Universitat Autònoma de Barcelona

Light-motion interaction in disordered nanostructures

Guillermo Arregui Bravo

ADVERTIMENT. L'accés als continguts d'aquesta tesi queda condicionat a l'acceptació de les condicions d'ús establertes per la següent llicència Creative Commons: http://cat.creativecommons.org/?page_id=184

ADVERTENCIA. El acceso a los contenidos de esta tesis queda condicionado a la aceptación de las condiciones de uso establecidas por la siguiente licencia Creative Commons: http://es.creativecommons.org/blog/licencias/

WARNING. The access to the contents of this doctoral thesis it is limited to the acceptance of the use conditions set by the following Creative Commons license: https://creativecommons.org/licenses/?lang=en

Doctoral Thesis

Light-motion interaction in disordered nanostructures

Guillermo Arregui Bravo

Under the supervision of:

Dr. Pedro David García Fernández
Prof. Clivia Marfa Sotomayor-Torres

A thesis submitted in fulfilment of the requirements for the degree of Doctor of Philosophy in the

Universitat Autònoma de Barcelona
Facultat de Ciències
Departament de Física

Photonic and Phononic Nanostructures Group

Institut Català de Nanociència i Nanotecnologia

2021

Abstract

The interaction of trapped light and motional degrees of freedom has recently emerged as one of the mechanisms enabling both fundamental research in mesoscopic quantum physics and high-performance microscale laboratory devices for practical applications such as sensing or optical signal processing. To do so, a solid theoretical and experimental understanding of the exploitable physics in (cavity) optomechanical systems has been achieved during the past two decades. Their dynamics can be reduced to a small set of governing parameters, the preferred setting for engineered solid-state classical and quantum devices. However, those parameters are usually determined by a fine-tuned combination of material properties and geometry, the control of which becomes extremely challenging in nanometer-scale device-like structures. It is well accepted that unavoidable fabrication imperfections impose severe limits on the achievable control over these parameters in state-of-the-art optomechanical systems. However, this role has so far not been analysed in depth. In this thesis, I study the role of this ubiquitous form of disorder in the optomechanical coupling at the nanoscale, both from a numerical and experimental perspectives.

Understanding and quantifying the effect of disorder in engineered cavity optomechanical systems is crucial to reduce its impact. Taking this approach, based on our propensity towards order and symmetry over anything else, eventually leads to the following conclusion: critical dimensions need to be controlled down to a few nanometers. If instead of considering disorder as a nuisance, we explore how to harness its potential, the conclusions are less obvious. In the field of photonics the role of multiple scattering in disordered dielectric structures has been largely studied, evidencing the particular role of disordered lattices, where the interplay between order and disorder offers an alternative route to strong light confinement, i.e., Anderson localization, a phenomenon well known for electrons in solid-state physics since the mid-1950s. In principle, the same wave-like multiple interference should happen for elastic waves, leading to tightly localized mechanical modes at similar wavelengths. However, direct observation of Anderson localization of phonons in the GHz range remains elusive, due to the lack of practical phonon transitions in the solid state and limited far-field radiation for read-out. Can these disorder-induced optical cavities be used to locally probe Anderson localization of GHz phonons via their optomechanical interaction? What is the likelihood to find spatially co-localized photons and phonons? Are these two waves equally sensitive to fabrication imperfection? Can we explore cavity optomechanical dynamical back-action in such a system? These scientific questions articulate this thesis.

Due to the limited control over the intrinsic dissipation channels of the mechanical resonator at room temperature, the quality factor of the optical modes and the level of co-localization are identified as the key parameters to statistically enable optomechanical interaction in disordered semiconductor nanostructures. The first requirement is achieved in slow-light photonic crystal waveguides. Using

evanescent fiber-taper coupling, we observe high-Q ($\sim 10^5$) optical Anderson localization in a novel silicon photonic crystal waveguide that simultaneously operates as a phononic waveguide. Trigger of non-linear material effects via the strongly confined light coherently self-modulates the random cavities, hindering the observation of optomechanical modulation. The inclusion of a sub-wavelength air slot along the waveguide core allows confinement in the narrow air region, preventing the rapid onset of material non-linearities while simultaneously increasing the achievable optomechanical coupling rate g_o. We observe optomechanical modulation of Anderson-localized optical modes in slotted photonic crystal waveguides at two frequency ranges: low-frequency in-plane mechanical modes spanning 100-500 MHz and high-frequency $\sim$ 7 GHz phonons. Optomechanically-induced amplification up to coherent self-sustained oscillations is evidenced at both frequency ends. At the 7 GHz band, the explored system constitutes a perfect platform to observe high-frequency phonon localization phenomena in cryogenic conditions.

These simultaneous slow-light and slow-sound two-dimensional photonic crystal waveguides however lack an a priori mechanism that guarantees a high degree of colocalization. In principle, the modes appear at uncorrelated positions due to their complex interference nature. To explore and understand this colocalization process, I proposed a way to address this challenge using periodic-on-average one-dimensional GaAs/AlAs Distributed Bragg Reflectors. A statistical enhancement of the vacuum optomechanical coupling rate, g_o, is found, making this system a promising candidate to explore Anderson localization of even higher frequency ($\sim$ 20 GHz) phonons using ultra-fast pump-probe coherent phonon spectroscopy. I have employed this experimental technique to all-optically probe a spacer-less phononic nanocavity created by concatenating two perfectly periodic multilayers, i.e., a 0D topological state, a testbed to understand the most basic implications of bulk topology on interfaces.

Last, I apply my knowledge and understanding of disordered waveguide nanostructures to explore propagating topological interface states and quantify their potential for robust backscattering-free photon transport at the nanoscale, a premise for compact and efficient circuit and cavity optomechanics based on topological edge states.

Acknowledgements

When I started my PhD at the end of 2016 all I really knew about optics was that they obey Maxwell's equations, and even these were quite obscure to me. Needless to say then, I had no idea what things such as Anderson localization meant. Four years later, after a lot of work and emotions, I find myself writing these lines and wondering how I actually got here. Luckily, *how I got here* has names and surnames and it is therefore the goal of these lines to thank all those that were by my side along the way.

First of all, I want to thank my supervisor David. He took me in when I first arrived as clueless as a civil engineer can be for a PhD in physics. He understood that the path from km-scale bridges to nano-bridges is shorter than one would think. I really value that you prioritized my willing to learn over a specific background. I thank you for your trust and understanding since I am aware that I am not always easy to deal with. I also thank you for the choice of the thesis subject: intelectually enriching, prospective and innovative, while sufficiently down-to-earth to produce steady results. I do think that disorder will always remain, to my will or not, part of my mindset as a scientist. I also thank Clivia for the opportunity and challenge she gave me by joining her group. I think I am not alone in saying that your vision is an integral part of the group's DNA. I am grateful for the freedom you gave me and the rest to get involved in many different research lines and to get hands-on experience with multiple equipment. I will always be in debt with you for the variety of skills I have acquired and that will definately help me in my future career.

Most projects, scientific or not, are succesfull whenever they build upon the brains and souls of many people. The accomplishment of the results here presented are no exception and I therefore want to thank all of the P2N group for their invaluable help. A special mention for Dani and Martin, with who I shared hours and hours in the lab. Dani, it has been insightfull to see you working in the lab with passion and attention to detail, only adding new bricks of knowledge when the foundations are well settled. I owe you that. Mano, I will miss your company and our endless conversations about the details of the experiments and simulations we were doing. I am glad that we shared most of the way. To Jordi, who always found some time within his own constant stress. Sometimes two or three kind words are the most rewarding of prizes. To Omar, Francisco, Juliana, San Emigdio, Alex, Jeremie, Peng and Ryan for making life at ICN2 feel like home.

This thesis would have not been possible without the high quality samples measured. I thank Daniel Lanzillotti and part of his team at CN2, Martin and Omar, for that and for overall contributing to a considerable part of this work.

I also thank Søren Stobbe and Marcus from DTU Fotonik, whose samples completely changed the path my thesis was taking. For those samples and the ones to come.

El camino que me trae hasta aquí tampoco lo he hecho sólo en lo personal. Quiero agradecer a mi familia, a los que estan y a los que ya no estan, su constante apoyo y cuidado, su capacidad para aguantar mi humor cambiante, especialmente durante este último año. También quiero acordarme de aquellos que estan cerca y te animan sin apenas darse cuenta. A los salchichas, un pilar desde tiempos que ya ni recuerdo.

Et en dernier, je te remercie Claire pour ne jamais me laisser tomber, pour mettre un peu d'ordre dans ce désordre. Si j'écris cette dernière phrase avec un sourire c'est, surtout, grâces à toi.

List of Publications

Publications arising from the research in this thesis

Part of the work presented in this thesis has been published or accepted in peer-reviewed journals during the course of these four years. These are:

- *Optomechanical coupling in the Anderson-localization regime*, P. D. García, R. Bericat-Vadell, G. Arregui, D. Navarro-Urrios, M. F. Colombano, F. Alzina and C. M. Sotomayor-Torres, Physical Review B, **95**, 115129 (2017).
- *All-optical radio-frequency modulation of Anderson-localized modes*, G. Arregui, D. Navarro-Urrios, N. Kehagias, C. M. Sotomayor-Torres and P. D. García, Physical Review B, **98**, 180202(R) (2018).
- *Anderson Photon-Phonon Colocalization in Certain Random Superlattices*, G. Arregui, N. D. Lanzillotti-Kimura, C. M. Sotomayor-Torres and P. D. García, Physical Review Letters, **122**, 043903 (2019).
- *Coherent generation and detection of acoustic phonons in topological nanocavities*, G. Arregui, O. Ortíz, M. Esmann, C. M. Sotomayor-Torres, C. Gomez-Carbonell, O. Mauguin, B. Perrin, A. Lemaître, P. D. García and N. D. Lanzillotti-Kimura, APL Photonics, **4**, 030805 (2019).
- *Quantifying the robustness of topological slow light*, G. Arregui, J. Gomis-Bresco, C. M. Sotomayor-Torres and P. D. García, Physical Review Letters, **126**, 027403 (2021).

Other publications

I have also contributed substantially to other cavity optomechanics experiments performed within the group, which have led to the following publications:

- *Optical modulation of coherent phonon emission in optomechanical cavities.*, J. Maire, G. Arregui, N. E. Capuj, M. F. Colombano, A. Griol, A. Martínez, C. M. Sotomayor-Torres and D. Navarro-Urrios, APL Photonics, **3**, 126102 (2018).
- *Synchronization of optomechanical nanobeams by mechanical interaction*, M. F. Colombano[1], G. Arregui[1], N. E. Capuj, A. Pitanti, J. Maire, A. Griol,

[1] Equal contribution.

B. Garrido, A. Martínez, C. M. Sotomayor-Torres and D. Navarro-Urrios, Physical Review Letters, **123**, 017402 (2019).

- *Ferromagnetic Resonance Assisted Optomechanical Magnetometer*, M. F. Colombano, G. Arregui, F. Bonell, N. E. Capuj, E. Chávez-Angel, A. Pitanti, S. O. Valenzuela, C. M. Sotomayor-Torres, D. Navarro-Urrios and M. V. Costache, Physical Review Letters, **125**, 147201 (2020).
- *Injection locking in an optomechanical coherent phonon source*, G. Arregui, M. F. Colombano, J. Maire, A. Pitanti, N. E. Capuj, A. Griol, A. Martínez, C. M. Sotomayor-Torres and D. Navarro-Urrios, Nanophotonics 1 (ahead-of-print)

Contents

List of Figures

List of Abbreviations

ASOPS	**As**ynchronous **O**ptical **S**ampling
BZ	**B**rillouin **Z**one
DBR	**D**istributed **B**ragg **R**eflector
DMS	**D**ensity of **M**echanical **S**tates
DOS	**D**ensity of **O**ptical **S**tates
ESA	**E**lectronic **S**pectrum **A**nalyzer
FCA	**F**ree **C**arrier **A**bsorption
FCD	**F**ree **C**arrier **D**ispersion
FDT	**F**luctuation **D**issipation **T**heorem
FEM	**F**inite **E**lement **M**ethod
FFT	**F**ast-**F**ourier-**T**ransform
FP	**F**abry-**P**érot
FSR	**F**ree **S**pectral **R**ange
GME	**G**uided-**M**ode-**E**xpansion
IBZ	**I**rreducible **B**rillouin **Z**one
MBE	**M**olecular **B**eam **E**pitaxy
OM	**O**pto**m**echanics / **O**pto**m**echanical
OMC	**O**pto**m**echanical **C**rystal
PhBG	**P**hotonic **B**and **G**gap
PhC	**P**hotonic **C**rystal
PhCW	**P**hotonic **C**rystal **W**aveguide
PML	**P**erfectly **M**atched **L**ayer
PnBG	**P**hononic **B**and **G**gap
PnC	**P**hononic **C**rystal
PnCW	**P**hononic **C**rystal **W**aveguide
QNM	**Q**uasi-**N**ormal **M**ode
RF	**R**adio**f**requency
SEM	**S**canning **E**lectron **M**icroscopy
SL	**S**uper**l**attice
SP	**S**elf-**p**ulsing
TIR	**T**otal **I**nternal **R**eflection
TO	**T**hermo-**o**ptic
TPA	**T**wo**P**hoton **A**bsorption
WGM	**W**hispering **G**allery **M**ode
ZC	**Z**one-**C**enter
ZE	**Z**one-**E**dge

Chapter 1

Motivation and introduction

The role that symmetry and order play on the underlying structure of nature has fascinated the human mind since the Greeks, to the point that science operates on the fundamental assumption that nature is ordered and that symmetries determine its dynamical laws. However, the role of complexity in understanding the world around us does not escape us either. Entropy, one of the foundations of thermodynamics and statistical physics, is often understood, at least under particular circumstances, as a measure of the level of disorder in a physical system. Going beyond the simplicity of regular systems and accepting this inherent complexity of nature has been crucial in the last century physics.

In particular, the history of condensed matter physics gives us a clear example. Before 1958 solid-state physicists were convinced that the effect of disorder in crystals could be treated by considering electrons as point-like particles suffering random scattering events with a characteristic length-scale denoted as the mean free path ℓ. A stronger scattering could always be cast into a smaller ℓ. Building on this simple picture, electronic transport in the presence of defects can be described as a Brownian motion with a drift velocity and macroscopically manifests itself as the well-known Ohm's law. Lack of experimental evidence suggesting the necessity for a more fundamental treatment of scattering from lattice defects was probably the main reason for that simple description. Faced with anomalously long relaxation times of electron spins in doped semiconductors [1] that he thought could be explained by localized electrons, Phillip Warren Anderson decided to account for the quantum wave nature of the electron in a disordered lattice. In a seminal paper [2] he proposed that strong enough scattering can halt the classical diffusive motion of the electron, whose wave function becomes exponentially localized. As the mean free path becomes smaller and smaller by larger disorder it encounters another fundamental length scale: the electronic wavelength, beyond which wave effects cannot be ignored anymore. This effect was later understood to arise from the localization of the system eigenstates [3], prompting intense mathematics research on the spectral properties of random operators [4]. These ideas completely revolutionized the understanding of physics back in the 60s. As put by Anderson himself during his Nobel Prize speech (1977): "Localization was a different matter" [5]. Far from being the most mathematically rigorous paper in theoretical solid-state physics, what was *different* and supposed a profound

breakthrough was his choice of treating disorder not as the exception, but as the rule. We now know that the localization of the electron wave function is actually not limited to perturbed lattices but to generic random potentials and, ultimately, the theory of bands –periodicity, order- and the theory of localization –disorder- need to be considered in an equal footing [6] to understand why some materials conduct electricity and why others do not.

The profound effect of complexity that emanates from Anderson's ideas has strongly permeated physics, generating strong research efforts on the behaviour of disordered systems [7] in fields such as solid-state physics, biophysics, optics or acoustics. In particular, as localization is essentially a wave-interference phenomenon, it should be universal to all wave-systems [8], generating a long-lasting quest for Anderson localization in a large variety of *classical* waves such as water waves [9], light [10] or sound [11]. The non-interacting and time-invariant nature of Anderson's model to predict electron localization were proving too stringent simplifications for an unambiguous experimental confirmation and classical waves offered a promising platform for the observation of localization in its *pure* form. Manipulating and controlling excitations whose wavelengths are of the order of millimeters or micrometers instead of nanometers as well as the occurrence of interference effects without the need of low-temperature operation were some of the advantages offered by classical waves. Experimental attempts to observe Anderson localization have often relied on the analysis of transport parameters [12–14], an approach that strongly relates to Anderson's first description of the phenomenon. The fingerprint of the localization regime in transport measurements is the exponential, rather than linear, fall of transmission with system size. However, classical waves suffer from artifacts like absorption, that also show up as an exponential decay [15]. Fortunately, classical waves often offer the possibility to measure other observables than conduction, specially in the case of photons. One can look at the relative size of the fluctuations in different transport parameters, an approach first proposed in the microwave domain [16]. In optics, the far-field emission of excellent point sources, i.e., quantum emitters, allows direct access to the statistics of Anderson localization and to spatially resolve localized fields [17]. For elastic waves, experiments have been so far restricted to ultrasound [11,18] while the direct observation of localization at higher frequencies with explicit inspection of the individual localized wave fields simultaneously in the spatial and spectral domain remains elusive. The lack of practical phonon transitions in the solid state, the limited number of commercially available high frequency coherent phonon sources and their limited far-field radiation complicate the read-out and prevent the analogy to optics.

Optics and acoustics constitute two pillars of modern scientific knowledge and are the two disicplines, along with electronics, that have had a stronger influence in the advent of the chip-based technological era. They have been explored separately since *time immemorial* but have happened to find common grounds during the last century. Brillouin's predictions of diffraction of light by an acoustic wave in 1922 [19] was the departure line of acousto-optics, a field that has recently received huge attention due to the fast developments in cavity optomechanics [20]. Among the most commonly used optomechanical (OM) systems

figure optomechanical crystals [21] (OMCs), precisely fabricated nanometer-scale devices used to efficiently interface light with the mechanical vibrations of matter at the nanoscale. They constitute a clear example where order and spatial symmetries are crucial for current functionalities and often used at an early design stage. Fabrication imperfections, that impose severe performance limits by increasing the energy dissipation of the optical and mechanical elements [22], are seen as a nuisance. We propose this form of ubiquitous disorder as a tool to simultaneously localize both the electromagnetic and acoustic fields by Anderson localization of photons and phonons in nanostructured media, offering an alternative route to precisely designed confining potentials that is, by the nature of its construction, imune to disorder. In particular, the interplay of order and disorder in dielectric/acoustic perturbed lattices provides an ideal platform for studying strong localization effects, as was early predicted by S. John [23] for photonic crystals. Since disorder localizes both fields, the confined optical modes can interact with the localized mechanical motion via the same mechanisms as in standard engineered cavity OM systems [24]. Simultaneous localization of photons and phonons via randomness may have limited practical applications for tasks requiring small foot-print, highly engineered cavity OM systems, but light-localization can be used as a fundamental local probe to observe Anderson localization of high frequency mechanical vibrations, circumventing the aforementioned issues so far encountered for phonons. The main objective of the research reported here is to identify the limiting factors encountered with this approach and to assess, both numerically and experimentally, the convenience of different optomechanical platforms to overcome them. In the context of OM cavity arrays, site-to-site disorder and its effects on the OM building blocks can also lead to Anderson localization of hybrid photon-phonon excitations [25]. The question of what role does disorder play for photons and phonons that are allowed to interact in nanoscale structures has therefore become relevant.

Understanding the effect complexity has in nanoscale photonics and phononics and their possible interactions seems even more crucial in a scientific landscape that is now strongly influenced by the concepts of topology coming from fermions in condensed matter physics. At the heart of this growing interest is the possibility of opening dissipationless information channels by providing robust backscattering-free topological waveguides. Nearly every paper on topological bosonics published during the last years claims robust topological edge states, but few describe the role of unavoidable fabrication disorder on the allowed propagation lengths. It is therefore necessary to study the supposed robustness using the concepts of coherent backscattering and localization, where the interplay between the properties of the ordered system, the density of states, and the type and amount of randomness is a key factor to determine the backscattering length ξ, the average ballistic propagation length. In particular, this length-scale strongly depends on the group index n_g, the slow-down factor of the propagating wave. These two figures of merit, ξ and n_g should be taken into account to obtain a quantitative assesment of any particular protection mechanism in the propagation equation due to topology.

In this thesis, I discuss the general role of disorder in OM systems and

explore key aspects that could enable the observation of Anderson phonon localization at frequencies where direct observation of the wave fields is otherwise ellusive. The thesis starts with two background chapters (Chapters 2 and 3) that provide an extensive introduction to the field of cavity optomechanics and its development in nanostructures. Both are ended with a brief section that underlines the concepts exposed that are required for a proper understanding of the numerical and experimental results later described on Chapters 4 and 5, the core results of this doctoral thesis. Chapter 6 is used to provide conclusions to this thesis, to explain how it contributes to the different fields involved and to give an overview of possible future research. In particular, we build upon the knowledge gained earlier in this work to assess the robustness of topological edge states to backscattering, one of the typically assumed properties granted by topology. The contents of the individual chapters are given below.

- In **Chapter 2** the fundamentals of cavity OM systems in the very generic system of a Fabry-Pérot cavity with a movable end mirror are introducted. This particular setting is introduced via a historical perspective on radiation-pressure interaction of light and matter, going from point-like particles (atoms) to gram-scale mirrors. The hamiltonian of such a system is described and the governing equations for the optical and mechanical resonators derived. The basic physical effects induced by dynamical back-action of the light field on the mechanical resonator are explained, with special emphasis on optomechanically-induced coherent amplification and lasing. The strongly-driven non-linear dynamical response of an optical cavity via intrinsic material non-linearities is also given, as well as how to couple it to the mechanical degree of freedom via radiation-pressure in order to produce mechanical lasing at low frequencies.

- In **Chapter 3** a clear and detailed introduction to the properties of light and motion propagation in periodic lattices, i.e. photonic and/or phononic crystals, is provided. The traditional notions of band gaps and localization via point and smooth defects are described, but special attention is set to the role of distributed defects in the form of geometrical disorder, providing the tools to understand the interplay of order and disorder in the occurrence of Anderson localization in such structures. Last, the coupling mechanisms in standard semiconductor nanostructures are described and the way to compute an OM coupling rate g_o from first order perturbation theory.

- In **Chapter 4** the interaction of photons and phonons in purely one-dimensional structures based on GaAs/AlAs multilayers is presented and discussed. I analyze the particular role of the photon/phonon co-localization occuring with such specific material choice on g_o, an enabling aspect for their interaction in the Anderson-localization regime. Due to their lack of confiment in the in-plane direction, multilayers are less-suited for OM measurements based on brownian motion. We introduce all-optical ultra-fast pump probe coherent phonon spectroscopy as an alternative spectroscopic technique. Selection rules for generation and detection of coherent phonons via light are explored and their relation to g_o analyzed. These rules are finally used to conceive and

perform an experiment that demonstrates a topological phononic nanocavity and the band inversion underlying it.

- In **Chapter 5** OM effects in dual photonic/phononic crystal waveguides subject to unintentional fabrication imperfection are explored. Two dimensional numerical simulations and experimental data provide conclusive evidence of strong photon localization in both standard and slotted photonic crystal waveguides, ultimately leading to non-linear behaviour. For the latter, OM coupling to extended low-frequency and high-frequency guided modes is experimentally observed with Anderson-localized optical modes, a milestone observation in this thesis. Finally, dynamical-backaction induced phonon lasing is experimentally achieved in both frequency ranges. This chapter comprises the most relevant results of the thesis towards anwering the questions initially set.
- In **Chapter 6** the main results presented in the thesis are reviewed and a perspective on future research is provided. In particular, recent numerical results on the role of topological phases and the bulk-edge correspondance are discussed as a means to produce guided edge states that are immune to backscattering. The backscattering mean-free path ξ and the group-velocity n_g are presented as the key parameters for wave-transport in the presence of disorder to compare the robustness of different topological edge states. A comparison with conventional edge states is also provided.

Chapter 2

Fundamentals of cavity optomechanics

The field of cavity optomechanics studies the interaction of light confined inside an optical cavity with the mechanical degrees of freedom of the structure supporting it. A myriad of coupling mechanisms have been explored in the last two decades, howevever, most of the physical implementations and the observed phenomena can be explained with a simple model: a Fabry-Pérot interferometer with a movable end mirror, the latter being attached with a spring to a fixed support. In this chapter, we describe the basic theory of cavity optomechanical (OM) systems that is required for the understanding of the chapters to follow, based on this well-known toy model. Even though the results in this thesis belong to the realm of classical physics, a more general description starting from the quantum equations of motion is given for the sake of completeness. The classical description is simply derived from the quantum version by taking the expectation value of the operators in play. After a brief historical perspective on the role of radiative light forces on motional degrees of freedom of matter, the basic OM system and its Hamiltonian are derived. The equations of motion for the driven optical and mechanical resonators naturally emerge from such a description. The different physical phenomena that arise from the set of differential equations is then described, with special emphasis on mechanical mode amplification. An incursion into the non-linear behaviour of strongly driven optical cavities is made, with the goal of describing another type of self-sustained oscillation reported in this thesis. Finally, a description of optical transduction of the (thermal) motion of the mechanical oscillator is given. The chapter is finished with a brief summary describing how the concepts herein relate to the results given in Chapters 4 and 5.

2.1 The effect of light on mechanical objects and viceversa

The idea that electromagnetic radiation exerts pressure on objects dates back to the early days of the scientific revolution in the 17$^{\text{th}}$ century, when Kepler observed that the tail of comets always point away from the sun [26]. Far from being aware that electromagnetic radiation carries momentum, and even from the notion of momentum itself, his interpretation in terms of a force exerted by sunlight was foundational. Around 250 years were necessary for setting the theoretical grounds of Kepler's intuition. In 1873, Maxwell described how light, as a form of electromagnetic radiation, has the property of momentum and thus exerts a pressure upon any surface it encounters [27], i.e., radiation pressure, and he derived a closed-formula for it. Radiation-pressure effects had largely been explored experimentally during the century [28–30], however observations in agreement with Maxwell's predictions remained ellusive until the early 20$^{\text{th}}$ century, namely due to the relative strength of the induced force compared to other effects in the studied systems. Indeed, if one imagines a mirror upon which a photon impinges (Figure 2.1(a)), conservation of momentum dictactes that the sum of momentum vectors after reflection/absorption must be equal to the momentum of the incoming photon. Particle-wave duality and De Broglie's hypothesis [31] impose the momentum p of the photon of wavelength λ to be

$$p = \frac{\lambda}{h} \tag{2.1}$$

where h is Planck's constant. In terms of wavenumber $k = \frac{2\pi}{\lambda}$ the momentum of each photon obeys the well-known relation $p = \hbar k$ where we use the reduced Planck's constant $\hbar$. Reflection upon the mirror implies a momentum transfer of $\Delta p = 2\hbar k$, i.e., $\Delta p = 1.25{\cdot}10^{-27}$ kg·m/s for a green photon ($\lambda = 532$ nm), which is a tiny number for most of electromagnetic radiation. Observing this momentum transfer or the force that results when an incoherent light source is used, e.g. a light bulb or an halogen lamp, requires extreme precision measurement and disentangling the effect from the action of other forces, in particular those mediated by the residual gases surrounding the body in study. This resulted in famous and controversial experiments, like the Crookes radiometer experiment [32], where optical momentum was said to make a vane spin. The vane did spin, but Maxwell was not the one pushing. The radiometer was actually spinning in the opposite direction to what is expected from radiation pressure and it was even shown later that spinning of the vanes halted for even lower vacuum levels than the ones Crookes could achieve. Constructing upon the ideas of Crookes, more sophisticated experimental set-ups and thorough consideration of the ubiquitous residual gases allowed the russian scientist Lebedew [33] and americans Nichols and Hull [34] to observe true radiation-pressure effects, the latter with such an accuracy that no subsequent physicists reproduced their experiments.

With Nichols and Hull experiment as a starting point and with the advent of the laser in the 70s, a new era in the study of light-matter interaction started.

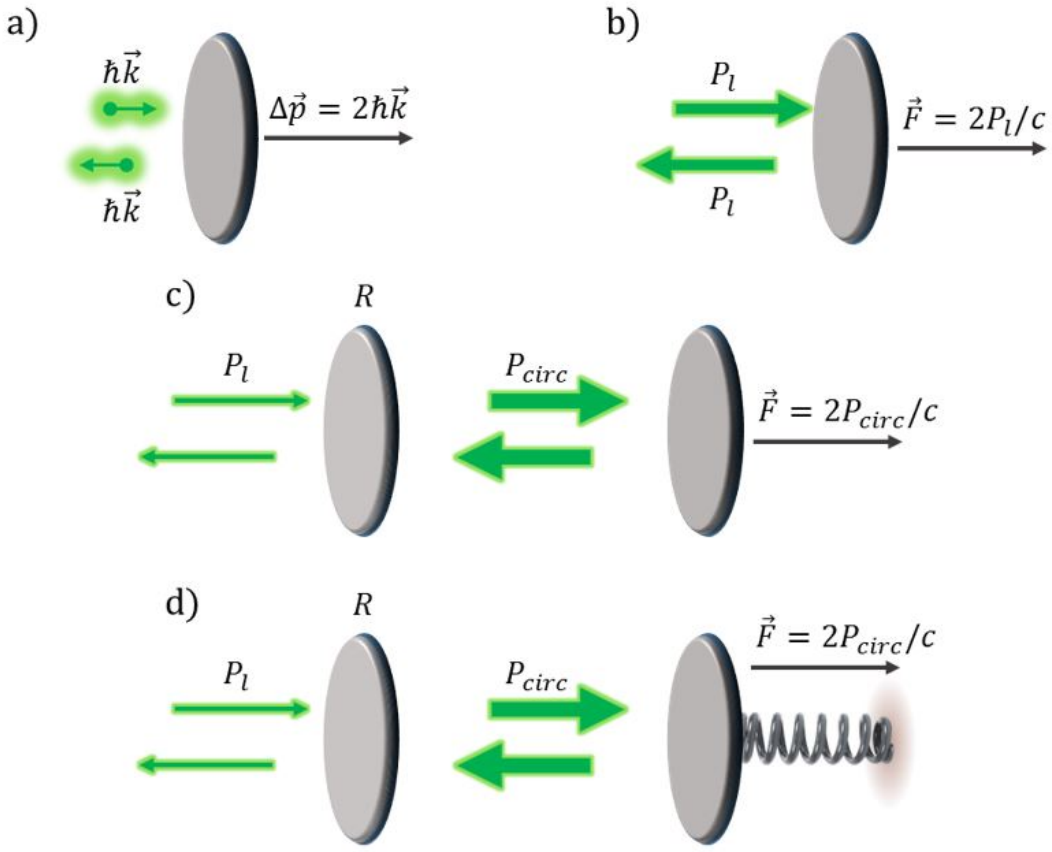

Figure 2.1: Radiation pressure force: a route towards a tangible interaction in macroscopic systems. (a) Conservation of momentum of the system composed by the photon and the mirror where it is reflected fixes the momentum transfer. This instantaneous momentum transfer puts the mirror into motion with a negligible velocity. (b) The use of a coherent laser source of power P_l generates a net force upon the mirror, resulting from the *continuous* photon arrival rate. This force is still very small in most situations. A possible path towards increased radiation pressure is enclosing the light in a partially open cavity (c), where the circulating power is much larger than the input power. Finally, (d) the movable mirror is held in place via a suspension or a spring.

If instead of a single photon travelling towards a mirror, a coherent light beam with a photon rate $|a_{in}|^2 = N_l/\Delta t$ and a frequency ω_ℓ is used for illumination (Figure 2.1(b)), the radiation pressure force reads

$$F_{RP} = \frac{\Delta p}{\Delta t} = \frac{2\hbar k N_l}{\Delta t} = \frac{2kP_l}{\omega_l} = \frac{2P_l}{c} \tag{2.2}$$

with c the speed of light. This is still a tiny force for everyday objects, e.g.1 W of laser power exerts a force of 6.7 nN, but can be readily used to manipulate the motional degrees of freedom of very lightweight objects such as atoms, ions or molecules, where the force is mediated by absorption. The quest for better spectroscopic measurements of atomic lines and for readily available physical systems to study quantum-optical phenomena led to important research efforts

in using radiative light forces to cool down the heat-induced random motion of atoms. The simultaneous works of Hänsch and Schawlow [35] and Wineland and Dehmelt [36] concerning laser cooling, followed by proposals from Ashkin [37] and Chu [38] to trap the aforementioned atoms using optical dipole forces, set the ground for a revolution in atomic physics, with radiative forces used to manipulate atoms to form exotic states of matter, such as Bose-Einstein condensates [39], superfluidity [40] and optical lattices [41], or to generate our most accurate clocks. With the increasingly lower temperatures achieved, the necessity of using quantum mechanics to understand both the motion of trapped particles and the limits in temperature [42] became evident. Refined excitation schemes of the atomic clouds taking into account the quantum nature of the object allowed even lower temperatures down to the quantum ground state [43], where further manipulation allows generation of intricate quantum states such as superposition [44] or entangled states [45,46].

The question of how big, in terms of mass, can we make the system to be cooled down, eventually to its zero-energy state, follows naturally seeing the tremendous accomplishments of atomic physics during the end of the 20^{th} century. From a fundamental perspective, ground-state cooling of massive resonators could help in studying the quantum-classical boundary and the decoherence mechanisms that define it. Generating superposition or entangled states of mechanical motion at a mass scale where gravity is non-negligible could allow the observation of gravitation-induced spontaneous quantum state reduction [47], a milestone towards a unfied theory in physics. The radiation-pressure force exerted by a laser beam upon a macroscopic mirror is well described by Equation (2.2). It is obvious that for massive objects the effect on velocity is, most of the time, negligible, unless photons can be recycled. An effective way of recycling photons starting from Fig. 2.1(b) is by using a second mirror prior to the object of study, i.e., photons travel in an optical cavity. In it, a resonant photon makes multiple round-trips before being lost either via leakage or absorption, making the built-up circulating optical power much larger than the input power driving the cavity (Fig. 2.1(c)). This increases the radiation pressure force acting on the mirrors. For the particular case of a partially transparent input mirror of reflectivity R at a distance L of the studied mirror, the internal enhancement the resonator provides to the light launched into it scales as $1/(1-\sqrt{R})^2$ and therefore the radiation pressure force can be given by

$$F_{RP} = \frac{\Delta p}{\Delta t} = \frac{2P_{circ}}{c} = \frac{2P_l}{c(1-\sqrt{R})^2} \tag{2.3}$$

where the effect of using an optical cavity is evident as compared to Equation (2.2). If the circulating power P_{circ} is written in terms of the cavity photons n_c and the round-trip time $\tau_{rt} = 2L/c$, the formula can be also written as

$$F_{RP} = \frac{2P_{circ}}{c} = \frac{2n_c\hbar\omega_c}{\tau_{rt}c} = \frac{n_c\hbar\omega_c}{L} \equiv \hbar G n_c \tag{2.4}$$

where we have introduced the OM coupling rate $G \equiv \omega_c/L$, the radiation-pressure force of a single cavity photon. We will see on Section 2.2 that this parameter

also represents the frequency shift induced by a unitary mechanical displacement of the mirror.

When such an optical feedback system is used to increase radiation pressure, effective action can be achieved on more massive objects. The most striking in this quest to understand how to manipulate objects of increasing mass is that most of the theoretical foundations were set by people working with objects at the other end of the size spectrum and for who that specific light-matter interaction was more of an impediment than a goal itself. In order to detect space-time oscillations generated by gravitational waves (with strain levels on the order of 10^{-21} [48]), gravitational astronomers conceived kilometer-scale laser-driven interferometers with pendulum-like mirrors to avoid spurious environmental noise. The building block of these interferometers is therefore equivalent to the one depicted in Fig. 2.1(d), a Fabry-Pérot (FP) resonator with an end mirror attached to a spring, and experimentalists were soon confronted with the fact that radiation pressure exerted by the high power laser on the massive interferometer mirrors led to displacements higher than the wobbles they were seeking to mesure, overwhelming the signal. Braginsky's group pioneered the development of a theory of OM interactions in such a system. The physics that derive from such an interaction turned out to be extremely rich. While the cavity photons put the mirror in motion, the subsequent displacement of the mirror changes the length of the cavity and therefore the resonance condition. The driving laser finds itself detuned from respect to the cavity, producing a change of the intracavity photon number, which again changes the radiation-pressure force. This closed loop and the retarded nature of the force change due to the finite lifetime of the cavity photons generates a broad collection of physical phenomena, in particular the control over the mechanical oscillator [20]. Both optically-induced changes in the stiffness and the viscous damping of the mechanical oscillator dynamics were evidenced during the early days [49]. Control over the dissipation rate was soon envisioned as a means to amplify -up to the self-sustained level- or cool -down to the ground-state- the motion of the mechanical oscillator [50]. Within the framework provided by the developed theory, Braginsky adressed the question of how accurate can we measure the mechanical resonator position using light, going down to the fundamental limits imposed by quantum fluctuations of radiation pressure in what is called quantum backaction [51]. His measurement theory approach to the problem allowed to conceive optimal driving strategies for the detection of gravitational waves, finally observed by the LIGO collaboration in September 2015 [52].

The developments of Braginsky soon reached the quantum optics community, initiating a lasting research on possible quantum effects in these systems. These efforts were initially focused on controlling the quantum properties of the light field via the mechanical resonator [53,54], but very soon the quantum behaviour of the motional degree of freedom itself was explored. Generation of non-classical states of motion with one or more mechanical resonators such as supersposition [55] or entangled [56] states are only some examples of the physics that were studied at the time. However, most of the ideas remained as theoretical proposals for many years. The observation of quantum effects in these systems is

a great experimental challenge. The first reason is simply because the interaction strength G discussed above is generally weak, even inside an optical cavity. More fundamentally, this is due to the natural scale of the displacements involved in quantum motion, given by the zero point fluctuations $x_{zpf} = \sqrt{\hbar/2m\Omega_m}$, where m is the mechanical oscillator's mass and Ω_m its frequency. Due to the masses involved and to the impossibility to tailor Ω_m at will, x_{ZPF} of a spring-attached mirror is many orders of magnitude smaller than for trapped atoms, requiring extreme displacement sensitivity that can only recently be achieved [22,57–59]. Even when control over Ω_m constitutes a possible path to increase x_{ZPF}, this may worsen the role of thermal noise -how the energy scale k_BT compares to the quantum of energy $\hbar\Omega_m$- to levels that mask quantum effects, even at the lowest attainable temperatures in closed-cycle cryogenic environments.

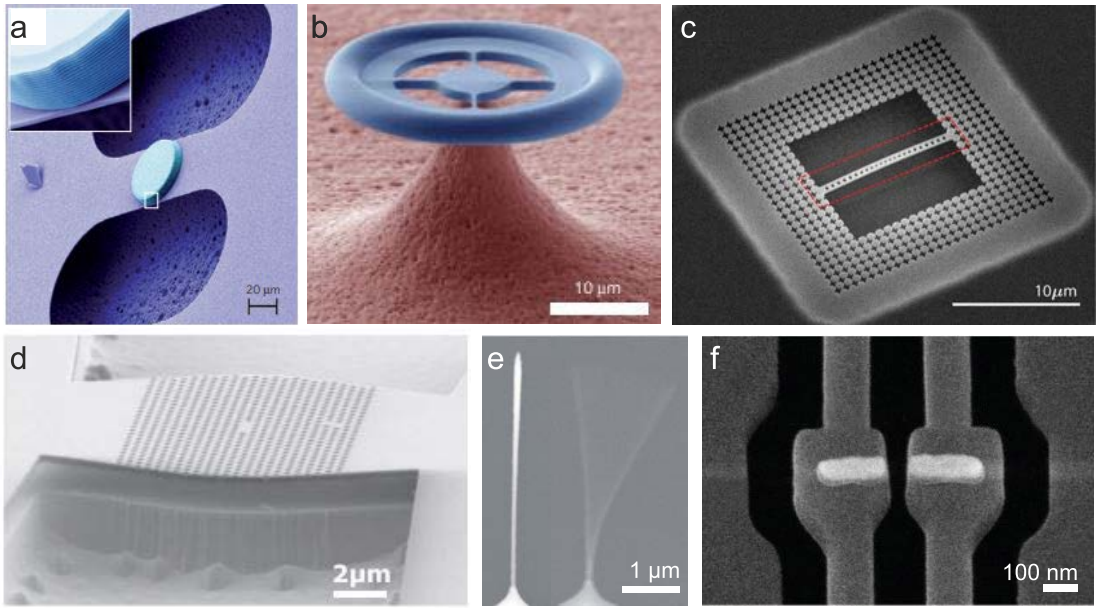

Figure 2.2: Micro and nanometer-scaled optomechanical (OM) systems. (a) Suspended high-reflectivity micromechanical system in a Fabry-Perót (FP) OM system [60] (b) Whispering gallery modes (WGMs) along the rim of a microtoroid couple to radial mechanical modes of the structure supported via a thin pedestal [61]. (c) One dimensional [62] and (d) two dimensional [63] suspended photonic crystals couple diffraction-limited optical photons to extended and localized mechanical motion. (e) A nanoresonator embedded in the middle of an optical cavity couples to the cavity light field and enables mapping of the full cavity. (f) Plasmonic resonators exhibit much lower quality factors but extreme nanoscale light confinement, allowing values of the coupling rate g_o hard to attain with dielectrics [64].

It comes as no surprise that the community pushed towards the miniaturization of both the mechanical element (lower m) and the optical cavity (increasing G). Despite the difficulty in fabricating FP resonators below the mm-scale, the breakthroughs in advanced micro-nanofabrication starting at the end of the century supposed a true revolution for the field of quantum optomechanics (OM). Instead of using an end-mirror configuration where the displacement in play is the

center-of-mass displacement of a test mass, increasing interest was put in mechanical motion resulting from relative atomic motion. In contrast to point-like atoms where the *external* degrees of freedom have a free-particle behaviour in the absence of other forces (like the force induced by the trapping potential), the natural motion of more massive objects results from collective motional degrees of freedom of ensembles of atoms, i.e., phonons, whose complex motion naturally evolves in time like a harmonic oscillator, at least at small displacements [65]. Control of solid-state matter at the sub-micrometer scale allowed the development of novel OM systems in which both the optical cavity and the mechanical resonator properties and their coupling can be tailored with great flexibility. The most natural micro-scale version of the system in Fig.2.1(d) is that of a microcavity where the suspended mirror is replaced by a highly-reflecting micromechanical device like a membrane or a cantilever (Fig. 2.2(a)) with naturally-occurring flexural mechanical modes. However, the first micron-sized OM systems employed were based on axi-symmetric structures such as microspheres, microdisks or microtoroidal resonators, as the one reported in Fig. 2.2(b). In these, light is confined via total internal reflection along the circular rim of the resonator, in the so-called whispering gallery modes (WGMs) [66]. These micrometric devices are obviously free to move and one of its natural mechanical displacements are radial-like breathing motion. In an analogous way to what was described for the FP resonator in Fig.2.1(d), the light field bouncing on the boundaries of the resonator exerts a radiation pressure force that drives this motion, while a change in the radius R of the structure changes the optical path length and therefore changes the optical resonance condition, leading to the same type of bidirectional OM coupling. Early experiments with this type of system also revelead the necessity to take into account another type of coupling mechanism beyond radiation pressure [67]. When the microresonator experiences a breathing-like motion, microscopic strain fields are both present in the radial and the azimuthal direction, which generates distortion of the host lattice and changes its refractive index. This effect, called photoelasticity, also alters the optical path of resonant light, dispersively coupling the optical resonator to the mechanical degree of freedom. The reverse process, the generation of strain fields via light, electrostriction, plays the role of radiation pressure and again produces bidirectional OM coupling. For optical microresonators, radiation pressure coupling still dominates over photoelastic coupling. The coupling rate G that were achieved were high enough to allow the observation of the parametric instability predicted by Braginsky [68] and radiation-pressure cavity cooling [69] in just one year.

These seminal experiments paved the way to a myriad of new physical implementations of the OM coupling mechanism [20], among which photonic crystal cavities play a major role. Chapter 3 will provide an in-depth description of OM systems based on photonic crystals, but it is worth noting here their role from a historical perspective. Photonic crystals are periodic dielectric lattices which result in the generation of optical bands with dispersions far more rich than those happening in a homogeneous material, eventually leading to the creation of band gaps where the total absence of density of states prevents light propagation, in analogy to electron waves in a crystal lattice [70]. The inclusion of an artifical defect in the lattice results in a localized electromagnetic mode that cannot decay

into the continuum due to the presence of the band gap. The photonic holy grail, a cavity in a three-dimensional photonic crystal at optical wavelengths, has however remained ellusive due to the difficulty of fabricating these structures at optical scales. To ensure 3D confinement and operate at optical wavelengths the typical approach has been to employ periodic structures in one or two directions and total internal reflection in the remaining. Photonic crystal slabs [71] or photonic crystal wires, two and one-dimensional photonic crystals etched into thin semiconductor slabs or wires are playground structures for applications in photonics [72]. A cavity is formed in such a system by introducing a defect in the underlying periodic lattice, regardless of the number of dimensions where Bragg reflection is employed. Underetching of a photonic crystal cavity results in the formation of nanomechanical membranes or beams, while maintaining light confinement due to total internal reflection with the new air substrate. Their mechanical motion produces both displacement of the boundaries and strain fields, i.e., it leads to dispersive OM coupling between the mechanical modes of the structure and the cavity photons. The possibility to engineer the cavity dimensions down to sizes of the order of the wavelength combined with the use of low-mass mechanical resonators produces OM coupling strengths that are much larger than in FP systems or WGMs [21]. In addition, the spatial dielectric modulation is inevitably accompanied with a modulation of the acoustic properties like the density and the elastic constants. A photonic crystal is generally also a phononic crystal, where the same confinement strategies are also valid. Periodic patterning therefore allows OM coupling to another family of mechanical modes that does not require the motion of the whole suspended photonic crystal [73]. It allows simultaneous confinement of optical photons and microwave phonons in volumes of diffraction-limited size. The higher mechanical frequencies in the gigahertz range also allow approaching a regime where low-temperature operation is achieved even without additional laser cooling.

Most of the work described in this thesis deals with the interaction of photons and phonons in photonic crystals. As will be seen in Chapter 3, the analogous behaviour of photons and phonons in periodic potentials and how their flow is perturbed in the presence of defects also allows confinement strategies based on distributed defects, which are the main object of study of this research. Despite the specificities of OM interactions in a photonic crystal platform and the ones added by employing localization via disorder, what truly matters to describe the basic physics of photon-phonon interactions in an optical cavity is having a cavity whose resonant frequency is dispersively coupled to the position of a mechanical resonator, something that is true for all of the aforementioned systems. Therefore, we use the FP resonator with a movable mirror as a toy model from which the Hamiltonian and the equations of motion are derived. For the sake of simplicity, other types of OM coupling explored, like dissipative [74] or quadratic [75] coupling, are omitted in our model.

2.2 Hamiltonian formalism and equations of motion

In a real OM system, light can usually be confined at more than one particular wavelength/frequency and the mechanical spectrum of the involved structure has a rich multi-lineshape spectral response. Therefore, in principle, such a system can only be described in terms of a set of optical modes with frequencies $\omega_{o,i}$ and a set of mechanical modes with frequencies $\Omega_{m,j}$. However, all of the involved mechanical frequencies are typically much smaller than the free spectral range of the optical cavity and we can restrict ourselves to one single optical mode of frequency ω_o, the one closest in frequency to the driving laser. Additionally, we also limit the analysis to one mechanical mode of frequency Ω_m under the assumption that the dynamics are linear with independently evolving normal modes. At the displacement levels typically achieved with such systems, the uncoupled optical cavity and mechanical mode can both be described by quantum harmonic oscillators with $\hat{a}$ ($\hat{a}^\dagger$) and $\hat{b}$ ($\hat{b}^\dagger$) the anihilation (creation) operators for photons and phonons, respectively. The system Hamiltonian then reads

$$\hat{H} = \hbar\omega_o \hat{a}^\dagger \hat{a} + \frac{1}{2} + \hbar\Omega_m \hat{b}^\dagger \hat{b} + \frac{1}{2} \tag{2.5}$$

When we consider an optical cavity with a movable end mirror, i.e., a cavity whose resonating frequency depends on the position of the mechanical resonator, the induced parametric coupling can be easily introduced in Eq. (2.5) by substituting ω_o by $\omega_o(\hat{x})$, where we have replaced the classical position amplitude by the position operator $\hat{x} = x_{zpf}(\hat{b}^\dagger + \hat{b})$. For most experimental realizations so far explored, including the ones of this thesis, the frequency dependence on the position can be Taylor-expanded to first order as $\omega_o(\hat{x}) \sim \omega_o + \hat{x}\partial\omega_o/\partial x \equiv \omega_o - G\hat{x}$, with G the frequency shift induced by a unitary displacement. When this expansion is included in the previous Hamiltonian, we get

$$\begin{aligned} \hat{H} &= \hbar(\omega_o - G\hat{x})\hat{a}^\dagger\hat{a} + \hbar\Omega_m\hat{b}^\dagger\hat{b} \\ &= \hbar\omega_o\hat{a}^\dagger\hat{a} + \hbar\Omega_m\hat{b}^\dagger\hat{b} - \hbar G x_{zpf}(\hat{b}^\dagger + \hat{b})\hat{a}^\dagger\hat{a} \end{aligned} \tag{2.6}$$

where the constant terms have been omitted. From this construction, the product Gx_{zpf}, the cavity frequency shift due to a displacement equal to the zero-point fluctuations of the mechanical resonator position, arises naturally. We define the vacuum optomechanical coupling rate $g_o = Gx_{zpf}$, which quantifies the interaction between a single phonon and a single photon. Unlike G, which suffers from the somehow arbitrary definition of the displacement amplitude for complicated space-dependent mechanical modes [76], g_o is a fundamental quantity. We see from (2.6) that the interaction term, $\hat{H}_{int} = -\hbar g_o(\hat{b}^\dagger + \hat{b})\hat{a}^\dagger\hat{a}$, is a three-wave operator and is therefore inherently nonlinear. From this interaction hamiltonian, the radiation-pressure force is given by

$$\hat{F}_{RP} = -\frac{d\hat{H}_{int}}{d\hat{x}} = \hbar\frac{g_o}{x_{zpf}}a^\dagger\hat{a} = \hbar G a^\dagger\hat{a} \tag{2.7}$$

whose expectation value recovers the formula derived in Eq. 2.4 for a FP resonator with a movable end-mirror, for which $G = -\partial\omega_o/\partial x = \omega_o/L$.

In order to have the full description of the OM system, a series of additional terms accounting for the openness of the system need to be added to (2.6). First, the optical cavity is being driven by an external laser that populates the cavity and enables acquisition of information on mechanical motion via photons exiting the cavity. Its effect can still be cast into the conservative hamiltonian as $\hat{H}_{drive} = i\hbar\sqrt{\kappa_l}\alpha_{in}\hat{a}^\dagger e^{-i\omega_\ell t} + c.c.$, with ω_ℓ the laser drive frequency [77]. However, the mere presence of this term implies that the optical cavity has some loss channels along which the cavity can be driven. Photon decay into that specific channel and into any other loss channel need to be considered, as do the possible quantum fluctuations entering via them. For the mechanical resonator, coupling to a thermally-populated bath should also be taken into account. First-principles consideration of all these additional terms in a Hamiltonian formalism would require a model for the optical and mechanical environment, typically that of an infinite collection of harmonic oscillators [78], and how these couple to the optical and mechanical resonator. To avoid tracking the evolution of both the OM system and the environment simultaneously, one can ressort to the input-output formalism [79]. This is a formal setting based on quantum Langevin equations derived from integrating the Heisenberg equations of motion over the environment and asuming some non-restrictive properties on the environment, notably its non-Markovian dynamics, i.e., whatever reaches the outside is irreversibly lost. A detailed derivation of these equations can be found elsewhere [80].

The quantum Langevin equations [81] for the field operator $\hat{a}$ can be written in the following form

$$\frac{d\hat{a}(t)}{dt} = -i(\omega_o - G\hat{x}(t))\hat{a}(t) - \frac{\kappa}{2}\hat{a}(t) + \sqrt{\kappa_\ell}(\overline{a}_{in}e^{-i\omega_\ell t} + \delta\hat{a}_{in}) + \sqrt{\kappa_b}\hat{f}_{in} \tag{2.8}$$

where we introduced the overall photon decay rate $\kappa \equiv \kappa_\ell + \kappa_b$ that takes into account both losses into the laser drive channel (κ_ℓ) and into all other bath channels (κ_b). The quantum fields $\hat{a}_{in}$ and $\hat{f}_{in}$ associated to these two channels enter as source terms in (2.8), where we split $\hat{a}_{in}$ into its coherent mean field $\overline{a}_{in}$ and its vacuum-like fluctuations $\delta\hat{a}_{in}$. The field is normalized in such a way that

$$P_{in} = \hbar\omega_\ell|\overline{a}_{in}|^2 \tag{2.9}$$

is the input power launched into the cavity. More complex field states such as squeezed or entangled states of the photonic environment $\hat{a}_{in}$ can also be treated within the input-output formalism, but we limit ourselves to highly coherent laser sources. Fortunately, the same formalism gives access to the field that is decoupled from the optical cavity into any of the loss channels via the energy-conserving boundary condition

$$\hat{a}_{out,j}(t) = \hat{a}_{in}(t) - \sqrt{\kappa_j}\hat{a} \tag{2.10}$$

where κ_j specifies the decay rate into the chosen j-th channel, whose contribution to Eq. (2.8) was either masked inside κ_b or in the driving term such that $\kappa_j = \kappa_\ell$. For the equation on the field operator $\hat{b}$, the same input-output formalism leads

to

$$\frac{d\hat{b}(t)}{dt} = (-i\Omega_m - \frac{\Gamma_m}{2})\hat{b}(t) + iG\hat{a}^\dagger(t)\hat{a}(t) + \sqrt{\Gamma_m}\hat{b}_{in} \tag{2.11}$$

where Γ_m is the dissipation rate. We have also asumed that the mechanical mode is not driven by any other external means and the only source term $\hat{b}_{in}$ accounts for the hot thermal bath to which the mechanical mode is coupled. Unlike for the optical cavity, the average number of quanta in the mechanical thermal bath $\overline{n}_{th} = k_B T/\hbar\Omega_m \gg 1$ is non-negligible, even when the system is operated in cryogenic environments.

The classical equations of motion for both the mechanical resonator position $x(t) = 2x_{zpf}\mathrm{Re}(\langle\hat{b}(t)\rangle)$ and the complex cavity field amplitude $a(t) = \langle\hat{a}(t)\rangle$ are readily obtained by taking the expectation values of Eqs. (2.8) and (2.11)

$$\frac{da(t)}{dt} = i(\Delta + Gx(t))a(t) - \frac{\kappa}{2}a(t) + \sqrt{\kappa_\ell}\overline{a}_{in} \tag{2.12a}$$

$$m_{eff}\frac{d^2x(t)}{dt^2} = -m_{eff}\Omega_m^2 x(t) - m_{eff}\Gamma_m\frac{d}{dt}x(t) + \hbar G|a(t)|^2 + F_{th}(t) \tag{2.12b}$$

where we have moved to a rotating frame at the laser frequency ω_l and introduced the detuning $\Delta = \omega_\ell - \omega_o$. The system is said to be blue-detuned for $\Delta > 0$ and red-detuned for $\Delta < 0$, while $\Delta = 0$ corresponds to a laser in perfect resonance with the optical cavity. As can be seen, the only fluctuations left are the ones associated to the thermal bath of the mechanical oscillator, which effectively leads to a stochastic Langevin force with correlation function $\langle F_{th}(t), F_{th}(t')\rangle = \hbar m_{eff}\Gamma_m \int_{\mathbb{R}} e^{i\omega(t-t')}\coth(\frac{\hbar\omega}{2k_BT})d\omega$ [82].

In the absence of interaction, i.e., $G = 0$, and with the classical analogue of the boundary condition in (2.10), i.e., $a_{out}(t) = \overline{a}_{in}(t) - \sqrt{\kappa_j}a(t)$, Equations (2.12a) and (2.12b) correspond to the equations for a driven optical cavity within a coupled mode theory framework [83] and to the dynamics of a thermally-driven damped harmonic oscillator, respectively.

2.3 Dynamics of optomechanical resonators

The two coupled non-linear differential equations in (2.12) do not present an easy analytical solution, making the use of numerical simulations unavoidable in most cases. However, it is instructive to analyze what happens in a series of simplified settings. The simplest one is probably what happens when the interaction strength is set to zero in both equations and the two resonators evolve independently. This will allow us to study the basic physics and response of a driven optical resonator and of a mechanical resonator in thermal equilibrium. With those in hand, the equations can be linearized around a steady state value and both the effect of the mechanical displacement on the optical cavity field and static and dynamical effects on the mechanical resonator induced by the light field, i.e., dynamical backaction, can be easily derived.

2.3.1 Basics of a driven optical cavity

Here, we only consider the optical subsystem with $G = 0$. We first analyze the dynamics in the case where the cavity is driven at low power and responds linearly and then add the necessary terms to Equation (2.12a) in order to account for the onset of material nonlinearities, which lead to nonlinear dynamics.

The linear regime

The behaviour of a weakly driven optical cavity can be derived by setting $G = 0$ in Eq. (2.12a). This is a simple first-order linear equation, whose solution for the initial condition $a(t = 0) = a_o$, after going back into the laboratory frame, yields

$$a(t) = \frac{\frac{\sqrt{\kappa_\ell}\overline{a}_{in}}{\frac{\kappa}{2}-i\Delta}(e^{(\frac{\kappa}{2}-i\Delta)t} - 1) + a_o}{e^{(\frac{\kappa}{2}-i\Delta)t}} e^{-i\omega_\ell t} \tag{2.13}$$

The intra-cavity photon number can be found by taking $n(t) = |a(t)|^2$. Its time dependence is depicted in Fig. 2.3(b) for two different initial conditions and for various detunings, with $\kappa_\ell = \kappa/2$ fixed. In all cases, the photon number saturates to a fixed value on a characteristic timescale of several κ^{-1}, the cavity build-up or decay time depending on the cavity initial condition. The saturation value corresponds to the steady state solution to the equation $(da(t)/dt = 0)$ and is found by taking the limit of Eq. (2.13) when $t \to \infty$. The solution corresponds to the prefactor

$$\overline{a} = \frac{\sqrt{\kappa_l}\overline{a}_{in}}{\frac{\kappa}{2} - i\Delta} \tag{2.14}$$

in the numerator, while the steady-state cavity population is given by

$$\overline{n} = \frac{\kappa_\ell}{(\kappa/2)^2 + \Delta^2} \frac{P_{in}}{\hbar\omega_l} \tag{2.15}$$

While the intra-cavity field $a(t)$ is the fundamental quantity that couples to the mechanical degree of freedom, the information on the dynamical state of the system is obtained via the outcoupled light into the channel of detection $a_{out,d}(t)$. Coupling light into an optical resonator and the conditions for an optimal coupling are extremely recurring problems in photonics, specially when the system size gets down to the nanoscale. How to read-out the decoupled light is however as important as how we couple it in. For the case of a FP cavity as the one depicted in Fig. 2.1 the openness of the cavity is directly used to drive it from one of its mirrors and measure the reflected light, but one could very well measure the transmitted light from the back-mirror. In a simplified picture, these two cases would correspond to a one-sided or a double-sided optical cavity coupled to one or two bus waveguides, respectively, the cases depicted in top and middle diagrams of Fig. 2.3(a). The optical cavities dealt with in this thesis are photonic crystal cavities based on disorder-induced localization and on-demand access to particular cavities becomes a crucial requirement. Therefore, we use a tapered optical fiber to evanescently couple to the near-field of the optical cavity and we use the fiber for both the driving and the detection, which can be done either in transmission or in reflection. The description of such an experimental configuration in the

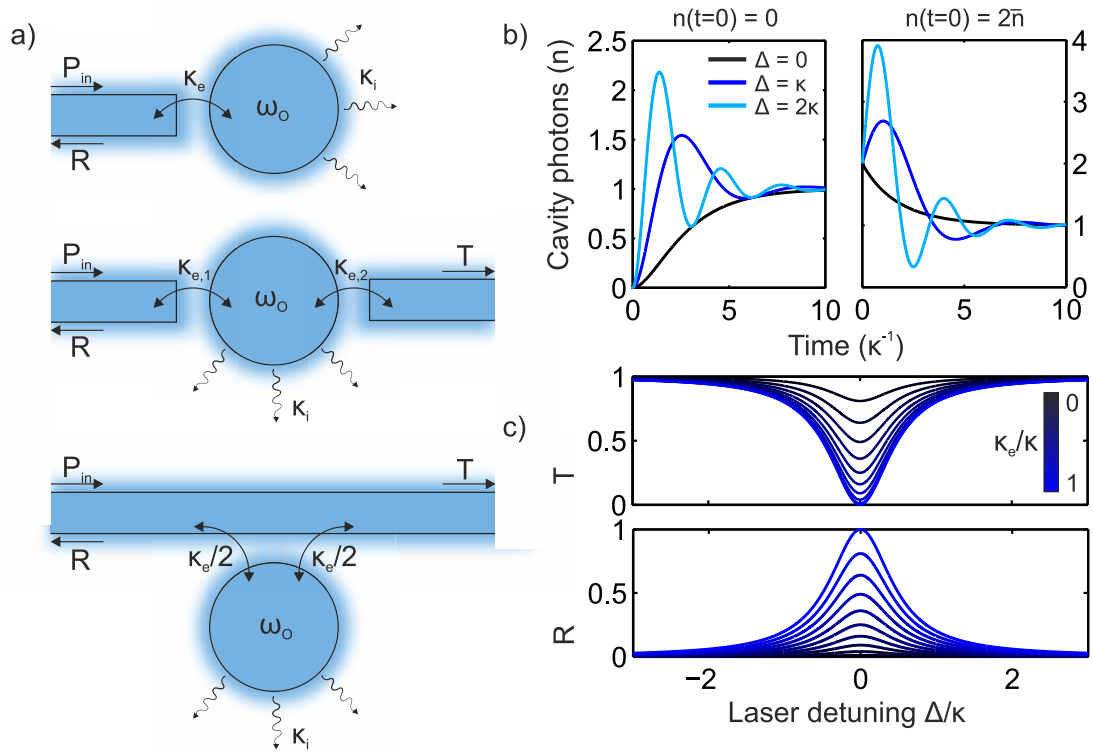

Figure 2.3: Optical response of a driven optical cavity. (a) Possible configurations for driving an optical cavity, where the blue rectangles represent the channels used for excitation and/or detection and the optical cavity is represented with a circle. The relevant parameters for a single-sided (top), a double-sided (middle) and a bus-waveguide-coupled (bottom) optical cavity are given. (b) Time evolution of the intracavity photon number $n(t)$ for different laser-cavity detunings Δ starting from an empty (left) and a filled cavity (right). (c) Transmission (top) and reflection (bottom) of an optical cavity bi-directionally coupled to an excitation/detection bus waveguide as a function of the ratio κ_e/κ.

input-output formalism corresponds to an optical cavity which is bi-directionally coupled to a bus waveguide, as depicted in the bottom of Fig. 2.3(a). This bi-directionality is typically perfect for the cases treated in this thesis, and we can therefore divide the losses into the bus waveguide κ_w into equal parts for the propagating ($\kappa_w/2$) and counter-propagating modes ($\kappa_w/2$). The total losses of the system $\kappa \equiv \kappa_i + \kappa_e$ can be split into the intrinsic losses κ_i that exist irrespective of the bus waveguide -mainly absorption or radiation losses- and the extrinsic losses κ_e associated to the fiber taper that obviously are $\kappa_e = \kappa_w/2 + \kappa_w/2 = \kappa_e/2 + \kappa_e/2$. In such case $\kappa_\ell = \kappa_e/2$. However, this symmetry can be broken for propagating cavity modes like those in ring resonators, where phase-matching can only occur in one particular direction [84]. The steady-state transmission for a bi-directionally

coupled cavity therefore reads

$$T(\Delta) = |t|^2 = \left|\frac{a_{out,t}}{a_{in}}\right|^2 = \left|\frac{a_{in} - \sqrt{\kappa_e/2}}{a_{in}}\right|^2 = \frac{\Delta^2 + (\kappa/2 - \kappa_e/2)^2}{\Delta^2 + (\kappa/2)^2} \tag{2.16a}$$

$$R(\Delta) = |r|^2 = \left|\frac{a_{out,r}}{a_{in}}\right|^2 = \left|\frac{-\sqrt{\kappa_e/2}}{a_{in}}\right|^2 = \frac{(\kappa_e/2)^2}{\Delta^2 + (\kappa/2)^2} \tag{2.16b}$$

whose lineshapes are represented in Fig. 2.3(c) as a function of the ratio κ_e/κ. Obviously, whenever $\kappa_e = 0$, R = 0 and T = 1 since the cavity is invisible to the bus waveguide, and when $\kappa_e = \kappa$ the inverse situation happens and the transmission is null, all light being back-reflected into the bus waveguide. The optical parameters of the cavity κ and κ_e can be obtained from fitting a measured normalized DC transmission or reflection spectrum to the above formula. Most measurements that will be described in this thesis are done in a transmission configuration, for which the response is an effective Lorentzian lineshape with linewidth κ and an on-resonance transmission $T(0) = (1 - \kappa_e/\kappa)^2$. With those parameters known, the typical figure of merit for an optical cavity, the (loaded) quality factor Q, can be calculated as $Q = \omega_o/\kappa$.

The non-linear regime

We see from Eqs. (2.16) that, as expected from the linearity of the equations, the normalized response of the system is independent of the power drive P_{in}. However, the experiments that will be described in Chapter 5 require relatively large laser power ($\sim$ 0.1-10 mW) and deal with cavities of rather high quality factors Q ($\sim 10^4 - 10^5$), where the cavity response is modified due to the onset of material non-linearities. The range of non-linearities in the materials used for optical resonators is extremely large and materials are chosen depending on the application targeted. In the field of cavity OM the situation is rather the opposite, with extensive research on finding materials that respond linearly up to very high power drives [85–88]. The main driving force for this material science research is to perform quantum OM experiments, since lowering photon absorption as much as possible is crucial in order to prevent heating effects when the mechanical resonator has been cooled to near its quantum ground-state [89,90]. Our experiments use a silicon platform and operate at telecommunication wavelengths, room-temperature and ambient conditions. We therefore restrict our description of the non-linear response of a driven optical cavity to the most prominent non-linearities for this particular setting.

Due to its central symmetry, the susceptibility tensor of second order of silicon is null and only third order terms need to be considered [91]. To such order, the main non-linear processes in silicon for single frequency operation in the telecom range are two-photon absorption (TPA) and a dispersive Kerr effect, arising from the real and imaginary parts of the third order suspceptibility of electronic origin [92]. Nevertheless, free carrier absorption (FCA) needs to be considered since a large population of free carriers N_e can be generated in such high-Q low-V cavities, precisely due to TPA. A schematic describing the microscopic nature of these two phenomena can be found in Fig 2.4 (top panel). Last, most of the

absorbed optical power in the cavity will be released to the lattice through the decay of the photoexcitated carriers, rising its temperature. The decay being much faster than the dynamics of the temperature, the energy transfer from the electron population to the lattice can be considered inmediate for the purposes of modelling the temperature field in the cavity. Such temperature rise in the cavity region will in turn produce a shift in the cavity resonant frequency ω_o of opposite sign to the one mediated by the presence of free carriers. Following the derivations in [93–95], all such non-linear processes can be microscopically introduced into Maxwell's equations with the corresponding non-linear polarization terms, and then cast into a non-linear coupled mode formalism by writing

$$\frac{da(t)}{dt} = i\Delta a(t) - \left(\frac{\kappa}{2} + \frac{c^2}{n_{Si}^2}\frac{\hbar\omega_\ell\beta_{TPA}|a(t)|^2}{2V_{TPA}} + \frac{c}{n_{Si}}\frac{\sigma_r N_e}{2V_{FCA}}\right)a(t) + \sqrt{\frac{\kappa_e}{2}}\overline{a}_{in} \tag{2.17a}$$

$$\Delta = \omega_\ell - \left(\omega_o - \frac{\omega_o}{n_{Si}}\frac{\sigma_i N_e}{V_{FCA}} + \frac{\omega_o}{n_{Si}}n_T\Delta T\right) \tag{2.17b}$$

where in addition to the cavity losses in the linear regime ($\kappa/2$) the absorbed power due to TPA and FCA have been considered in (2.17a). Dispersion due to free carriers N_e and temperature increases ΔT has also been introduced as can be seen on the equation for the detuning in (2.17b). Here β_{TPA} is the tabulated TPA coefficient, V_{TPA} and V_{FCA} the characteristic volumes of TPA/FCA processes respectively, n_{Si} the refractive index of silicon, c the speed of light, σ_r and σ_i the free-carrier absorption and dispersion *cross-sections* and n_T the first-order refractive index variation caused by temperature. We have already here dismissed the dispersion associated to the Kerr effect due to the difference in magnitude as compared to free-carrier dispersion (FCD) and to the thermo-optic (TO) effect. We note here that the linear absorption does not appear explicitly in (2.17a) since its effect is already taken into account through the intrinsic cavity losses κ_i, that contribute to κ. This implies that solely considering linear absorption already requires solving a much more complex system in which N_e and ΔT have a prominent role in the dynamics. The influence of the free carrier population N_e and the temperature increase ΔT in Eqs. (2.17a) and (2.17b) implies that their dynamics need to be tracked too. These are obviously very complex space and time-dependent processes, but its possible to have a simple physical picture in the following form,

$$\frac{dN_e(t)}{dt} = -\gamma_{fc}N_e + \frac{1}{2}\frac{c^2}{n_{Si}^2}\frac{\hbar\omega_l\beta_{TPA}}{V_{TPA}}|a(t)|^4 + \frac{c}{n_{Si}}\frac{\alpha_{lin}}{R_{eff}}|a(t)|^2 \tag{2.18}$$

$$\begin{aligned}\frac{d\Delta T(t)}{dt} =& -\gamma_{th}\Delta T + \frac{1}{\rho_{Si}C_{p,Si}V_{eff,T}}\left(\frac{c^2}{n_{Si}^2}\frac{\beta_{TPA}}{V_{TPA}}|a(t)|^4 + \frac{c}{n_{Si}}\frac{\sigma_r N_e(t)}{V_{FCA}}|a(t)|^2\right.\\ &\left.+\frac{c}{n_{Si}}\frac{\alpha_{lin}}{R_{eff}}|a(t)|^2\right)\end{aligned} \tag{2.19}$$

where we have considered unavoidable linear absorption in addition to TPA and FCA. Here α_{lin} is the linear absorption coefficient, R_{eff} represents the inverse of the fraction of the optical mode inside the silicon, ρ_{Si} and $C_{p,Si}$ the density and constant-pressure specific heat capacity of silicon, $V_{eff,T}$ an effective thermal volume for the cavity and γ_{fc} and γ_{th} the free-carrier and thermal decay rates. An understanding of the dynamical behaviour of an optical cavity driven at high enough power requires the simultaneous solution of Equations (2.17a), (2.18) and (2.19). In order to simplify those, we can use the characteristic times involved in

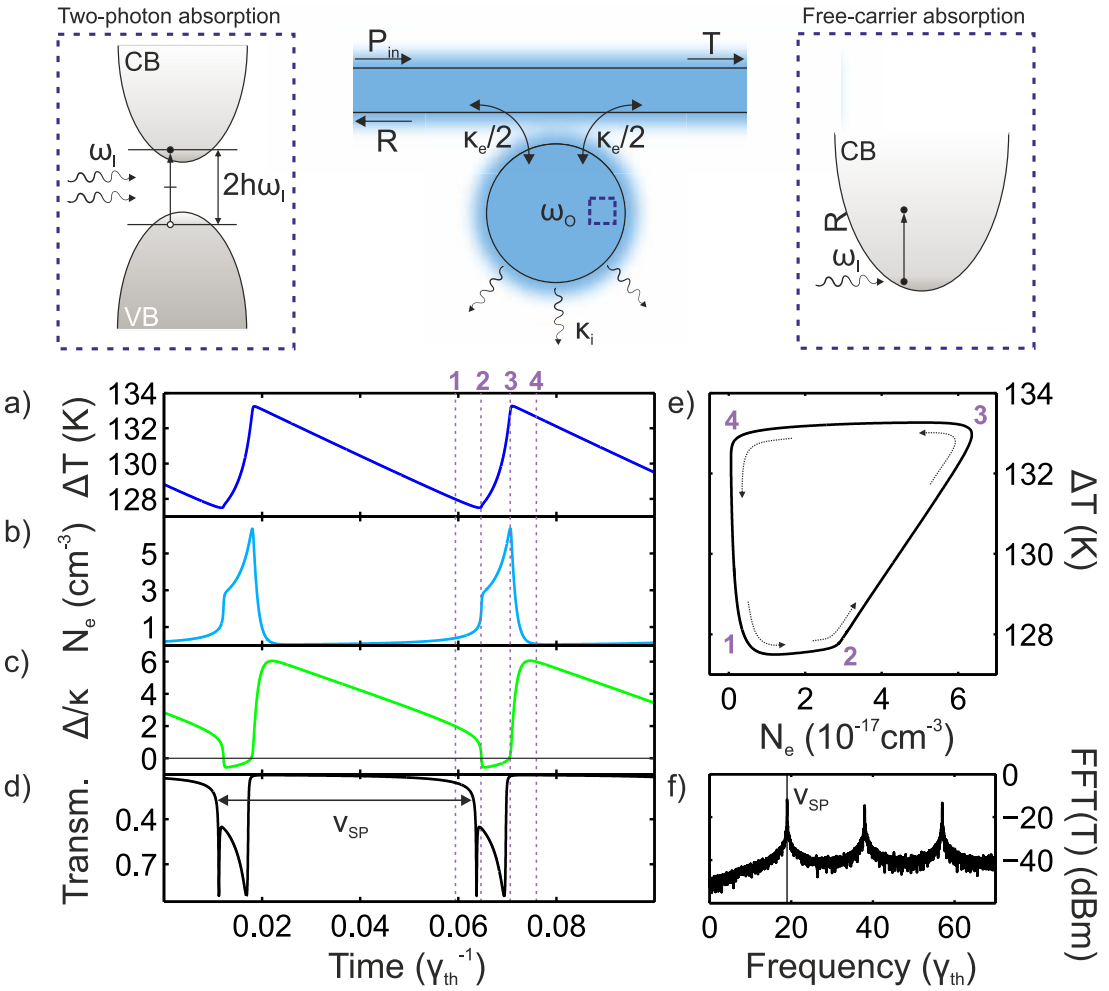

Figure 2.4: Self-pulsing (SP) dynamics of a highly driven silicon optical cavity. Driven at *high* powers, the dynamics of free-carriers N_e and temperature changes ΔT need to be tracked. They couple dispersively to the optical resonance and can end up leading to periodic but highly anharmonic dynamical states. Both dynamical variables ΔT (a) and N_e (b) display a periodic behaviour at frequency ν_{SP}, forming a closed trajectory in phase space (e). The resulting time-periodic detuning Δ (c) between the optical cavity and the driving laser modulates the photon number $\overline{n}_c$ and the transmission, the typical time trace of which is shown in (d). (e) Fast Fourier transform (FFT) of the time trace. Time and frequency are given relative to the thermal decay rate γ_{th}.

the different physical processes. For most of the optical modes dealt with in this work, the typical decay time of an optical mode ($\sim$ ps) is orders of magnitude faster than the nonlinear dispersion mechanisms ($\sim$ ns). As a consequence, we can asume N_e and ΔT to be constant in the time-scales involved in (2.17a). In addition, the non-linear losses, that we denote by κ_{nl}, can be at first neglected, since in most cases we have still $\kappa \gg \kappa_{nl}$. Solving for the steady state intracavity photon number $\overline{n}$, we can actually restrict our system of equations to (2.18) and (2.19) by considering the adiabatic response of the optical cavity using the steady state number of photons (2.15) with a time-dependent detuning (2.17b) and replacing $|a(t)|^2 = \overline{n}(t)$. This results in the simplified system of non-linear

equations

$$\frac{dN_e(t)}{dt} = -\gamma_{fc}N_e(t) + \frac{1}{2}\frac{c^2}{n_{Si}^2}\frac{\beta_{TPA}\hbar\omega_l\overline{n}(t)^2}{V_{TPA}} + \frac{c}{n_{Si}}\frac{\alpha_{lin}\overline{n}(t)}{R_{eff}} \tag{2.20}$$

$$\begin{aligned}\frac{d\Delta T(t)}{dt} = &-\gamma_{th}\Delta T(t) + \frac{\hbar\omega_l\overline{n}(t)}{\rho_{Si}C_{p,Si}V_{eff,T}}\left(\frac{c^2}{n_{Si}^2}\frac{\beta_{TPA}\hbar\omega_l\overline{n}(t)}{V_{TPA}} + \frac{c}{n_{Si}}\frac{\sigma_r N_e(t)}{V_{FCA}}\right.\\ &\left.+\frac{c}{n_{Si}}\frac{\alpha_{lin}}{R_{eff}}\right)\end{aligned} \tag{2.21}$$

which can be integrated without much computational effort and is able to capture the main experimental features that will be reported on Chapter 5, as well as in previous experiments in our group [96]. For the observed modes with largest Q-factor, the adiabaticity assumption does not hold and Equations (2.17a), (2.18) and (2.19) need to be solved. This has consequences in the temporal transmission trace when these are driven, as will be shown in Chapter 5.

We consider all of the parameteres defining the equations above, except the laser parameters P_{in} and ω_ℓ, as given. In most of the situations, the dynamic solution to the system of differential equations (2.20) and (2.21) is a fixed or equilibrium point in the phase space defined by $\{N_e, \Delta T\}$, which leads to a stable spectral shift of the cavity mode, which is typically dominated by the thermal part and will be simply referred to as the TO shift [97] from now on. For particular combinations of P_{in} and ω_ℓ stable limit cycles exist in phase space. With initial conditions $\{N_e(0), \Delta T(0)\}$ inside the basin of attraction of this limit cycle, the dynamic solution in the limit $t \to \infty$ tends to the cycle, forming a periodic closed trajectory in phase space $\{N_e^*(t), \Delta T^*(t)\}$ - a self-pulsing (SP) limit cycle [98]- which is generally highly anharmonic. The typical shape of this closed trajectory, as well as the resulting temporal traces for N_e and ΔT are obtained by numerical integration of equations (2.20) and (2.21) and are depicted in Fig. 2.4(a,b). The dynamical solution can be readily understood by heuristically considering the physical processes taking place at several points, the ones highlighted as 1, 2, 3 or 4 in Fig. 2.4. Let us imagine the system is set to an arbitrarily higher temperature by an external heat source, inducing a TO redshift of the optical resonance, and the laser is fixed somewhere in between the original *cold* and the modified *hot* optical resonance. The external source is shut down and the temperature starts decreasing progressively, until the driving laser is resonant with the cavity, which is exponentially returning to its original position due to the progressive temperature decrease. Then:

- At **point 1**, partial absorption of the optical energy that gets stored in the cavity (Fig. 2.4(b)) induces a fast increase of the free-carrier density N_e while the raise in temperature is slower. This induces a quick blueshift of the mode.
- The first minimum observed in transmission (Fig. 2.4(d)) occurring at **point 2** is related to this blueshift, which ends up leading to a change in the detuning sign (Fig. 2.4(c)). The sharpness of the dip is precisely related to the short characteristic time of the free carriers γ_{fc} decay.

- The resonance rapidly blueshifts up to the point where the temperature starts raising due to the previously absorbed light, redshifting the resonance. As the TO effect is much larger than FCD, the resonance progressively redshifts despite the increase in N_e. This leads to the second transmission minimum **point 3**, where the laser is again perfectly resonant with the cavity mode ($\Delta = 0$).
- After, the cavity progressively goes out of resonance and free-carriers decay much faster than temperature. This leads to a much faster redshift, up to **point 4**, where all free-carriers have decayed to the valence band and the cavity is back at the initial stage of its cooling. The cavity starts cooling down, eventually leading to point 1 again.

This periodic evolution occuring at a frequency ν_{SP} is highly anharmonic as shown by the time traces of N_e and ΔT. The anharmonicity of the observed transmission trace is even stronger since the non-sinusoidal evolution of ω_o is convoluted with the Lorentzian lineshape given by Eq. (2.16), which constitutes a highly non-linear filter for resonance oscillations that go up to several linewidths (Δ/κ reaches 6 in Fig. 2.4(c)). This generates a frequency-comb in the transmitted light with harmonics M up to $M = 100$ or more [96].

When the laser frequency ω_ℓ or the power P_{in} are changed, the limit cycle is both displaced and occurs at a different pace ν_{SP}. Since the instantaneous decay rate of ΔT depends on the absolute value of the temperature, ν_{SP} can be enhanced up to five times by increasing the amount of total heat in the cavity, which can be done by increasing the time-averaged photon number. This is experimentally achieved by either increasing the power P_{in} or by further decreasing ω_ℓ, i.e., increasing the wavelength λ_ℓ, to be more resonant with the optical mode. However, initial conditions inside the basin of attraction of the limit cycle are required to end up in the cycle. In order to enter this basin of attraction experimentally one needs either additional drive terms to prepare the initial condition [99] or to sweep the laser wavelength starting from the blue-side of the resonance. The resulting dynamics as a function of λ_ℓ, the typical parameter over which we have experimental control, are shown in Fig. 2.5(a,b). The DC transmission $\langle T(t)\rangle_t$, the quantity that one would measure with a slow photodetector, is depicted in (a) for several input powers P_{in}. Above $P_{in} =$ X mW a kink in the DC transmission appears at some particular wavelength λ_ℓ^*, which corresponds to an intracavity photon threshold $\overline{n}_{th}$. The Fast-Fourier-Transform (FFT) of the transmission temporal trace above that wavelength is shown in (b) and exhibits the spectral features of the SP limit cycle (Fig. 2.4(f)). The panel at $P_{in} = 2$ mW shows the most commonly observed behaviour of the SP, with ν_{SP} progressively increasing with the number of cavity photons as the average detuning $\langle\Delta(t)\rangle_t$ is lowered. At some point, after reaching $\nu_{SP,max}$, ν_{SP} starts decreasing again, until the resonance irreversibly returns to its original *cold* position. Although this is the spectral map we typically observe experimentally, other more intricate behaviours can be found numerically for particular locations in the multiparameter phase space. A particular example observed experimentally (see Chapter 5) is shown in the right panel of Fig. 2.5(b), with a pronounced change in the onset and die-out of the SP limit cycle.

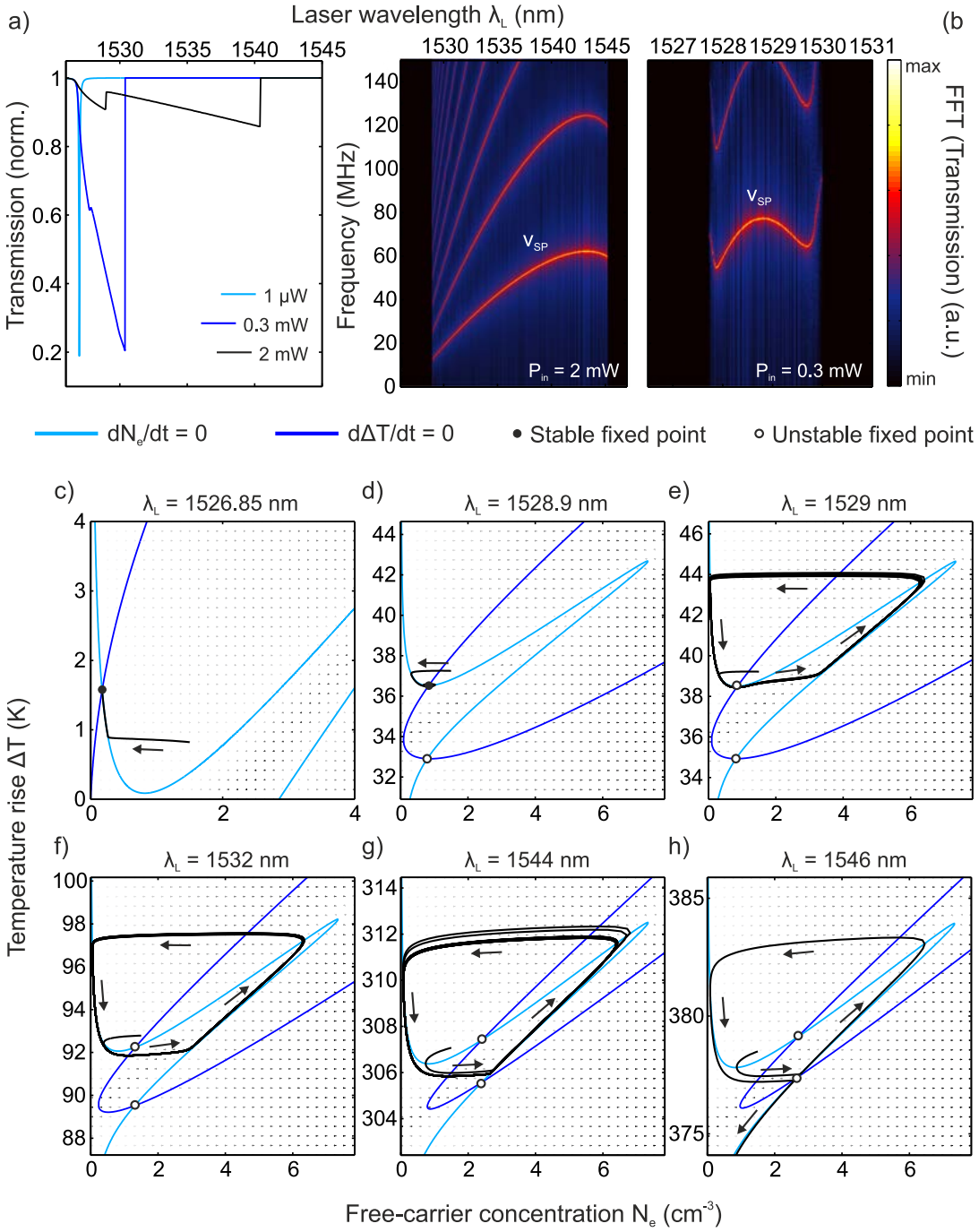

Figure 2.5: Typical wavelength-dependence and phase portrait of the self-pulsing (SP) dynamics. (a) DC transmission at various input powers P_{in}. (b) Radiofrequency (RF) spectrum of the transmission time trace $T(t)$ as a function of the laser wavelength λ_ℓ for two of the powers in (a). The left panel shows the most common type of SP RF spectral map, while the right panel shows a more intricate evolution of $\nu_{SP}(\lambda_\ell)$. In both panels the first harmonic of the SP is highlighted. (c-h) Phase portraits as of function of N_e and ΔT for λ_ℓ below the Hopf bifurcation (c), at the bifurcation (d), above the bifurcation (e-g) and when the resonance is lost (h). The nullclines of Eqs. (2.20) and (2.21) are plotted in light ($dN_e/dt = 0$) and dark ($d\Delta T/dt = 0$) blue, while the system trajectories are in black. The background arrows show the temporal derivatives at each point in phase space. Solid black dots and open dots represent stable and unstable fixed points respectively.

It is also instructive to observe the phase portrait of the dynamic solution while sweeping λ_ℓ [100]. The long-term solutions of any one or two-dimensional nonlinear system restrict to nothing more complicated than stable/unstable fixed points or limit cycles and the existence of one such limit cycle grants the presence of an unstable fixed point in the space bounded by the closed trajectory [101]. Therefore, we depict in Fig. 2.5(c-h) both stable and unstable fixed points in the region close to where the effective trajectory takes place. First, when the laser is only slightly inside the optical resonance (c), the long-term solution to which the system evolves towards is a stable fixed point (•) with a steady-state free-carrier density N_e^* and a fixed temperature rise ΔT^*. When gently increasing the laser wavelength λ_ℓ, we adiabatically follow the stable fixed point, although an unstable fixed point appears close in phase space (d). Although not shown, another stable fixed point also appears close to the origin within a given region where the cavity has a bistable behaviour. It results from the intersection of the lower branch of the free-carrier nullcline ($dN_e/dt = 0$) in light blue with a temperature nullcline ($d\Delta/dt = 0$) that remains close to $\Delta T = 0$. The physical origin of this other fixed point is simply the solution that one would obtain with the laser directly turned on at that particular wavelength λ_ℓ, since we have already TO-shifted the resonance by much more than its own linewidth κ. At some particular wavelength, the fixed point in (d) undergoes a supercritical Hopf bifurcation [102], transmuting into an unstable fixed point surrounded by a stable limit cycle (e), effectively our SP state. Further increasing the laser wavelength increases the average temperature of the system $\langle \Delta T(t) \rangle_t$ ((e) to (g)) and increases the SP frequency ν_{SP}. We also observe that the SP trajectory, whose shape remains rather constant, starts approaching the second unstable fixed point. The optical resonance is lost and returns to its *cold* wavelength whenever the limit cycle encounters the second unstable point. There, the trajectory closely follows the free-carrier nullcline and ends up in the stable fixed point very close to $0, 0$. The resonance is therefore irreversibly lost and further sweeping the laser wavelength does not produce any more interesting dynamics.

The overall dynamics described above asumes that the cavity photon number $\overline{n}_o$ adiabatically responds to changes in both temperature and free-carrier density and that no steady-state effect of the non-linear losses is induced in the cavity lineshape. Despite being a crude approximation for optical cavities above $Q \sim 10^5$, the dynamics of the system including the free evolution (2.17a) of the complex cavity field leads to very similar type of solutions in most situations. However, since more than two dimensions are at play, trajectories may become much more complex, eventually displaying aperiodicity and extreme sensibility to initial conditions, that is, exhibiting chaos. We have chosen to depict their solution under simplifying assumptions to enable their visualization in phase space, although these will be solved exactly for quantitative comparison to an experiment. This phenomenon, which has already been observed in different photonic engineered nanostructures such as microdisks [94], photonic crystals [103] or optomechanical crystals [96], will be of importance to understand the experimental observations of Chapter 5.

2.3.2 Basics of a mechanical resonator in thermal equilibrium

The main characteristics of an optical cavity driven at both low and high powers given, the behaviour of the mechanical resonator when the coupling constant $G = 0$ remains to be explored. The simplest case to evaluate is the mechanical resonator dynamics under free-evolution, with no drive terms. We denote $x_h(t)$ the solution to the resulting homogeneous equation obtained by setting $F_{th}(t) = 0$ in (2.12b). The equation of motion can be easily solved in the time domain and $x_h(t)$ is given by

$$x_h(t) = A_o e^{-\Gamma_m/2} \sin\left(\sqrt{\Omega_m^2 - \left(\frac{\Gamma_m}{2}\right)^2}\, t + \phi_o\right) \tag{2.22}$$

where constants A_o and ϕ_o are found from the initial conditions. The system oscillates at a frequency close to the resonance frequency Ω_m and gradually decays to zero. The quality factor of the mechanical resonator, i.e., $Q_m = \Omega_m/\Gamma_m$, determines the number of oscillations the resonbator undergoes before its amplitude decays by a factor e. In addition, its value categorizes the system as underdamped ($Q > 1/2$), critically damped ($Q = 1/2$) or overdamped ($Q < 1/2$). Fig. 2.6(a) depicts the behaviour of (2.22) for various values of the quality factor Q_m and evidences how in any case the resonator ends up being at its equilibrium position after a time $t \gg \Gamma_m^{-1}$.

If the mechanical resonator is driven by any external force, including any type of noise, like the one resulting from coupling to a thermal bath $F_{th}(t)$, the general solution to the equation of motion comprising the force term will be the sum of the solution to the homogeneous equation given in (2.22) and a particular solution. The particular solution is best found in the frequency domain. We define the Fourier transform of $x(t)$ via $x(\omega) = \int_{-\infty}^{\infty} x(t) e^{i\omega t} dt$, which leads to the following equation in frequency coordinates

$$-\omega^2 m_{eff} x(\omega) = -\Omega_m^2 m_{eff} x(\omega) - i\omega\Gamma_m m_{eff} x(\omega) + F_{th}(\omega) \tag{2.23}$$

which is now a simple algebraic expression. The generic mechanical susceptibility $\chi(\omega)$ of the mechanical resonator is

$$\chi(\omega) = \frac{1}{m_{eff}(\Omega_m^2 - \omega^2) - i\Gamma_m m_{eff}\omega} \tag{2.24}$$

such that $x(\omega) = \chi(\omega)F(\omega)$ and the full trajectory in time can be calculated as

$$x(t) = x_h(t) + \frac{1}{2\pi}\int_{-\infty}^{\infty} \chi(\omega) F(\omega) e^{-i\omega t} d\omega \tag{2.25}$$

where again constants A_o and ϕ_o set the initial conditions. Due to the decaying transient nature of $x_h(t)$, very often one ends up considering only the second term in (2.25), the one relevant for observation times $t > \Gamma_m^{-1}$. The response

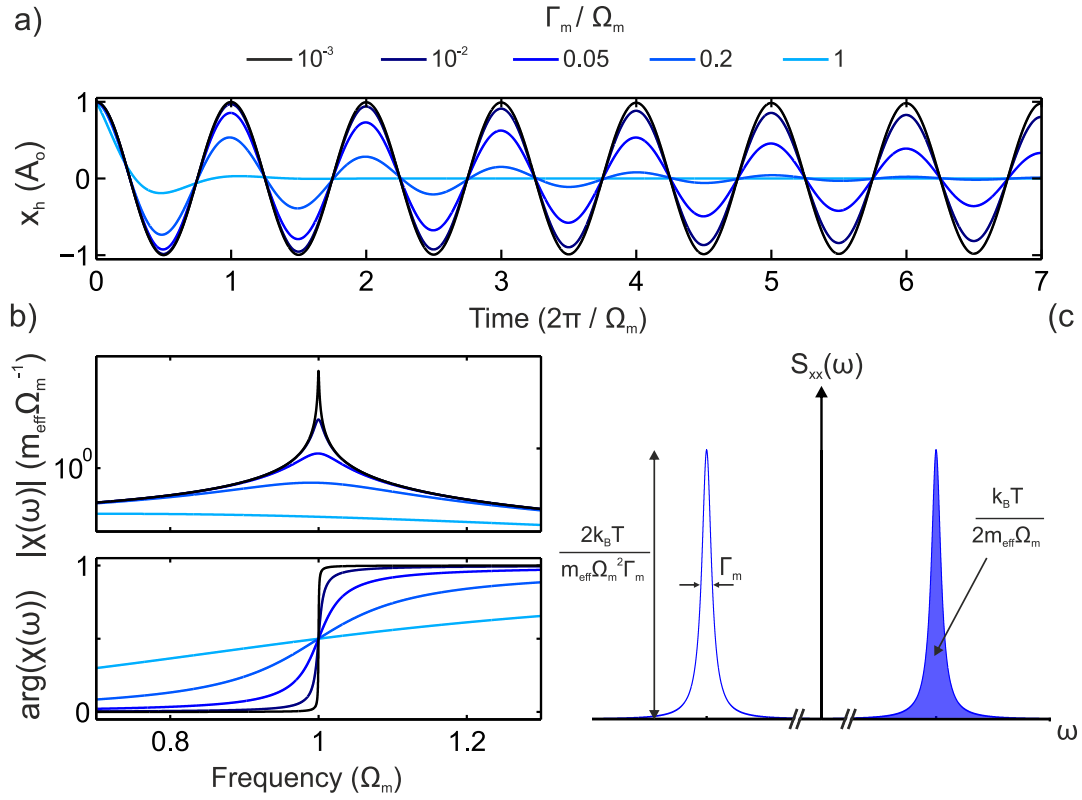

Figure 2.6: Free and forced mechanical resonator response. (a) Time-evolution of a damped free harmonic oscillator for different ratios of Γ_m/Ω_m. (b) Amplitude and phase response of a damped driven harmonic oscillator as a function of the drive frequency ω for the same values of Γ_m/Ω_m. (c) Power spectral density of a mechanical resonator in thermal equilibrium with a high-temperature bath at T. In the low-dissipation limit, i.e., $\Gamma_m \ll \Omega_m$, it corresponds to a pair of Lorentzian lineshapes centered at $\omega = \pm\Omega_m$, each of which contributes to one half of the variance $\langle x^2 \rangle$ due to thermal motion.

given by (2.24) can be approximated by a Lorentzian for high-Q_m ($\Gamma_m \ll \Omega_m$) mechanical oscillators as,

$$\chi(\omega) = \frac{1}{m_{eff}\Omega_m(2(\Omega_m - \omega) - i\Gamma)} \tag{2.26}$$

Figure 2.6(b) depicts the shape of $|\chi(\omega)|$ for several values of Q_m, evidencing that the oscillator responds with an intensity proportional to Q_m when driven at resonance ($\omega = \Omega_m$), while Fig. 2.6(c) shows how the phase of the resonator motion evolves from 0 to π across the resonance.

In the set of experiments described in this thesis, the mechanical resonator is solely driven by the optical field or by the thermal bath. The first driving force being null for $G = 0$, only the latter needs to be considered. We therefore want to solve Eq. (2.12b) with a force term $F_{th}(t)$ that is inherently stochastic. The resulting trajectory $x(t)$ obviously inherits the nature of the drive force and needs to be considered as a random process. When the force acting upon the mechanical resonator is the thermal Langevin force, the motion of a single harmonic oscillator in thermal equilibrium corresponds to an oscillating motion at frequency

Ω_m with time-varying amplitude and phase whose changes occur on a time scale given by the damping time Γ_m^{-1} [104]. Direct observation of the thermally-active trajectory of the mechanical resonator $x(t)$ is rare due to the simultaneous contribution of many normal modes. Observations are often done in the frequency domain via noise spectra, acquired in radiofrequency (RF) spectrum analyzers. In such apparatus, like in any measurement, one only measures over a given time τ or, equivalently, with a given bandwith. Given one particular realization of the trajectory $x(t)$ obtained during such time, the gated Fourier transform over τ is defined [105] as

$$x_\tau(\omega) = \frac{1}{\sqrt{\tau}} \int_0^\tau x(t) e^{i\omega t} dt \tag{2.27}$$

whose average over independent experimental runs leads to the gated power spectral density $\langle |x_\tau|^2 \rangle$, the quantity we measure with spectrum analyzers. The power spectral density of the signal $x(t)$ is therefore defined [105] as

$$S_{xx}(\omega) = \lim_{\tau\to\infty} \langle |x_\tau|^2 \rangle \tag{2.28}$$

From a theoretical standpoint, the main quantitiy of interest in a random process $x(t)$ is its autocorrelation function $R_{xx}(t,t') = \langle x(t')x(t) \rangle$. Since a mechanical oscillator in thermal equilibrium can be considered as a wide-sense stationary (WSS) process [106], i.e., there is no special time t in the first and second order moments of the process, the autocorrelation function can be written as $R_{xx}(t,t') = \langle x(t-t')x(0) \rangle \equiv \langle x(t)x(0) \rangle = R_{xx}(t)$. Fortunately, the Fourier Transform $R_{xx}(\omega)$ of the autocorrelation function, a theoretical quantity, can be connected to the experimentally-accesible expression (2.28) via the Wiener-Khinchin theorem [107]

$$S_{xx}(\omega) = R_{xx}(\omega) \tag{2.29}$$

for a WSS processes. With this relation, the area under the noise spectrum $(1/2\pi) \int_{-\infty}^{\infty} S_{xx}(\omega) d\omega$ yields the variance of the mechanical displacement $\langle x(0)^2 \rangle = \langle x(t)^2 \rangle = \langle x^2 \rangle$.

As the resonator is in thermal equilibrium, the classical fluctuation-dissipation theorem (FDT) relates the Fourier transform of the autocorrelation function $R_{xx}(\omega)$ to the dissipative part of the mechanical susceptibility introduced in (2.24),

$$R_{xx}(\omega) = 2\frac{k_B T}{\omega} \mathrm{Im}(\chi_m(\omega)) \tag{2.30}$$

which in the case of a high-Q_m resonator gives rise to two Lorentzian peaks of width Γ_m and central frequency $\omega = \pm\Omega_m$. The integral of such a lineshape is readily obtained, leading to the well-known equipartition theorem $\langle x^2 \rangle = k_B T / m_{eff} \Omega_m^2$ after using (2.29). This allows to calibrate the temperature T of the mechanical oscillator by integrating over the power spectral density $S_{xx}(\omega)$. Note that $R_{xx}(\omega)$ is a symmetric function and the real observable, which is composed of the spectrum folded back on itself, $\overline{R}_{xx}(\omega) = (R_{xx}(\omega) + R_{xx}(-\omega))/2$ retains this property. On the contrary, a generalization of the previous derivations to a quantum mechanical resonator taking the products of the Heisenberg operators $\langle \hat{x}(t)\hat{x}(0) \rangle$ and using the quantum FDT [108] leads to an asymmetric function due to the

non-commuting nature of $\hat{x}(t)$ and $\hat{x}(0)$. In that case, accessing $R_{xx}(\omega)$ requires a more advanced readout scheme where the positive and negative frequency components of the observable are determined separately. This was achieved in Ref [109] and the observed asymmetry used to prove the quantum nature of a mechanical oscillator close to its quantum ground state.

2.3.3 Optomechanical effects

So far we have considered the behaviour of the driven optical cavity and the mechanical resonator separately. We now set $G \neq 0$ and intend to solve simultaneously the equations in (2.12).

Static effects

We first search for the fixed points of the system $\{\overline{x}, \overline{a}\}$ in the absence of an external force. These are the points at which all time derivatives vanish and are given by the two relations

$$\overline{a} = \frac{-\sqrt{\kappa_l}\overline{a}_{in}}{i(\Delta + G\overline{x}) + \kappa/2} \tag{2.31a}$$

$$|\overline{a}|^2 = \frac{m_{eff}\Omega_m^2}{\hbar G}\overline{x} \tag{2.31b}$$

The phase of the complex cavity field $\overline{a}$ can always be adjusted via $\overline{a}_{in}$ in order to fulfill (2.31a). We can therefore multiply it by its complex conjugate $\overline{a}^*$ without loss of generality. The resulting implicit relations are plotted in Fig. 2.7(a) for different values of the normalized detuning Δ/κ, exhibiting the possibility of multiple fixed points. The existence of such values is conditioned to the inequality

$$|\overline{a}_{in}|^2 \geq \frac{\sqrt{3}\Omega_m^2 m_{eff}\kappa^3}{9\kappa_e \hbar G^2} \tag{2.32}$$

that is obtained by comparing the slope of the straight line (2.31b) to the maximum slope of the Lorentzian resulting from (2.31a). Above this power, the system may develop bistability, i.e., values of Δ for which two stable fixed points exist. These are represented as filled dots (•) in Fig. 2.7. In between these, an unstable fixed point develops. The unstable nature of such point is better understood if one considers the particular dynamic case when the light force reacts instantaneously to mechanical motion, i.e., the regime in which $\kappa \gg \Omega_m$. In the phase space representation of Fig. 2.7(a) this is a trajectory that always follows the Lorentzian photon number curve (dark blue). We can restrict ourselves to trajectories exactly along the nullcline. In that case, the equation of motion for the mechanical resonator sees a radiation pressure force $F_{rp}(x)$ that depends on its position via the steady-state intracavity photon number $\overline{n}(x)$ as

$$F_{rp}(x) = \hbar G\overline{n}(x) = \frac{\hbar G\kappa_\ell |\overline{a}_{in}|^2}{(\kappa/2)^2 + (\Delta + Gx)^2} \tag{2.33}$$

which is then a conservative force deriving from a light-induced potential $V_{rp}(x)$

$$V_{rp}(x) = 2\hbar\frac{\kappa_\ell}{\kappa}|\overline{a}_{in}|^2 \mathrm{atan}\left(\frac{2(\Delta + Gx)}{\kappa}\right) \tag{2.34}$$

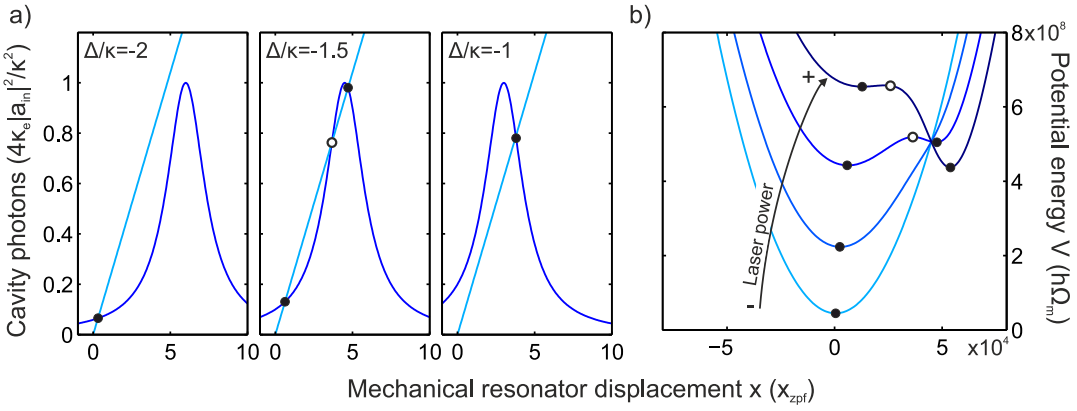

Figure 2.7: Static optomechanical effects. (a) Graphic representation of the fixed points $\{\overline{x}, \overline{a}\}$ of the driven ptomechanical system for different detunings Δ/κ. These are obtained as the intersection of (2.31a) and (2.31b), given with dark and light blue solid lines. Filled (empty) circles represent stable (unstable) solutions. The unstable fixed point is better understood in the limit $\Omega_m \ll \kappa$, where the number of photons adiabatically follows the mechanical displacement. In that case, the radiation pressure force F_{rp} derives from a potential, which added to the harmonic oscillator potential leads to the energy landscape shown in (b) for different input powers P_{in}.

that needs to be added to the bare harmonic potential $V_m(x) = (1/2)m_{eff}\Omega_m^2 x^2$. The overall potential landscape in which the mechanical degree of freedom evolves is depicted in Fig. 2.7(b) for different values of the laser field $\overline{a}_{in}$. Above some threshold power the system develops into a double-well potential, evidencing the presence of the two aforementioned stable fixed points and the presence of an unstable fixed point in between the two local minima. Under other less restrictive conditions, the stability of these points may be lost. This bistability has been observed with a micromirror OM system [110] and manifests itself in a hysteretic behaviour of a transmission curve upon direct/reverse scanning of either the input power or the detuning. The addition of $V_{rp}(x)$, as evidenced in Fig. 2.7(b), also leads to a change in the curvature at the minimum of the potential, thus changing the effective spring constant. This effect is derived later.

Dynamic effects

We now analyze the dynamical reponse of the system evolving around a stable fixed point $\{\overline{x}, \overline{a}\}$ satisfying (2.31a) and (2.31b). We first numerically solve the equations of motion (2.12) starting from an initial position $\{\overline{x} + \delta x, \overline{a}\}$ in close proximity to the fixed point and observe the evolution of the mechanical resonator when the cavity is driven. What one observes for a large fraction of phase space is that the mechanical resonator returns back to the equilibrium fixed point as a free damped mechanical resonator, whose evolution is shown in Fig. 2.6, with modified dissipation rate Γ_m and modified resonance frequency Ω_m. In Fig. 2.8(a) the trajectory of a mechanical resonator with and without the laser driving the optical cavity are depicted, where the fixed position $\overline{x}$ is taken as the zero reference.

For clarity, the curves have been shifted to start with a common phase reference and normalized in amplitude to their value at time $t = 0$. For a negative detuning (top panel), there is an exponential decay with an increased dissipation rate Γ_m, as can be seen by the the fastest decay of the driven OM system (light blue) compared to the free mechanical resonator (black). The change in the resonance frequency is less evident, but careful look at times $t \gg \Gamma_m^{-1}$ show that a small phase mismatch is present, a consequence of the modified spring constant in the potential resulting from the radiation pressure force. When driven on the blue-side, i.e., $\Delta > 0$, the influence on the damping Γ_m is inverted and the OM system decays slower than the bare mechanical resonator. A simple thermodynamical picture displaying the underlying mechanism behind the modified friction force is shown in Fig. 2.8(b). When the cavity is red detuned and the equilbrium position $\overline{x}$ lies somewhere on the rising slope of the steady-state radiation-pressure force (2.33), putting the resonator into motion by a small momentum transfer leads to a radiation-pressure force that is smaller than the steady-state force due to the time-lag associated to the cavity decay or build-up rate κ. After this instantaneous kick, the resonator follows the curve depicted by the arrow, along which the light-induced radiation-pressure force is doing negative work since $\oint_S F \cdot dx < 0$. Therefore, the work done during one oscillation, i.e., the area swept in the force-displacement diagram, leads to additional damping of the mechanical resonator. On the other side of the optical resonance, the thermodynamic picture is inverted and the work done by the radiation-pressure leads to antidamping. In that case, the level of antidamping can even surpass the natural decay rate of the mechanical resonator, leading to self-sustained oscillation, as we see later.

To understand the dynamics obtained via direct numerical integration of the equations it is instructive to linearize them. We assume that the system undergoes small excursions $\delta a(t)$ and $\delta x(t)$ out of the equilibrium position and set $a(t) = \overline{a} + \delta a(t)$, $x(t) = \overline{x} + \delta x(t)$. Plugging these expressions into (2.12) and discarding second-order terms one finds

$$\frac{d\delta a(t)}{dt} = i(\Delta + G\overline{x})\delta a(t) - \frac{\kappa}{2}\delta a(t) + iG\overline{a}\delta x(t) \tag{2.35a}$$

$$\begin{aligned} m_{eff}\frac{d^2\delta x(t)}{dt^2} = &-m_{eff}\Omega_m^2\delta x(t) - m_{eff}\Gamma_m\frac{d\delta x(t)}{dt} \\ &+ \hbar G\overline{a}(\delta a(t) + \delta a^*(t)) + F(t) \end{aligned} \tag{2.35b}$$

where both (2.31a) and (2.31b) are used and we have set $\overline{a} \in \mathbb{R}$, i.e., $\overline{a} = \overline{a}^*$, which can be done due to the free phase of the driving laser term $\overline{a}_{in}$. The solution to this system of equations is easier in the frequency domain, so we Fourier transform the set of equations to obtain

$$-i\omega\delta a(\omega) = i(\Delta + G\overline{x})\delta a(\omega) - \frac{\kappa}{2}\delta a(\omega) + iG\overline{a}\delta x(\omega) \tag{2.36a}$$

$$\begin{aligned} -m_{eff}\omega^2\delta x(\omega) = &- m_{eff}\Omega_m^2\delta x(\omega) - im_{eff}\Gamma_m\omega\delta x(\omega) \\ &+ \hbar G\overline{a}(\delta a(\omega) + \delta a^*(\omega)) + F(\omega) \end{aligned} \tag{2.36b}$$

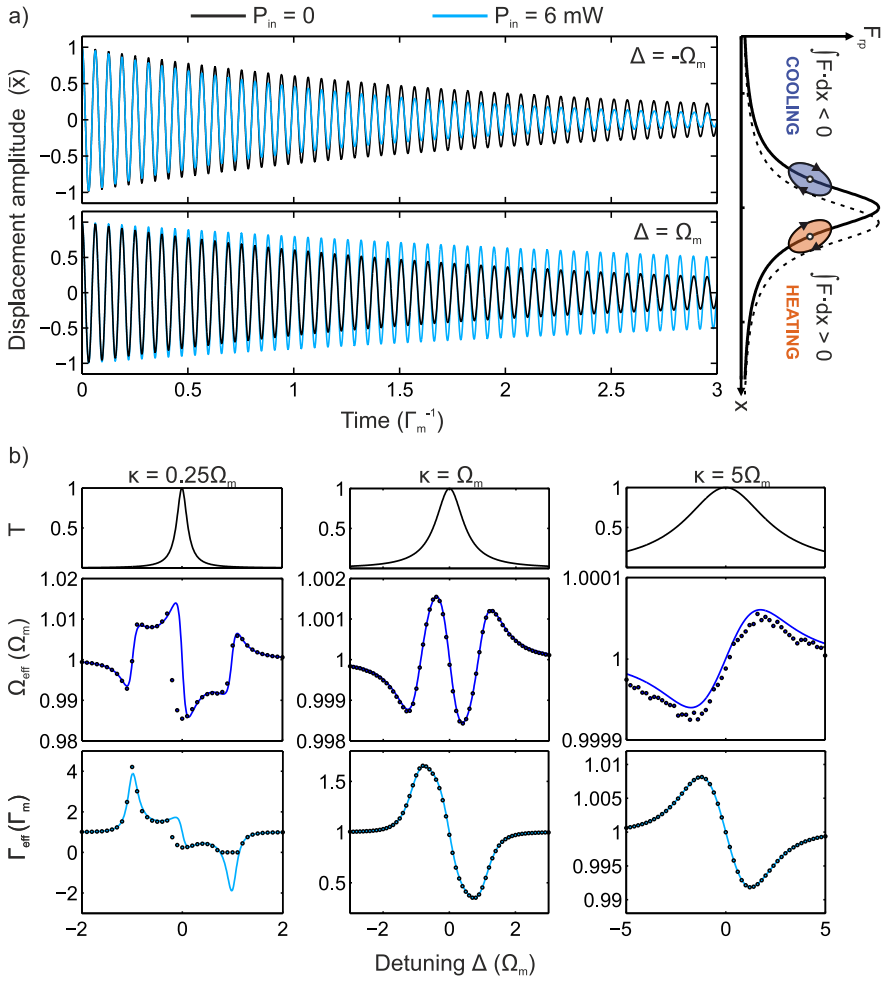

Figure 2.8: Dynamic optomechanical effects. The effect of radiation pressure force on the dynamics of the mechanical resonator depend on the sign of the detuning Δ. On the red-detuned side, i.e., $\Delta > 0$, the backaction of the light field on the mechanical resonator leads to an increased damping and a frequency shift, while it leads to antidamping on the blue side. This is shown for $\Delta = \pm\Omega_m$ from direct numerical integration of 2.12 with a mechanical oscillator displaced from its equilbrium position $\overline{x}$ at time t=0 and left to evolve while the optical cavity is simultaneously driven. (b) Optomechanical spring effect and damping for different sideband resolutions (Ω_m/κ) as obtained from fitting the numerically-integrated displacement with (2.22) (points) and as given from the predictions (2.40a) and (2.40b) obtained from the linearized optomechanical equations of motion.

Using the Fourier transform property $\delta a^*(\omega) = (\delta a(\omega))^*$ and (2.36a) we find

$$\delta a(\omega) = \frac{iG\overline{a}}{-i(\Delta + G\overline{x} + \omega) + \frac{\kappa}{2}}\delta x(\omega) \tag{2.37a}$$

$$\delta a^*(\omega) = \frac{-iG\overline{a}}{i(\Delta + G\overline{x} - \omega) + \frac{\kappa}{2}}\delta x(\omega) \tag{2.37b}$$

Here, the displacement field $x(t)$ acts as a modulator, spectrally resulting in the generation of sidebands to the cavity field at frequencies $\omega_\ell \pm \omega$. These

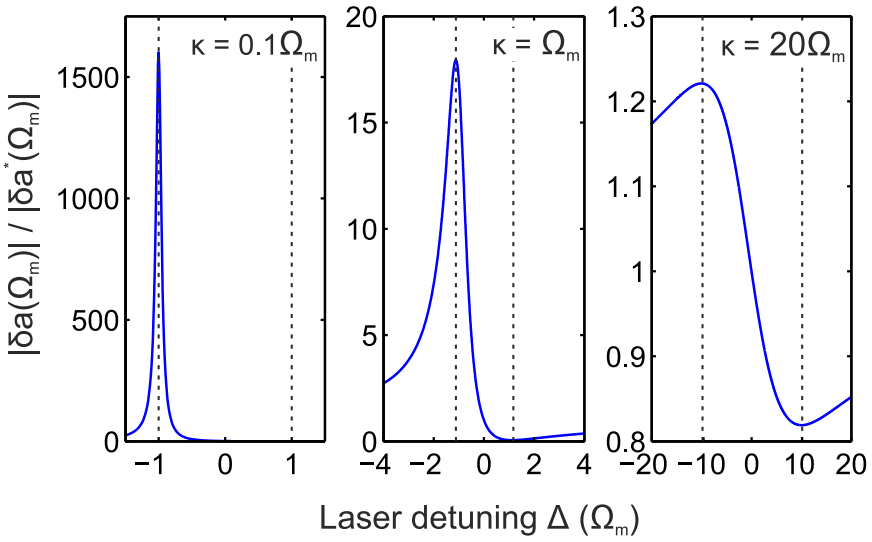

Figure 2.9: Optomechanical sideband asymmetry. Ratio of the Stokes and anti-Stokes sidebands at Ω_m for different levels of sideband resolution κ/Ω_m.

sidebands are weighted with a Lorentzian lineshape, where the detuning Δ enhances or supresses either the Stokes (2.37a) or the anti-Stokes (2.37b) sideband. The mechanical resonator typically has a peaked response $\delta x(\omega)$ at a frequency $\omega = \Omega_m$ and it suffices to evaluate there. Fig. 2.9 depicts the sideband asymmetry $|\delta a(\Omega_m)|/|\delta a^*(\Omega_m)|$ as a function of the detuning, where for simplicity we set $\Delta = \overline{\Delta} = \Delta + G\overline{x}$. The largest asymmetry is found for $\Delta = \pm\sqrt{\Omega_m^2 + (\kappa/2)^2}$, i.e., the highest unbalance depends on the ratio κ/Ω_m. When the generated sidebands at Ω_m are spectrally resolved with respect to the cavity itself, i.e., the sideband-resolved regime ($\Omega_m \gg \kappa$), the highest asymmetry happens at $\Delta \sim \pm\Omega_m$. This case is shown in the leftmost panel of Fig. 2.9. When the sidebands are not resolved, i.e., the sideband-unresolved regime ($\Omega_m \ll \kappa$), the highest asymmetry occurs at $\Delta \sim \pm\kappa/2$.

The induced intracavity energy modulation gives rise to an oscillating light-induced force $F_{rp}(\omega) = \hbar G\overline{a}(\delta a(\omega) + \delta a^*(\omega))$ called dynamical backaction, that can be expressed as originating from the displacement by using (2.37a) and (2.37b). If we substitute for $x(t)$ in the frequency-domain, i.e., Eq. (2.36b), we see that the dynamical response of the mechanical oscillator to the external force $F(t)$ changes to

$$\begin{aligned}\delta x(\omega) &= \frac{F(\omega)}{m_{eff}(\Omega_m^2 + \Omega_{om}^2(\omega) - \omega^2) - i\omega m_{eff}(\Gamma_m + \Gamma_{om}(\omega))} \\ &= \chi_{m,eff}(\omega)F(\omega)\end{aligned} \tag{2.38}$$

with

$$\Omega_{om}^2(\omega) = \frac{\hbar G^2|\overline{a}|^2}{m_{eff}}\left(\frac{\overline{\Delta}+\omega}{(\overline{\Delta}+\omega)^2 + (\kappa/2)^2} + \frac{\overline{\Delta}+\omega}{(\overline{\Delta}-\omega)^2 + (\kappa/2)^2}\right) \tag{2.39a}$$

$$\Gamma_{om}(\omega) = \frac{\hbar G^2|\overline{a}|^2}{2m_{eff}\omega}\left(\frac{\kappa}{(\overline{\Delta}+\omega)^2 + (\kappa/2)^2} - \frac{\kappa}{(\overline{\Delta}-\omega)^2 + (\kappa/2)^2}\right) \tag{2.39b}$$

With the above ω-dependent expressions for the OM spring constant $m_{eff}\Omega_{om}(\omega)^2$ and damping Γ_{om}, the effective susceptibility has a non-Lorentzian line shape. By using the relation $\hbar G^2 = 2m_{eff}\Omega_m g_o^2$, with g_o as introduced in Section 2.2, and defining a new coupling rate by $g = g_o|\overline{a}|^2$, the laser-enhanced OM coupling rate, expressions (2.39a) and (2.39b) can be further simplified. When the laser drive is weak ($g \ll \kappa$), one can evaluate them at the unperturbed oscillation frequency $\omega = \Omega_m$. Then, the mechanical oscillator effectively behaves like a damped harmonic oscillator with resonance frequency and damping given by

$$\Omega_{eff}^2 = \Omega_m^2 + 2\Omega_m g_o^2|\overline{a}|^2 \left(\frac{\overline{\Delta} + \Omega_m}{(\overline{\Delta} + \Omega_m)^2 + (\kappa/2)^2} + \frac{\overline{\Delta} - \Omega_m}{(\overline{\Delta} - \Omega_m)^2 + (\kappa/2)^2} \right) \tag{2.40a}$$

$$\Gamma_{eff} = \Gamma_m + g_o^2|\overline{a}|^2 \left(\frac{\kappa}{(\overline{\Delta} + \Omega_m)^2 + (\kappa/2)^2} - \frac{\kappa}{(\overline{\Delta} - \Omega_m)^2 + (\kappa/2)^2} \right) \tag{2.40b}$$

The magnitude of Γ_{om} and Ω_{om} are determined by multiple device parameters like the OM coupling rate g_o or the optical decay rate κ. However, the operating conditions, $\overline{\Delta}$ and P_{in}, which enters the expressions via $|\overline{a}|^2$, allow controlling the overall behaviour, in particular the sign. The solid lines in Fig. 2.8(b) plot the effective oscillation frequency and damping rate of an OM system at various levels of sideband-resolution κ/Ω_m. The effective parameters of the mechanical resonator obtained via the linearized system quantitatively reproduce the results obtained upon numerical integration of the dynamical equations, even up to values where Γ_{eff} is very close to zero, where self-sustained oscillations are expected to happen since any perturbation blows up in time until the non-linearities of the system saturate the signal amplitude. Whenever $\Gamma_{eff} < 0$, the time trace does not decay exponentially, as the bottom panel in Fig. 2.8(b) shows for $\kappa = 0.25\Omega_m$. The linear approximation also fails within the optical resonance red-detuned flank, since the condition $g \ll \kappa$ does not hold.

2.4 Mechanical amplification

The work done by radiation-pressure can lead to amplification or damping of the mechanical mode, effectively heating or cooling the resonator when this is coupled to a hot environment. This process leads to a thermal state with a modified effective temperature T_{eff} [20]. On the blue-side, amplification can be strong enough to induce OM self-oscillation, where these thermal fluctuations blow up. However, the system requirements to reach the self-sustained oscillation state are quite restrictive in terms of device parameters and operating conditions, specially at low frequencies where operation in the sideband-resolved regime is extremely complicated due to limitations imposed by fabrication disorder on the achievable optical quality factors Q. The onset of optical non-linearities as described in Subsection 2.3.1 can lead to dynamical solutions of the optical cavity that are self-sustained oscillating solutions. This phenomenon is very often seen as detrimental, since it prevents operation of a resonant photonic device at a fixed cavity-laser detuning Δ. Here, we exploit these non-linearities and their intercoupling with the mechanical degrees of freedom to unveil another mechanism for mechanical

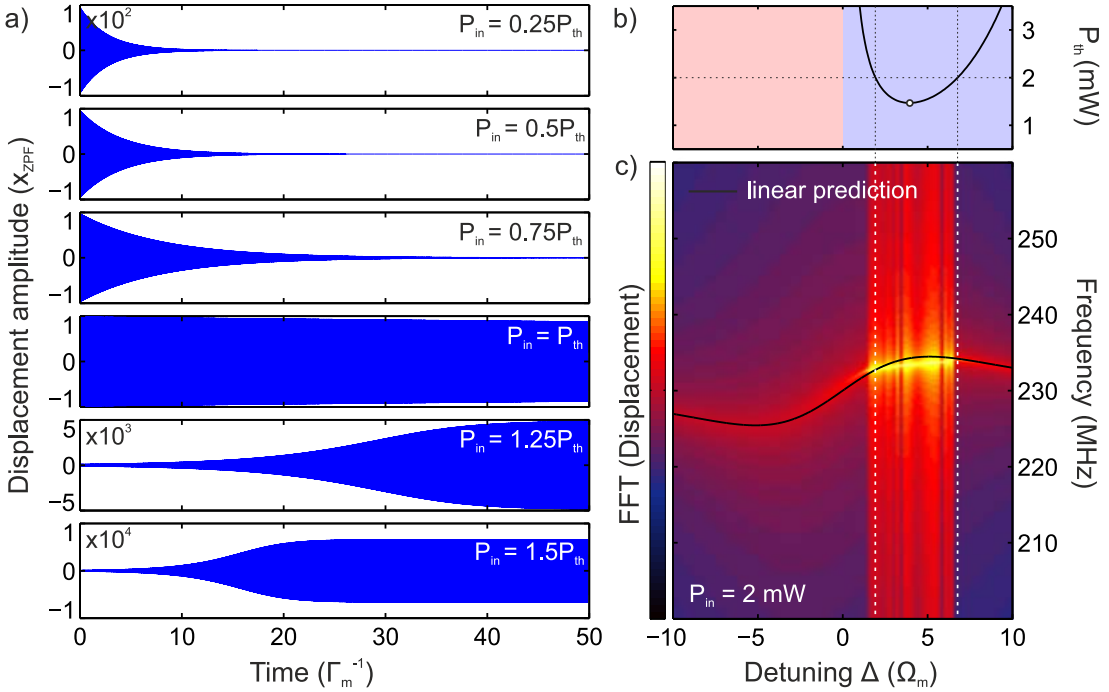

Figure 2.10: Optomechanical oscillation via dynamical backaction. (a) Numerically obtained displacement amplitude of a mechanical resonator coupled to a driven optical cavity after displacing it from its fixed position $\overline{x}$. The time traces are given for different input powers as a function of the threshold powe P_{th} given by Eq. (2.41). Above P_{th}, optomechanical oscillations are evidenced by the stable high-amplitude displacement. (b) P_{th} as a function of cavity-to-laser detuning Δ. (c) Spectral map of the Fast Fourier Transform (FFT) of the obtained numerical traces as a function of Δ. The solid black line gives the prediction of the linearized system (Eq. (2.40a)). The vertical dashed lines across (b) and (c) delimit the detuning region where $P_{in} = 2$ mW $\geq P_{th}$.

lasing. This type of OM oscillation requires much less stringent conditions on the OM system parameters and it can be effectively used to have low-noise coherent phonon sources [96]. These two ways to achieve OM oscillation obviously coexist in an OM system based on silicon, as will be shown in Chapter 5, but are here independently discussed for the sake of clarity.

2.4.1 Dynamical backaction

As explained in Subsection 2.3.3, a blue detuned laser reduces the effective damping of the mechanical resonator. Whenever the optomechanically-induced damping Γ_{om} completely cancels out the intrinsic Γ_m, the fixed point $\{\overline{x}, \overline{a}\}$ becomes unstable and a limit cycle develops around it. The approximate condition for the onset of self-sustained oscillations can be derived in the framework of the linearized equations by imposing $\Gamma_{om} = -\Gamma_m$, with the first taken as (2.39b). After some algebraic manipulation to introduce the input power P_{in}, the power

threshold condition reads

$$P_{th} = -\Gamma_m \frac{\hbar\omega_l\omega}{\Omega_m g_o^2}\left(\frac{(\kappa/2)^2+\overline{\Delta}^2}{\kappa_l}\right)\left(\frac{\kappa}{(\overline{\Delta}+\omega)^2+(\kappa/2)^2}-\frac{\kappa}{(\overline{\Delta}-\omega)^2+(\kappa/2)^2}\right)^{-1} \tag{2.41}$$

where we have kept the explicit frequency dependence that was set to $\omega = \Omega_m$ in (2.40). We will see that Ω_{eff} as given in (2.40a) roughly holds even when $\Gamma_{eff} < 0$, so we set here $\omega \equiv \omega_{osc} = \Omega_{eff}$ to be the frequency already modified due to the optical stiffening, with which Eq. (2.41) becomes implicit since Ω_{eff} depends on the input power. We show in Fig. 2.10(a) the temporal trace of the mechanical displacement $x(t)$ obtained from numerical integration of (2.12) with a presrcibed small perturbation δx from the fixed point $\{\overline{x}, \overline{a}\}$ as an initial condition. This is done for different powers given as a fraction of P_{th} for an OM system with the following parameters: $\omega_o = 2\pi\cdot$ 187 THz, $\kappa_i = 2\pi \cdot 2.42$ GHz, $\kappa_e = 2\pi \cdot 1.6$ GHz, $\Omega_m = 2\pi\cdot$ 230 MHz, $\Gamma_m = 2\pi\cdot$ 1.2 MHz, $g_o = 2\pi\cdot$ 200 kHz. Whenever $P_{in} > P_{th}$, high amplitude coherent mechanical oscillations are activated and their trajectory can be very well approximated by a sinusoidal shape once the steady-state is reached [111,112]. The detuning Δ in panel (a) is chosen such that the power threshold P_{th} is minimal. That precise point is higlighted in Fig. 2.10(b), where P_{th} is given as a function of detuning. Fig. 2.10(c) provides the FFT of the temporal transmission trace obtained when sweeping the laser-cavity detuning from the blue-detuned side. The solid black line highlights the prediction (2.40a) of the linearized theory. While this prediction agrees very well with the FFT peak whenever the OM oscillation is not reached, the oscillation frequency seems to evolve linearly within the lasing bandwith rather than follow the black curve, something that is observed in Chapter 5.

2.4.2 Intrinsic optical non-linearities

The non-linear behaviour of a strongly driven optical cavity made of silicon has been described in Section 2.3.1, evidencing the existence of thermal/free-carrier self oscillations, i.e., self-pulsing, that lead to a strongly anharmonic modulation of the intracavity photon number $\overline{n}(t)$ (see Fig. 2.4(d)). If the driven optical cavity is dispersively coupled to a mechanical resonator and the SP is active, the photon modulation results in a comb-like radiation pressure force $F_{RP} = \hbar G\overline{n}(t)$. As would happen with any driven harmonic oscillator, we expect a modulated force close to the mechanical resonator frequency Ω_m to drive its motion with a response proportional to the mechanical susceptibility $\chi_m(\omega)$ given by (2.24). Due to the highly anharmonic nature of the optical force $F_{RP}(t)$, many of the SP harmonics M may drive its motion; whenever $\nu_{SP} \sim \Omega_m/M$ with $M \in \mathbb{N}$. When this is achieved with one of the first high-amplitude SP harmonics, the dispersive effect of the activated motion on the optical frequency via G provides enough feedback to the cavity dynamics and leads to self-sustained motion.

If we assume $\Omega_m \ll \kappa$ and a moderate value of g_o, we can rule out the dynamical backaction effects previously described and consider the response of the intracavity photons $n(t)$ to deformation to be adiabatic, as done in Subsection 2.3.1 for the free-carriers N_e and temperature ΔT. Under such asumptions,

the system of equations governing the dynamics of the OM system is given by,

$$\frac{dN_e(t)}{dt} = -\gamma_{fc}N_e(t) + \frac{1}{2}\frac{c^2}{n_{Si}^2}\frac{\beta_{TPA}\hbar\omega_l\overline{n}(t)^2}{V_{TPA}} + \frac{c}{n_{Si}}\frac{\alpha_{lin}\overline{n}(t)}{R_{eff}} \tag{2.42a}$$

$$\frac{d\Delta T(t)}{dt} = -\gamma_{th}\Delta T(t) + \frac{\hbar\omega_l\overline{n}(t)}{\rho_{Si}C_{p,Si}V_{eff,T}}\left(\frac{c^2}{n_{Si}^2}\frac{\beta_{TPA}\hbar\omega_l\overline{n}(t)}{V_{TPA}} + \frac{c}{n_{Si}}\frac{\sigma_r N_e(t)}{V_{FCA}} + \frac{c}{n_{Si}}\frac{\alpha_{lin}}{R_{eff}}\right) \tag{2.42b}$$

$$m_{eff}\frac{d^2x(t)}{dt^2} = -m_{eff}\Omega_m^2 x(t) - m_{eff}\Gamma_m\frac{d}{dt}x(t) + \hbar G\overline{n}(t) \tag{2.42c}$$

with the adiabatic photon number $\overline{n}(t)$ and the detuning Δ given by

$$\overline{n}(t) = \frac{\kappa_\ell}{(\kappa/2)^2 + \Delta(t)^2}\frac{P_{in}}{\hbar\omega_\ell} \tag{2.43a}$$

$$\Delta(t) = \omega_\ell - \left(\omega_o - \frac{\omega_o}{n_{Si}}\frac{\sigma_i N_e(t)}{V_{FCA}} + \frac{\omega_o}{n_{Si}}n_T\Delta T(t) - Gx(t)\right) \tag{2.43b}$$

We solve numerically the system of equations using the same set of parameters employed to obtain the colormap of Fig. 2.5(b). The mechanical resonator dynamics are solved for a resonator of effective mass $m_{eff} = 5$ pg, frequency $\Omega_m/2\pi$ = 54.6 MHz, $\Gamma_m/2\pi$ = 0.1 MHz and coupling given by $G/2\pi$ = 0.76 THz/nm, which corresponds to $g_o/2\pi$ = 175 kHz. Fig. 2.11(a) compares the spectral map obtained in the presence/absence of the mechanical resonator. While the left map reproduces the one in Fig. 2.5, the right map evidences both wavelength regions where the dynamic solution corresponds to SP and matches the one seen for g_o = 0 and others where the frequency of the limit cycle does not change with the laser wavelength. These result in the sharp plateaus of the right panel. The frequency of the first harmonic in these regions corresponds to $2\pi\nu = \Omega_m/M$, i.e., the SP drives the mechanical motion and the two oscillators are frequency-entrained due to the OM feedback. The simulated temporal transmission traces in these plateaus are shown in Fig. 2.11(b) at the wavelengths highlighted with dashed lines in panel (a). The displacement of the mechanical resonator is also provided with a solid blue line in the case $G \neq 0$. The observed transmission traces qualitatively agree with those of pure SP (see Fig. 2.4) at a frequency ν_{SP} with the superposition of an additional sinusoidal component at $\nu = M\nu_{SP}$ resulting from the activated mechanical motion. The fact that the mechanical oscillations do not decay at all inside a cycle of the SP implies that the driving strength overcomes the mechanical dissipation Γ_m, leading to mechanical lasing. The appearance of abrupt plateaus seen in (a) precisely result from the onset of mechanical lasing. If self-oscillation is not achieved, the SP follows its natural evolution $\nu_{SP}(\lambda)$ and merely activates mechanical motion at its own frequency with an amplitude proportional to $\chi_m(\nu_{SP})$.

The mechanism to generate coherent mechanical oscillations described here operates deeply in the unresolved-sideband regime ($\kappa \gg \Omega_m$) and therefore represents a viable solution to generate and feed phonons to waveguides or membranes. The relatively low standards in terms of system parameters make coherent phonon generation readily available to researchers not having access to state-of-the-art

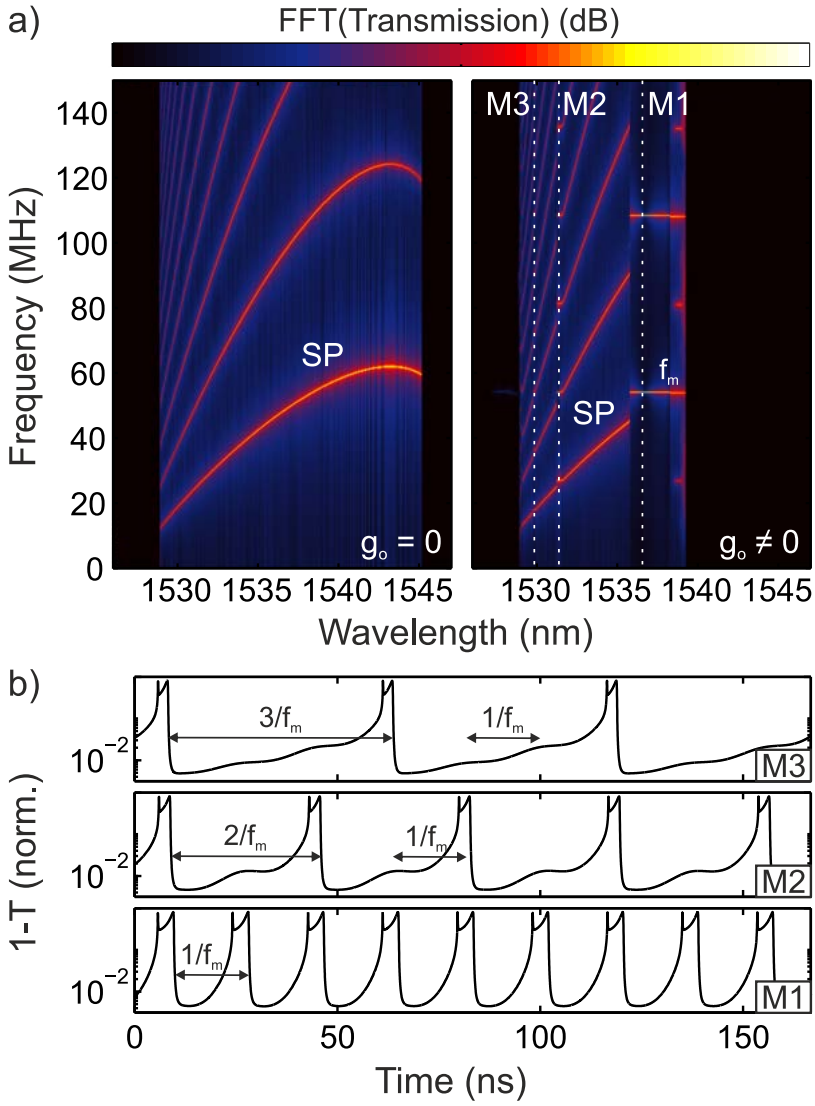

Figure 2.11: Self-pulsing (SP) driven mechanical lasing. (a) Numerically-obtained spectral maps as a function of laser wavelength with (left) $g_o = 0$ and (right) $g_o = 2\pi \cdot 175$ kHz, for a driven optical cavity with parameters as in Fig. 2.5. The effect of having the optical cavity undergoing SP dispersively coupled to a mechanical resonator is to activate mechanical lasing whenever $\nu_{SP} \sim f_m/M$, where M is the harmonic of the optical force driving the motion. This leads to the plateaus shown in the right panel. The mechanical resonant frequency is marked with f_m and the vertical dashed lines mark the $M = 3$, $M = 2$ and $M = 1$ mechanical lasing states, the transmission temporal traces of which are given in (b).

fabrication facilities and experimental setups. In addition, we have recently evaluated the phase noise of such type of phonon sources and shown how to control it via injection-locking to an external RF tone [113].

2.5 Mechanical motion detection

The dispersive coupling of the optical cavity mode and the mechanical resonator motion via the OM coupling rate G allows precise monitoring of mechanical motion via the reflected or transmitted light, with measurement imprecision that has reached the standard quantum limit of weak continuous measurements [114]. This limit can even be beaten by using alternative measurement schemes belonging to the family of quantum non-demolition (QND) measurements, like single quadrature measurements or single-photon-assisted phonon counting. In this thesis, mechanical motion is detected using the most basic and direct detection scheme, in which the amplitude of the outcoupled light is continuously measured with a fast photoreceiver. We provide here the basic steps that lead to the measured power spectral densities.

Given the detuning $\Delta = \omega_\ell - (\omega_o - Gx(t)) \equiv \Delta_0 + Gx(t)$, the mechanical motion state can be obtained from any of the scattering properties of the system which depends on Δ. If one considers a small oscillation of the mechanical resonator, the effect on the transmitted light is proportional to its derivative with respect to the bare detuning Δ_0 as

$$T(t,\Delta) = T(\Delta_0) + \left.\frac{dT}{d\Delta}\right|_{\Delta=\Delta_o} \frac{d\Delta}{dx(t)} x(t) = T(\Delta) + \frac{dT}{d\Delta} G x(t) \tag{2.44}$$

where we have considered that there is no backaction of the light field on the mechanical motion. Expression (2.44) comprises the steady-state DC value one measures with a slow photodetector (see Fig. 2.3) and a time-dependent term proportional to both the coupling rate G and the derivative of the transmission lineshape, the last given by

$$\frac{dT}{d\Delta} = \frac{\Delta\kappa_e \left(\kappa - \frac{\kappa_e}{2}\right)}{\left(\Delta^2 + \left(\frac{\kappa}{2}\right)^2\right)^2} \tag{2.45}$$

where we have used Eq. (2.16a) for a bi-directionally coupled cavity.

Figure 2.12 diagramatically shows the mechanism to detect mechanical motion and plots the derivative $\frac{dT}{d\Delta}$, where we have set $\kappa_e/\kappa = 0.4$ and both axis are given normalized to κ. The depicted curve shows that the OM transduction of mechanical motion is optimal at two very precise detunings, i.e., $\Delta = \pm\frac{1}{2\sqrt{3}}\kappa$ and is null exactly at resonance with the optical mode, i.e., $\Delta = 0$. This last property is unfortunate since $\Delta = 0$ corresponds to the detuning for which dynamical backaction effects, as given by Eqs. (2.39a) and (2.39b), are ruled out and backaction-evading measurements can be done. However, phase sensitive detection schemes like homodyne detection have maximum sensitivity at $\Delta = 0$ since the derivative of the transmitted/reflected phase is maximal. With expression (2.45), we can now calculate the total modulated power due to the coherent mechanical motion $x(t)$ to be

$$P_m(t) = P_{in}\frac{dT}{d\Delta} G x(t) = 2\hbar\omega_\ell G |a_{in}|^2 \frac{\Delta\kappa_e \left(\kappa - \frac{\kappa_e}{2}\right)}{\left(\Delta^2 + \left(\frac{\kappa}{2}\right)^2\right)^2} \tag{2.46}$$

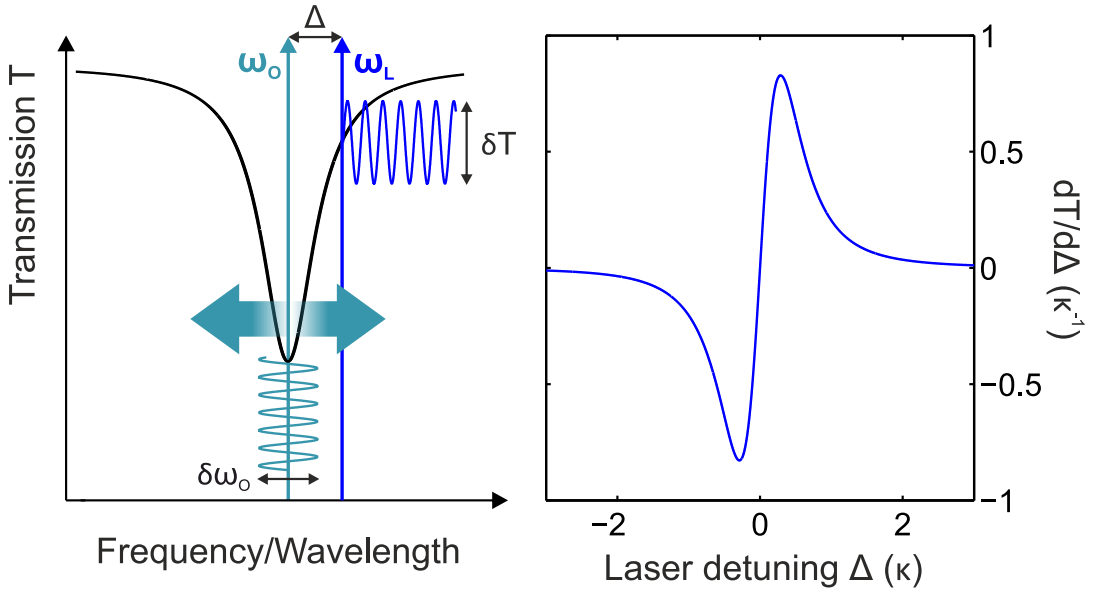

Figure 2.12: Optomechanical transduction of motion.

The optical power $P_m(t)$ is measured on a photodetector, leading to a voltage $V_m(t) = \eta_{det} G_{det} P_m(t)$, where we have introduced the detector efficiency η_{det} and its transimpedance gain G_{det}. The photodetector signal is then fed to an electronic spectrum analyzer (ESA), which measures the electrical power $P_e = \langle V_m(\omega)^2 \rangle / R$, with R the characteristic impedance of the detector. The measured signal is therefore

$$P_{ESA}(\omega) = 2 \left(\frac{\eta_{det} G_{det}}{\sqrt{R}} \right)^2 G^2 \hbar \omega_\ell |a_{in}|^4 \left(\frac{dT}{d\Delta} \right)^2 \langle x(\omega)^2 \rangle \tag{2.47}$$

As we can obtain the variance from integrating over the power spectral density, we can write the measured power spectral density as

$$S_{PP}(\omega) = 2 \left(\frac{\eta_{det} G_{det}}{\sqrt{R}} \right)^2 G^2 \hbar \omega_\ell |a_{in}|^4 \left(\frac{dT}{d\Delta} \right)^2 S_{xx}(\omega) \tag{2.48}$$

where the expression for $S_{xx}(\omega)$ for the resonator in thermal equilibrium is given in (2.30). This is the signal we measure in our spectrum analyzer.

2.6 Summary

The main conceptual developments of the chapter and how they relate to the results provided in Chapters 4 and 5 are given. These are:

- Spectrally and spatially confined light in the form of an optical cavity enhances the interaction with the mechancial modes of the structure. The interaction of a particular optical cavity / mechanical mode pair is weighted by the vacuum optomechanical coupling rate g_o, which also determines the accuracy with which its motional state can be measured when the optical

cavity is driven (Section 2.5). In Chapters 4 and 5, we show (both numerically and experimentally) how the light and acoustic fields spontaneously localize in a periodic-on-average nanostructure. The achievable g_o in such a regime is studied for intentionally disordered superlattices (Chapter 4) and for dual photonic/phononic crystal waveguides in the presence of unavoidable fabrication disorder (Chapter 5). By optically driving such random cavities, they become an accesible read-out mechanism for phonon spectroscopy, a key ingredient to observe mechanical Anderson localization and to understand phonon transport in disordered nanostructures.

- In addition to mechanical motion read-out, driving the optical cavity enables the manipulation of the motional state, as described in Subsection 2.3.3. On the blue-side of the optical resonance, amplification up to optomechanical self-oscillation (Subsection 2.4.1), i.e., mechanical lasing, can be achieved. In Chapter 5 dynamical backaction effects obeying the laws here derived is observed.

- The optical input power P_{in} is a key knob to explore the physics that derive from the OM coupling. However, high drive powers in low-V/high-Q optical cavities activate material non-linearities, which can lead to self-triggered optical oscillations, i.e., self-pulsing (Subsection 2.3.1), even before any OM effect sets in. In Chapter 5 these oscillations are observed. When these oscillations coexist with a highly-coupled MHz mechanical mode, the resulting modulated radiation pressure force can also be used to drive OM oscillations (Subsection 2.4.2). This regime, i.e., self-pulsing driven mechanical lasing, is also explored in Chapter 5.

Chapter 3

Confining light and motion in photonic and phononic crystals

In this background chapter, we discuss the basic propagation properties of electromagnetic and elastic waves in periodic structures in order to understand how to simultaneously trapped light and motion in exceedingly small interaction volumes increases the rates at which these couple. Using the rapid advances in nanofabrication techniques, lithographically defined chips with multiple optical and mechanical elements allow access to regimes in optomechanics that are difficult to achieve with other optomechanical (OM) systems. However, highly-engineered optomechanical crystals (OMCs) are sensitive to random disorder due to fabrication fluctuations in the few nm range. While acoustic losses might be compensated by larger acoustic shields in full phononic band gaps, the optical quality factors are strongly affected by out-of-plane scattering on such random defects, compromising the OM interaction. However, disorder can also naturally lead to highly confined Anderson-localized optical (and mechanical) modes in OMCs, a localization mechanism that we explore at the end of this Chapter and in the rest of this thesis. The chapter is finished with a brief summary describing how the concepts herein relate to the results given in Chapters 4 and 5

3.1 The governing equations

3.1.1 Maxwell's equations in matter

The propagation of electromagnetic waves in a periodic medium, like in any medium, is governed by the four macroscopic Maxwell's equations, which are [115]

$$\boldsymbol{\nabla} \cdot \mathbf{B}(\mathbf{r}, t) = 0 \tag{3.1a}$$

$$\boldsymbol{\nabla} \cdot \mathbf{D}(\mathbf{r}, t) = \rho(\mathbf{r}, t) \tag{3.1b}$$

$$\boldsymbol{\nabla} \times \mathbf{E}(\mathbf{r}, t) + \frac{\partial \mathbf{B}(\mathbf{r}, t)}{\partial t} = 0 \tag{3.1c}$$

$$\boldsymbol{\nabla} \times \mathbf{H}(\mathbf{r}, t) - \frac{\partial \mathbf{D}(\mathbf{r}, t)}{\partial t} = \mathbf{J}(\mathbf{r}, t) \tag{3.1d}$$

where $\mathbf{E}(\mathbf{r},t)$ and $\mathbf{H}(\mathbf{r},t)$ represent the macroscopic electric and magnetic fields, the scalar function $\rho(\mathbf{r},t)$ in (3.1b) accounts for the free charge density and $\mathbf{J}(\mathbf{r},t)$ in (3.1d) represents the current density. The displacement $\mathbf{D}(\mathbf{r},t)$ and the magnetic induction $\mathbf{B}(\mathbf{r},t)$ fields are defined by

$$\mathbf{D}(\mathbf{r},t) = \epsilon_o \mathbf{E}(\mathbf{r},t) + \mathbf{P}(\mathbf{r},t) \tag{3.2a}$$
$$\mathbf{B}(\mathbf{r},t) = \mu_o(\mathbf{H}(\mathbf{r},t) + \mathbf{M}(\mathbf{r},t)) \tag{3.2b}$$

with $\mathbf{P}(\mathbf{r},t)$ the polarization and $\mathbf{M}(\mathbf{r},t)$ the magnetization fields. The mathematical description of $\mathbf{P}$ and $\mathbf{M}$ as a function of $\mathbf{E}$ and $\mathbf{H}$ in the form of local consitutive relations describing the response of the bound charges and currents in the medium sets the equations to solve. These can be generally written as power series expansions of $\mathbf{E}$ and $\mathbf{H}$ depending on a set of tensors $\{\boldsymbol{\chi}_j\}$ of order $j+1$ [116]. Asuming small field strengths only the first terms $\boldsymbol{\chi}_{1,e}$ and $\boldsymbol{\chi}_{1,h}$, i.e., the electric and magnetic susceptibility, might be kept. Since a material cannot polarize instantaneously, the time-dependence of $\mathbf{P}$ is formulated via

$$\mathbf{P}(t) = \epsilon_o \int_{-\infty}^{t} \boldsymbol{\chi}_e(t-t')\mathbf{E}(t')dt' \tag{3.3}$$

where we omit the index "1" in $\boldsymbol{\chi}_e$ since the response is linear. As is obvious from the expression, causality is preserved. Since the dielectric materials treated here present a very small magnetization, we simply set $\mathbf{B}(\mathbf{r}) = \mu_o \mathbf{H}(\mathbf{r})$. The free charges $\rho(\mathbf{r},t)$ and currents $\mathbf{J}(\mathbf{r},t)$ can be discarded if one aims at understanding the intrinsic propagation properdies inside the medium. Setting ρ and $\mathbf{J}$ to zero and using (3.3) in Equations (3.1) leads to

$$\boldsymbol{\nabla} \cdot \mathbf{H}(\mathbf{r},t) = 0 \tag{3.4a}$$
$$\boldsymbol{\nabla} \cdot (\mathbf{E}(\mathbf{r},t) + \int_{-\infty}^{t} \boldsymbol{\chi}_e(t-t')\mathbf{E}(t')dt') = 0 \tag{3.4b}$$
$$\boldsymbol{\nabla} \times \mathbf{E}(\mathbf{r},t) + \frac{\partial \mathbf{B}(\mathbf{r},t)}{\partial t} = 0 \tag{3.4c}$$
$$\boldsymbol{\nabla} \times \mathbf{H}(\mathbf{r},t) - \epsilon_o \frac{\partial}{\partial t}\left(\mathbf{E}(\mathbf{r},t) + \int_{-\infty}^{t} \boldsymbol{\chi}_e(t-t')\mathbf{E}(t')dt'\right) = 0 \tag{3.4d}$$

whose Fourier transform reads

$$\boldsymbol{\nabla} \cdot \mathbf{H}(\mathbf{r},\omega) = 0 \tag{3.5a}$$
$$\boldsymbol{\nabla} \cdot (\boldsymbol{\epsilon}(\mathbf{r},\omega)\mathbf{E}(\mathbf{r},\omega)) = 0 \tag{3.5b}$$
$$\boldsymbol{\nabla} \times \mathbf{E}(\mathbf{r},\omega) - i\omega\mu_o \mathbf{H}(\mathbf{r},\omega) = 0 \tag{3.5c}$$
$$\boldsymbol{\nabla} \times \mathbf{H}(\mathbf{r},\omega) + i\omega\epsilon_o \boldsymbol{\epsilon}(\mathbf{r},\omega)\mathbf{E}(\mathbf{r},\omega) = 0 \tag{3.5d}$$

We have introduced the relative permittivity $\boldsymbol{\epsilon}(\omega) = (\mathbf{1} + \boldsymbol{\chi}_e(\omega))$ with $\boldsymbol{\chi}_e(\omega)$ the Fourier transform of $\boldsymbol{\chi}_e(t)$. This complex-valued tensor describes the response of the bound charges in a material to an harmonic electromagnetic field. The tensorial nature of $\boldsymbol{\epsilon}(\omega)$ can however be dropped for the materials considered in this thesis since we employ isotropic dielectrics, i.e., $\boldsymbol{\epsilon}(\omega) = \epsilon(\omega)\mathbf{1}$.

In the *special* case of a monochromatic field at frequency ω, i.e., $\mathbf{E}(\mathbf{r},t) = \mathbf{E}(\mathbf{r})e^{-i\omega t}$ and $\mathbf{H}(\mathbf{r},t) = \mathbf{H}(\mathbf{r})e^{-i\omega t}$, the frequency dependence of $\mathbf{E}$ and $\mathbf{H}$ can be dropped. If we combine equations (3.5c) and (3.5d) and introduce the vacuum speed of light $c = 1/\sqrt{\epsilon_o \mu_o}$ we get

$$\boldsymbol{\nabla} \times \left(\frac{1}{\epsilon(\mathbf{r},\omega)} \boldsymbol{\nabla} \times \mathbf{H}(\mathbf{r}) \right) = \left(\frac{\omega}{c} \right)^2 \mathbf{H}(\mathbf{r}) \tag{3.6}$$

Together with the divergence equation (3.5a) and the appropriate boundary conditions, the master equation (3.6) fully determines the magnetic field $\mathbf{H}(\mathbf{r})$. The electric field can be readily found as

$$\mathbf{E}(\mathbf{r}) = \frac{i}{\omega \epsilon_o \epsilon(\mathbf{r},\omega)} \boldsymbol{\nabla} \times \mathbf{H}(\mathbf{r}) \tag{3.7}$$

that automatically satisfies its own divergence equation (3.5a). Equation (3.6) has the form of a non-linear eigenvalue problem with $(\omega/c)^2$ the eigenvalue and $\mathbf{H}(\mathbf{r})$ the eigenvector.

Most standard textbooks in photonic crystals (PhCs) [72,117,118] build upon Eq. (3.6) and state that the operator acting on the magnetic field $\mathbf{H}(\mathbf{r})$ is an hermitian operator with respect to the standard inner product of two complex functions. This property is based on two particular aspects: i) the permittivity $\epsilon(\mathbf{r},\omega)$ is real and ii) the fields $\mathbf{H}(\mathbf{r})$ are well behaved at the boundary S of the physical domain V, which clearly depends on the particular boundary conditions one imposes. When these two conditions are true, the operator is indeed hermitian and the theory behind hermitian operators, like their real eigenspectrum, holds [119]. However, the equations are valid even in the presence of losses or gain induced by an imaginary part $\epsilon_i(\mathbf{r},\omega)$ of the complex permittivity $\epsilon(\mathbf{r},\omega) = \epsilon_r(\mathbf{r},\omega) + i\epsilon_i(\mathbf{r},\omega)$ which obviously precludes the existence of modes with real eigenvalues ω, unless very specific conditions on the potential $\epsilon(\mathbf{r})$ are met in parity-time (PT) symmetric systems [120], a class of systems which are currently gathering much attention in optics [121,122]. A second type of situation refers to an optical system occupying a volume of physical space V' and surrounded by a *rather homogeneous* unbounded environment. Such situations are extremely common in photonics and are found, for example, in a planar dielectric slab or in a PhC cavity, cases that will be described later in this Chapter. These situations can either be treated by considering V to be all space, in which case the system is hermitian and exhibits radiation states with continuous eigenspectrum, or by considering the finite volume of interest V' as the physical domain V and treating it as an open system exhibiting irreversible radiation losses. In that case, the eigenvalue problem (3.6) has to be supplied with outgoing boundary conditions [123] to ensure that energy leaks away. Both in the presence of loss/gain or when such an outgoing boundary condition is imposed, the problem is not (necessarily) hermitian with respect to the conventional inner product and the eigenvalue problem (3.6) needs to be considered within the theory of non-hermitian physics [124]. The solutions to the system $\{\widetilde{\mathbf{E}}(\mathbf{r}), \widetilde{\mathbf{H}}(\mathbf{r})\}$ are denoted quasinormal-modes (QNMs) and have complex eigenfrequencies $\widetilde{\omega} = \omega_r - i\omega_i$, where the imaginary part ω_i represent the losses and plays the role of $\kappa_i/2$ for the

optical cavity dynamics described in Chapter 2. This type of formalism is well suited to describe resonant states in optical systems[1], states whose energy can be stored in a bounded region of space for a certain time but inherently decaying into a continuum of radiative states that carry the energy away. This continuum is typically made of plane or spherical waves. The use of optical QNMs to study the scattering properties of a medium [126,127] or light-matter interactions [128,129] has gained widespread acceptance and is a growing field in theoretical photonics.

For most of this thesis we focus on the optical response of semiconductor (nano)structures around particular frequency regions where they do not absorb linearly, e.g. silicon in the telecommunication bands 1.4-1.6 μm. We therefore disregard gain/loss and dispersion provided that the obtained eigenvalues ω lie within a narrow frequency band around some ω_o for which $\epsilon(\mathbf{r},\omega) \approx \epsilon(\mathbf{r},\omega_o) \equiv \epsilon(\mathbf{r})$. This leads to a linear eigenvalue problem of the form

$$\hat{\Theta}_o(\mathbf{r})(\mathbf{H}(\mathbf{r})) = \left(\frac{\omega}{c}\right)^2 \mathbf{H}(\mathbf{r}) \tag{3.8}$$

with the differential operator given by

$$\hat{\Theta}_o(\mathbf{r})\bullet = \boldsymbol{\nabla} \times \left(\frac{1}{\epsilon(\mathbf{r})}\boldsymbol{\nabla} \times \bullet\right) \tag{3.9}$$

The operator $\Theta_o(\mathbf{r})$ is a linear operator and two field patterns differing only by an overall multiplier are taken to be the same mode. If one is interested in the energy carried by a particular eigenmode, its excitability from the far-field or its interaction with matter makes proper normalization of the modes critical, specially within the framework of QNMs [130–132], where the fields diverge towards infinity due to the complex eigenfrequencies and the outgoing boundary conditions.

3.1.2 Elastodynamics of solids

The discrete nature of the atomic lattice can generally be ignored when finding the vibrational modes of a mechanical element, thus treating it as a continuum. This is similar to what is done when one transitions from the microscopic version of Maxwell's equations to their corresponding version in matter (3.1). This model can be directly derived from the theory of lattice vibrations if one considers that the deformations vary slowly at the inter-atomic force scale [133] and is typically valid for acoustic wavelengths sufficiently larger than the atomic lattice constant. In that case, the theory of continuum mechanics [134] dictates the behaviour of the body under study by imposing Newton's second law to each differential volume dV,

$$\boldsymbol{\nabla}\cdot\boldsymbol{\sigma}(\mathbf{r},t) + \mathbf{F}(\mathbf{r},t) = \rho(\mathbf{r},t)\frac{\partial^2 \mathbf{U}(\mathbf{r},t)}{\partial t^2} \tag{3.10}$$

where $\mathbf{U}(\mathbf{r},t)$ is the unknown displacement field, $\boldsymbol{\sigma}(\mathbf{r},t)$ the Cauchy stress tensor, $\rho(\mathbf{r},t)$ the mass density and $\mathbf{F}(\mathbf{r},t)$ the body force per unit volume. In order to

[1] The formalism was first developed to study the properties of resonant states in quantum mechanics, quantums states that are *long lived* but are inherently coupled to a continuum of modes. This is the case, for example, of autoionization states [125].

solve for the displacement, we need a constitutive relation, i.e., a function $\mathcal{G}$ relating the nearly-always symmetric tensor $\boldsymbol{\sigma}(\mathbf{r},t)$ and the displacement field $\mathbf{U}(\mathbf{r},t)$. This relation typically depends on the relative displacement between neighboring volume elements. We introduce the strain tensor $\mathbf{S}(\mathbf{r},t)$, that is defined for low displacements as,

$$\mathbf{S} = \frac{1}{2}[\boldsymbol{\nabla}\mathbf{u} + \boldsymbol{\nabla}\mathbf{u}^{\mathbf{T}}] \equiv \boldsymbol{\nabla}_S\mathbf{u} \tag{3.11}$$

$\boldsymbol{\nabla}_S$ is the symmetric gradient and $\mathbf{S}$ is a symmetric tensor by construction. We can generally expand $\boldsymbol{\sigma}$ as a power series of $\mathbf{S}$ and keep only the first-order term, i.e., $\boldsymbol{\sigma} = \mathbf{C} : \mathbf{S}$, where the stiffness tensor $\mathbf{C} = \{C_{ijkl}\}$ is a fourth order tensor. This is the constitutive relation for linear elasticity.

Using the fact that both $\boldsymbol{\sigma}$ and $\mathbf{S}$ are second order symmetric tensors with at most 6 different elements, the tensor $\mathbf{C}$ has at most 36 different components C_{ijkl}. As $\boldsymbol{\sigma}$ and $\mathbf{S}$ are 6-component vectors using the Voigt notation [135], $\mathbf{C}$ is a 6x6 matrix $C_{\alpha\beta}$ in that same notation. By using energy considerations, the matrix $\mathbf{C}$ is itself symmetric, therefore reducing its number of independent parameters to 21 for the most general anisotropic material. This number is further reduced by using the symmetry operations that leave the underlying crystalline lattice invariant. For the case of silicon, the standard material platform used in this thesis, the cubic symmetry leads to

$$C_{\alpha\beta} = \begin{bmatrix} C_{11} & C_{12} & C_{12} & 0 & 0 & 0 \\ C_{12} & C_{11} & C_{12} & 0 & 0 & 0 \\ C_{12} & C_{12} & C_{11} & 0 & 0 & 0 \\ 0 & 0 & 0 & C_{44} & 0 & 0 \\ 0 & 0 & 0 & 0 & C_{44} & 0 \\ 0 & 0 & 0 & 0 & 0 & C_{44} \end{bmatrix} \tag{3.12}$$

in the material coordinate system ($x \equiv [100]$,$y \equiv [010]$ and $z \equiv [001]$). This reduces the tensor to only three different elastic coefficients, which are $C_{11} = 166$ GPa, $C_{12} = 64$ GPa and $C_{44} = 79.6$ GPa [136]. Unlike for the electromagnetic response, isotropy is rather unusual in mechanics since crystalline materials are always, by construction, anisotropic. Isotropy only applies for acoustic wavelengths much larger than the scale where the system displays atomic order. Let's note here that an arbitrary rotation of the physical coordinate system with respect to the material coordinate system will in general transform all of the coefficients in (3.12) and this should therefore be carried out before any calculation. Additionally, the orientation of a patterned structure displaying discrete symmetries, e.g.., a phononic crystal (PnC), with respect to the material axis is critical, as will be discussed later.

We solve for the normal modes of a mechanical object assuming no volume (or boundary) forces, i.e., $\mathbf{F}(\mathbf{r},t) = 0$, and a stationary setting, i.e., no time-dependent physical parameters. We look for harmonic solutions of the type $\mathbf{U}(\mathbf{r},t) = \mathbf{U}(\mathbf{r})e^{-i\Omega t}$, leading to,

$$\hat{\Theta}_m(\mathbf{r})(\mathbf{U}(\mathbf{r})) = \Omega^2\mathbf{U}(\mathbf{r}) \tag{3.13}$$

with the differential operator $\hat{\Theta}_m(\mathbf{r})$ given by,

$$\hat{\Theta}_m(\mathbf{r})(\bullet) = -\frac{1}{\rho(\mathbf{r})}\boldsymbol{\nabla}\cdot(\mathbf{C}\,(\mathbf{r}):\boldsymbol{\nabla}_S\bullet) \tag{3.14}$$

which constitutes a linear eigenvalue problem for the displacement field $\mathbf{U}(\mathbf{r})$. Due to the anharmonicity of phonons, the mechanical excitations in such a system are intrisically lossy and the system is non-hermitian, even in the absence of radiation losses. The eigenfrequencies Ω are generally complex eigenfrequencies $\widetilde{\Omega} = \Omega_r + i\Omega_i$, although the QNM framework in the description of mechanical resonances has only recently been addressed [137,138].

Despite the apparent differences between the electromagnetism operator (3.6) and the elastodynamics operator (3.14), the structure of the problem to solve is similar as are the numerical methods suited for it. In addition, fundamental properties of their eigensolutions can be understood from a general inspection of the respective operators, in particular their underlying symmetries [139].

3.2 Symmetries and mode categorization

The use of symmetries, i.e., coordinate transformations that leave a system unchanged, and, under some circumstances, the breaking of those same symmetries is of utter importance in physics. In this case, symmetries of the the eigenvalue operators $\hat{\Theta}_o(\mathbf{r})$ and $\hat{\Theta}_m(\mathbf{r})$ are reflected in the form of the solution and or allow clsssification of the normal modes supported by the structures, often reducing the computational cost of their numerical resolution. We discuss here particularly important symmetries for OMCs such as discrete and continuous translational and rotational symmetries, mirror symmetries and time-reversal symmetry.

We consider an operator $\hat{A}$ that acts on $\mathbb{C}^3$ vector fields $\mathbf{F}(\mathbf{r})$ in $\mathbb{R}^3$. In some cases $\hat{A}$ admits a matrix representation $\mathbf{A}$ with which the action of the operator is given by $\hat{A}(\mathbf{F}(\mathbf{r})) \equiv \mathbf{A}\mathbf{F}(\mathbf{A}^{-1}\mathbf{r})$, i.e., the inverse matrix $\mathbf{A}^{-1}$ acts on the argument $\mathbf{r}$, the field is taken at the new argument and then the field itself is multiplied by matrix $\mathbf{A}$. The system studied is said to have $\hat{A}$-symmetry if it does not matter whether we directly apply the operator $\hat{\Theta}(\mathbf{r})$ or we first apply $\hat{A}$, then $\hat{\Theta}(\mathbf{r})$ and operate back with the inverse $\hat{A}^{-1}$ to change them back. Formally

$$\hat{\Theta}(\mathbf{r})(\mathbf{F}(\mathbf{r})) = \hat{A}^{-1}(\hat{\Theta}(\mathbf{r})(\hat{A}(\mathbf{F}(\mathbf{r})))) \implies [\hat{A}, \hat{\Theta}(\mathbf{r})] = 0 \tag{3.15}$$

with the commutator $[\hat{B}, \hat{C}] \equiv \hat{B}\hat{C} - \hat{C}\hat{B}$. Therefore, if $\mathbf{F}(\mathbf{r})$ is an eigenfield of $\hat{\Theta}(\mathbf{r})$ with eigenvalue ω, then $\hat{A}(\mathbf{F}(\mathbf{r}))$ is also an eigenmode with equivalent eigenvalue ω. In the absence of degeneracies in the eigenspectrum of $\hat{\Theta}(\mathbf{r})$, this means that they need to be equivalent up to a multiplicative factor, i.e., $\hat{A}\mathbf{F}(\mathbf{r}) = \beta\mathbf{F}(\mathbf{r})$, which is nothing more than the eigenvalue problem for the operator $\hat{A}$. Therefore, eigenstates of $\hat{\Theta}(\mathbf{r})$ are also eigenstates of $\hat{A}$, which is an extremely powerful tool since the eigenstates of $\hat{A}$ are often easily obtained. In the presence of degeneracies, $\mathbf{F}(\mathbf{r})$ and $\hat{A}(\mathbf{F}(\mathbf{r}))$ might have the same frequency ω but not be related by a multiplicative factor. However, under particular circumstances the field $\hat{A}(\mathbf{F}(\mathbf{r}))$ is adscribed to a particular eigenstate among the degenerate set,

generating redundancies in the calculation of the full energy spectrum and reducing the computational cost. In general, one can show that the two operators do posses simultaneous eigenfunctions even in the presence of degeneracies. Therefore, a common strategy consists of finding the eigenfunctions of the symmetry operator first and then use them to simplify the search of the eigenfunctions of $\hat{\Theta}(\mathbf{r})$. Even when the eigenfunctions of the symmetry operator $\hat{A}$ are degenerate, as is typically the case, we only need to search in the lower-dimension degenerate eigenspaces by building eigenstates of the operator $\hat{\Theta}(\mathbf{r})$ as a linear combination of the degenerate set. This can drastically reduce the complexity of the problem.

3.2.1 Discrete translational symmetry and Bloch theorem

A particularly important role in PhCs and PnCs, as in matter in general, is played by discrete translational symmetry because it leads to the well-known concepts of Bloch modes with energies represented via a band structure. If the operator $\hat{\Theta}(\mathbf{r})$ possesses translation invariance with respect to some vector $\mathbf{R}$, i.e $\hat{\Theta}(\mathbf{r}) = \hat{\Theta}(\mathbf{r}+\mathbf{R})\ \forall \mathbf{r}$, then $[\hat{\Theta}(\mathbf{r}), \hat{T}_{\mathbf{R}}] = 0$, where $\hat{T}_{\mathbf{R}}$ is the translation operator whose action upon a vector field is given by $\hat{T}_{\mathbf{R}}(\mathbf{F}(\mathbf{r})) = \mathbf{F}(\mathbf{r}+\mathbf{R})$. Due to the composition law $\hat{T}_{\mathbf{R}}\hat{T}_{\mathbf{R}'} = \hat{T}_{\mathbf{R}+\mathbf{R}'}$, the eigenvalues of the translation operator $\hat{T}_{\mathbf{R}}$ are given by $\beta(\mathbf{R}) = e^{i\mathbf{k}\cdot\mathbf{R}}$ and its eigenfields satisfy $\mathbf{F}(\mathbf{r}+\mathbf{R}) = e^{i\mathbf{k}\cdot\mathbf{R}}\mathbf{F}(\mathbf{r}+\mathbf{R})$, where we have introduced the quasi-momentum $\mathbf{k}$, a conserved quantity. The functions $\mathbf{F}(\mathbf{r})$ satisfying such condition can be written as

$$\mathbf{F}_{\mathbf{k}}(\mathbf{r}) = \mathbf{f}_{\mathbf{k}}(\mathbf{r})e^{i\mathbf{k}\cdot\mathbf{r}} \quad \text{with} \quad \mathbf{f}_{\mathbf{k}}(\mathbf{r}) = \mathbf{f}_{\mathbf{k}}(\mathbf{r}+\mathbf{R})\ \forall \mathbf{r}, \mathbf{R} \tag{3.16}$$

which is a formulation of the Bloch-Floquet theorem [133]. It is worth noting that, as posed, nothing constraints the wavevector $\mathbf{k}$ to be real. One would physically expect it to be real in an infinite lattice to avoid divergent solutions, but formal solutions with $\mathbf{k} \in \mathbb{C}^3$ do exist [140]. These have particular importance when a surface or a defect is introduced as happens with, for example, evanescent Bloch waves or the role of perturbative disorder.

A corollary of Bloch's theorem is that wave-vectors $\mathbf{k}$ are redundant outside a region of reciprocal space that is called the Brillouin Zone (BZ). The particular boundaries and shape of this region depend on the underlying periodic lattice, with its dimension set by the dimensionality of the lattice in real space. The shape of the BZ for a one-dimensional system is simply given by $-\pi/a < k \leq \pi/a$ but in 2D and 3D there is many possible ways of arranging a periodic pattern in what are called Bravais lattices. Starting with a set of elementary vectors $\mathbf{a}_i$ one builds the Bravais lattice of the crystal by setting all points $\mathbf{R} = \sum_i n_i\mathbf{a}_i$ with n_i integers and repeating an elementary unit cell in all directions given by the lattice $\mathbf{R}$. This elementary block, the unit cell, is, however, not unique. A particular choice is given by the *primitive* unit cell or Wigner-Seitz cell [133], which has minimal volume and is constructed by taking the perpendicular bisectors to the lines joining a lattice site to its neighbours and finding the volume enclosed by those. This is depicted in Fig. 3.1(a) for a triangular lattice. Analogous to this construct in real space, a lattice is built in reciprocal space using lattice vectors $\mathbf{b}_i$ found by imposing $\mathbf{a}_i\mathbf{b}_j = 2\pi\delta_{ij}$ and with lattice sites spanned by $\mathbf{K} = \sum_i k_i\mathbf{b}_i$, with k_i integers. The BZ is obtained by finding the Wigner-Seitz

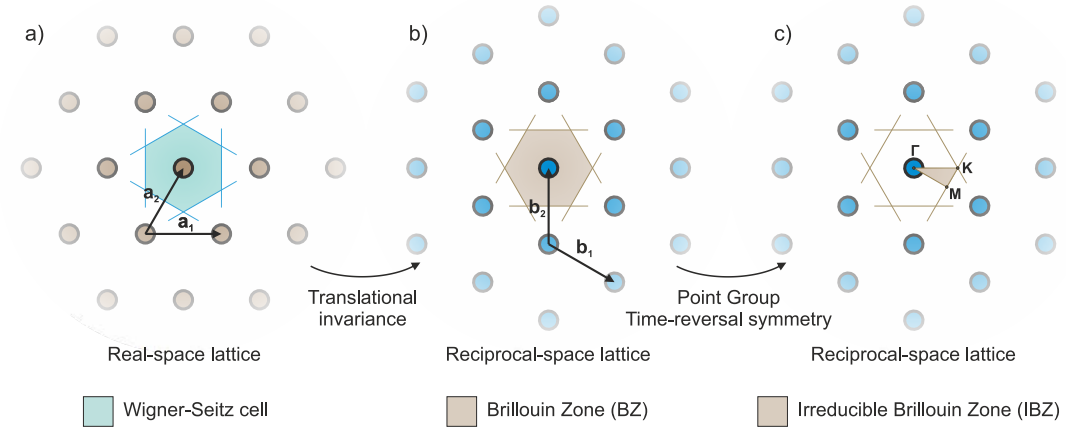

Figure 3.1: Real and reciprocal space lattices in a discrete translational invariant 2D system. Triangular lattice of circles in (a) real space and (b) reciprocal space, with the Wigner-Seitz (WS) cell shaded in blue and brown respectively. For reciprocal space, the WS cell corresponds to the 1^{st} Brillouin Zone (BZ). The primitive vectors in both lattices are also shown. (c) By using additional symmetries of the system like its point group or time-reversal invariance, the 1BZ is reduced to the irreducible Brillouin Zone (IBZ), the minimum region in reciprocal space not connected by symmetry operations.

cell of the reciprocal lattice, as is depicted in Fig. 3.1(b) for the triangular lattice. The case where *continuous* translational symmetry in a direction $\mathbf{s}$ holds, i.e., $[\hat{T}_{d\mathbf{s}}, \hat{\Theta}(\mathbf{r})] = 0 \ \forall d \in \mathbb{R}$, can be thought of as satisfying Bloch's theorem (3.16) for any vector $\mathbf{R}$ in that direction, which only holds if the periodic part does not depend on that particular coordinate. If we take, for clarity, the system to be homogeneous along z, then the eigenfield can be written as $\mathbf{F}(\mathbf{r}) = \mathbf{f}_{\mathbf{k}}(x, y)e^{ik_z z}$ and k_z can take any value in $\mathbb{C}$.

The Bloch eigenmodes are therefore described by their continuous conserved quasi-momentum $\mathbf{k}$, so it seems appropiate to ask what is the minimum space that has to be sampled in the 1BZ to capture all features of the eigenspectrum $\omega(\mathbf{k})$. To answer this, additional symmetries of the unit cell are considered.

3.2.2 Discrete rotational symmetry and other spatial symmetries

Depending on the symmetries of the *motif* inside the unit cell and the symmetries of the material at the atomic scale, the PhC/PnC might possess a discrete set of rotational symmetries in addition to their translation invariance. Asuming a constituent insotropic reponse, it is clear that rotating a circle around its center by any angle θ leaves the circle unchanged. We say that the circle has C_∞ rotational symmetry. If a full lattice of circles, like the one depicted in Fig. 3.1(a), is rotated by some angle θ about an axis $\mathbf{n}$ that leaves the lattice unchanged, then the full crystal remains unchanged. For the particular case of the triangular lattice of circular holes we see that any rotation of angle $\theta = p2\pi/6$ with $p \in \mathbb{Z}$ leads to the exact same lattice.

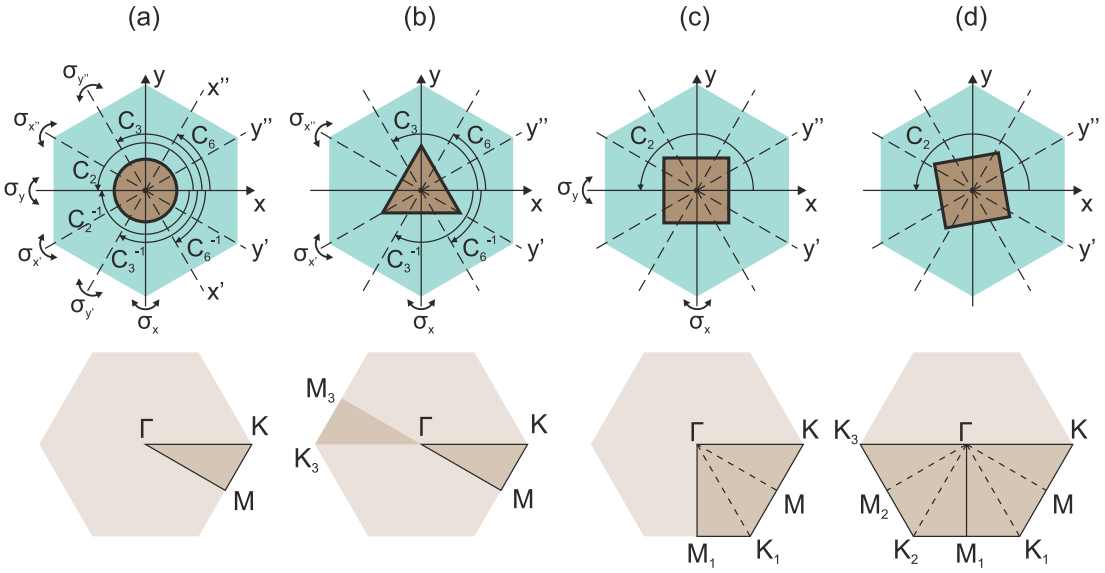

Figure 3.2: Point group representation and the Irreducible Brillouin Zone (IBZ). The symmetries of the unit cell motif that map the lattice into itself are called the point group of the crystal and define the IBZ, the minimum region in k-space that needs to be sampled to access the full eigenspectrum $\omega_n(\mathbf{k})$. (a) A circle preserves all mirror symmetries $\sigma_{x,x',x'',y,y',y''}$, all rotational symmetries $C_{\pm 6,\pm 3,\pm 2}$ and the inversion symmetry $C_{\pm 2}$ of the hexagonal WS cell of a triangular lattice, leading to the Γ-K-M IBZ shaded in brown. (b) An equilateral triangle breaks the $\sigma_{x',y,y'}$ mirror symmetries and the inversion symmetry $C_{\pm 2}$, which leads to the shaded reregion. Use of time-reversal invariance finally leads to the same Γ-K-M IBZ. Larger IBZs occur when the motif breaks additional symmetries, as does (c) a square or (d) a tilted square, which lead to an IBZ of size 1/4 and 1/2 in units of the 1BZ area, respectively. Even if the $C_{\pm 2}$ inversion symmetry in (d) is lost by employing an arbitrary shape, time-reversal invariance still leads to the region shown.

More generally, let us imagine that the system under study possesses a discrete rotational symmetry, which is a set of rotations denoted by $\boldsymbol{\mathcal{R}} \equiv \boldsymbol{\mathcal{R}}(\mathbf{n}, \theta)$ with $\mathbf{n}$ the rotation axis and $\theta = p2\pi/N, p \in [0, ..., N-1]$ the rotation angle, whose associated operators $\hat{\mathcal{R}}$, applied in the way described above, commute with the differential operator $\hat{\Theta}(\mathbf{r})$. Unfortunately, operators $\hat{\mathcal{R}}$ and the translation operator $\hat{T}_{\mathbf{R}}$ do not generally commute even if they both commute with the differential operator $\hat{\Theta}(\mathbf{r})$. Even if this prevents a common eigenbasis, the use of the discrete rotational symmetry allows a reduction of the BZ that needs to be sampled. When operating on a Bloch eigenstate with wavevector $\mathbf{k}$, $\hat{\mathcal{R}}(\mathbf{F}_{\mathbf{k}}(\mathbf{r}))$, the rotation leads to nothing else than the Bloch eigenstate with the rotated wavevector $\boldsymbol{\mathcal{R}}\mathbf{k}$ up to a multiplicative constant

$$\hat{\mathcal{R}}(\mathbf{F}_{\mathbf{k}}(\mathbf{r})) = e^{i\phi}\mathbf{F}_{\boldsymbol{\mathcal{R}}\mathbf{k}}(\mathbf{r}) \tag{3.17}$$

and by the commutation relation they possess the same eigenvalue, therefore $\omega(\boldsymbol{\mathcal{R}}\mathbf{k}) = \omega(\mathbf{k})$. The dispersion relation $\omega(\mathbf{k})$ of the system eigenstates inherits the discrete rotation.

A comprehensive study of all the spatial symmetries of the crystal lattice can further reduce the size of the 1BZ. This is in principle done based on group theory [141], but can be understood rather intuitively by doing analogous arguments to the one given for discrete rotations. The set of transformations (e.g. rotation, mirror-symmetry and inversion) leaving the dielectric function $\epsilon(\mathbf{r})$ and mechanical pair $\{\rho(\mathbf{r}), \mathbf{C}(\mathbf{r})\}$ respectively unchanged is called the point group. Taking the point group into account reduces the 1BZ to what is denoted as the irreducible Brillouin zone (IBZ), i.e., all of the points in the 1BZ that cannot be connected by symmetry. For example, if we define $\hat{\sigma}_{\mathbf{d}}$ as the mirror symmetry with respect to an axis $\mathbf{d}$ and $[\hat{\Theta}(\mathbf{r}), \hat{\sigma}_{\mathbf{d}}]$=0, then it can be shown that

$$\hat{\sigma}_{\mathbf{d}}(\mathbf{F}_{\mathbf{k}}(\mathbf{r})) = e^{i\phi}\mathbf{F}_{\boldsymbol{\sigma}_{\mathbf{d}}\mathbf{k}}(\mathbf{r}) \tag{3.18}$$

and $\omega(\mathbf{k}) = \omega(\boldsymbol{\sigma}_{\mathbf{d}}\mathbf{k})$ in an analogous way to what has been said for the discrete rotations in the point group. Figure 3.2 illustrates how the existing symmetries of the unit cell of a triangular lattice give rise to reduced sizes of the BZ via some examples, where the top panel represents the real-space WS cell and the bottom panel the corresponding 1BZ. The circle in Fig. 3.2(a) possesses full rotational symmetry (C_∞) and the 12 operations that map the hexagonal WS cell to itself are preserved, leading to an IBZ (the shaded region inside Γ-K-M) of size 1/12, in units of the 1BZ. The equilateral triangle in (b) breaks the inversion symmetry (C_2) and three mirror symmetries ($\hat{\sigma}_y$,$\hat{\sigma}_{y'}$ and $\hat{\sigma}_{y''}$) leading to an IBZ two times bigger. Other geometrical entities like a square can preserve inversion symmetry but break a higher number of mirror symmetries, leading to an IBZ of one quarter of the 1BZ (c). Finally, if the same square is tilted an angle different from a multiple of $\pi/6$, only inversion symmetry is left, leading to an IBZ half the size of the original BZ.

Even though these symmetry arguments might appear obvious to the reader, a literature review over the past decade [142] has shown how the IBZ is often misjudged. Ref. [142] addresses only PnCs but the issues presented are found to be generic and present in the literature on photonic systems. This analysis is even more complex in phononics if the isotropy condition on the constituent materials is dropped, since symmetries of the artifical lattice might not apply to the constitutive stiffness tensor $\mathbf{C}$. Therefore, special care has to be taken on the definition of the IBZ even for artificial lattices using an elemental crystalline material like silicon.

3.2.3 Time-reversal symmetry

An extremely important and subtle symmetry across physics that we have left out so far is time-reversal invariance, or the fact that a system is invariant to an operation that inverts the time dependence t to $-t$ as well as instantaneously preserves or reverses some fundamental quantities at fixed t, e.g., position x is preserved, momentum p is reversed, the electric field $\mathbf{E}$ is preserved, but the magnetic field $\mathbf{H}$ is reversed, etc. [143]. The definition of a time-reversal operation in physics is actually an important source of debate [144]. When set via the eigenvalue problems (3.8) or (3.13), which are inherently written in the frequency domain, the time-reversal operator acts by taking the complex conjugate of the field [145].

Time-reversal invariance implies that if $\{\omega, \mathbf{F}(\mathbf{r})\}$ is an eigenstate of the system, the complex conjugate $\mathbf{F}^*(\mathbf{r})$ is also an eigenstate with eigenfrequency ω^*. Now, if the system is periodic and hermitian, the eigenstate can be represented by a Bloch state with ω real and its complex conjugate is nothing more than a Bloch eigenstate at wavevector $-\mathbf{k}$ and the same eigenvalue. When time-reversal invariance holds, the IBZ of the periodic structure may therefore be further reduced. This is shown in Fig. 3.2(b), where the point group leads to the shaded region and time-reversal invariance crops the IBZ to the delimited region inside Γ-K-M. Therefore, regardless the symmetry of the crystal, only half of the BZ needs to be considered.

The systems we consider in this thesis are time-reversal invariant and the necessary existance of two eigenstates with equivalent frequency ω and opposite value of $\mathbf{k}$ plays a very prominent role in the behaviour of the Bloch mode in the presence of small disorder, when translational symmetry is perturbatively broken. However, when any of the materials considered is lossy, $\mathrm{Im}(\epsilon(\mathbf{r}, \omega)) > 0$, time-reversal symmetry of the macroscopic Maxwell's equations can be broken and the mentioned property is lost, usually needing a larger IBZ. Breaking time-reversal symmetry is actually the main strategy to induce topologically non-trivial periodic structures that support edge states [146], propagating states immune to elastic coherent backscattering due to the absence of the time-reversed state at frequency ω and wavevector -$\mathbf{k}$. This strategy is analyzed at the end of this thesis where topological photonic structures are discussed.

3.2.4 Mirror-symmetry and field polarizations

In subsection 3.2.2 the effect of mirror symmetries was explored, leading to (3.18) and to a reduction of the $\mathbf{k}$-space redundancies. Despite this reduction, relation (3.18) does not say much about the reflection properties of the mode eigenfield $\mathbf{F}_\mathbf{k}(\mathbf{r})$. However, if $\boldsymbol{\sigma}_\mathbf{d}\mathbf{k} = \mathbf{k}$, (3.18) is an eigenvalue problem. The eigenvalues of the mirror symmetry operator $\boldsymbol{\sigma}_\mathbf{d}$ are simply +1 and -1, since two applications of the operator restores the original system. Without loss of generality, we set $\mathbf{d} = \mathbf{z}$ and apply the operator in the way described before, $\boldsymbol{\sigma}_\mathbf{z}\mathbf{F}(\boldsymbol{\sigma}_\mathbf{z}^{-1}\mathbf{r})$ with

$$\boldsymbol{\sigma}_\mathbf{z} = \begin{bmatrix} 1 & 0 & 0 \\ 0 & 1 & 0 \\ 0 & 0 & -1 \end{bmatrix} \tag{3.19}$$

the matrix associated to the mirror operator $\hat{\sigma}_z$. For the eigenvalue $p_z = +1$, this leads to

$$F_x(x, y, -z) = F_x(x, y, z) \tag{3.20a}$$
$$F_y(x, y, -z) = F_y(x, y, z) \tag{3.20b}$$
$$-F_z(x, y, -z) = F_z(x, y, z) \tag{3.20c}$$

while multiplying the left-hand-side of (3.20) by -1 sets the restrictions on $\mathbf{F}(\mathbf{r})$ for $p_z = -1$. For the case of the electromagnetic field, using (3.7) shows that if the magnetic field $\mathbf{H}(\mathbf{r})$ transforms as (3.20), the electric field transforms as if

it were a $p_z = -1$ eigenstate[2]. For points in the symmetry plane, like $\boldsymbol{\sigma_z}\mathbf{r} = \mathbf{r}$, the field takes the form $[F_x, F_y, 0]$ for $p_z = +1$ and $[0, 0, F_z]$ for $p_z = -1$. This restrictions on the field are essentially boundary conditions imposed in a surface of the volume V where the problem is solved and can be used to reduce the size of the computational domain in real-space solvers.

Whenever the condition $\boldsymbol{\sigma_d}\mathbf{k} = \mathbf{k}$ is satisfied for all $\mathbf{k}$ values, $\hat{\sigma}_\mathbf{d}$ commutates with the operator $\hat{\Theta}(\mathbf{r})$ restricted to the eigenspace defined by $\mathbf{k}$, making the categorization extremely useful. This property is satisfied for a system exhibiting two dimensional periodicity in the $\rho = (x, y)$ plane and a mirror symmetry along z, like a PhC slab. In the case of a two dimensional PhC which is translationally invariant, and therefore infinite in that same direction, the mirror symmetry becomes very restrictive with respect to the polarizations allowed to propagate. Based on Subsection 3.2.1, the general form of the eigenstates is

$$\mathbf{F}(\mathbf{r}) = e^{ik_z z} e^{i\mathbf{k}\cdot\boldsymbol{\rho}} \mathbf{f}_{k_z,\mathbf{k}}(\boldsymbol{\rho}) \tag{3.21}$$

with $\mathbf{k} = (k_x, k_y)$ the in-plane Bloch wavevector and k_z the out-of-plane wavevector. Since translational invariance along z can be thought as being a continuum of mirror symmetries $\boldsymbol{\sigma_d}$ with respect to any plane, we have both $\boldsymbol{\sigma_z}\mathbf{r} = \mathbf{r}$ and $\boldsymbol{\sigma_z}\mathbf{k} = \mathbf{k}$ for all $\mathbf{r}$ and $\mathbf{k}$, and solutions at $k_z = 0$ can be classified according to their polarizations. In the case of electromagnetic waves this classification leads to trasnverse electric (TE) and transverse magnetic (TM) modes

$$\text{TE} : \{\mathbf{H}, \mathbf{E}\} = \{[0, 0, h_{z,\mathbf{k}}(\boldsymbol{\rho})], [e_{x,\mathbf{k}}(\boldsymbol{\rho}), e_{y,\mathbf{k}}(\boldsymbol{\rho}), 0]\} \tag{3.22a}$$

$$\text{TM} : \{\mathbf{H}, \mathbf{E}\} = \{[h_{x,\mathbf{k}}(\boldsymbol{\rho}), h_{y,\mathbf{k}}(\boldsymbol{\rho}), 0], [0, 0, e_{z,\mathbf{k}}(\boldsymbol{\rho})]\} \tag{3.22b}$$

while in the case of elastodynamics it leads to a decoupling of the displacements into transverse and in-plane motional waves

$$\text{Transverse} : \mathbf{U} = [0, 0, u_{z,\mathbf{k}}(\boldsymbol{\rho})] \tag{3.23a}$$

$$\text{In-plane} : \mathbf{U} = [u_{x,\mathbf{k}}(\boldsymbol{\rho}), u_{y,\mathbf{k}}(\boldsymbol{\rho}), 0] \tag{3.23b}$$

3.3 Band structures and band gaps

Supplied with Bloch's theorem (3.16), the eigenvalue problems for electromagnetic and acoustic waves can be rewritten inside the eigenspace defined by wavevector $\mathbf{k}$. The eigenvalue problem (3.6) can be cast as finding $\mathbf{h}_\mathbf{k}(\mathbf{r})$ obeying

$$\hat{\Theta}_{o,\mathbf{k}}(\mathbf{r})(\mathbf{h}_\mathbf{k}(\mathbf{r})) = \left(\frac{\omega(\mathbf{k})}{c}\right)^2 \mathbf{h}_\mathbf{k}(\mathbf{r}) \tag{3.24}$$

with the $\mathbf{k}$-dependent differential operator $\hat{\Theta}_{o,\mathbf{k}}$ being defined by

$$\hat{\Theta}_{o,\mathbf{k}}(\mathbf{r})(\bullet) = (i\mathbf{k} + \boldsymbol{\nabla}) \times \left(\frac{1}{\boldsymbol{\epsilon}(\mathbf{r})}(i\mathbf{k} + \boldsymbol{\nabla}) \times \bullet\right) \tag{3.25}$$

[2]This difference stems from the fact that $\mathbf{H}(\mathbf{r})$ is a pseudovector and $\mathbf{E}(\mathbf{r})$ a vector.

Additionally, the solution needs to satisfy both the transversality condition $(i\mathbf{k} + \boldsymbol{\nabla})\cdot\mathbf{h}_\mathbf{k}(\mathbf{r}) = 0$ and periodicity $\mathbf{h}_\mathbf{k}(\mathbf{r}) = \mathbf{h}_\mathbf{k}(\mathbf{r} + \mathbf{R})$.

For the case of acoustic waves in solids the eigenvalue problem (3.13) transforms to

$$\hat{\Theta}_{m,\mathbf{k}}(\mathbf{r})(\mathbf{u}_\mathbf{k}(\mathbf{r})) = \Omega(\mathbf{k})^2\mathbf{u}_\mathbf{k}(\mathbf{r}) \tag{3.26}$$

with the $\mathbf{k}$-dependent differential operator $\hat{\Theta}_{m,\mathbf{k}}$ being defined by

$$\hat{\Theta}_{m,\mathbf{k}}(\mathbf{r})(\bullet) = -\frac{1}{\rho(\mathbf{r})}\left(\boldsymbol{\nabla} + i\mathbf{k}\right)\cdot\left(\mathbf{C}(\mathbf{r}){:}\left(\boldsymbol{\nabla}_S \bullet + \frac{i}{2}(\mathbf{k}\otimes\bullet + \bullet\otimes\mathbf{k})\right)\right) \tag{3.27}$$

where we have introduced the outer product $\mathbf{a}\otimes\mathbf{b}$, in index notation $(\mathbf{a}\otimes\mathbf{b})_{ij} = a_i b_j$. The periodic boundary condition $\mathbf{u}_\mathbf{k}(\mathbf{r}) = \mathbf{u}_\mathbf{k}(\mathbf{r} + \mathbf{R})$ needs also to be satisfied.

Since periodic boundary conditions are imposed on the fields to solve, the eigenfields for a fixed $\mathbf{k}$ are determined by their value inside a small region of space, a single unit cell. This results in a discrete spectrum of eigenvalues ω_n at a fixed value of $\mathbf{k}$ [72]. In addition, due to the continuity of $\hat{\Theta}_{o/m,\mathbf{k}}(\mathbf{r})$ with respect to $\mathbf{k}$, we expect a particular frequency ω at a fixed $\mathbf{k}$ to evolve continuously when $\mathbf{k}$ is changed. Therefore, the modes of a PhC or PnC can be cast into a set of continuous functions $\omega_n(\mathbf{k})$ indexed by the number n, the band number. In order to obtain the band diagram of a phot(n)onic crystal we need to solve Equation (3.24) or (3.26). In general, numerical methods are needed to obtain the band structure $\omega(\mathbf{k})$ and the corresponding eigenstates $\mathbf{F}_\mathbf{k}(\mathbf{r})$.

One of the most salient features of periodic structures is the possibility to have frequency regions $\Delta\omega$ where propagation is forbidden, at least for some of the allowed polarizations, i.e., frequencies ω for which there is no Bloch state with $\mathbf{k} \in \mathcal{R}$. The analogy with the behaviour of electrons in atomic crystals is, for this particular feature, obvious. If such a region is to be found, one typically needs to solve for all possible values of $\mathbf{k}$ inside the IBZ. This is done for the $k_z = 0$ modes of a two-dimensional PhC made of a triangular lattice of infinite cylindrical air inclusions in silicon. The results, which can be split between TE and TM polarizations, are shown in Figure 3.3. The unit cell size is given by the parameter a, the radius of the circles is $r = 0.3a$ and the refractive index of silicon is taken as $n_{Si} = 3.48$. Here, we solve the modes for the entire BZ to show the convenience of using the IBZ (the shaded region depicted in the xy-plane), since the rest are only replicas. Along with the band structure, the density of optical states (DOS), defined as

$$\mathrm{DOS}(\omega) = \sum_n \int_{IBZ} \delta\left(\omega - \omega_n(\mathbf{k})\right)\mathbf{dk} \tag{3.28}$$

is given. This quantity essentially counts the number of available states at a particular frequency ω, and scales as ω^2 in a bulk material. The DOS for the TE polarization evidences the presence of a photonic band gap (PhBG) for frequencies spanning $[0.206c/a, 0.272c/a]$, while the TM polarization possesses no gaps.

An important result that has been derived in the frame of group theory tells us that the extreme points (maxima and minima) of all bands occur along the

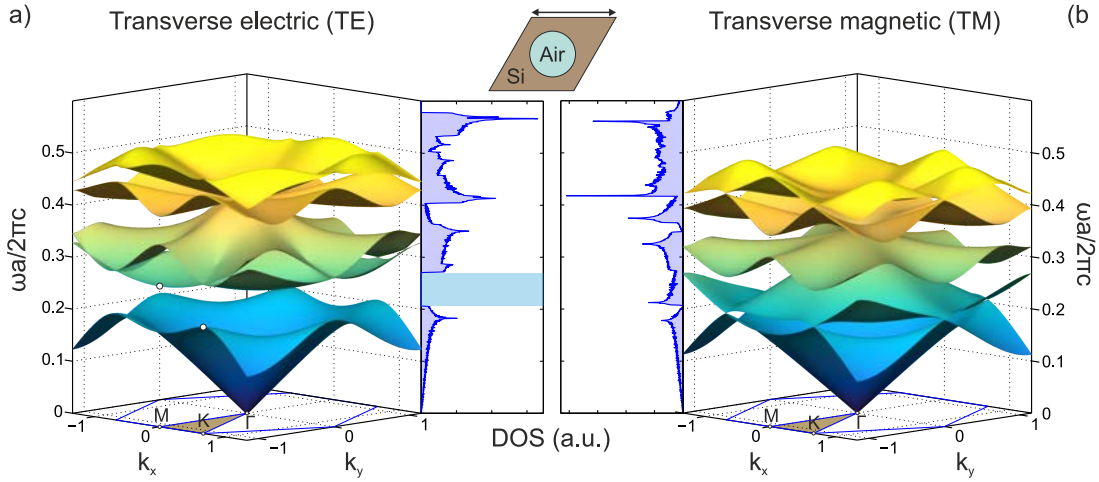

Figure 3.3: Band structure of a two-dimensional photonic crystal (PhC) made of air holes in silicon. Transverse electric (TE, left) and transverse magnetic (TM, right) band structure of a 2D PhC made of infinite cylindrical air inclusions in silicon, whose unit cell is given on top. The parameters used are period a, radius $r = 0.3a$ and $n_{Si} = 3.48$. The bands are given as continuous manifolds within the full Brillouin Zone (BZ), where the color represents the frequency and is only employed for visualization purposes. The irreducible BZ (IBZ) is highlighted in the xy-plane in shaded brown, along with the revelant high-symmetry points Γ-K-M. The density of optical states (DOS) as obtained from Eq. (3.28) is depicted for both polarizations, evidencing a band gap -blue shaded rectangle- for TE modes and none for TM modes. All frequencies are given in normalized units.

high symmetry directions, and most of the time at the high symmetry points in the IBZ. This happens for the case shown in Fig. 3.3, where the maximum and minimum bounding the gap are depicted with a white dot at the K and M points respectively. Most of the research community in photonics and phononics tends to sample a reciprocal space path that follows those directions in the IBZ and the band structure is calculated and displayed in a single line graph. However, Maurin et al [142] numerically assessed the probability that a band-gap extremum is located on the IBZ contour for the 17 different plane crsytallographic lattices (in 2D) and showed that the assumption inherited from group theory only holds for crystallographic groups *p4mm* and *p6mm*, the groups with the highest number of symmetry operations [147], to which the silicon-air structure of Fig. 3.3 belongs. This said, we often plot the bands along the IBZ contour since the likelihood of finding a full gap in such path is still relatively high and serves as a design guideline. However, the effective width of a band gap should always be obtained after solving in the (properly-defined) full IBZ.

Examples of different photonic band diagrams along that high-symmetry IBZ path for a material system consisting of a two-dimensional crystal of infinite cylindrical inclusions in a matrix are shown in Figure 3.4. Figure 3.4(a) shows the photonic band diagram already depicted in 3.3, with its indirect PhBG for TE polarization (shaded blue) and no gap for TM polarization. This is a typical feature of low-index inclusions in a high-index matrix [72]. The band diagram for

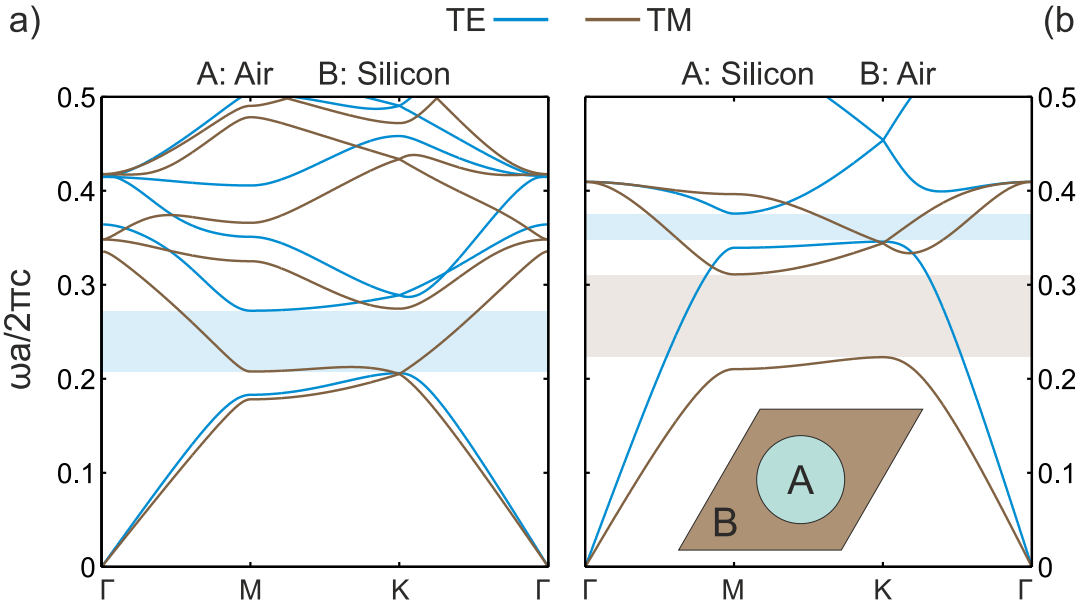

Figure 3.4: Band structure of two-dimensional photonic crystals (PhCs): the role of the inclusion's refractive index. Transverse Electric (TE, light blue) and Transverse Magnetic (TM, brown) band structure of a 2D PhC made of infinite cylindrical inclusions of (left) air in silicon and (right) silicon in air. The results are given along the Irreducible Brillouin Zone (IBZ) contour, which suffices since the structure belongs to the *p4mm* crystallographic group. Low-index inclusions in a high-index matrix typically lead to a TE band gap between the first and second bands, as shown with the blue-shaded region. On the contrary, high-index inclusions in a low-index matrix open a TM band gap, shown in shaded brown.

the reverse situation, that of an array of silicon cylinders in an air matrix, is given in Fig.3.4(b). The situation is also reverted and we have now a wide PhBG for TM polarization spanning $[0.224c/a, 0.31c/a]$.

3.4 Three-dimensional confinement with lower-dimensional periodicity

One of the main quests in both photonics and phononics is controlling the propagation properties in three dimensions, something possible with periodic structures in all three directions. The possibility of having omnidirectional band gaps would allow perfectly-shielded spatially-confined excitations, a task that is extremely complicated otherwise, specially in optics since electromagnetic radiation can propagate in vacuum. Three-dimensional PhCs with full band gaps are therefore a sort of grail for physicists and engineers and their realisation was the main goal of the early PhC research. Since then, a number of 3D PhC implementations have been realized. Some examples are the famous 'Yablonovite' [148], self-assembled colloids/inverse opals [149,150] or woodpile structures [151,152]. Nevertheless, they are still highly undeveloped in practice, specially at the nanoscale, where only approaches based on stacked layer-by-layer 2D crystals [153–155] have been

experimentally realized. The reason for the lack of scalable 3D PhCs at frequency ranges nowadays relevant for technology applications is both the challenge to fabricate them and the difficulty to integrate them with the existing (and mature) planar technology. In order to effectively confine light or motion in the three dimensions, other strategies have therefore been explored, among which PhC/PnC slabs are the most widely investigated.

3.4.1 Index guiding and free surfaces

For the case of elastic waves, the solution that enables ominidirectional confinement is extremely simple. It consists in using physical boundaries between a solid material and vacuum to force any propagating elastic wave in the direction of the boundary to be perfectly reflected. In a more realistic environment, the surrounding medium is filled with air, where pressure waves can be launched, however, the mismatch is so large that a boundary between a solid and air can be effectively modelled as a perfectly reflecting interface. In terms of the stress tensor, this condition is denoted as a free surface condition and can be written as

$$\boldsymbol{\sigma}\cdot\mathbf{n} = 0 \quad \forall \mathbf{r} \in \partial V \tag{3.29}$$

where ∂V denotes the boundary of the considered domain V. In principle, elastic energy can be confined in such a way in all three directions, but any object typically needs to be supported to avoid the effect of gravity. The supporting points, like the clamping regions of a suspended solid beam or the contact area of a solid object with a substrate, are both a source of damping and of thermal noise, which prevents strict confinement without energy decay in time. Recently, the motion of trapped particles inside the potential generated by light beams, in essence a levitated object, has gathered increasing attention [156] since they precisely allow motion confinement without any source of radiative losses and/or thermal loading and are candidates to study collapse models that go beyond standard quantum mechanics [157].

Confinement of electromagnetic radiation is achieved via a similar principle by using total internal reflection. We consider an interface between two semi-infinite media of permittivity ϵ_1 and ϵ_2 and asume that $\epsilon_1 > \epsilon_2$. We consider a plane wave inside medium 1 with wavevector $\mathbf{k}_1$ and frequency ω_1 incident at an angle θ_1 upon the interface, as depicted in Fig. 3.5. Energy conservation and translational invariance impose the equality of frequencies $\omega_1 = \omega_2 \equiv \omega$ and the conservation of momentum parallel to the interface, $\mathbf{k}_{1,\parallel} = \mathbf{k}_{2,\parallel} \equiv \mathbf{k}_\parallel$. Given these and the dispersion relation in both media we have

$$\left(\frac{n_2\omega}{c}\right)^2 = |\mathbf{k}_\parallel|^2 + |\mathbf{k}_{2,\perp}|^2 \tag{3.30}$$

which can only hold for imaginary values of $\mathbf{k}_{2,\perp}$ if $\omega < c\mathbf{k}_\parallel/n_2$. This implies that the modes are evanescent away from the interface into the medium 2 and are fully confined to the semi-infinite medium 1, a result which is known as total internal reflection (TIR). This result is actually nothing more than a formal statement of Snell's refraction law in ray optics [158], i.e., $n_1\sin(\theta_1) = n_2\sin(\theta_2)$, above the critical angle $\theta_1 > \theta_c = \text{asin}(n_2/n_1)$, that only exists with the set condition $\epsilon_1 > \epsilon_2$.

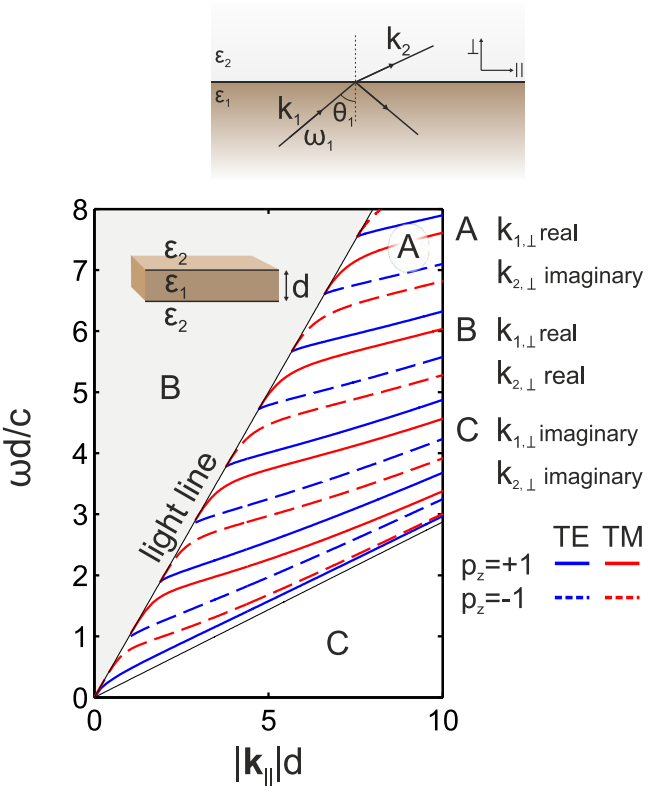

Figure 3.5: Index guiding in an infinite dielectric slab. The interface between two dielectric media of permittivities ϵ_1 and ϵ_2 leads to total internal reflection (TIR) when the incidence angle from medium 1 satisfies $\theta_1 \geq \text{asin}(n_2/n_1)$. When a layer of thickness d and permittivity ϵ_1 is surrounded by a lower index homogeneous medium as shown in the inset, multiple interference of light bouncing between the two interfaces due to TIR leads to a discrete set of modes with frequencies lying between lines given by $\omega = c|\mathbf{k}_\parallel|/n_2$ -the light line- and $\omega = c|\mathbf{k}_\parallel|/n_1$. Within this region (A), modes are labelled as Transverse Electric (TE, blue) or Transverse Magnetic (TM, red) in relation to their symmetry with respect to a plane $\mathbf{z}\mathbf{k}_\parallel$ and as $p_z = +1$ (solid) or $p_z = -1$ (dashed) with respect to the mid-plane of the slab. Region B hosts a continuous eigenspectrum of radiation modes called the light cone, while region C contains no physically meaningful solutions.

Based on TIR, a slab of material with refractive index $n_1 = \sqrt{\epsilon_1}$ embedded between two semi-infinite media of lower refractive indexes n_2 and n_3 can totally confine light into the slab region for frequencies $\omega < c|\mathbf{k}|/\max(n_2, n_3)$. In particular, a slab surrounded on both sides by air supports slab-confined modes with in-plane wavevector $\mathbf{k}$ at frequencies below $\omega = c|\mathbf{k}|$, which we denote by the light line. The condition for constructive interference, i.e., phase matching, of slab-confined light recurrently bouncing at the two interfaces leads to the formation of well-isolated bands below this light line. The discrete nature of the spectrum could have also been deduced via the argument used in Section 3.3, i.e., the equations at a fixed $\mathbf{k}$ are effectively solved for a finite volume of space. The $\omega - \mathbf{k}$ region above that line, the light cone, supports a continuum of radiation modes which far away from the interfaces must approximate plane waves, which are supported at all frequencies ω and $\mathbf{k}_\perp$.

The photonic dispersion relation for a slab of thickness d and refractive index $n_1 = 3.48$ is given in Fig. 3.5. Since the slab has a continuous rotational symmetry around the axis $\mathbf{n}$ perpendicular to the interfaces, the dispersion only depends on the wave vector amplitude $\omega(\mathbf{k}) = \omega(|\mathbf{k}|)$. With the symmetry arguments given in subsection 3.2.4, modes can be categorized into two polarizations, that we again denote by TE and TM. For a particular choice of the wavevector $\mathbf{k}_{\|}$, that we denote from now simply $\mathbf{k}$, the system has a mirror symmetry with respect to any plane defined by $\mathbf{z}$ and $\mathbf{k}$, whose mirror operator we denote $\hat{M}_{\varepsilon_\mathbf{k}}$ with $\hat{\boldsymbol{\varepsilon}}_\mathbf{k} \equiv \hat{\mathbf{z}} \times \hat{\mathbf{k}}$ and $\hat{\mathbf{k}}$ the unit vector along $\mathbf{k}$. Solutions can therefore be split into TE modes with fields $\{\mathbf{E}(\rho, z) = E(\rho, z)\hat{\boldsymbol{\varepsilon}}_\mathbf{k},\ \mathbf{H}(\rho, z) = H_k(\rho, z)\hat{\mathbf{k}} + H_z(\rho, z)\hat{\mathbf{z}}\}$ and TM modes with fields $\{\mathbf{E}(\rho, z) = E_k(\rho, z)\hat{\mathbf{k}} + E_z(\rho, z)\hat{\mathbf{z}},\ \mathbf{H}(\rho, z) = H(\rho, z)\hat{\boldsymbol{\varepsilon}}_\mathbf{k}\}$. In addition, for a slab with common cladding and substrate as shown in Fig. 3.5 the mid plane of the slab is a plane of symmetry and modes can therefore be categorized with respect to the mirror symmetry $\hat{M}_z$ as even ($p_z = +1$) or odd ($p_z = -1$). The particular form and trascendental equation for the optical modes of an isotropic material slab are described in detail in Appendix A, since they constitute an extremely well-suited basis to expand the solutions of the eigenvalue problem for PhC slabs, as done in the Guided Mode Expansion (GME) [159].

One should note here that not all eigenmodes at a particular $\mathbf{k}$ above the light line possess the same behaviour. Solving the eigenproblem (3.8) for QNMs with complex eigenfrequencies as described in Subsection 3.1.1 leads to solutions with $\mathrm{Im}(\omega) \neq 0$ above the light cone which represent resonant states for which the fields are highly concentrated in the slab but over time leak into the radiation continuum [160]. These are therefore modes with a finite lifetime and can be well represented by QNMs [161]. The particular case of $\mathbf{k} = 0$ will be described in more detail on the next Chapter in the context of propagation of normal-incidence light in a multilayer structure.

3.4.2 Photonic and phononic crystal slabs

Photonic and phononic crystal slabs are structures exhibiting 2D in-plane periodicity and a slab structure as the one described above in the vertical out-of-plane direction. In this thesis we limit ourselves to suspended structures for which both cladding and substrate are made of air, which behave as some sort of hybrid between the two pictures already described and depicted in Figs. 3.3 and 3.5. They exhibit band gaps due to the high degree of dispersion control allowed by the in-plane periodicity while confining in the transverse direction due to TIR. They constitute the most widely used approach to engineer light and motion propagation in three dimensions and can be routinely realized at submicrometer length-scales by advanced lithography and etching.

Figure 3.6 depicts the photonic band diagram of a silicon slab into which a triangular lattice of cylindrical air holes has been etched. The in-plane parameters are chosen as in Fig. 3.3, the period is $a = 500$ nm and the thickness is set to $d = 250$ nm. As evidenced by the grey shaded regions in Figure 3.6(a,b), the occurrence of a radiation continuum above the light line is preserved for the etched slab since the cladding and substrate remain homogeneous unstructured

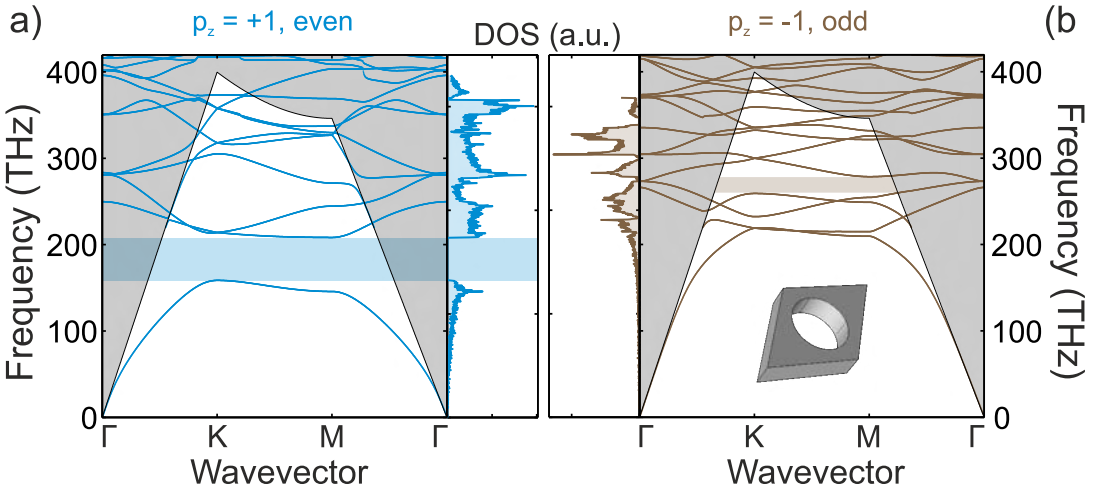

Figure 3.6: Band structure of a two-dimensional photonic crystal (PhC) slab of air holes in silicon. Eigenspectrum of a 2D PhC slab obtained by etching a triangular lattice of holes in a silicon slab. The band structure for modes of even (odd) parity with respect to the mid-plane, i.e., $p_z = +1$ ($p_z = -1$), is given along the Irreducible Brillouin Zone (IBZ) contour Γ-K-M on the left (right). The inset to (b) shows the unit cell. The in-plane parameters are chosen as in Fig. 3.4 and the thickness is set to $t = 0.5a$. The density of optical states (DOS), as obtained from applying Eq. (3.28) over the bundle of guided and quasi-guided bands inside the full IBZ, is depicted with the corresponding color for both polarizations. The DOS evidences a band gap -shaded rectangle- for z-even or TE-like modes which is faithfully captured by the minima/maxima along the IBZ contour. A band gap for guided z-odd or TM-like modes is also evidenced. The pitch a has been set to 500 nm, which leads to a z-even gap around 190 THz.

media. However, the band diagrams of Figure 3.6 also depict discrete bands in the radiation continuum. The portion of the folded bands at frequencies above the light cone suffers from diffraction by the periodic potential, which leads to lossy slab-confined bands, i.e., they become *quasi-guided* or *leaky*. For the particular thickness d used for Fig. 3.6, a critical parameter for the dispersion [71], the PhC slab inherits the TE PhBG observed for the 2D PhC at $k_z = 0$, but now associated to $p_z = +1$ even eigenstates with respect to the mid plane of the slab, often called TE-like modes. Since a true complete PhBG is not possible due to the presence of the radiation continuum, we define two different types of gaps for PhC slabs. First a guided PhBG, which we define as a range of frequencies ω for which there are no guided modes. The second type of gap, that we denote as in-plane PhBG, extends accross both the guided and the leaky resonances. Achieving an in-plane PhBG is of great importance to reduce radiation losses in real fabricated structures, since unintentional fabrication imperfections or any other perturbation, can easily couple a guided mode to a quasi-guided lossy band at the same frequency due to the large local DOS. While the PhBG spanning 158.5 - 208.3 THz shown in Fig. 3.6(a) is of the second type, the structure also exhibits a narrow PhBG of the first type spanning 259-8 - 278.5 THz for odd or TM-like modes. The depicted bands are computed using an in-house GME code, whose

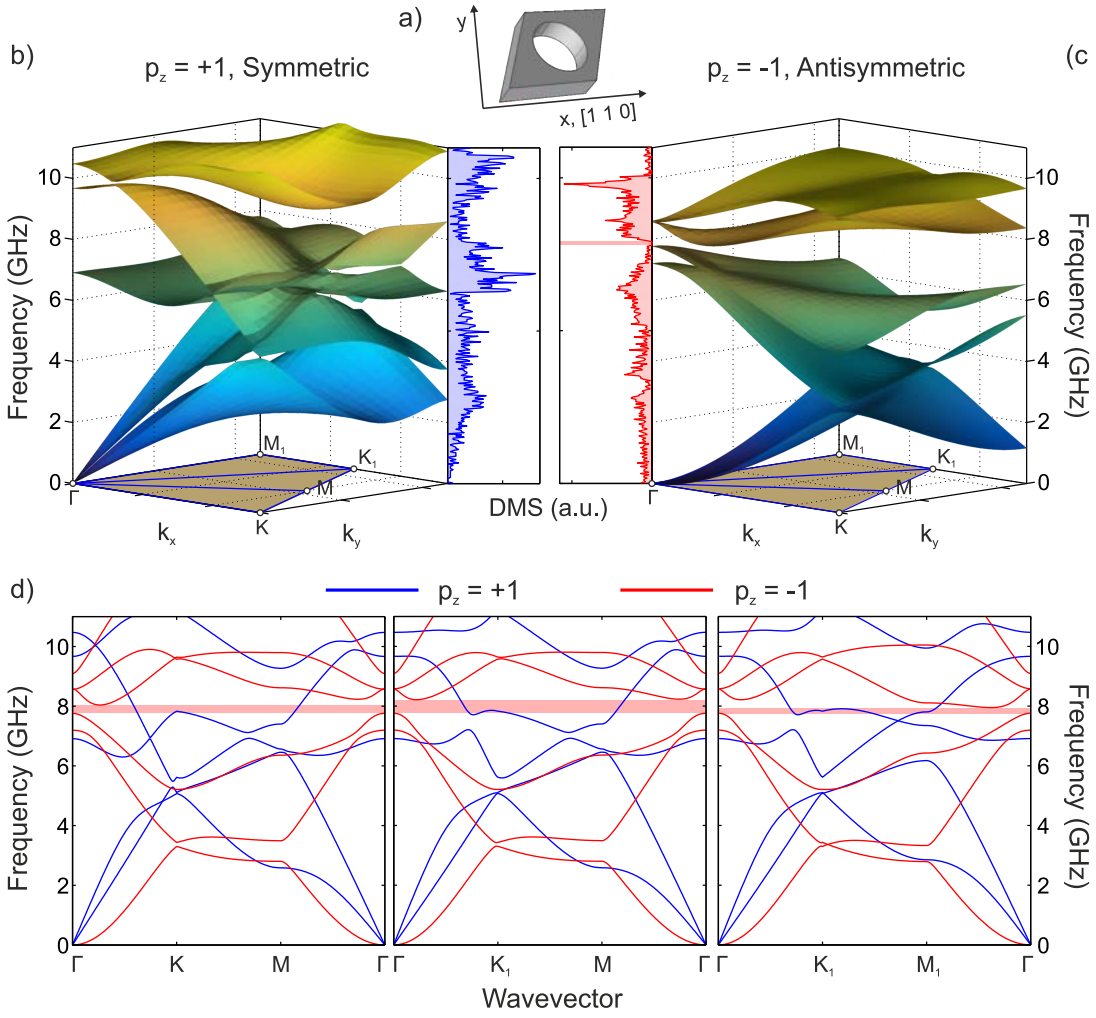

Figure 3.7: Band structure of a two-dimensional phononic crystal (PnC) slab of circular air holes in silicon. Eigenspectrum of a 2D PnC slab obtained by etching a triangular lattice of holes in a silicon slab. The unit cell is given in (a), with the crystalline axis of silicon given for reference. The band structure for modes of (b) even ($p_z = +1$) and (c) odd ($p_z = -1$) parity with respect to the mid-plane is given inside the Irreducible Brillouin Zone (IBZ). All parameters are chosen exactly as in Fig. 3.6. The density of mechanical states (DMS), from Eq. (3.28), is depicted for symmetric (blue) and antisymmetric (red) polarization. (d) The mechanical band diagram is shown along three high-symmetry paths within the IBZ, the edges of which are given within the brown shaded IBZ depicted in (a) or (b).

underlying principle is posing the eigenvalue problem (3.8) in a basis made of the guided modes of an effective dielectric slab, which are shown in Fig. 3.5. The leaky modes of the dielectric slab are not considered and the basis is therefore incomplete, resulting in a band structure with only guided and lossless quasi-guided modes. The losses associated to the portion of the bands above the light line can however be calculated using a Fermi golden rule approach [162]. More details are given in Appendix A.

The phononic band structure for the same crystal is calculated using the

Finite Element Method (FEM) in the commerical solver COMSOL Multiphysics. The band diagram is given in Fig. 3.7. As for the optical eigenstructure, two polarizations can be defined with respect to the mid plane of the slab. However, the PnC band structure needs to be computed in a larger IBZ than in the photonic case due to the cubic crystallography of silicon (see Eq. 3.12). We asume here that the slab surface corresponds to the (001) plane and that the lattice vector $\mathbf{a_1}$ is oriented along x and along the [1 0 0] crystalline direction as depicted in the unit cell of Fig. 3.7(a). Given this information, the IBZ of the PnC is a quarter of the BZ and cannot be reduced to Γ-K-M as for the optical case. The three-dimensional plots in Fig. 3.7(b,c) show the band structure inside the IBZ and the corresponding density of mechanical states (DMS) for even and odd modes. They evidence that there is only a very narrow phononic band gap (PnBG) for the asymmetric modes. Figs. 3.7(c) shows the band diagram for both polarizations along three paths in the high symmetry directions of the artifical crystal. These illustrate that the results yield by considering those paths, very often asumed to give the same bands, differ and that the presence of a full PnBG needs to be assessed within the full IBZ.

The shamrock crystal

As shown in Fig. 3.7(a,b), the typically employed triangular photonic lattice with circular air holes [163] only opens a narrow mechancial bandgap for antisymmetric modes, which is of limited practical use for OM devices. Mohammadi et al. [164] have shown that such a lattice displays no sizeable PnBG for a large range of radius r and thicknesses t and that in order to open a full PnBG square or hexagonal lattices are required. Nevertheless, these lattices lead to a reduced PhBG and the large hole sizes required make them unsuitable to realize high-Q optical cavities [165]. In order to allow simultaneous confinement of light and motion while maintaining the triangular lattice,variations in the shape of the hole have been explored in Ref. [166]. The heuristic design rule to achieve the PnBG is as follows: the mass has to be distributed in such a way that the PnC effectively behaves as a collection of alternating heavy and light masses attached by springs, in analogy to the two-mass phonon toy model in solid-state physics [133], where optical and acoustic phonons are separated by a bandgap. Despite this design rule, numerical studies and experimental evidence of simultaneous PhBG/PnBG in two-dimensional crystal slabs are rather limited, with the most well-known structure being the *snowflake* crystal design from Oskar Painter's group [167,168]. It consists of a triangular lattice of holes with *snowflake* shape or equivalently, by an hexagonal lattice of triangular drumheads connected by small bridges. With this second interpretation, the snowflake crystal faithfully follows the mentioned design rule. This OMC has recently led to cavities with high quantum cooperativity [169] or to back-scatter free topological phononic edge states [170], althought the latter in the MHz range. Despite these major breakthroughs, the community of nanoscale optomechanics may benefit from a simplified design that can be experimentally realized with the current nanofabrication in multiple material platforms.

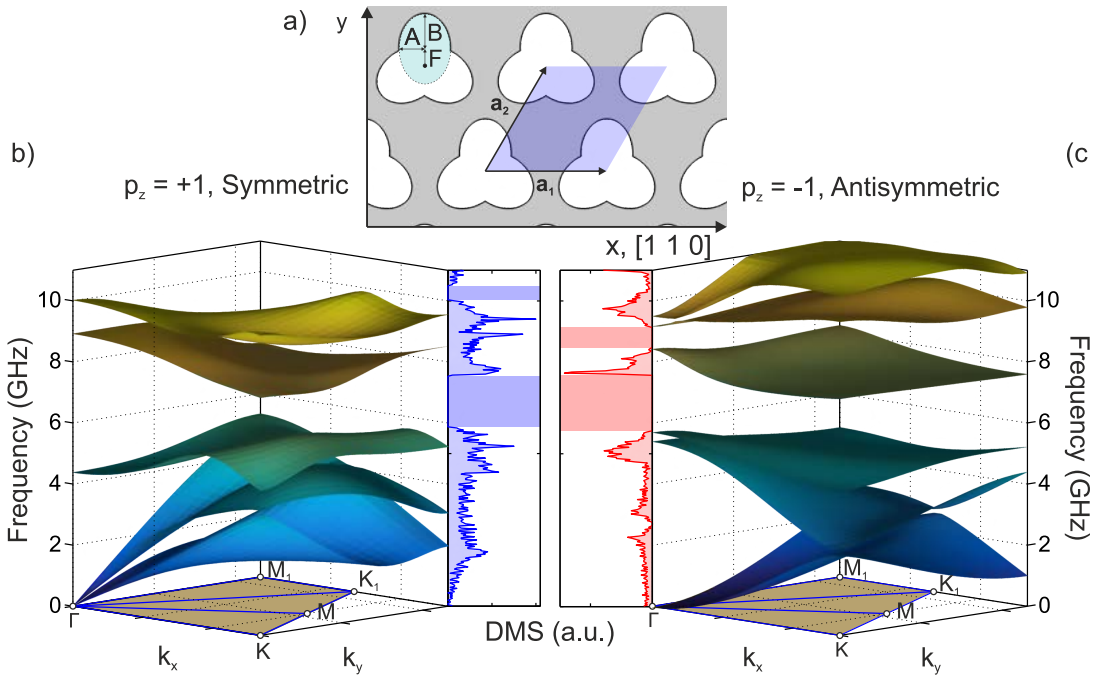

Figure 3.8: Band structure of a two-dimensional phononic crystal (PnC) slab of *shamrock*-shaped air holes in silicon. Eigenspectrum of a PnC slab obtained by etching a triangular lattice of shamrock-shaped holes in a silicon slab. The lattice showing the unit cell, the parameters defining the shamrock and the crystalline orientation, is given in (a). A shamrock is obtained by overlapping three ellipsoids (semi-axis A and B) rotated by $2\pi/3$ with respect to each other and displaced by F along the direction of axis B. The band structure inside the Irreducible Brillouin Zone (IBZ) is given for modes of (b) even ($p_z = +1$) and (c) odd ($p_z = -1$) parity with respect to the mid-plane of the slab. The density of mechanical states (DMS), from Eq. (3.28), is depicted for symmetric (blue) and antisymmetric (red) polarization. The DMS evidences that two wide band gaps are found for each polarization, the first of which coincides in energy and leads to a wide full phononic gap.

In this thesis we explore the geometry initially proposed in Ref. [171] to achieve simultaneous TE and TM gaps in 2D PhC and later shown [172] to allow the opening of a full PnBG in a slab architecture, where the photon-phonon interaction mediated by an embedded Zeeman-split quantum dot was studied. It consists of a triangular lattice of *shamrock*-shaped holes. Each hole is made by the union of three overlapping ellipses rotated by $2\pi/3$ with respect to one another, as shown in Fig. 3.8. The minor and major semiaxes of the ellipse are denoted by A and B, and each ellipse is shifted outwards along its major axis by a distance F. With the [1 1 0] crystalline axis aligned with the $\mathbf{a_1}$ lattice vector, the IBZ of the PnC is given by the region bounded by the path Γ-K-M-K_1-M_1 (see Fig. 3.2(c)), which coincides with the IBZ given in Fig. 3.7 despite the additional symmetries broken. Note that Ref. [172] misjudged the IBZ despite mentioning that the full anisotropy of GaAs was considered.

The band structure for both symmetric and antisymmetric mechanical modes for a structure with parameters $a = 500$ nm, $A = 0.21$a, $B = 0.28$a, $F = 0.15$a

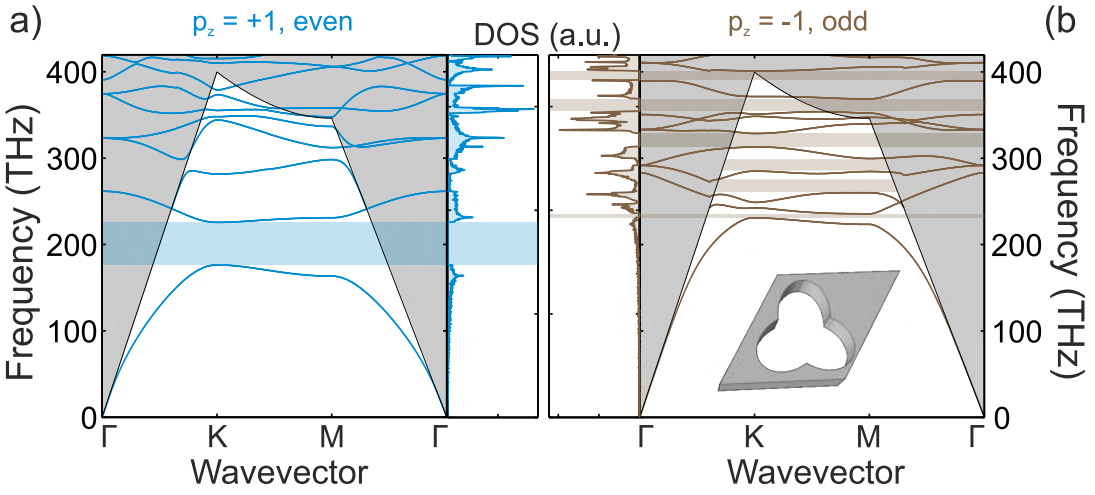

Figure 3.9: Band structure of a two-dimensional photonic crystal (PhC) slab of *shamrock*-shaped air holes in silicon. Eigenspectrum of a PhC slab obtained by etching a triangular lattice of shamrock holes in a silicon slab. The band structure inside along the Irreducible Brillouin Zone (IBZ) contour is shown for modes of (a) even and (b) odd parity with respect to the mid-plane of the slab. The density of optical states (DOS), as obtained from Eq. (3.28), is depicted for both polarizations. The DOS evidences that the wide z-even in-plane photonic band gap (PhBG) is preserved in the shamrock crystal, while both guided and in-plane PhBGs open for the z-odd polarization.

and $t = 0.5$a is shown in Fig. 3.8(a,b), along with the DMS. Two PnBGs are found for each polarization, the first of which coincides in energy and leads to a wide 1.7 GHz full PnBG p at ~ 7 GHz. The photonic band diagram for the same structure along the Γ-K-M path, which corresponds to the IBZ for the photonic case, is shown in Fig. 3.9. The wide in-plane PhBG for z-even modes is preserved, which makes the shamrock crystal a potential platform for high-frequency optomechanics with strong radiation-pressure interaction of cavity photons and cavity phonons. In Chapter 5 of this thesis we will see how to employ the shamrock crystal as a building block to mediate OM interactions in the presence of unavoidable fabrication imperfection, both with guided mechanical resonances in a linear defect and with low-frequency MHz motion.

3.4.3 Photonic and phononic crystal nanobeams

The dimensionality of the periodic pattern can be even further reduced by using dielectric waveguides with a one-dimensional pattern in the propagation direction with finite thickness and width. Confinement in both directions perpendicular to the propagation axis is provided by TIR while the periodic pattern provides a high degree of dispersion control.

Most of the work devoted to patterned nanobeams has focused on straight ridge waveguides with a pattern of circular or elliptical holes [73], whose basic unit cell is shown in an inset to Fig. 3.10(a). For vertically etched holes centered along the axis in the nanobeam, the structure possesses both a $\hat{\sigma}_z$ and a $\hat{\sigma}_y$ symmetry

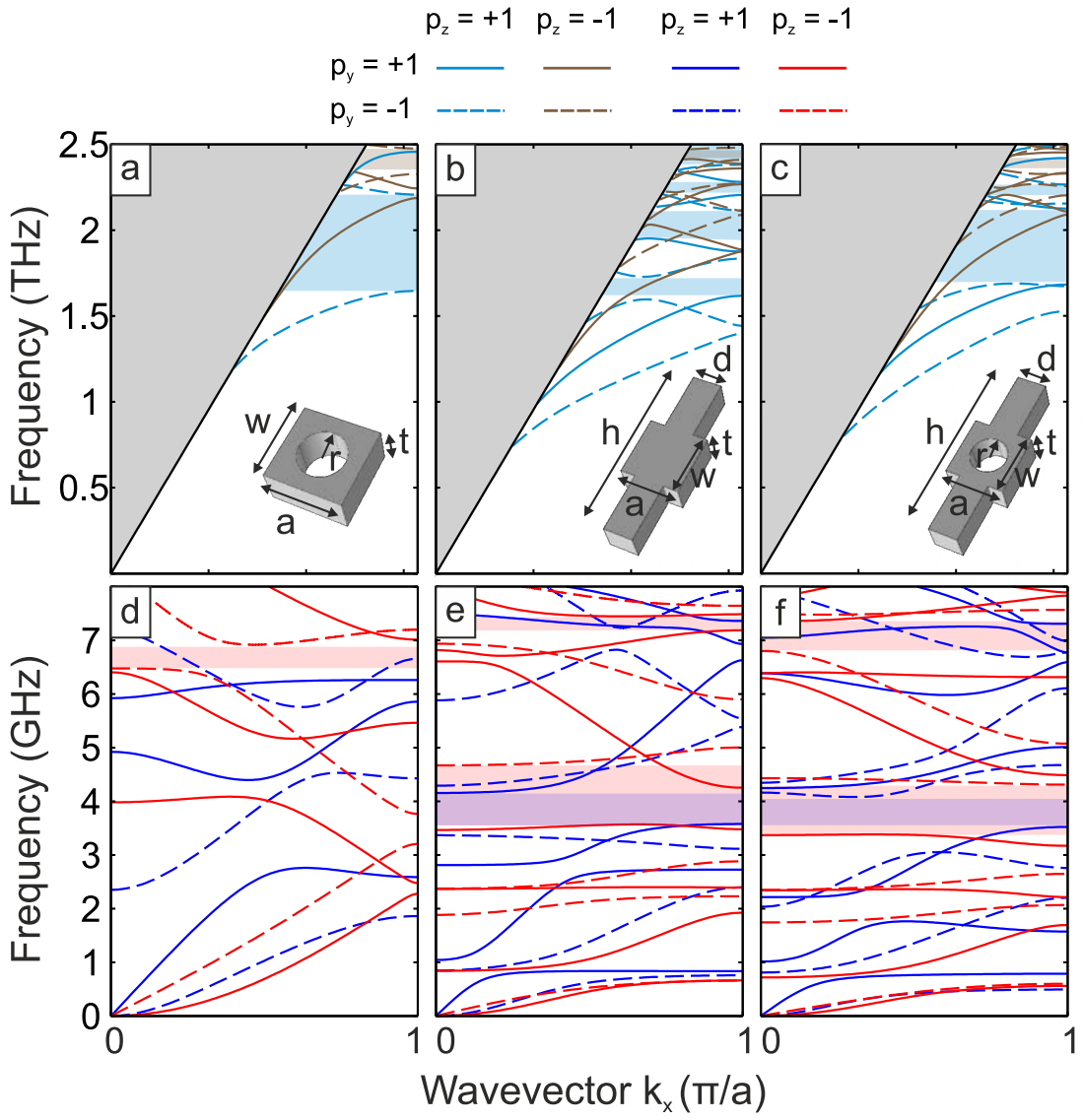

Figure 3.10: Photonic and phononic band structure of patterned nanobeams. Suspended dielectric wires, i.e., nanobeams, can be patterned along their axis to tailor the propagation of both light and acoustic waves. (a,b,c) provide the optical (top) and mechanical (bottom) band diagram for three possible choices of the unit cell. The first case shown (a) consists of a strip waveguide with a pattern of etched circular holes. The parameters used are $a = 500$ nm, $w = a$, $r = 0.3a$ and $t = 0.5a$. It exhibits a wide photonic band gap (PhBG) for z-even modes and a small phononic band gap (PnBG) for z-odd modes. To open a mechanical gap for both polarizations, a unit cell based on long rectangular corrugations of length $h = 3a$ and width $d = 0.5a$ is shown in (b), where the rest of common parameters remain unmodified. Despite the full PnBG that opens around 4 GHz, the wide PhBG is replaced by smaller ones. The structure shown in (c), a combination of (a) and (b), inherits their properties, notably the two gaps.

with respect to the mid-z and mid-y planes, respectively. This leads to splitting the modes into four categories: $\{p_z = +1, p_y = +1; p_z = +1, p_y = -1; p_z = -1, p_y = +1; p_z = -1, p_y = -1\}$. For a nanobeam with periodicity a, circular holes of radius $r = 0.25a$, width $w = a$ and thickness $d = 0.5a$, a PhBG between the lowest guided bands can be observed (Fig. 3.10(a)) for TE-like modes ($p_z = +1$), somehow inherited from the one observed along Γ-K for the 2D PhC slab of Fig. 3.6(a). The phononic band structure of that same beam is depicted in Fig. 3.10(d) and shows that only a narrow gap for antisymmetric modes is open. If a full PnBG is sought after, an alternative structure consisting of a strip waveguide with corrugations [173,174] can be designed. Its photonic and phononic band structures are depicted in Fig. 3.10(b) and (e), respectively. While the latter evidences the presence of a mechanical band gap spanning Ω = [3.6-4.15] GHz, the wide PhBG is lost, since the previously described *thumb* rule of having low-index inclusions in high index material is not fulfilled.

A corrugated nanobeam that exhibits both a TE-like in-plane PhBG and a full PnBG was conceived [175] and characterized [176]. It merges the two previous systems into a structure like the one depicted in the inset to Fig. 3.10(c). The photonic and mechanical properties of such a design strongly inherit the features observed in (a) and (e) respectively. While the individual gaps are wider in (a) and (e), the structure posseses both a wide photonic and mechanical band gap in the same frequency regions, as shown in Fig. 3.10(c) and (f), respectively. The geometry of the holes and the wings provides independent control over the optical and mechanical dispersion, a key figure in designing OMC cavities based on this unit cell [177]. This has been recently used to design for the first time a silicon OM oscillator which operates within a full mechanical gap [178]. We later use this property when we assess the role of intentional disorder in localizing the optical and mechanical fields.

3.5 Optomechanical crystal cavities: the case of nanobeams

It is a well-known concept in solid-state physics that local defects in the crystal structure of a band-gap material introduce energy eigenstates inside the band gap [179]. In addition, the spatial extent of these eigenmodes is localized in the region of the defect. Analogously, defects in PhCs and PnCs posessing a band gap can lead to mid-gap states. The large degree of control allowed by nano-fabrication makes this property very convenient. One can deliberately create *defects* by mere design of the nano-fabricated pattern and thus build integrated elements that serve a particular function. Examples of these are the introduction of a line defect in a two-dimensional PhC slab to create waveguides or the introduction of a 0D or point defect to create a cavity. Since the dispersion of both the optical and acoustic fields can be shaped via a periodic pattern in a thin silicon slab, defects can then be used to achieve co-localization of vibrational and light modes in a small volume. We review here the traditional strategy to confine photons and phonons using the corrugated nanobeam described in the previous section and explain how to compute the OM coupling coefficient g_o introduced in Chapter 2.

We then evaluate how the presence of distributed disorder in an otherwise periodic lattice can also lead to localized optical and mechanical eigenfields, providing a new strategy to achieve OM coupling in nanoscale structures [180].

3.5.1 Point and other engineered defects

The introduction of a local defect of finite extent in a PhC/PnC nanobeam can lead to the creation of cavities, i.e., resonant localized states. The resulting confinement can either be understood in analogy to solid-state physics or by considering the system as having two PhBG/PnBG mirrors facing each other and an intermediate small region (the defect) where light or motion can eventually oscillate at certain frequencies inside the band gap. We explore here two different types of such defects.

Point-like defects

We first describe a point-like defect, as shown in Fig. 3.11(a), where a strong perturbation is introduced inside an otherwise periodic lattice made of unit cells as the one in Fig. 3.10(c). The defect corresponds to a single unit cell with no wings and no holes, i.e., a suspended strip waveguide of length $a = 500$ nm surrounded by two silicon corrugated PhCs/PnCs. Since the defect preserves the $\hat{\sigma}_z$ symmetry, z-even and z-odd bands do not couple and we can restrict to even optical modes of the defect, for which the gap is open. The chosen geometry also preserves the $\hat{\sigma}_y$ symmetry of the unit cell, which implies that bands of different y-symmetry do not couple via the defect. Additionally, the defect+mirror has a $\hat{\sigma}_x$ symmetry with respect to the plane that cuts the beam at the center of the defect. Using all these symmetries allows us to decouple the calculation of the eigenspectrum of the full structure into that of 1/8 of it. The structure is simulated using COMSOL and surrounding the system by perfectly matched layers (PMLs) [181] to mimic an open system. The use of PMLs in finite-element simulations coupled to complex eigensolvers has been shown to accurately provide both the optical and mechanical QNMs [130] . The latter is particularly important for the optical eigenproblem because the modes are not confined to the slab. Fig. 3.11(b,c) illustrate the optical eigenmodes supported by such a point defect. The spectral position of the allowed states is shown within the TE-like bandstructure in (a), while (b) displays the y-component of the field profile $E_y(x, y, z = 0)$ of the localized optical modes. All three allowed modes have common $p_y = -1$ parity, which probably results from the much higher frequency of second order modes in the central strip waveguide [182].

Adiabatic confinement potentials

While this type of abrupt point defect suffices to confine the optical and mechanical modes to extremely low modal volumes, it is rather poor in terms of light storage. The simulated optical quality factors Q for this type of abrupt defect (Fig. 3.11(c)) show that it is not suitable to obtain long-lived optical resonances. Confining light to a given region of space in the slab leads to a finite extension of the cavity field profile in k-space, whose wavevector components within the light cone couple to the radiation continuum. While multiple strategies both in real

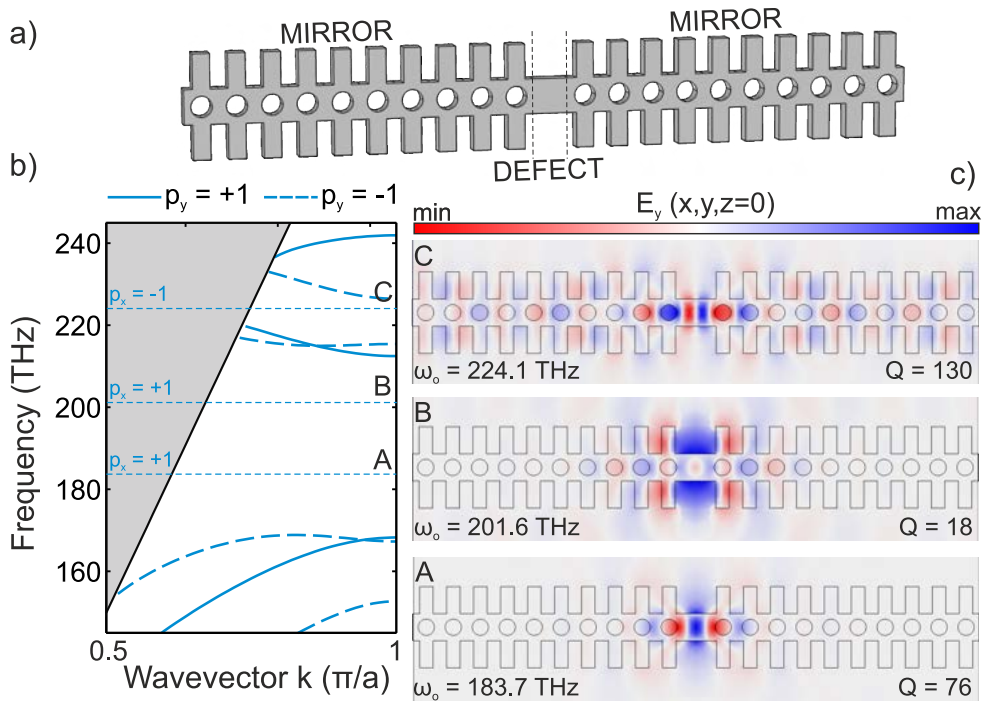

Figure 3.11: Point defect optical cavities in a silicon optomechanical crystal (OMC). (a) A point defect consisting of a strip waveguide embedded between two finite OMCs leads to spatially localized defect states within the TE-like photonic band gap (PhBG). The optical band diagram is reproduced in (b), with y-even (odd) modes given with solid (dashed) blue lines. (c) Electric field component $E_y(x, y, z = 0)$ of the allowed defect states, with their frequencies ω_o and Q-factors. Their position within the band gaps is shown with either solid or dashed horizontal lines in (b) along with the symmetry of the field with respect to the plane intersecting the beam at the center of the defect. All of the supported defect states have $p_y = -1$ parity.

and reciprocal space have been pursued to circumvent this issue [183–185], all of them agree on the importance of the smoothness of the cavity envelope. A Gaussian envelope is Fourier transform-limited, which leads to the smallest possible extension in k-space and therefore constitutes an efficient way to supressess those k-vector components.

The most straightforward way to achieve a smooth cavity envelope is to use a smooth potential. This strategy relies on engineering the band structure by adiabatically changing the unit cell geometry in the direction of periodicity. In this way one can construct an optical or a mechanical trap [186,187]. A standard strategy to define the trap corresponds to changing the pitch a quadratically/cubically from the mirror cell a_{mir} to a central defect cell $a_{def} = \Gamma a_{mir}$ and back to a_{mir}. The rest of geometrical parameters, which are defined in fractions of a, change accordingly. Although the thickness t remains constant, the conditions to use the scaling properties of Maxwell's equations [72] are approximately satisfied for small values of Γ, which implies that the band structure is approximately scaled by a factor of Γ. This allows a progressive shift of the bands for the same corrugated nanobeam. If one changes the geometrical parameters following a cubic

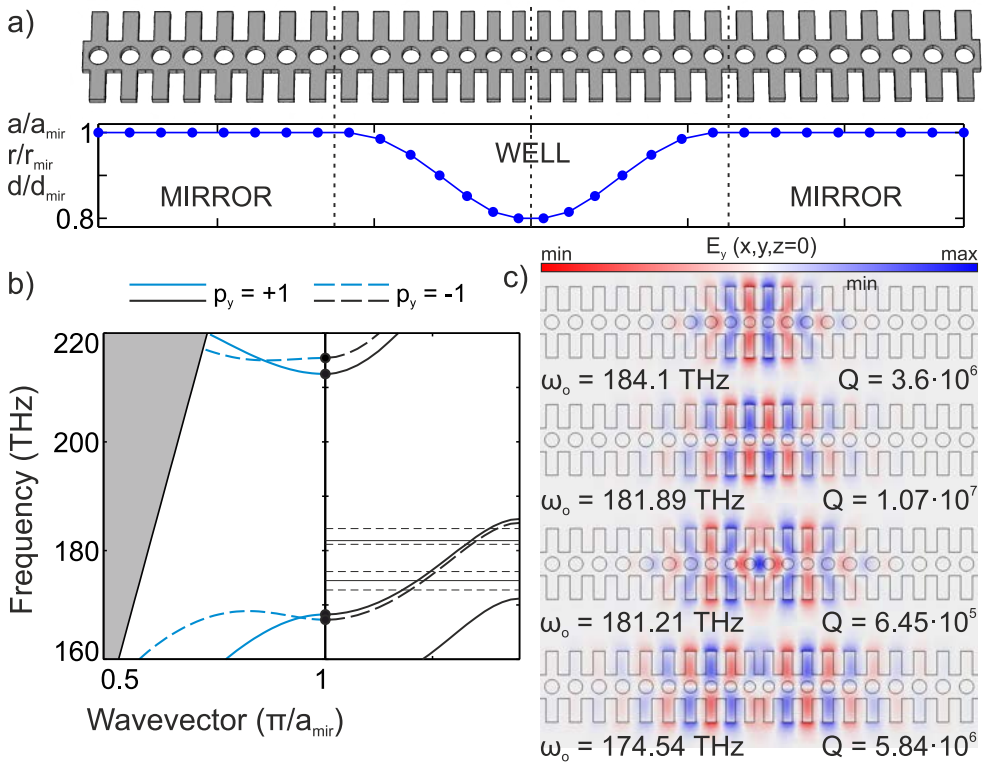

Figure 3.12: Adiabatic optical cavities in a silicon optomechanical crystal (OMC). (a) A typical adiabatic defect consists of a geometrical transformation that smoothly transitions from a nominal unit cell with characteristic width a_{mir} to a defect unit cell of width $a_{def} = \Gamma a_{mir}$, and back to a_{mir} following the mirror transformation. In addition to changing the unit cell size a, other parameters may change accordingly, as the radius r and the corrugation width d. (b) Optical band diagram of the mirror unit cell ($a = 500$ nm, $w = 500$ nm, $t = 250$ nm, $h = 1500$ nm, $r = 0.3$a and $d = 0.5$a), with the zone edge ($k = \pi/a$) modes highlighted with black dots. The evolution of their frequencies along the potential well shown in (a) is drawn with solid or dashed black lines depending on their y-symmetry. The two lower bands are smoothly drawn into the photonic band gap (PhBG) of the mirror cells, creating a potential well for photons in the adiabatic defect region. This leads to spatially confined states, whose frequencies are highlighted with horizontal lines. (c) Electric field component $E_y(x, y, z = 0)$ of the allowed states, showing a steadily decreasing mode volume towards the top of the well. The Q-factors are given, evidencing how such a strategy is radically superior to the one shown in Fig. 3.11.

function, as shown in Fig. 3.12(a), the lower band edge of the even PhBG generates a smooth potential for photons in the central region of the defect, as shown with green lines in Fig. 3.12(b). Solving Maxwell's equations leads to the set of confined optical modes shown in Fig. 3.12(c), whose quality factors are now all above $5 \cdot 10^5$. Cavity modes formed from both the band edge of the y-symmetric and the y-antisymmetric bands are found. Their symmetries are given by either dashed or solid horizontal lines in Fig. 3.12(b). The same strategy followed here allows confining mechanical modes provided that the geometrical transformation pushes the mechanical band inside a (quasi-)band gap. This is shown in the next

section.

3.5.2 Optomechanical coupling

The introduction of controlled defects in PhC/PnC slabs allows confining the electromagnetic and displacement fields to a tiny region of space. The nearly diffraction-limited level of confinement has been used to enhance the OM interaction [73,178,188–190] up to levels that are hardly achievable with other types of mesoscopic OM resonators, like those based on whispering gallery resonators [191] or Fabry-Perot microcavities [192]. Nevertheless, not all defect cavity modes result in coupled photon-phonon pairs and proper design of the confinement potential is of utter importance. This is due to the symmetries of the resulting cavity fields and to the physical coupling mechanisms.

The interplay between optical and mechanical modes results from changes in the material permittivity due to deformation, i.e., $\Delta\epsilon(\mathbf{U}(\mathbf{r}))$. In silicon OMC cavities two mechanisms need to be considered. The first one is a moving boundary (MB) effect applying to any material. The displacement introduced by the motion during the mechanical oscillation shifts the boundary S of the silicon nanostructure and changes the overall shape of the patterned structure, which in turn affects the frequency ω_o and losses κ of the optical mode. This is equivalent to the radiation pressure force term used in Chapter 2 for the Fabry-Perot cavity with a movable end mirror. Second, the stress induced in the system by the vibration locally modifies the dielectric constant of silicon via the photoelastic effect [193]. Although several approaches for evaluating the interaction strength are possible [194,195], the most easily deployed is perturbation theory, which in addition may provide physical insights through simple mathematical expressions. Since the optical cavities used are designed to have extremely high Q-factors, the commonly chosen approach consists in using an hermitian perturbation theory for closed photonic systems [196]. However, dissipation is unavoidable and can be accounted for by using a non-hermitian treatment and the associated perturbation theory [197,198], which allows computing both the dispersive $g_{o,\omega}$ and dissipative $g_{o,\kappa}$ OM coupling rates, as recently pointed in [199].

The complex coupling rate $\widetilde{g}_o$ between an optical QNM $\{\widetilde{E}(\mathbf{r}), \widetilde{H}(\mathbf{r})\}$ of unperturbed complex eigenfrequency $\widetilde{\omega}_o$ and a mechanical eigenmode $U(\mathbf{r})$ of frequency Ω_m is given by,

$$g_o = \frac{d\widetilde{\omega}_o}{d\alpha} x_{zpf} \equiv (G_{MB} + G_{PE}) \sqrt{\frac{\hbar}{2\Omega_m m_{eff}}} \tag{3.31}$$

where α represents a generalized displacement coordinate [200] associated to a unit-normalized displacement field $\mathbf{u}(\mathbf{r})$, i.e., $\mathbf{U}(\mathbf{r}) = \alpha\mathbf{u}(\mathbf{r})$, and the effective mass m_{eff} is calculated by requiring that the potential energy of the parametrized oscillator is equal to the true potential energy [201]

$$m_{eff} = \int \rho(\mathbf{r})|\mathbf{u}(\mathbf{r})|^2 \mathbf{dr} \tag{3.32}$$

The non-hermiticity manifests in the form of the first-order (complex) perturbation coefficients G_{MB} and G_{PE}, which are given by

$$G_{MB} = -\frac{\widetilde{\omega}_o}{2}\frac{\int_S (\mathbf{u}(\mathbf{r})\cdot\mathbf{n})\left[\Delta\epsilon\widetilde{\mathbf{E}}_\parallel(\mathbf{r})\cdot\widetilde{\mathbf{E}}_\parallel(\mathbf{r}) - \Delta(\epsilon^{-1})\widetilde{\mathbf{D}}_\perp(\mathbf{r})\cdot\widetilde{\mathbf{D}}_\perp(\mathbf{r})\right]}{\frac{1}{2}\int_V \left[\epsilon(\mathbf{r})\widetilde{\mathbf{E}}_\parallel(\mathbf{r})\cdot\widetilde{\mathbf{E}}_\parallel(\mathbf{r}) - \mu(\mathbf{r})\widetilde{\mathbf{H}}(\mathbf{r})\cdot\widetilde{\mathbf{H}}(\mathbf{r})\right]} \tag{3.33a}$$

$$G_{PE} = \frac{\widetilde{\omega}_o}{2}\frac{\int_V \frac{\epsilon(\mathbf{r})^2}{\epsilon_0}\widetilde{\mathbf{E}}\cdot(\mathbf{p}:\mathbf{S})\cdot\widetilde{\mathbf{E}}}{\frac{1}{2}\int_V \left[\epsilon(\mathbf{r})\widetilde{\mathbf{E}}_\parallel(\mathbf{r})\cdot\widetilde{\mathbf{E}}_\parallel(\mathbf{r}) - \mu(\mathbf{r})\widetilde{\mathbf{H}}(\mathbf{r})\cdot\widetilde{\mathbf{H}}(\mathbf{r})\right]} \tag{3.33b}$$

where we have introduced the normal unit vector $\mathbf{n}$ to surface S between media 1 and 2, $\Delta\epsilon = \epsilon_1 - \epsilon_2$, $\Delta(\epsilon^{-1}) = \left(\frac{1}{\epsilon_1} - \frac{1}{\epsilon_2}\right)$, the fourth-rank photoelastic tensor $\mathbf{p}$ and the strain tensor $\mathbf{S}$ as given by (3.11). Expressions (3.33a) and (3.33b) correspond to the typically employed expressions [67,202], provided that the terms $\widetilde{\mathbf{F}}\cdot\bullet\cdot\widetilde{\mathbf{F}}$ are replaced by $\widetilde{\mathbf{F}}^*\cdot\bullet\cdot\widetilde{\mathbf{F}}$, with $\mathbf{F} = \mathbf{E}$ or $\mathbf{H}$. These transformations arise from replacing the standard power orthogonality of normal modes in hermitian systems [182], by the bi-orthogonality of QNMs [123,203]. To ensure completeness of the QNM basis [204], the integration volume V comprises the PMLs used to truncate the computational domain. Once $\widetilde{g}_o$ given, the dispersive and dissipative coupling rates are found respectively by $g_{o,\omega} = \mathrm{Re}(\widetilde{g}_o)$ and $g_{o,\kappa} = 2\mathrm{Im}(\widetilde{g}_o)$, respectively. The vacuum OM coupling rate g_o as defined in Chapter 2 corresponds to $g_{o,\omega}$ and its value is very well aproximated by the hermitian theory in the case of high-Q cavities. Since we only consider the dispersive coupling in this thesis, we restore from now to the common notation $g_o \equiv g_{o,\omega}$. The non-hermitian perturbation theory provides the right theoretical framework to engineer devices with strong dissipative coupling, e.g. plasmonic systems, and deserves increasing attention in the optomechanics community. In addition, the deformation $\mathbf{u}(\mathbf{r})$ has no time dependence and Eq. (3.33a) can be used to calculate the first-order changes in both frequency and losses with respect to any prescribed displacement, i.e., its gradient. One can therefore compute the change in Q with respect to, e.g., the rigid displacement of a particular hole. I am currently using the computed gradient to optimize the in-plane and out-of-plane Q-factor of point-like PhC cavities in a large parameter space, but that work goes beyond the scope of this thesis.

Once the first order perturbation expressions are found, the challenge is to select a geometry transformation to a mirror unit cell that not only allows simultaneous confinement of light and motion, but a high dispersive OM coupling rate. Inspection of expressions (3.33a) and (3.33b) is rather instructive in that sense, since they allow determining which mechanical modes are optomechanically dark, i.e., $g_o \approx 0$, in the presence of mirror symmetries. The moving boundary effect results from the product of *squared* terms, e.g. $\mathbf{E}\cdot\mathbf{E}$, with a linear term, i.e., $\mathbf{u}\cdot\mathbf{n}$, and therefore vanishes for mechanical modes which are antisymmetric accross any mirror plane. Although the photoelastic term is more involved, developing the numerator in (3.33b) evidences that for a mode with a dominant optical polarization, which is the case in the structures used in this thesis and in particular in the nanobeams shown in Fig. 3.12, the same selection rule applies [205]. Mechanical modes that are formed from bands with Bloch modes that are symmetric accrosss the y and z planes should therefore be privileged. In addition, mechanical modes

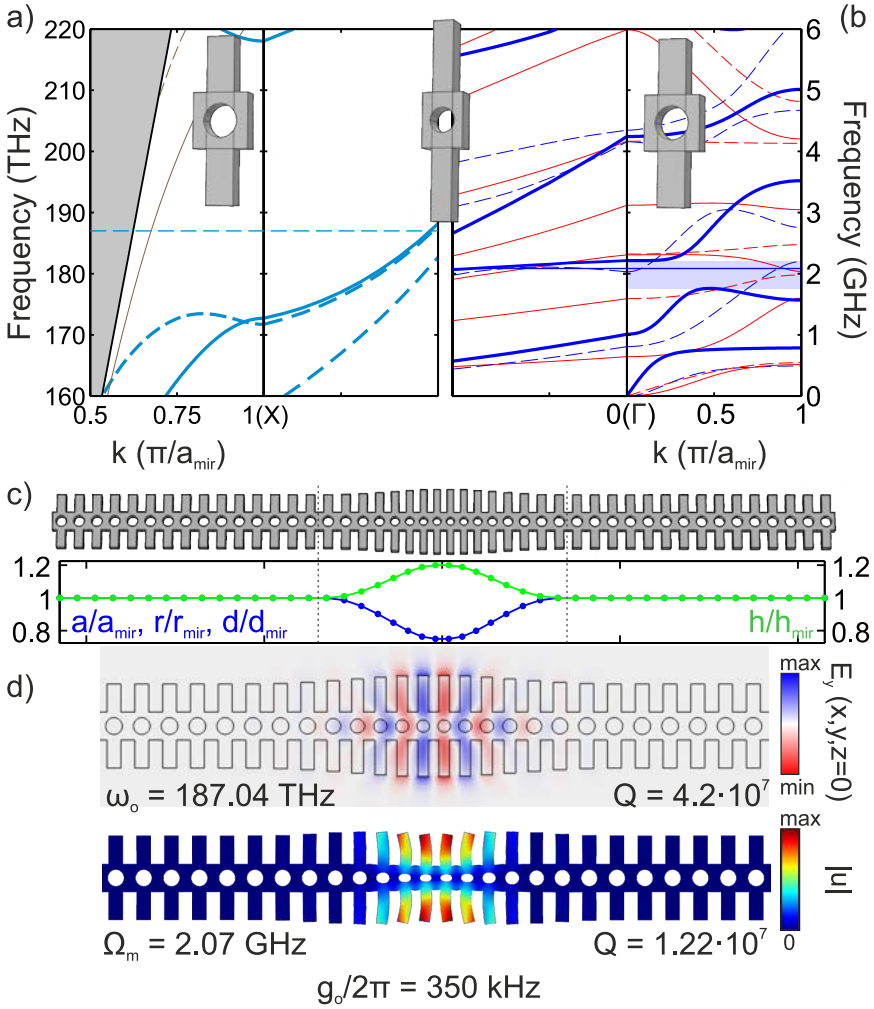

Figure 3.13: Optomechanical crystal (OMC) cavities based on adiabatic potentials. The optical and mechanical band structure of a corrugated silicon OMC can be engineered to (a) push the lower TE-like band edge inside the photonic band gap (PhBG) while (b) pushing a mechanical band of $x/y/z$-symmetric mechanical modes (thick solid blue lines) into a partial phononic band gap (PhBG) (shaded blue). This is done by scaling the geometry in the direction of periodicity while simultaneously increasing the stub height, as shown by the unit cells in the insets, where a, r and d are scaled by $\Gamma = 0.75$ and h by $\Gamma_h = 1.2$. (c) An OMC cavity is created by a cubic transformation from the mirror to the defect cell, leading to the geometry shown in the upper panel. (d) Mode profiles of the calculated optical and mechanical modes having the highest coupling $g_o = 2\pi \cdot 350$ kHz.

originating from the Γ point are preferred since neighboring cells add up constructively, while modes from the X point experience a π phase shift at the unit cell boundary and single cell contributions cancel out. Note that modes at the Γ point of a crystal with a centro-symmetric unit cell are also either symmetric or antisymmetric with respect to the inversion center and that this feature also needs to be considered.

Figure 3.13 shows the design of an OMC cavity based on the corrugated

nanobeam and following the design rules just given. The geometrical transformation proposed employs the same defect cell shown in Fig. 3.12(a) with $\Gamma = 0.75$ with the additional enlargement of the corrugation height h by a factor $\Gamma_h = 1.2$. Panels (a) and (b) show, respectively, the optical and mechanical band diagram of the mirror cell and the evolution of the band edges when linearly transforming the geometry from the mirror cell to the defect cell. This is done at the X (optical) and Γ (mechanical) points, respectively. The stub height has a minimal effect on the optical bands, which increase their frequency due to the scaling of Maxwell's equations. However, it strongly influences the mechanical band structure and counterbalances the frequency rise induced by the decreasing unit cell width a, radius r and stub width d, as shown by the negative slope of the mechanical modes shown as solid blue lines in (b). The band edges of these bands at the Γ point therefore enter the quasi-PnBG for vibrations that are symmetric across the y plane. When a smooth transition along the beam axis -over N_d unit cell periods- from the mirror region unit cell to the central defect unit cell is designed, it leads to a confinement potential and allows both the localization of TE-like optical modes and of z/y symmetric mechanical modes. Fig. 3.13(b) shows the resulting geometry using a smooth cubic function [73] over $N_d = 7$ cells and a mirror of $N_m = 15$ cells. The frequency of the most OM-coupled photon and phonon is highlighted in (a,b) via a horizontal line. This pair is represented in Fig. 3.13(c) along with their vacuum OM coupling rate $g_o/2\pi = 350$ kHz, calculated from the real part of Eq. (3.31). Note that the dissipative coupling $g_{o,\kappa}$ is equal to $2\pi \cdot 247$ Hz, which is much smaller than the dispersive contribution. This is the case for most of the photon-phonon pairs considered in this thesis.

3.5.3 The role of disorder: dissipation and localization

Purposely designed high-Q PhC/PnC cavities exhibiting high OM coupling rates are created via controlled nanopatterning based on engineering the band structure, as shown in Fig. 3.13. Nevertheless, uncontrolled distributed defects are always introduced in the fabricated nanostructures in the form of fabrication disorder. Regardless of the type of disorder, any deviation from the perfect design generally introduces additional dissipation channels, both in the crystal plane and in the out-of-plane direction. The first channel operates both in PhCs and PnCs by coupling the cavity mode to isofrequency propagating modes with other spatial symmetries, if any are present. This is precisely why confining phonons inside a full mechanical gap is particularly appealing, as has recently been done with shrunken wings in Ref. [178]. In the case of photonics, the second dissipation channel also operates and results from the coupling to the radiation continuum. These two mechanisms lead to a decrease of the radiation-limited optical and mechanical quality factors. Fig. 3.14(a) shows the results of simulating 200 realizations of the OMC cavity described in Fig. 3.13 in which the holes are randomly displaced by $\Delta\mathbf{r}$, with $\Delta\mathbf{r}$ distributed according to a normal distribution $\mathcal{N}(0, \sigma^2)$. From now on, whenever we refer to disorder, normal distributions are assumed. The results shown use $\sigma = 0.005a = 2.5$ nm, with $a = 500$ nm the periodicity in the mirror

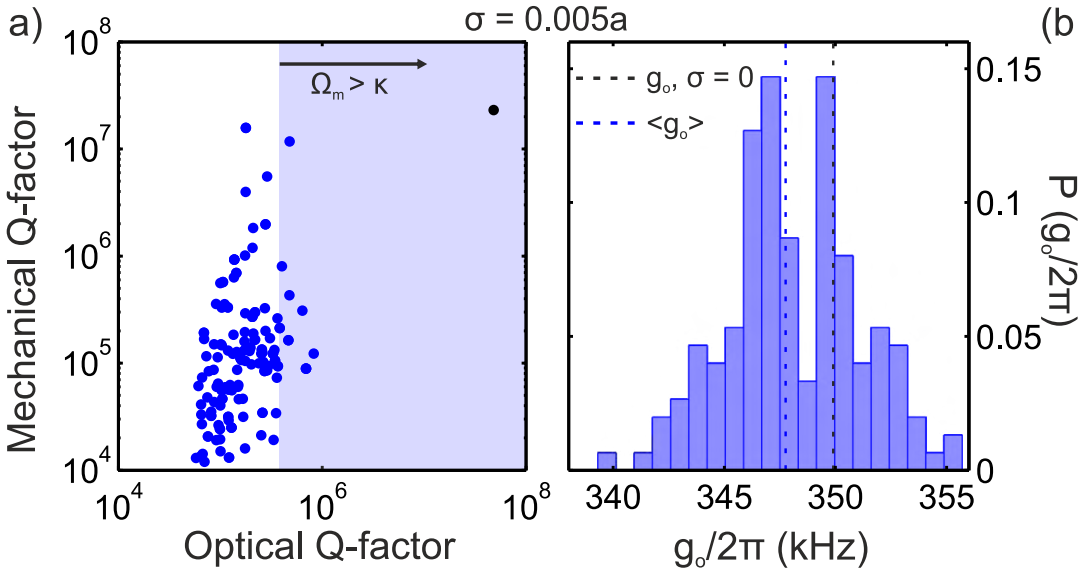

Figure 3.14: Disorder-mediated dissipation in an optomechanical crystal (OMC) cavity. The OMC cavity of Fig. 3.13 is subject to unintentional disorder the position of the holes $\Delta\mathbf{r}$, with $\Delta\mathbf{r}$ distributed according to a normal distribution $\mathcal{N}(0, \sigma^2)$. (a) Optical and mechanical quality factors of 200 disorder realizations (blue dots) with $\sigma = 0.005a$ and of the unperturbed structure (black dot). The shaded region marks the space where the OMC cavity is in the sideband resolved regime $\Omega_m > \kappa$. (b) Histogram of the obtained $g_o/2\pi$ for the same set of disordered structures. The black vertical line marks the unperturbed value and the blue one the average on the set shown.

section, a value that can only be achieved with state-of-the-art nanofabrication technologies.

The optical Q-factor is shown to be dramatically affected by the presence of fabrication disorder, with an average decrease in Q of over two orders of magnitude. This constitutes the main effect of unintentional disorder for the optical Q, since the Q-factors otherwise spread over a rather limited region. The strong effect on $\langle Q \rangle$ stems from breaking the underlying x and y symmetries of the confinement potential, which are crucial in canceling out radiation channels via interference [206]. In contrast, the radiation-limited mechanical Q-factor presents a much broader distribution, with some subset of values close to the unperturbed one (black dot). Nevertheless, the average decrease in Q is also two orders of magnitude. Note that the mechanical mode under study is found in a partial PnBG instead of in the full PnBG (see Fig. 3.13(b)). Random disorder breaks the symmetry that protects the mechanical mode, coupling the otherwise y-even mode to the isofrequency y-odd band of the mirror region, i.e., it adds a dissipation channel. While the cavity OM system is designed to operate in the sideband resolved regime ($\Omega_m \gg \kappa$), the presence of unavoidable fabrication disorder brings the system to the unresolved one, as shown via the blue shaded region of Fig. 3.14(a). This critically limits the possible physical phenomena experimentally accessible, as discussed in Chapter 2. On the contrary, the field profiles do not change significantly and the OM coupling rate g_o is practically unaffected as shown via the

histogram in Fig. 3.14(a). Since disorder is considered detrimental, efforts are usually made to minimize it [73] or finding designs as immune to fabrication disorder as possible [207,208]. We propose here a different strategy focused on exploiting disorder as a resource.

When a crystal is structurally perturbed such as a crystalline solid, a PhC, or an OMC, the ideally propagating Bloch modes undergo random multiple scattering and are sensitive to imperfections, especially at the edges of the band gap [23]. Depending on the propagation frequency or energy, the dimensionality of the system, the nature and level of disorder and the interaction of the system with the environment, disorder-induced scattering can completely change the energy spectrum of the perturbed crystal and the transport properties with respect to the unperturbed one. In the three dimensional case [209], a phase transition from diffusive to insulating occurs when the disorder level is sufficiently high and the modes become localized states, decaying exponentially when ensemble-averaged with a characteristic length scale, called the localization length, ξ. In a quasi-one-dimensional structure like the OMCs described here, the crossover from extended to localized modes occurs at $\xi = L$, where L is the total length of the structure [209]. These disorder-induced narrow resonant states populate the spectrum around the band edges forming a band of localized modes, known as the Lifshitz tail [210], which exponentially decays away from the band edge when ensemble averaging. This band-edge tail in the density of states broadens with increasing disorder and has been measured in, e.g., a photonic crystal waveguide (PhCW) [211]. This type of disorder-induced confinement, also known as Anderson localization, was originally proposed in the context of electronic transport to explain the metal-insulator phase transition induced by structural imperfections in a semiconductor [2]. The idea here is to induce localization of both photons and phonons via intentional disorder and to study the potential of such an approach for cavity optomechanics and as a tool to observe Anderson localization of GHz mechanical vibrations. In Chapters 4 and 5 we will discuss the physics of light and motion localization in some detail, in particular its occurrence within the frequency regions where propagating Bloch modes exist in the unperturbed structure and the connection between the spontaneously localized modes and the density of states given by Eq. (3.28). Here we restrict instead to modes that spectrally appear inside the full mechanical gap or the TE-like photonic gap of the corrugated OM nanobeam, i.e., modes deep inside the Lifshitz tail, which guarantees their localized nature and allows comparison to engineered cavities. Close to the band edge and to first-order, localization can be pictured in close analogy to what we have shown in Fig. 3.13 for an engineered potential. Random geometrical perturbations in an otherwise periodic lattice lead to random fluctuations of the band edge frequencies, which in turn results in a potential landscape where photons and/or phonons can be spatially trapped. This is schematically depicted in Fig. 3.15(a), where the band edge frequencies of the full mechanical gap are shown in the presence of normally distributed wing widths ($\sigma = 0.05a$) across a nanobeam of length $L = 100$a. The approximate extension of the Lifshitz tail, at least for low values of σ depends, therefore, on how sensitive is the gap to variations in the parameter of choice. This is confirmed in panels (b) and (c),

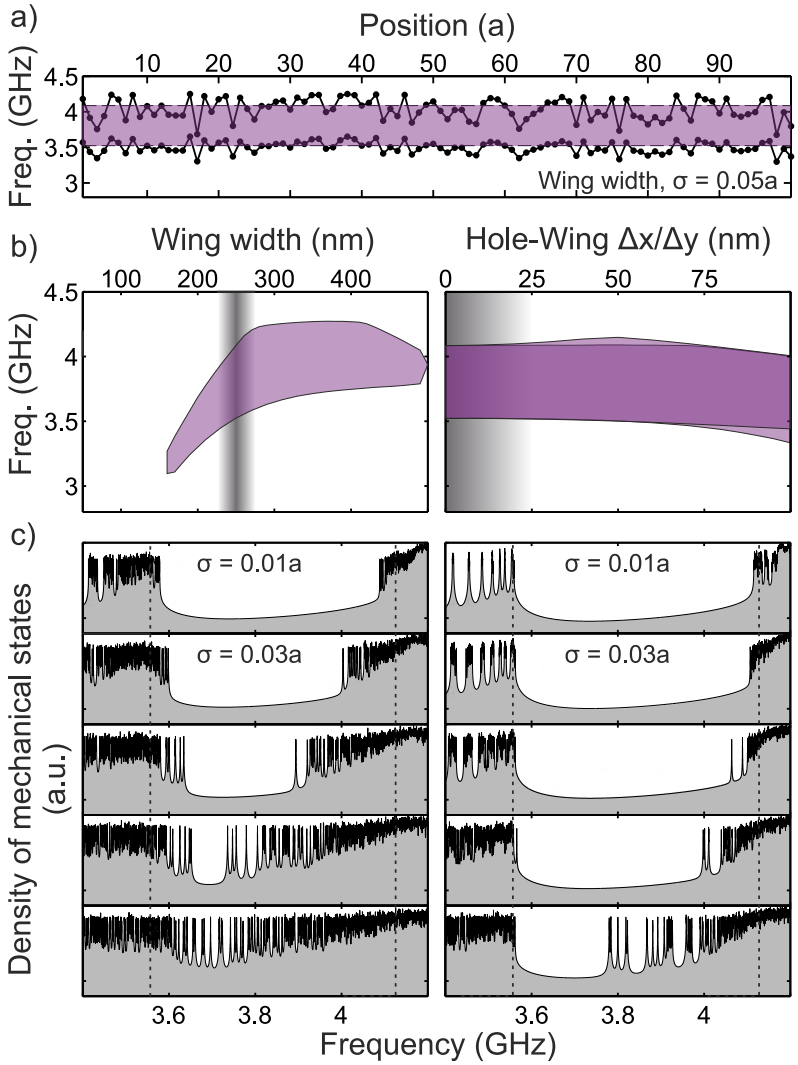

Figure 3.15: Gap maps and sensitivity to disorder. (a) Geometrical disorder leads to a random spatially-dependent potential at the band edges of a photonic/phononic crystal, as shown for disorder in the wing width ($\sigma = 0.05a$) of a corrugated nanobeam of length $L = 100a$. The position of the full mechanical gap band edges is extracted from the corresponding gap map shown below (left). The gap map obtained when changing the position of the circular hole by Δx or Δy is also shown (right). (b) Density of mechanical states (DMS) obtained for disorder in the wing width (left) and hole position (right). Disorder levels $\sigma = \{0.01a, 0.03a, 0.05a, 0.07a, 0.09a\}$ are shown. The Lifshitz band-edge tail is evidenced in both cases, as is the enhanced sensitivity of the DMS to disorder in the wing parameters.

where we show both the gap map and the density of mechanical states for various σ obtained after ensemble averaging over 30 different disorder realizations. The DMS is shown both for disorder in the wing widths and the hole positions (both in x and y). The unperturbed structure has a wing width of $w = 250$ nm and the holes are centered in the unit cell. Such positions are marked in the gap maps with a graded shading, which represents the uncertainty in the value due to the imposed disorder. While the gap position and size is quite sensitive

to the wing width at the values chosen, it is rather independent of variations in the hole position relative to the center of the unit cell. Indeed, the evolution of the gap width with respect to these two has to correspond to either a minima, a maxima or a saddle point since moving the hole in one or the other direction is equivalent. As a result, the Lifshitz tail extends much deeper in the gap for wing disorder. Positional disorder only starts having a strong effect on the band-edge tail at disorders above $\sigma = 0.05a$, a disorder level above which the gap is nearly *destroyed* for wing disorder. Similar results are found for wing height disorder (left) or hole radius disorder (right). Although not shown here, the behaviour for the optics is reverted, with the holes having a much stronger effect than the wings, as was suggested with the simulations shown in Fig. 3.10. At very large levels of disorder, i.e., $\sigma > 0.07a$, the simple picture used here might be considerably wrong, which leads to a sudden increase of the Lifshitz tail, which otherwise grows linearly with σ [180]. This different response opens the exciting possibility to engineer independently their disorder-induced localization.

Finally, we calculate the vacuum OM coupling rate $g_o/2\pi$ between all the photonic and phononic Anderson-localized modes found in a set of structures perturbed by different amounts of disorder using Eq. (3.31). An example of a highly coupled photon-phonon pair ($g_o/2\pi = 183$ kHz) found for a structure with $\sigma = 0.08a$ in the hole positioning is depicted in Fig. 3.16(a), exhibiting a highly localized mechanical mode of effective volume of $V_{eff} = 0.1\mu\text{m}^3$, which represents half of the effective volume of a perfectly engineered mechanical cavity as the one shown in Fig. 3.13. The optical mode shown is spatially broader than an engineered cavity even if intentional hole disorder is employed. The probability distribution of the calculated coupling for ten structures perturbed by $\sigma = 0.04a$ (black dots), $\sigma = 0.08a$ (red dots), and $\sigma = 0.12a$ (blue dots) is shown in Fig. 3.16(b). Deep in the localization regime, many variables deviate from a normal distribution showing heavy-tailed distributions such as the quality factor and the volume of localized modes [212,213], the transmission intensity [214], or the conductance fluctuations [215]. In this case, we also observe a log-normal distribution of $g_o/2\pi$ in the localization regime. The mean value of the log-normal distribution increases with disorder, while the variance has a maximum value for $\sigma = 0.08a$ and then decreases. We attribute this dependence on disorder to a nontrivial interplay between the localization length and the photonic leakage out of the structure. Up to $\sigma = 0.08a$, the localization length is comparable to the total length of the structure thus giving rise to extended leaky modes with poor coupling rates in the range of 0.1 kHz. With increasing disorder, the localization length decreases giving rise to strongly confined modes within the structure with larger coupling rates. For larger perturbation, however, also the leakage of photonic modes increases which reduces both the photonic confinement and the OM coupling. For completeness, the probability distribution of $g_o/2\pi$ calculated when perturbing the width of the wings and the position of the holes by $\sigma = 0.08a$ is shown in the bottom panel of Fig. 3.16(b).The maximum rates are calculated in the hundreds of kHz range and correspond to strongly overlapping photonic and phononic localized modes. These are lower than values attainable for an engineered cavity in the same silicon platform (see Fig. 3.13 or Refs. [176–178]) but place the observation of OM modulation in the Anderson-localization regime at

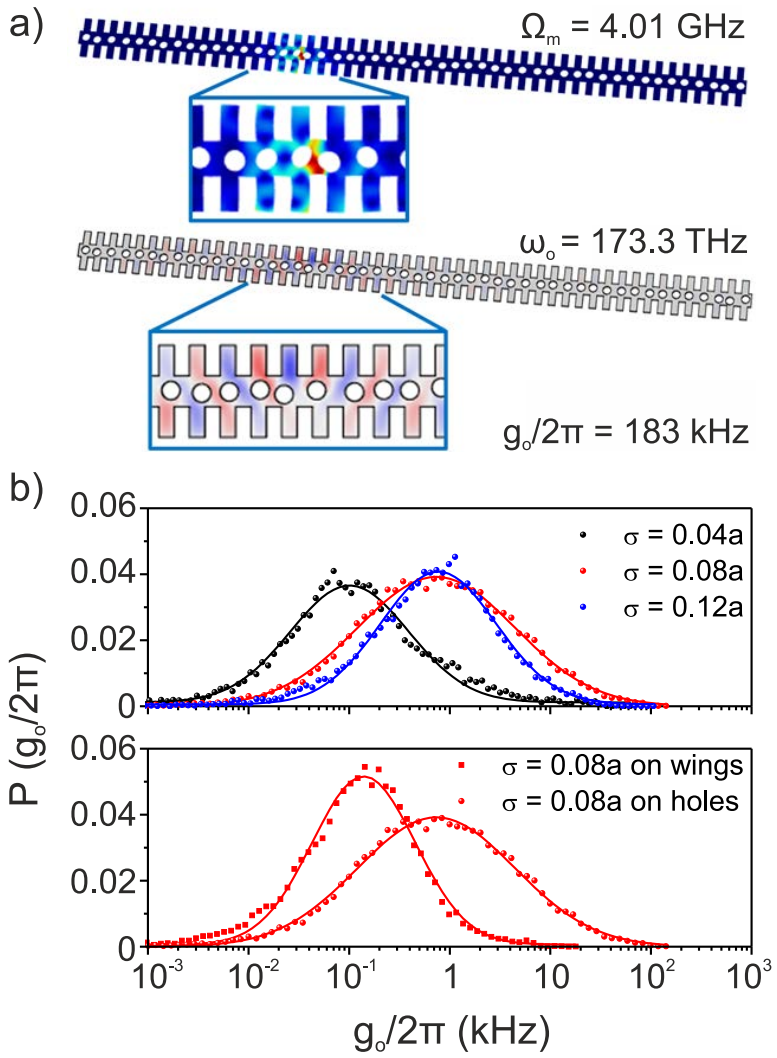

Figure 3.16: Optomechanical coupling in the Anderson localization regime. (a) An Anderson-localized mechanical and optical mode in a corrugated nanobeam of length $L = 50a$ ($a = 500$ nm) where the hole positions are distributed with $\sigma = 0.08a$. Their vacuum optomechanical coupling rate $g_o/2\pi$ is given. (b) Probability distribution of $g_o/2\pi$ calculated between all the Anderson-localized mechanical and photonic modes found in ten nanobeams randomized with a standard deviation $\sigma = 0.04a$ (black dots), $\sigma = 0.08a$ (red dots) and $\sigma = 0.12a$ (blue dots). We fit them with a log-normal distribution. (b) As (a) but with a perturbation of the wings width by $\sigma = 0.08a$ (red squares), compared to the coupling calculated when perturbing the holes by the same amount (red dots).

experimental reach, as only twenty structures have been used to obtain the distributions of Fig. 3.16(b).

Motivated by these calculations, corrugated nanobeams with intentional disorder in several parameters were fabricated in collaboration with Universitat Politècnica de Valencia. The fabricated samples had a fixed amount of $\sigma = 0.02a$

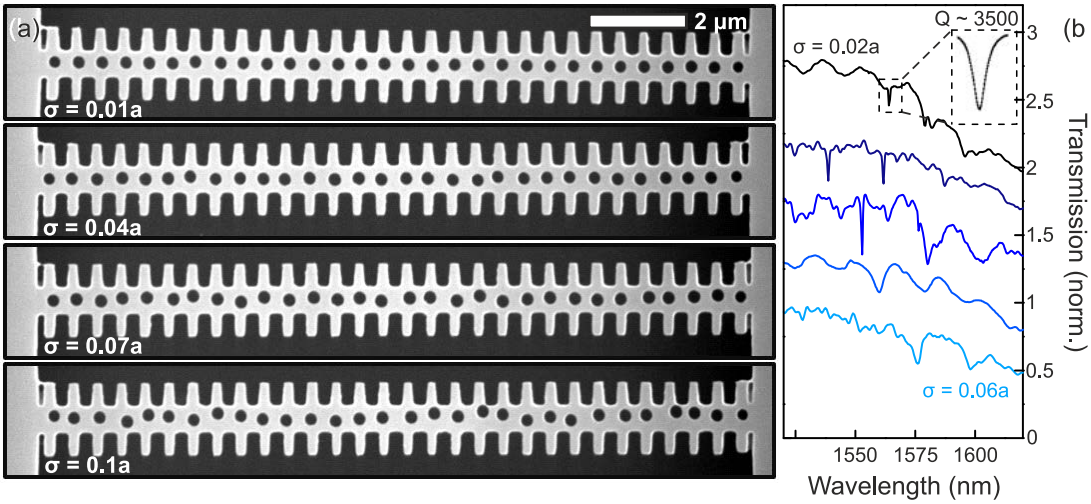

Figure 3.17: Photonic localization in disordered corrugated silicon nanobeams. (a) SEM micrographs of disordered corrugated nanobeams with a deterministic disorder in the wing width ($\sigma = 0.02a$) and increasing disorder in the hole position. (b) Optical transmission spectra measured with an evanescently-coupled fiber taper (see Chapter 5 for experimental details) for a single disorder realization of various values of σ. The inset shows a single optical resonance fitted with a Lorentzian, from which a $Q \sim 3500$ is extracted.

deterministic disorder on the width of the wings to guarantee phonon localization close to the band edge and varying levels of disorder on the hole position to significantly alter the photonic localization properties leaving the phononic ones relatively unaltered. Scanning Electron Micoscopy (SEM) images of the fabricated structures are shown in Fig. 3.17(a). These were optically characterized using an optical fiber taper experimental setup (discussed in detail in Chapter 5). Localized optical modes were observed but with very low Q-factor ($Q < 5 \cdot 10^3$), as exemplified by the transmission spectra of Fig. 3.17(b). The low Q-factors, even lower than in the simulated structures, probably prevented the observation of any OM modulation in the GHz-range.

3.6 Summary

The main notions and results are summarised and the relationship to the content provided in the next Chapters 4 and 5 is given.

- To observe optomechanical interaction in first-order approximation we need to co-localize light and displacement within the same volume. Deterministic defects in periodic structures allow this to happen. Since periodicity in three directions is difficult to achieve at the nanoscale, an alternative is to reduce the dimensionality of the system and use 2D or even 1D periodic structures. In these cases, the confinement in the dimension(s) left is achieved by other mechanisms such as total internal reflection (Subsection 3.4.1). These structures exhibit eigenmodes described by Bloch waves distributed in frequency bands (Section 3.3). An embedded deterministic defect creates localized

eigenstates in otherwise forbidden regions, i.e., band gaps. This is achieved even in quasi-band gaps for modes sharing the symmetries of the introduced defect, i.e., the modes are protected by symmetry. Spatially co-localized photons and phonons can be obtained by appropriate engineering of the band structure (Fig. 3.13).

- The dispersive coupling of an optical cavity mode to a mechanical mode displacement is given by the vacuum optomechanical coupling rate g_o (Chapter 2). We presented here (Subsection 3.5.2) a general treatment to calculate it based on a non-hermitian perturbation theory which uses quasinormal modes, the naturally-ocurring resonances of a lossy system, and goes beyond ultra-high Q cavities. The theory yields a complex coupling $\widetilde{g}_o = g_{o,\omega} + i g_{o,\kappa}$, which also provides the dissipative coupling, i.e., changes in Q depending on the mechanical resonator position x. The dissipative part $g_{o,\kappa}$ is not considered in the rest of this thesis, but the Q factor in an Anderson-localized optical cavity is typically lower than in a designed optical cavity and justifies the use of this theory even for the dispersive part $g_{o,\omega}$. The expressions given here should gain widespread use as they unveil the often neglected role of dissipative coupling in current experiments and offer a way to engineer it. We also analyzed the selection rules that govern the value of g_o when an adiabatic potential is employed. These rules are equally relevant in understanding the role of g_o in the Anderson-localization regime since the localized fields are roughly given by the product of a Bloch mode and a cavity envelope [216]. These ideas are employed to understand optomechanically transduced spectra in Chapter 5 and constitute a set of first-order rules to consider when engineering an optomechanical structure optimal for the observation of phonon localization.

- Cavity-optomechanical systems are parametrized by a few coefficients set either by design or by the optical drive conditions. In a lithographically patterned optomechanical crystal cavity, the presence of unavoidable fabrication disorder typically alters the calculated values for these coefficients. This random disorder leads to additional loss channels, as shown for an optomechanical crystal cavity in a silicon corrugated beam (Subsection 3.5.3), and is often seen as a nuisance. However, disorder can also be exploited as a tool to induce both light and motion confinement. This was illustrated at band gap frequencies for the same corrugated optomechanical nanobeam with intentional positional disorder. However, to bring Anderson-localization optomechanics within experimental reach, one needs to tackle two main issues: lack of co-localization and poor light confinement over time. The first is inherent to the independence of the two interference processes and will generally push the probability distribution function of the dispersive coupling rate g_o to peak at rather low values, as shown for the nanobeams in Figure 3.16. In Chapter 4 we show how to circumvent this limitation using GaAs/AlAs periodic-on-average multilayers. The second issue, low optical quality factors, makes it difficult to the detect mechanical motion by lowering the transduction factor (see Eq. (2.45)). When the disorder levels required to induce localization are very high, as for the nanobeams explored here, the

Q-factor of the Anderson-localized optical cavities are dramatically reduced due to enhanced out-of-plane losses ($Q_{max} \sim 4 \cdot 10^3$). Ideally, the minimum disorder that can be assumed in a fabricated structure, i.e., intrinsic fabrication disorder, should suffice to tightly localize both fields. In the case of optics, photonic crystal waveguides (PhCWs) have proven resourceful for experiments in the Anderson-localization regime even with fabrication deviations as low as 1.5 nm [217]. A dual photonic/phononic crystal waveguide should therefore enable both optical and mechanical localization of waveguided modes with Anderson-localized optical modes at much higher Q-factors. We show in Chapter 5 how a well-chosen line defect in the full mechanical gap of the shamrock crystal we proposed here (Fig. 3.8) enables both light and mechanical guiding and explore this approach in detail.

Chapter 4

Photon-phonon interaction in one-dimensional structures

The simplest photonic and phononic crystal one can envision is a one dimensional structure in the form of a periodic multilayer, also known as a superlattice. Despite its simplicity, the physics of periodic multilayer stacks provide deep insights into the general physics of periodic systems and how propagation can be controlled via alternating material properties. It also allows some analytical derivations, which can cast light on some of the most fundamental effects described in the rest of the chapters. Since this type of system can be grown with epitaxial techniques [218], the quality of the crystalline materials and the atomic-scale level of precision that one can attain on the thicknesses of the constituent layers has opened the door to highly engineered optical and mechanical nanostructures with applications in a broad range of disciplines. We will therefore review the acoustooptic properties of this type of system and how disorder can be introduced to induce localization of both the light and acoustic fields. The last part of the chapter will be devoted to explain how to coherently generate and detect high frequency phonons by pulsed optical means in this type of structure. With the selection rules that result, one of the main experimental results of this thesis, the coherent generation and detection of a topological nanocavity phonon will be described.

4.1 Acoustics and optics in multilayered structures

4.1.1 Acoustic and optical eigenproblem

Following the structure developed on the previous Chapter our goal is to solve the elastodynamic (3.13) and optical (3.8) eigenproblems for a system with a stacking of transversely homogeneous layers of different materials $\{A, B, C, D, ..\}$. We give here the basic mathematical developments and physical assumptions that lead to the simple transfer matrix formalism that is used both in the optical and acoustic domains in the rest of the chapter.

Longitudinal acoustic phonons

Using the translational invariance property in the in-plane direction we can describe the acoustic modes sustained by such a system as

$$\mathbf{U}_{\mathbf{k}_\parallel}(\mathbf{r}) = e^{i\mathbf{k}_\parallel \cdot \boldsymbol{\rho}} \mathbf{u}_{\mathbf{k}_\parallel}(z) \tag{4.1}$$

with $\mathbf{k}_\parallel$ the in-plane wavevector taking any value and function $\mathbf{u}_{\mathbf{k}_\parallel}(z)$ dependent only on the z coordinate. For a generic crystalline material, $\mathbf{U}_{\mathbf{k}_\parallel}(\mathbf{r})$ can have all three components non-null simultaneously and no further polarization information can be given on the supported modes, except when $\mathbf{k}_\parallel = \mathbf{0}$. In such case, the eigenmodes can be split between longitudinal $\mathbf{U} = [0, 0, U_z(z)]$ and transverse waves $\mathbf{U} = [U_x(z), U_y(z), 0]$. Due to the experimental conditions used during this thesis, we can limit our analysis to modes with propagation normal to the interfaces; we set $\mathbf{k}_\parallel = 0$. For the very same reason, we will only consider longitudinal vibrations, for which the only non-null component is U_z, i.e. we define $U(z) \equiv U_z(z)$. The eigenproblem, prior to using any condition on the materials and/or thicknesses, becomes the following scalar eigenproblem

$$-\frac{1}{\rho(z)}\frac{\partial}{\partial z}\left(C(z)\frac{\partial U}{\partial z}(z)\right) = \Omega^2 U(z) \tag{4.2}$$

where we asume that the z direction corresponds to the [100] crystalline direction of all materials and set $C \equiv C_{11}$. The solution inside each homogeneous layer j is known to be a plane wave with a linear dispersion relation and we can locally decompose the field inside the j-th layer as the sum of a propagating and a counterpropagating plane wave

$$U_j(z) = a_{j,+}e^{ik_j z} + a_{j,-}e^{-ik_j z} \text{ for } 0 < z \leq d_j \tag{4.3}$$

with $k_j = \Omega/v_j$ the local wavevector and $v_j = \sqrt{C_j/\rho_j}$ the longitudinal speed of sound in the material j. Note that we define here a local coordinate z at the beginning of each layer. The solution inside layer j can now be given by a two-component vector $\mathbf{a}_j = [a_{j,+}, a_{j,-}]$. At the interfaces between each two layers, the boundary conditions of the elasticity problem impose the continuity of both displacement and stress

$$U_j(d_j) = U_{j+1}(0) \tag{4.4a}$$

$$C_j\frac{\partial u_j}{\partial z}(d_j) = C_{j+1}\frac{\partial u_{j+1}}{\partial z}(0) \tag{4.4b}$$

whose algebraic manipulation leads to the following recursion relation for the vector $\mathbf{a_j}$

$$\mathbf{a}_j = \mathbf{M}_{j,j+1} \cdot \mathbf{a}_{j+1} \tag{4.5}$$

with matrix $\mathbf{M}_{j,j+1}$ given by

$$\mathbf{M}_{j,j+1} = \frac{1}{2}\begin{bmatrix} \left(1+\frac{Z_{j+1}}{Z_j}\right)e^{-iq_j d_j} & \left(1-\frac{Z_{j+1}}{Z_j}\right)e^{-iq_j d_j} \\ \left(1-\frac{Z_{j+1}}{Z_j}\right)e^{iq_j d_j} & \left(1+\frac{Z_{j+1}}{Z_j}\right)e^{iq_j d_j} \end{bmatrix} \equiv \mathbf{L}_j \cdot \mathbf{I}_{j,j+1} \tag{4.6}$$

where we have introduced the acoustic impedance $Z_j = C_j/v_j$. The last equivalence in (4.6) decomposes matrix $\mathbf{M}_{j,j+1}$ into a matrix $\mathbf{L}_j$ that accounts for propagation in layer j and an interface matrix $\mathbf{I}_{j,j+1}$ that connects the field and stress just to the left of the interface between j and $j+1$ to the one just on the right of it. These are

$$\mathbf{L}_j = \begin{bmatrix} e^{-iq_j d_j} & 0 \\ 0 & e^{iq_j d_j} \end{bmatrix} \tag{4.7a}$$

$$\mathbf{I}_{j,j+1} = \begin{bmatrix} \left(1 + \frac{Z_{j+1}}{Z_j}\right) & \left(1 - \frac{Z_{j+1}}{Z_j}\right) \\ \left(1 - \frac{Z_{j+1}}{Z_j}\right) & \left(1 + \frac{Z_{j+1}}{Z_j}\right) \end{bmatrix} \tag{4.7b}$$

which are the two main algebraic building blocks to find the coefficients at a given position once they are known elsewhere. Solving the eigenproblem (4.1) therefore implies using these algebraic relations to construct a global transfer matrix $\mathbf{M}$ together with the appropriate boundary conditions in what is called a transfer matrix formalism [219].

Normal-incidence light

The same stacking behaves as an optical multilayered structure, provided that the different materials $\{A, B, C, D, ..\}$ have different complex permittivities. We assume that all materials are non magnetic, i.e. $\mu = 1$. Much like in the acoustic eigenproblem, translational invariance in the xy-plane allows us to write the eigenmodes sustained by such a structure as

$$\mathbf{E}_{\mathbf{k}_\parallel}(\mathbf{r}) = e^{i\mathbf{k}_\parallel \cdot \boldsymbol{\rho}} \mathbf{e}_{\mathbf{k}_\parallel}(z) \tag{4.8}$$

with $\mathbf{k}_\parallel$ the in-plane wavevector taking any value and function $\mathbf{e}_{\mathbf{k}_\parallel}(z)$ depending only on the z coordinate. Note that we give here the form of the solutions for the electric field $\mathbf{E}$ but the same applies to the magnetic field $\mathbf{H}$. Since we only consider optically isotropic materials, any plane defined by $\mathbf{k}_\parallel$ and $\mathbf{z}$ (the plane of incidence) is a symmetry plane and modes can be split between Transverse Electric (TE) and Transverse Magnetic (TM) polarization, as was seen in Chapter 3, which reduces the vectorial wave equation (3.8) to two uncoupled scalar equations [219]. For TE (TM) waves the electric (magnetic) field is perpendicular to the plane of incidence. For the particular case of on-axis propagation, i.e. $\mathbf{k}_\parallel$=$\mathbf{0}$, the two polarizations are degenerate. We will limit ourselves to this particular case and fix an arbitrary polarization $\mathbf{p} \equiv i\mathbf{x} + j\mathbf{y}$. One can then solve for the scalar field $E(z)$ satisfying

$$-\frac{1}{\epsilon(z)} \frac{\partial^2 E(z)}{\partial z^2} = \left(\frac{\omega}{c}\right)^2 E(z) \tag{4.9}$$

whose solution inside each layer is simply given by the superposition of a propagating and a counterpropagating plane wave

$$E_j(z) = a_{j,+} e^{ik_j z} + a_{j,-} e^{-ik_j z} \text{ for } 0 < z \leq d_j \tag{4.10}$$

with $k_j = \frac{\omega}{c}\sqrt{\epsilon_j}$ the local wavevector and $\sqrt{\epsilon_j} = n_j$ the refractive index of layer j. As in the acoustic case, the solution in a given layer is given by the vector

$\mathbf{a}_j = [a_{j,+}, a_{j,-}]$. At the interfaces between each two layers, Maxwell's boundary conditions impose the continuity of both the tangential electric field (here $E(z)$) and magnetic fields (here $-\frac{i}{\omega\mu_o}\frac{\partial E}{\partial z}(z)$), that lead to

$$E_j(d_j) = E_{j+1}(0) \tag{4.11a}$$

$$\frac{\partial E_j}{\partial z}(d_j) = \frac{\partial E_{j+1}}{\partial z}(0) \tag{4.11b}$$

The use of such boundary conditions leads to a relation of the form (4.5), with the matrix $\mathbf{M}_{j,j+1}$ given by

$$\mathbf{M}_{j,j+1} = \frac{1}{2}\begin{bmatrix} \left(1+\frac{n_{j+1}}{n_j}\right)e^{-ik_jd_j} & \left(1-\frac{n_{j+1}}{n_j}\right)e^{-k_jd_j} \\ \left(1-\frac{n_{j+1}}{n_j}\right)e^{ik_jd_j} & \left(1+\frac{n_{j+1}}{n_j}\right)e^{ik_jd_j} \end{bmatrix} \tag{4.12}$$

The obtained matrix is equivalent to (4.6) provided that the acoustic impedances Z_j are replaced by refractive indexes n_j and the longitudinal acoustic velocities v_j by the speed of light, c/n_j. The equations governing on-axis propagation of light in a multilayer structure therefore mimic longitudinal acoustic phonons propagating in the same structure, the similarity being most apparent when the problem is set via a transfer matrix formalism.

Due to the strong analogy between longitudinal acoustic phonons and normal-incidence light propagation in multilayered systems, most of the discussed physics for the acoustic case can be directly generalized to the case of optical multilayers and viceversa. The analogy can also be extended to other one-dimensional systems governed by scalar wave equations. We will therefore devote most of this chapter to the description of acoustic phenomena in multilayers and their optical properties will only be explored when studying photon-phonon interaction.

4.1.2 Acoustic superlattices

We focus now on the propagation of elastic waves in an infinitely periodic planar stacking, i.e. an acoustic superlattice (SL). In this setting, the eigenmodes can be set to be Bloch modes of the form

$$U_{q,n}(z) = e^{iqz}u_{n,q}(z) \tag{4.13}$$

where $u_{n,q}(z)$ is a periodic function of period D. As described in the previous chapter, q, the Bloch wavevector, belongs to the Brillouin Zone (BZ), i.e. $-\pi/D < q \leq \pi/D$.

From now on, only periodic systems with two different materials A/B, a binary SL, are considered (see Fig. 4.1(a)). Unlike in the previous chapter, where we resorted to numerical methods to find the band structure of the allowed modes, the simplicity of this particular system allows for a direct analytical solution. If we concatenate the operation (4.5) two times we know that the coefficients should

obey both the result of applying (4.6) twice and Bloch's theorem for the Bloch wavevector q in (4.13). They therefore need to fulfill simultaneously

$$\mathbf{a}_j = \mathbf{M}_{j,j+1} \cdot \mathbf{M}_{j+1,j+2} \cdot \mathbf{a}_{j+2} \equiv \mathbf{B} \cdot \mathbf{a}_{j+2} \tag{4.14a}$$

$$\mathbf{a}_j = e^{-iqD}\mathbf{a}_{j+2} \tag{4.14b}$$

an eigenvalue problem that leads to the following transcendental equation [220] for q

$$cos(qD) = cos\left(\frac{\Omega d_A}{v_A} + \frac{\Omega d_B}{v_B}\right) - \frac{\eta^2}{2}\sin\left(\frac{\Omega d_A}{v_A}\right)\sin\left(\frac{\Omega d_B}{v_B}\right) \tag{4.15}$$

where

$$\eta = \frac{1 - \frac{Z_A}{Z_B}}{\sqrt{\frac{Z_A}{Z_B}}} \tag{4.16}$$

represents the phononic modulation that arises from the difference in the acoustic impedances Z_A and Z_B. The corresponding eigenvector is given by

$$\begin{bmatrix} a_{j+2,+} \\ a_{j+2,-} \end{bmatrix} = \begin{bmatrix} B_{12} \\ e^{-iqD} - B_{11} \end{bmatrix} \tag{4.17}$$

with B_{ij} the i,j-th coefficient of matrix $\mathbf{B}$ in (4.14a). If we assume that $\eta \ll 1$, which is the case for the most commonly used III-V materials, we can neglect the second term in (4.15), which leads to [221]

$$qD = \pm\frac{\Omega}{v} + n2\pi \ \forall n \in \mathbb{Z} \tag{4.18}$$

where v is the effective speed of sound given by

$$v = \frac{Dv_Av_B}{d_Av_B + d_Bv_A} \tag{4.19}$$

and corresponds to the mean velocity for the transit time across one period. Equation (4.18) evidences the band folding effect induced by the periodicity D, although the dispersion remains a simple linear dispersion with an effective velocity v and no acoustic band gap. This dispersion ($Z_A/Z_B = 1$) is depicted with a black solid line in Fig. 4.1(b). The folded dispersion relation (4.18) leads to a degeneracy of order two at frequencies

$$\Omega_n = \frac{n\pi v}{D} \ , \forall n \in \mathbb{N} \tag{4.20}$$

with even values of n corresponding to zone-center (ZC) phonons ($q = 0$) and odd values corresponding to zone-edge (ZE) phonons ($q = \pi/D$). When the quadratic term on η is considered, there exists values of Ω for which the modulus of the RHS in (4.15) is greater than 1 and the equation has no solutions for $q \in \mathbb{R}$. The role of the acoustic impedance mismatch is therefore to open acoustic band gaps around the frequencies Ω_n in (4.20). The size of such gap can be approximated as

$$\Delta\Omega_n = 2\frac{v}{D}\left|\eta\sin\left(n\pi\frac{d_A}{D}\frac{v}{v_A}\right)\right| \tag{4.21}$$

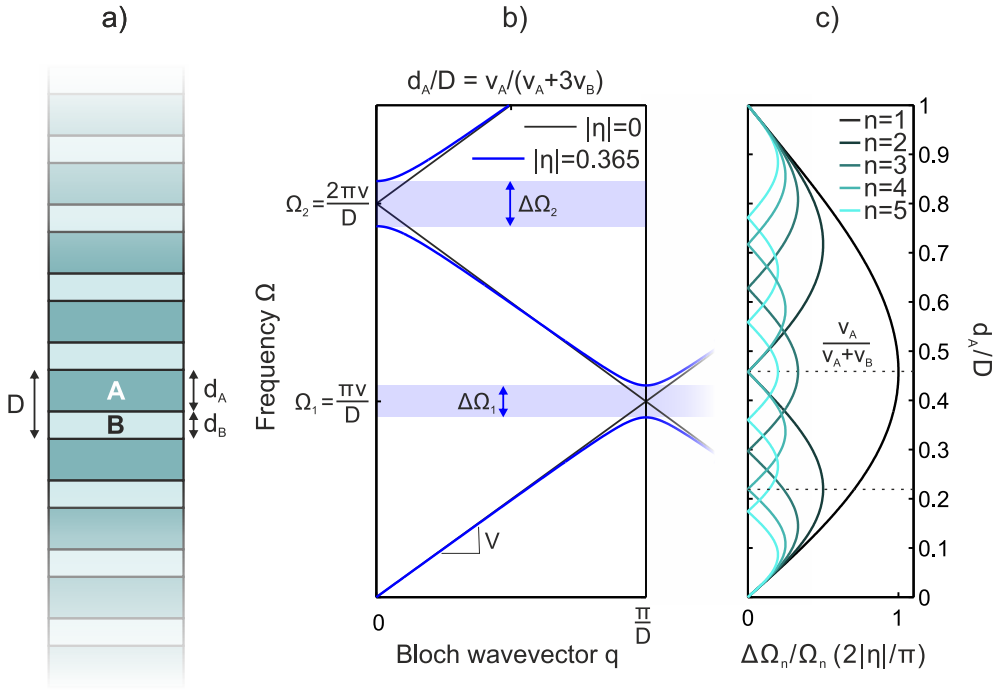

Figure 4.1: Schematic principle of an acoustic superlattice (SL). An acoustic SL is made by infinitely stacking layers of different materials in such a way that the governing parameters, the mass density $\rho(z)$, the elastic coefficient $C(z)$ and the longitudinal acoustic velocity $v(z)$ are periodic in z. The typical bilayer setting, with a period D given by two layers A and B of thicknesses d_A and d_B, is depicted in (a). (b) Acoustic band diagram of the allowed propagating Bloch modes for a SL with (blue) and without (black) acoustic impedance contrast. While band folding and a modification of the acoustic velocity to v occurs without impedance mismatch, i.e. $\eta = 0$, impedance mismatch is required to open band gaps of width $\Delta\Omega_n$ at frequencies $\Omega_n = n\pi v/D$. The gap to midgap ratio $\Delta\Omega_n/\Omega_n$ for the first 5 bands is depicted in (c) for varying d_A/D.

by Taylor expanding the RHS of (4.15) around Ω_n and its normalized behaviour is depicted for the first 5 bands in Fig. 4.1(c). We see that both Ω_n and $\Delta\Omega_n$ are inversely proportional to the period D, which can be used to increase both the width and central frequency of a minigap, without altering their ratio. However, if a particular Ω_n is targeted, choosing materials with high η constitutes the main way of increasing the gap. In addition, the presence of the sinusoidal term in (4.21) allows particular choices of the thicknesses (d_A, d_B) to close certain minigaps. For the n-th minigap, we have

$$\frac{d_A}{D} = \frac{pv_A}{nv_B + p(v_A - v_B)} \implies \Delta\Omega_n = 0 \ , \ \forall p \in [0, n] \cap \mathbb{N} \tag{4.22a}$$

$$\frac{d_A}{D} = \frac{(2p-1)v_A}{2nv_B + (2p-1)(v_A - v_B)} \implies \max\left(\frac{\Delta\Omega_n}{\Omega_n}\right) \ , \ \forall p \in [1, n] \cap \mathbb{N} \tag{4.22b}$$

such that all ZC minigaps cancel out for $d_A/D = v_A/(v_A + v_B)$ while the ZE minigap relative width $\Delta\Omega_n/\Omega_n$ are always maximal for this particular choice of d_A. Since we usually deal with the lowest order minigaps, it is interesting to

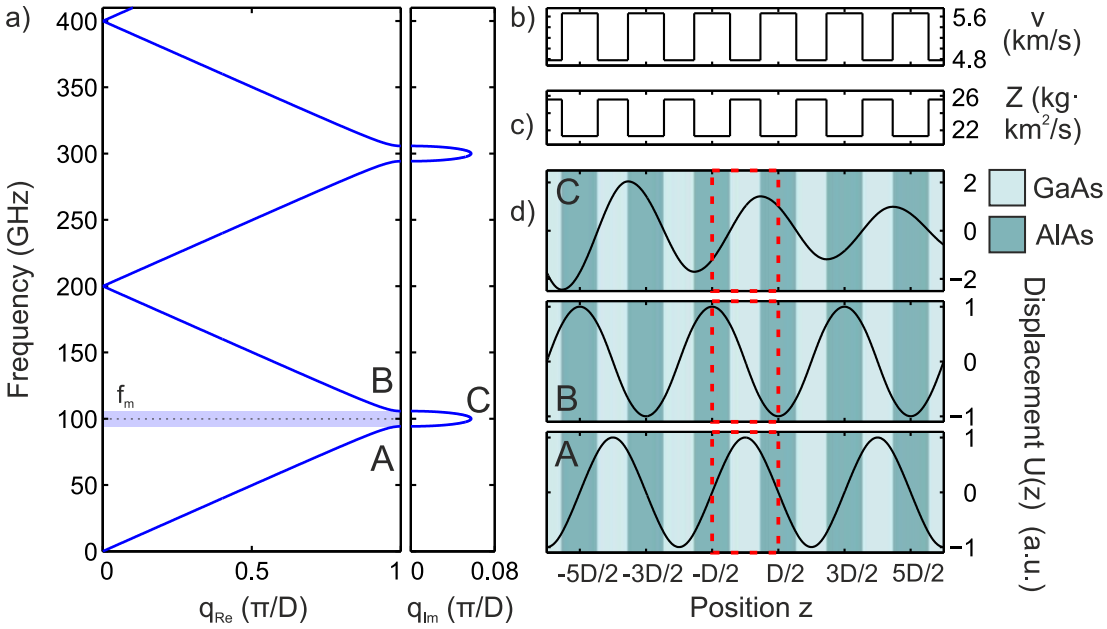

Figure 4.2: Band diagram and Bloch modes of a GaAs/AlAs $(\frac{\lambda}{4}, \frac{\lambda}{4})$ superlattice (SL). (a) Complex band diagram of a $(\frac{\lambda}{4}, \frac{\lambda}{4})$ SL for a design frequency $f_m = 100$ GHz. The zone-edge (ZE) minigaps are maximized for the thicknesses chosen, while all the zone-center minigaps are closed. Inside the minigaps, evanescent Bloch solutions with $q = \frac{\pi}{D} + iq_{Im}$ exist. (b) and (c) represent the acoustic velocity v and impedance Z profiles. (d) The displacement field $U(z)$ associated with the Bloch modes at the lower (upper) edge A (B) of the first ZE minigap is given. Due to symmetry considerations, these have to be either symmetric or antisymmetric in a unit-cell chosen to be centro-symmetric (dashed red). We see that the edge mode A (B) is symmetric (antisymmetric) with respect to the central GaAs layer.

note that for $n = 2$, the choice of thicknesses $d_A/D = v_A/(v_A + 3v_B)$ or $d_A/D = v_A/(3v_A + v_B)$ leads to a maximal relative gap width. Also note that the first minigap $\Delta\Omega_1$ is never closed for a finite value of η by sole control of the relative thicknesses of the two layers A and B, but closes only when $d_A = 0$ ($d_A = D$), i.e. bulk material of only material B (A).

When designing an acoustic SL and nanostructures that derive from it, one typically wants to control the phononic properties in a particular minigap n, at a frequency f_m and with a given gap size (typically maximal). These criteria set the values of the layer thicknesses. For example, if we aim at having a SL with a design frequency f_m=100 GHz at the the first ZE minigap and with maximal minigap width, the chosen thicknesses would be $d_A = {}^{v_A}/_{4f_m}$ and $d_B = {}^{v_B}/_{4f_m}$ [222]. This particular geometry is called a $(\frac{\lambda}{4}, \frac{\lambda}{4})$ SL, since the wavelength of a mechanical plane wave propagating at frequency f_m is ${}^{v_{A/B}}/_{f_m}$ for alternating materials A/B. The band diagram of this SL made of GaAs/AlAs is shown in Fig. 4.2(a), while (b) and (c) show the acoustic velocity and impedance profiles. The eigenvalue problem we solve is formulated in the reverse direction than (3.13), since we asume Ω given and we look for eigenvalues q [223]. With this approach, Equation (4.15) admits an analytic continuation in the complex plane and we can find solutions

with $\Omega \in \mathbb{R}$ and $q \equiv q_{Re} + iq_{Im} \in \mathbb{C}$. Within the ZC (ZE) band gaps, solutions with $q_{Re} = 0$ ($q_{Re} = \pi/D$) and $q_{Im} \neq 0$ satisfy (4.15). Although these solutions lack physical meaning for an infinite SL (spatially divergent eigenfields in either the positive or negative z-direction) they are relevant whenever one considers a finite or semi-infinite SL or when one studies what would happen to a system in the presence of an oscillating source term at frequencies within the band gap. For this particular choice of thicknesses, the minigaps at the ZC are closed (see Fig. 4.1(b)) and evanescent Bloch modes only exist at the ZE. The propagating Bloch eigenfields at the two extrema A and B of the first ZE minigap and the evanescent Bloch mode at the deepest point within the same minigap (at the design frequency f_m=100 GHz) are depicted in Fig. 4.2(d). The centro-symmetric unit cell is depicted by the red dashed lines and reveals the exchange of the mode symmetry with respect to the center of the unit cell accross the minigap. The different symmetry of the band edge modes can be generalized to all other minigaps and will be of importance in the following sections. For the first minigap, the lower band-edge mode A is symmetric (antisymmetric) with respect to the middle of the central GaAs (AlAs) layer, while the upper band-edge mode (B) is antisymmetric (symmetric) with respect to the GaAs (AlAs) layer. The evanescent Bloch mode at f_m has obviously no inherent symmetry since it decays towards +z and grows towards -z, but one can see that the minima and maxima of the field are located at the interfaces between materials.

4.1.3 Acoustic Distributed Bragg Reflectors

An acoustic SL is an infinitely extended ideal one-dimensional phononic crystal and cannot be strictly realized in practice. The finite version of such a system, an acoustic Distributed Bragg Reflector (DBR) is however of great technological relevance and inherits its basic features from the properties described for the infinite SL. A DBR is a structure composed of N periods of an acoustic SL and embedded between bulk material, as depicted in Fig. 4.3(a) for a $(\frac{\lambda}{4}, \frac{\lambda}{4})$ GaAs/AlAs stacking embedded in bulk GaAs, where we have added a last AlAs layer since the substrate is GaAs (N+0.5 periods).

The structure being of finite nature the problem does not possess discrete translational invariance as it does in the infinite case and little to nothing can be said *a priori* about the eigenfrequencies or eigenfields. However, using the recurrence relation given in (4.5) one can easily study what happens in the presence of a source far away in the cladding or substrate layers, whose effect can be thought of as a plane wave impinging from one of the sides. We can then study how acoustic waves are reflected, transmitted (or absorbed) by the DBR as well as the fields that result from such excitation. For this purpose, the coefficients $\mathbf{a}_o^{end}$ at the end of the semi-infinite cladding layer (0) need to be related to the coefficients $\mathbf{a}_{N_{layer}+1}$ at the origin of the semi-infinite substrate layer ($N_{layer}+1$). This is done by concatenating the matrices $\mathbf{M}_{j,j+1}$ introduced in (4.6) as

$$\mathbf{a}_0^{end} = \left(\mathbf{I}_{0,1} \prod_{j=1}^{N_layer} \mathbf{M}_{j,j+1} \right) \cdot \mathbf{a}_{N_{layer}+1} \equiv \mathbf{M} \cdot \mathbf{a}_{N_{layer}+1} \tag{4.23}$$

where $N_{layer} = 2N+1$ for the particular multilayer of Fig. 4.3(a). For a plane wave impinging from layer 0 and arbitrarily choosing a phase reference, we have $\mathbf{a}_0^{end} = [1, r]$ and $\mathbf{a}_{N_{layer}+1} = [t, 0]$. The transmission and reflection of the multilayer stack can be found via

$$T(\Omega) = \frac{Z_{N_{layer}+1}}{Z_0} |t|^2 = \frac{Z_{N_{layer}+1}}{Z_0} \left| \frac{1}{M_{11}(\Omega)} \right|^2 \tag{4.24a}$$

$$R(\Omega) = |r|^2 = \left| \frac{M_{21}(\Omega)}{M_{11}(\Omega)} \right|^2 \tag{4.24b}$$

where M_{ij} is the i,j-th element of matrix $\mathbf{M}$ in (4.23). The reflection and transmission properties of any multilayer structure can be found by computing (4.24), which is typically done by the direct matrix multiplication. For an absorptionless N-period DBR embedded between bulk semi-infinite media of the same material, the transmittance is given by [224]

$$T(\Omega) = \frac{1}{1 + \frac{\sin^2(q(\Omega)ND)}{\sin^2(q(\Omega)D)} \left(\frac{1}{|t_1(\Omega)|^2} - 1 \right)} \tag{4.25}$$

where we see the Bloch wavevector q of the SL appear, while the coefficient t_1 is the complex transmission coefficient of a single unit cell, which can be obtained directly by computing the matrix $\mathbf{M}$ for a single unit cell using (4.23). This provides a direct link between the eigenstructure of the infinite SL and he behavior of its respective finite DBR and shows the importance of computing the complex band structure inside the bands gaps where $q(\Omega)$ in (4.25) is complex.

The band diagram of the underlying $(\frac{\lambda}{4}, \frac{\lambda}{4})$ GaAs/AlAs SL and the reflectivity of the $N = 20$ period DBR shown in Fig. 4.3(a) are reproduced in panels (b) and (c) of the same figure. Since the structure can both be thought of as being composed of N bilayer unit cells plus an additional AlAs layer at the end or in terms of $N + 1$ centro-symmetric unit cells with AlAs as the central layer, the reflectivity is computed using Equation (4.25) for $N = 21$. At frequencies within the band gap region of the underlying SL no propagating Bloch modes are supported, which leads to a region of high reflectivity R, called the stop band. Outside this stop band, whenever the underlying SL supports propagating Bloch modes, the overall reflectivity drops significantly while exhibiting fast spectral oscillations called Bragg oscillations, whose occurrence can be understood using (4.25). They occur at frequencies Ω_{DBR} satisfying either $q(\Omega_{DBR})ND = m\pi$ or $|t_1(\Omega_{DBR})|^2 = 1$, giving rise to two different families of resonances. The first family corresponds to Bragg resonances and one can find $N - 1$ per band (for values $m = 1, .., N - 1$), while the other family, whose number per band is not precisely defined [225], stem from resonances of the single unit cell. The free spectral range (FSR) and the linewidth of such resonances decrease both towards the band edges and with increasing number of periods N, see the colormap in Fig. 4.3(d), where the horizontal dashed line highlights the position of the reflectivity curve of Fig. 4.3(c). The dependence of the FSR with increasing number of layers N and towards the band edge is due to the difference between two of the Bragg resonances in q-space, given by $\Delta q = \pi/(ND)$, and to the flattening of the

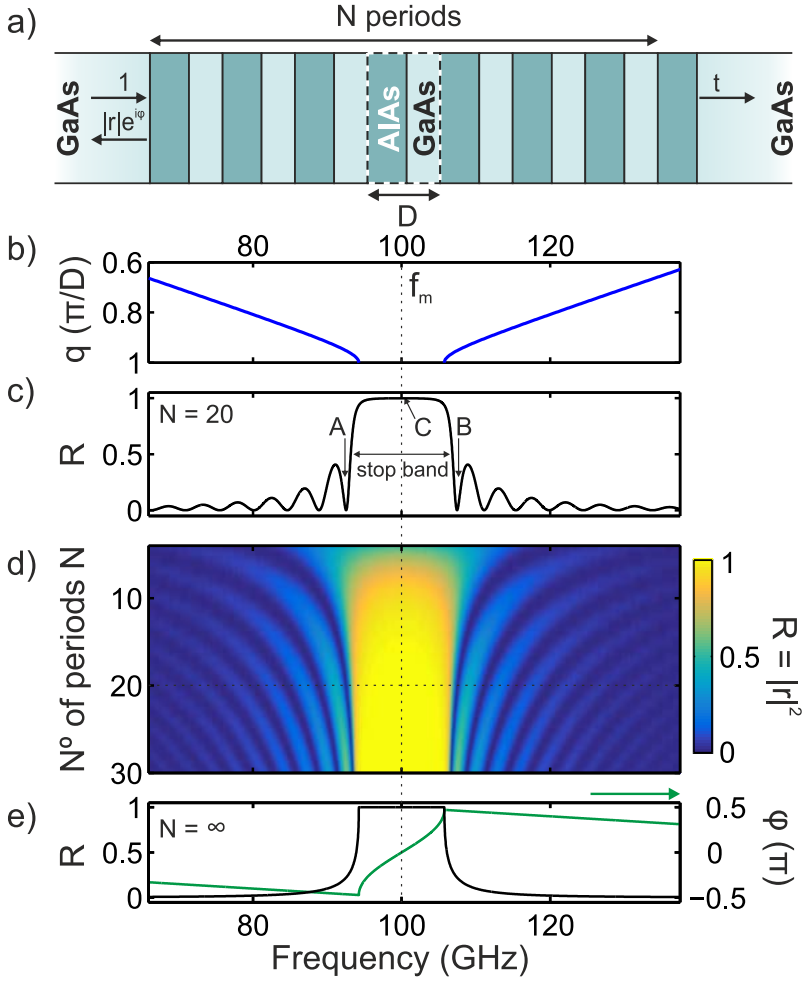

Figure 4.3: Basic features of an acoustic Distributed Bragg Reflector (DBR). (a) A DBR is made of N periods of an acoustic superlattice (SL) bounded by semi-infinite bulk media. (b) Band diagram of the infinite GaAs/AlAs SL around the first zone-edge (ZE) minigap, centered at frequency f_m=100 GHz, and (c) reflectivity of its finite counterpart, a DBR consisting of N=20 periods. The stop band tends to the minigap with increasing number of DBR periods N (d), with the highest reflectivity reached at f_m. (e) Reflectivity R (black) and reflection phase ϕ (green) spectra for a plane wave impinging on the semi-infinite SL from a GaAs cladding, mimicking the behaviour of (d) when $N \to \infty$.

bands towards the band edges. The stop band, bounded by these reflectionless resonances, approaches the minigap width for $N \to \infty$ and one intuitively expects that the fringes disappear when $N \to \infty$. The reflection R in this case, a semi-infinite SL, is computed by imposing the boundary conditions (4.11) between a perfect Bloch mode in the semi-infinite periodic medium and plane waves on the cladding medium. Using (4.17) and $\mathbf{a}_0^{end} = [1, r]$, the complex reflection coefficient r is given by

$$\frac{1+r}{1-r} = \left(\frac{Z_{cladd}}{Z_A}\right) \frac{B_{12} + (e^{iqD} - B_{11})}{B_{12} - (e^{iqD} - B_{11})} \tag{4.26}$$

whose spectral evolution is given in Fig. 4.3(e). Perfect reflectivity R occurs

throughout the full minigap of the underlying SL while it progressively drops within the band with a lineshape that closely follows[1] the mean value of the aforementioned Bragg oscillations. This steady decrease in reflectivity is associated with an effective frequency-dependent impedance of the semi-infinite SL, that goes from infinity exactly at the band edge to a fixed value in the region of linear dispersion.

The resonant transmission occurring at frequencies Ω_{DBR} is associated to (quasi-)resonant excitation of dissipative eigenmodes of the system [226]. A lossy optical cavity or a damped mechanical resonator exhibits a resonant response when subject to a periodic drive via one of its loss channels (Chapter 2). In the low-dissipation limit, the response has a Lorentzian lineshape with a central frequency given by the resonator frequency (Ω_m or ω_o) and linewidth given by its dissipation rate (Γ_m or κ). Bulding on these ideas, we can think of the full physical volume of Fig. 4.3(a) as a finite closed acoustic system having discrete energy levels to which we add the cladding and substrate layer, which are irreversible sources of losses. When driven periodically, in this case via the cladding layer itself, the response at the fixed drive exhibits the resonant behaviour observed. The linewidth Δf_{DBR} of such resonances is therefore associated to losses of these dissipative modes of the system. This rationale used for unbounded systems corresponds to finding the quasinormal-modes (QNMs) of the structure (see Chapter 3), which are modes $\widetilde{U}(z)$ satisfying the eigenproblem (4.2) with outgoing boundary conditions, the eigenfrequencies of which are complex, i.e. $\widetilde{\Omega}_m = \Omega_m - i\Gamma_m/2$.

For the case of a multilayered structure with N_{layer} layers, satisfying the outgoing boundary conditions implies setting $\mathbf{a}_0^{end} = [0, a_{o,-}^{end}]$ and $\mathbf{a}_{N_{layer}+1} = [a_{N_{layer}+1,+}, 0]$ in (4.23), i.e. only outgoing plane waves exist in the cladding and substrate layers. This implies finding $\widetilde{\Omega}_m \in \mathbb{C}$ satisfying

$$M_{11}(\widetilde{\Omega}_m) = 0 \tag{4.27}$$

with M_{11} the 1,1-th coefficient of matrix $\mathbf{M}$. Since $M_{11} = 1/t$ in a transmission configuration, finding the QNM frequencies $\widetilde{\Omega}_m$ corresponds to finding the complex poles of the scattering matrix [227]. Whenever the transmission/reflection resonances calculated are narrow and well isolated from other spectral dependencies, both Ω_m and Γ_m can be extracted from the central frequency and width of the resonant Lorentzian feature. Fig. 4.3(b) shows that this low-dissipation limit is not satisfied and the trascendental complex equation (4.27) has to be solved. We use a standard complex root-finding Müller method [228] for its numerical resolution, calculating the initial values from the central frequency and the linewidth of the transmission resonances. When the method fails to converge, as in the case of closely spaced eigenvalues, we use a method based on the argument principle method (APM) of complex analysis [229]. Both methods were occasionally employed depending on the intricacy of the basins of attraction of the zeros using

[1] The spectral evolution of $R(\Omega)$ resembles that of the envelope of the Bragg oscillations but the exact value depends on the impedance of the substrate Z_{subs} chosen, a choice that is obviously irrelevant inside the minigap, where the matching is perfect.

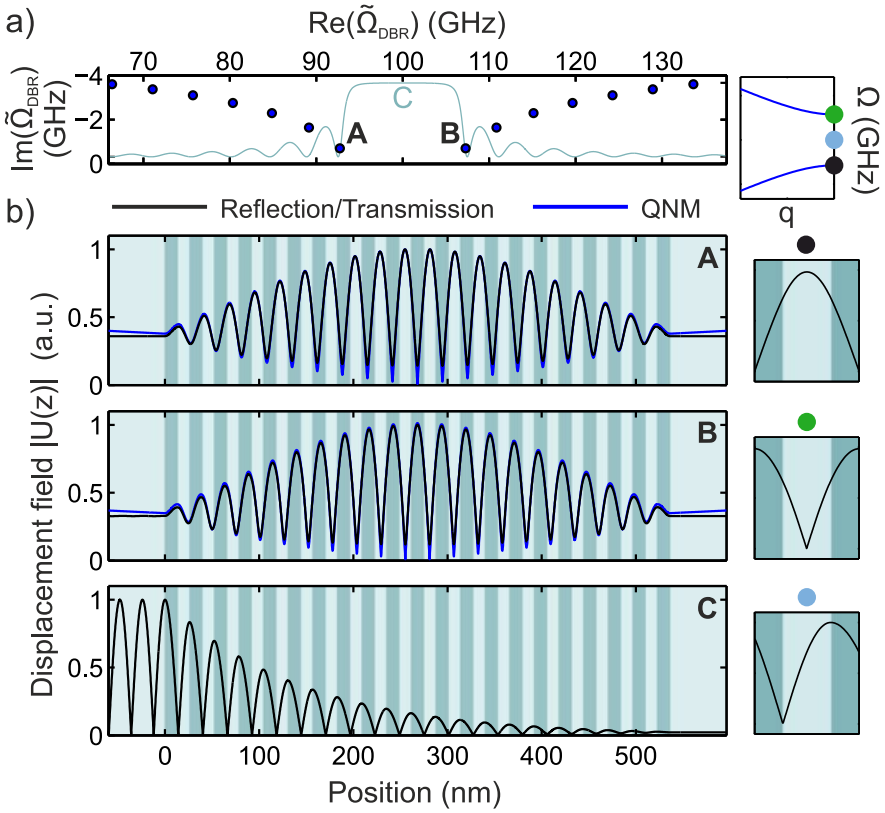

Figure 4.4: Displacement fields at the edges of and inside the stop band of an acoustic Distributed Bragg Reflector (DBR). (a) Eigenfrequencies $\widetilde{\Omega}_m$ of the supported quasinormal-modes (QNMs) in a GaAs/AlAs DBR around the first zone-edge (ZE) minigap (blue dots). Its reflection spectrum is given with a solid light blue line for reference. (b) (Blue) Absolute value of the QNM fields $|\widetilde{U}(z)|$ associated to QNMs highlighted with letters A, and B in (a). Along with the QNM fields, the transmitted fields $|U(z)|$ (black) are shown. These are associated to either the closest reflectivity dip to the real part of frequencies A and B or to frequency f_m (C). The Bloch modes $|U(z)|$ for the lower (upper) band edge, whose frequency is marked by a black (green) dot, and for the evanescent Bloch mode at f_m (light blue dot) are depicted on the right. The observed resonances inherit some of the field properties of the *corresponding* Bloch modes, including their symmetries.

the iterative method. The complex eigenfields $\widetilde{U}_m(z)$ are obtained by fixing the coefficients in a given layer, e.g. in layer $N_{layer}+1$, and propagating the solution via matrix multiplication, with matrices (4.7a) and (4.7b) evaluated at $\widetilde{\Omega}_m$. These are defined up to a an arbitrary phase factor. Note that the eigenmodes diverge when $z \to \pm\infty$ since the outgoing plane waves in layer 0 (or $N_{layer}+1$) will have an exponential term diverging as $\Gamma_m/2v_0)z$.

The QNM eigenfrequencies $\widetilde{\Omega}_{DBR}$ of the $N = 20$ $(\frac{\lambda}{4}, \frac{\lambda}{4})$ GaAs/AlAs DBR are given in the complex frequency plane in Fig. 4.4(a). The reflection spectrum from Fig. 4.3(b) is reproduced in the background for clarity. There are no QNMs with $\mathrm{Re}(\widetilde{\Omega}_{DBR})$ inside the minigap. The QNM frequencies lie inside the pass bands and $\mathrm{Re}(\widetilde{\Omega}_{DBR}) \sim \Omega_{DBR}$. In addition, the associated losses as given by

$\mathrm{Im}(\widetilde{\Omega}_{DBR})$ steadily drop towards the gap edges, as expected from the observed linewidths. Among such QNMs and their associated reflectivity resonance, the modes bounding the stop band are of special importance. Their spectral position tends to the band edge when $N \to \infty$ (Fig. 4.3) and we expect the QNM eigenfields to resemble the Bloch eigenmodes of the infinite SL. Fig. 4.4 depicts the absolute value of the displacement fields $|U(z)|$ at frequencies A, B and C of Fig. 4.3(b) in a transmission/reflection configuration along with $|\widetilde{U}(z)|$ for the associated QNMs at frequencies $\widetilde{\Omega}_{DBR}$[2]. For reference, $|U(z)|$ in the unit cell for the Bloch band-edge (black and green dots) and mid-gap (light blue dot) modes are given along with the field profiles. We see how the QNM eigenfields A and B inherit the symmetry properties of the SL Bloch modes and how the transmission field excites such modes. The transmission field C possesses the displacement profile corresponding to the midgap evanescent Bloch mode at f_m, evidencing the importance of these family of evanescent modes in finite structures. The last has obviously no QNM associated since there is no natural resonant state at that or close to that frequency, therefore no QNM field (blue) is plotted.

4.2 Acoustic nanocavities

More complex and compact acoustic nanostructures can be envisioned, notably nanocavities which can be formed following several approaches, such as introducing a local defect [230,231], an adiabatic potential [232] or distributed disorder [233]. These strategies solely use the frequency band structure (the eigenenergies) of their underlying periodic counterpart as a confinement strategy, with the spatial distribution of the Bloch modes having no particular role in controling the density of states. Such spatial distributions, thoroughly discussed in the previous section, can also be used to achieve spectrally and spatially confined states by relating the symmetries of the band-edge modes to reflection phases within a stop band. Since the latter are linked to a topological invariant of one-dimensional periodic systems, the Zak phase [234], this confined mode will be described as stemming from the topological properties of the bulk acoustic SL.

4.2.1 Fabry-Pérot cavities

Due to the presence of band gaps, semi-infinite SLs can be used to confine mechanical waves by bounding a spacer layer. When two SLs are placed top and bottom of a given intermediate layer of different acoustic length[3], as is depicted with DBRs in Fig. 4.5(a) for a GaAs spacer layer, this confined state allows propagation within the stop band. One expects mechanical confinement to happen for specific frequencies within the minigap, forming a Fabry-Pérot (FP) acoustic

[2]The displacement field itself, $U(z)$, depends in both cases on a chosen phase reference. In the transmission configuration this corresponds to the phase chosen in the cladding layer, i.e. the real displacement depends on the position of the source in the that layer, while in the QNM fields it is just an overall factor of the field. It therefore seems clearer to depict the absolute value, which is insensitive to that arbitrary phase

[3]This can be achieved by either changing the material or by choosing a thickness different from the ones used in the SLs.

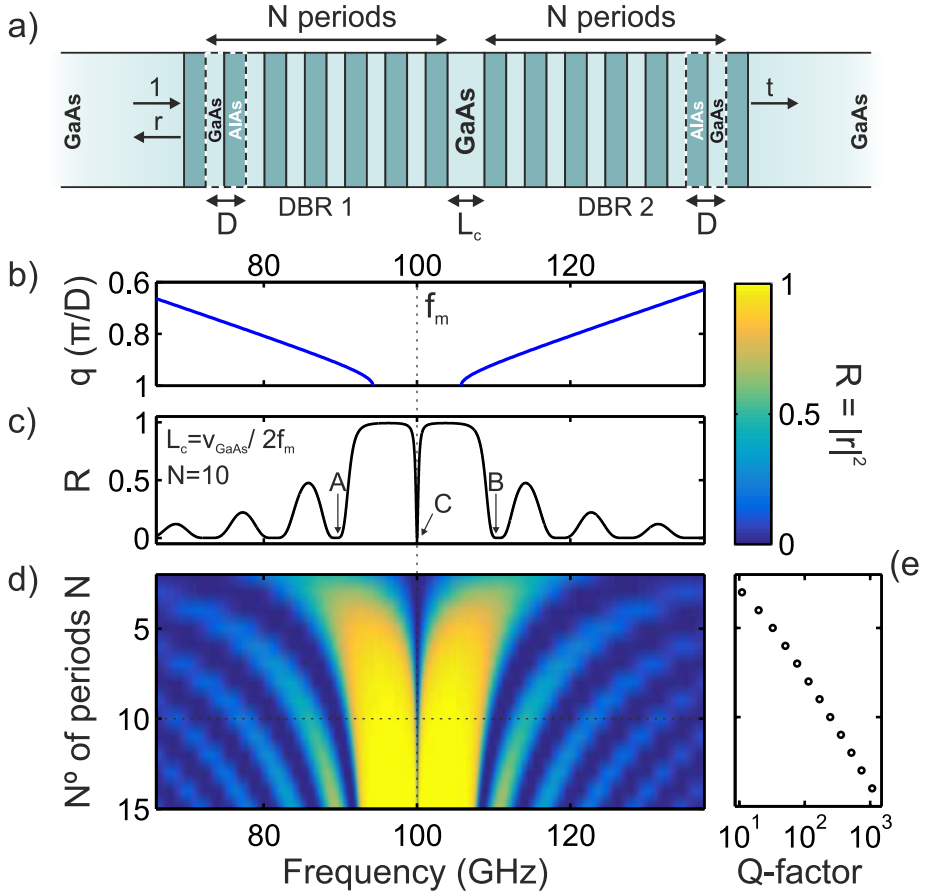

Figure 4.5: Basic features of an acoustic Fabry-Pérot (FP) resonator. (a) Schematic of a GaAs FP resonator. (b) Band diagram of the infinite GaAs/AlAs superlattices (SLs) around the first zone-edge (ZE) minigap, centered at frequency f_m=100 GHz, and (c) reflectivity of its finite counterpart, a GaAs spacer ($L_c = v_{GaAs}/2f_m$) bounded by two DBRs of N=10 periods. The stop band tends to the common minigap with increasing number of DBR periods N (d), while the transmission resonance associated to the FP cavity at f_m gets narrower. The value of the Q-factor of the resonance is given in (e).

resonator. Let us imagine that a longitudinal acoustic phonon is propagating in the spacer layer towards the top (left) DBR at a frequency inside the minigap. As it encounters the SL, it is fully reflected and acquires a phase ϕ_1. Upon interaction with the bottom (right) SL, the same happens, acquiring a phase ϕ_2, while during the round-trip a propagation phase $2q_cL_c$ is acquired, with q_c the wavevector in the cavity (c) layer, i.e. $q_c = \Omega/v_c$. Constructive interference results from fulfilling the condition

$$2q_cL_c + \phi_1 + \phi_2 = 2\pi n \quad \text{with} \quad n \in \mathbb{Z} \tag{4.28}$$

which applies to any two SLs 1 and 2 and cavity length L_c within the minigap. Usually one deals with equivalent SLs at both sides of the cavity layer, leading to $\phi_1 = \phi_2$. If the two are $(\frac{\lambda}{4}, \frac{\lambda}{4})$ GaAs/AlAs SLs equivalent to the ones described in Fig. 4.3, we see (Fig. 4.3(e)) that $\phi_{1/2}(f_m) = 0$ and the system sustains a confined mode at f_m for $L_c = {}^{nv_c}/_{2f_m}$. The case $n = 1$ corresponds to a $\frac{\lambda}{2}$ FP resonator. In addition, since (4.28) is satisfied for the rest of the open minigap centers $f = pf_m$, a

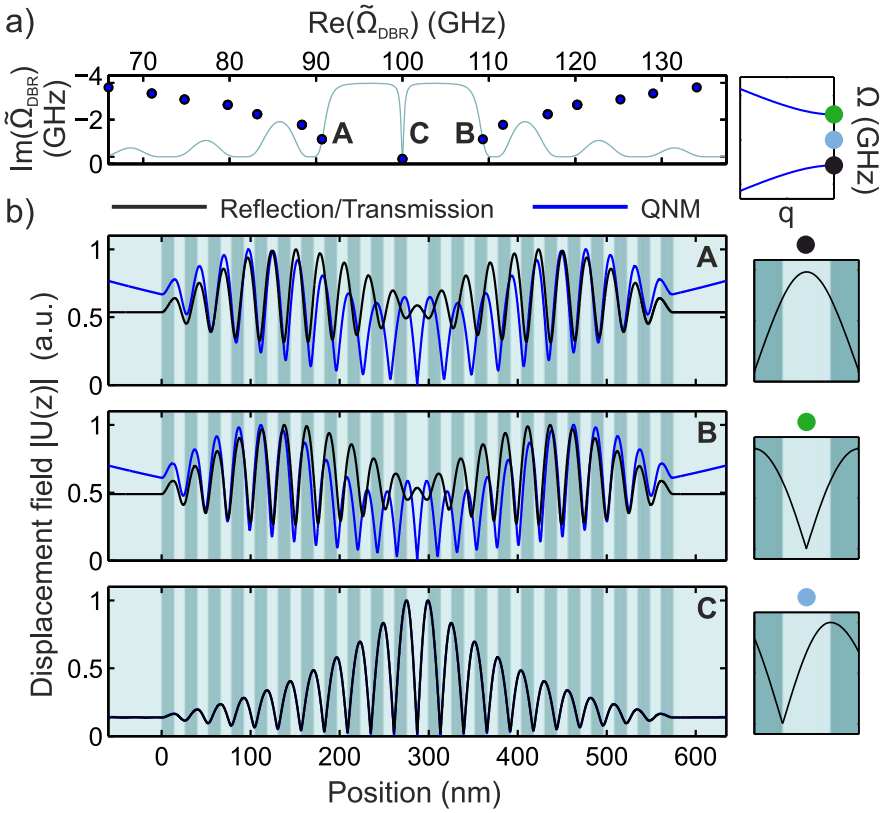

Figure 4.6: Relevant displacement fields in a Fabry-Perot (FP) nanophononic resonator. (a) Eigenfrequencies $\widetilde{\Omega}_m$ of the supported quasinormal-modes (QNMs) in a structure made of a GaAs spacer bounded by two finite 10-period Distributed Bragg Relfectors (DBRs) (blue dots). The reflection spectrum of the structure is given with a solid light blue line for reference. (b) (Blue lines) Absolute value of the QNM fields $|\widetilde{U}(z)|$ associated to QNMs highlighted with letters A, B and C in (a). Along with the QNM fields, the transmitted fields $|U(z)|$ (black lines) are shown. These are associated to the reflectivity dip closest to the real part of frequencies A, B and C. The Bloch modes $|U(z)|$ for the lower (upper) band edge, whose frequency is marked by a black (green) dot, and for the evanescent Bloch mode at f_m (light blue dot) are given on the right. The observed resonances inherit some of the field properties of the *corresponding* Bloch modes, including their symmetries.

FP mode is found at any such frequency (not shown). Cropping the two bounding SLs into DBRs leads to a finite system open to external radiation. The band structure of the underlying SLs and the reflection spectrum of a symmetric $\frac{\lambda}{2}$ GaAs FP cavity with N = 10 (+0.5) ($\frac{\lambda}{4}$, $\frac{\lambda}{4}$) GaAs/AlAs DBRs are shown in Figs. 4.5(b) and (c). The latter evidences a spectrally isolated resonance (C) appearing within the stop band, at the design frequency f_m.

The evolution of the spectral reflectivity as a function of the number N of periods in the bounding DBRs is depicted in Fig. 4.5(d), which evidences that the cavity spectral width decreases for increasing N. The quality factor, extracted as $Q = f_m/\Delta f_m$, with Δf_m the full width at half maximum (FWHM) of the

Lorentzian reflectivity dip, is depicted in (d) and can be approximated as [235]

$$Q_m = -\frac{f_m(L_c + L_{DBR})}{v_c ln(\sqrt{R_1 R_2})} \tag{4.29}$$

where L_{DBR} is the penetration depth into the bounding DBRs, extracted as in Ref [236]. We again observe similar Bragg oscillations as in the case of the single DBRs, with a stop band that approaches the (common) minigap as dips A and B in Fig. 4.5(c) tend to the band edges with increasing N. The wide resonances A and B are composed of two dips, a behaviour that can be understood as (strong) coupling between the QNM band-edge modes of the two DBRs (which were depicted in Fig. 4.4) via the GaAs spacer. Fig. 4.6(a) shows the presence of two QNMs per wide reflection dip. The transmission fields associated with the peak bounding the stop band at each band edge are shown in black in Fig. 4.6(b), showing how the resonances are built up from the respective band-edge modes of the conforming $N = 10$ DBRs and mantaining the *in-cell* symmetries. The FP cavity transmission field profile $|U(z)|$ is also depicted in C. The QNM fields $|\widetilde{U}(z)|$ are also given in the respective panels (blue lines). These match the structure observed on the transmission field at the core of the two DBRs, but the central part differs. This is because a plane wave impinging from the left at frequency Ω_{DBR} close to two QNMs will likely excite both of them and result in an interference pattern.

Condition (4.28) is satisfied for other in-gap frequencies f_c for nearly any value of L_c, as shown in Fig. 4.7. For example, if the cavity length is changed to $L_c = 1.2v_c/2f_m$, the condition is satisfied for a frequency lower than f_m. This is illustrated in Fig. 4.7(b), where the zero-crossing of the black curve, the total phase acquired, gives the resonant frequency of the supported mode in a spacer bounded by the same $(\frac{\lambda}{4}, \frac{\lambda}{4})$ semi-infinite SLs, with the reflection phases ϕ_1 and ϕ_2 obtained again from (4.26). When the system is finite, i.e. $N = 10$ periods for each DBR, the resonant frequencies are obtained via the dips in the reflectivity spectrum, which are depicted for varying cavity length in Fig. 4.7(c). The resonant frequencies obtained from the reflectivity map remain very close to those extracted via condition (4.28), as is evidenced in Fig. 4.7(d). The $N \to \infty$ approximation only fails close to the borders of the minigap, with the disagreement caused by deviation of the reflection phases $\phi_{1/2}$ from ϕ_{SL} close to these edges. Using the exact reflection phases $\phi_{1/2}$ for finite $N = 10$ DBRs leads to perfect matching.

4.2.2 Topological cavities

Spacer-less Fabry-Perot resonators

The presence of a resonant state trapped between two semi-infinite SLs obeys the phase-matching condition (4.28). Whether or not the condition can be satisfied in the limit $L_c \to 0$, a spacer-less cavity, can be cast as

$$\phi_1 + \phi_2 = 2\pi n \quad \text{with} \quad n \in \mathbb{Z} \tag{4.30}$$

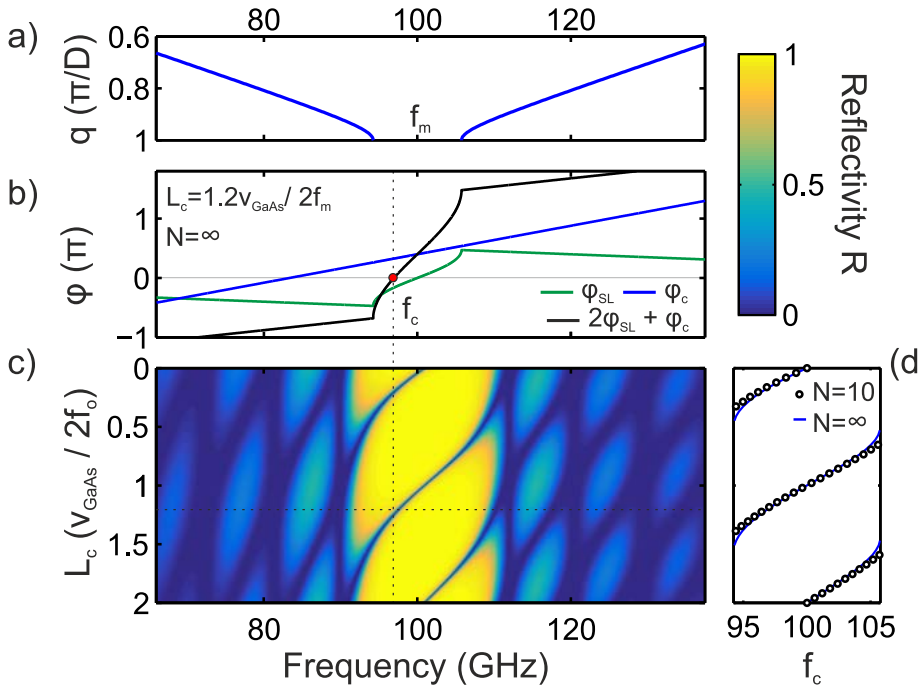

Figure 4.7: Influence of the cavity spacer thickness on the Fabry-Pérot (FP) resonant frequency. The frequency of the FP cavity can be controlled by changing the spacer thickness L_c. (a) Band diagram of the infinite GaAs/AlAs SL around the first zone-edge (ZE) minigap, centered at frequency f_m=100 GHz. (b) Phase matching condition (4.28) for a FP mode with a spacer of width $L_c = 1.2v_{GaAs}/2f_m$. The phases of the two semi-infinite superlattices (SLs) are equal and given by ϕ_{SL} (green), while ϕ_c (blue) represents the linear phase acquired during propagation. The black curve gives the sum of the two and the red dot highlights the frequency f_c for which phase matching occurs. (c) Colormap showing the reflectivity as a function of the value of $L_c \in [0, 2]$ in units of $v_{GaAs}/2f_m$. The horizontal dashed line highlights the reflectivity for the case shown in (b). (d) The position of the reflectivity dip, the resonance in the finite system, can be predicted from the phase matching condition for semi-infinite SLs, with small disagrement whenever f_c approaches the band edges.

with ϕ_1 and ϕ_2 the phases acquired upon reflection on both sides of the infinitesimally thin spacer. In Fig. 4.7(c) the case for $L_c = 0$ was already solved; it exhibits resonant transmission exactly at frequency f_m. Whenever L_c goes to zero in the configuration used there, we end up with the two bounding layers of AlAs joining and creating a $\lambda/2$ FP cavity with AlAs as the spacer layer. An AlAs $\lambda/2$ FP cavity can be interpreted both via condition (4.30) with the two semi-infinite SLs starting with a full AlAs layer or via condition (4.28) with an AlAs $\lambda/2$ spacer and the two semi-infinite SLs starting with full GaAs layers. This observation gives a much more general purpose to (4.30) and explains nearly any interface state inside the gap. This phase condition is extremely general and consequently applies to other physical systems such as localized surface plasmons [237], electromagnetic waves pinned at the interface between two optical materials [238,239], or an electronic wave localized at the interface between two semiconductors [240].

In the field of nanophononics it is used to study the emergence of surface states in a semi-infinite SL, a surface being nothing more than an interface between the SL and vacuum [241]. Using it to understand the formation of cavities more often approached as spacer-based cavities points to the key ingredient being how/where the interface is defined and how does $\phi(\Omega)$ behave inside the band gap. The question is then, how can we design or control the spectral dependence of the reflection phase? This is determined by some geometrical phase of the bulk bands, giving a topological view to the resulting interface states.

The choice of the origin in the unit cell upon concatenation of two DBRs has a large influence on the allowed states at the interface via their reflection phases ϕ from a semi-infinite cladding (Fig. 4.8). The schematic of Fig. 4.8(a) shows two DBRs 1 and 2 prior to being concatenated and being cut at specific points within the unit cell denoted by α_1 and α_2. We study how the reflection phase ϕ from a semi-infinite SL at frequencies in a minigap depends on how the SL is connected to the semi-infinite cladding from which a plane wave impinges. For now, we restrict ourselves to the same $(\frac{\lambda}{4}, \frac{\lambda}{4})$ GaAs/AlAs SL, with design frequency $f_m =$ 100 GHz. We define the parameter $\alpha \in [0, 1)$ that continuously shifts the initial position of the SL, with $\alpha = 0$ being set by a SL starting with the full AlAs layer in what is usually called a bilayer unit cell. For $\alpha < \frac{d_{AlAs}}{D}$ $(\geq)$, the plane wave first reaches an AlAs (GaAs) layer. This parameter is evidenced in the schematic of the two semi-infinite SLs of Fig. 4.8(a) and it essentially determines how the origin is chosen inside the unit cell. The evolution of the reflection phase ϕ is depicted in Fig. 4.8(b), where we see that this can be highly controlled by appropriately choosing the interface position via α. The phase variation $\Delta\phi$ across the minigap always equals π, but the bounds change depending on the unit cell. For a bilayer unit cell with AlAs at its origin ($\alpha = 0$), ϕ grows from $-\frac{\pi}{2}$ to $\frac{\pi}{2}$ when going from the lower to the upper band edge, while for the bilayer unit cell with GaAs at the origin ($\alpha = {}^{d_{AlAs}}/_{D}$) it goes from $\frac{\pi}{2}$ to $\frac{-\pi}{2}$. Interestingly, at $\alpha = \frac{d_{AlAs}}{2D}$ the value goes from $-\pi$ to 0 and at $\alpha = 1 - \frac{d_{GaAs}}{2D}$ from 0 to π. These last two cases correspond to centro-symmetric unit cells with GaAs and AlAs as the central layer, respectively. If two SLs with values α_1 and α_2 are concatenated, condition (4.30) is satisfied for f_c inside the gap for nearly any pair $[\alpha_1, \alpha_2]$, as depicted in Fig. 4.8(c) for three particular cases. The colormap in Fig. 4.8(d) highlights the frequency f_c for any pair $[\alpha_1, \alpha_2]$. The two red diagonals represent pairs for which the concatenated system is a simple DBR and they correspond to lines for which no values of f_c satisfying (4.30) are found. The lower-left (upper-right) region corresponds to cavities made of an AlAs (GaAs) spacer bounded by bilayer GaAs/AlAs DBRs. Green dots correspond to a $\lambda/2$ AlAs spacer cavity, whose phase matching condition is represented on the topmost graph of Fig. 4.8(c). The background of that graph represents the reflectivity, R, of a finite stack made of $N = 10$ periods for each one of the two phases. The light blue dot represents a $\lambda/2$ GaAs spacer cavity, found when $\alpha_1 = \alpha_2 = \frac{d_{AlAs}}{D}$, whose condition is also fulfilled in the center of the gap f_m, as depicted in the mid panel of Fig. 4.8(c). Again, traditional spacer-based cavities can be understood as stemming from a condition solely dependent on the reflection phases ϕ_1 and ϕ_2. The most interesting regions in this phase space are the outer diagonal regions, since the cavities

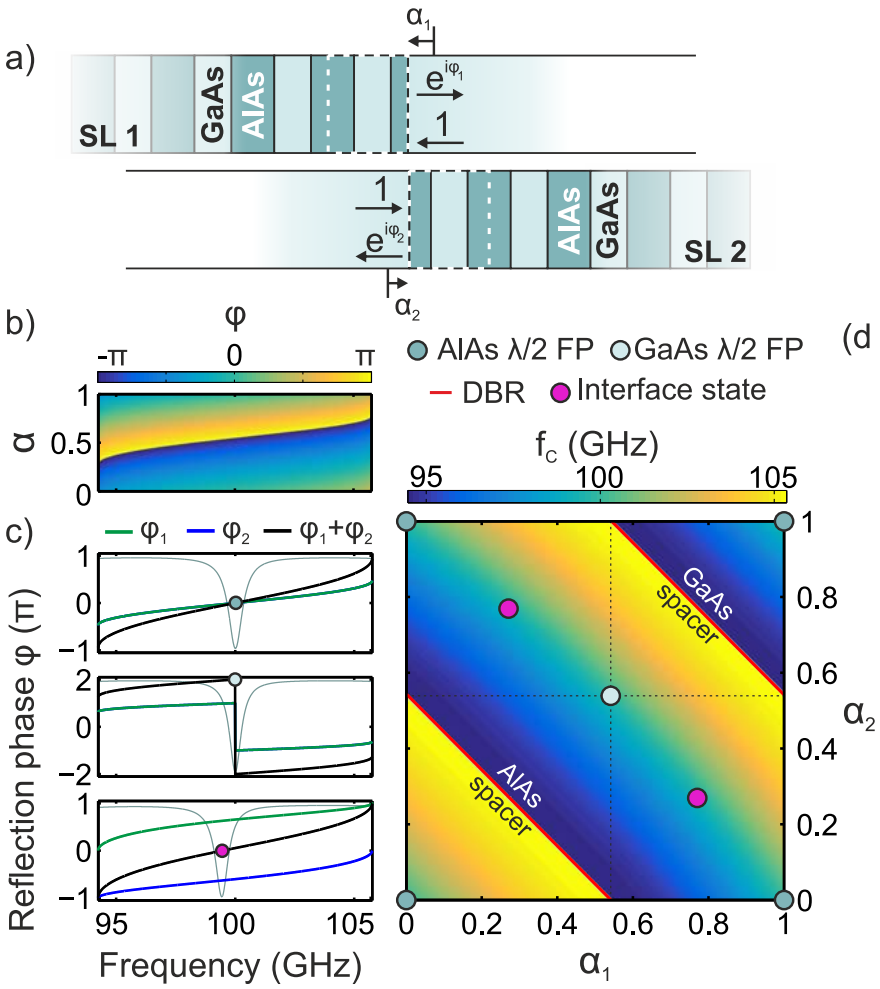

Figure 4.8: Spacer-less Fabry-Pérot (FP) nanophononic resonators. (a) Schematic of two semi-infinite superlattices (SLs) with unit cell defined by parameters α_1 and α_2 prior to being concatenated at their interface. (b) Reflection phase ϕ of a SL as a function of the unit-cell origin α. (c) An interface state is created when the spacer-less phase matching condition (4.30) is satisfied, as shown for $[\alpha_1,\alpha_2]=[0,0]$ (top), $[\alpha_1,\alpha_2]=[d_{AlAs}/D, d_{AlAs}/D]$ (middle) and $[\alpha_1,\alpha_2]=[d_{AlAs}/2D, 1-\frac{d_{GaAs}}{2D}]$ (bottom). (d) Colormap showing the cavity frequency f_c resulting from the phase matching condition for all $[\alpha_1,\alpha_2]$. For clarity, $\frac{\lambda}{2}$ FP cavities are marked with green (AlAs) and light blue (GaAs) dots. The outer diagonal quadrants delimit the regions where the FP picture given above cannot be directly applied. The positions highlighted with magenta dots represent states at the interface of the two SLs with centro-symmetric unit cells, albeit with different central layer.

do not correspond to a bounded spacer. The central points in those two regions, highlighted with magenta dots, correspond to two centro-symmetric concatenated SLs with the central layer exchanged. The existence of confined intra-gap states in those regions would not be expected from traditional band structure arguments as no defect is introduced. Without loss of generality, let us focus on the choice of $[\alpha_1, \alpha_2] = [\frac{d_{AlAs}}{2D}, 1-\frac{d_{GaAs}}{2D}]$, i.e., the magenta points in Fig. 4.8(d).

Phononic topological invariants

The notion of a topological invariant [242] enables the prediction of the unintuitive resonant state(s) discussed in the previous section from the intrinsic properties of the bulk bands without consideration of condition (4.30), providing easy design rules for interface states. Here, the relevant topological invariant is the Zak phase [234], although this choice is not unique [243]. We consider an isolated band with Zak phase given by

$$\theta_n^{Zak} = i \int_{-\frac{\pi}{D}}^{\frac{\pi}{D}} \langle u_{n,q} | \partial_q | u_{n,q} \rangle \, dq \tag{4.31}$$

where the bra-ket notation is used for historical reasons [244]. $|u_{n,q}\rangle$ represents the periodic-in-cell part of the Bloch mode as was introduced in (4.1). The Zak phase θ_n^{Zak} in (4.31) is the one dimensional geometric Berry phase [245], which is obtained by integrating the Berry connection $A(q) = \langle u_{n,q} | \partial_q | u_{n,q} \rangle$ in the full BZ. The latter is given by [246],

$$A(q) = \int_{unitcell} \frac{1}{2\rho(z)v(z)^2} u_{n,q}^*(z) \partial_k u_{n,q}(z) dz \tag{4.32}$$

For the case of binary A/B SLs considered here, the system posseses inversion symmetry and the Zak phase is known to be quantized at either 0 or π if the origin is chosen to be in an inversion center [234]. The definition provided by (4.31) depends on the unit cell choice [247] and a linear phase $\frac{2\pi s}{D}$ is acquired by shifting the unit cell origin by s. If the Zak phase equals 0 (π) relative to the inversion center in layer A, it must be π (0) relative to the other inversion center B. Therefore, the Zak phase is not a gauge-invariant topological quantity [248] since it cannot characterize the bulk bands uniquely. However, the classical bulk-boundary correspondance using the Zak phase has been applied in multiple 1D systems [249–252] since the Zak phase difference between bands is a properly defined topological number. We apply it here to nanophononic systems. For simplicity, we assume that we have centro-symmetric unit cells and then derive the case of a bilayer cell.

Each of the bands and band gaps are numbered beginning from 0 and 1, respectively. This numbering holds even for closed minigaps, i.e. two bands crossing count as two bands and a closed minigap counts as a gap. The relation between the reflection phase ϕ_n inside the n-th band gap of a semi-infinite SL terminated in a centro-symmetric unit cell and the Zak phases of the bulk SL has been formally derived for photonic crystals in [249]. The derivation is analogous for the longitudinal acoustic phonons considered here, noting the already mentioned analogy between optics and acoustics. For a phase reflection $\phi_n \in [-\pi, \pi]$, we have

$$sgn(\phi_n) = (-1)^n (-1)^l \exp(i \sum_{m=0}^{n-1} \theta_m^{Zak}) \tag{4.33}$$

The integer n denotes the considered band gap and the integer l denotes the number of croissing points or closed band gaps under the considered gap. In the

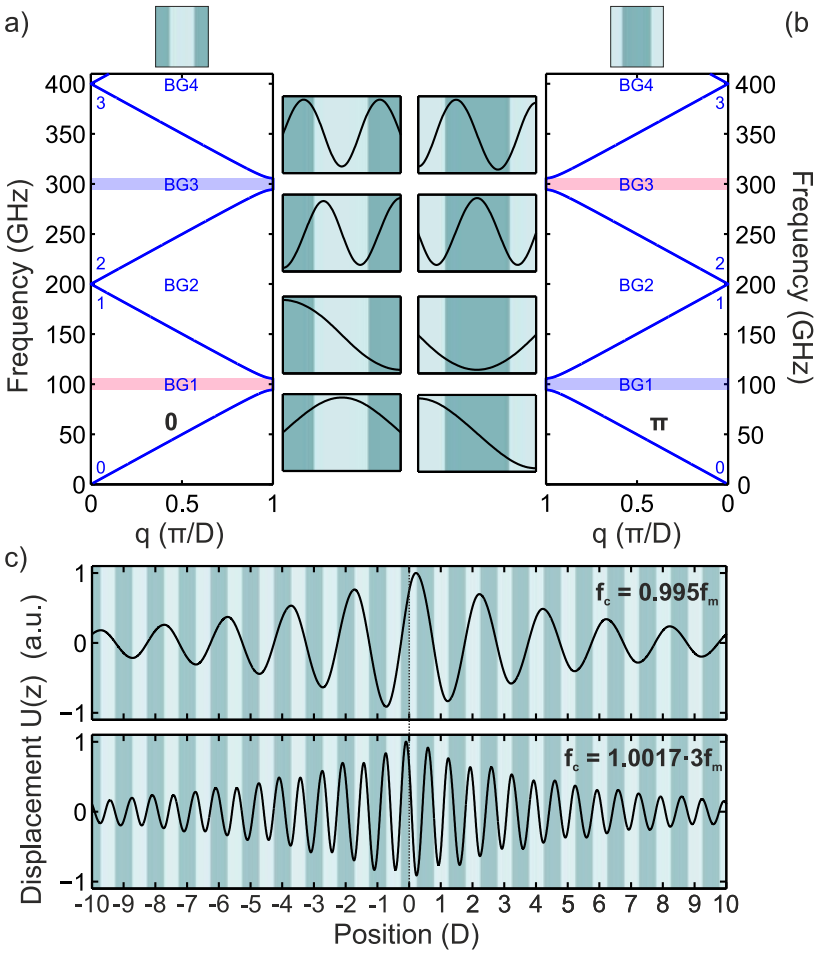

Figure 4.9: Topological origin of the simplest interface state. The Zak phase of an isolated band depends on the choice of the unit cell origin. (a) Acoustic band diagram of a $(\frac{\lambda}{4}, \frac{\lambda}{4})$ GaAs/AlAs superlattice (SL) with the unit cell shown schematically above the band diagram, with a central GaAs layer. The bands and band gaps (BGs) are numbered in blue. The Zak phases are given and the sign of the reflection phase inside the open zone-edge (ZE) minigaps is highlighted by shaded blue (+) and red (-). The displacement fields of the corresponding band edge modes are also given (in spectral order). (b) Acoustic band diagram analagous to (a) but with a centro-symmetric unit cell centered in the AlAs layer. Concatenating these two SLs at their origin leads to interface states at the *center* of all ZE minigaps, as evidenced by the difference in the sign of ϕ (shown for BG1 and BG2) and by the magenta dots in Fig. 4.8(c). The two lowest energy states are shown in (c), evidencing the exponential decay towards both sides of the interface.

summation in (4.33) only well defined Zak phases, i.e. of isolated bands, are considered. Recalling that centro-symmetric unit cells are chosen, the RHS of (4.33) takes values ± 1 and everything is well defined.

Relation (4.33) holds for any centro-symmetric unit cell, even for continuously varying periodic impedances $Z(z)$ and mass densities $\rho(z)$, making it extremely useful as the reflection phases are harder to compute for such conditions.

In addition, since the phase-matching condition (4.30) only requires being in band gaps of any order n_1 and n_2 for both SLs 1 and 2, (4.33) determines the presence of an interface state even for SLs of different period D. In particular, a simple way of building such an interface state consists of having a given SL 1 and concatenating it with a particular scaled version of itself. If SL 1 has minigaps n with $sgn(\phi_n) = +1$ and m with $sgn(\phi_m) = -1$, concatenating it with a SL 2 with a geometry scaled by a factor n/m leads to a common band gap region around the frequency of the m-th gap in SL 1. This is due to the scaling properties of the governing equations, which do not change the Zak phases of each band, leading to a common gap with inverted sign of the phase reflection ϕ on both sides of the interface.

Now we return to the localized interface states that were highlighted with magenta dots in the analysis of Fig. 4.8. The band diagram of the base SLs is reproduced twice in Fig. 4.9(a,b), but now the Zak phases and the mode profiles at all visible band edges are given for the particular choice of the unit cell highlighted on top. The bands and band gaps have been numbered for clarity and the reflection phase sign (4.33) for all ZE minigaps (we recall that ZC minigaps are closed for a $(\frac{\lambda}{4}, \frac{\lambda}{4})$ SL) is given in blue (+) and red (-). The respective Zak phase θ_n^{Zak} as calculated from (4.31) is also given above each band. As expected from the phase evolution of θ_n^{Zak} with the unit cell choice, all bands having Zak phase equal to 0 (π) in (a) become π (0) in (b). Another important aspect that needs to be explored is the relation of the Zak phase of a band to the spatial profiles of the band edge modes. Using the seminal result from Kohn [253], the Zak phase of the n-th band is 0 if both the ZC and ZE modes profiles satisfy $U(z = 0) = 0$ or both satisfy $U(z = 0) \neq 0$. In any other case, its value is π. From this point, this argument is used to adscribe θ_n^{Zak} to a given band. Here, the only band having a well defined Zak phase is the lowest lying band, i.e. θ_0^{Zak}, all the rest exhibit a crossing at the ZC. Having the null solution at the origin, the lowest band edge modes depicted explain the calculated Zak phases. The reflection phase signs highlighted are found by direct use of (4.33). The inversion of the reflection phase sign guarantees the existence of an interface state inside all ZE minigaps. The eigenfrequencies f_c of such states are not exactly centered in the corresponding minigaps, as has already been discussed. The mode profile $U(z)$ associated to the the first and second ZE minigap interface modes are depicted in Fig. 4.9(c). Both modes decay exponentially from the interface. The profile associated to the first ZE minigap mode at each side of the interface closely resembles the evanescent Bloch mode given in Fig. 4.4.

Topological band inversion

The interface states found at the ZE minigaps by the strategy just described are often referred to as topological interface/edge states. The used nomenclature is not necessarily related to the use of the Zak phases to predict the sign of the reflection phase, but to the fact that they are obtained by tuning the system parameters across a topological transition point [254]. To understand this, we explore how an

interface state can be formed solely by tuning of the layer thicknesses at the first ZC minigap.

In Fig. 4.9, the first minigap is closed and the first requirement would be to open it. If we additionally want the central frequency to remain the same, the total acoustic path length of one SL unit cell needs to remain half a phonon wavelength, i.e., to satisfy

$$\frac{d_{GaAs}}{v_{GaAs}} + \frac{d_{AlAs}}{v_{AlAs}} = \frac{1}{2f_m} \tag{4.34}$$

which can be accomplished by setting

$$d_{GaAs} = \frac{v_{GaAs}}{4f_m}(1+\delta) \quad \text{and} \quad d_{AlAs} = \frac{v_{AlAs}}{4f_m}(1-\delta) \tag{4.35}$$

where $\delta \in (-1, 1)$. The two bounds correspond to bulk AlAs ($\delta = -1$) and bulk GaAs ($\delta = 1$), while $\delta = 0$ corresponds to the $(\frac{\lambda}{4}, \frac{\lambda}{4})$ SL explored so far. The band diagram for $\delta = -0.25$ and $\delta = +0.25$ are given in Fig. 4.10(a,b), along with the information for band topological invariants and reflection phases similar to in Fig. 4.9(a,b) previously. When only considering the dispersion relations, $\pm\delta$ provide the exact same information. However, the opening of the gap towards $+\delta$ and towards $-\delta$ is accompanied by the acquisition of different Zak phases in the bands that cross at the ZC for $\delta = 0$. In addition, the symmetry of the band edge modes associated to those gaps is inverted, as can be seen for the two first even band gaps, BG2 and BG4 (Fig. 4.10(c)). The Zak phases of these bands here are topological invariants because it is possible to deform the set of bands inside the Brillouin Zone by changing the value of δ without altering the associated Zak phases. The only way to change the values of θ_n^{Zak} for any n (and consequently θ_{n-1}^{Zak}) is to pass through a discontinuity, here associated with band inversion, where we close and reopen the n-th gap. This topological band inversion is represented in Fig. 4.10(c) for both BG2 and BG4.

We first focus on BG2: for $\delta < 0$ the lower band has $\theta_1^{Zak} = 0$ and the upper band $\theta_2^{Zak} = \pi$ and we say that we are in a given topological phase (with respect to this particular gap). For $\delta > 0$, the values of θ_1^{Zak} and θ_2^{Zak} are flipped and we are in another topological phase. At the topological transition point, i.e. $\delta = 0$, the gap is closed and the Zak phases of the two bands cannot be defined. The color code for the GaAs and AlAs layers used for the mode profiles represent that both are different topological phases. The cell insets in Fig. 4.10(c) show that for $\delta < 0$ the Bloch mode at the lower (upper) band edge has a symmetric (antisymmetric) displacement pattern. The insets also how these symmetries are exchanged precisely at the topological transition point. The symmetry is not associated to the particular value of the Zak phases bounding the gap, but to all Zak phases below it. In the case of band gap BG4, we have the same Zak phase exchange as produced for BG2 for small values of δ. However, for $|\delta| > 0.5$, the bands are inverted another time. For simplicity, the associated mode edges are not shown, but the swapping of the Zak phases at all three points is associated to an inversion of the edge mode symmetries. By continuously varying δ, BG4

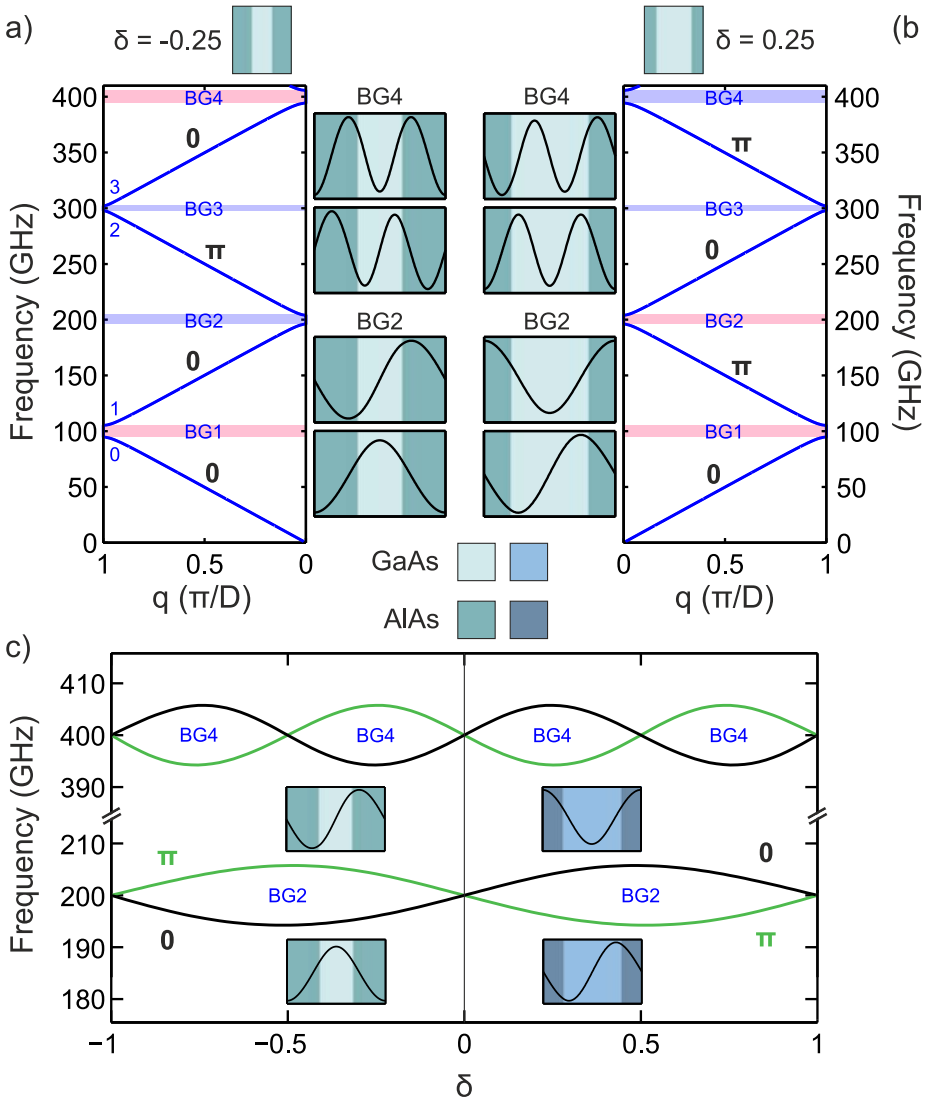

Figure 4.10: Topological band inversion in a phononic superlattice (SL). The acoustic band diagram of a $\left(\frac{\lambda}{4}(1+\delta), \frac{\lambda}{4}(1-\delta)\right)$ GaAs/AlAs SL is given for (a) $\delta = -0.25$ and (b) $\delta = 0.25$, the corresponding unit cells shown on top. Bands and band gaps (BGs) are numbered, Zak phases are given above the bands and the sign of the reflection phase inside the minigaps is highlighted by shaded blue (+) and red (-). The displacement fields of the band (BG2 and BG4) edge modes are also given (in spectral order). (c) Band edge frequencies as a function of $\delta \in (-1, 1)$ for the edges bounding the first (BG2) and second (BG4) ZC minigaps. The Zak phases of the associated bands are given in green (π) and black (0). The insets reproduce the mode profile shape of the modes bounding BG2. The value δ=0, for which the gaps are closed, represents a topological transition point that is characterized by an exchange of the symmetries of the Bloch modes. Accordingly, the Zak phases bounding the gap are exchanged. Therefore, $\delta > 0$ and $\delta < 0$ represent two distinct topological phases. This is visually represented by using a different colour code in the layers, with a dark (light) palette corresponding to GaAs (AlAs) layers.

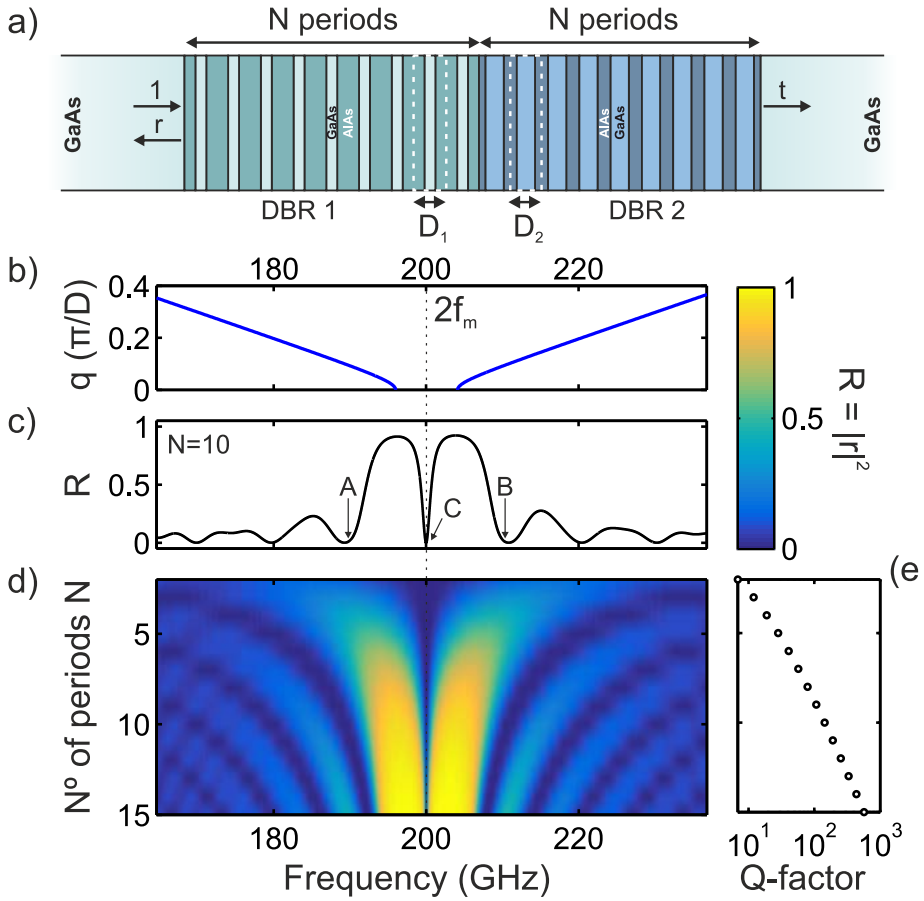

Figure 4.11: Basic features of an acoustic topological nanocavity. (a) Schematic of a structure supporting an interface state between two centrosymmetric GaAs/AlAs superlattices (SLs) belonging to two different topological phases. (b) Common band diagram of the $\left(\frac{\lambda}{4}(1+\delta), \frac{\lambda}{4}(1-\delta)\right)$ GaAs/AlAs SLs around the first zone-center (ZC) minigap for $\delta = \pm 0.25$, centered at frequency $2f_m$=200 GHz. (c) Reflectivity of a finite sample consisting of a $\delta = -0.25$ and a $\delta = 0.25$ concatenated 10-period Distributed Bragg Reflectors (DBRs). The stop band tends to the common minigap with increasing number of DBR periods N (d), while the transmission resonance associated with the topological cavity at f_m gets narrower. The value of the Q-factor extracted from the corresponding quasinormal-mode (QNM) is given in (e).

can undergo three topological phase transitions. For this system, passing through two of these transition points necessarily implies that one returns to the same original phase. This behaviour can be generalized to the n-th even gap by noting that the variation in δ at a fixed acoustic path length corresponds to varying α in Fig. 4.1(b), where we have $2^{n/2} - 1$ topological band transitions (gap closings) and that $\delta = 0$ ($\alpha = v_{AlAs}/(v_{AlAs} + v_{GaAs})$) is a crossing point for all ZC minigaps. Due to the periodic evolution of the band edges with δ, this implies that for a fixed value of δ_*, the topology of $-\delta_*$ is exchanged for any open ZC minigap. Therefore, for the particular case shown in Fig. 4.10(a,b), $\delta = \pm 0.25$, all minigaps of the two systems are not topologically equivalent since the only way to obtain one structure from the other is through band inversion.

As described before, a common minigap associated with two different topological phases exhibits, by construction, a different reflection phase sign, as shows Fig. 4.10(a,b). This provides the foundation for what is more generally known as the bulk-edge correspondance [255], which guarantees the presence of an in-gap edge state when two systems of different topological phase are interfaced. For the first ZC minigap: θ_0^{Zak} remaining the same for any δ, the change in the value of the θ_1^{Zak} changes the value of (4.33). For any higher-order ZC minigap, i.e. $n = 2p$ with $p > 1$, the inversion of the reflection phases ϕ_n upon passing through an odd number of topological transition points simply follows from the fact that all the bands beneath the $n-1$ -th band either keep the same Zak phase or there is a Zak phase exchange at lower order crossings, but the sum below the $n-1$ -th band remains fixed. Therefore the n-th band Zak phase, which has swapped from 0 to π or from π to 0 determines the sign. For a transition from $-\delta_*$ to δ_* all ZC minigaps are closed an even number of times and this leads to topologically different ZC minigaps. By concatenating two semi-infinite SLs with inverted bands and centro-symmetric unit cells an interface state is created. An example of the finite version of such a structure, two finite DBRs with inverted bands, is given in Fig. 4.11(a), where the two DBRs correspond to $\delta = -0.25$ (left) and $\delta = 0.25$ (right). For clarity, the band diagram of the base SL around the first ZC minigap is shown in Fig. 4.11(b). When the structure is driven from the left, a clear reflectivity dip at frequency $2f_m$ (Fig. 4.11(c)) evidences the presence of a topological interface state, as predicted from the fact that the two are topologically different. The reflectivity as a function of the number of periods N in the DBRs is given in Fig. 4.11(d). The Q-factor of the topological interface state obtained from the complex eigenfrequency $\widetilde{\Omega}_m$ of the associated QNM, is depicted in (e). The overall Q is lower than for the FP cavity discussed previously though this stems from the lower reflectivity of the mirrors R_1 and R_2. At $\delta = \pm 0.25$, the width of the first ZC minigap is not maximal, unlike the first ZE minigap for $\delta = 0$, likely leading to a smaller reflectivity.

The resonant transmission at A and B in Fig. 4.11(b) is associated to a pair of dissipative normal modes which arise from coupling of the band edge modes of the respective DBRs. In this particular case, the two-mode structure is not even visible from the reflectivity spectrum, but two QNMs exist with $\mathrm{Re}(\widetilde{\Omega}_m)$ close to the frequencies of both A and B. Fig. 4.12 shows both the transmission field and the QNM eigenfield (of the mode closest to the band edge) for both of these edges, along with the same fields for the topological interface state. The behaviour of both the QNMs and the transmitted fields at A and B are rather complex. However, the fields at both DBRs interchange their overall field structure when one switches from A to B. Although $|U(z)|(|\widetilde{U}(z)|)$ of A and B do not perfectly follow the mode profiles associated with the edge modes of the SL as was seen in Figs. 4.4 and 4.6, the modes do retain some field properties associated with the band inversion process. In addition, for much larger values of N the modes do follow accurately the displacement field associated to the Bloch band edge modes. On the contrary, the topological nanocavity decays exponentially into both DBRs.

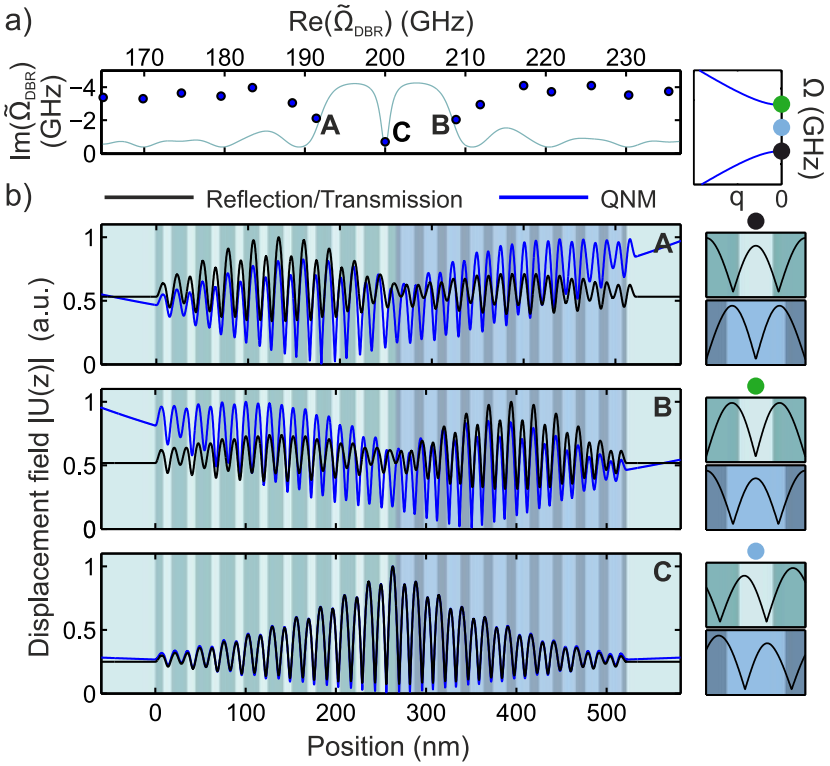

Figure 4.12: Relevant displacement fields in a topological nanophononic resonator. (a) Eigenfrequencies $\widetilde{\Omega}_m$ of the supported quasinormal-modes (QNMs) in a structure with two concatenated Distributed Bragg Reflectors (DBRs) based on superlattices (SLs) exhibiting different topology (blue dots). The reflection spectrum of the structure is given with a solid light blue line for reference. (b) (Blue lines) Absolute value of the QNM fields $|\widetilde{U}(z)|$ associated with QNMs highlighted with letters A, B and C in (a). Along with the QNM fields, the transmitted fields $|U(z)|$ (black lines) are shown. These are associated to the reflectivity dip closest to the real part of frequencies A, B and C. The Bloch modes $|U(z)|$ of both inverted superlattices for the lower (upper) band edge, whose frequency is marked by a black (green) dot, and for the evanescent Bloch mode at f_m (light blue dot) are given on the right. The observed resonances inherit some of the field properties of the *corresponding* Bloch modes, including their symmetries.

The described interface state, which has been designed using the bulk topological properties of the SLs that are interfaced, can still be interpreted as a FP resonator. While the left and right acoustic mirrors are $\left(\frac{\lambda_m}{4}(1-\delta), \frac{\lambda_m}{4}(1+\delta)\right)$ and $\left(\frac{\lambda_m}{4}(1+\delta), \frac{\lambda_m}{4}(1-\delta)\right)$ DBRs for an acoustic wave propagating at frequency $f_m = 100$ GHz, they are $\left(\frac{\lambda}{2}(1-\delta), \frac{\lambda}{2}(1+\delta)\right)$ and $\left(\frac{\lambda}{2}(1+\delta), \frac{\lambda}{2}(1-\delta)\right)$ for a phonon of frequency $2f_m$. When interfaced with the same material in contact, AlAs in this context, it leads to a $\frac{\lambda}{2}$ FP resonator between two different mirrors. Nevertheless, we can now create a localized interface state between the two DBRs in which the mode is confined between layers of different materials, a mode that lives between two bilayer DBRs. For that purpose, the last unit cell of each DBR can be redefined. The procedure is schematically shown in Fig. 4.13(a). We perturb the interface via the addition of a thin AlAs layer of thickness d_{mid} (black

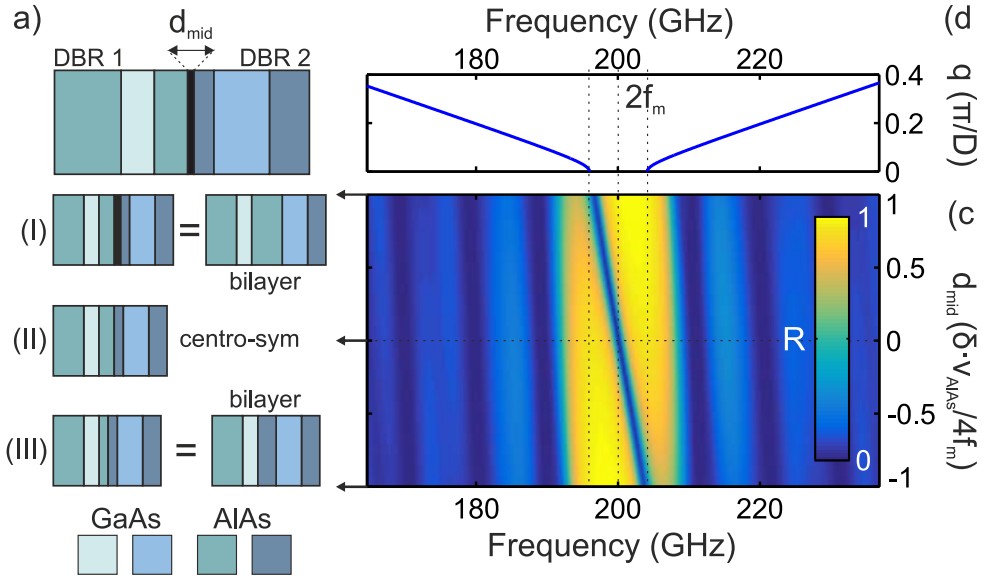

Figure 4.13: Topological nanophononic state at an interface made of two different materials. The spectral position of the topological cavity mode can be tailored by adding a thin AlAs layer of thickness d_{mid} at the interface, as shown on the top schematic in (a). Three particular cases are depicted. Case (I) corresponds to $d^*_{mid} = \delta\frac{v_{AlAs}}{4f_m}$, for which the compound central AlAs layer has the thickness of AlAs layers in the left superlattice (SL1). Case (II) shows the structure for $d_{mid} = 0$, in which case two concatenated centro-symmetric SLs terminated in AlAs are joined, effectively leading to a $\lambda/2$ Fabry-Pérot (FP) resonator at $f_c = 2f_m$. Case (III) represents $d^*_{mid} = -\delta\frac{v_{AlAs}}{4f_m}$, for which the compound central AlAs layer has the thickness of AlAs layers in the right SL (SL2). (b) Common band diagram of the $\left(\frac{\lambda}{4}(1+\delta), \frac{\lambda}{4}(1-\delta)\right)$ GaAs/AlAs SLs around the first zone-center (ZC) minigap for $\delta = \pm 0.25$, centered at frequency $2f_m$=200 GHz. (c) Reflection spectrum colormap of a finite structure composed of two 20-period concatenated DBRs as a function of the interface layer thickness d_{mid}. For $d_{mid} > 0$ ($d_{mid} < 0$), the mode continuously redshifts (blueshifts). The two limiting cases, i.e., $d_{mid} = \pm d^*_{mid}$, which represent two bilayer DBRs in contact, still lead to an in-gap resonant state as shown by the vertical dashed lines across (b) and (c).

layer). When $d_{mid} = \delta\frac{v_{GaAs}}{4f_m}$, or more generally when $d_{mid} = (\delta_R - \delta_L)\frac{v_{GaAs}}{8f_m}$, if δ is chosen to be different in both DBRs, the thickness of the central AlAs compound block becomes equivalent to the thickness of an AlAs layer in the left DBR, as is illustrated in Fig. 4.13(a) (I). By redefining the position of the interface between the two topologically different DBRs, the perturbation introduced corresponds to changing from centro-symmetric unit cells to a standard GaAs/AlAs bilayer unit cell, where the interface directly connects layers of different materials. Allowing d_{mid} to also take negative values leads to the case depicted in Fig. 4.13(a) (III), where the interface is now between a GaAs layer of the left DBR and an AlAs layer of the right DBR. In both cases an interface state prevails, although its frequency f_c is red-shifted (blue-shifted) with respect to the $d_{mid} = 0$ case shown in Fig. 4.13(a) (II). This results from the added (suppressed) propagation

phase through the layer. The colormap in Fig. 4.13(c) shows how it is possible to continuously tune the spectral position of the mode inside the minigap by continuously varying the intermediate layer thickness. The extreme cases are particularly interesting, since the bilayer configuration is the one typically employed in nanophononic devices and the one that was experimentally realized in the frame of this thesis and explored in Subsection 4.4.4.

4.2.3 Disorder-induced localization

Intentional disorder can lead to the formation of optical/mechanical cavity modes, in the classical analogue of Anderson strong localization for electrons [2] (see Chapter 3). Here, we introduce geometrical disorder to induce acoustic Anderson localization in a periodic-on-average SL and focus our analysis in a frequency range around the band edge of the corresponding acoustic SL, where stronger multiple scattering is expected [23,256]. Localization of photons [6,256–258] and phonons [259–262] has been largely explored in these systems due to their ease of modelling. Some relevant notions are described here.

Calculating the localization length

Crystals are rather robust to disorder [17], i.e., one requires considerable disorder levels to induce localization in realistic structures. The first requirement to understand the emergence of localized displacement fields in a finite-size multilayer is to compute the frequency-dependent localization length ξ. In this case, it corresponds to the back-scattering mean free-path of the system since this is the only possible source of losses for a propagating acoustic phonon.

We study the $(\frac{\lambda}{4}, \frac{\lambda}{4})$ SL with design frequency $f_m = 100$ GHz that has been previously discussed. Disorder is introduced by randomly setting the natural position z_{int} of the interface between AlAs and GaAs inside a bilayer unit cell, a type of geometrical disorder that keeps the length L of the structure fixed and that can be readily obtained in molecular beam epitaxy (MBE) grown multilayers. For a fixed amount of disorder and a fixed sample length L, we calculate the intensity transmission T of many different realizations of disorder. A single realization is given by a set of interface positions $\{z_{int,i}\}$ taken from a Gaussian distribution $\mathcal{N}(d_{AlAs}, \sigma^2)$ with standard deviation σ. The ensemble-averaged transmission $\langle T \rangle$ decays exponentially with the length L. However, the logarithm of T is typically chosen due to its self-averaging nature [263], which leads to [264]

$$\langle \log(T(L)) \rangle = -\frac{L}{\xi} \tag{4.36}$$

Note that a single realization of length L_* can be used to extract T for all $L < L_*$ provided that Equation (4.36) is used at each layer. The results of fitting $\langle \log(T(L)) \rangle$ with (4.36) are shown in Fig. 4.14(a) for a disorder level $\sigma = 0.025D$ and for several frequencies (both in the pass and stop bands). Both the value of the frequency and the extracted ξ are given. The localization length ξ is rounded to the closest integer number of periods and the fit error is omitted when

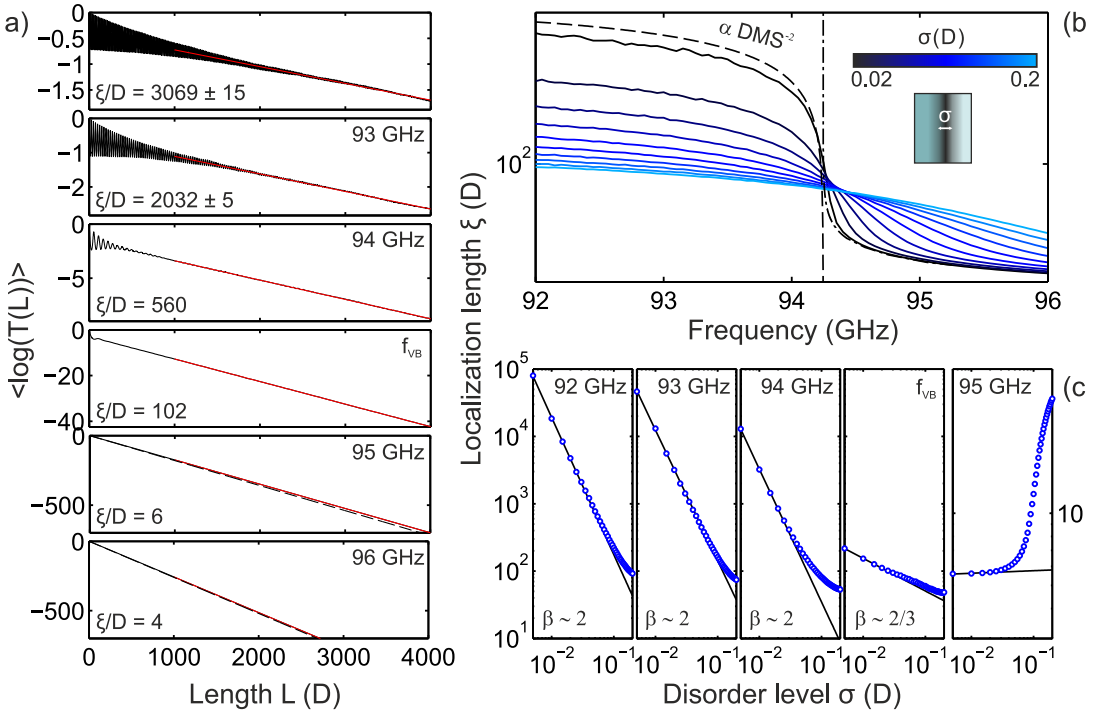

Figure 4.14: Localization length in a disordered acoustic superlattice (SL). The acoustic transmission through N-period Distributed Bragg Reflectors (DBRs) based on a $(\frac{\lambda}{4}, \frac{\lambda}{4})$ GaAs/AlAs superlattice (SL) with design frequency $f_m = 100$ GHz is studied in the presence of Gaussian-distributed geometrical disorder, with the standard deviation σ as the measure of disorder. (a) Ensemble average logarithmic transmission as a function of N for frequencies accros the lower band edge of the first zone-edge (ZE) minigap, whose frequency is denoted by f_{VB}. Red lines give the best fit to Eq. (4.36), with the extracted localization length ξ given in each panel. Repeating the procedure in (a), we obtain ξ as a function of both frequency and disorder level (b). The vertical dotted-dashed line marks f_{VB}, while the dashed lines on both sides represent (left) the squared-inverse density of mechanical states (DMS^{-2}) and (right) the Bragg attenuation length. (c) Disorder-level dependance for several frequencies, with their assymptotic behaviour at low σ fitted to a straight line whose slope gives the the Lyapunov exponent β.

smaller than D. Finite size effects, which are relevant for lengths $L < \xi$, result in fast oscillations for small values of L in Fig. 4.14(a). Nevertheless, the non-oscillatory baseline of $\langle \log(T(L)) \rangle$ in that region also decays exponentially and roughly shares the exponent ξ computed by omitting the first region, as shown from the shifted origin of the red fit. While the effect of this is minimal due to the low computational cost of these simulations, this can be relevant for higher dimensional systems where the length of the simulated structure can be a limiting factor.

The localization length ξ decreases quickly when going from the *valence* band, across the valence band edge frequency f_{VB} and into the band gap. The full dependence of ξ with both frequeny and disorder level σ is shown in Fig. 4.14(b), where two different regimes are observed. Outside the band gap within the bulk

bands, an increasing level of disorder leads to a decreasing ξ, since backscattering is the only source of losses. Within the band gap, the situation is reversed and ξ starts at half the Bragg length for $\sigma = 0$ and increases with σ. In the former, the density of mechanical states (DMS) controls the localization length ξ [265], while the Bragg attenuation length, i.e. twice the Bragg length $1/q_{Im}$, is that which controls ξ within the gap [6,266]. The two last panels in Fig. 4.14(a) include the Bragg exponential decay as a dashed line. Both the DMS and the Bragg length diverge at the band edge, necessarily implying that a crossover in which the two mechanisms compete takes place around the band edge [267], determinining the precise value of ξ. Fig. 4.14(b) also evidences that an increasing level of disorder enlarges the frequency range over which this crossover takes place. For clarity, Fig. 4.14(b) provides the inverse square of the DMS in the passband and the Bragg attenuation length in the gap as a black dashed and black dotted-dashed lines, respectively. The used scaling with the DMS has been largely discussed [180,268,269] and observed in photonic-crystal waveguides [270] and three-dimensional photonic crystals [271]. To explain this scaling, there are three approximations to take into account. First, in a one-dimensional single-mode structure, the localization length equals the scattering mean-free path [215], i.e., $\xi \approx \ell_s$. In addition, the scattering mean-free path can be expressed as $\ell_s = 1/\rho_s\Sigma$, where ρ_s is the density of scatterers and Σ is the scattering cross section [209]. Finally, two separate mechanisms determine Σ in a periodic structure: how the Bloch mode couples to the scatterer and how the scatterer radiates the scattered wave. While the former is described by the DMS along the incident wave vector q [272], the latter also reduces to the DMS when considering only in-plane scattering [273], as is the case for this one-dimensional geometry.

To evaluate the strength that the disorder level σ has on the localization length ξ, we plot the detail of this dependence for several characteristic frequencies in Fig. 4.14(c). At sufficiently low σ, all panels exhibit a linear dependence on a log-log plot. This linear dependence is lost for an increasingly lower value of σ when approaching the cutoff, which reflects the widening of the crossover region with σ. We fit the calculated values in the first region as $\xi = a\sigma^{-\beta}$, shown with a solid black line in each panel. This dependence has been studied in the literature in terms of the Lyapunov exponent, γ, which under certain hypotheses fulfilled here quantifies the exponential decay of the eigenfunctions in a disordered system [274]. Therefore, γ is the inverse of the localization length. The asymptotic dependence of γ with the amount of disorder, $\gamma \sim \sigma^{\beta}$, has been analyzed in perturbed periodic photonic structures [275] where a value of $\beta \sim 2$ is obtained in the bulk of the dispersion relation, i.e., spectrally far from the cutoff frequency. Here, we recover this dependence for frequencies 92, 93 and 94 GHz, i.e., well within the band. Near the cutoff frequency, the parameter β is expected to asymptotically behave as 2/3, as observed in Ref. [275]. When the fit is done exactly at the cutoff, i.e. f_{VB} here, we obtain a value of $\beta = 0.62$, which is in good agreement with the expected asymptotic. As previously mentioned, at 95 GHz inside the gap, the behaviour of ξ with σ changes sign, but we still observe an asymptotic power-law behaviour with β strongly dependent on frequency.

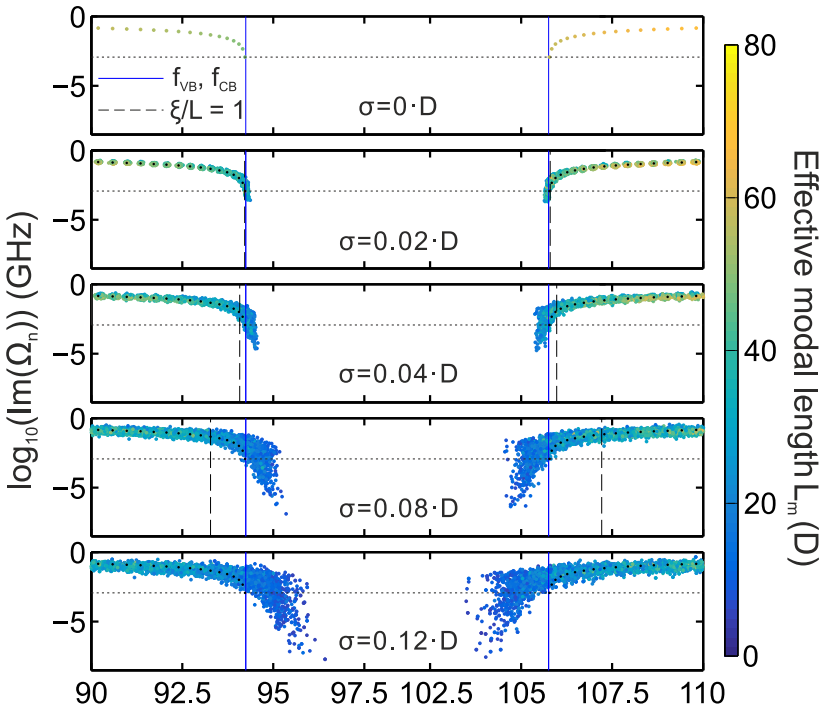

Figure 4.15: Quasinormal-modes (QNMs) of a disordered acoustic Distributed Bragg Reflector (DBR). Eigenfrequencies $\widetilde{\Omega}_m$ of the supported QNMs in a set of 250 geometry-disordered 200-period Distributed Bragg Reflectors (DBRs). These are based on a $(\frac{\lambda}{4}, \frac{\lambda}{4})$ GaAs/AlAs superlattice (SL) with design frequency $f_m = 100$ GHz. The top panel gives the eigenfrequencies for the unperturbed structure ($\sigma = 0$) and is reproduced in the rest of the panels with black dots. Vertical blue lines mark the band edges, while black vertical dashed lines mark the frequency for which $\xi \approx L$ as extracted from Fig. 4.14. The horizontal dashed line marks, for reference, the lowest losses $\mathrm{Im}(\widetilde{\Omega}_m)$ found for the unperturbed structure. The color code gives an effective modal length L_m for the QNM, calculated via Eq. (4.37).

Anderson-localized modes

Whenever the sample length L exceeds ξ, the system is expected to exhibit spatially localized and spectrally distinct modes, unlike in the ballistic and/or diffusive regime where modes overlap spectrally. However, we consider finite disordered DBRs either embeded between two semi-infinite media or terminated with fixed/free boundary conditions. Even in the unperturbed case, such systems exhibit well-defined spectral resonances close to the band edge (see Fig. 4.3) and it is therefore instructive to explore how the spectral features of the unperturbed structure transform under the introduction of disorder with increasing σ. Fig. 4.15 shows the eigenfrequencies $\widetilde{\Omega}_m$ found for a set of 250 disorder realizations in the regions bounding the two band edges of the SL discussed so far. In addition to the real and imaginary parts of the QNM eigenfrequencies $\widetilde{\Omega}_m$, the colorscale represents the effective modal length of the considered mode, calculated as,

$$L_{eff} = \frac{\int \rho(z)|\widetilde{U}(z)|^2}{\max(\int \rho(z)|\widetilde{U}(z)|^2)} \tag{4.37}$$

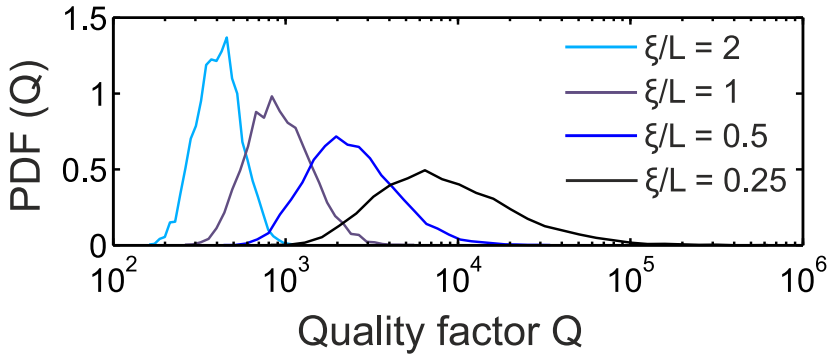

Figure 4.16: Quality factor distributions in a disordered acoustic Distributed Bragg Reflector (DBR). Log-scale probability distribution function of the quality factors Q found in a narrow frequency region $\Omega_m \in [93.2, 93.28]$ for different lengths $L/D = \{100, 200, 400, 800\}$ of a disordered DBR ($\sigma = 0.08 \cdot D$). The localization length is obtained from Fig. 4.14 to be ξ=200D.

For the lowest value of σ, i.e. $\sigma = 0.02 \cdot D$, the QNM eigenfrequencies are found to be distributed (both real and imaginary parts) around the eigenfrequencies of the unperturbed structure, nearly up to the band edge frequencies f_{VB} and f_{CB}, where modes with considerably smaller losses $\Gamma_m \equiv 2\text{Im}(\widetilde{\Omega}_m)$ appear both at the band edge and slightly inside the band gap. For reference, the QNM eigenfrequencies for the unperturbed DBR are given with black dots and the horizontal dashed line marks the minimum losses achieved for the unperturbed structure, which corresponds to the band edge modes. For a stronger disorder level $\sigma = 0.04 \cdot D$, only the lowermost and uppermost frequency regions exhibit well-defined clustered data. This clear characteristic of ballistic propagation is lost towards the band edges rather quickly, both for frequency and losses, and we cannot attribute a single eigenmode in the perturbed structure to the unperturbed one, despite having $\xi < L$ (marked with the vertical dashed black lines). Further increasing σ leads to the appeareance of low losses and low modal length L_m modes inside the band gap. This set of modes extends further inside the gap with increasing σ, a feature that leads to the well-known Lifshitz tail in the density of states when ensemble averaging, as seen in Chapter 3 for the corrugated nanobeams. At frequencies close to the band edge, the spread in losses increases with σ, leading to a distribution unrelated to the original eigenmodes in the unperturbed structure. Note that the losses at the band edge frequency (marked by the crossing of the vertical blue line and the horizontal dashed line) spread over a region with values lower than the losses of the unperturbed band edge mode, showing that the spectral properties at that frequency are no longer determined by the properties of the finite-sized acoustic DBR.

The long tails in the distribution of $\text{Im}(\widetilde{\Omega}_m)$ describe a non-vanishing probability to observe very high Q-factor Anderson-localized modes. This probability grows with the ratio ξ/L, as is shown in Fig. 4.16 for a narrow frequency region $\text{Re}(\widetilde{\Omega}_m) \in [93.2, 93.28]$ MHz close to the band edge and a disorder level $\sigma = 0.08 \cdot D$. All of the distributions shown are in good agreement with the

predicted log-normal distributions [276,277] that are given by,

$$\mathrm{P}(Q) = \frac{1}{Q\sqrt{2\pi}\sigma} e^{-\frac{(\mu - \ln(Q))^2}{2\sigma^2}}. \tag{4.38}$$

with μ and σ the mean and standard deviation. Moreover, each distribution is in principle uniquely assigned to a given ratio ξ/L as a consequence of the single-parameter scaling and universality [278] exhibited by most one-dimensional disordered systems, i.e. μ and σ only depend on the ratio ξ/L. This holds for any mesoscopic-transport observable in the system as long as the frequencies are chosen within the bands of the unperturbed periodic structure. States from the interior of the band gaps and in a narrow region around the band edge do not have universal behavior and require two parameters to describe their scaling properties [258]. In our case, this leads, for the same ratios ξ/L, to different distributions as those shown in Fig. 4.16. The Q-factors of the Anderson-localized modes appearing inside the band gap of the unperturbed structure are considerably higher and we therefore restrict the following analysis to that particular region.

4.3 Optomechanical coupling in the Anderson-localization regime

Due to the strong analogy between longitudinal acoustic phonons and normal-incidence light in multilayers, one would expect that photon localization behaves in a qualitatively similar manner for the corresponding wavelength range. Nevertheless, the specific values of the governing parameters in the binary SL, i.e. the refractive indices n_A and n_B, strongly influence both the average behaviour of the supported eigenmodes (both localized and extended) and the specific eigenfields and eigenfrequencies associated to a particular disorder realization. Due to the inherently complex nature of the underlying interference processes that lead to phonon/photon localization, the likelihood of having simultaneous localization along with spatially co-localized fields in space is extremely low. This decreases the achievable optomechanical coupling rates as was outlined in Chapter 3. We propose a way to address this challenge by noting that for the specific binary multilayers dicussed so far (i.e. GaAs/AlAs multilayers), a remarkable coincidence in the physical parameters governing light and motion propagation occurs [279].

4.3.1 The double magic coincidence

The similarities in the formal description of light and motion propagation in multilayered structures previously discussed imply that, under some conditions on the physical parameters of all the layers j, the two problems may become equivalent. When cast in a transfer matrix formalism, the matrices governing the propagation of light ($\mathbf{M}_{\mathrm{op}}$) and those governing the propagation of acoustic waves ($\mathbf{M}_{\mathrm{ac}}$) are equivalent under the substitutions $Z \leftrightarrow n$ and $c/n \leftrightarrow v$. This implies the following

property

$$\left.\begin{array}{l}\dfrac{Z_{j+1}}{Z_j}=\dfrac{n_{j+1}}{n_j}\\[2ex]\dfrac{c/n_j}{v_j}=K\end{array}\right.\quad\rightarrow\quad\mathbf{M}_{\mathrm{op}}(K\Omega)=\mathbf{M}_{\mathrm{ac}}(\Omega)\tag{4.39}$$

which states that if the impedance ratios at all interfaces are equal and the acquired propagation phases obey some proportionality relation, with proportionality constant, K, the problems to solve become exactly equivalent by scaling of the frequency by K.

Condition (4.39) is extremely stringent and is generally not satisfied. However, for stacks made of GaAs and AlAs grown in the [100] direction, an exceptional coincidence occurs for near-infrared photons and microwave phonons. Using standard values [280] for the optical and mechanical coefficients of GaAs and AlAs at those frequencies, we have

$$\frac{n_{GaAs}}{n_{AlAs}}=1.193\sim 1.199=\frac{Z_{GaAs}}{Z_{AlAs}}\tag{4.40a}$$

$$\frac{n_{GaAs}}{n_{AlAs}}=1.193\sim 1.186=\frac{v_{AlAs}}{v_{GaAs}}\tag{4.40b}$$

which approximately satisfies (4.39). Despite this slight departure from the ideal case, we expect that any *arbitrary* GaAs/AlAs multilayer exhibiting a mechanical eigenmode with field profile $U(z)$ and angular frequency Ω_m will also support an optical eigenmode with angular frequency $\omega_o\approx K\Omega_m$ and field profile $E(z)\approx U(z)$. In particular, any geometrically disordered GaAs/AlAs multilayer should satisfy the condition, guaranteeing the existence of perfectly co-localized photon-phonon pairs in the Anderson-localization regime. This property has already been exploited in engineered nanophononic devices to achieve enhanced optoacoustic interaction and spectrally-tuned coherent phonon generation with light [281,282]. In particular, the topological cavity discussed in Subsection 4.2.2 has been recently designed at a phononic frequency of 18 GHz, leading to a perfectly co-localized near-infrared photonic topological cavity at 920 nm and showing simultaneous band inversion [283]. However, spatial co-localization in engineered nanocavities such as FP resonators or topological interface states is already granted by the purposely designed confinement potential. The true potential of such double magic coincidence relies in using the co-localization effect to explore more subtle interference effects such as those induced by randomness. The question is then: is the depature from condition (4.39) enough to prevent the emergence of co-localization in a regime where both the optical and acoustic modal structure are induced by disorder?

4.3.2 Spectral and spatial co-localization

To illustrate the role of the double magic coincidence [284] in a disordered multilayer we depart from a $(\frac{\lambda}{4},\frac{\lambda}{4})$ DBR structure and we choose the layer thicknesses to have the first optical ZE minigap centered at $\lambda=870$ nm ($f_o=344.6$ THz).

This opens the first acoustic ZE minigap at $f_m = 19.28$ GHz. Note that we already have $f_o \approx K f_m$, with $K = \frac{c/n_{AlAs}}{v_{AlAs}}$, as expected. The layer thicknesses are therefore given by $d_{GaAs} = 61.88$ nm and $d_{AlAs} = 73.48$ nm. In the exact same manner as in the previous section, we introduce geometrical disorder in the position of the interface between the two materials. Its natural position inside a bilayer unit cell at $z_{int} = d_{AlAs}$ is normally distributed $\mathcal{N}(z_{int}, \sigma^2)$ with varying standard deviation σ, whilst the period $D = d_{AlAs} + d_{GaAs} = 135.36$ nm is kept constant. Whenever the obtained interface position z_{int} enters the previous or following unit cell, the interface is set at the end of the corresponding layer.

We compare first the transmission of normal-incidence light and longitudinal acoustic phonons in the same disordered sample for a high disorder level of $\sigma = 0.15 \cdot D$, for which we have verified that $L = 600a \gg \xi_m \sim \xi_o$ across the entire frequency region shown. The optical spectrum is almost identical to the mechanical one when plotted with scaled frequency, as shown in Fig. 4.17(a). The QNMs associated to such resonances are calculated as discussed previously, assuming an air layer as a cladding. When the real parts of the mechanical and optical QNM frequencies are mapped onto each other in spectral order, we recover the predicted spectral behavior with $\omega_o \approx C\Omega_m$ and $C = 1.82 \cdot 10^4 \approx 1.79 \cdot 10^4 = K$ (Fig. 4.17(b)). Figures 4.17(c) and (d) show the displacement and electric field intensities for the photon-phonon pair highlighted in Fig. 4.17(b), demonstrating that they are indeed localized modes within the same region of the multilayer. A zoomed in region indicated between the dashed black lines in Fig. 4.17(c,d) is shown in Fig. 4.17(e), where the two fields are perfectly overlapping in space, with the only observed mismatch corresponding to minor intensity differences.

To quantify the degree of spatial co-localization we define the following overlap integral between the two eigenfields

$$\Delta_{nm} = \frac{\int |\widetilde{U}_m(z)||\widetilde{E}_n(z)|dz}{\sqrt{\int |\widetilde{U}_m(z)|^2 dz \int |\widetilde{E}_n(z)|^2 dz}} \tag{4.41}$$

where $\Delta \in [0,1]$, with $\Delta = 1$ indicating full co-localization. Here $\widetilde{U}_m(z)$ is the mechanical displacement of the m-th mechanical QNM and $\widetilde{E}_n(z)$ the electric field of the n-th optical QNM. The fields are normalized by the amplitude of the field in the substrate and by the electromagnetic energy, respectively. As a reference, the calculated value of Δ for the pair depicted in Fig. 4.17 is $\Delta = 0.997$. We calculate the co-localization parameter Δ between all the $\{m, n\}$ phonon-photon pairs in a narrow frequency range around the lower band edge in a set of 1500 disorder realizations. The disorder level is kept at $\sigma = 0.15 \cdot D$, which guarantees the presence of multiple Anderson-localized modes per disorder realization. The histogram of Δ, plotted in Fig. 4.18(a), is strongly peaked for $\Delta > 0.95$. On the contrary, the histogram presents rather low and evenly disitrbuted values for the $\Delta < 0.95$ bins. We set this value as the criteria for perfect co-localization. For comparison, we calculate the distribution of Δ for another commonly used binary SL in nanophononics [285–287], that based on silicon (Si) and germanium (Ge). The Si and Ge layer thicknesses ($d_{Si} = 115.97$ nm, $d_{Ge} = 93.88$ nm, $N = 600$) are chosen to tune the band edge of interest to approximately half the frequency of

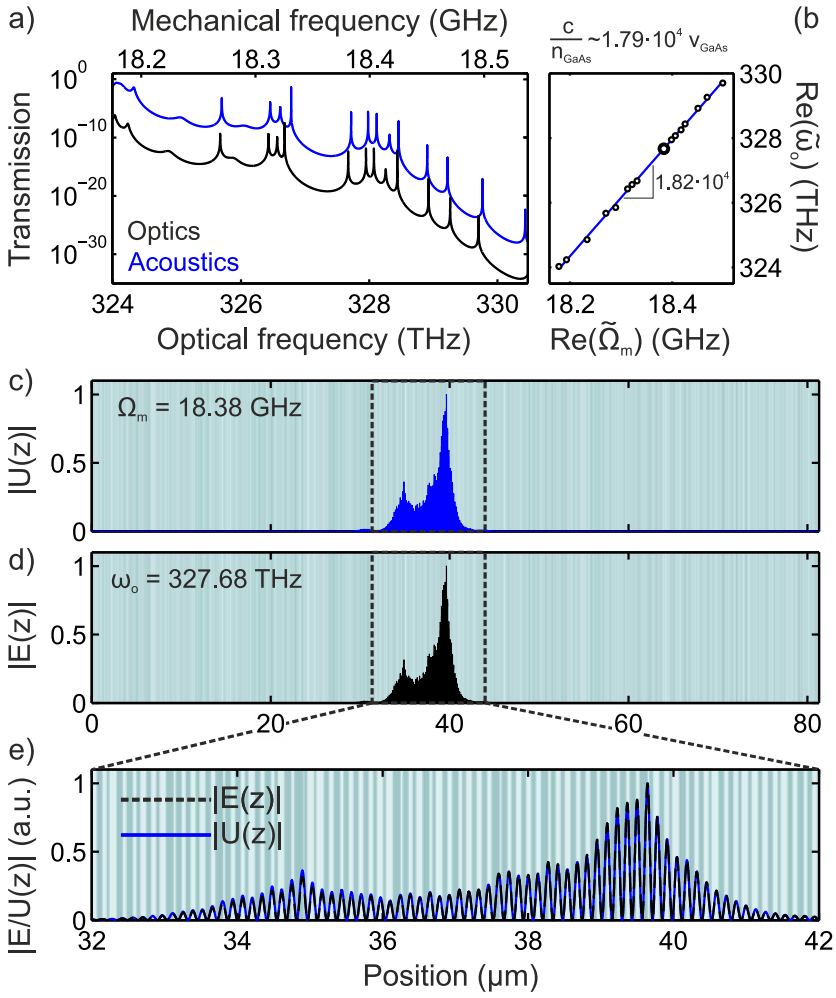

Figure 4.17: Anderson photon-phonon co-localization in GaAs/AlAs Distributed Bragg Reflectors (DBRs) with geometrical disorder. (a) Optical and acoustic transmission spectrum of a single disordered $(\frac{\lambda}{4}, \frac{\lambda}{4})$ DBR with design frequency $f_m = 19.28$ GHz and disorder level $\sigma = 0.15D$. Both spectra have been shifted for clarity. (b) Real part of the quasinormal-mode optical eigenfrequencies $\widetilde{\omega}_o$ as a function of the real part of the QNM acoustic eigenfrequencies $\widetilde{\Omega}_m$ when these are paired in spectral order. The blue line gives a linear fit to the obtained QNM pairs, showing a proportionality relation given by $C = 1.82 \cdot 10^4$ close to the one expected, given by $K = 1.79 \cdot 10^4$. QNM field profile (c) $|\widetilde{U}(z)|$ and (d) $|\widetilde{E}(z)|$ of the pair highlighted in (b), evidencing the localized nature of the modes. (e) The region highlighted with dashed boxes in (c,d) is shown in more detail, demonstrating that both field profiles are virtually the same.

that of the GaAs/AlAs SL to avoid absorption. The disorder level is also shifted to $\sigma = 0.11 \cdot D$ to satisfy the condition $\xi_{Si/Ge} \sim \xi_{GaAs/AlAs}$. In this case, the probability distribution of Δ, shown in Fig. 4.18(b), shows no level of co-localization at all, clarifying the statistical difference granted by the use of GaAs and AlAs as the SL materials.

The physical parameters governing both light and motion transport of even

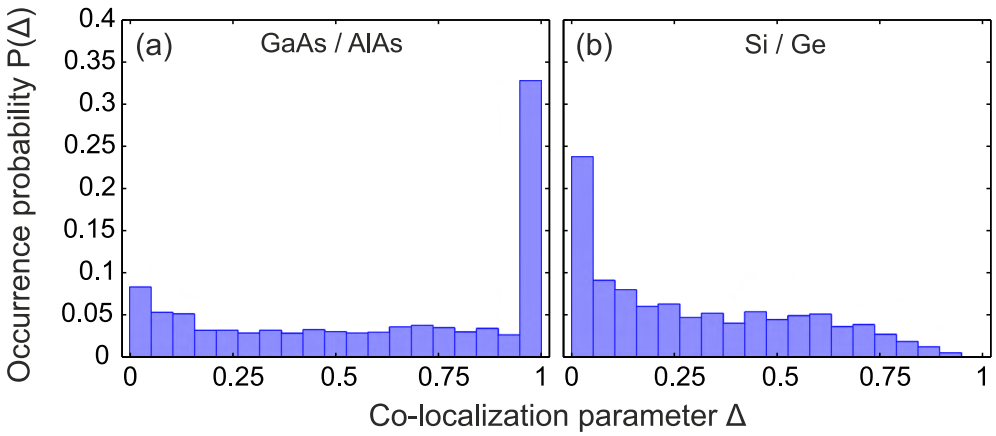

Figure 4.18: Statistical assesment of the co-localization level. The level of co-localization between a photon-phonon pair is evaluated with the overlap integral Δ given by (4.41), whose value is equal to 1 for perfectly overlapping fields. The case for GaAs/AlAs Distributted Bragg Reflectors (DBRs) is shown in (a), with the distribution effectively peaked at $\Delta > 0.95$. For comparison, Si/Ge DBRs ($d_{Si} = 115.97$ nm, $d_{Ge} = 93.88$ nm, $N = 600$) are also simulated and their co-localization properties are shown in (b).

the most well-known parameters are subject to some uncertainty. To verify the robustness of this significant co-localization effect, we calculate the distribution of Δ while adding additional Gaussian disorder to the material parameters $\{\rho,v,n\}$ of both GaAs and AlAs, with standard deviations $\sigma_p = [0.002, 0.005, 0.01] \cdot \mu_p$, where μ_p is the mean value for the given physical parameter. As plotted in the series of panels of Fig. 4.19(a), a disorder level bigger than $\sigma_p = 0.01 \cdot \mu_p$ or more is required to fully wipe out the co-localization effect, well above the layer-by-layer statistical fluctuations achievable in actual MBE-grown samples [288]. Such distributions are obtained from the same set of 1500 geometrically disordered multilayers. Fig. 4.19(b) plots the obtained optic and acoustic transmission spectra for one disordered multilayer, which shows that spectral *co-localization* is lost simultaneously. It is remarkable that spectral co-localization seems to be lost faster than the spatial counterpart. A possible heuristic explanation would be that additional phases acquired due to the randomized parameters are compensated by slight changes in frequency, leading to fields that remain close to the original ones.

4.3.3 Statistics of the optomechanical coupling rate

The double magic coincidence ocurring for GaAs and AlAs ensures that for a given frequency range exhibiting an average of N Anderson-localized photonic modes, a scaled frequency region will on average host N Anderson-localized acoustic eigenmodes. Among all possible N^2 pairs, N will be fairly co-localized, even in the presence of certain parameter randomness. These well-confined spatially-overlapping modes can interact with each other and are therefore candidates as optomechanical systems. As was already discussed in Chapter 3 for a silicon nanostructure, the deformation profile associated with a normal mode $u_m(z)$ will locally change

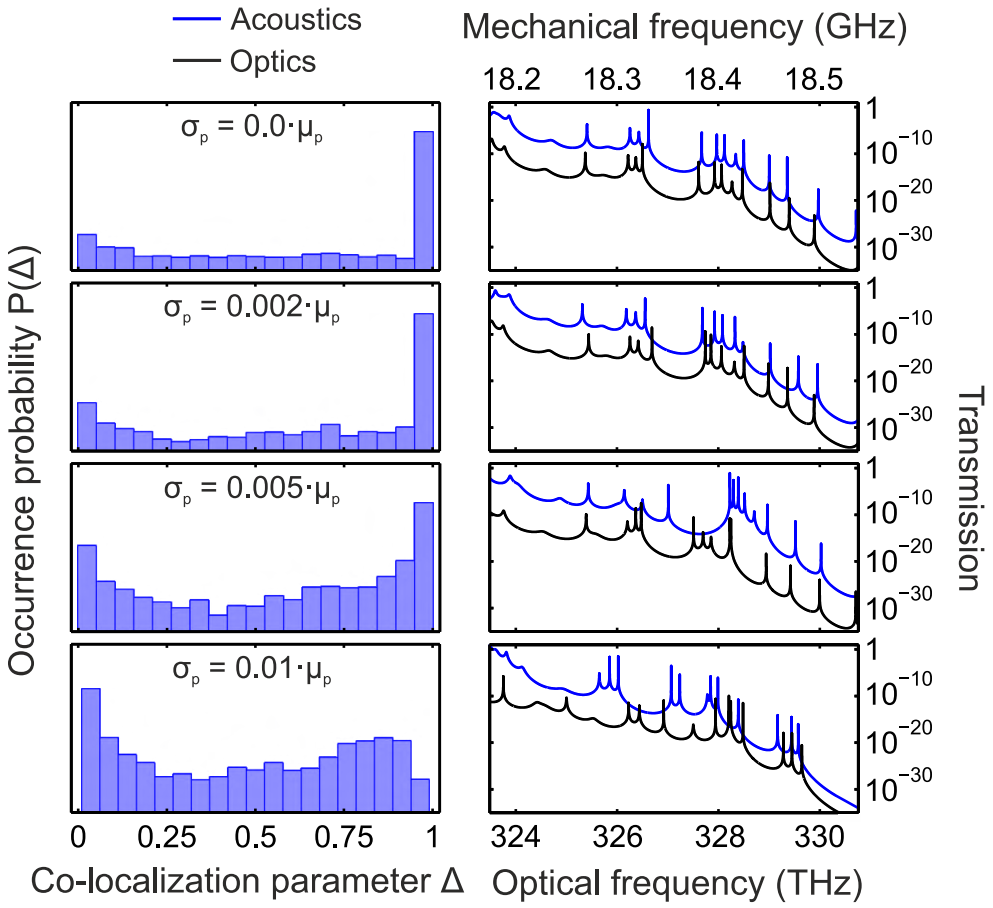

Figure 4.19: Effect of parameter uncertainty on the co-localization properties. Physical quantities governing light and motion transport are very precisely known, but small levels of uncertainty are still expected. (a) Statistical assessment of the co-localization levels achieved in the presence of increasing levels of uncertainty on $\{\rho,v,n\}$ of both GaAs and AlAs, with standard deviations $\sigma_p = [0.002, 0.005, 0.01] \cdot \mu_p$, μ_p the mean value for the given physical parameter. The same 1500 disordered geometries are used for each distribution. (b) Transmission spectra of a single disorder realization for increasing level of parameter uncertainty, exhibiting how spectral co-localization is lost. The top panels in (a) and (b) correspond to Fig. 4.18(a) and Fig. 4.17(a) respectively.

the optical properties of the structure. The inherent reason for such a change is that the optical eigenmodes themselves depend on such displacement. The coupling of an acoustic and an electromagnetic QNM gives rise to both an optical frequency shift (dispersive interaction) and a quality factor change (dissipative interaction). In GaAs/AlAs SLs and in the frequency range of interest, mainly two acousto-optic interaction mechanisms need to be considered [289,290]. First, the displacement of the $N+1$ boundaries, or moving boundary effect, will change the interference pattern of multiple light paths. Second, the photoelastic effect will induce a change in the bulk permittivity tensor ϵ that can be written as the tensor product $d(\epsilon^{-1})_{ij} = P_{ijkl}Ukl$, where $\mathbf{U}$ is the second-order strain tensor and $\mathbf{P}$ the fourth-order photoelastic tensor [291]. These two correspond precisely to the mechanisms evoked for silicon in Chapter 3. Employing the hermitian limit

of the first-order perturbation theory discussed in Chapter 2 to a multilayered system leads to,

$$g_{mb} = -\frac{\omega_o}{2}\frac{\sum_{i=1}^{N+1}\widetilde{U}_m(z_i)(\epsilon_{i-1}-\epsilon_i)|\widetilde{E}_n(z_i)|^2}{\int_0^L \epsilon(z)|\widetilde{E}_n(z)|^2 dz}x_{zpf} \tag{4.42a}$$

$$g_{pe} = -\frac{\omega_o}{2}\frac{\int_L^0 P_{12}(z)\frac{\partial\widetilde{U}_m}{\partial z}(z)\epsilon(z)^2|\widetilde{E}_n(z)|^2}{\int_0^L \epsilon(z)|\widetilde{E}_n(z)|^2 dz}x_{zpf} \tag{4.42b}$$

The hermitian limit is used because for a 1D system deep in the localization regime ($\xi << L$), the quality factor of the observed QNMs is extremely large and the limit provides an extremely good approximation for the dispersive shift. The strength of the coupling parameter $g_o = g_{mb} + g_{pe}$ between two (n-optical,m-mechanical) eigenmodes strongly depends on the overlap of the displacement $\widetilde{U}_m(z)$ or strain $\frac{\partial\widetilde{U}_m}{\partial z}(z)$ field with the electric field squared-modulus $|\widetilde{E}_n(z)|^2$, which highlights the importance of co-localizing the displacement and the electric field profiles. Since our model is by definition one-dimensional, we have chosen an *arbitrary* size in the x-y plane of 2×2 μm^2 -for the area excited by a focused laser beam- in order to calculate the effective mass m_{eff} of the mechanical resonator and the zero point fluctuations $x_{zpf} = \sqrt{\frac{\hbar}{2m_{eff}\Omega_m}}$. The product of the coupling integral by x_{zpf} quantifies the interaction between a single phonon and a single photon (Chapter 2) and is required since otherwise the parameter would depend on the normalization chosen for $\widetilde{U}_m(z)$.

We evaluate g_o between optical and mechanical QNMs of the GaAs/AlAs disordered SLs simulated for Fig. 4.19(a). Due to the strongly dispersive nature of the localization length ξ (Fig 4.14), we consider only a narrow frequency window and thus minimize the effect of varying the effective volume of both field profiles. The coupling values in the densely-packed *diagonal* of Fig. 4.20(a), which roughly corresponds to perfectly co-localized photon-phonon pairs ($\Delta > 0.95$), exhibit values higher than those far from the diagonal. This plot is again compared to the values obtained for Si/Ge SLs (Fig. 4.20(b)), where lack of any co-localization effect leads to uniformly distributed pairs inside the frequency-frequency space considered. The probability density function of the vacuum optomechanical coupling rate g_o for the case of interest is plotted in Fig. 4.20(c). The distribution considering either poorly co-localized (blue bars) or perfectly co-localized (red bars) modes are shown separately, pointing out a statistical increase of g_o for this material combination. For comparison, we also calculate the coupling coefficient for a perfect $\lambda/2$ FP cavity formed by two 300 cells DBR-mirrors, highlighted with a dashed line in panel Fig. 4.20(c).

Similar as in the case of the co-localization parameter Δ, the role of parameter uncertainty is evaluated in the statistics of the optomechanical coupling rate g_o. The probability distribution function of Δ transforms from a nearly δ-like distribution at $\Delta \sim 1$ over a uniform background when no uncertainty is considered, i.e. $\sigma_p = 0$, to a broad peak around that same, or slightly lower, value of

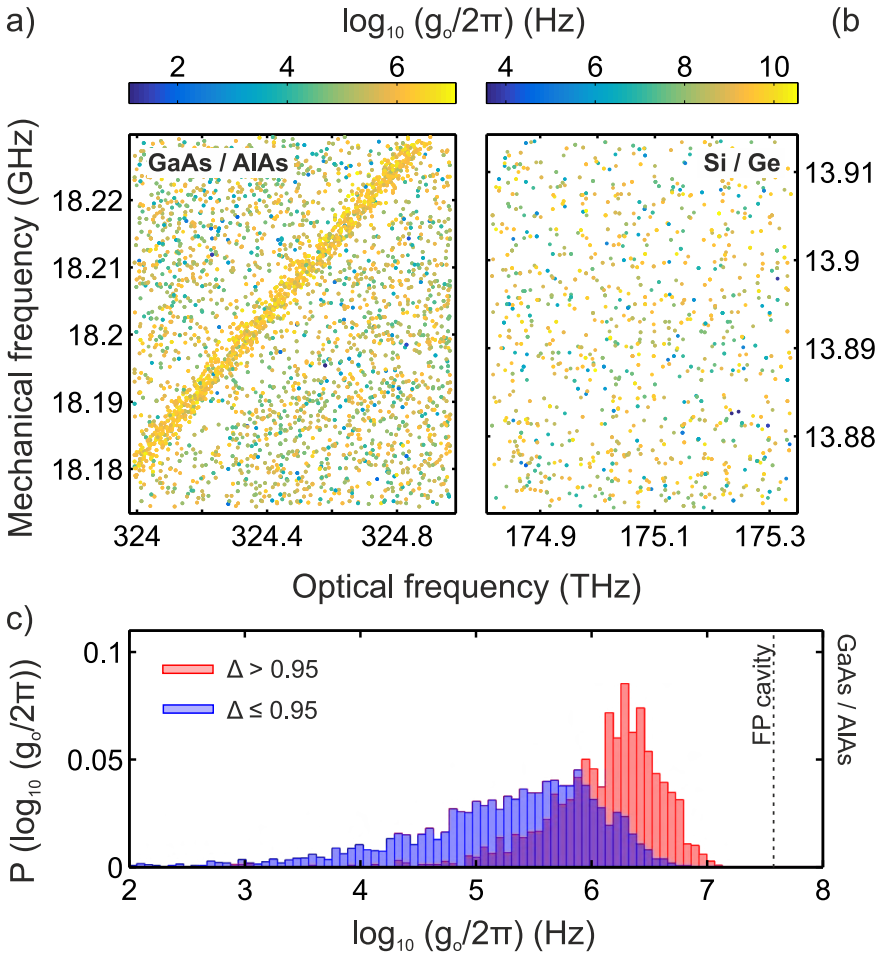

Figure 4.20: Vacuum optomechanical coupling rate $g_o/2\pi$ in disordered Distributed Bragg Reflectors (DBRs). Scatter plots of the mechanical and optical frequencies of the resonant modes found in (a) a set of 2000 disordered 600-period GaAs/AlAs DBRs ($\sigma = 0.15 \cdot D$) and (b) a set of 1000 disordered 400-period Si/Ge DBRs ($\sigma = 0.11 \cdot D$). The lengths are chosen such that ξ/L is roughly equal for the acoustic case. The color represents the coupling rate $g_o/2\pi$ between the considered pair in logarithmic scale. (b) Histogram of the coupling rate $g_o/2\pi$ considering poorly co-localized photon-phonon pairs ($\Delta < 0.95$, blue bins) and only perfectly co-localized pairs ($\Delta > 0.95$, red bins), with Δ the co-localization parameter given by Eq. (4.41). The dashed line gives the value expected for a perfect $\frac{\lambda}{2}$ GaAs Fabry-Pérot (FP) cavity with unperturbed DBR-mirrors of 300 cells each.

Δ when uncertainty is considered (Fig. 4.19). However, we expect that rather large values of Δ in this broadened feature are inherited from the perfect case. In the presence of uncertainty we have chosen $\Delta = 0.75$ as the threshold value that determines co-localization between two modes arising from the double magic coincidence. This value is also chosen taking into account the distribution observed for the Si/Ge SLs, where $\Delta > 0.75$ is extremely unlikely. Fig. 4.21 depicts the probability distributions for differents levels of uncertainty σ_p. The full distribution is represented in green, while the partial contributions from co-localized pairs ($\Delta > 0.75$) and non-colocalized pairs ($\Delta < 0.75$) are represented in red

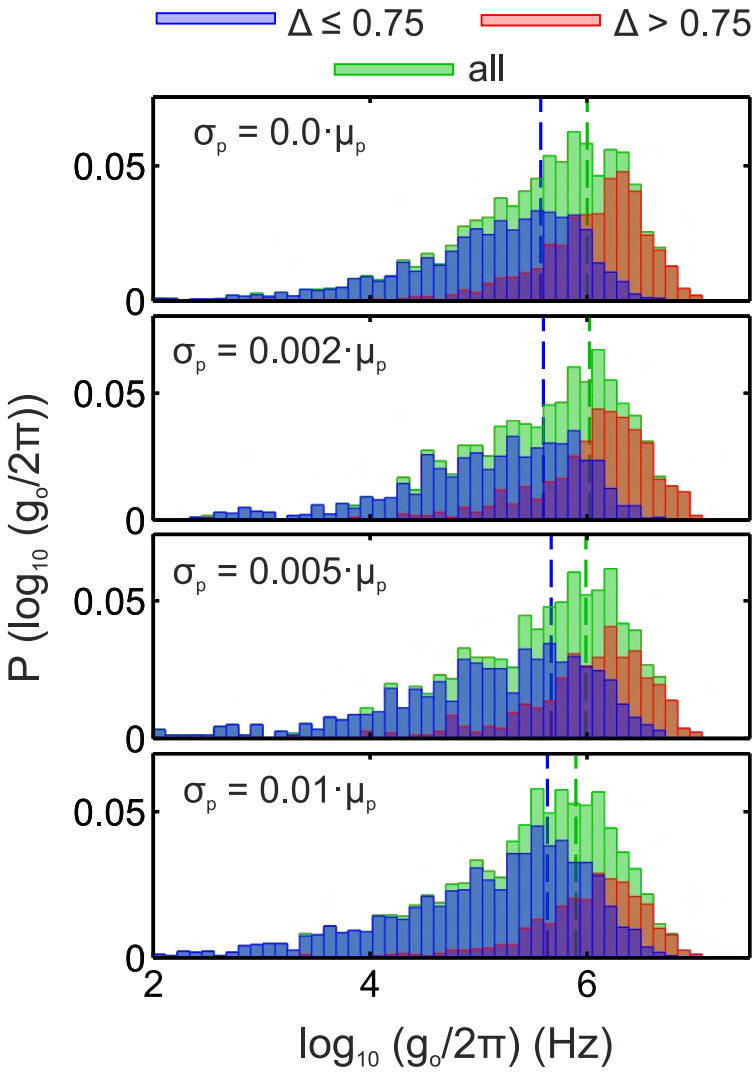

Figure 4.21: Vacuum optomechanical coupling rate $g_o/2\pi$ with uncertain physical parameters. Histogram of the logarithm of the photon-phonon optomechanical coupling values for poorly co-localized ($\Delta < 0.75$, blue bins), co-localized ($\Delta > 0.75$, red bins), and for their sum (green bins) as a function of the uncertainty σ_p on the governing physical parameters. The mean values from the distributions in blue and green are given with a dashed line of the same color.

and blue, respectively. The mean values obtained for the co-localized distribution and total distribution are indicated by a dashed line across the panels with the color chosen accordingly. The co-localized pairs (red) contribute to the high-g_o side of the distribution as expected from the chosen cut-off. They constitute the majority of photon-phonon pairs above the mean value of the full distribution for the cases without uncertainty and with $\sigma_p = 0.002 \cdot \mu_p$. For greater uncertainties we see how the mean value drops slightly, but the overall distribution shape remains the same. In any case, comparison of the mean value with and without the co-localized portion shows the important role of this set of photon-phonon pairs in the statistical properties of the optomechanical coupling rate g_o.

However, one could expect a more pronounced difference after seeing the statistics of Δ in Fig. 4.18, particularly for $\sigma_p = 0$. The photoelastic coupling mechanism considered in Eq. (4.42b) dominates over Eq.- (4.42a) and can allow us to understand why the expected *blow-up* effect is rather moderate. Expression (4.42b) is based on the product of the oscillating function $\frac{\partial \widetilde{U}_m}{\partial z}(z)$ by the always positive $\epsilon(z)^2|\widetilde{E}_n(z)|^2$. When two fields $\widetilde{U}_m(z)$ and $\widetilde{E}_n(z)$ are perfectly co-localized, the function $\frac{\partial \widetilde{U}_m}{\partial z}(z)$ ($\pi/2$-shifted version of $u_m(z)$) is null whenever $|\widetilde{E}_n(z)|^2$ attains a maximum, and vice versa for the maxima/minima of $\frac{\partial \widetilde{U}_m}{\partial z}(z)$. The fields coincide perfectly but the integrand values stay low, since $\epsilon(z)^2$ and $p_{12}(z)$ have their own particular spatial-dependence. As a consequence, partially overlapping photon-phonon pairs may present similar couplings than perfectly-overlapping ones, which reduces the effect of co-localization for this particular photoelastic coupling when compared to other light-matter processes. In addition, $\frac{\partial \widetilde{U}_m}{\partial z}(z)$ is an oscillating function and only part of the field in each unit cell ends up contributing to the integral coupling, so the effect of co-localization does not result in a blow-up. Nevertheless, a clear change in the distribution can be observed even when the complicated spatial distribution of the three functions involved in the mechanism is considered. To emphasize the general interest of the co-localization effect, we calculate the role of co-localization on different possible types of light-matter interactions, i.e with different functional forms of the parametric coupling. While a purely photoelastic coupling yields a moderate effect of co-localization (Fig. 4.22(a)) for the reasons explained above, other functional forms are best suited to the situation in hand. Fig. 4.22(b) shows the distribution for a non-integral coupling rate, that we denote g_δ, considering a Dirac-like photoelastic response at the given depth of the multilayer. This coupling is interesting because it is not affected by the oscillation of the strain field $\frac{\partial \widetilde{U}_m}{\partial z}(z)$, but allows us to see the effect of the first issue described above. It shows that when the maximum value of the product of the two functions $\frac{\partial \widetilde{U}_m}{\partial z}(z)$ and $|\widetilde{E}_n(z)|^2$ is considered, partially co-localized photon-phonon pairs can be competitive when compared to perfectly co-localized modes. The case of coupling mediated by the modulus squared electric field $|\widetilde{E}_n(z)|^2$ and the modulus squared strain field is considered in Figure 4.22(c), where we see an important effect on the full distribution. This g_2 coupling describes a second order photoelastic interaction. The most prominent effect of co-localized modes on their interaction is depicted in Figure 4.22(d), for which the maxima and minima of the two terms $|\widetilde{U}_m(z)|^2$ and $|\widetilde{E}_n(z)|^2$ coincide and the integrand is positive everywhere. We denote this coupling by g_{mod}. For this case, the co-localized photon-phonon pairs have an obvious effect on the full distribution and any light-matter interaction that share these characteristics would also benefit from this enhancement. The precise values given in the x-axis and their different scales are not to be taken literally, since the the z-dependent function p_{12} has numerically been kept the same for all interactions; the importance here is the shape of the distributions as a way to understand why the observed effect is smaller than what could in principle have been expected.

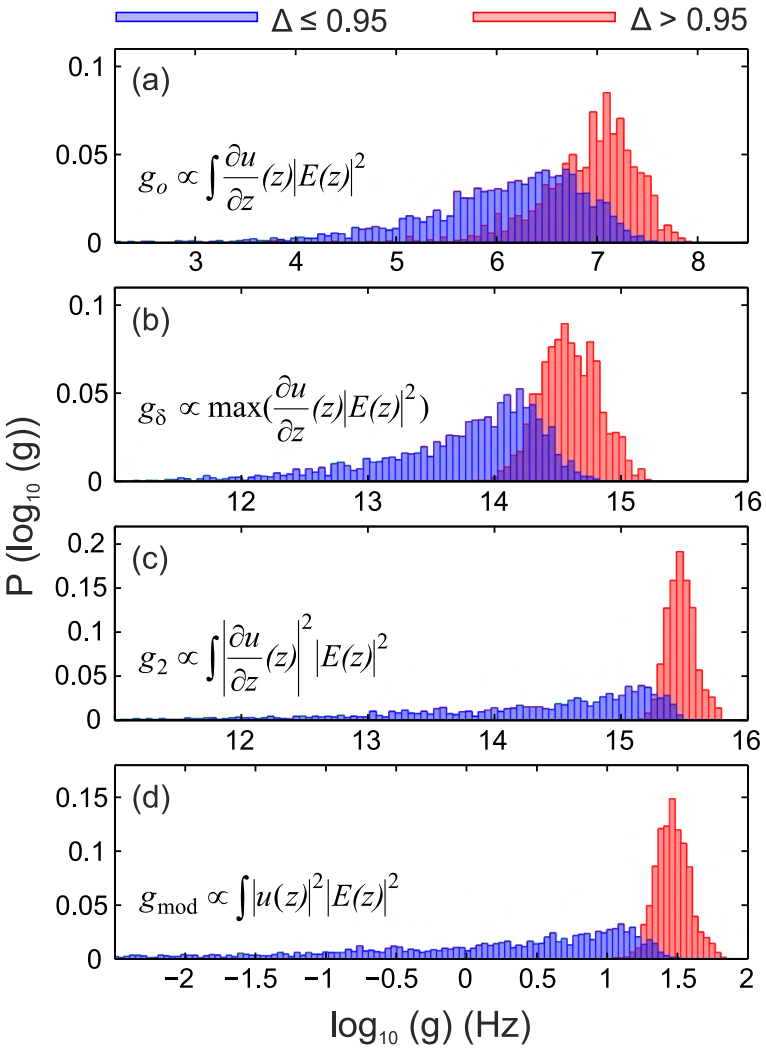

Figure 4.22: Photon-phonon coupling rate distributions for different functional forms. Histogram of the poorly co-localized ($\Delta < 0.95$, blue bins) and perfectly co-localized ($\Delta > 0.95$, red bins) photon-phonon pairs coupling values for the coupling terms indicated in panels (a) to (c).

4.4 Optical generation and detection of longitudinal coherent acoustic phonons

The optomechanical coupling in a deformable and driven optical cavity allows the detection of mechanical motion and the generation of coherent phonons via parametric amplification processes (Chapter 2). In these systems, the mechanical frequencies Ω_m explored are limited to several tenths of GHz due to the detection bandwidths and signal-to-noise ratios available as well as to a reduced thermal Brownian motion. The spectrum of optical techniques to both generate and detect acoustic vibrations is not limited to such a setting and some allow exploration of (much) higher mechanical frequencies. With the advent of femtosecond light pulses delivered by pulsed lasers, the realm of non-equilibrium ultra-fast processes, like high-frequency coherent acoustic phonons, can be explored by the use

of pump-probe techniques.

4.4.1 Time-domain pump-probe phonon spectroscopy

Pump-probe experimental techniques to generate and detect coherent acoustic phonons consist of using ultrafast light pulses as both a mechanism to *instantaneously* create a non-equilibrium population of coherent mechanical vibrations at a given time t_0 and to read the deformation state of the sample of study at a certain time t from the creation event. If the delay time Δt between the initial time t_0 and the read-out time t, i.e. $\Delta t = t - t_0$, can be controlled, one can in principle reconstruct the dynamics of the vibrational state by repeatedly generating exactly the same coherent population and changing Δt at each run. This simple picture already points to some of the requirements needed to perform such type of experiments. First, the pump pulse needs to be able to generate mechanical vibrations, so it needs to be at the origin of a source term in the elastodynamic equation of motion. Second, the optical property to be measured via the delayed pulse needs to be affected by the presence of mechanical vibrations in the sample. Third, the measurement itself needs to leave the state of the sample unaffected, which is typically achieved by using a much weaker low-power probe pulse or by employing two-color pump probe spectroscopy [292]. Lastly, one needs to be able to control the delay between the two pulses and, at each time delay, to repeat the experiment multiple times in order to increase the signal-to-noise ratio. Here, we describe the different possible physical mechanisms leading to the generation of coherent acoustic phonons by the pump pulse and detection of these phonons by the probe pulse. Then, we introduce the experimental technique and apparatus used to achieve the different requirements just mentioned.

Generation mechanisms

Whenever a light pulse is incident on a material it interacts with the bound and/or free electrons and the atomic lattice. Several of the processes occuring can give rise to the generation of coherent acoustic phonons [293,294]. This can be cast into the elastodynamics equation by adding a source term consisting of the derivative of the tension σ_p induced by the pump pulse. In the case of a laser spot much larger than both the characteristic dimensions of a multilayer and the penetration depth of light, the equation of motion reads

$$\frac{\partial^2 U}{\partial t^2}(z,t) - \underbrace{\frac{1}{\rho(z)}\frac{\partial}{\partial z}\left(C(z)\frac{\partial U}{\partial z}(z)\right)}_{\hat{L}(z)U(z)} = \frac{1}{\rho(z)}\frac{\partial \sigma_p}{\partial z}(z,t) \tag{4.43}$$

Despite important controversy on the microscopic origin of the tension σ_p leading to the generation of coherent acoustic phonons in many pump-probe experiments [290], the following origins are typically acknowledged to take place:

- *Thermal expansion*: In the presence of absorption, electrons (and holes in the case of semiconductors) acquire an excess energy which, on a picosecond

timescale, is given to the lattice by phonon-mediated intra-band relaxation. The excess energy given to the lattice leads to an out-of-equilibrium population of incoherent phonons. Whenever the timescales to explore are much larger than several picoseconds, that phonon population can be considered in thermal equilibrium at a higher temperature, i.e. we have a sudden increase of the temperature of the material $\Delta T(z,t)$, whose spatiotemporal dynamics have to be solved using Fourier's law [295,296]. This ΔT produces in turn a change of the elementary differential volumes due to anharmonicity effects [297], generating a tension in the material σ_T that is given by [294]

$$\sigma_T = -3B\beta\Delta T(z,t) \tag{4.44}$$

where B is the bulk compressibility module and β the linear expansion coefficient. Only isotropic materials are considered here. This constitutes the leading tension term in metals after the initial picosecond dynamics, because the electronic heat capacity is much smaller than the phonon heat capacity.

- *Deformation potential*: The thermal picture just depicted gives a sufficient description when absorption and relaxation happens fast and inside the same band, as it does in metals [298]. In semiconductors, electrons can remain in an excited state at the bottom of the conduction band for up to a fraction of a μs [299]. The same is true for holes at the top of the valence band. Under this condition, the equilibrium state of the crystalline lattice is not equal to that of the unexcited state, leading to what is called a deformation potential [300]. The tension associated with this mechanism is given by [301]

$$\sigma_{DP} = -B\frac{\partial E_g}{\partial P}n(z,t) \tag{4.45}$$

where E_g is the band gap energy, P is the pressure and $n(z,t)$ is the electron (hole) density. This electronic tension is often around one order of magnitude greater than the thermal equivalent in semiconductors [302].

- *Electrostriction*: For excitation energies below an electronic gap, the above mechanisms cannot lead to the generation of acoustic vibrations. The main mechanism to generate coherent acoustic phonons is electrostriction or stimulated Raman scattering [303], which stems from the polarization of the medium induced by the pump pulse electric field. It is the inverse process of photoelasticity and the tension term is found by taking the derivative with respect to deformations of the electromagnetic field energy in the material [304]

$$\sigma_{RS,ij} = \frac{1}{8\pi}\sum_{ijkl} p_{klji}\epsilon_{km}\epsilon_{ln}E_m(z,t)E_n(z,t) \tag{4.46}$$

where $\mathbf{P}$ is the photoelastic tensor, $\boldsymbol{\epsilon}$ the dielectric tensor and $\mathbf{E}(z)$ the incident electric field.

These three generation mechanisms can have very intricate space and time dependence and are all interlinked. However, some approximations using the

characteristic timescales and the space dependence of the light field can be made. Since the thermal and electronic tensions will subsist after several nanoseconds, their time dependence can approximately be considered as a step or Heavyside function in time, i.e. $\sigma_p = F(z)\mathcal{H}(t)$, when acoustic phonons with periods smaller than a fraction of a nanosecond are considered. On the other hand, the electrostrictive tension only lasts while the pulse transits the sample, which is typically done in a timescale much shorter than the period of phonons up to the THz, i.e. $\sigma_p = F(z)\delta(t)$. Concerning the spatial dependence, what can be very generally said is that higher electric field intensities $|E(z)|$ lead to higher tensions. This is a direct consequence of (4.46) for the electrostrictive term and a consequence of increased absorption for both the thermal (4.44) and electronic (4.45) stresses. Thus, one can very generally asume the following expression for the induced tension [305]

$$\sigma_p(z,t) = K(z)|E(z)|^2 T(t) \tag{4.47}$$

with $K(z)$ a material and process dependent constant and $T(t)$ either a step-like or delta-like function depending on the generation mechanism considered. Even though many observed dynamics go beyond what can be explained by considering the functional form (4.47), this expression allows us to obtain simple selection rules for the generation of coherent acoustic phonons in SLs, as well as a closed analytical expression for the mechanical displacement $U(z,t)$.

Detection mechanisms

The optical detection of the generated coherent acoustic phonons is done via the photoelastic mechanism, which has already been described. The presence of an acoustic strain $\eta_{ij}(z,t) = \frac{1}{2}\left(\frac{\partial u_i}{\partial x_j}(z,t) + \frac{\partial u_j}{\partial x_i}(z,t)\right)$ modifies the dielectric tensor $\boldsymbol{\epsilon}$ according to

$$\Delta\epsilon_{ij}(z,t) = \sum_{kl} p_{ijkl}\eta_{kl}(z,t) \tag{4.48}$$

where again $\mathbf{p}$ is the photoelastic tensor. The movement of the boundaries in the system also contribute to change the dielectric tensor by the moving boundary effect. These two detection mechanisms are precisely the ones that were evoked when considering the optomechanical coupling g_o in Section 4.3.3. Other phenomena in play will change the light scattering properties of the pumped system. We have already referred to changes in temperature and in the electronic distribution, which have an important effect on the observed optical response.

Asynchronous optical sampling (ASOPS)

The traditional scheme in ultrafast pump-probe time-domain spectroscopy experiments employs a single mode-locked laser. The pulsed laser emits a train of picosecond (ps) or femtosecond (fs) light pulses with a given repetition rate f_{rep} and the high-energy pulses are guided to a beam splitter (BS), which divides the primary laser into two independent trains that act as the pump and the probe.

In the optical path followed by the probe (or the pump), a mechanical translation stage with mounted mirrors is introduced and allows control on the delay time Δt between the arrival of pump and probe pulses. However, the use of a scanning mechanical delay line has several inconveniences. The first and more obvious is the impossibility to eliminate residual variations of the beam pointing and spot size on the sample as the stage is translated by tens of centimeters, the required distance to achieve time delays of hundreds of picoseconds. These lead to experimental artifacts that are sometimes hard to distinguish from the real dynamics. Another issue concerns the scanning speed, which is currently limited. Higher scanning rates allow much faster measurement times and higher throughput, which could enable the analysis of *slow* transient behaviour [306–308] or acoustic imaging [309,310] by the acquisition of succesive data sets within just a few milliseconds.

ASynchronous OPtical Sampling (ASOPS) is an elegant technique that enables ultrafast pump-probe time-domain spectroscopy without the use of such a mechanical delay line [311]. The pump and probe pulses that will respectively interact and monitor the sample are generated by two different mode-locked lasers that are actively stabilized (via a single electronic feedback loop) to have a small repetition rate difference $\Delta f_{rep} = f_1 - f_2$. The working principle of the method and the practical implementation used in this thesis are depicted in Fig. 4.23. The detuning of the repetition rate Δf_{rep} causes the interval between the pump and probe pulses to vary monotonically as a function of time, allowing the dynamics of the system to be probed without the need of re-adjusting a mechanical stage. The scan rate is given by Δf_{rep} which means that one can acquire the response of the system every $\frac{1}{\Delta f_{rep}}$ s. The available time window is given by the inverse of the repetition rate of the pump laser f_1, i.e. the dynamics to be probed should ideally die out before $t = 1/f_1$, since otherwise the system enters a resonantly pumped regime [312]. If only laser pulses coming from the probe reach the detector and the electronics are able to follow the dynamics at the repetition rate f_2 of the probe laser, then the photocurrent signal will reproduce the sample's reflection curve. This acquisition process is schematically depicted in Fig. 4.23(a). Note that the schematic uses a very high Δf_{rep} for the sake of clarity, while in reality this is set to Δf_{rep} = 2-10 kHz.

The experimental setup used for the measurements shown in this thesis is represented in Fig. 4.23(b). The overall system has been set up in reflectometric configuration using colinear pump and probe pulses, which are focused into the surface of the sample using a long working-distance, high NA, 100x microscope objective. Filtering of reflected pump light is achieved by means of polarization. The setup was originally set to filter by wavelength using an extremely sharp low-pass filter. This configuration was changed as the operation of the dual-mode-locked lasers at a common wavelength of λ = 800 nm is easier. The polarization filtering is achieved by using two half-wave plates ($\lambda/2$) at the beginning of the pump and probe optical paths, from which the two beams propagate with orthogonal polarization. Placing a polarizing beam splitter (PBS) prior to the objective joins the

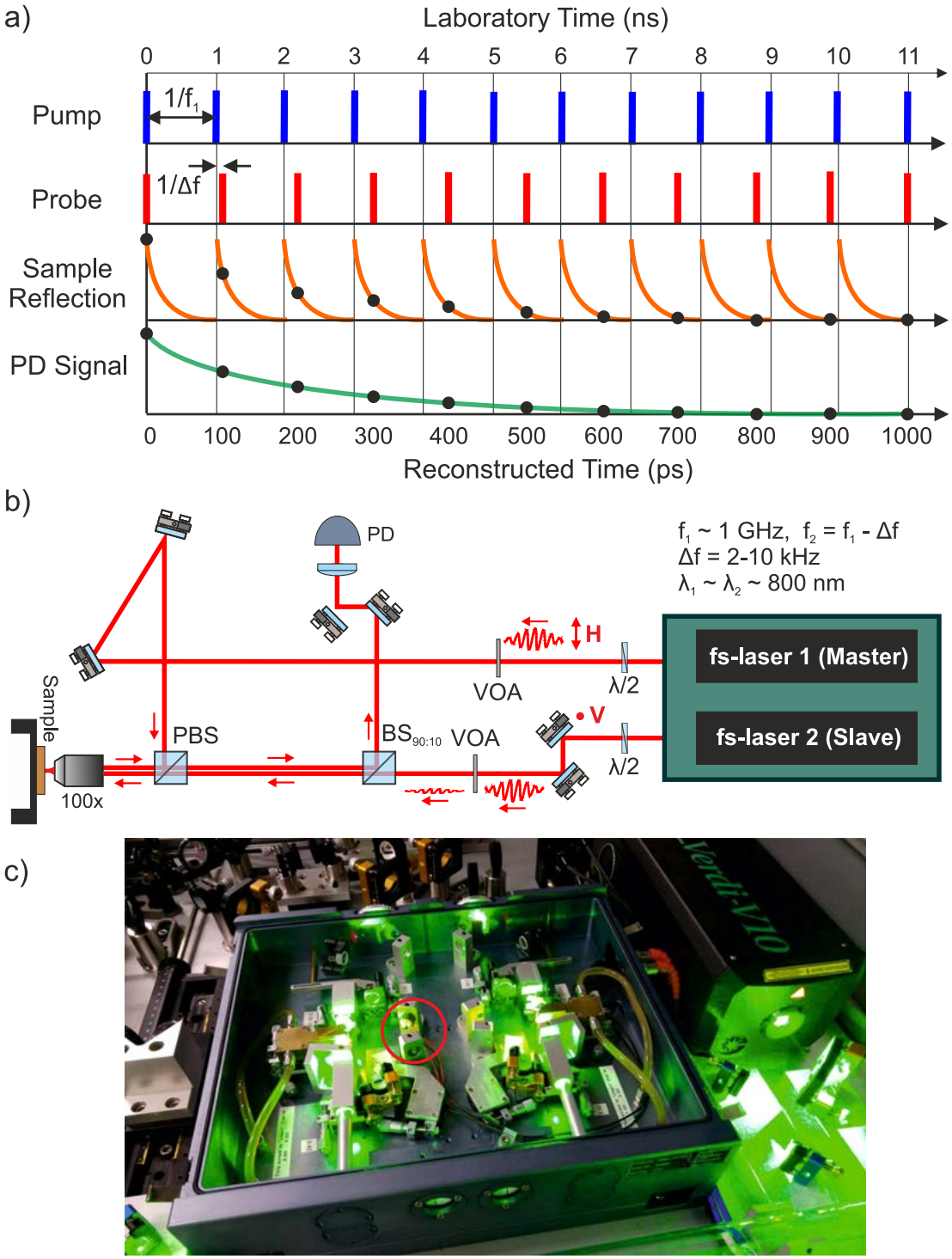

Figure 4.23: Ultra-fast pump probe spectroscopy based on asynchronous optical sampling (ASOPS). (a) Illustration of time-domain signal acquisition by ASOPS, including (1) pump pulses at repetition rate f_1, (2) probe pulses at repetition rate $f_2 = f_1 - \Delta f$, (3) sample reflection after the pump photo-induced stress and (4) photodetector signal. (b) Schematic of the reflectometric colinear pump-probe setup used during this thesis. The dual-GHz femtosecond oscillators from LaserQuantum GmbH are shown in (c), with the piezocontrolled mirrors of the slave (left) cavity highlighted.

two optical paths and forces the reflected light to take the same path when propagating backwards, effectively filtering all the pump light. An additional beamsplitter (BS) is placed in the probe optical path and used to redirect the reflected probe light towards the fast photodetector. The R/T ratio of the BS is chosen to be 90/10 since the employed pulsed lasers deliver more than enough fluence for a weak probe but we want as much of the reflected light to reach the photodetector as possible. The power delivered by both pulse trains is controlled by two variable optical attenuators (VOA). The employed Ti:Sapphire pulsed lasers are commercial femtosecond lasers from Laser Quantum GmbH [313], delivering 30-50 pulses of energy X fJ. The two ring laser cavities are perfectly symmetric and are built on the same metallic box, which allows minimizing relative fluctuations between the two pulse trains. A picture of the two under continuous wave pumping by a green Coherent Verdi laser is shown in Fig. 4.23(c). As highlighted, two of the mounted mirrors in the left cavity are piezo-controlled, which allows very precise tuning of their position. This degree of freedom is used to control the repetition rate f_2 of the left cavity and to stabilize it at Δf_{rep} from f_1.

4.4.2 Coherent phonon generation

Here we derive in detail the level of excitation associated with the different eigenmodes of a structure. This will then allow us to obtain selection rules for simple systems such as acoustic SLs. Their finite version in the form of acoustic DBRs largely inherit the found selection rules and help the interpretation of experimental data of pump-probe experiments in systems comprising DBRs. This section relies heavily on Refs. [314] and [305].

Generation spectral function

The presence of a source term in a wave equation leads to the excitation of the normal modes of the medium. It is therefore instructive to seek a solution to (4.43) based on spectral decomposition of the displacement field $U(z)$ into its eignmodes. The first requirement is therefore knowing the eigenspectrum of the differential operator $\hat{L}(z)$ in (4.43) under practical boundary conditions. This has been done previously for the Bloch modes of an acoustic SL and to find the QNMs of open nanophononic structures, i.e. with outgoing boundary conditions. Real fabricated acoustic nanostructures are nevertheless closed structures due to the finite thickness of both the substrate and the grown nanostructure and they typically have a free surface on the excitation side, i.e. at the beginning of layer 1, and either a free-surface or a fixed boundary on the substrate side, at the end of layer N. In the absence of acoustic dissipation, the eigenfields are purely real, whcih implies that the displacement field in any layer j can be written as $U_j(z) = U_j cos(q_j z + \theta_j)$. The boundary conditions are enforced by setting U_1 and θ_1 in layer 1 and θ_{N+1} in a (irrelevant) fictitious $N+1$ -th layer. On the

propagating/counterpropagating plane wave basis, this leads to

$$\begin{bmatrix} a_{1,+} \\ a_{1,-} \end{bmatrix} = \begin{bmatrix} e^{i\theta_1} \\ e^{-i\theta_1} \end{bmatrix} \tag{4.49a}$$

$$\begin{bmatrix} a_{N+1,+} \\ a_{N+1,-} \end{bmatrix} = \begin{bmatrix} \frac{U_{N+1}}{2} e^{i\theta_{N+1}} \\ \frac{U_{N+1}}{2} e^{-i\theta_{N+1}} \end{bmatrix} \tag{4.49b}$$

with $\theta = 0$ for a free-surface and $\theta = \frac{\pi}{2}$ for a fixed boundary. Note that the amplitude in layer 1 has been arbitrarily set to $U_1 = 2$ since the eigenfields are defined up to a multiplicative constant. These two pair of coefficients are linked via the full transfer matrix of the system $\mathbf{M}$, i.e. $\mathbf{a}_{N+1} = \mathbf{M} \cdot \mathbf{a}_1$, which leads to

$$\begin{aligned} &\mathrm{Re}(M_{11})\cos(\theta_1 - \theta_{N+1}) - \mathrm{Im}(M_{11})\sin(\theta_1 - \theta_{N+1}) \\ &+\mathrm{Re}(M_{12})\cos(\theta_1 + \theta_{N+1}) + \mathrm{Im}(M_{11})\sin(\theta_1 - \theta_{N+1}) = 0 \end{aligned} \tag{4.50}$$

Expression (4.50) is satisfied for a discrete set of real frequencies Ω_n, that can be found using a standard Newton method. The eigenfields are found by concatenating the individual transfer matrices starting from $\mathbf{a}_1$. Lastly, the obtained eigenfields need to be normalized to fulfill the following orthonormality relation [315]

$$\int_0^L \rho(z) U_n(z) U_m(z) dx = \delta_{nm} \tag{4.51}$$

Once the spectral decomposition of operator $\hat{L}(z)$ is known, we use the Green function formalism for second order differential equations in the time variable to obtain a general solution to equation (4.43), which is formally written as [316]

$$U(z,t) = U_h(z,t) - \sum_n \frac{U_n(z)}{\Omega_n} \int_{-\infty}^{t} \sin(\Omega_n(t-t') \left(\int_0^L U_n(z') \frac{\partial \sigma_p}{\partial z}(z',t') dz' \right) dt' \tag{4.52}$$

where $U_h(z,t)$ is the homogeneous solution to equation (4.43). This is usually disregarded as the system is either at rest at time $t = 0$ or undergoing incoherent Brownian motion which goes undetected in pump-probe time-domain spectroscopy. Integrating by parts and introducing the functional form $\sigma_p(z,t) \equiv K(z)|E(z)|^2 T(t)$ given in (4.47), the displacement field can be written as

$$U(z,t) = \sum_n G(\Omega_n) U_n(z) f(\Omega_n, t) \tag{4.53}$$

with

$$G(\Omega) = \frac{1}{\Omega^s} \left[-u_\Omega(z) K(z) |E(z)|^2 |_0^L + \int_0^L \frac{\partial U_\Omega}{\partial z}(z) K(z) |E(z)|^2 \right] \tag{4.54}$$

and

$$f(\Omega, t) = \begin{cases} \sin(\Omega t) & \text{for } T(t) = \delta(t) \ (s = 1) \\ 1 - \cos(\Omega t) & \text{for } T(t) = \mathcal{H}(t) \ (s = 2) \end{cases} \tag{4.55}$$

We will refer to $G(\Omega)$ as the generation spectral function, whose evaluation at the eigenfrquency Ω_n and with the eigenmode field $U_n(z)$, gives the amplitude

of oscillation of that particular mode upon incidence of the pump pulse. The function is in principle only defined for $\{\Omega_n, U_n(z)\}$ and one should compute the normal modes with the guidelines described above. Here, $G(\Omega)$ is an analytical continuous function of frequency Ω as the examined nanostructures are typically grown on a thick substrate, which implies that the eigenfrequencies of two modes are extremely close, much closer than the typical experimental resolution. We can therefore assume a continuum of frequencies Ω and choose the sampling in (4.53) according to the experimental resolution. In this case the fields $U_\Omega(z)$ are computed by considering the free-surface boundary condition at the top, i.e. $\mathbf{a_o} = [1, 1]$ and using the transfer matrices up to the substrate. This essentially corresponds to neglecting the boundary condition at the bottom of the substrate and taking $L \to \infty$. The system is therefore equivalent to an open system on the bottom surface. Unavoidable sound absorption at room-temperature while phonons propagate through the thick substrate [317] also strengthen this formal argument, since vibrations cannnot reach the bottom surface to generate standing waves.

The temporal dependence of (4.53) is provided by the term $f(\Omega_n, t)$. The particular form this function takes for two limiting cases, i.e. a delta and step time dependence for σ_p, is given in (4.55). The difference between their two temporal dynamics is a phase factor of $\pi/2$ and an overall offset given by the factor 1. The latter is associated to the sudden change in equilibrium position described previously. Any other temporal dependence will simply produce a different phase and offset. Note that the choice of a step time-dependence $\mathcal{H}(t)$ also leads to an additional factor Ω^{-1} in $G(\Omega)$, a factor that can be neglected when considering the behaviour of $G(\Omega)$ on a particular frequency region.

Selection rules for an acoustic superlattice

The spectral behaviour of $G(\Omega)$ in an infinite SL and in the absence of optical absorption, i.e. via electrostriction, can be found by taking the limits 0 and L in (4.54) to $\pm\infty$ and using the periodicity of the structure. Since the typical wavelengths used in the experiments ($\lambda \sim 800$ nm) are considerably larger than the modulation of the optical properties induced by the SL considered ($d_{A/B} \sim$ 5-100 nm), the system optically behaves as an effective medium with effective refractive index n_{eff}. The electric field is therefore approximately given by $E(z) = Ee^{ik_{eff}z}$ with $k_{eff} = n_{eff}k$ and k the free-space wavevector; therefore $|E(z)|^2 = |E|^2$. Both the displacement field $U_\Omega(z)$ and any of its spatial derivatives are Bloch functions, i.e. $\frac{\partial U_\Omega}{\partial z}(z) = \eta_\Omega(z)e^{iqz}$ with $\eta_\Omega(z)$ a periodic function of period D. In addition, $K(z)$ is also a periodic function whenever light absorption is disregarded. Expanding both $\eta_\Omega(z)$ and $K(z)$ in the Fourier basis spanned by the reciprocal lattice vectors Q and disregarding the first term of (4.54) leads to

$$G(\Omega) = |E|^2 \sum_{QQ'} K_{Q-Q'}\eta_{\Omega,Q'}\delta(q - Q) \tag{4.56}$$

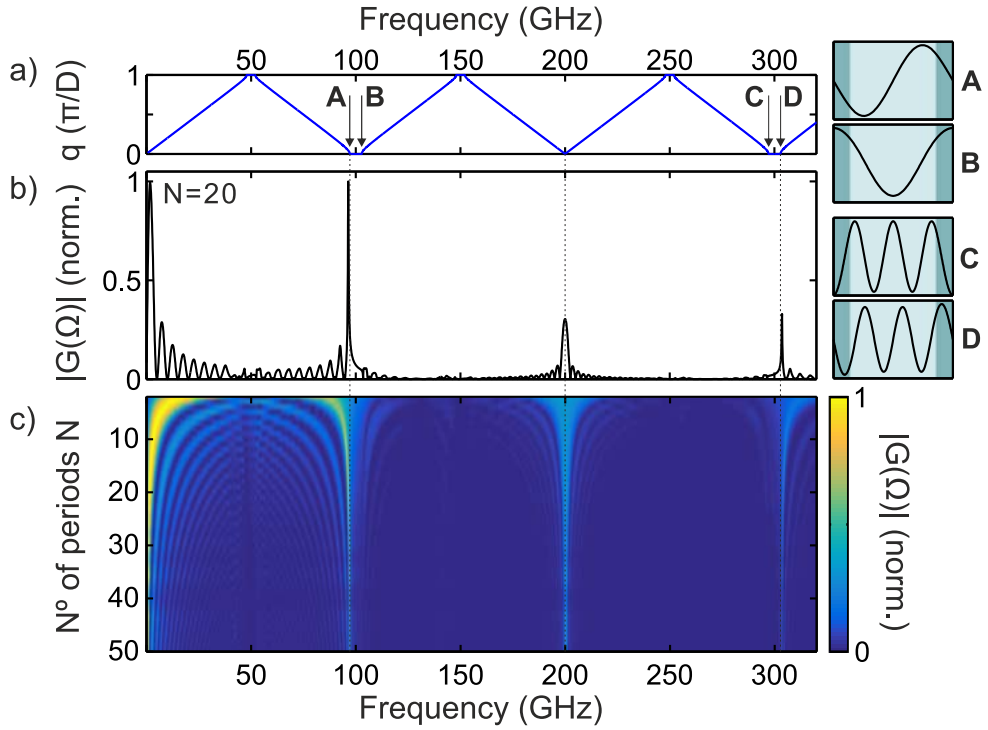

Figure 4.24: Coherent acoustic phonon generation function in an acoustic Distributed Bragg Reflector (DBR). (a) Band diagram of a $(\frac{3\lambda}{4}, \frac{\lambda}{4})$ GaAs/AlAs superlattice (SL) for a design frequency $f_m = 100$ GHz. The displacement profile of $q = 0$ modes highlighted with letters A-D are given. (b) Generation spectral function $|G(\Omega)|$ for a DBR of $N = 20$ periods. The evolution of the spectral function with N is shown as a colormap in (c), with each spectrum normalized to its maximum. It demonstrates how in the limit $N \to \infty$ the selection rules for an acoustic superlattice are recovered.

which is only non-null when $q = 0$ in the first BZ. This leads to the following selection rule: only phonons with $q = 0$ in the band-folded scheme, often called forward-scattering (FS) modes, are generated in an infinite absorptionless SL.

An additional selection rule can be obtained when one considers the symmetry properties of the band edge modes at $q = 0$. The two modes bounding a ZC or ZE minigap are either symmetric or antisymmetric with respect to reflections in the bisector planes and if one is symmetric, the other one is antisymmetric (Section 4.1). In addition, the displacement $U_\Omega(z)$ and the strain $\eta_\Omega(z)$ are $\pi/2$ out of phase, which inverts the symmetry property with respect to the bisector. Since $K(z)$ is an even function, the second term in (4.54) vanishes for symmetric modes since $\eta_\Omega(z)$ is odd. The selection rule is further reduced to: only $q = 0$ phonons with odd parity with respect to the bisector planes can be generated in an absorptionless SL.

Finite size and absorption effects

In a realistic experiment the SL is finite and light is at least partially absorbed or scattered away by defects. What are the role of these two on the selection rule just

introduced? Finite-size effects for the generation of coherent acoustic phonons in a SL, a DBR of N periods, can be partly deduced from the behaviour of (4.56). The integration leading to $\delta(q-Q)$ leads to a $\mathrm{sinc}(q)$ function when the integral bounds are set at finite positions, which slightly relaxes the selection rule. Considering the exact acoustic and optical fields slightly modifies this $\mathrm{sinc}(q)$ dependence, but the resulting functions will be of similar shape, leading to satellite oscillations whose spectral position gets closer to the central peak with an increasing number of layers N [318]. In addition, the first term in (4.54) cannot be neglected for a DBR, especially outside the frequencies Ω for $q = 0$ phonons and can contribute to the relaxation of the selections rules. The inclusion of absorption in the sample has more or less the same effect. The presence of a real exponential term $e^{\mathrm{Im}(k)z}$ in $E(z)$ does not lead to $\delta(q - Q)$ after integration. Whenever strong absorption takes place, the three mechanisms for coherent generation simultaneously operate and $K(z)$ cannot be assumed to follow the sample's geometrical profile. Despite these finite size and absorption effects, the spectral behaviour of the generation function $G(\Omega)$ for a DBR is dominated by the peaks at $q = 0$ (band diagram in Figs. 4.24(a)), as can be seen in Figs. 4.24(b,c), where we have considered an impulsive mechanism for generation based on electrostriction. The spectral oscillations are clearly visible, as is the odd parity $q = 0$ selection rule evidenced by the accompanying field profiles of the Bloch modes.

4.4.3 Coherent phonon detection

The spectrum of the generated phonons, given by $G(\Omega)$, provides simple selection rules. Now we want to study if the probe pulse is sensitive to the generated phonons. By finding the reflection coefficient r of the structure, we derive a detection spectral function and study what selection rules follow from the detection process and how compatible they are with the rules for generation.

Detection spectral function

The presence of excited coherent acoustic phonons leads to a modulation of the optical properties via the photoelastic effect, as defined in (4.48), and via the displacement of the interfaces between the layers. Due to the nature of the longitudinal phonons generated and to the cubic crystallography of the materials employed in this thesis, the dielectric tensor remains isotropic when normal-incidence light is considered. Maxwell's equations remain practically unchanged, although the displacement field $D(z,t)$ is in principle time-dependent via $\epsilon(z,t) \equiv \epsilon^{(0)}(z)+\Delta\epsilon(z,t)$, with $\epsilon^{(0)}(z)$ the contribution from the nanostructure in the absence of vibrations and $\Delta\epsilon(z,t) = \Delta\epsilon_{pe}(z,t) + \Delta\epsilon_{mb}(z,t)$ the perturbation induced by the vibrations. Note that we typically have the following situation: first, $|\Delta\epsilon(z,t)| \ll |\epsilon^{(0)}(z)|$ and second, the timescale associated with the variations $\Delta\epsilon(z,t)$ is much longer than both the optical period and the probe pulse duration. Given these two assumptions, we can make a quasi-static approximation and employ the Green function of the unperturbed system to solve for the reflectivity of the optical nanostructure at optical frequency ω [291]. This corresponds to solving at a given snapshot of the coherent mechanical oscillation. Up to the first order in $\Delta\epsilon(z)$, the electric

field $E(z)$ at the cladding layer can be written as

$$E(z) \simeq E^{(0)}(z) + \frac{ik^2}{2k_0 a^{(0)}_{0,+}} e^{-ik_0 z} \left\{ \int_0^L P(z) \frac{\partial U}{\partial z}(z) E^{(0)}(z)^2 + \sum_{m=0}^{N} (\epsilon_{m-1} - \epsilon_m) u(z_m) (a^{(0)}_{m,+} + a^{(0)}_{m,-})^2 \right\} \tag{4.57}$$

where the form of the photoelastic and moving boundary terms have been used. For SLs made of GaAs and AlAs, the photoelastic coefficients can be set to around 200 for GaAs [319] and null for AlAs [320]. With these values, the first term in (4.57) largely dominates over the second term and we can safely restrict our analysis to just the first. Introducing the expression found for the generated displacement (4.53) into (4.57) leads to the following expression for the reflection coefficient change Δr

$$\Delta r(t) = \sum_n G(\Omega_n) D(\Omega_n) f(\Omega_n, t) \tag{4.58}$$

with

$$D(\Omega) = \frac{ik^2}{2k_0 (a^{(0)}_{0,+})^2} \int_0^L \frac{\partial U_\Omega}{\partial z}(z) P(z) E^{(0)}(z)^2 dz \tag{4.59}$$

We will refer to $D(\Omega)$ as the detection spectral function, whose evaluation at the eigenfrquency Ω_n and with the eigenmode field $U_n(z)$ gives the achieved sensitivity in the reflection coefficient at the frequency of that particular eigenmode. $\Delta r(t)$ is the sum over the eigenmodes of the product of the generation and the detection function times the corresponding temporal evolution given by (4.55).

Selection rules for an acoustic superlattice

Here, we deduce a selection rule for the detection process using (4.59) and the periodicity of the functions within when the light field $E^{(0)}(z)$ is simply given by a plane wave with an effective refractive index n_{eff}. This leads to,

$$D(q(\Omega)) \propto \sum_{QQ'} P_{Q-Q'} \eta_{\Omega,Q'} \delta(q - Q + 2k_{eff}) \tag{4.60}$$

which has the same form as (4.56) but the Dirac delta is not taken at $q = Q$ but at $q = Q - 2k_{eff}$, which implies that in the folded scheme only $q = 2k_{eff}$ can be detected, as depicted in Fig. 4.25(a). This results from the momentum conservation in the backscattering of light induced by the coherent acoustic phonons. In the same manner as for the generation spectral function, finite size effects and optical absorption relax these selection rules and lead to a sinc-like response, as can be seen in the spectrum of Fig. 4.25(b). Due to the slope of the dispersion at $q = q_{eff}$, the detection peaks are broader than those in $G(\Omega)$. Nevertheless, these narrow for an increasing number of DBR periods N, as shown in the colormap of Fig. 4.25(c), recovering the selection rules for the infinite SL. Small peaks that mimic $G(\Omega)$ are also visible at $q = 0$ in both Fig. 4.25(b) and (c). These are due to the fact that the effective index approximation for $E(z)$ is weakly satisfied, which hints at engineering the light field confinement as a tool to tailor the generation/detection spectral responses [321].

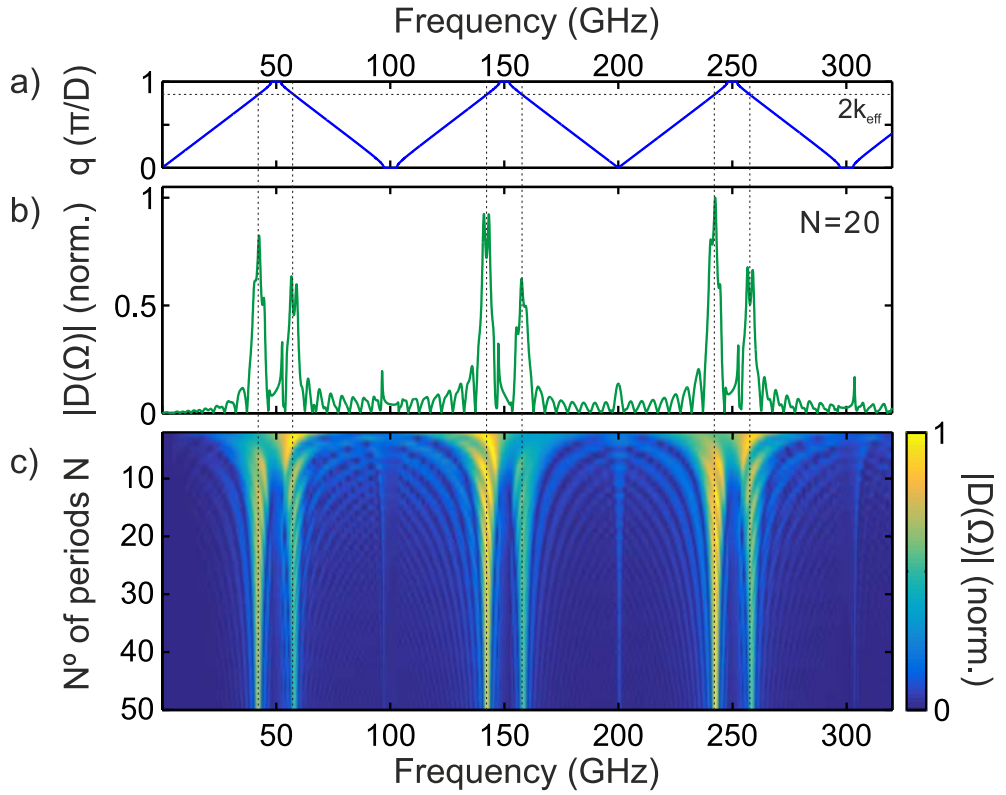

Figure 4.25: Coherent acoustic phonon detection function in an acoustic Distributed Bragg Reflector (DBR). (a) Band diagram of a $(\frac{3\lambda}{4}, \frac{\lambda}{4})$ GaAs/AlAs superlattice (SL) for a design frequency $f_m = 100$ GHz. (b) Detection spectral function $|D(\Omega)|$ for a DBR of $N = 20$ periods. The evolution of the spectral function with N is shown as a colormap in (c), with each spectrum normalized to its maximum. It shows how in the limit $N\infty100$ the selection rules for an acoustic superlattice are recovered, with additional spectral features at $q = 0$ arising from backpropagating components in the electric field $E(z)$.

Differential reflectivity in the time and spectral domain

The quantity we measure with the configuration shown in Fig. 4.23(b) is the variation of the reflectivity of the sample at at given time t with respect to its value in the absence of vibrations $R^{(0)}$. This quantity can be written as

$$\Delta R(t) = 2\mathrm{Re}[r^{(0)}]\mathrm{Re}[\Delta r(t)] + 2\mathrm{Im}[r^{(0)}]\mathrm{Im}[\Delta r(t)] \tag{4.61}$$

where both the real and imaginary part of $\Delta r(t)$ can contribute to the observed temporal trace. If expression (4.58) is used, the differential reflectivity $\Delta R(t)$ is

$$\Delta R(t) = \sum_n \Delta R_n f(\Omega_n, t) \tag{4.62}$$

with

$$\Delta R_n = 2\mathrm{Re}[r^{(0)}]\mathrm{Re}[G(\Omega_n)D(\Omega_n)] + 2\mathrm{Im}[r^{(0)}]\mathrm{Im}[G(\Omega_n)D(\Omega_n)] \tag{4.63}$$

Given expression (4.62), the spectrum of $\Delta R(t)$ can be found, since all the spectral information is essentially contained in ΔR_n. However, we have so far ignored

that the eigenmodes of the structure have a finite lifetime even in the absence of radiation lossess. To improve the matching between the measured spectra and the expected reflectivity traces, we add an exponential decay e^{-t/τ_n} to the temporal dependence of each normal mode. In addition, the experimental trace is only acquired over a given time interval. The theoretical expression (4.62) is therefore convoluted with the Fourier transform of the rectangular function $\mathcal{H}(t)\mathcal{H}(t_f - t)$ where we have set the initial measurement time to $t = 0$ and the temporal measurement window ends at the final time t_f, which corresponds to 1 ns in our experimental apparatus. Combining both the finite lifetime and the convolution, the spectrum is

$$\begin{aligned}\Delta R(\omega) = \sum_n \Delta R_n \Bigg[& e^{i(\omega+\Omega_n+i/\tau_n)t_f/2)} \frac{\sin((\omega+\Omega_n+i/\tau_n)t_f/2)}{\omega+\Omega_n+i/\tau_n} \\ & + e^{i(\omega-\Omega_n+i/\tau_n)t_f/2)} \frac{\sin((\omega-\Omega_n+i/\tau_n)t_f/2)}{\omega-\Omega_n+i/\tau_n} \Bigg]\end{aligned} \tag{4.64}$$

In addition to these aspects, the frequency cut-off induced by the finite size of the pulses (∼50 fs) is also taken into account, as is the full spectral width of the pump and probe pulses by doing a weighted average of the generation and detection functions over the linewidth of the laser spectrum. Since the spectral dependence of the losses τ_n goes well beyond the scope of the measurements reported here, we set $\tau_n \equiv \tau$ and we use it as a free parameter to be adjusted by comparing the theoretical expression (4.64) to the Fast Fourier Transform (FFT) of the measured data.

4.4.4 Experimental evidence of a topological nanocavity

In this section we numerically and experimentally study how the selection rules just described manifest in a system comprising of two concatenated and band-inverted DBRs, for which the inversion of the ZC band edge mode symmetries and its manifestation in coherent pump probe spectra indicate the topological nature of the measured confined state inside the corresponding minigap.

Cavity design

We study two different nanoacoustic multilayer structures made by combining different types of DBRs (labelled A, B, and C) as building blocks. Both samples are grown on a 200 μm thick GaAs substrate starting with a DBR of type B followed by DBR of type A (we label this the topological sample) or type C (control sample), respectively. While the topological sample is designed to confine a topological acoustic mode at the interface between the two DBRs, the control sample only supports extended propagating and stationary band edge modes. The design of both samples is based on the $\left(\frac{\lambda_m}{4}(1+\delta), \frac{\lambda_m}{4}(1-\delta)\right)$ DBRs introduced before, for which we have shown that $\delta = 0$ corresponds to a topological transition point for all ZC minigaps. The design frequency is chosen at $f_m = 100$ GHz, which means that the first ZC minigap lies at 200 GHz. We choose $\delta = -0.1$ for DBR A, $\delta = 0.1$ for DBR B and $\delta = 0.3$ for DBR C. Each DBR contains 20

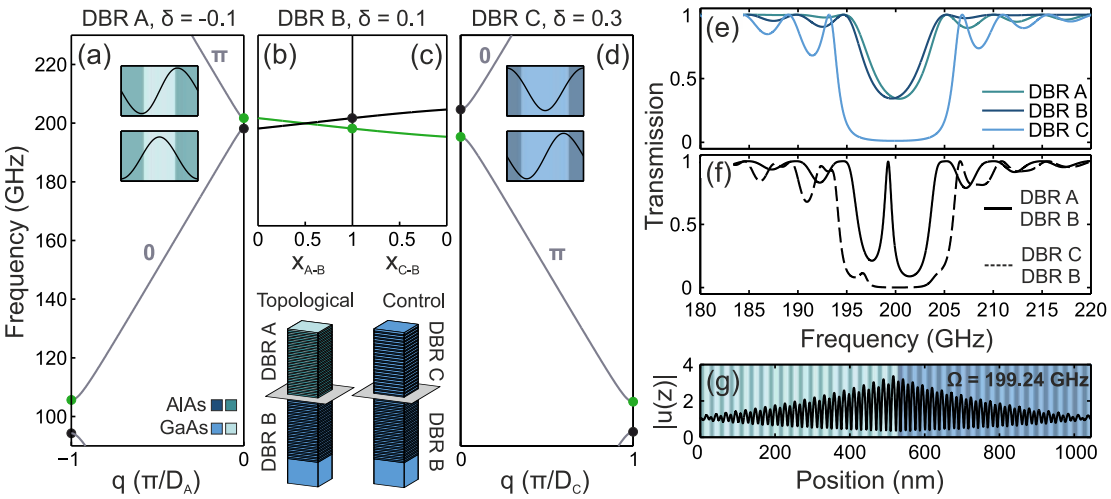

Figure 4.26: Topological interface state through band inversion in GaAs/AlAs superlattices (SLs). (a) Band structure corresponding to the Distributed Bragg Reflector (DBR) A. Zak phase values of different bands depicted on top of them. Minigap edges at the center and border of the Brillouin Zone (BZ) are marked with green and black dots. Black (green) dots represent edge modes with an even (odd) displacement profile as shown in the insets. (b) and (c) present plots of the edge positions as a function of parameters x_{A-B} and x_{C-B}, respectively. Edges corresponding to DBR B are represented as dots at $x_{A-B} = x_{C-B} = 1$ using the same even/odd color code for both lines and dots. A schematic of the two samples with their corresponding DBRs labeled and the interface plane highlighted is provided. (d) Band structure corresponding to DBR C using the same representation as in (a). (e) Reflectivity spectra for DBRs A, B, and C composed of 20 periods. (f) Reflectivity spectra for topological (DBR A - DBR B) and control samples (DBR C- DBR B). (g) Displacement profile of the topological interface state at $f_c = 199.24$ GHz.

GaAs/AlAs layer pairs with 10.76 nm/15.57 nm (A), 13.15 nm/12.74 nm (B), and 15.54 nm/9.91 nm (C) nominal thicknesses, respectively.

As explained in Subsection 4.2.2, the difference in the topological properties of the two samples can be understood from an analysis of the SL bandstructures and the associated mode symmetries and/or Zak phases, as is shown in Figs. 4.26(a-d). While Fig. 4.26(a) and Fig. 4.26(d) show the band structures of SLs A and C, Fig. 4.26(b) and Fig. 4.26(c) illustrate that upon a topological phase transition the energetic order of the band edge modes change. To that end, we define a continuous parameter, x_{A-B}, that deformS DBR A into DBR B. An analogous parameter, x_{C-B}, transforms DBR C into DBR B. That is, we define the thickness of a DBR's GaAs and AlAs layers as

$$d_{GaAs} = d_{GaAs,Y} \cdot (1 - x_{Y-B}) + d_{GaAs,B} \cdot x_{Y-B} \tag{4.65a}$$

$$d_{AlAs} = d_{AlAs,Y} \cdot (1 - x_{Y-B}) + d_{AlAs,B} \cdot x_{Y-B} \tag{4.65b}$$

with $x_{Y-B} \in [0, 1]$, and Y being either A or C. We plot the evolution of the band edges bounding the second acoustic minigap as a function of x_{A-B} (Fig. 4.26(b))

and x_{C-B} (Fig. 4.26(c)). Continuously transforming DBR C into B merely implies a change in the size of the common minigap, but the energetic order of mode symmetries persists. This corresponds to moving from $\delta = 0.3$ to $\delta = 0.1$ in Fig, 4.10. In contrast, Fig. 4.26(b) shows that a continuous transition between DBR A and B necessarily implies a band crossing, i.e. the minigap closes and re-opens, and an associated exchange of the band edge symmetries. This happens for $x_{A-B} = 0.5$, which corresponds to $\delta = 0$ in Fig. 4.10. DBRs B and C are hence in the same topological phase, whereas DBRs B and A cannot be continuously transformed into one another, that is, they are in different topological phases. Acoustic transmission spectra of the individual DBRs (Fig. 4.26(e)) and of the two concatenated structures (Fig. 4.26(f)) show the different behaviour of the two stackings. For the control sample (dashed line, Fig. 4.26(f)) only a broad stop band is found, as in the case of the individual DBRs. The small peak at around 196 GHz corresponds to the band edge mode of DBR B, which is confined between the substrate and DBR B, whose minigap is much wider. For the topological sample (solid line), a clear peak appears at 199.24 GHz, indicating the presence of a confined mode. The spatial acoustic displacement profile of the corresponding QNM $|\widetilde{U}(z)|$ is shown in Fig. 4.26(g), superimposed with the layer structure of the topological sample. We observe that the mode is centered at the interface between the two bilayer DBRs and decays exponentially into both extremes of the structure.

Both samples were grown by MBE at the Centre de Nanosciences et de Nanotechnologies (C2N) in Palaiseau, France. These were grown on a [001]-oriented GaAs substrate and without any thickness gradient. They were pre-characterized by means of high resolution x-ray diffraction (HRXRD). As an important tool for structural characterization, HRXRD provides valuable information on the periodicity, layer sizes and overall quality of both samples. A $\theta - 2\theta$ HRXRD scan using Cu K-α 1 radiation was performed, diffractograms were measured, and further analysis of their peaks provided information about the different parts of the structure. For the topological sample, the results showed that DBR A is formed by GaAs/AlAs layers of 11.1/15.5 nm and DBR B of 13.5/12.7 nm. For the control sample DBR C presents layers of 16/10 nm of GaAs/AlAs while DBR B of 13.5/12.8 nm. For the topological sample, these thickness values represent a reduction of the AlAs layers by 0.6% of their nominal values, while for the GaAs layers the change corresponds to an increase of 2.8%. For the control sample both AlAs and GaAs layers present an increase of 0.5% and 2.8%, respectively. Despite this deviation from the design values, this band structure analysis remains valid for both samples as we will show via coherent pump-probe spectroscopy.

Pump-probe measurements

The samples described were first characterized in Dr. Daniel Lanzillotti-Kimura's team at C2N via Raman scattering spectroscopy [252]. The measurements carried out there demonstrated the presence of a confined topological phononic mode, yet the resolution did not suffice to determine lifetimes or to identify other acoustic modes in the same frequency region. Fig. 4.27 reproduces Fig. 3(c) in Ref. [252],

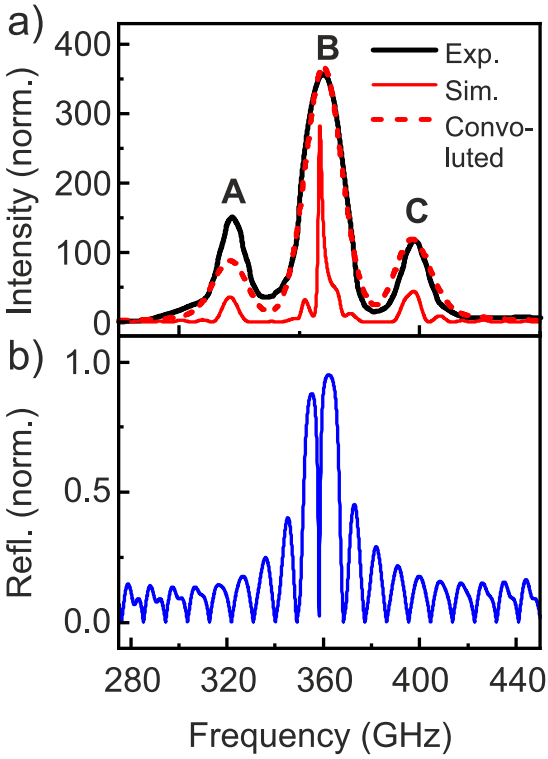

Figure 4.27: Raman scattering spectrum of a topological nanocavity mode. (a) Raman spectrum of a bilayer topological phononic nanocavity with design frequency $2f_m$ = 360 GHz. The solid black line represents the experimental spectrum, while the solid red trace shows the simulated spectrum using a photoelastic model similar to that used for coherent phonon generation/detection experiments. The limited resolution of the experimental set-up is taken into account by convoluting the simulated Raman spectrum with a Gaussian (2σ = 13 GHz), as shown with a dashed red line. The agreement between the measurement and the convoluted spectrum is remarkable. Nevertheless, the different mechanical modes leading to the broad peak B cannot be resolved. (b) Simulated acoustic reflectivity of the sample. The topological interface mode at 360 GHz corresponds to peak B in the Raman spectrum. The two panels have been adapted from Fig. 3 in Ref. [252] ©American Physical Society.

where the measured and simulated Raman spectrum and the calculated reflectivity of a topological sample with higher design frequency ($2f_m$ = 360 GHz) are shown. As compared to the resolution-limited (13 GHz) broad peak (B) observed with Raman (solid black line in Fig. 4.27(a)), the use of time-resolved pump-probe measurements can unveil the detailed structure of the nanoacoustic modes around the band gap region (the inner structure ok peak B in the solid red line in Fig. 4.27(a)), allowing a clear assignment of the different peaks to topological and other stationary modes. Therefore, we perform measurements using the ASOPS technique described in Subsection 4.4.1 to overcome these resolution limitations.

The measurements shown are done at a fixed central wavelength of λ = 800 nm for the pump beam (40 mW) and a varying central wavelength λ = 760-840

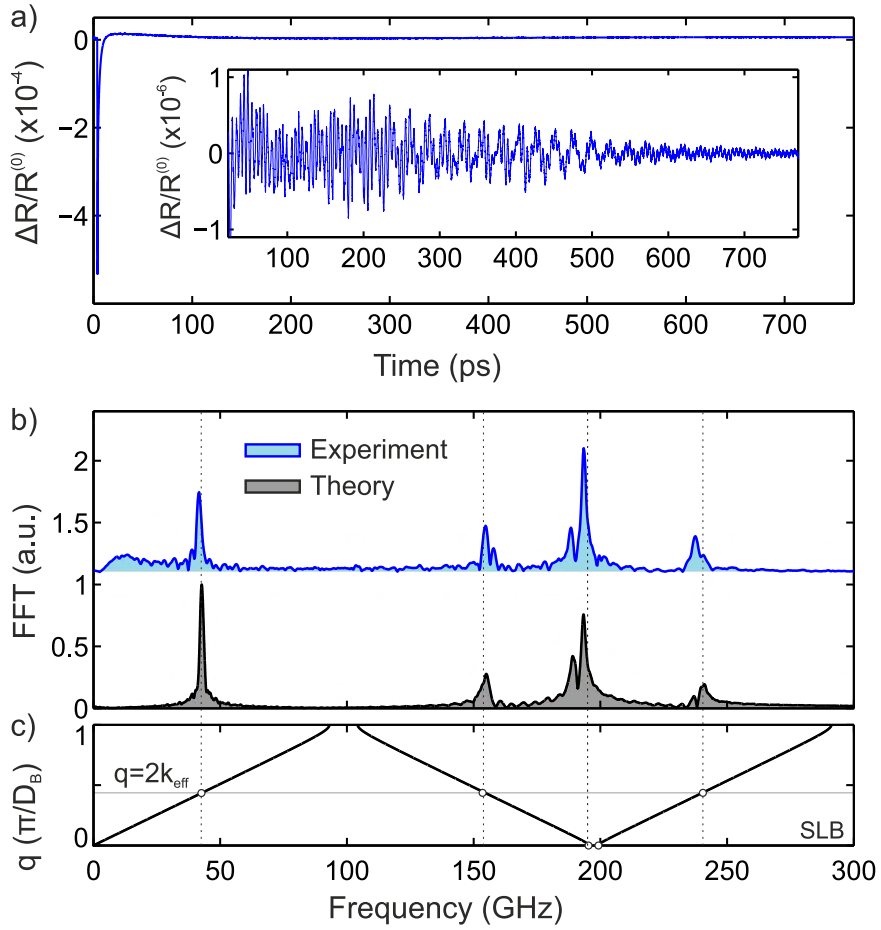

Figure 4.28: Reflection-type pump-probe coherent acoustic phonon experiments in a control sample. (a) Time-resolved differential reflectivity obtained with both pump (40 mW) and probe (4 mW) at $\lambda = 800$ nm. The as-obtained data is treated by cutting the initial electronic peak and using appropriate Savitzky-Golay filters to extract low-frequency backgrounds, leading to the trace in the inset. (b) The Fast Fourier Transform (FFT) of the treated time trace is given (blue) and compared to the theoretical spectra obtained from a simple electrostriction-photoelastic model (grey). (c) Band diagram of the bottom superlattice (SL B), with the spectral position of the generation/detection selection rules highlighted with vertical dashed lines.

nm for the probe (4 mW) beam, collinearly focused to a 2 μm spot on the sample surface. Measurements at different magnifications and powers were done to rule out the presence of additional power density dependent temperature variations of the sample reflectivity. In addition, measurements at different positions in the sample were done to confirm the observed signals. The differential reflectivity signal $\Delta R(t)/R^{(0)}$ obtained for the control sample is shown in Fig. 4.28(a). The temporal trace is *initiated* by a sharp dip of electronic origin, that marks the point of coincidence between the pump and probe pulses. When this peak is disregarded, only slow dynamics related to the temperature field $\Delta T(t)$ are usually left in addition to the modulation associated with the mechanical vibrations. Supervised application of Savitzky-Golay filtering [322] allows extraction of this low-frequency background which also includes a 1 GHz background coming from

spurious light from the pump. The inset of Fig. 4.28(a) shows the result of this data processing. This time trace shows that specific coherent acoustic vibrations have been excited and that those vibrations can be observed via the reconstructed differential reflectivity. The discrete Fourier transform of the differential reflectivity signal in the spectral region below 300 GHz is shown in Fig. 4.28(b) and compared to the expected differential reflectivity spectra as obtained from Equation (4.64). The experimental time trace has been zero-padded for increased readability of the discrete Fourier Transform and special care has been taken to ensure that the padding does not add any spectral features. This is achieved whenever the signal has reached zero after the final time over which the FFT is taken, which is essentially the case here. We see that a purely electrostrictive model for the phonon generation process and photoelasticity-based detection reproduces the main features of the measured spectra for the control sample under the experimental conditions considered here. Several acoustic modes are observed in Fig. 4.28(b). First, we observe the Brillouin peak [323] of both SLs and the substrate at ~ 42 GHz, as well as two groups of peaks at 150 and 245 GHz, which are linked to the detection $q \sim 2k_{eff}$ selection rule introduced before, which applies even in the presence of two different concatenated SLs. This is demonstrated in Fig. 4.28(c), where the band structure of the bottom SL (SL B) is depicted, with the horizontal line representing the $q = 2k_{eff}$ condition at the detection wavelength $\lambda = 800$ nm. Although we have two different DBRs B and C, their bands far from the minigap are virtually equivalent, which makes it hard to observe any particular substructure in those regions. The analysis of the region around the first ZC minigap of the underlying SLs A, B and C (185-210 GHz), where the generation selection rule $q = 0$ applies, is studied in a separate figure.

The equivalent treatment of the obtained differential reflectivity for the topological sample is shown in Fig. 4.29, where the initial electronic response leads to a peak instead of a dip. The same processing of the data as the one done for the control sample leads to the time trace shown as an inset, where the initial modulation $\Delta R(t)/R^{(0)}$ is ≈ 3 times larger than for the control cavity for similar levels of power. Using the same impulsive electrostriction mechanism for generation and photoelastic-based detection also leads to quantitative agreement between the experimental spectrum and the modeled spectrum for the topological sample, as seen in Fig. 4.29(b). The black dashed lines highlight the same set of modes associated with detection and selection rules. The additional peak between the two dashed lines bounding the first ZC minigap at ~ 200 GHz corresponds to the topological nanocavity mode. The structure around this peak is studied in more detail in Fig. 4.30. We expect the differential reflectivity spectrum $\Delta R/R^{(0)}(\Omega)$ for the topological sample to exhibit a modal structure involving three modes. First, the $q = 0$ odd mode of each SL should lead to a generation peak in the corresponding DRBs. This is shown in Figs. 4.30(a,b), which respectively show the acoustic band diagrams and the active modes if the two DBRs were assessed individually. Owing to the inverted symmetry of the band edge modes of the underlying SLs A and B, the lower band edge mode of DBR B (that we denote L_B) and the upper band edge mode of DBR A (that we denote U_A) are respectively excited. When the two DBRs are concatenated, the corresponding modes, evidenced by peaks in the derivative of the reflection phase from the substrate side (Fig. 4.30(c)),

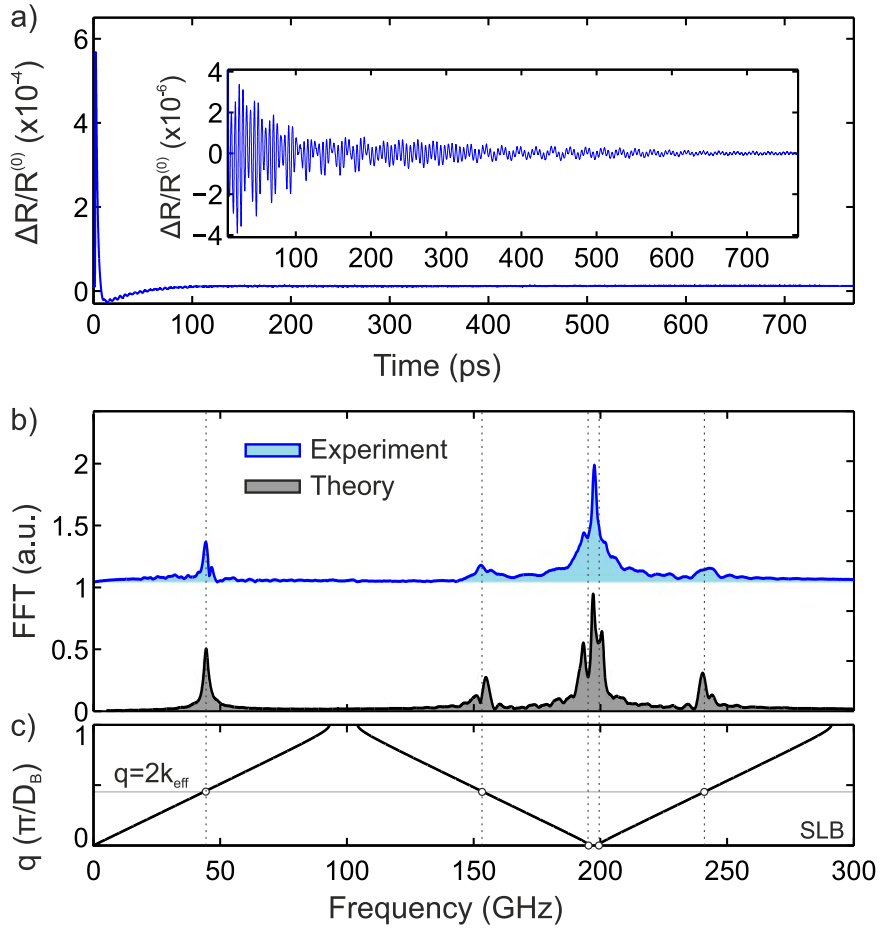

Figure 4.29: Reflection-type pump-probe coherent acoustic phonon experiments in the topological sample. (a) Time-resolved differential reflectivity obtained with pump (40 mW) at $\lambda = 800$ nm and probe (4 mW) at $\lambda = 765$ nm. The as-obtained data is treated by cutting the initial electronic peak and using appropriate Savitzky-Golay filters to extract low-frequency backgrounds, leading to the trace in the inset. (b) The Fast Fourier Transform (FFT) of the treated time trace is given (blue) and compared to the theoretical spectra obtained from a simple electrostriction-photoelastic model (grey). (c) Band diagram of of the bottom superlattice (SL B), with the spectral position of the generation/detection selection rules highlighted with vertical black dashed lines. A peak, corrresponding to the position of the topological interface state, is observed in between the two dashed lines bounding the first zone-center (ZC) minigap at ~ 200 GHz.

are also generated/detected, as is the topological mode (T), which arises precisely from this symmetry exchange. These three peaks are present in the modeled spectrum shown in Fig. 4.30(d). The spectrum obtained from zooming in Fig. 4.29(b) around 185-210 GHz (shown in Fig. 4.30(e)) shows qualitative agreement with the theoretical spectrum, although what are clear peaks in the theoretical curve (grey) only show up as shoulders in the experimental curve (blue). However, these shoulders are individually present as more prominent peaks in spectra taken at different points of the sample surface and do not arise from the zero padding of the time signals. For completeness, the calculated mode profiles $U_n(z)$ for the three

modes are shown in Fig. 4.30(f) clearly highlighting the band edge and confined nature of the observed modes, respectively.

The same analysis is carried out for the control sample, as shown in Figs. 4.30(g)-(l). The simple selection rules for photoelasticity-based infinite non-absorbing SLs are also conclusive for the control sample. The two modeled and observed peaks correspond to the lower ZC band edge modes of DBRs C (that we denote L_C) and B (L_B) respectively. When looking at the displacement profile of the $q = 0$ (FS) mode of DBR B (L_B) in both the topological and control sample we observe a different spatial profile, despite being at a very similar frequency. It must be noted that the FS peak is mainly generated in the second DBR (DBR B) and thus its intensity is almost independent of the spatial profiles in the first DBR

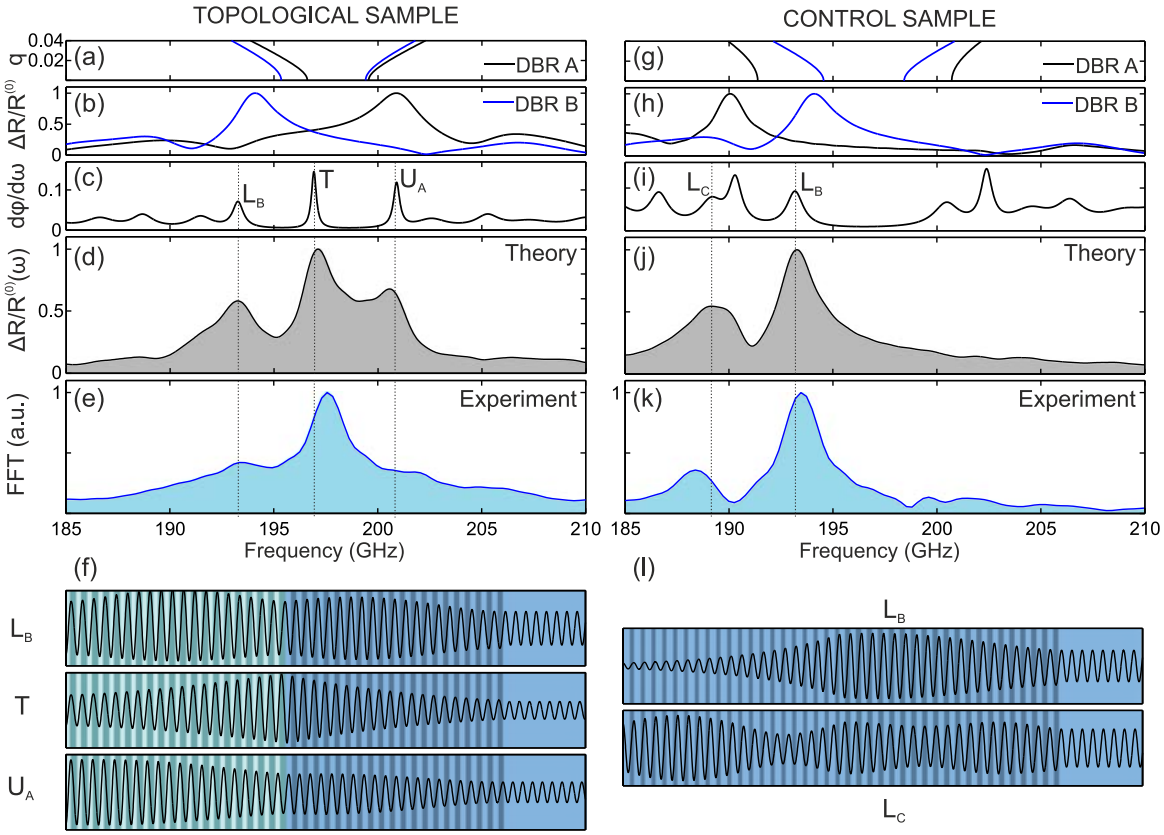

Figure 4.30: Optical transient reflectivity spectra of the topological and control sample around the first zone-center (ZC) minigap. (Left) (a) Band diagram of the underlying superlattices SL A (black) and SL B (blue). (b) Pump-probe phonon spectra of the individual uncoupled Distributed Bragg Reflectors (DBRs) A and B. The same color code as in (a). (c) Simulated derivative of the phase shift ϕ for a substrate-incident acoustic plane wave, allowing identification of supported resonances for a closed structure at the top layer. The three relevant modes are identified as L_B, U_A, and T and are also present in the (d) theoretical $\Delta R/R_o(\Omega)$ and (e) experimental spectra. (f) Mode profiles of the topological nanophononic cavity (T) as well as the detected lower (upper) band edge mode L_B (U_A). (Right) Equivalent plots for the control sample, with the two lower band edge modes L_B and L_C depicted instead in (l).

(DBRs A or C). In the first DBR, the L_B mode grows exponentially from the surface to the interface for the control sample while it is fully propagating for the topological sample. This difference arises from the different matching conditions with the second DBR. Fig. 4.30(a) shows how the lower band edge associated with DBR B lies inside a frequency region where propagating modes exist for DBR A, while Fig. 4.30(g) shows that the same band edge lies deep inside the band gap of DBR C. Note that the profiles in Fig. 4.30(f,l) directly give the displacement field $U(z)$, i.e. its real part, in contrast with Fig. 4.26, where we show the absolute value of the complex-valued displacement field $|U_n(z)|$ since an arbitrary complex phase can be added to the transmitted field.

In conclusion, in a pump-probe measurement in a semiconductor superlattice we observe peaks that are related to $q = 0$ (FS) and $q = 2k_{eff}$ acoustic phonons. For symmetry reasons, only one of the two FS modes is accessible by the experiment. In the case of the control sample, two FS peaks appear on the same side of the common minigap. In the case of the topological cavity, the two FS peaks appear on opposite sides of the gap, validating the band inversion concept. The symmetry-dependence of the observed peaks is based on very well established selection rules in Raman scattering that are mapped into photoelastic mediated processes in pump-probe coherent phonon generation/detection experiments. Even though the existence of the topological mode could also be probed by means of transmission/reflection experiments, similar to the ones reported in Ref. [324], this kind of experiments does not provide any information on the mode symmetries, a critical feature to prove the topological nature of the most intense observed central peak. Moreover, they require the growth of metallic transducers that would generate additional acoustic modes. Therefore, the use of time-resolved pump-probe measurements directly on the semiconductor superlattices is essential to spectrally resolve and distinguish the three modes around 200 GHz. The possibility of identifying individual modes that are closely spaced in frequency is of central importance for the study of dynamics in more complex topological acoustic structures where the interaction with the optical field can be engineered [279], e.g. in topological resonators for light and acoustic phonons [283].

Chapter 5

Cavity optomechanics in the Anderson-localization regime

In this chapter, we discuss the optomechanical (OM) experiments performed on photonic crystal waveguides (PhCWs) in the presence of unintentional fabrication disorder. We first give an introduction to the optical and mechanical properties of unperturbed photonic and phononic waveguides, which allows us to understand how to control the behaviour of light and motion propagation in the presence of fabrication imperfection. After that, we describe the experimental technique and apparatus employed to couple light into the optical modes emanating from the bands of these PhCWs, notably Anderson-localized optical modes. Multiple features evidencing the onset of localization are adressed, choosing the most appropriate on a case by case basis. With these tools in hand, the OM characterization of slotted PhCWs (sPhCWs) is described, showing both OM interaction with low-frequency mechanical modes using circular holes and with high-frequency modes using shamrock-shaped holes.

5.1 Photonic and phononic crystal waveguides: order and disorder

Photonic crystal (PhC) slabs enable control over the phase and amplitude of light due to the combined effect of the slab geometry and the dielectric pattern. In particular, they allow creating photonic band gaps (PhBGs), where light cannot propagate. A similar effects occurs for acoustic waves provided that the hole shape is chosen properly. Cavities based on point defects in a periodic nanostructure possesing a bandgap, like a patterned nanobeam, have been discussed in Chapter 2. In a two-dimensional system, one can also create a linear defect which guides light or sound from one point to another using Bragg reflection confinement within the lateral in-plane directions. Owing to the periodic pattern, the bands that arise from this type of defect are very dispersive. This allows a high density of propagating states at particular frequencies, in general close to the band edges [72], but

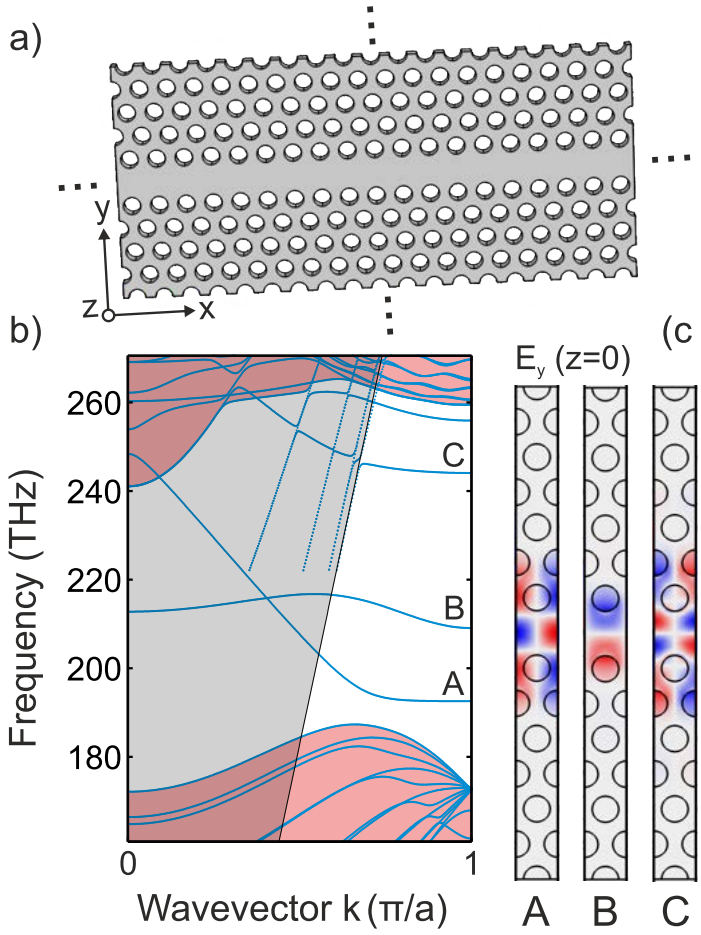

Figure 5.1: Band structure of a photonic crystal waveguide (PhCW). (a) Schematic of a W1 PhCW, which consists of a triangular lattice of circular holes with one missing row in the Γ-K direction. (b) Band structure of the structure shown in (a) for $r = 0.31a$, $t = 0.5a$ and $a = 500nm$. The light cone and the bulk bands are shown with shaded grey and red respectively. (c) $E_y(x, y, z = 0)$ for the highlighted bands (A,B and C) at the band edge ($k = \frac{\pi}{a}$), showing either even or odd parity with respect to the waveguide axis.

not limited to. We have already discussed how a high density of states can lead to enhanced multiple scattering and localization for a 1D multilayer and we explore here its manifestation in PhCWs and phononic crystal waveguides (PnCWs).

5.1.1 Line defects in two-dimensional lattices

A line defect is formed in a regular lattice by altering the periodic pattern in a given direction. The most typical line defect consists of omitting a single row of holes [325] in a high-symmetry direction, but many other possibilities have been explored [326,327]. The effect of omitting a row of holes in the $\Gamma - K$ direction of a triangular lattice of circular holes leads to the geometry depicted in Fig. 5.1(a). As seen in Chapter 2, when this lattice is etched in a silicon slab it exhibits a PhBG for z-even or TE-like modes, provided that the value of the hole radii and

the slab thickness are properly chosen. Since the vertical thickness invariance is mantained, we denote the resulting geometry of Fig. 5.1(a) a TE-like PhCW. The disruption of the translation symmetry in the in-plane direction perpendicular to the defect (y) creates a set of photonic states in the PhBG. Similar to the point-like defects, these states are roughly localized within the defect volume, since they cannot propagate through the lattice. The system still retains the translational symmetry along the direction x, i.e., Bloch theorem (see (3.16)) applies. We define k as the Bloch wavevector that characterizes the variation of the phase along that direction. The photonic band diagram for the system in Fig. 5.1(a) is calculated using Guided-Mode-Expansion (GME) and its bands are shown in (b). Only z-even modes are shown for clarity. We see that four bands populate the band gap region of the original lattice below the light line, the region above which is marked with shaded grey. The field profile of these guided modes is confined within the defect and decays exponentially into the bulk of the bounding PCs, as shown in Fig. 5.1(c) via the component $E_y(z = 0)$ of modes A, B and C ($k = \pi/a$). In addition, the modes have a well-defined and differing vector symmetry with respect to the axis of the defect, which will be of relevance later in this Chapter. The discrete nature of the bands shown for the bulk regions only results from the artificial periodicity that the GME method imposes in the perpendicular direction, i.e. it is a finite size effect. The structure supports in reality a continuum of states, which is also shown with shaded red in Fig. 5.1(b).

In order to achieve the same waveguiding effect for acoustic waves, an acoustic band gap is required. The lattice used in Fig. 5.1(a) does not exhibit band gaps for either z-symmetric or antisymmetric modes, as shown in Fig. 3.7 of Chapter 3. A mechanical waveguide or PnCW can be created by employing a different geometry for the scatterer like the shamrock used in Chapter 3. This is shown in Fig. 5.2(a) by employing a phononic crystal (PnC) on one side and a free-surface on the other. This boundary strategy is less suited for the photonic counterpart since the in-plane total internal reflection (TIR) is easily lost in the presence of any perturbation, but it provides lossless confinement for the guided mechanical waves, which we employ for cavity-optomechanics experiments. The band diagram of the waveguide with the $\Gamma - X$ direction of the PnC oriented along the [110] crystalline direction of silicon (as in Fig. 3.7) is shown in Fig. 5.2(b). Both z-symmetric (blue) and z-antisymmetric modes (red) are calculated due to the presence of the full mechanical gap. Panel (c) highlights the deformation profile of the modes of different bands and at different high-symmetry points. In the frequency range spanning 6.7 - 7.3 GHz, a multimode symmetric band operates at frequencies where two asymmetric bands are also present. This has an important effect on our measurements, where the vertical invariance is lost due to irregular etching.

5.1.2 Light localization

Compared to other light waveguiding technology, the supported propagating modes in PhCWs allow smaller confinement volumes and more compact architectures. The modal volumes can be much smaller than that of the high-refractive-index

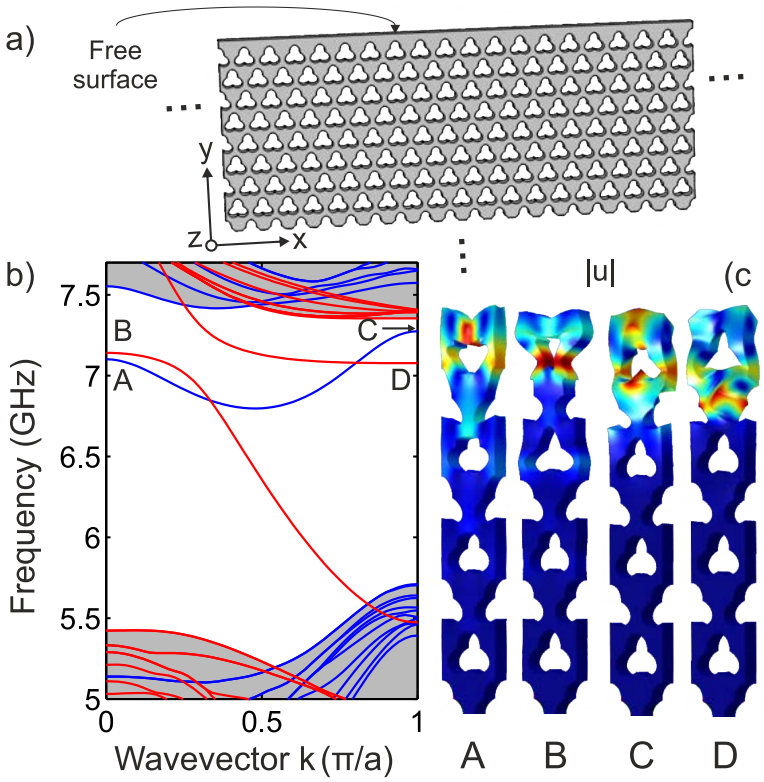

Figure 5.2: Band structure of a phononic crystal waveguide (PnCW). (a) Schematic of a mechanical *strip* waveguide bounded by a triangular lattice of shamrock holes and a free-surface. (b) Band structure of the structure shown in (a) for $A = 0.31a$, $B = 0.5a$, $f = 0.13a$, $t = 0.5a$ and $a = 500nm$. The width of the waveguide is $Ws = 0.2a$. Bands are split between modes that are symmetric (blue) and asymmetric (red) with respect to the mid-plane. The bands extending in the bulk of the crystal are shown with shaded grey. (c) Displacement fields (color gives $|u|$ at the surface) of the band edge modes highlighted with A, B, C and D.

core of an optical fiber and of similar magnitude or smaller (and thus compatible) than those of high-index waveguiding structures (see light fields in Fig. 5.1(c)). In addition, distortion or bending at a microscopic scale in fibers or high-index waveguides leads to scattered waves with angles of incidence for which TIR is lost, while in a PhCW light cannot radiate in-plane because there are no electromagnetic modes to scatter into. However, in the presence of a scattering center like a sharp corner or a misplaced hole, the propagating Bloch mode of frequency ω and wavevector k scatters in the forward or backward direction into isofrequency modes, i.e. Bloch states of another (or the same) k propagating at the same frequency ω [209]. The number of scattering channels depends on the number of available guided states, while the scattering cross sections are linked to the quantity of allowed states at ω, i.e. the density of optical states (DOS) [270]. The paradigmatic case of a W1 PhCW presents a y-even monomode band (see band labeled A in Fig. 5.1(b)), with no other guided (or quasi-guided) isofrequency modes than its time-reversed state at $-k$. This easily allows the interpretation of

the backscattering properties in terms of the group velocity of light in the waveguide [328].

The fast speed of light in vacuum or through transparent materials (which can circumvent the Earth in just 0.1 seconds) allows us to see very distant objects in the Universe and enables unbeatable fast information transmission. However, when strong light-matter interaction is needed, the fast speed of light is a drawback [329]. Slowing down light is a scientific and technological goal of paramount importance for applications ranging from nonlinear optics [330] to quantum information processing [331] and PhCWs are likely the most suited platform to achieve it [332]. The velocity at which the phase of a single frequency wave propagates in a given system is given by the frequency-dependent refractive index as $v_p = c/n(\omega)$. However, in a realistic setting where light is used one typically deals with an electromagnetic wave-packet. The velocity at which its envelope moves, i.e., the group velocity v_g, is given by

$$v_g = \frac{\partial \omega}{\partial k} = \frac{c}{n(k)} - ck\frac{\partial n}{\partial k} \tag{5.1}$$

where the refractive index dependence on k is made explicit. Both v_p and v_g coincide in non-dispersive media, but they can be extremely different in the presence of dispersion, i.e., when $\frac{\partial n}{\partial k} \neq 0$. The factor at which the wave slows down with respect to the light speed in vacuum is defined by the group index $n_g = c/v_g$. One possible way to achieve high values of n_g, i.e. slow light, is to rely on the natural dispersion of materials resulting from the interaction of light and matter at the atomic scale, which has allowed the production of extreme slowdown factors in, e.g. atomic clouds [333]. This category often requires controlled pressure and temperature environments and are restricted to laboratory-scale settings [334]. Another way of achieving controlled, guided, slow light can be easily understood by looking at the dispersion shown in Fig. 5.1(b). At the band edge X ($k = \pi/a$) both bands are flat: at those frequencies light is completely halted. At frequencies very close to the cut-off, n_g has extremely high values, which would make a photon wavepacket travel freely within the waveguide channel at nearly human paces (m/s).

However, in real devices there is a limitation to the maximum n_g achievable due to slight deviations of the fabricated parameters compared to the designed values. Even fluctuations in the nm-range [217] give rise to backscattering of the guided light, especially within the slow-light bandwith. The slower the wave propagates, the more time it has to interact with the imperfection, therefore increasing its chances of being (back-)scattered. Recurrent coherent backscattering can actually induce a strong interference [335] which localizes the light field, a photonic manifestation of Anderson localization in low dimensions. We have already discussed and numerically assesed in Chapter 4 how the presence of disorder in a multilayered structure can halt transport and how this absence of difusion originates from a localization of the corresponding eigenfields. While a superlattice seems to constitute the perfect setting to observe the physics of localization

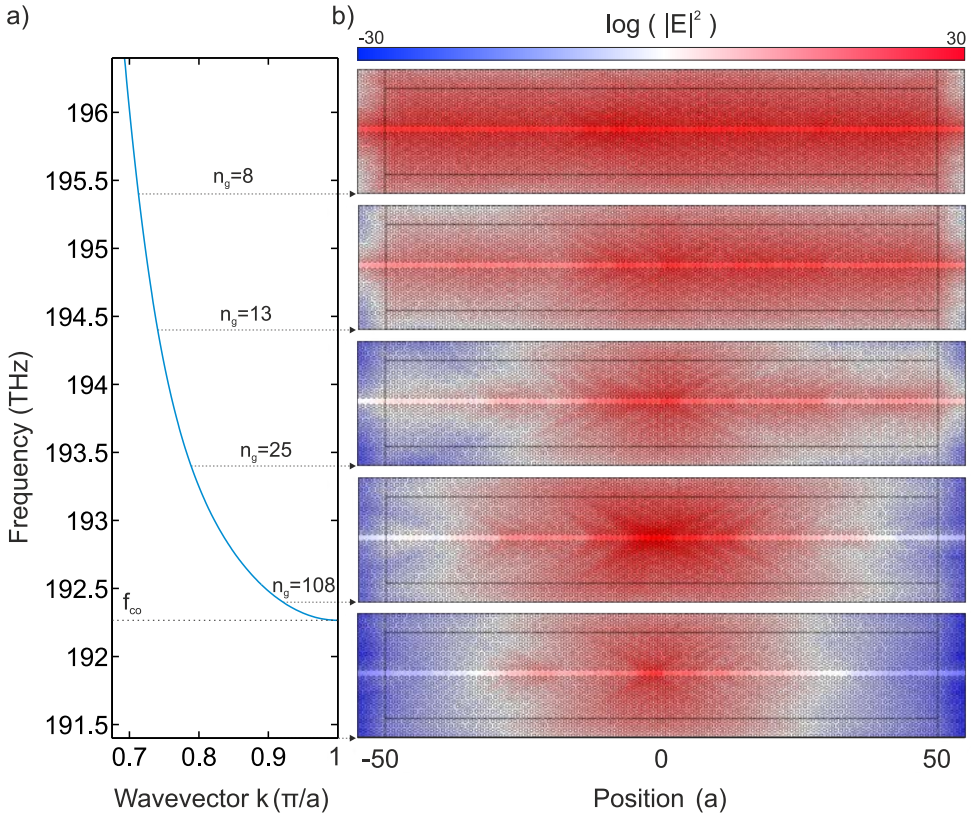

Figure 5.3: Dipole emission in disordered photonic crystal waveguides (PhCWs). (a) Band structure of a 2D W1 PhCW around the cut-off of the z-even mode, with the group index n_g of the propagating modes highlighted at some particular frequencies. (b) Logarithmic scale map of the field emitted by a y-oriented dipole source at the middle of the waveguide oscillating at the frequencies highlighted in (a). The color scale is fixed for all of the maps and evidences the different length-scale associated to the field decay. All simulations are based on the Finite Element Method (FEM).

because an imperfection can only elastically scatter the incident Bloch mode into itself or its backward state, observations in such systems are limited [336–338]. On the other hand, the picture in PhCWs may seem more complex due to an important additional channel for scattering, i.e., out-of-plane radiation. Although the propagating Bloch modes below the light cone have no intrinsic out-of plane losses, the considered disorder can induce coupling to the radiation continuum. However, in plane back-scattering is largely the dominant loss mechanism at large values of n_g and low disorder levels [339] for most traditionally employed PhCWs.

Localization length in a W1 photonic crystal waveguide

Given that in-plane scattering dominates in the slow light regime, we use two-dimensional Finite Element Method (FEM) simulations of perturbed PhCWs to study its localization properties around that frequency region (Fig. 5.3), instead of more computationally heavy 3D simulations. In this case, we can use an effective (lower) refractive index for silicon of $n_{eff} = 2.84$ to mimick the real 3D system.

With this choice the photonic bands of the 2D system reproduce the bands shown in Fig. 5.1(b) rather accurately. The effective refractive index method [340] provides accurate results whenever the fundamental TE mode of an unpatterned silicon slab suffices to describe the PhC slab [71] and we have checked using GME that only that guided mode is required to have a converged band structure. Under these hypotheses and for the particular case of the y-even guided mode of the W1 PhCW, the only source of losses is backscattering and the localization length ξ coincides with the backscattering mean free path [215,341].

The localization length ξ is obtained from numerical simulations of the light emitted by a light source embedded in the medium, following Ref. [267] as

$$-\frac{x}{\xi(\nu)} = < \ln[I(\nu)] > \tag{5.2}$$

where I is the FEM solution of the electromagnetic field intensity emitted by a single y-oriented dipole at frequency ν, x is the distance from the dipole position along the waveguide and the brackets indicate the statistical ensemble average over different configurations of positional disorder. The emitter is placed at the middle of a waveguide of length length $L = 100a$ in the x direction and with eleven unit cells on each side of the waveguide in the y direction. This domain is surrounded by perfectly matched layers (PMLs) to mimic an open system. The effect of fabrication imperfection is introduced by randomizing the position of the air holes around their ideal value according to a normal distribution whose standard deviation σ is our measure of disorder. Note that the exponential damping (5.2) is not found in all types of disordered single-mode waveguide systems [342], especially as v_g decreases, but it is commonly assumed and numerically obtained [270,343–345]. Fig. 5.3 shows the electromagnetic field intensity excited by a dipole source in a single realization of disorder ($\sigma = 0.03a$) and for several oscillating frequencies. The values of n_g for the corresponding frequencies ν are given in the band diagram of Fig. 5.3(a). Regardless of the fine structure of the excited electromagnetic field for this particular disorder realization, we observe that as n_g increases the field profile decays faster, a clear fingerprint of the mentioned correlation between the DOS of the unperturbed structure and backscattering in the perturbed one. In addition, for frequencies inside the band gap of the perfect structure, bottommost field of Fig. 5.3(b), the field is not a simple exponential decay as would be expected from coupling to an evanescent Bloch mode, but has an intricate structure, also pointing to a change in the DOS induced by disorder. The localization length ξ is extracted after ensemble averaging the emitted fields over 100 disorder realizations, a number of samples for which the extracted parameter ξ is already converged. For clarity, the exponential fit corresponding to the frequencies shown in Fig. 5.3 are given with a red and blue line in Fig. 5.4(a), evidencing well-behaved exponential decays with decreasing characteristic lengthscale. Taking ξ as the mean between the two fitted lengths, we extract the frequency-dependent $\xi(\nu)$, which is given in Fig. 5.4(b). For reference, the cut-off frequency for the guided band is given with a dashed line. As expected, we observe a progressive decrease of ξ with decreasing frequency ν, a dependence that stems from the increasing group index n_g. Inside the band gap, where n_g is an ill-defined quantity,

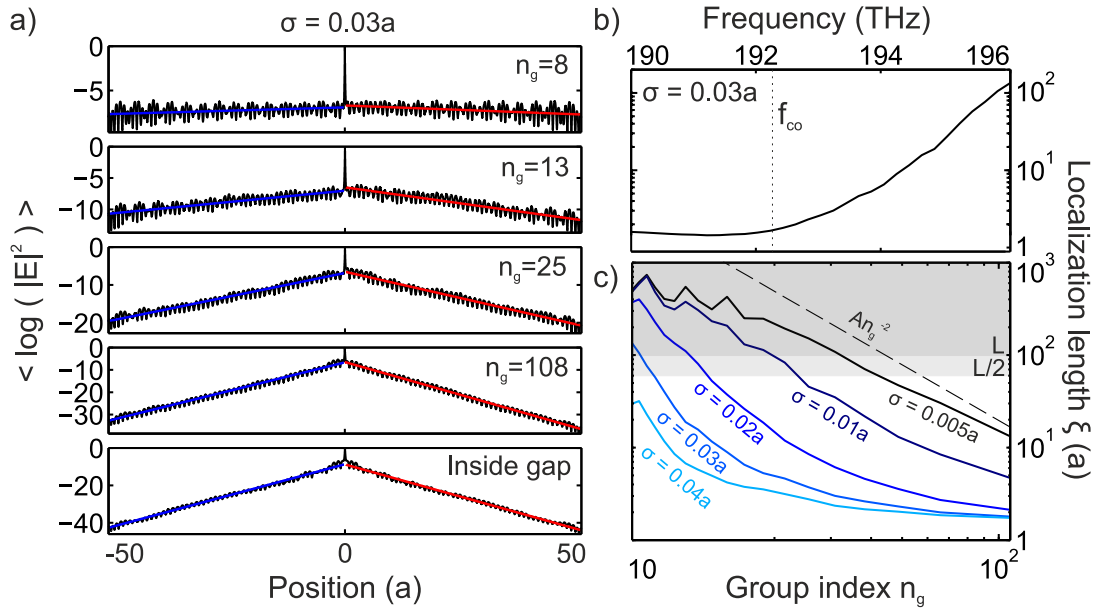

Figure 5.4: Photonic localization length ξ in a disordered photonic crystal waveguide (PhCW). (a) Averaged intensity $|E|^2$ emitted by a dipole along the axis of a disordered PhCW ($\sigma = 0.03a$). Both sides are fitted (blue and red) with an exponential from which the localization length ξ is extracted. The value of n_g for the used frequencies is given. (b) $\xi(\nu)$, with the cut-off f_{co} given as a black dashed line. The analysis done in (a,b) is repeated for multiple disorder levels σ and ξ as a function of n_g is shown in (c). Shadings mark the region where the fields decay less than a factor e^{-1} and the dashed line shows the perturbative [328] slope n_g^{-2}.

the localization length also exhibits some slight dispersion. To emphasize the importance of the group index n_g of the unperturbed structure on the backscattering properties of the PhCW and on the localization length ξ, Fig. 5.4(c) shows the dependence of $\xi(\nu)$ with σ, where we see that a negative correlation between n_g and ξ is always found. Shadings mark the region where the fields decay less than a factor e^{-1} and the dashed line shows the perturbative slope n_g^{-2} [268,346]. We recover here very similar results to those obtained for a three-dimensional Fourier-Bloch mode method [328], notably that the perturbative approach is only valid for very high n_g and very low σ.

Anderson-localized modes in a W1 photonic crystal waveguide

Whenever the length L of the system explored is considerably larger than the localization length ξ ($L \gg \xi$), we expect the photonic eigenspectrum to be composed of spectrally and spatially localized modes with an average lengthscale given by ξ [213]. This can be observed for $\sigma = 0.03a$ in Fig. 5.5, where $E_y(x, y)$ is shown for the eigenmodes with eigenfrequencies closest to the ones considered in the previous two figures. The localization length ξ at those particular frequencies are given for reference. For $\xi = 80a$ the localization length is approximately the size of the considered system and the eigenmode field extends over the whole structure, although the field profile of the perfectly propagating Bloch mode is considerably

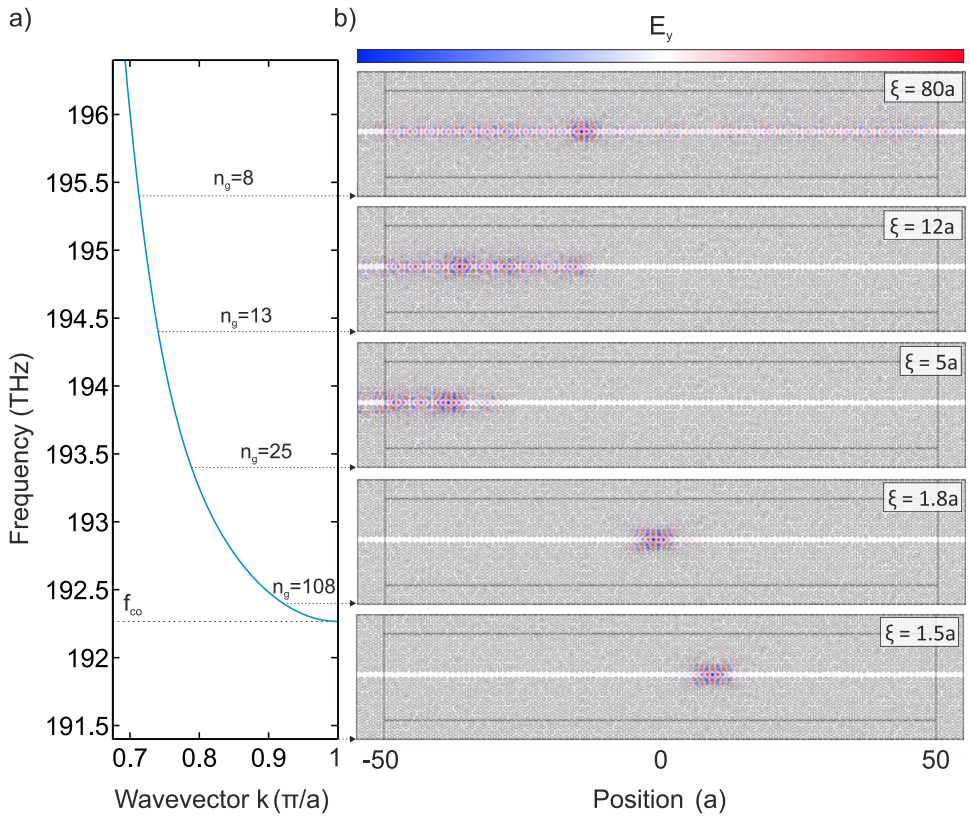

Figure 5.5: Anderson-localized optical modes in a disordered photonic crystal waveguide (PhCW). Eigenfields of several representative modes of a 2D disordered PhCW with $\sigma = 0.03a$, evidencing light localization. (a) Band structure of a 2D W1 PhCW around the cut-off of the z-even mode, with the group index n_g of the propagating modes in the perfect structure highlighted at some particular frequencies. (b) $E_y(x, y)$ of the eigenmodes with eigenfrequency closer to the ones highlighted in (a).

altered. For lower values of ξ, the eigenmodes are localized within the sample length with correspondingly lower mode volumes. The last two eigenfields, one of eigenfrequency inside the propagating bands and one inside the PBG, have tightly confined fields that are of similar size to engineered heterostructure PhCW cavities [186] and therefore possible good candidates for cavity OM experiments.

Anderson-localized modes in LN cavities

In general, characterizing ξ is very challenging [347]. In transport experiments, where the trasmission of light through the waveguide is detected for various lengths of the system, many artifacts can arise, mainly absorption [14]. It is therefore important to find alternative ways of measuring, or at least estimating, such a quantity based on other spectral features. Here, we suggest an alternative solution to estimate the value of ξ based on finite samples and show how this applies in the case of 2D simulations.

To characterize the dispersion of a fabricated PhCW, it is interesting to

enclose the waveguide portion between high-reflectivity mirrors and use the resulting Fabry-Pérot (FP) resonances and their free spectral range (FSR). The case of enclosing a W1 PhCW is particularly straightforward, since instead of omitting a full row of holes as in Fig. 5.1 one can omit only a portion of a row composed of N cells, creating or forming a long LN cavity [348]. The field confinement in disordered LN cavities [349] is mainly determined by the local structural disorder as long as the confinement region is far away from the cavity mirrors and the localization length ξ is considerably smaller than the cavity length $L = Na$, while in the opposite case it effectively behave as a W1 waveguide. This LN cavities enable simultaneously FP resonances and Anderson-localized modes depending on the value of ξ/L, which is also strongly dispersive (see Fig. 5.4(b,c)). This makes them interesting candidates to study the transition between a frequency range where ballistic transport is allowed -and thus FP resonances are created- when $L \ll \xi$ and another frequency range where Anderson localization happens when $L \gg \xi$. Analyzing this transition might give valuable insights into the n_g dependence of the localization length ξ, at least qualitatively. In addition, Anderson-localized modes do not appear as additional resonances inside the spectral region covered by the original FP resonances of an unperturbed LN cavity, i.e. the number of eigenmodes within the band remains constant [349]. This points towards resonance counting as a possible tool to understand the experimentally observed spectra and whether or not to expect additional resonances when locally probing the density of states.

We have simulated a number of these LN cavities with different lengths $L = \{50a, 100a, 150a\}$ to analyze the onset of localization in a W1 PhCW and its relation with n_g. Disorder is introduced here as positional disorder with strength $\sigma = 0.005a$, a value that is on the lower bound of the fabrication disorder expected from our fabrication process. Fig. 5.6(a) plots the first 8 modes of a perfect (left panel) and a disordered (right panel) L50 cavity. The associated W1 band is also given, with the eigenfrequencies highlighted with solid lines of the corresponding colour. From the 4^{th} to the 8^{th} eigenmode there is a strong link between the profiles and eigenfrequencies of the perfect and the perturbed structure, while they differ for eigenmodes 1 to 3, when the eigenfrequencies approach the cut-off frequency f_{co}. The disordered L50 cavity exhibits tightly localized modes which are difficult to link to the modes of the perfect L50. Below a certain frequency, the condition $Na > \xi$ is satisfied and the LN cavity behaves like an open W1 waveguide, the boundary conditions imposed by the end mirror playing no role. From the FSR between two resonances, i.e. $\Delta\nu_{FSR} = \nu_{i+1} - \nu_i$, one can obtain the group index n_g of the propagating mode in the central region as,

$$n_g = \frac{c}{\Delta\nu_{FSR} L} \tag{5.3}$$

where the frequency ν at which n_g is evaluated is simply taken to be the mean value $\nu = (\nu_i + \nu_{i+1})/2$. The extracted n_g^{LN} for both the perfect and the disordered LN cavity are shown in Fig. 5.6(b), with the theoretical curve n_g^{W1} as obtained from (5.1) given by the solid black line. The curve for the unperturbed L50 cavity exactly recovers n_g^{W1} (both superimposed in Fig. 5.6(b)) and this holds even for

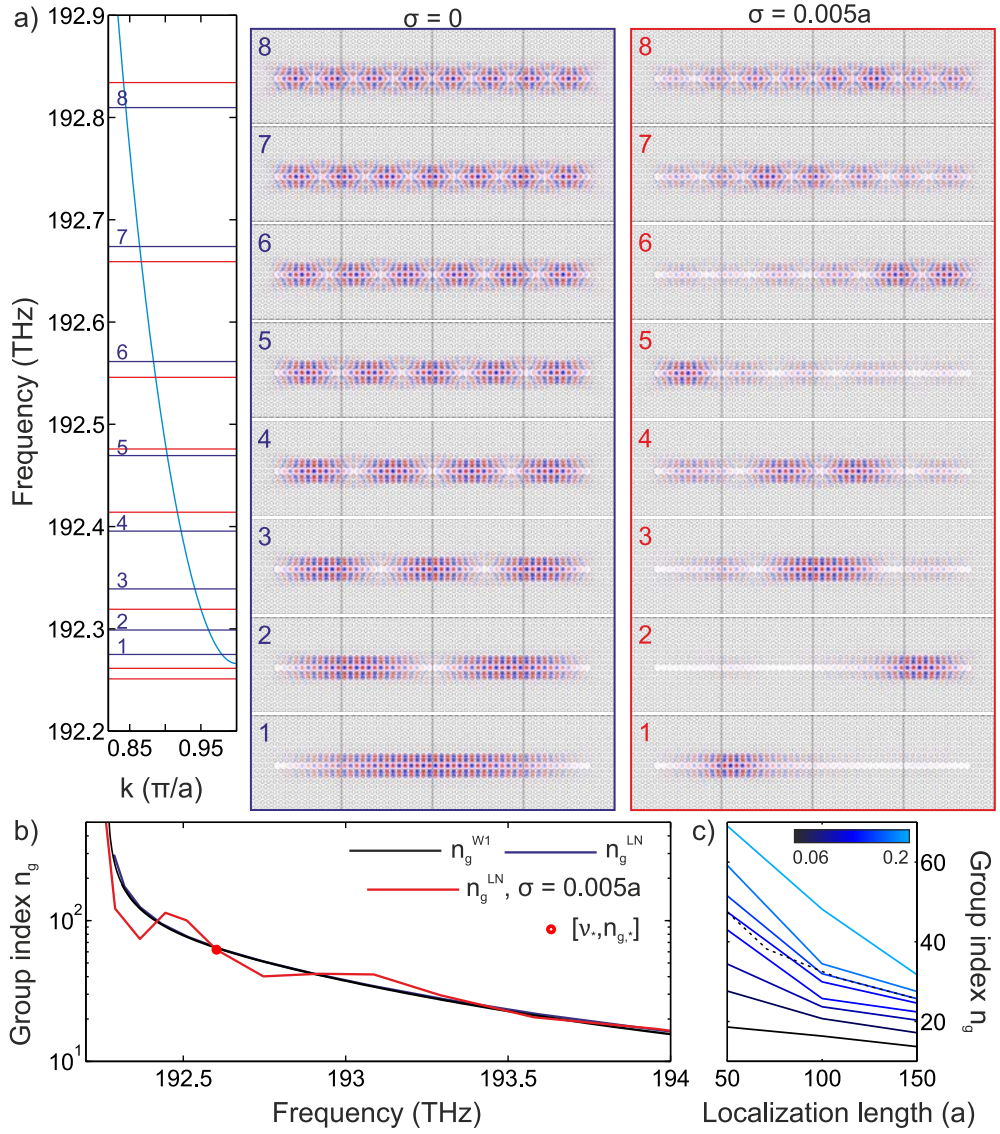

Figure 5.6: Localized optical modes in a disordered LN cavity. (a) Eigenfields of the first 8 modes of a 2D L50 cavity in the absence (left) and the presence (right) of positional disorder. The disorder level is set to $\sigma = 0.005a$. The band dispersion of the underlying 2D W1 photonic crystal waveguide (PhCW) is given in the left, with the obtained eigenfrequencies highlighted with solid lines. (b) The group index n_g^{LN} is recovered from the corresponding eigenfrequencies and, in the case of the disordered L50 cavity shows deviations from n_g^{W1}. (c) Extracted $\xi(n_g)$ using Eq. 5.4 on 100 disordered LN cavities of lengths $L = \{50a, 100a, 150a\}$.

very small N. Secondly, the effect of disorder leads to a deviation of the extracted $n_g^{LN}(\nu)$ from $n_g^{W1}(\nu)$, since the frequency of the random cavities is not determined by the bounding mirrors but by the disordered potential. This deviation can be used as a fingerprint of strong backscattering in closed waveguides and as a means to obtain a good approximation to the localization length $\xi(\nu)$. To this aim, we

define a normalized deviation as,

$$\delta(\nu) = \frac{|n_g^{W1}(\nu) - n_g^{LN}(\nu)|}{n_g^{W1}(\nu) + n_g^{LN}(\nu)} \tag{5.4}$$

where the numerator accounts for extreme deviations at very high n_g values. Once this deviation is defined, one must set a criterion, i.e. a limiting value δ_*, that allows extracting the pair $\{\nu_*, n_{g,*}\}$ for which the perfect LN system starts deviating or $\delta(\nu_*) > \delta_*$. This approach is applied in panel Fig. 5.6(b), where the point $\{\nu_*, n_{g,*}\}$ is marked with a red dot for a value of $\delta_* = 0.13$. After repeating this same procedure for many different disorder realizations, finding the average $\overline{n_{g,*}}$ and iterating over LN cavities of different lengths L, one obtains a curve relating the length L to $\overline{n_{g,*}}$. Since the modes are localized roughly whenever $\xi \geq L$, one can approximate the localization length at group index $n_g = \overline{n_{g,*}}$ to be L, i.e. $\xi(n_g) = L$. The dependence obtained for different values of the threshold value δ_* is shown in Fig. 5.6(c) for the three lengths explored here and the dotted black line gives the reference curve as extracted from Fig. 5.4(c). This analysis gives an appropriate trend for the localization length, although the value of δ_* is obviously arbitrary and has a strong influence on the analysis. For this reason, this analysis is by no means quantitative and it is only intended to estimate $\xi(\nu)$ in a well-behaved monomode optical band without the need of cumbersome transport measurements, which are usually affected by artifacts [13].

5.2 Near-field coupling to photonic crystal waveguides

A significant challenge in the development and characterization of integrated nanoscale optical devices lies in the efficient coupling of light from conventional optical elements such as lenses and fibers to confined or distributed nanoscale optical mode volumes and viceversa [350]. The most relevant challenge is the considerable modal mismatch in spatial extent, polarization, and propagation constant between radiation in free-space or in a glass fiber with weak refractive index contrast and that of a typical integrated waveguide with high refractive index contrast and sub-micron dimensions [351]. Possible solutions include the use of on-chip grating couplers [352], with efficiencies that can go up to 80% [353] for free-space radiation and for near-normal fiber-based coupling [354,355], end-fire butt-coupling into inverse tapered integrated ridge waveguides [356], and/or adiabatic mode transfer [351,357]. In all such cases, tapered structures with rather high footprints are usually required to avoid losses at the interface and/or to increase the operational bandwith.

In any technique that couples light from the outside world into the photonic chip, one needs to engineer the interface between different functional elements, e.g., a nanoscale strip waveguide and the PhC (waveguide, cavity, etc.), to avoid on-chip back-reflection or out-of plane losses at the interface. The strong impedance mismatch occuring due to the large difference in group index between

the fundamental mode of a strip waveguide and a PhCW guided mode is the main impediment in the case of PhCWs [358]. Several adiabatic couplers changing the PhCW width [359], the hole radii [360] or the crystal periodicity [361] have been designed and experimentally assesed, exhibiting extremely high coupling efficiencies of above 95%. Resonant coupling using interface states [150] has also been proposed, especially in slotted PhCWs using a multimode interference (MMI) coupler [362], although with limited bandwith. With such advanced coupling schemes, PhCW dispersion characterization observing reflection/transmission FP resonances [325] or interference fringes in external Mach-Zehnder interferometers [363] is achieved. Insertion efficiency in these systems is however still a challenge, especially in the slow light regime, which leads to poor signal-to-noise ratios. The experimental observation of the onset of Anderson localization in that frequency region is also hard to assess by such a *transport* approach because any optical loss in the system, like absorption or out-of-plane scattering also results in an exponential decay of the intensity profile with an average loss length. This problem can be circumvented by studying the fluctuations in the transmitted light intensity [16], but only modes having a non-vanishing amplitude at the initial part of the PhCW are efficiently excited [270,364]. All these issues point to the necessity to locally probe the spectral properties of the PhCW of study, which can be achieved by using internal emitters such as quantum wells or quantum dots [365] both by far-field [366] or near-field excitation [367,368].

Evanescent coupling from an optical tapered fiber to the photonic structure of interest is the alternative method employed in cavity optomechanics [369]. A standard single mode optical fiber supports a single propagating optical mode in the wavelength range of interest through TIR of light between the core of the fiber and its lower-index cladding. At telecom wavelengths, this is typically achieved with an 8 μm diameter core and a 125 μm cladding, where most of the optical mode is confined in the core. If the lateral dimensions of the fiber are reduced and air chosen as a cladding, most of the guided mode propagates as an evanescent tail which can be brought in close proximity to a photonic structure. Overlap of the evanescent fields of the two modes or, equivalently, frustrated total internal reflection enables their coupling. This approach has been used to efficiently probe a large variety of micro and nanophotonic devices [370], including PhCWs [93], and allows to extract its dispersion properties without the need of integrated access waveguides. In this section we will explain how to use this approach to couple light into a silicon PhCW, how to characterize its dispersion properties, and how to locally probe Anderson-localized optical modes close to the cut-off frequency of the considered waveguide. We will also see how the boundary conditions of the considered waveguide can clarify the nature of the observed spectral features and the behaviour of such locally probed resonances when driven at high power.

5.2.1 Fiber-taper: theory and fabrication

The evanescent coupling between two optical modes occurs whenever the two oscillate at the same frequency and have some overlap in their k-space distribution, i.e., they are phase-matched. For propagating modes with eigenstates defined by

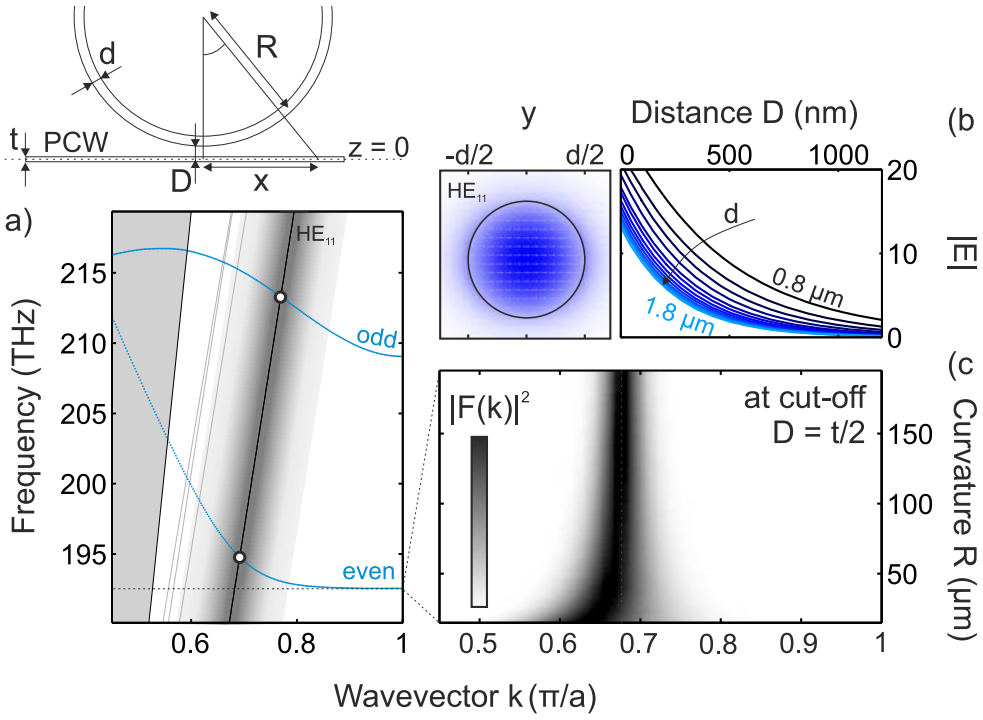

Figure 5.7: Phase matching between an air-cladded fiber and a photonic crystal waveguide (PhCW). The coupling geometry is shown schematically on top: an air-cladded curved fiber of diameter d is placed at a distance D from the mid-plane of a slab of thickness t in which a PhCW is patterned. (a) Band diagram portrait of the phase matching condition between the fiber taper and the PhCW. The even and odd defect TE-like bands are shown in light blue, while the optical modes of a fiber taper of diameter d=1.5 μm are shown in black (HE_{11} mode) and light grey. For a straight fiber taper, the phase matching condition is only achieved at the points marked with a white-filled dot, while a finite curvature R relaxes the condition by increasing the k-space distribution of the fiber taper mode in the PhCW plane $z = 0$, as shown by the shading around the HE_{11} mode. (b) Electric field norm $|E(x, y)|$ and vector field (arrows) of the fiber HE_{11} mode at frequency f_{co} (left) and its decay in the air-clad (right) for different diameters d, with fields normalized to carry the same power. (c) Approximated Fourier transform of taper mode at the PC plane as a function of R, showing how the phase-matching region broadens with decreasing R.

a well-conserved momentum k in a given common direction, this translates into finding a crossing in a band diagram. This is the case for the evanescent coupling of the propagating Bloch modes of a PhCW (of wavevector k) and the modes of a silica fiber (of wavevector β). The thick lines in Fig. 5.7(a) show the dispersion of both the PhCW of Fig. 5.1(b) and of an air-cladded fiber taper of diameter d =1.5 μm, where a refractive index of 1.445 has been used for SiO_2.

For the diameter chosen, the fiber is not single mode in the frequency range of interest. However, we will only consider the fundamental HE_{11} for the purpose of understanding the phase-matching condition. When an infinitely long fiber and a PhCW are considered only a single point of intersection between the two

continuous dispersion curves leads to efficient energy transfer [371]. Evanescent coupling is therefore possible for both the fundamental even mode and for the first higher order odd mode of the eW1 PhCW. Nevertheless, due to the symmetry of the taper-guided mode (shown in Fig. 5.7(b)), the y-odd mode of the PhCW is optically dark when the fiber is perfectly aligned with respect to the axis of the PhCW. The positioning of the fiber relative to the PhCW axis is a critical parameter and that slight misalignment can induce coupling to the odd band. Measurements with fiber tapers of different (and well-known) diameters should be carried out [372] to characterize a PhCW, which clearly precludes its use as a chip-scale fast characterization technique. An alternative approach was suggested in Ref. [373], where a single taper with an increased curvature radius R allows coupling over a much higher bandwith. This can be understood by mapping the curved fiber eigenfield to the PhC plane and taking its Fourier transform. This last can be approximated as

$$F(k_z) = \int_{-\infty}^{\infty} f(0, \sqrt{x^2 + (R+D)^2} - R) e^{i\beta R \mathrm{atan}(\frac{x}{R+D})} e^{ik_z z} dz \tag{5.5}$$

where the curvature is considered small enough to mantain the transverse profile $f(x', y')$ of the straight fiber at any θ, with θ and all other parameters defined as shown on top of Fig. 5.7. Accurate description of the coupling should consider the exact fields, but this simply evaluated integral shows that the k-space extension of the taper mode increases in the presence of a finite curvature R. The smaller the radius R, the broader the reciprocal space broadening. This allows an overall transition from a δ-like taper dispersion to a Gaussian-like one and facilitates the phase-matching condition over a large portion of the dispersion. Fig. 5.7(a) shows that a thicker taper is beneficial to couple light into the PhCW over the slow-light region at telecom wavelengths in terms of phase matching. However, this also leads to a thinner evanescent field extension, as seen in Fig. 5.7(c), which considerably reduces the coupling for a fixed distance d. In addition, the presence of other higher order propagating modes can lead to beating between different propagating modes in the taper when this one is driven from either side. In our case, the diameter of 1.5 μm simulated here is chosen to allow both a sufficient exponential tail at D = 120-125 nm, i.e. half the thickness of the used slabs, while mantaining the center of the broadened dispersion close to the cut-off of the y-even band.

The fiber tapers are produced using a telecom optical fiber (SMF-28) which is stretched in a controlled way via two independent motorized stages while the central part is being heated to a temperature of 1180°C using an electric ceramic microheater [374]. This allows direct coupling to the air-cladded region by employing standard SMF technology, provided that the tapered region is made adiabatic [375], since the guided field mode in the standard step-index unstretched regions needs to adiabatically transform into a guided mode in the waist of the taper. Nevertheless, extremely high and optimized transmission as the ones reported in [376,377] are not necessary for the purposes herein. The used setup is shown in Fig. 5.8(a). Since we typically work with structures designed to operate at λ = 1.5 μm, the fiber transmission at that wavelength is monitored during

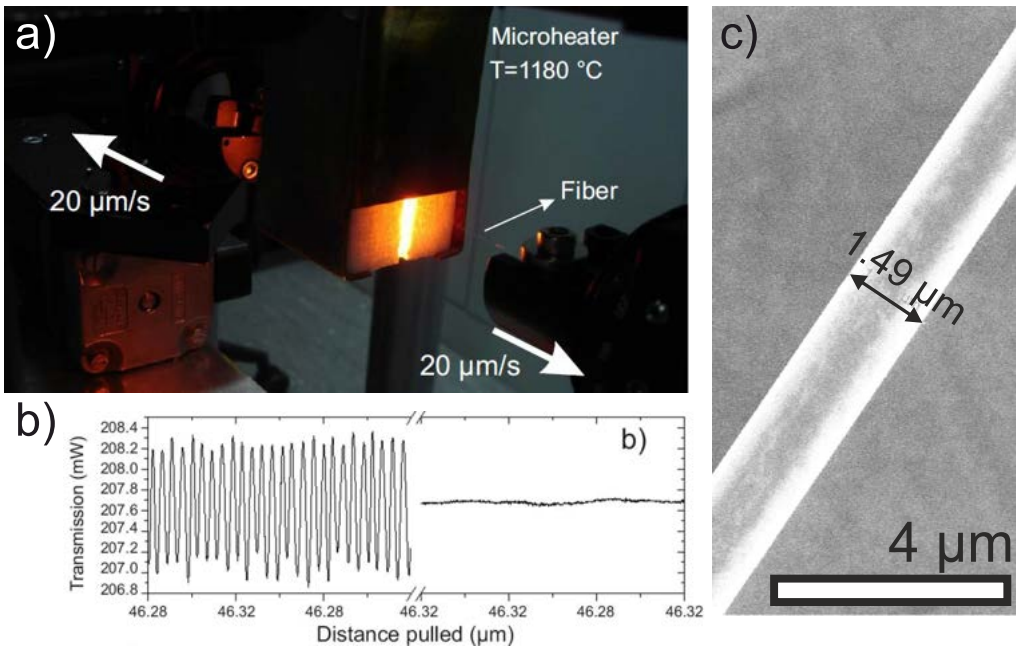

Figure 5.8: Fabrication of wavelength-scale fiber tapers. (a) Experimental arrangement used to produce a fiber taper with a wavelength-scale diameter at its waist. Two independent motorized stages operating at a 20 μm/s speed are used to symmetrically pull the fiber, which is supported by magnetic clamps. The central part is embedded in a ceramic microheater with a narrow slot, which permanently heats the region to a temperature around T = 1180 °C. The transmission at a central wavelength of λ =1.5 μm is monitored while pulling and exhibits oscillations that arise from interference between the supported guided modes, as seen in (b). When the observed oscillations die off, the pulling is stopped. (c) SEM image of the waist of a fabricated taper using the described technique.

the pulling process, allowing us to understand the modal structure of the taper. Heating of the structure by the microheater melts the core and cladding into a single effective material and the initially SMF becomes multimode. Power loss from the fundamental mode can therefore happen via the excitation of higher order modes, which leads to interference between the supported modes at the operating wavelength, as shown in the left region of Fig. 5.8(b). As discussed in several works [374,378] the beating notes vanish when the supported modes go above the cut-off. When all oscillations have vanished, the taper waist is single mode (right region of Fig. 5.8(b))[1]. Strictly single-mode fibers are best suited to couple light to tighly confined engineered optical cavities or in light-atom interaction experiments [379]. However, in our case we stop pulling slightly before the single mode operation to ensure that the HE_{11} band crosses the PhCW in close proximity to the region of interest. A Scanning Electron Microscopy (SEM) micrograph of a typical fabricated taper is shown in Fig. 5.8(c), with its diameter highlighted. The achievement of a curved geometry is guaranteed by creating a micro-loop with the taper's waist at its lower part. After removing the taper from the microheater,

[1]The single mode operation at λ = 1.5 μm for a taper of refractive index n_{SiO_2} = 1.445 is achieved at d = 1.23 μm.

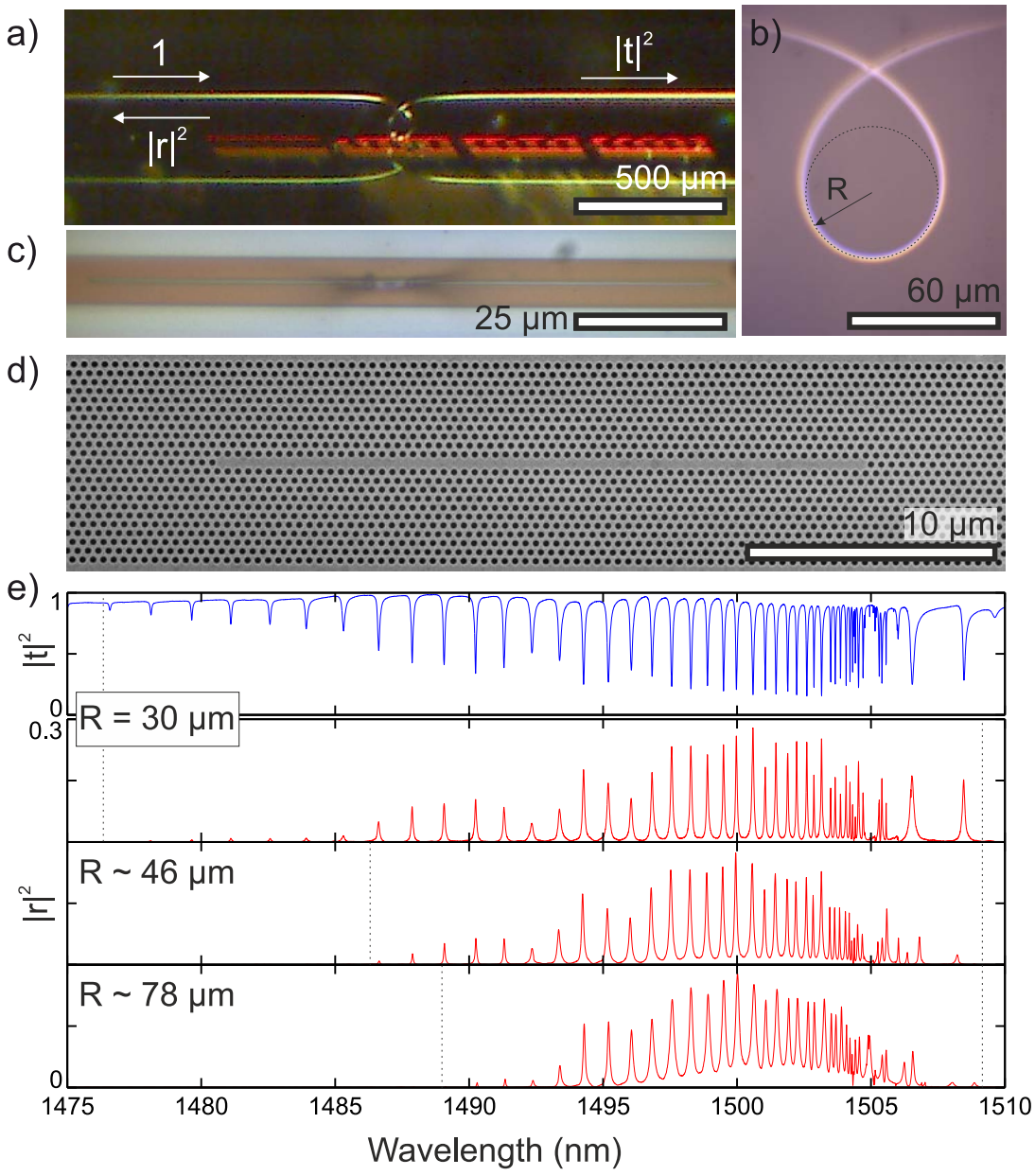

Figure 5.9: Experimental evidence of evanescent coupling to a silicon photonic crystal waveguide (PhCW). (a) Lateral image of the employed optical excitation scheme, where both the chip and the fiber with the loop are clearly visible. (b) Detailed image of the obtained loop as observed with a 100x microscope objective, with the curvature R schematically shown. (c) Microscope image of the PhCW surface with the loop in contact and aligned with the waveguide axis, our typical measurement configuration. (d) SEM image of a closed W1 PhCW or an LN cavity. The micrograph shown here corresponds to an L31 cavity and differs from the one shown in (c), an L255 cavity, for clarity. (e) Reflection coefficient $|r|^2$ for different curvatures R, where only the first one has been explicitly calibrated with the top microscope after a $90°C$ tilt of the fiber taper loop. The scale is common to the three spectra, which are given in arbitrary units. The dashed lines mark the region where resonances are observed, clearly evidencing the increased bandwith with decreasing radius R.

the loop of desired size/curvature is created by a 3-step procedure: first, twisting the stretched fiber using rotating magnetic clamps (one full turn each); second, approaching the two translation stages by approximately 3 mm and, last, pulling the fiber again up to the desired loop size. The obtained shape has a fine dependence on the amount of pulling but a typical shape is shown in the image of Fig. 5.9(b), obtained with a 100x microscope objective. The curvature radius R in the region that will approximate the sample is highlighted, with an approximate radius of $R = 30$ μm. A lateral image of the fiber loop over a photonic chip is shown in Fig. 5.9(a), where the reflection over the surface of the full fiber/loop is also visible. The one-sided optical driving configuration is sketched with arrows, allowing us to measure both transmission $T = |t|^2$ and reflection $R = |r|^2$. The PhCWs are characterized by measuring the fiber transmission/reflection with the loop on top of the waveguide axis, as is shown in Fig. 5.9(c) with a microscope image of the chip surface, where both waveguide and loop can be seen. Whenever the PhCW is enclosed by using mirrors on each side, FP resonances are formed and their FSR can be used to characterize the dispersive properties of the band (see Subsection 5.1.2). These modes are mainly composed of a propagating and a counterpropagating Bloch mode of wavevector k, with discrete modes at each $\Delta k = \pi/L$, with L the length of the PhCW region. Those FP modes with k inside the shaded region shown in Fig. 5.7(a,b) are therefore phase-matched to the fiber taper mode and can therefore be probed both in transmission and reflection.

The dispersion characterization using FP resonances is achieved in a W1 waveguide by measuring LN cavities with $N \gg 1$, as the one on the SEM micrograph of Fig. 5.9(d), where $N = 31$. Both T and R obtained with a calibrated loop radius of 30 μm are shown in blue and red in Fig. 5.9(e), where a tunable near-infrared (NIR) external cavity diode laser (Yenista T100S-HP) is used for excitation and a wavelength-calibrated multiport powermeter (Agilent 8164B) for detection. Although we typically measure in a transmission configuration, the reflection spectrum (red) is often cleaner since virtually no other mechanism than light outcoupled from the FP resonances can contribute to the reflection signal. On the contrary, the transmission spectrum exhibits both low-amplitude oscillations due to the fiber-taper loop ring esonances [374] as well as contributions from any residual coupling to, e.g. a TM-like quasi-continuum. The effect of diminishing the taper curvature R is observed in the reflection spectra of Fig. 5.9(e), where R is only approximately obtained from the pull-back distance of the translation stages. The specific value of R is here of little relevance, what matters is that it confirms that the basic phase-matching rule described in Fig. 5.7 qualitatively describes our experimental conditions, as shown with the dashed lines which mark the range over which resonances are observed. We conclude that a minimum curvature R is desirable, although going below 25 μm is extremely complicated since the loop unwinds when the fiber is detached from the sample surface.

5.2.2 Experimental signatures of Anderson localization

The PhCWs explored in this thesis have been designed without any intentional disorder, but slight unintentional deviations of the fabricated structures from the as-designed geometry effectively lead to disordered PhCWs. These deviations are due to the fabrication process itself and include surface roughness, shape inhomogeneity, loss of wall verticality, etc. These types of distributed disorder have various effects on the transport properties of the PhCWs like out-of plane scattering [380,381], TE-TM like coupling [211,382] and/or backscattering [335]. The lattermost eventually leads to strong localization in a narrow frequency region around the slow-light region of the perfect waveguide, as thoroughly discussed before. Assessing the level and type of unintentional disorder in a fabricated photonic nanostructure is a topic of extreme interest and the most novel and accurate approaches actually rely on the scattering properties of light in the medium [217] rather than on high-resolution direct spatially-resolved imaging techniques like SEM, where charging effects and drift, edge effects, and scale bar miscalibration can lead to uncertainty in the geometrical feature extraction.

Nevertheless, since the precise assessment of the level of unintentional disorder is beyond the scope of this thesis, we employ high-quality and fast-scan SEM images to evaluate the fabricated geometrical parameters of the measured PhCWs. Special attention is devoted to the extraction of the average parameters, since this enables the calculation of the as-realized band structure, provided that the thickness t and the refractive index of silicon n_{Si} are well-known. We obtain the former from nearly tangent SEM inspection of the used structures in purposely introduced trenches, as can be seen in Fig. 5.10(a), while the latter is obtained from ellipsometry measurements[2] to be $n_{Si} = 3.482$. The image processing of a normal-incidence SEM micrograph of the LN cavity of Fig. 5.9 is shown in Fig. 5.10(b), with the fitted circles drawn in blue. The distributions of both the extracted radii r and the 1^{st} neighbour distances are shown in (c), where the conversion from pixels to nm is done by setting the mean of the distribution in (d) to be $a = 410$ nm, the design pitch of the fabricated structure. Although the resolution of the image is only of 0.5 nm/pixel, this treatment gives a mean radius of $\overline{r} = 131.5$ nm and together with t, n_{Si} and an average etch angle of $\theta_{etch} = 3°$ [Fig. 5.10(a)] allows us to calculate the expected band dispersion and group index n_g.

Group index fluctuations

With spectra like the one shown in Fig. 5.9(e) one can also reconstruct the experimental band dispersion (Subsection 5.1.2), and identify the frequency region where the waveguide enters the localization regime. This is done in Fig. 5.10(d) by comparing the simulated n_g obtained after FEM simultation of the extracted geometry (solid blue curve) and the experimentally obtained using the FP resonances shown in Fig. 5.9(e) and Eq. (5.3) (solid black curve). Despite a fairly good matching between the spectral lineshape of the simulated and experimental n_g, a better understanding of the deviations from ballistic transport is obtained when

[2]The ellipsometry measurements were done at DTU Fotonik.

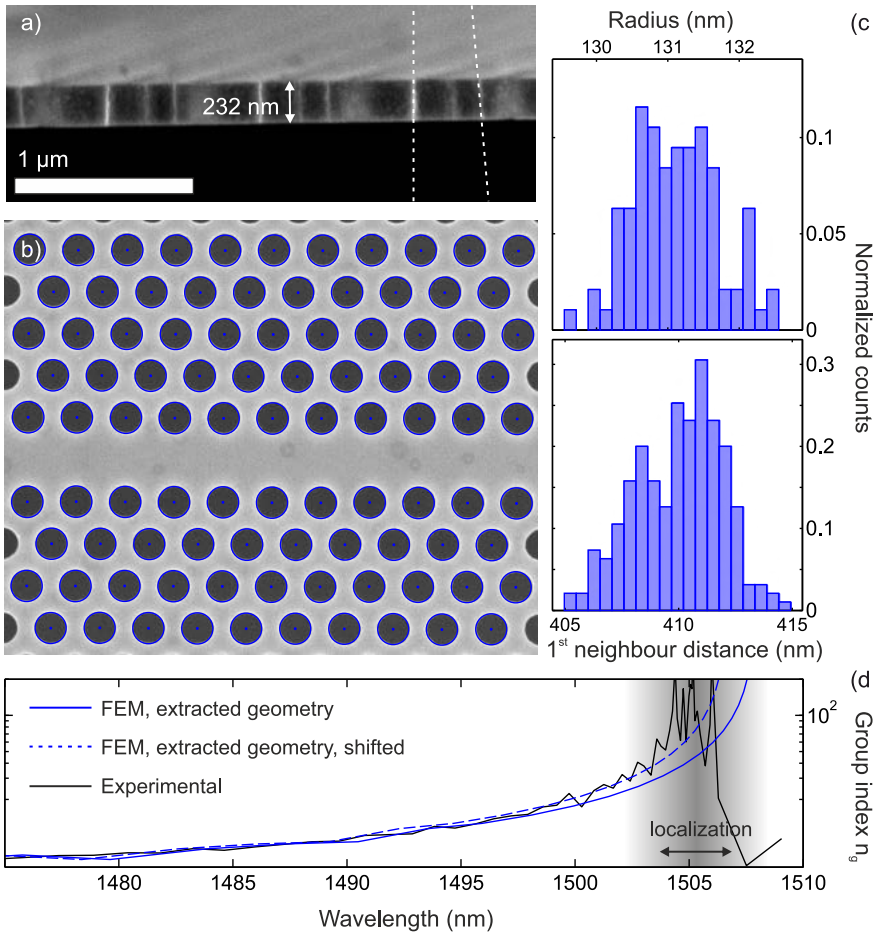

Figure 5.10: Experimental evidence of Anderson localization of light in an L255 cavity. (a) Nearly-tangent SEM micrograph of a trenched photonic crystal waveguide (PhCW), showing both the slab thickness and hole etching profile. (b) Normal-incidence SEM micrograph of a representative region of a L255 cavity, with blue circles showing the extracted holes after image processing. (c) Histograms of the extracted radii r (top) and first neighbour distance (bottom). The mean value $\overline{r}$ along with t, θ_{etch} and n_{Si} are used to compute the photonic band diagram using the Finite Element Method (FEM). The comparison of the FEM simulated (solid blue) and the experimentally extracted (black) group-index $n_g(\lambda)$ is shown in (d). The blue dotted line shows a wavelength-shifted version of the theoretical curve which corresponds to the best fit of experiment and theory over the ballistic region below $\lambda = 1503nm$.

the FEM simulated curve is shifted by $\delta\lambda = 1.25$ nm, which corresponds to the best fit in the region below $\lambda = 1503$ nm, i.e. in the ballistic regime. We find our 2D calculations shown in Fig. 5.6 to describe the full 3D bandstructure accurately by comparing the blue dotted and solid black curves. In a different collaboration with DTU Fotonik, we actually performed fiber-taper measurements on a set (5 realizations) of W1 waveguides of varying length L. Those were terminated with high-reflectivity grating couplers at the two end facets (see [383] for details) since they were originally conceived for free-space measurements. Fig. 5.11(a) shows the spectrum and n_g curve measured for a single realization of length L, while (b) shows the extracted maximum $n_{g,*}$ using a threshold value of $\delta_* = 0.13$. One needs

to recall or take into account that, as explained in Fig. 5.6, the x-axis showing the length L gives us a good approximation of the localization length ξ.

We attribute the appearance of strong n_g fluctuactions in these PhCWs to the onset of light localization and the spectral dips in that region to Anderson localized optical modes. An additional hint of the localized nature of the mentioned optical cavity modes can be obtained from comparing the spectral behaviour of a LN cavity and a W1 waveguide of same length. The pronounced difference in the boundary conditions at the end facets leads to a completely different spectrum in the region where light propagates freely, since light easily escapes the W1 waveguide, i.e. there are no FP resonances. On the contrary, the spectrum contains randomly located transmission dips in the frequency range where light localizes, as the effect of the boundary conditions is negligible since $L \gg \xi$. Fig. 5.12 plots the spectrum of an L255 cavity and a W1 waveguide with $L = 255a$ terminated with the silicon slab. While the L255 cavity exhibits strong FP resonances with a rather monotonously evolving FSR until λ = 1504-1505 nm (mid panel of Fig. 5.12(a)), the W1 shows only a nearly-continuous reduction of the transmission below that wavelength (mid panel of Fig. 5.12(b)). Minor oscillations are also present since index mismatch at the silicon slab termination still leads to some reflection at the end facets. Above λ = 1504-1505 nm, the two exhibit a series of unequal transmission dips with strong fluctuations in both frequency and linewidth, again a fingerprint of Anderson localization [384]. We hypothesize that some of these dips, specially at wavelengths above the cut-off, are not associated solely to the photonic structure but are due to a local confinement potential induced by the presence of the fiber taper loop, which increases the refractive index of the upper cladding and tunes the band edge [385]. These typically show up as broader dips with extreme sensitivity to the exact positioning of the loop.

Spectro-spatial mapping

Although several works have shown spatial mapping of a localized optical mode using a tapered optical fiber [370,386], the presence of a densely packed eigenspectrum combined to the sensitivity of the central wavelength and the coupled fraction to the positioning of the fiber taper makes spatially-resolved measurements rather complex in our case. Due to the atmospheric pressure conditions employed, we are forced to work with the fiber loop in contact with the waveguide surface, which leads to strong friction forces when the sample is displaced relative to the loop, complicating any automatization. Even when the loop is manually lifted and re-positioned somewhere else along the axis of the PhCW, the preceding exact transverse placement of the loop relative to the PhCW axis is lost, notably changing the optical coupling conditions. Placing the fiber and waveguide at an angle α can facilitate the task at the expense of lower average coupled fraction. Despite these difficulties, we show in Fig. 5.13 a spatial scan of size 39 μm with a spectrum taken each 3 μm. The spectral region above λ = 1505 nm corresponds to the region where Anderson localized modes show up. Although we are not able to assess the spatial shape of the modes, we see that some of the peaks only

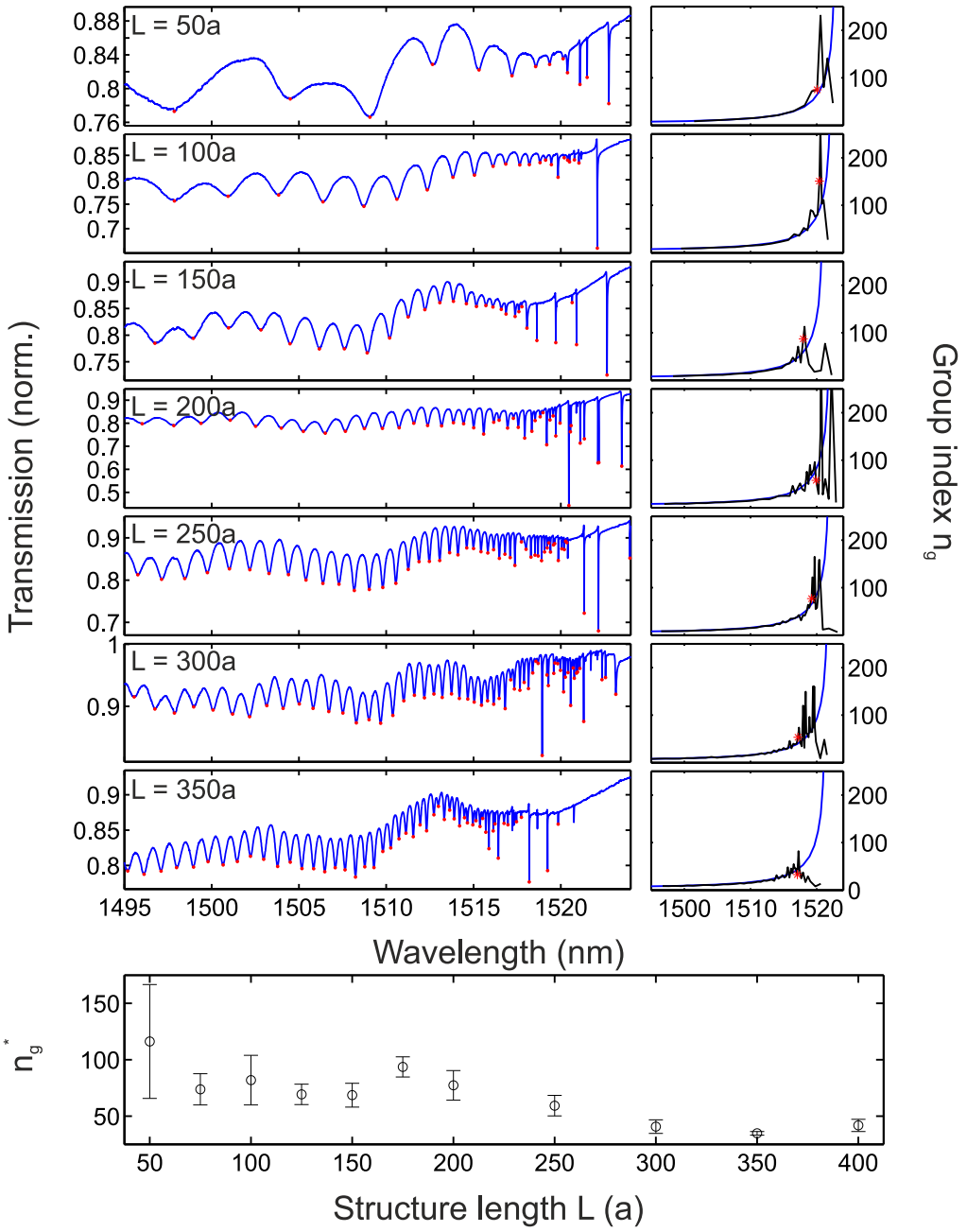

Figure 5.11: Estimating the localization length in closed photonic crystal waveguides (PhCWs). (a) Transmission spectra (left) of 7 W1 PhCWs of varying length L, with the extracted frequencies highlighted with red asteriks. The obtained group index n_g is given (right) with a solid black line, while the simulated -and shifted- is given with a solid blue line. (b) Mean value of the maximum n_g^* as obtained from the set of 5 measured waveguides, the error bar giving the standard deviation. The threshold is set to $\delta^* = 0.13$.

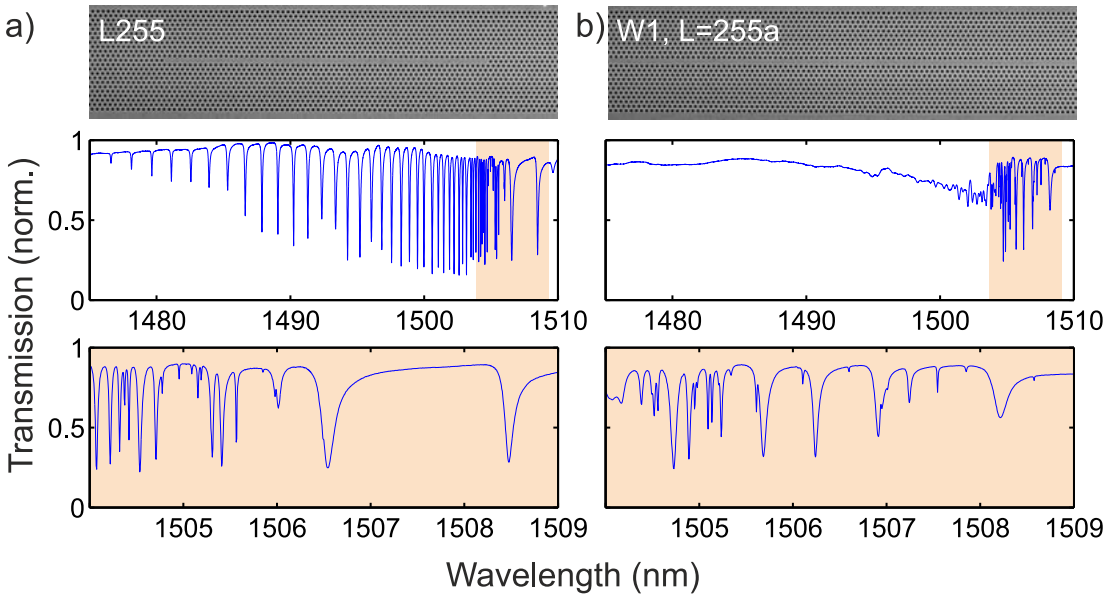

Figure 5.12: Spectral features of closed and open PhCWs. The transmission of an L255 cavity (a) over a broad (top) and narrow (bottom) wavelength range is compared to the one of a W1 waveguide of length $L = 255$a (b).

appear in a very narrow spatial region, another fingerprint of strong Anderson localization. Further work along these lines is currently underway.

Shamrock photonic crystal waveguides and alternative hints for Anderson localization

Up to now we have given strong evidence of how unintentional fabrication disorder localizes the light field in the slow-light spectral region of a standard W1 PhCW. Nevertheless, this type of waveguide does not support guided mechanical modes, making their use in optomechanics rather limited. For this reason, we have fabricated and explored the behaviour of PhCWs with shamrock-shaped holes instead of circles. A normal-incidence SEM micrograph of the geometry explored is shown in Fig. 5.14(a) with automatically fitted shamrocks included in blue and the main parameters highlighted. As can be seen from Fig. 5.14(b), the quality of the etching was rather poor both in terms of roughness and verticality, which complicates the fitting of the real structure with the imaged geometrical parameters. However, a better fit between the simulated band structure and the measured resonances is found when the average blue fit is expanded isotropically by $\delta x = 4$ nm, which corresponds well to the observed outer border around the shamrock. The band diagram of a structure with the fitted parameters and with that same shamrock extended by δx are shown in Fig. 5.14(b) in blue and red respectively. The position of the band edge for the latter fits well with the observed transmission resonances in the panel $\Gamma = 1$ of Fig. 5.14(d). The band of observed modes is frequency tuned by scaling the full in-plane structure by a factor Γ, as shown in the set of panels in Fig. 5.14(d), although the spectral position of individual

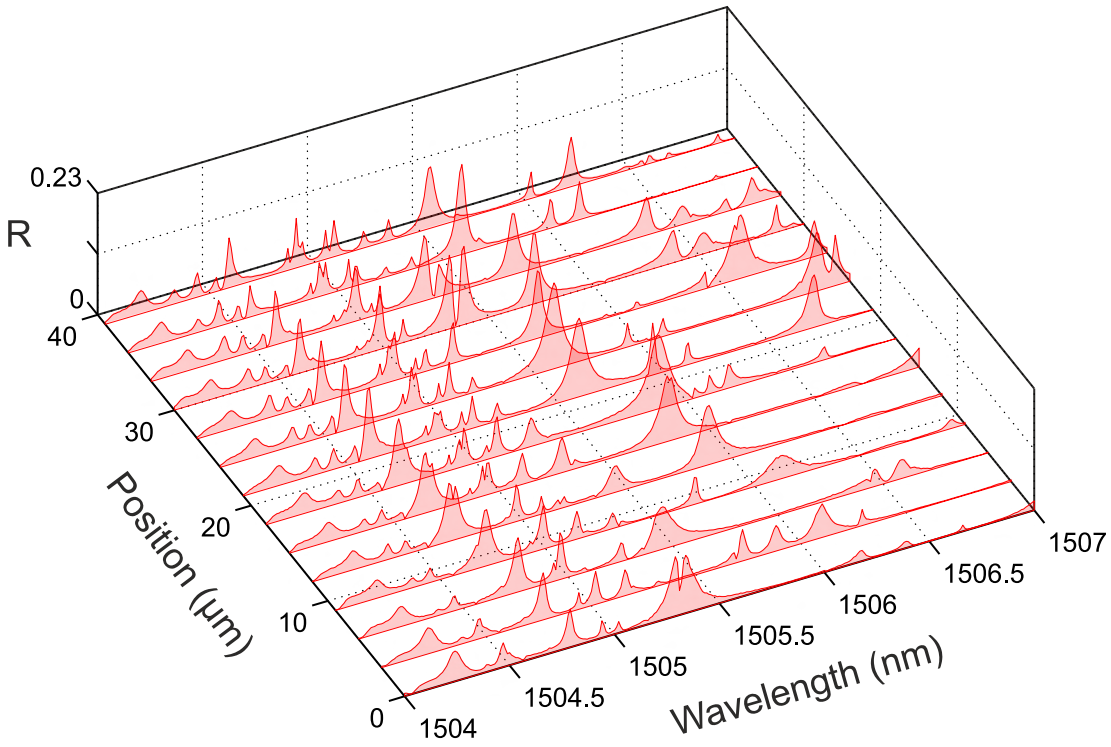

Figure 5.13: Spectro-spatial imaging of a W1 photonic crystal waveguide (PhCW) in the slow light region. Reflection spectrum obtained with a fiber taper loop aligned and in contact with the axis of a W1 PhCW when the sample is displaced along the axis of the PhCW in steps of 3 μm.

modes within this band is uncertain due to the complex nature of the system. Another collection of modes is observed at shorter wavelengths at aproximately 10 nm distance, which matches well the spectral position of the other simulated band. The small coupled fraction of the transmission resonances is due to the y-odd nature of the optical band, i.e. it corresponds to residual coupling from a slight misalignment with the waveguide axis.

Unlike with circular holes, these PhCWs do not exhibit a monomode y-even guided band as shown in Fig. 5.14(c), where we consider the full band above the light cone. This is the case unless the shamrock parameters are chosen to closely resemble a circle, which undermines the mechanical properties that we aim to explore. The multimode characteristics of the band has very important implications in the localization properties of the PhCW, since the elastic scattering into a (quasi)guided mode with momentum k' differing from k or $-k$ is allowed [339]. In addition, enclosing the waveguides with PhBG mirrors as done for LN cavities leads to a more intricate spectrum of FP resonances. This makes the interpretation of the transmission spectra in terms of Anderson localization harder than in the standard waveguides discussed in prevous sections. We analyze here both the distribution of the observed Q-factors as well as the spectral fluctuations in either the transmission or reflection spectrum, as shown in Fig. 5.15 for the case of $\Gamma = 1$ shamrock PhCWs. Transmission or reflection spectra as the one shown in (a) are taken at different positions of an $L = 150$ μm waveguide and treated

independently. The transmission resonances are fitted with a Lorentzian lineshape and used to obtain the intrinsic quality factor Q_i of the observed optical modes by employing the procedure described in Subsection 2.3.1. The values obtained for a particular resonance are given as an inset in Fig. 5.15(a). The broad distribution of Q factors obtained and shown in Fig. 5.15(b) has values in the range $10^3 < Q < 1.5 \cdot 10^5$ and a mean value of $Q \sim 1.6 \cdot 10^4$. By comparing these values with the ones calculated with a fully three-dimensional Bloch mode expansion technique [213], we can estimate the amount of fabrication imperfection as $\sigma = 0.005 - 0.007a$, although only out-of-plane losses are considered therein while our system is likely limited by in-plane radiation at the waveguide terminations as well. In addition, this implies that we map all the possible sources of intrinsic disorder to zero-mean Gaussian random displacements in the shamrock positions with a standard deviation σ. In any case, the value of σ found by comparison seems to be in good agreement with previous estimations of the tolerance of the fabrication process. By analogy with 1D systems as the one described in Chap-

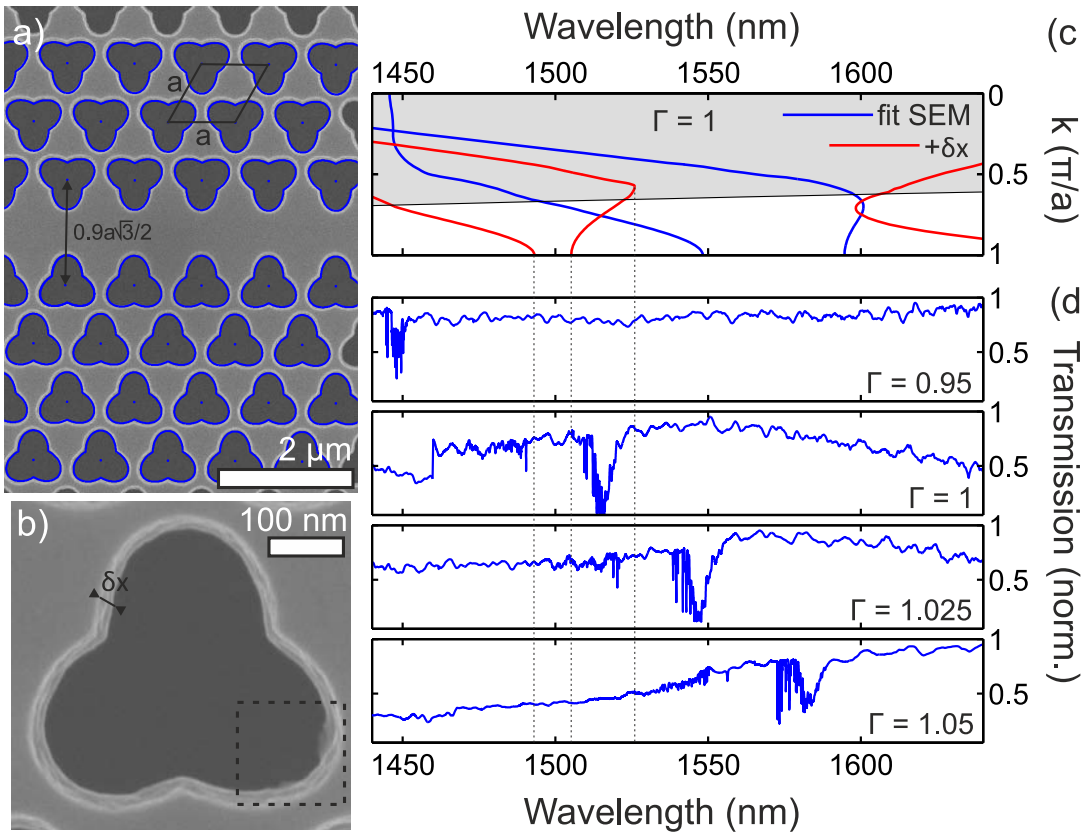

Figure 5.14: Optical characterization of shamrock photonic crystal waveguides (PhCWs). (a) SEM micrograph of a W=0.9 shamrock PhCW, with the two crystals facing each other. (b) Detail of a single shamrock hole highlighting the observed border of size δx that results from the low quality of the dry etching process. (c) Band diagrams of the PhCW with the parameters obtained from the mean values of the blue fits (blue) and with an expanded feature by δx (red). (d) Fiber-taper transmission spectra of waveguides with different overall scalings Γ, clearly evidencing the deterministic tuning of the overall band region.

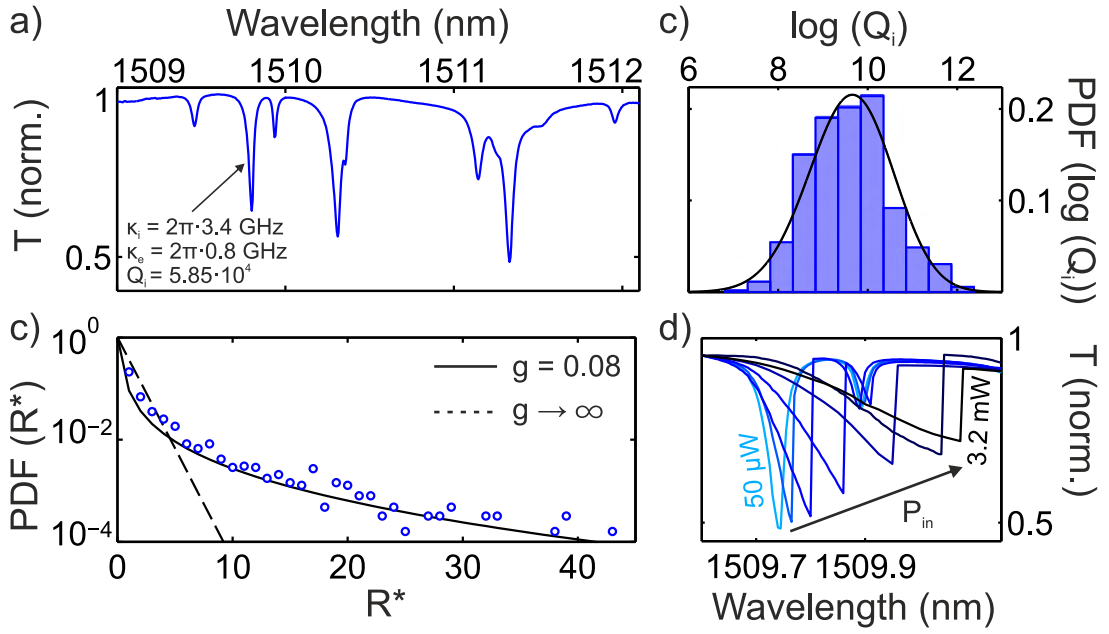

Figure 5.15: Experimental signatures of Anderson-localization in sharmcok photonic crystal waveguides (PhCWs). (a) Transmission spectrum of a $\Gamma = 1$ shamrock PhCW around the band edge. The properties of one mode as obtained from fitting the lineshape with a Lorentzian are given for reference. This is done for all modes around the band edge, at multiple locations and for several waveguides in order to acquire the Q-factor statistics shown in (b). The solid line gives a log-normal fit. (c) Reflection spectrum fluctuatins deviating from those expected in the Rayleigh scattering limit and fitted with the theory of Ref. [214] using $g = 0.08$. (d) Thermo-optic effect in an Anderson-localized optical mode driven at high power.

ter 4, in the limit of narrow resonances, we expect the Q-factor to be log-normal distributed in the localized regime [365,387,388]. Assuming no long-range correlations and in the absence of any other loss mechanism than leakeage at the boundaries of the disordered region, the in-plane Q, i.e. $Q_{\parallel}$, is distributed according to Eq. 4.38. In our structures, however, ξ/L is not enough to fully describe the experimental distributions. Other leaky channels such as out-of-plane scattering or material absorption have to be taken into account in addition to the in-plane losses. Although out-of-plane losses obey some distribution as well [213,339] we incorporate them to our model by adding a generic loss length, ℓ/L, which represents a truncation to the log-normal distribution expressed in Eq. (4.38). A detailed analysis of this procedure can be found in Refs. [365,389]. The final distribution is,

$$\mathrm{P}(Q) = \frac{1}{\sqrt{2\pi}\sigma} e^{-\frac{\left[\mu - \ln\left(\frac{QQ_{\perp}}{Q_{\perp}-Q}\right)\right]^2}{2\sigma^2}} \frac{Q_{\perp}\theta(Q_{\perp}-Q)}{Q(Q_{\perp}-Q)} \tag{5.6}$$

where Q is the quality factor including in-plane and out-of-plane losses and $Q^{-1} = Q_{\parallel}^{-1} + Q_{\perp}^{-1}$. Here, $Q_{\perp}$ represents the limit to the highest value that can be measured in the system, imposing a truncation to its log-normal distribution and is given by $Q_{\perp} = \frac{n_{Si}\pi}{\langle\lambda\rangle}\ell$. Using a Bayesian inference [390] approach, we calculate the

probability that ξ/L and ℓ/L determine the set of measured values of the Q-factor, $\{Q_i^m\}$ over the modes observed at 10 different positions. This leads to a fitting of the measured distribution (black line in Fig. 5.15(b)) with parameters $\xi/L = 0.045 \pm 0.015$ and $\ell/L > 10^4$. Here, the extra loss channel associated to the quasi-guided band to which the observed Anderson-localized modes can couple, does not impose a significant truncation to the observed Q-factor distribution, leading to narrow cavity resonances as in Ref. [335]. In addition, these values open the possibility for strong light-matter coupling induced by disorder [389].

A second fingerprint of localization in shamrock PhCWs is found by analyzing the fluctuations in the reflection spectra. These are preferred to transmission due to the absence of interference effects arising from the ring-like modes of the fiber-taper loop. The statistical analysis of these (strong) fluctuations is a powerful tool used to characterize the regime of localization [209]. In particular, the existence of very bright and spectrally well separated peaks is a fingerprint of Anderson localization and their analysis can provide significant information on the degree of confinement induced by disorder in our structures. To quantify the degree of confinement, we use a parameter, the dimensionless conductance g, initially proposed [391] in the scaling theory as a single scaling parameter to describe the conductor-insulator phase transition induced by disorder. This theory was extended to the case of classical waves by Van Rossum and Neuwenhuizen [214] and defined as the total transmittance, i.e., the sum over all the transmission coefficients connecting all input-output modes. It governs all the statistical aspects of light transport in a random medium [16] and sets the boundary for Anderson localization in absence of absorption at ($g \leq 1$) for three-dimensional structures [11]. For lower-dimensional structures, g determines the degree of confinement and can be extracted as a single parameter by fitting the reflected intensity distribution with the theory developed in Ref. [214] as

$$\mathrm{P}(R^*) = \int_{-i\infty}^{i\infty} \frac{\mathrm{d}x}{\pi i} \mathrm{K}_0(2\sqrt{-R^* x}) e^{-\Phi_{\mathrm{con}}(x)}, \tag{5.7}$$

where R^* is the normalized intensity, i.e. $R^* = R/\langle R \rangle$. Here, K_0 is a modified Bessel function of the second kind and $\Phi_{\mathrm{con}}(x)$ is obtained by assuming plane-wave incidence to be,

$$\Phi_{\mathrm{con}}(x) = g \ln^2 \left(\sqrt{1 + \frac{x}{g}} + \sqrt{\frac{x}{g}} \right) \tag{5.8}$$

This formula is valid in the regime of perturbative scattering and in the absence of absorption. For low values of the parameter g, Eq. (5.7) leads to a heavy tail of the intensity distribution which can only be explained in terms of Anderson localization. The extracted fluctuations (Fig. 5.15(c)) can be reasonably well fitted with a dimensionless conductance of $g = 0.08 \pm 0.01$, which is lower than in previous experiments [11,17]. We are aware that the experimental conditions herein are far from the hypothesis assumed to use Eq. 5.8 and from other experimental configurations where this has been used [392]; nonetheless, the large tail and the low value of g extracted constitutes a solid fingerprint of the localized nature of the modes.

5.2.3 Self-pulsing in Anderson-localized cavities

The shamrock geometry was inteded to enable the mechancial modulation of Anderson-localized cavities in the GHz range resulting from guided mechacial modes at these high frequencies. Unfortunately, we were unable to observe any OM modulation of the optical modes therein, even at the highest powers P_{in} of the available lasers. However, we do observe a modulation of the AL modes induced by a different mechanism at sufficient power P_{in}. The fundamentals of this modulation mechanism are explained in Subsection 2.3.1, where we describe how a highly-driven optical cavity can be brought into a state of self-oscillation by triggering material optical non-linearities. In this section, we describe this mechanism applied to AL modes, leading to all-optical RF modulation of a disorder-induced optical resonance [393].

So far, the optical transmission spectra shown were acquired at an incident power $P_{in} = 20\ \mu W$, which is low enough to obtain the linear Lorentzian response of the driven optical cavities. Driving the Anderson-localized mode at higher powers leads to more complex transmission spectra. The fiber DC transmission spectrum shows a thermo-optically mediated sawtooth-shaped transmission bistability at an input power typically around 150 μW, as plotted in Fig. 5.15(d). This power is rather high when compared to other nanostructures where only confined modes are allowed [96]. The coexistence of confined and propagating modes in our waveguides may open leaky channels to the coupled light, thus increasing the power required to achieve the nonlinear behavior. Finally, sweeping the excitation laser wavelength at higher powers drags the resonant wavelength to higher values, broadening the range of the hysteresis loop, as shown for powers up to $P_{in} = 3.2$ mW. This behaviour is a clear fingerprint of the presence of high Q/V photonic cavities and is observed for multiple of the resonances in the spectral range explored. An example can be seen in Fig. 5.16(a), where the linear response is shown in light blue. While some of the modes are strongly dragged by the thermo-optic (TO) effect, others are only slightly affected despite similar Q-factors, a manifestation of their differing mode volumes V. When the transmitted light is detected instead with a fast 12 GHz photoreceiver (New Focus 1544-B) and processed by a spectrum analyzer (Anritsu MS2830A) it reveals a frequency comb whenever the laser is resonant with the optical modes which exhibit a strong TO effect, as shown in Fig. 5.16(b). The revealed RF spectra in resonance with those optical modes exhibits many of the features that are shown in Fig. 2.4 for a simulated cavity undergoing self-oscillation. The origin of the anharmonic modulation is therefore attributed to the onset of a self-pulsing (SP) limit cycle. This is confirmed by time-resolving the transmitted light using a 4 GHz digital oscilloscope (Tektronix TDS7404) and using the signal itself as a trigger. The acquired time trace at wavelength $\lambda_L = 1510.7$ nm and driving the mode with a *cold* wavelength of $\lambda_o = 1510.34$ nm is shown in Fig. 5.16(c). This time trace shows most of the features of the simulated trace in Fig. 2.4. To recall the dynamics of this optical modulation, the set of panels in Fig. 5.16(c) sketches different frames of the period of the Anderson-localized mode oscillation around the laser wavelength, which is marked as a black solid line. Figures 5.16(c)(1-3) plot the first half period of the

oscillation when the cavity mode is progressively blueshifted due to a slow temperature recovery and a fast free-carrier population buildup. Far from resonance, at position (1), the transmission through the fiber at λ_L is maximum due to the poor coupling to the cavity mode. When the cavity is tuned on resonance with the laser —position (2)— the transmission through the fiber drops to the minimum due to the evanescent coupling of the transmitted light to the Anderson-localized cavity. The oscillation still continues to the maximum blueshift at position (3), for which the effect of heating of the sample overcomes the effect of the excess of free carriers and redshifts the localized mode back to its initial position.

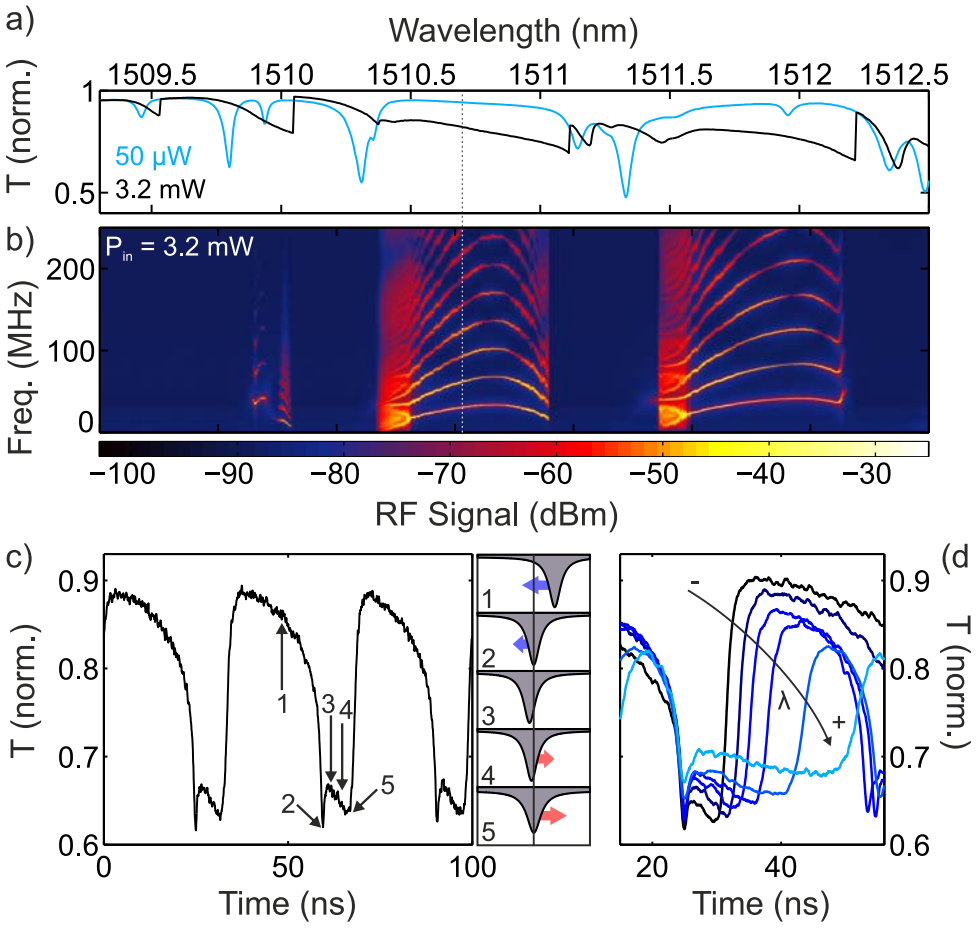

Figure 5.16: Self-pulsing (SP) dynamics in a shamrock photonic crystal waveguide (PhCW). (a) Optical transmission spectrum around the band edge of a shamrock PhCW in the linear (light blue) and non-linear (black) regime, exhibiting pronounced thermo-optic (TO) effect for many of the modes. (b) Radiofrequency (RF) spectral map as a function of wavelength obtained when detecting the transmitted signal with a fast photoreceiver. The modes with the highest TO effect enter a SP regime as described in Chapter 2. (c) Time-resolved transmission as obtained with an oscilloscope at the wavelength highlighted with a vertical dashed line in (b). A sketch of the relative position of the laser line relative to the cavity is given for points numbered 1 to 5. (d) Evolution of the duty cycle of the SP dynamics as a function of wavelength for the optical mode with a cold resonance wavelength $\lambda_o = 1510.3$ nm.

Table 5.1: Model parameters for the coupled differential equations governing the behaviour of a highly driven optical cavity.

Parameter	Value	Units	Origin
Refractive index (n_{Si})	3.458	-	[394]
Density (ρ_{Si})	$2.33 \cdot 10^{3}$	kg/m^3	[394]
Constant-pressure specific heat capacity ($C_{\mathrm{p,Si}}$)	$0.7 \cdot 10^{3}$	$J/(kg \cdot K)$	[394]
Two-photon absorption coefficient (β_{TPA})	$8.4 \cdot 10^{-12}$	m/W	[395]
Free-carrier absorption cross-section (σ_r)	$1.45 \cdot 10^{-21}$	m^2	[396]
Free-carrier dispersion cross-section (σ_i)	$-5.3 \cdot 10^{-27}$	m^2	[396]
Linear absorption coefficient (α_{lin})	3.68	m^{-1}	[397]
Refractive index temperature coefficient (n_{T})	$1.86 \cdot 10^{-4}$	K^{-1}	[398]
Thermal decay rate (γ_{th})	33	MHz	fit
Free-carrier decay rate (γ_{fc})	4.62	GHz	fit
Effective thermal volume ($V_{\mathrm{eff,T}}$)	$2.3 \cdot 10^{-18}$	m^3	fit
Free-carrier absorption volume (V_{FCA})	$8 \cdot 10^{-18}$	m^3	fit
Two-photon absorption volume (V_{TPA})	7	$(\lambda_c/n_{Si})^3$	[213]

Beyond the temporal modulation of the cavity, the material nonlinearities have an effect in the Anderson localization process. The optical nonlinearity has two main effects on the Q-factor of the Anderson-localized modes. First, the material two-photon absorption induces a dissipation mechanism which increases the optical leakage, thus reducing the Q-factor of the modes. This has been observed in previous experiments with resonant nonlinearity in standard silicon-photonic structures [93]. However, the nonlinear process probably induces an additional dephasing mechanism in the interference process leading to Anderson localization [399]. This decoherence mechanism further reduces the Q-factor and it is expected to fully destroy the localization effect in an infinite system [400]. As sketched in Fig. 5.16(c), the Q-factor of the Anderson-localized mode is considerably reduced from position (2) to position (5). This *fast* modulation of Q explains why the two resonant conditions shown in the time trace of Fig. 5.16(c) do not drop to the same value, a feature that cannot be explained by solely considering the dissipation induced by two-photon absorption and free-carrier absorption in the numerical model detailed in Subsection 2.3.1. This fast modulation is further evidenced in Fig. 5.16(d), where the shape of the time trace is shown at different wavelengths λ_L. Along with an increase of the duty cycle of the trace as was described theoretically, we see that the difference between the two resonant dips increases with the power dropped into the cavity, a fingerprint of stronger dephasing. The multiple scattering process adds yet another complexity to the picture. When few modes overlap spectrally and spatially, a complex collective behavior could be expected in the dynamics of the system due to their interaction. This spatial and spectral mode overlap can eventually result in complex temporal transmission traces that cannot be explained with a single-cavity model [337]. However, we do not observe these interaction effects in our experiment. This can be atributed to the suppression of mode interaction in the localization regime, even between modes that have significant spatial and frequency overlap, as predicted in Ref. [401] and confirmed by experiments on multimode lasing in the Anderson localized regime [402].

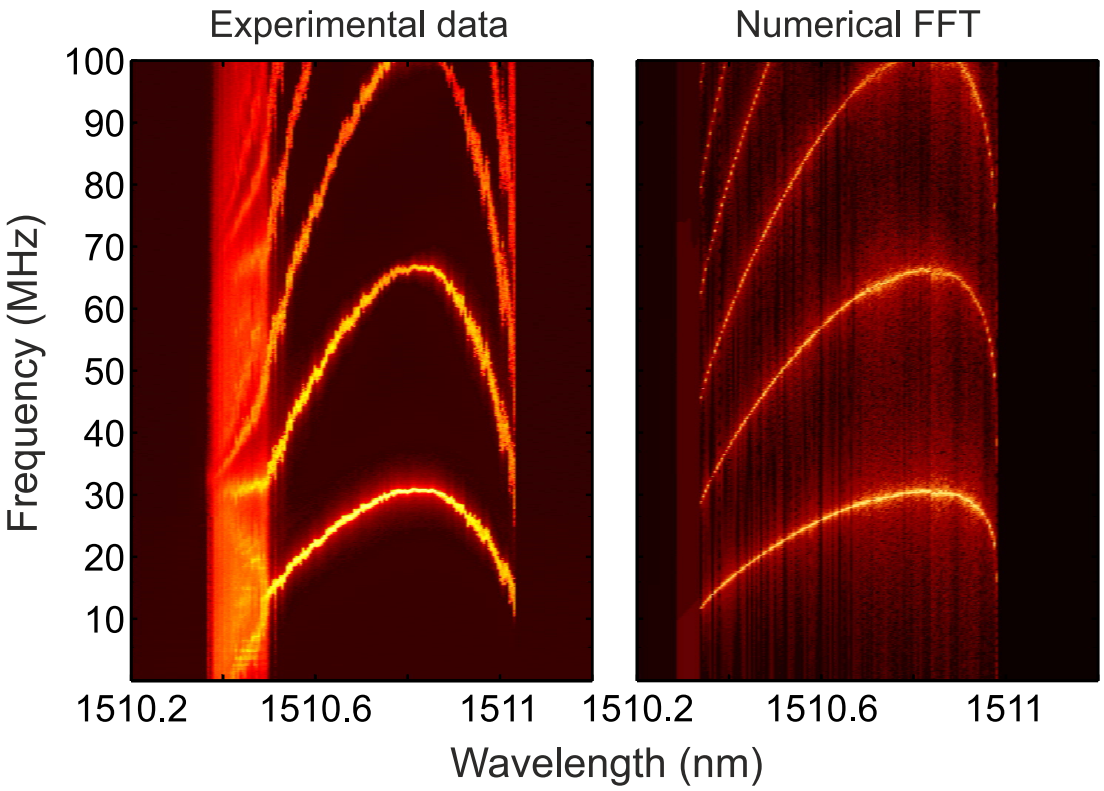

Figure 5.17: Comparison of the experimental radiofrequency (RF) spectral map to numerical simulations. The RF spectral map obtained for the optical resonance having a cold resonance wavelength $\lambda_o = 1510.3$ nm is compared to the Fast Fourier Transform (FFT) from the numerical simulations using the linear optical response and the parameters given in Table 5.1.

In the absence of multimode interference effects, we can use the model developed in Chapter 2 and extract the values of the unknown physical parameters therein, e.g. γ_{th} or γ_{fc}, by comparing the experimentally observed radiofrequency map to the FFT of the simulated transmission traces. Using the values in Table 5.1, we see that the numerical FFT in Fig. 5.17(right) qualitatively and quantitatively agrees with the experimental colormap, the only prominent differences being the initial region and the speed at which the system escapes the limit-cycle at the end of the resonance. Despite the considerable number of free parameters and the extensive use of data from the literature, an analysis of the sensitivity of the colormap to changes in those parameters confirm that the values have to be close to those given in Table 5.1. Particularly interesting are the different mode volumes $V_{eff,T}$, V_{FCA} and V_{TPA}, which confirm that the optical modes probed are highly localized. We observe this behaviour for shamrock waveguides and also for standard waveguides fabricated with circular holes, as the origin of this modulation mechanism are the silicon material nonlinearities common to both systems. The possibility to extract meaningful information on the modal volumes of Anderson-localized modes via its SP maps, combined with the estimates of ξ obtained by probing LN cavities makes this system a test bed to study the interplay between structural complexity and material nonlinearities and their impact

on localization phenomena. In addition, this radiofrequency modulation introduces a different functionality to the toolset of disordered photonics [403].

5.3 MHz-Optomechanics with Anderson localized optical modes

The PhCWs discussed so far don't exhibit any type of OM modulation either at low (MHz) or high (GHz) frequencies. This is probably due to a rather low OM coupling g_o or simply due to our experimental conditions, since the fiber loop is in contact with the structure and considerably damps the motion. Physically separating both sides of the crystal by introducing an air slot enables us to probe the OM modulation at both high and low frequency using our evanescent coupling scheme. In Chapter 3 we have discussed both TIR and PhC mirrors as means to confine light in a given physical volume. However, another confinement strategy based on a narrow sub-wavelength low refractive index region surrounded by a higher index medium can be achieved in a specific direction in what is called a slot waveguide [404]. The combination of a nanoscale air slot and a line-defect PhCW leads to slotted photonic crystal waveguides (sPhCW). The sub-wavelength confinement provided by the slot and geometry-controlled dispersion engineering provided by the PhC pattern make sPhCWs an ideal building block for three-dimensional confinement with minimal footprint and a relevant platform for free-space cavity quantum electrodynamics (cQED) experiments with atomic ensembles [405,406] and index-sensitive sensing [407]. High-Q slot-confined cavities based on linear sPhCWs have been observed in slot-width [408] and waveguide-width [409] modulated configurations, as well as on heterostructures [410]. Additionally, the tightly localized electric field near the air/dielectric boundary imposes a large radiation pressure force on the slot sidewalls, which leads to a pronounced coupling of the slot-guided optical modes with low-frequency differential motion of the two sides of the waveguide [411]. Light-motion interaction in nanoscale slotted systems has also been explored in near-field evanescently-coupled pairs of OM structures [386], single or multiple slot-in-the middle PhC cavities [412,413] and one-dimensional sliced PhC nanobeams [189], the latter exhibiting a many-fold increase in the vacuum OM coupling rate g_o introduced in Chapter 2 as compared to previously existing OM systems.

This approach allows us to exponentially increase the coupling strength by simply decreasing the width of the slot [414,415]. However, several tenths of nanometers-wide air slots along many micron-long structures unavoidably suffer from (additional) uncontrolled imperfections appearing during the fabrication process, e.g., sidewall roughness. Extremely high as-designed Q-factor cavities ($Q \sim 10^6$) become specially sensitive to such imperfections, leading to additional radiation channels and experimentally observed quality factors far from the calculated values [408,409,416,417]. Nevertheless, the interplay between order and disorder in a sPhCW may itself induce strong light confinement as explained for standard PhCWs. In this section we assess how to use the air slot width as

a deterministic parameter enabling low-frequency cavity-optomechanics experiments with Anderson-localized optical modes and we experimentally evidence a pronounced OM coupling in unintentionally disordered sPhCWs where Anderson-localized optical cavities couple to extended mechanical modes with observed frequencies up to 600 MHz.

5.3.1 Slotted photonic crystal waveguides

First, we explore sPhCWs based on a standard W1 PhCW with an additional slot of variable width s along the waveguide axis. The resulting geometry for a slot of size $s = 78$ nm, circular hole radii $r = 147.5$ nm, pitch $a = 470$ nm and thickness $t = 240$ nm is shown in Fig. 5.18(a). Its TE-like band structure is shown in Fig. 5.18(b), where the same color code as in Fig. 5.1 is used. The band of interest in the sPhCW is plotted with a thick blue line, while the field

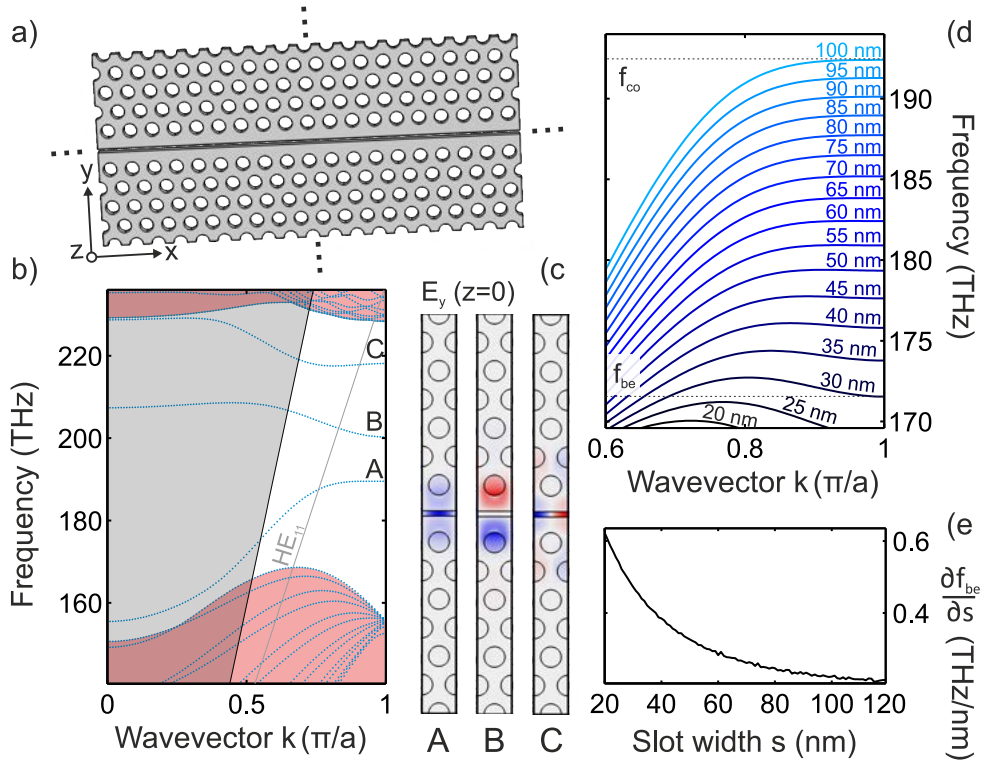

Figure 5.18: Band structure of a slotted photonic crystal waveguide (sPhCW). (a) Schematic of a sPhCW, which consists of a W1 waveguide with an additional air slot in the direction of the line-defect. (b) Band structure of the structure shown in (a) for the geometrical parameters $s = 78$ nm, $r = 147.5$ nm, $t = 240$ nm and $a = 470nm$. The light cone and the bulk bands are shown with shaded grey and red respectively. (c) $E_y(x, y, z = 0)$ for the highlighted bands (A,B and C) at the band edge ($k = \frac{\pi}{a}$), showing either even or odd parity with respect to the waveguide axis. (d) Fundamental slot-band as a function of the slot width s from $s = 20$ nm (black) to $s = 100$ nm (light blue). The cut-off f_{co} and band-edge f_{be} frequency are highlighted for two of the slots. (d) Rate of change of f_{be} as a function of the slot width s, showing an exponential behaviour.

profile $E_y(x, y, z = 0)$ of that band (A) and the two above (B and C) at the high-symmetry point $k = \pi/a$ are given in Fig. 5.18(c). We see that both A and C have a strong fraction of the electromagnetic field inside the air slot but the field partially extends into the surrounding PhC. This leads to a diverging group index n_g and allows slot-guided slow light. We denote these two bands as the fundamental and first order slot-bands. On the contrary, mode B looks very similar to the corresponding mode in Fig. 5.1(c), and we denote it as the W1-like mode. In addition, this sPhCW does not sustain any other guided or quasi-guided mode in the frequency range of the fundamental slot-band, which avoids excessive extrinsic out-of-plane losses in the presence of fabrication disorder [339,411].

Due to the strong confinement of the light field inside the slot, the highlighted band is extremely sensitive to the slot width s. Fig. 5.18(d) plots the band dispersion as a function of s, showing how the cut-off f_{co} and band edge f_{be} frequencies of this mode change by more than 20 THz when going from $s = 20$ nm to $s = 100$ nm, while the overall dispersion conserves the monomode condition for all slots above $s = 50$ nm. Any differential displacement of the two high-index regions leads to a change Δs of the slot width. The high sensitivity $\frac{\Delta f}{\Delta s}$ has a strong impact on the OM coupling rates g_o between an optical cavity drawn from that band and any in-plane relative displacement of the slot walls. This stems from the definition of g_o, which evaluates the frequency shift of an optical cavity mode with respect to a displacement of amplitude x_{zpf}, the zero-point fluctuations of the mechanical resonator considered. Fig. 5.18(e) depicts the rate of change of f_{be}, which increases with decreasing slot size s. The expected g_o increases exponentially with decreasing s. Strong light localization along the slot will therefore lead to pronounced coupling between light and motion in this system, which is our main approach to analyze the OM coupling mediated by disorder.

Similarly to the PhCWs analyzed in previous sections, the full 3D slotted waveguide is very challenging to be modelled with current numerical tools if we add complexity or disorder. 2D FEM simulations are therefore our only option to understand the behaviour of sPhCWs. Unfortunately, unlike the W1 waveguide, the effective refractive index approximation allowing us to transform the 3D problem into a 2D problem does not hold in this case because the bands of this system are not well described by the first TE mode of the slab. While the simulated bands shown in Fig. 5.18(d) exhibit a monomode band with monotone increasing n_g up to nearly the band edge for most values of s, their 2D counterpart using an effective index n_{eff} for silicon do not. Our strategy to approximate the band diagram of the 3D structures keeping the value of s fixed consists on changing the geometrical parameters of the waveguide. Fig. 5.19 plots the results following this strategy to calculate the localization length ξ for a sPhCW with W = 0.84, $s = 78$ nm, $a = 470$ nm, $r = 147.5$ nm and $n_{eff} = 2.844$. As shown in panel (a), the band is not single mode, so we calculate ξ as a function of frequency ν and not as a function of n_g (Fig. 5.19(c)). We calculate the localization length for positional disorder with $\sigma = 0.01a$, a value larger than the one used for the W1 waveguides, to account for the surface roughness on the slot itself. Under this condition, the localization length is not equal to the backscattering mean free

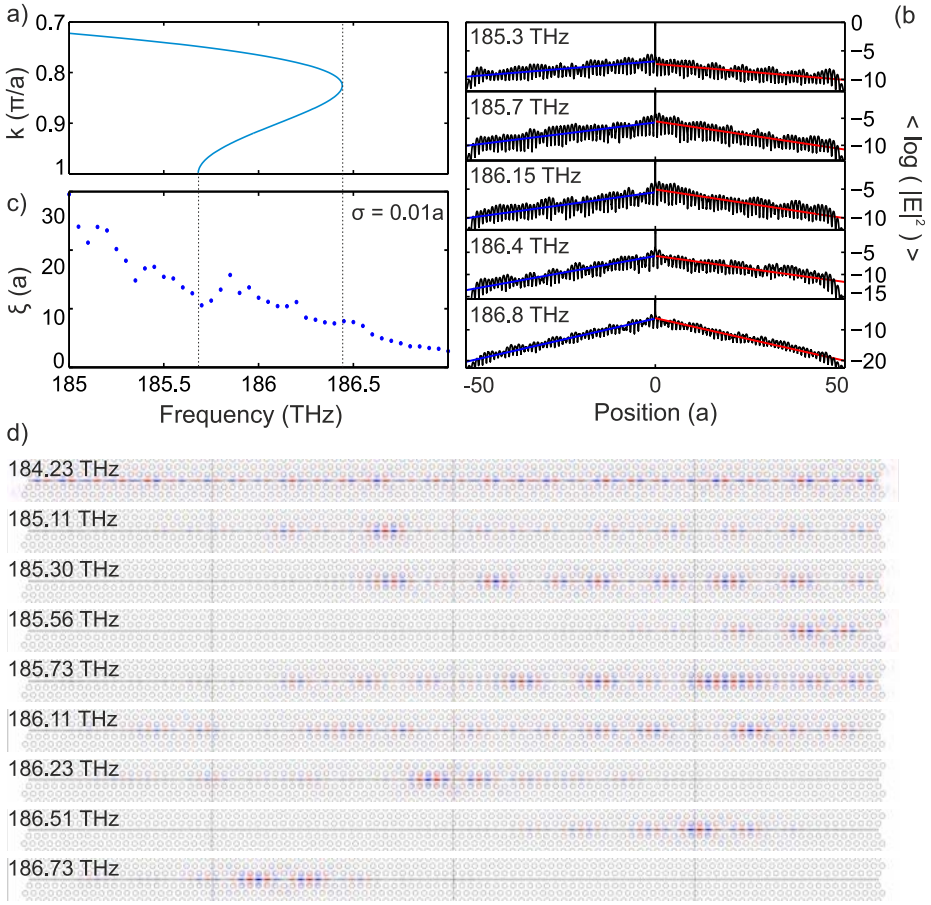

Figure 5.19: Photonic localization length ξ in a disordered slotted photonic crystal waveguide (sPhCW). (a) Slot-guided band dispersion close to the cut-off frequency f_{co} for a 2D sPhCW of parameters $s = 78$ nm, $r = 147.5$ nm, $a = 470$ nm and W=0.84. (b) $\xi(\nu)$ for a positional disorder of $\sigma = 0.01a$, as obtained from the averaged intensity $|E|^2$ emitted by a dipole along the axis of a disordered waveguide. (c) Both sides are fitted (blue and red) with an exponential from which the localization length ξ is extracted. (d)

path in this particular waveguide. The fits of the ensemble-average emitted light intensity are given for some of the calculated frequencies ν in panel (c), showing anomalously different slopes on both sides for some frequencies, a behaviour that is under exploration. For the range 185-187 THz the extracted localization length ξ is below 30 unit cells. This is associated to the formation of slot-guided localized modes, as shown in panel (d), where the geometry in the y-direction has been cropped for clarity. These calcualtions allow us to visualize the effect of disorder in a sPhCW and give us a qualitative description of the dispersion of ξ and the modal volumes of the localized modes in the system.

5.3.2 Optomechanical coupling to in-plane differential motion

The strong dependence of the fundamental slot-band on the slot width s can be used to design efficient cavity OM systems as, e.g., an engineered heterostructure optical cavity coupled to the fundamental in-plane differential mode of the membranes bounding the slot. Although the 3D simulation of the mechanical eigenmodes is computationally feasible due to the absence of surrounding air boxes and PMLs, the calculation of the coupling rates requires both the optical and mechanical eigenfields. We therefore continue with 2D simulations as described in the previous section to have a qualitative estimation of the expected OM couplings. Additional trenches etched on each side of the waveguide are introduced to enable efficient in-plane motion of the membranes. The particular geometry for a $L = 100a$ waveguide is shown in Fig. 5.20(a) along with the displacement profile of the main breathing-like mechanical resonance.

While this 2D approach has certain limitations on the analysis of the optical properties of our structure, the mechanics of the in-plane mechanical modes[3] are well captured by using a plane stress approximation [418]. We have simulated a set of 100 realizations of 2D sPhCW as the ones used for Fig. 5.19 and computed the OM coupling rate g_o between the first 30 mechanical eigenmodes and the 30 optical modes with eigenfrequencies closest to the cut-off frequency f_{co}, which comprises the modes within the 185-187 THz range for which $\xi(\nu)$ has been given in Fig. 5.19. In this system, the moving boundary contribution $g_{o,mb}$ (Eq. 3.33a) in the slot-guided mode largely surpasses the photoelastic contribution $g_{o,pe}$ (Eq. 3.33b), so here only the former is considered. In addition, the effective mass m_{eff} of the mechanical eigenmodes is computed by considering the 2D solutions to be invariant across a slab of thickness $t = 240$ nm, which leads to values with the right order of magnitude. Unlike a standard PhCW whose naturally achieved end-facets (a silicon slab) lead to a rather weak confinement, as confirmed by Fig. 5.12, a slotted waveguide bounded at its ends with silicon slabs effectively behaves as a closed system due to the abrupt termination of the air slot, leading to prominent FP resonances. We use the sPhCW without disorder as a reference to estimate the enhancement of g_o in the Anderson-localization regime. The calculated OM coupling in a perfect sPhCW and a set of disordered sPhCWs is plotted in Fig. 5.20(b) for a disorder strength $\sigma = 0.01a$. For an unperturbed waveguide the mechanical eigenmodes can be split into symmetric and antisymmetric with respect to the plane defined by the waveguide axis and z. Here we only include the symmetric modes, since the antisymmetric ones are optomechanically dark. One should nevertheless bear in mind that each eigenmode is actually associated to a nearly-degenerate antisymmetric mode in which the two sides oscillate in phase. On the contrary, disorder breaks that particular symmetry and to some extent hybridizes the two modes [414]. For this reason, we include all the mechanical modes in the case of the disordered sPhCW.

[3] We here limit our scope to z-symmetric in-plane eigenmodes since flexural antisymmetric modes are optomechanically dark.

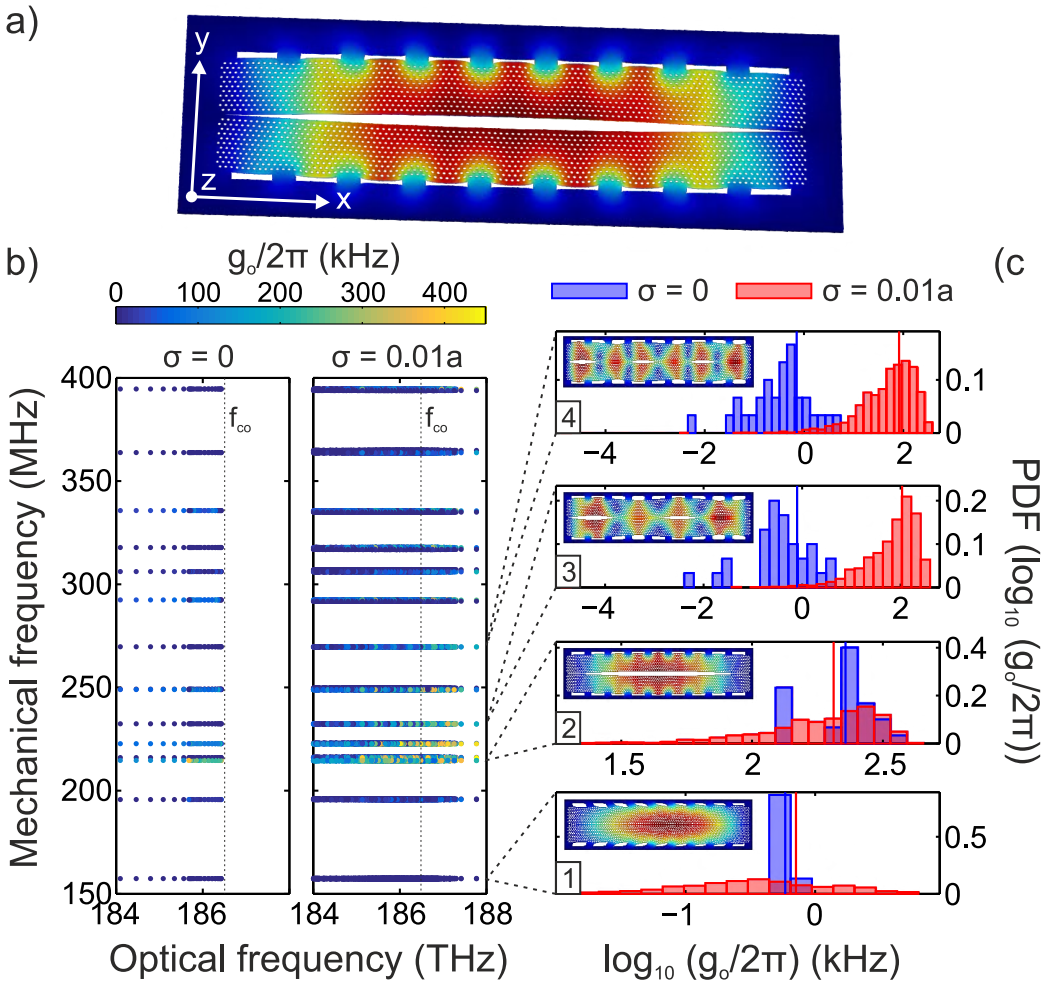

Figure 5.20: Optomechanical (OM) coupling in a disordered slotted photonic crystal waveguide (sPhCW). (a) Geometry and fundamental in-plane differential mode of a slotted photonic crystal waveguide with lateral trenches. (b) Scatter plot of the optical and mechanical eigenfrequencies in (left) an unperturbed L=100a 2D sPhCW and (right) a set of 100 disordered L=100a 2D sPhCW, with positional disorder of level $\sigma = 0.01$a. The slot-guided mode cut-off f_{co} is marked with vertical lines in both panels. The mechanical eigenmodes of the perturbed structures are easily attributed to the original unperturbed modes (the scattered dots roughly remain on horizontal lines) and the distribution of g_o associated to a given mechanical mode with all optical modes can be computed. This is shown in (c) for the 4 mechanical modes shown in the insets, both for the unperturbed (blue bins, $\sigma = 0$) and disordered (red bins, $\sigma = 0.01$a) structures.

Several conclusions can be drawn from Fig. 5.20. First, the optical eigenfrequencies in the disordered sPhCWs are not distributed into clusters around the eigenfrequencies of the unperturbed case, showing a strong effect of disorder which is associated to light localization. In addition, resonant optical modes are clearly visible above the cut-off frequency f_{co} (marked with a dashed line in Fig. 5.20(b)) which evidences the formation of a Lifshitz tail. On the contrary, the mechanical eigenmodes are barely sensitive to the imposed disorder and they

remain easy to identify by the sole observation of their frequency. This is especially the case for the type of disorder introduced, since it does not change the masses of both sides. In terms of the coupling rates g_o achievable, disorder can turn modes that are poorly coupled into highly coupled mechanical modes, altough some mechancial modes induce high coupling for the perfect and disordered system indistinctly. Fig. 5.20(c) shows the log-scale histogram of g_o as obtained from all 30 optical modes and each of the four highlighted mechanical modes, with red (blue) bars showing the distribution for the (un)perturbed sPhCW. The bottommost panel shows how shear modes without pronounced y displacement –and therefore $\Delta s \sim 0$– are not importantly coupled in any of the cases. In the case of the the fundamental breathing mode at $f_m = 212$ MHz (histogram 2), a nearly-rigid Δs leads to coupling values as high as $g_o = 2\pi\cdot$ 400 kHz both in the ordered and disordered case, with an actual lowering of the mean value for the disordered platform (the mean values are shown with the vertical lines). In the case of the n-th order breathing mode with n being an odd integer, the situation is similar but with a slight increase of the mean $< g_o >$, although not shown. On the contrary, breathing modes with even n are in principle optomechanically dark in the absence of disorder, but the localization of the light field radically enhances their coupling, as shown in histograms 3 and 4. The blue histogram should in principle be pinned to $g_o = 0$, but the numerical imprecision leads to distributed finite values, while in the disordered case values nearly as high as for the fundamental breathing mode can be reached. The same generally applies for higher even order modes.

We evaluate the overall effect of disorder by taking the distribution of the obtained g_o between all 30x30 pairs. The resulting histograms are shown in Fig. 5.21 for two different values of the slot width $s = [78,100]$ nm and three different disorder levels $\sigma = [0.005, 0.01, 0.02]a$. The distribution for the unperturbed case ($\sigma = 0$) is also given and the mean value $\langle g_o \rangle$ is pin pointed with a vertical line in each panel. The probability distribution functions evolve from a rather broad distribution in the unperturbed case to one that peaks around $g_o \sim 2\pi\cdot$ 100 kHz, for all three values of s. The extracted mean $\langle g_o \rangle$ for the three slots is given in Fig. 5.21(b). To evaluate quantitatively the role of s in the OM coupling properties, one should compare the distributions obtained for structures operating under the same localization length ξ. This is not done here, but these simulations show how reducing s induces an enhanced OM coupling in the Anderson-localization regime, something that is experimentally checked later in this thesis. Narrower widths have not been considered here since the 2D approximation increasingly fails to reproduce the bands for shrinking s. In addition, the shape and dimensions for the trenches have not been engineered at all, so we expect that more carefully designed structures [419] can achieve higher values of g_o.

5.3.3 Optomechanical spectroscopy

sPCWs with several overall scalings including different nominal slot widths $s =$

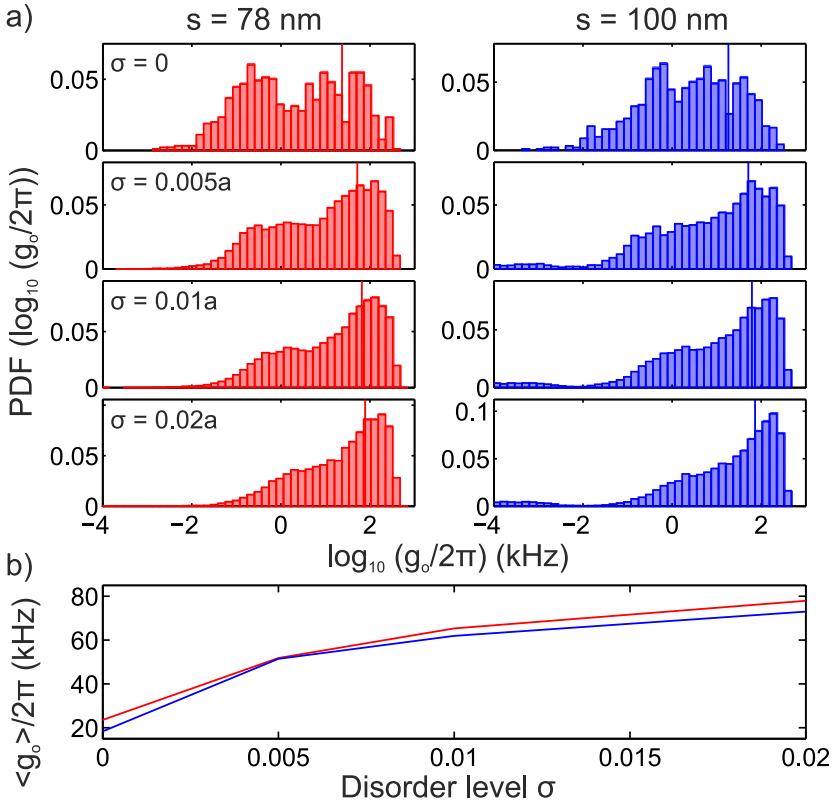

Figure 5.21: Statistical assessment of g_o in disordered slotted photonic crystal waveguides (sPhCWs). (a) Log-scale histogram of the obtained optomechanical (OM) couplings g_o for three different levels of disorder $\sigma = \{0.005, 0.01, 0.02\}a$ and for two slot widths $s = 78$ nm (left, red) and $s = 100$ nm (right, blue). The distribution in the unperturbed case is also given on top and the mean values are marked with vertical lines of the corresponding color. (b) Mean OM coupling $\langle g_o \rangle$ as a function of disorder level σ for both slot widths. The color of the line is chosen accordingly.

$\{20, 40, 60, 80, 100\}$ were fabricated at DTU Fotonik. The type of devices that are described herein correspond to sLN cavities, i.e. slotted LN cavities. Although direct termination also leads to pronounced FP resonances, their quality factor Q is highly improved when embedded between PhC mirrors. An SEM micrograph of the termination of one such cavity with $s = 100$ nm and $N \gg 1$ is shown in Fig. 5.22(a).

Waveguides with nominal $s = 20$ nm were unfortunately not fully developed since the dry-etching process did not reach the top of the silicon oxide layer of the SOI wafer, leaving a very thin (≈ 10 nm) silicon layer at the base of the slot, as evidenced by the contrast of the leftmost SEM micrograph of Fig. 5.22(b). The rest of the slots were fully etched and Fig. 5.22(b) shows a typical normal-incidence SEM image of the fabricated structures, with the realized widths s given above. These were extracted as the average over multiple normal-incidence SEM micrographs of the width of the rectangle best-fitting the slot. These SEM images also reveal the surface roughness of the slot walls and its width dependence, a type of disorder that probably controls out-of plane and backscattering losses to

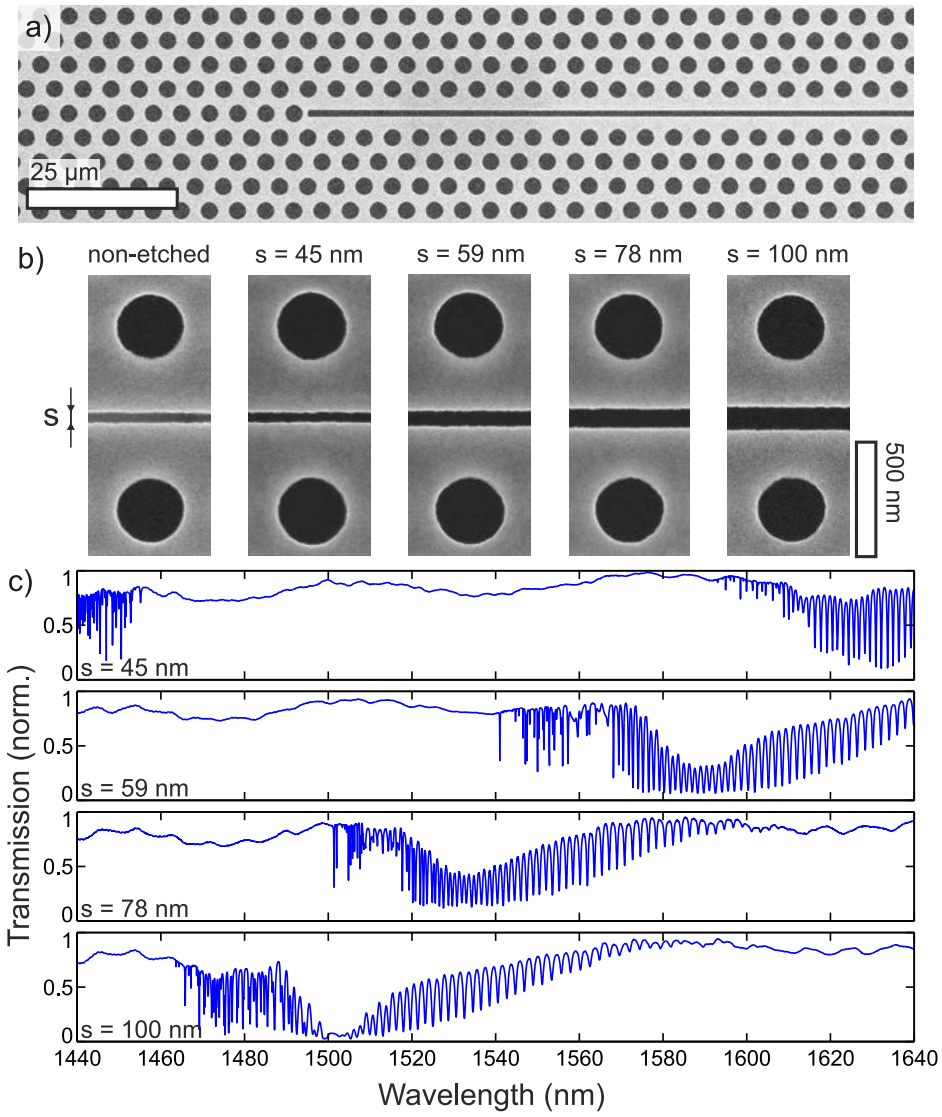

Figure 5.22: Optical characterization of slotted photonic crystal waveguides (sPhCWs). The optically probed sPhCWs are enclosed between photonic crystal mirrors to form sLN cavities, the left boundary of which is shown in (a) for a sPhCW with $s = 100$ nm and $N \gg 1$. (b) Detailed SEM micrograph of a representative region of the sPhCWs, with fabricated slots of widths $s = \{45, 59, 78, 100\}$. (c) Transmission spectra using the fiber-taper evanescent coupling technique of a sL309 cavity with varying s, showing the strong effect of the slot width on the spectral position of the band.

a much larger extent than hole radii or position fluctuations [420].

Optical characterization

We chacacterize optically the sLN structures using the fiber setup described previously. Due to the positive slope exhibited by the slot-guided mode within the first BZ, phase-matching is expected within a considerable bandwith, nearly up to the crossing with the light line, as shown in Fig. 5.18(b) by the precise dispersion of the HE_{11} mode of a $d = 1.5$ μm. The fiber is placed parallel to the waveguide

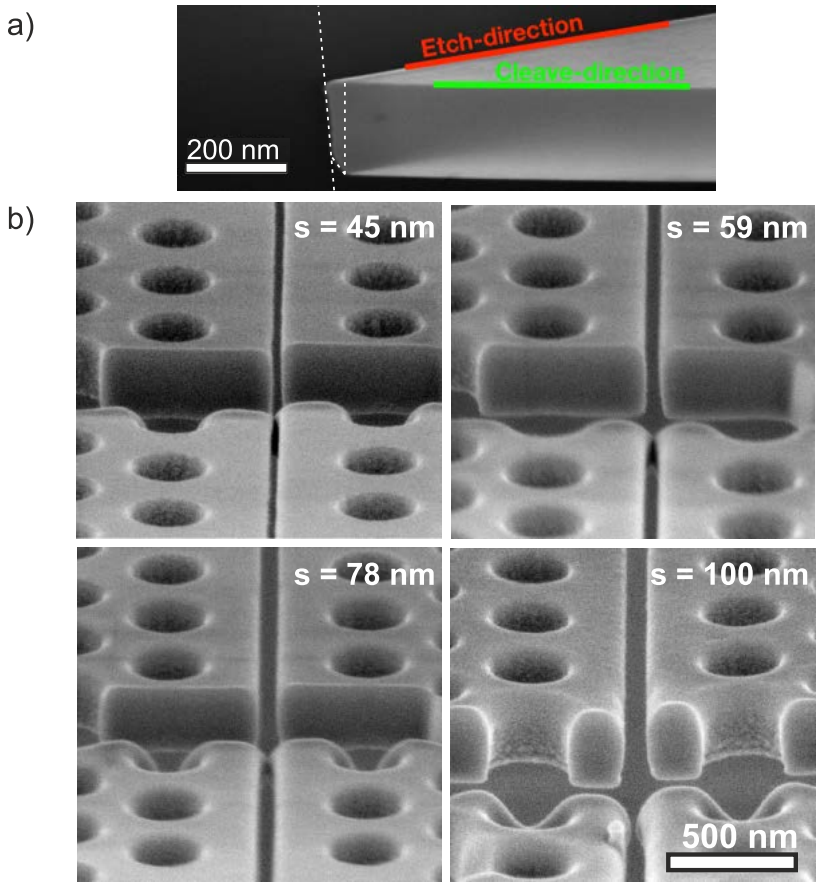

Figure 5.23: Etch verticality in fabricated features. (a) Etch profile along a [1 0 0] cleaved trench, with white dashed lines highlighting a possible geometrical representation of the sidewall. (b) Nearly-tangent SEM micrographs of focused-ion beam cut slotted photonic crystal waveguides (sPhCWs), showing the vertical profile of the slot trenches.

axis and aligned with it. Transmission spectra of sL309 cavities with varying slot width s are shown in Fig. 5.22(c). For the smallest slot of $s = 45$ nm, two sets of modes are visible close to the limits of the employed tunable laser. We asume that the band that starts close to $\lambda = 1590$ nm at $s = 45$ nm and shifts towards lower wavelengths with increasing s is the fundamental slot-guided band. Transmission resonances with monotonously increasing FSR appear on the long wavelength side, which is lost towards lower wavelengths where a collection of resonances at random spectral positions is observed. This represents an underlying band structure with a positive slope in the first BZ, which is a clear fingerprint of the fundamental slot-band. Nevertheless, the simulated band structure as obtained with the geometrical parameters extracted from the SEM micrographs does not allow us to indentify unambiguously the observed bands. The matching between the experimental spectral position and the simulated one is rather poor in this case, with an approximate offset of $\Delta\lambda = 100$ nm.

In-plane parameters $\{s, r, a\}$, thickness t and refractive index n_{Si} are known

with considerable accuracy, so we attribute the observed large systematic mismatch between simulation and measurement to a pronounced loss of the etch verticality, certainly larger than the one shown for the W1 PhCW of Fig. 5.10, where we had $\Delta\lambda = 25$ nm. The etch profile obtained by cleaving the sample perpendicular to an exposed trench is shown in Fig. 5.23(a). The etch profile is not vertical. An overall etch angle of approximately $\theta = 5°$ is observed and remains rather constant up to a depth $h_1 = 200$ nm, with an additional notching effect at the bottom 40 nm of the slab. This profile can be acounted for by considering a two slope profile given by parameters $[h_1, \theta_1] = [200$ nm, $5°]$ and $[h_2, \theta_2] = [40$ nm, $30°]$. Nevertheless, notching effects are often highly dependent on the exposed feature [421]. To assess the etch profile at the level of the sPhCWs, some of the devices were cut using a focused ion beam (FIB) accross both the circular holes and the slot trench[4]. Some SEM micrographs taken at a tilt angle of 20° are shown in Fig. 5.23(b). Although FIB exposure has an effect on the region surrounding the cuts [422], these SEM images show a non-vertical profile of the slot. This effect seems less pronounced than the one shown in (a). Aside from the slot trench, the verticality of circular holes seems to be preserved with only some minor notching.

Even with these structural imperfections considered, the matching of the simulated and experimental bands is still complicated. To estimate the role of the different geometrical parameters in this mismatch, we calculate the position of the band edge λ_{be} while varying them independently as shown in Fig. 5.24 for the sPhCW with $s = 78$. Each panel plots the variation of a single parameter while keeping the rest fixed. The structure with the as-extracted in-plane geometry therefore lies at the origin of the x-axis. The wavelength $\lambda = 1500$ nm of the approximate experimental cut-off is marked with a dashed line. We cannot acount for the observed mismatch with the effect of each parameter independently, which pinpoints the fact that several effects might be occurring simultaneously. Instead of doing a complex multiparameter optimization to fit the experimental data, we use the profile measured on the isolated trench as an etch reference which we use for all features equally.

The analysis of the group index n_g extracted from the observed resonances is shown in Fig. 5.25, with the different extracted band structures given as a reference. The considered vertical profile does not suffice to reach the deviation $\Delta\lambda$ and the best fit to the experimental data on the region where FP resonances are clear requires an additional rigid shift of $\delta\lambda = 25$ nm. With this shift given, we see that strong n_g fluctuations occur and the system deviates from a smooth ballistic behaviour at around $\lambda = 1515$ nm. We attribute these deviations to the onset of light localization. To ensure that we are probing Anderson-localized resonances we restrict the measurements from now on to the first 5 - 10 resonances appearing in the slow light regime.

[4]The FIB exposure was carried out by a technician at the Barcelona Institute of Microelectronics IMB-CNM.

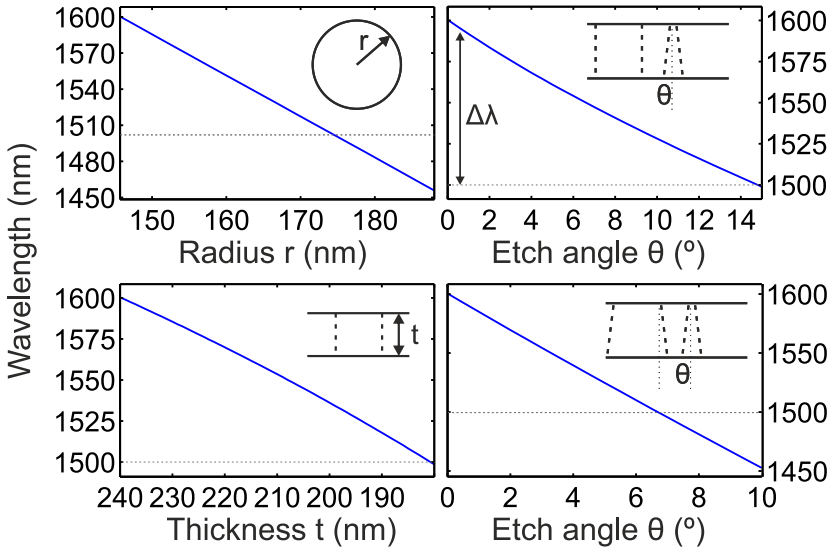

Figure 5.24: Band edge dependence on geometrical parameters in a slotted photonic crystal waveguide (sPhCW). Single-parameter sensitivity analysis of the band edge wavelength λ_{be} to the hole radius r, the slab thickness t, the slot etch angle θ and the overall etch angle θ. The dashed line highlights the experimentally observed approximate band edge.

Mechanical characterization

The OM coupling between an optical cavity and a mechanical mode allows the transduction of the latter's thermally activated motion, as described in Section 2.5. The RF signal as a function of laser wavelength obtained when probing the lowest wavelength mode of a $s = 78$ nm sL309 cavity with a laser drive of power $P_{in} = 80\ \mu W$ is shown in Fig. 5.26. The left panel shows the RF spectrum at the wavelength where the transduction is stronger and evidences the presence of multiple Lorentzian peaks. The evolution of the RF spectrum as a function of wavelength is represented via a colormap and shows the expected behaviour from frequency fluctuations of the optical mode frequency. Despite the presence of the TO effect leading to a saw-tooth resonant lineshape (top of Fig. 5.26), the transduction reaches a maximum close to the maximum slope of the transmission resonance at detuning $\Delta \sim \kappa/2$, progressively decreases again and vanishes in resonance. Then it appears again in the rising slope of the red-detuned side of the resonance. This dependence of the RF signal with wavelength constitutes a clear fingerprint of OM modulation of an Anderson-localized cavity mode with MHz-mechanical modes. The RF signal obtained when probing multiple optical resonances in the same sPhCW provides strong evidence for the mechanical origin of the transduced signal, as shown in Fig. 5.27. For reference, panel (a) shows the low-power transmission spectrum measured prior to the acquisition of the different RF spectra shown in (b), which are labeled with letters A-H accordingly. A rather high drive power of $P_{in} = 0.7$ mW is employed to enable the above-noise level transduction of as many mechanical modes as possible. The dashed grey lines accross all the spectra pinpoints the central frequency of the mechanical peaks visible in at least two of the spectra. We use additional spectra than the shown here. The optically transduced density of mechanical states (grey

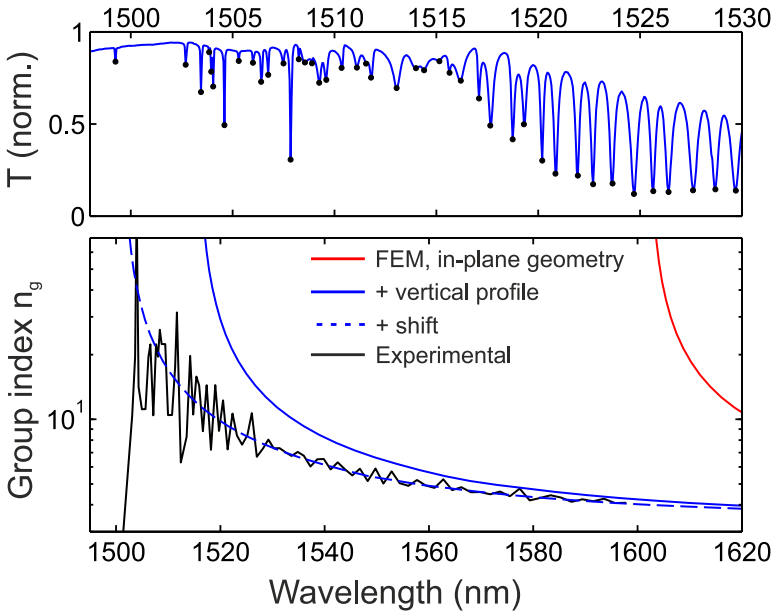

Figure 5.25: Signatures of optical Anderson-localization in slotted photonic crystal waveguides (sPhCWs). The transmission spectrum in the region λ = 1500-1530 nm is shown on top for an s = 78 nm sL309 cavity, showing both Fabry-Pérot (FP) resonances with a well-defined and predictable free spectral range (FSR) and a more unpredictable set of resonances above λ = 1520 nm. The detected peaks are used to extract the experimental group index n_g, which are compared to the progressively refined theoretical n_g.

lines in Fig. 5.27) can be compared to the simulated one to back the mechanical origin of the observed signal. Fig. 5.28 compares in detail the observed mechanical eigenspectrum (a single RF spectrum is given for reference) to the FEM simulated mechanical modes. The exact in-plane geometry of the sL309 cavity with s = 78 nm is considered, including the size of the underetched region (3.25 μm) from the lateral trenches to the SOI wafer where we impose a fixed boundary condition. Only modes simultaneously y and z-symmetric are simulated, allowing us to calculate just a quarter of the structure. However, z-antisymmetric flexural modes densely populate the full frequency range considered here. Two types of modes are found in our simulations. First, 5 shear modes with negligible y-displacement populate the spectrum up to 169 MHz, where the shear stress becomes considerable and it is released via a non-negligible y-displacement, as can be seen in C. The rest of the shear-like modes (I,K,N) have spatial regions where this motion is clearly visible and become optomechanically bright. The second family of modes (D,E,F,G,H,J,L,M) constitutes the one of interest, with differential in-plane motion between the two slabs. The fundamental in-plane breathing mode (D) has a frequency $\Omega_m/2\pi$ = 178 MHz, which is higher than the first observed mechanical resonances by approximately 10 MHz. Above such frequency, both the simulated and measured structure exhibit densely packed spectra with mechanical modes. Despite a higher density of modes in the experimental trace, the overall agreement is sufficiently good to consider the simulated modes as those populating the observed signal. The higher density and the overall shift to lower

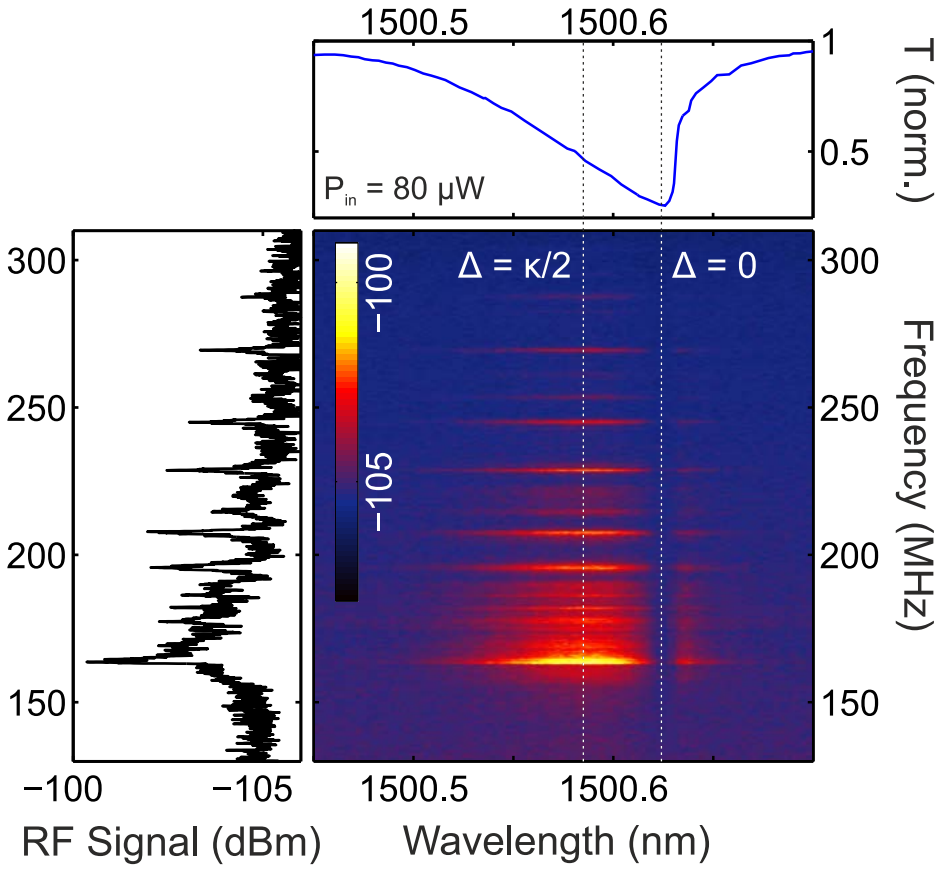

Figure 5.26: Optomechanical (OM) transduction with an Anderson-localized optical mode. The driving of an Anderson-localized mode at sufficiently low powers leads to the OM transduction of the thermally active motion of multiple mechanical modes, as shown with the left panel. The colormap in the middle shows the evolution of the radiofrequency (RF) spectrum with laser wavelength, which typically corresponds to the one expected from an optical cavity dispersively coupled to a mechanical resonator. This is highlighted with the dashed lines, corresponding to maximal transduction at $\Delta = \kappa/2$ and no transduction at $\Delta = 0$.

frequencies can be explained by considering both the presence of fabrication disorder and the real vertical profile of the sample, shown in Fig. 5.23. Coupling of the y-symmetric and antisymmetric modes due to disorder or the presence of the fiber taper loop can lead to the experimetal observation of two peaks instead of one, while the coupling of in-plane z-symmetric and flexural z-antisymmetric modes has a more unpredictable effect. We have simulated the eigenspectrum of a disordered structure of length $L = 100a$ including and excluding the vertical profile. FEM simulations indicate the presence of many flexural modes located within a few MHz of the the main in-plane modes, which can lead to mixing with in-plane motion through a breaking of the vertical symmetry of the slab. This mixing happens particularly for the non-vertical profile of these samples as does an aditional reduction of the frequencies of in-plane modes. The first can explain the presence of a highly packed spectrum in the 160-180 MHz region, since originally flexural modes become optomechanically active, while the latter probably

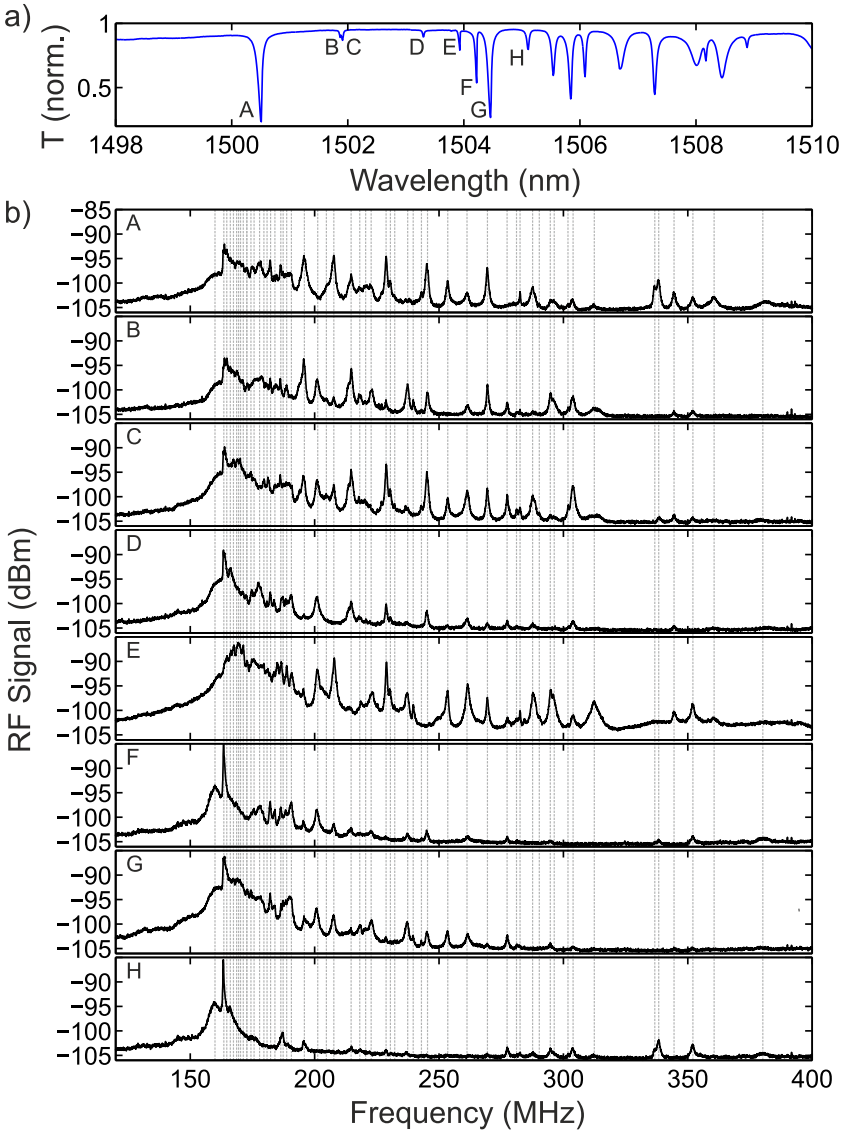

Figure 5.27: Low-frequency mechanical spectroscopy of a slotted photonic crystal waveguide (sPhCW) using multiple optical modes. (a) Optical spectrum of a $s = 78$ nm sL309 cavity in the frequency region where light localization occurs. Some of the optical modes are labeled with letters A to H. (b) Radiofrequency (RF) spectra of the transmitted light when probing the modes A-H, showing multiple Lorentzian peaks in the range from 120 MHz to 400 MHz. The peaks are manually inspected and the dashed lines represent those present in at least two from a large set of RF spectra.

explains why the first transduced modes are at lower frequency than expected from the as-designed structure. Similar observations have already been reported for weak stress-induced bowing in an engineered heterostructure cavity [411]. The high level of transduction of the fundamental drum mode of the full membrane at $\Omega_m/2\pi = 4$ MHz (not shown) also provides an important signature of the role played by the vertical profile in determining the final mechanical eigenspectrum of the structure under investigation.

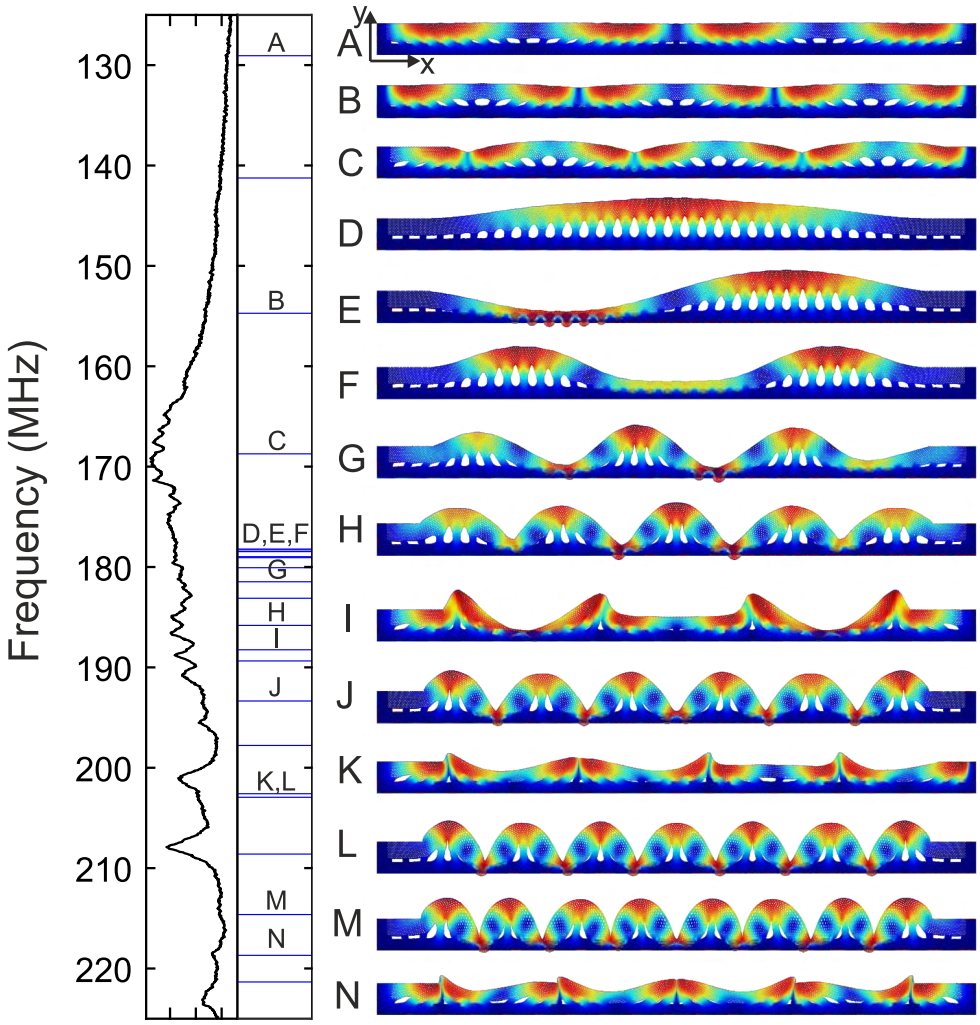

Figure 5.28: Simulated low-frequency mechanical eigenspectrum of a fabricated device. The experimentally extracted eigenspectrum is compared to that simulated via Finite Element Method (FEM), in which only the z and y-symmetric mechanical modes are included. Specific modes in the eigenspectrum are labelled from A to N and their deformation profiles given, with the deformation being unrealistically exagerated for visualization purposes.

We have made the same analysis for a set of sPhCWs with different s. The type of RF spectrum observed, including the precise frequencies of the detected peaks coincides across all devices, as the different values of s have negligible effect on the MHz modes being probed. However, the transduced signal was stronger for the narrower slots. The stronger signal can be due to different mechanisms, such as overall better quality factors Q in the Anderson-localization regime. Nevertheless, we observed that the Q-factors are within the same order of magnitude, which points towards higher values of the OM coupling rate g_o (see Fig. 5.18).

Experimental evaluation of the optomechanical coupling rate

The vacuum OM coupling rate g_o can be determined using several techniques. The most widespread employs a known frequency modulation as a calibration

signal [423] to which the thermomechanical radio frequency spectrum is compared. This technique is based on the equivalence of the transduction factor between a laser line undergoing frequency/phase fluctuations upon a fixed optical resonance and a fixed laser line driving an optical cavity undergoing (optomechanically-induced) frequency fluctuations. Details on the theoretical description of such a scheme can be found in the original article by Gorodetksy et al [423], and elsewhere [63,88].

We employ an electro-optic modulator (iXblue Photonics MPZ-LN-10, $V_\pi = 4.9$ V) driven by a vector network analyzer (Rohde&Schwarz ZVA 50) at a voltage $V = 0.178$ V to phase modulate the laser carrier before light is coupled into an optical cavity mode. The phase of the input signal can then be written as,

$$\phi(t) = \omega_L t + \beta \cos(\Omega_{mod} t) \tag{5.9}$$

where β is the phase shift factor, i.e. $\beta = V/V_\pi$, and Ω_{mod} the modulation angular frequency. The RF spectrum exhibits both the Lorentzian spectra of the mechanical modes and an additional calibration peak at $\Omega_{mod}/2\pi$, as can be seen with the solid black line of Fig. 5.29(a). Since the motional state of the mechanical resonators is incoherent, we assume there is only a single mechanical mode coupled to an optical cavity. The power spectral density of the mechanical resonator and of the calibration tone are given by

$$S^m_{\omega\omega}(\Omega) = 8 g_o^2 \overline{n}_{th} \frac{\Omega_m^2}{(\Omega^2 - \Omega_m^2)^2 + \Gamma_m^2 \Omega_m^2} \tag{5.10a}$$

$$S^{cal}_{\omega\omega}(\Omega) = \frac{1}{2} \Omega_{mod}^2 \beta^2 \delta(\Omega - \Omega_{mod}) \tag{5.10b}$$

with $\overline{n}_{th}$ the thermal occupany of the mechanical mode considered. The experimentally accesible power spectral density is given by $S_{VV}(\Omega) = |G_{V\omega}(\Omega)|^2 S_{\omega\omega}(\Omega)$, with $G_{V\omega}(\Omega)$ a transduction factor depending on frequency Ω. When the areas $\langle V^2 \rangle_m = 2 g_o^2 \overline{n} |G_{V\omega}(\Omega_m)|^2$ and $\langle V^2 \rangle_{cal} = \frac{\Omega_{mod}^2}{2} \beta^2 |G_{V\omega}(\Omega_{mod})|^2$ beneath both curves are compared, g_o can be determined by

$$g_o = \frac{\beta \Omega_{mod}}{2} \sqrt{\frac{1}{\overline{n}_{th}} \frac{\langle V^2 \rangle_m}{\langle V^2 \rangle_{cal}}} \left| \frac{G_{V\omega}(\Omega_{mod})}{G_{V\omega}(\Omega_m)} \right| \tag{5.11}$$

The typical approach consists in choosing a calibration tone placed just a few MHz apart from the mechanical mode of interest, since one can then assume that both transduction factors are the same and set $\left| \frac{G_{V\omega}(\Omega_{mod})}{G_{V\omega}(\Omega_m)} \right| \sim 1$. In our case, such approach would require the acquisition of as many RF spectra as mechanical modes present. Additionally, we would need to repeat this for many optical modes to assess the statistical role of the slot width s. However, the error commited in the extracted g_o by using such an assumption is spread by less than 10% of its mean value when Ω_{mod} is changed within a window spanning 150 to 300 MHz. We fix the calibration tone somewhere in the window and set $\left| \frac{G_{V\omega}(\Omega_{mod})}{G_{V\omega}(\Omega_m)} \right| = 1$ for all modes. We fit the low-power RF spectra obtained when driving the Anderson-localized optical modes present in a single sL309 cavity for different slot widths s

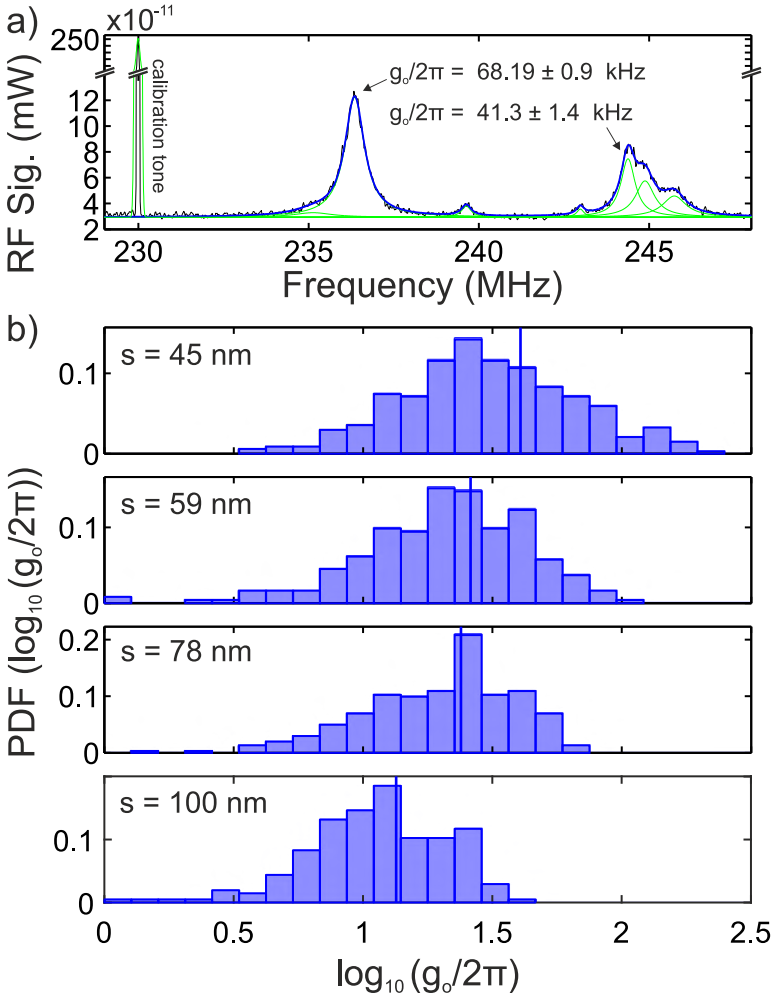

Figure 5.29: Optomechanical (OM) coupling statistics between MHz in-plane motion and Anderson-localized optical modes in a slotted photonic crystal waveguide (sPhCW). (a) Frequency modulation technique employed to extract the vacuum OM coupling rate between the observed mechanical modes and the driven optical cavity. The mechanical modes are fitted (blue line) using a sum of Lorentzian lineshapes and a background (green lines), while the EOM-generated calibration tone is fitted with a Gaussian lineshape. This procedure is repeated for multiple frequency windows and with multiple localized modes, leading to the statistical distributions shown in (b), where a clear shift towards higher g_o is seen with decreasing slot width s.

with a sum of Lorentzian lineshapes and a straight baseline. This is done in small spans of around 10 MHz to limit the number of observed modes and therefore enable efficient least-mean-squares fitting, while the extracted central frequencies from the analysis shown in Fig. 5.27(b) are used as a guideline for possible initial guesses. In addition, the calibration tone for each RF spectrum is fitted with a Gaussian, as the calibration tone lineshape is limited by the chosen SPA bandwith (RBW = 10 kHz). An example of such analysis is shown in Fig. 5.29(a), where each Lorentzian is given in green and their sum in blue. For clarity, the calibration tone is also shown at $\Omega_{mod}/2\pi = 230$ MHz. The extracted g_o is given for two of the observed peaks with an error solely given by the fit error for both the mechanical

and calibration signals.

The main result of this subsection is shown in Fig. 5.29(b), where the probability distribution function of g_o is shown in log-scale for the different slot widths s. There is an overall shift of the PDF towards higher values of g_o when s diminishes, confirmed by the progressive increase of the mean $\langle g_o \rangle$ marked with a vertical blue line in each panel. We also report measured values that can go up to $g_o \sim 2\pi \cdot 300$ kHz for the sPhCWs with $s = 45$ nm, a rather high value considering the absence of any design in these optical cavities. This constitutes a first proof of OM modulation of optical Anderson-localized modes. It also reveals the overall importance of the slot width in the OM coupling rate achieved in the localization regime. Strong efforts are currently ongoing at DTU Fotonik and Nanofab to further improve the fabrication process with the prospect of reaching $s = 10$ nm.

5.3.4 Mechanical amplification and lasing

To calibrate g_o very low probing powers are used to ensure that there is no backaction of the light field on the mechanical modes. However, on the RF spectra shown in Fig. 5.27, where higher powers were used to observe more modes, the sharpness of some of the observed peaks already preludes that such backaction is possible. In this subsection we show how Anderson-localized optical cavities in sPhCWs can host OM oscillation limit cycles and we use them to amplify mechanical motion at frequencies around 200 MHz. Additionally, silicon OMC cavities with both high optical Q, low mode volume V and high OM coupling rate g_o often suffer simultaneously from radiation-pressure backaction and material non-linear dynamical effects, which enriches the physics of the system under study. Despite the clear coexistence of both driving forces, we evidence mechanical lasing via either dynamical backaction or the self-pulsing (SP) mechanism.

Amplification based on dynamical backaction

The sPhCWs considered here constitute a rather rich OM system. First, many localized optical modes can be probed in a wavelength range of around 10 nm, which can be of interest for applications that benefit from large optical bandwiths like spectrometry [424]. Second, the optical modes probed are coupled with a considerable g_o to multiple closely packed mechanical modes spanning a large range of frequencies, with possible implications for high-bandwith sensing technology like, e.g. optomechanical magnetometry [425,426]. Considering the mechanical frequencies (they go up to $\Omega_m = 2\pi \cdot 600$ MHz) and the optical decay rates (the smallest of $\kappa = 2\pi \cdot 2.5$ GHz) measured and the laser driving a single optical cavity mode, the system constitutes a useful platform for sideband unresolved multimode optomechanics [415] where mechanical mode competition [427] and rich non-linear dynamics can be explored [428,429].

The high-power ($P_{in} = 200$ μW) transmission spectrum of an Anderson-localized optical mode in a sL309 cavity (with $s = 45$ nm) is shown in Fig. 5.30(a), along with its RF spectral map. The cold resonant wavelength of the mode corresponds to $\lambda_o = 1598.1$ nm, but rather moderate powers lead to a DC transmission

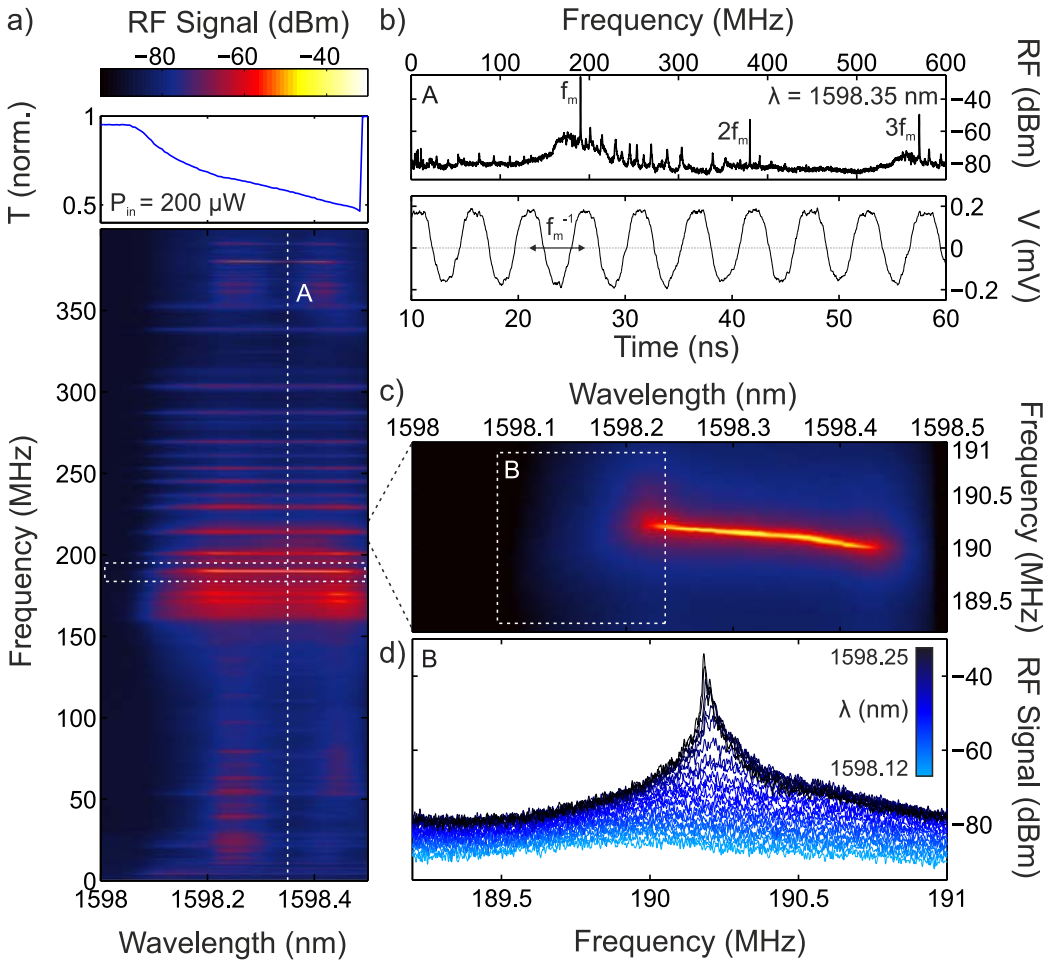

Figure 5.30: Dynamical backaction amplification and optomechanical (OM) oscillation with an Anderson-localized optical mode. (a) Optical transmission spectrum and radiofrequency (RF) spectral map of an Anderson-localized mode driven at $P_{in} = 200\ \mu$W, showing both transduction of in-plane mechanical modes as well as self-sustained oscillation at $f_m \sim 190.25$ MHz when driven above $\lambda_L = 1598.2$ nm. The RF spectrum at position A -marked with a white dashed line- is given in (b). The multiple harmonics at nf_m and the temporal trace trace evidence the coherent high amplitude nature of the dynamical mechanical state. (c) Detailed RF spectral map around f_m, with the region leading to lasing marked with a white dashed box. The spectra in that region are shown separately in (d), evidencing both stiffening and amplification of the motional state as the characteristic dynamical-backaction path towards self-oscillation.

with a saw-tooth lineshape, a fingerprint of cavity absorption leading to a TO shift. We attribute this non-linearity to a pronounced optical absorption mediated by surface states in the etched slot surface, since otherwise the air-guided nature of the mode should considerably limit the observed non-linearities. The first region of thermal transduction ($\lambda = 1598.05$-1598.2 nm) in the RF spectral map is followed by a more intricate spectrum ($\lambda = 1598.2$-1598.5 nm) in which a mode with natural frequency $f_m = 190$ MHz oscillates at high amplitude. However, the amplitude of the remaining mechanical modes stays rather constant.

The RF spectrum at a representative wavelength ($\lambda = 1598.35$ nm) is highlighted with a dashed white line in Fig. 5.30(a) and shown in (b). The mentioned peak is well above the rest of mechanical modes, as are its multiple harmonics ($2f_m$ and $3f_m$ shown). The temporal trace acquired with the oscilloscope (using the signal itself as a trigger) confirms the coherent nature of the motion and evidences that OM oscillation has been reached. Fig. 5.30(c) shows a detailed panel of the RF spectral map around f_m, where we see that the mechanical oscillation frequency linearly decreases with increasing wavelength. This behaviour has been numerically obtained in Chapter 2 (see Fig. 2.10), but has here an additional contribution from thermomechanical softening [97]. The region prior to the onset of the self-oscillation is marked with a white dashed box and further explored in Fig. 5.30(d), showing both a progressive lineshape narrowing and a stiffening of the mechanical resonator. These are two clear signatures of dynamical backaction-mediated amplification on the blue-detuned side of an Anderson-localized optical mode. Nevertheless, the presence of a nearly degenerate mechanical resonance (as seen from the bump on the high-frequency flank of the resonance) make the proper extraction of the linewidth and its comparison to Eq. 2.40b rather complicated. This analysis is left for another optical resonance where the nearly-degenerate mode appears to be optomechanically dark.

Figure 5.31 plots the OM amplification with the characteristic evolution of radiation pressure backaction given by Eq. 2.40b. These measurements were carried out on an $s = 45$ nm and $\Gamma = 0.95$ sL309 cavity, whose low-power transmission spectrum is shown in Fig. 5.31(a). In particular, we focus on the interaction of the lowest wavelength optical mode at a cold wavelength $\lambda_o = 1510.7$ nm and a mechanical mode of frequency $\Omega_m/2\pi = 230$ MHz. From Eq. 2.40b, we expect the overall damping rate Γ_m to evolve linearly with the input power P_{in} whenever the rest of the parameters are kept fixed. Unfortunately, the optical resonances exhibit a considerable TO effect (Fig. 5.30), which complicates the recurrent measurement at the same detuning Δ and forbids cooling on the red-detuned side. Fig. 5.31(b) shows the transmission spectrum at powers ranging $P_{in} = 20$ - 220 μW and highlights the simplified approach taken here. We assume here that absorption is strictly linear and the Q-factor of the optical resonance is fixed. We select the detuning $\Delta = \kappa/2$ by always measuring the RF spectrum at the wavelength λ_L corresponding to a fixed coupled fraction. The RF spectrum measured as a function of P_{in} is shown in Fig. 5.31(c). The trace in light blue was used used to extract g_o using the frequency modulation technique described before, from which $g_o \sim 2\pi \cdot 198$ kHz is obtained. Fitting the RF data with a Lorentzian lineshape allows us to obtain $\Gamma_m(P_{in})$, which indeed decays linearly up to $P_{in} = 150$ μW. Using the calibrated power P_{in}, the cold resonance characteristics $\kappa_{i/e}$ and the fitted slope, the use of Eq. 2.40b yields $g_o = 2\pi \cdot 228 \pm 7$ kHz, which is in good agreement with the value measured with the calibration tone. The mechanical linewidth increases above $P_{in} = 150$ μW and the mode vanishes from the RF spectrum for $P_{in} = 220$ μW (dashed black RF spectrum in Fig. 5.31(c)). For this drive power P_{in}, the gain Γ_{om} surpasses losses $\Gamma_{m,i}$ for another mechanical mode of frequency $\Omega_{m,2}/2\pi = 215$ MHz. This second mechanical mode presents a similar g_o to the driven optical cavity mode. The increase in Γ_m constitutes a fingerprint of mode competition, while we atribute the vanishing of the mode at

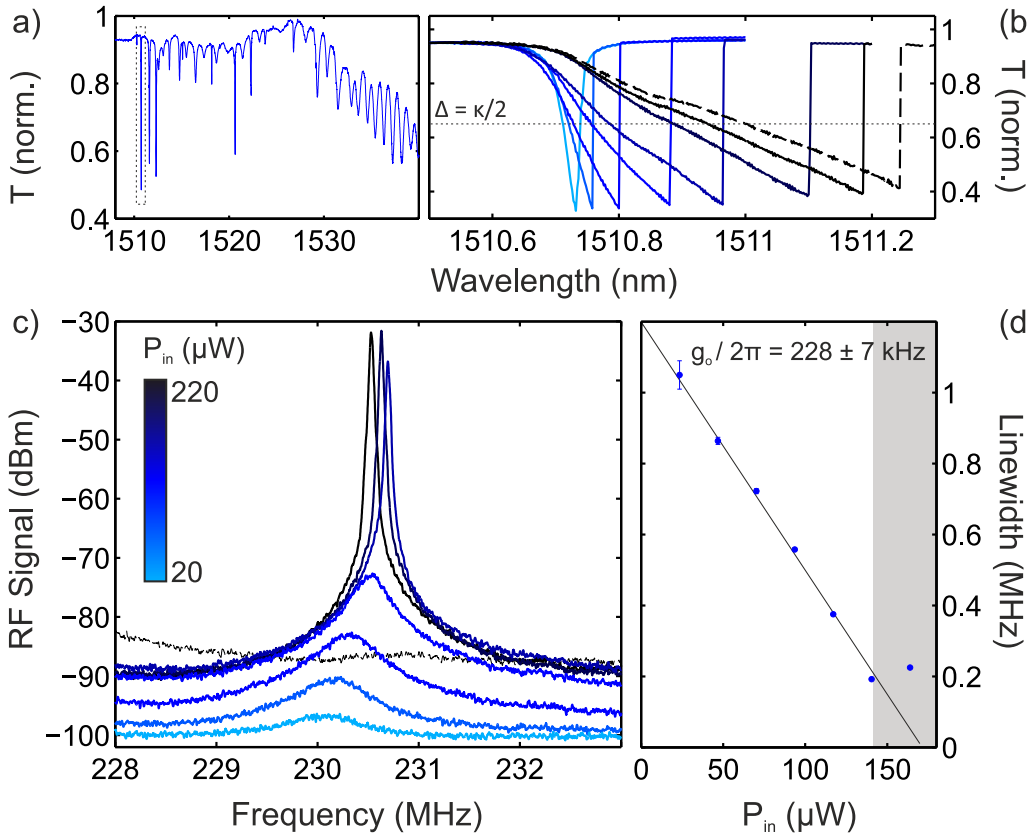

Figure 5.31: Power-dependence in dynamical backaction amplified mechanical motion. (a) Optical transmission spectrum of an $s = 45$ nm and $\Gamma = 0.95$ sPhCW, with the optical mode of interest highlighted. Its optical transmission at powers ranging from 20 μW to 220 μW are given in (b), with the dashed line crossing with each spectra representing the approximate detuning $\Delta \sim \kappa/2$. (c) RF spectrum taken at that precise detuning as a function of laser power, clearly evidencing both optomechanical stiffening and amplification. The latter corresponds to a change in linewidth depending linearly on the input power P_{in}, whose value is calibrated prior to the cavity. This is shown in (d), where the fitted slope is used to extract g_o.

even higher powers to anomalous cooling in multimode OM systems [430].

Self-pulsing triggered mechanical lasing

Air-slotted PhCWs enhance g_o in the Anderson-localization regime when compared to a standard PhCW. Additionally, this system allows us to avoid silicon absorption-mediated non-linearities. The onset of the self-pulsing limit cycle observed in Subsection 5.2.3 prevents the use of laser power as a knob to increase the mechanical transduction signal-to-noise ratio and limits the range of powers over which the backaction of the light field can be studied. Nevertheless, the probed resonances so far exhibit a dispersive TO shift which necessarily originates from absorption within the cavity volume. We attribute such effect to linear absorption by states at the surface of the slot sidewalls. Driving at sufficient power also leads

to the development of SP limit cycles in sPhCWs and its frequency tunability with laser wavelength leads to mechanical lasing whenever $\nu_{SP} \sim f_m/M$, with M being an integer (see Subsection 2.4.2). In addition, lasing via dynamical backaction and via SP can be achieved for a single OM resonator depending on the laser parameters (λ_L, P_{in}) employed.

When the Anderson-localized modes are probed at powers P_{in} higher than those for which backaction-based amplification is achieved, the dynamics become richer due to the onset of material nonlinearities. We give in Figure 5.32 the RF spectral maps at three different powers P_{in} when driving an optical mode in a sPhCW of slot size $s = 80$ nm. The specific values of P_{in} are only given for reference, since the power prior to the optical resonance was not calibrated and the fiber loop baseline transmission had considerably degraded. The left panel shows the spectral features of mechanical transduction (denoted with a T) and dynamical backaction-base OM oscillation (denoted with an L). The two other spectral maps evidence much more complex temporal dynamics and a large variety of attained dynamical states. We analyze in detail the spectral map at higher power (right), that we divide in different wavelength ranges associated to the leading physical process,

- *Transduction of thermally-active motion*, occurs in the first wavelength region spanning $\lambda_L = 1504.4$-1504.6 nm, with a most prominent transduction for the mechanical mode with $f_m = 163.6$ MHz.
- The *onset of self pulsing*, denoted by SP, occurs at $\lambda_L = 1504.6$ nm and is associated to an extremely broadband RF signal similar to the one shown for the shamrock PhCWs in Fig. 5.17. The broadband modulation of the intracavity photon number n_c effectively pumps the mechanical mode, as revealed by the associated increase of the amplitude at f_m in the region spanning $\lambda_L = 1504.6$-1504.78 nm, but does not lead to self-sustained mechanical oscillations.
- *Mechanical lasing mediated by the third harmonic of the SP*, denoted by M3, is activated when the underlying SP has periodicity of $\nu_{SP} \sim f_m/3$. The SP-induced modulation of n_c resonantly drives the mechanical motion via the radiation pressure force. The SP in this region is then entrained to oscillate at a third of the frequency of the mechanical oscillator, leading to mechanical lasing. The characteristic time trace in this narrow wavelength region is shown in the top panel of Fig. 5.32(b), where we observe the typical trace of an M3 mechanical lasing state (see Fig. 2.11), with the relevant periods highlighted with arrows.
- A *transition region*, denoted by P, takes place between the M3 plateau and the consecutive M2 plateau. Here, the appeareance of sideband peaks are characteristic of period doubling, one of the main routes to chaotic dynamics [431], and observed between the different lasing plateaus for other OM systems at the P2N group [100,113].

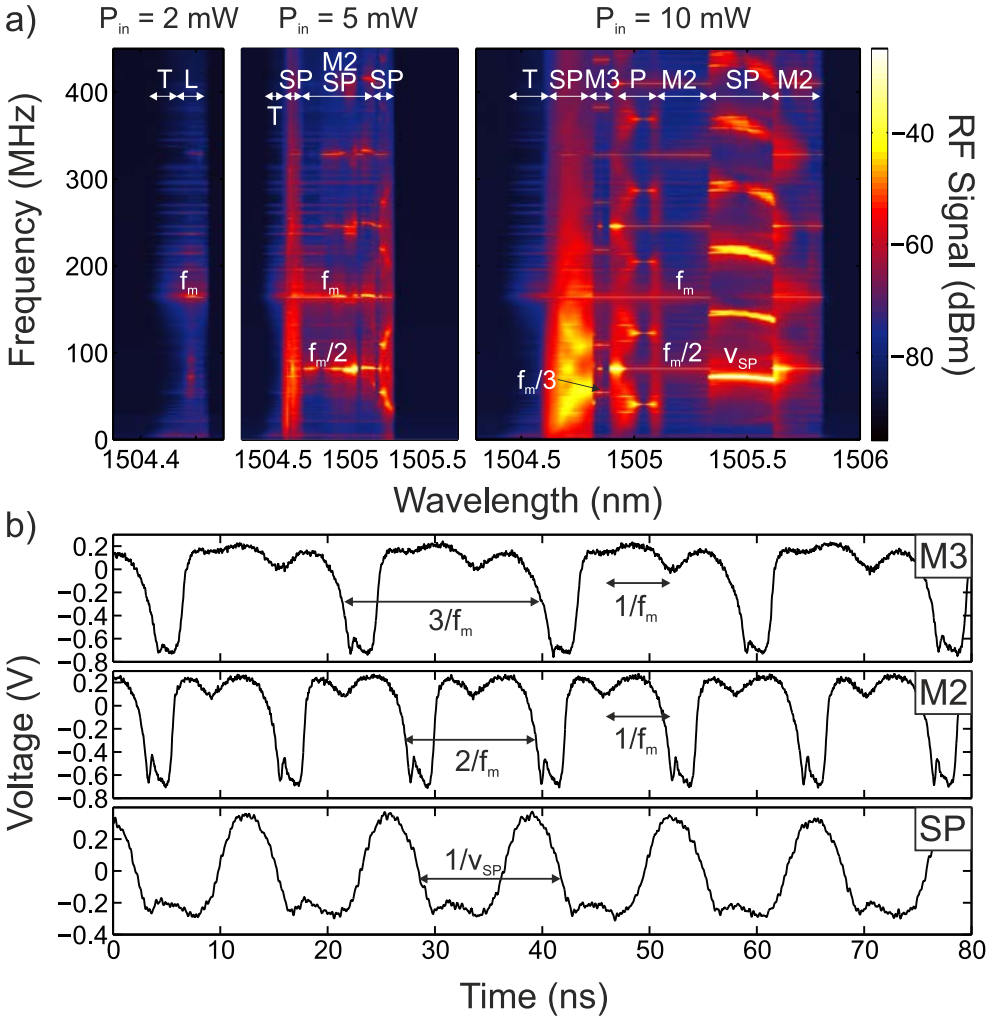

Figure 5.32: Non-linear optomechanical (OM) dynamics with a disorder-induced localized mode. (a) Radiofrequency (RF) spectral maps obtained driving an Anderson-localized optical mode in a $s = 78$ nm sL309 cavity with increasing laser power P_{in}. The attained dynamical states as a function of laser wavelength are synthesized with the following acronyms: transduction (T), dynamical backaction OM oscillation (L), self-pulsing (SP), period doubling (P) and SP-driven OM oscillation with the n-th harmonic (Mn). The relevant frequencies are also given. (b) Temporal traces corresponding to an M3 (top) and M2 (middle) mechanical lasing states and to a pure SP state (bottom) as measured simultaneously to the $P_{in} = 10$ mW RF spectral map in (a).

- *Mechanical lasing mediated by the second harmonic of the SP*, denoted by M2, starts at $\lambda_L = 1505$ nm and spans a region up to $\lambda_L = 1505.25$ nm. The characteristic time trace in this region is shown in the central panel of Fig. 5.32(b), with the specific initial phase of the SP in coincidence with the M3 panel, showing how the underlying mechanical signal remains fixed.
- *Self-pulsing* without any coherent mechanical motion is achieved between $\lambda_L = 1502.25$ nm and $\lambda_L = 1502.55$ nm, as evidenced by the broadening of the frequency comb linewidth and by the characteristic evolution of $\nu_{SP}(\lambda_L)$

already reported in Fig. 5.17. The time trace at the bottom of Fig. 5.32(b) also illustrates how the duty cycle of the limit cycle has considerably increased compared to the other two panels. This has already been reported for the shamrock PhCWs in Fig. 5.16.

- A second plateau of *mechanical lasing mediated by the second harmonic of the SP*, again M2, is suddenly activated above λ_L=1505.55 nm. Although the typical behaviour of the SP leads to a monotonously decreasing ν_{SP} once its maximum value is reached, we have seen in Fig. 5.16 that a sudden increase of the frequency can occur close to the wavelength where the limit cycle vanishes. This sudden rise of ν_{SP} could explain the occurrence of this second M2 plateau.

We observe mechanical lasing using the third and second harmonic of the SP and evidence the underlying physics behind the coherent oscillations by showing both the associated temporal traces and wavelength regions with pure SP. The spectral map at P_{in} = 5 mW exhibits some of these dynamical states, as labeled in white. In this case, the interpretation is more complicated since ν_{SP} does not efficiently lock to f_m/M and the system is constantly hopping between a self-sustained state of SP+mechanics and *independent* SP+mechanics. Fig. 5.33 depicts the same spectral maps for a localized optical mode in a s = 59 nm sPhCW. In this case, transduction and self-oscillation via backaction are observed at the lowest of the three powers, while increasing the drive power activates the SP dynamics. The first three harmonics of the SP frequency comb are considerably well defined in

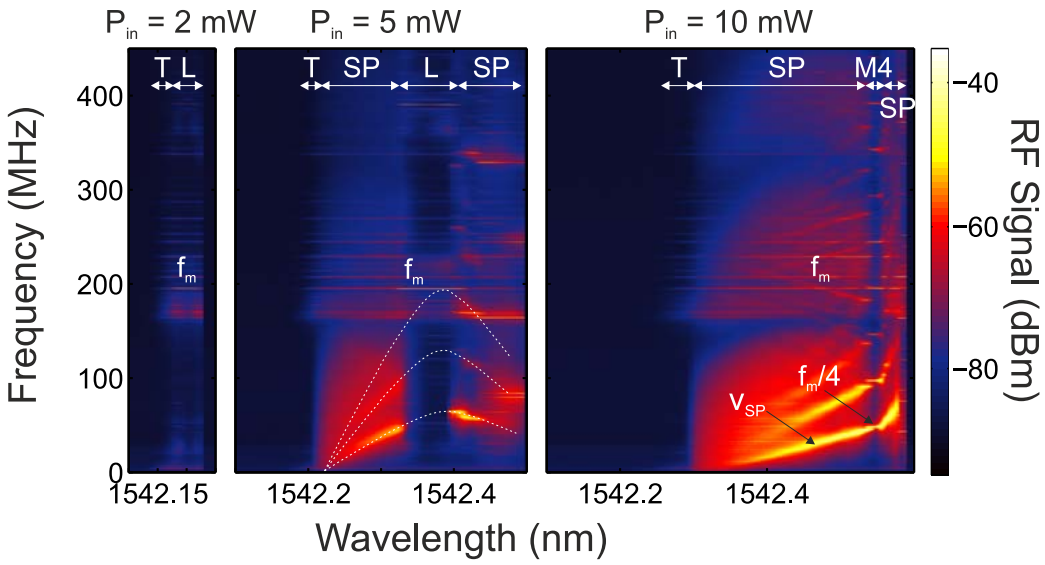

Figure 5.33: Signatures of competing physical mechanisms in optomechanical (OM) oscillation. Radiofrequency (RF) spectral maps obtained driving an Anderson-localized optical mode in an s = 59 nm sL309 cavity with increasing laser power P_{in}. The attained dynamical states as a function of laser wavelength are synthesized with the same acronyms as in Fig. 5.32 and the relevant frequencies are given. The white dashed lines in the central panel are guides-to-the-eye showing the spectral evolution of the self-pulsing (SP) frequency comb.

the middle and right panels compared to Fig. 5.32. Interestingly, at P_{in} = 5mW, the system starts lasing via dynamical backaction at around λ_L = 1542.32 nm even though the SP dynamics have been already triggered and despite the fact that the third harmonic is relatively close to f_m. This is backed by the vanishing of the SP spectral features in the range λ_L = 1542.32 - 1542.39 nm while the signal at f_m simultaneously becomes much higher. Above λ_L = 1542.39 nm, the backaction-based mechanical self-oscillation is lost and the SP reappears. The white dashed lines serve as guides-to-the-eye and mark the spectral position of the SP, even in the range where the SP is quenched. At even higher powers, P_{in} = 10 mW, we do not observe lasing via dynamical backaction but we do instead reach a M4 lasing state via the SP.

This set of qualitative measurements shows the richness of physical phenomena that can be explored within this platform and provides a unique tool to manipulate the state of an Anderson-localized optical mode by both material non-linearities and coupling to mechanical degrees of freedom. Additionally, at higher power drives the recurrent period doubling process preludes the entrance into a chaotic regime, a possibility currently being explored.

5.4 GHz-Optomechanics with Anderson localized optical modes

In the previous section we have thouroughly described the experiments carried out on sPhCWs employing circular holes, where we were able to transduce and actuate extended mechanical motion with frequencies always below 1 GHz. Despite the presence of unintentional fabrication disorder leading to light localization, the type of mechanical excitation probed is highly insensitive to disorder. One can consider even a negligible effect over the resonant frequencies and mode profiles. In order to study disorder-induced mechanical localization, a guided mechanical band at much higher frequencies is required. Our hypothesis is that a sPhCW with shamrock holes enables both light localization in the slow light region of a slot-guided band while supporting guided mechanical resonances on each side of the slot (Fig. 5.2(b)).

5.4.1 Optomechanical spectroscopy

Shamrocks sPCWs were fabricated at DTU Fotonik on the same chips containing the devices reported in the previous section. Waveguides with various overall scalings Γ and different slot widths s were included in the design file. In this case, the shamrock sPhCWs are not enclosed by PhC mirrors and waveguides are terminated with the bare silicon slab.

The optical characterization of waveguides with different slot widths over the full span of our tunable laser is shown in Fig. 5.34, where a typical SEM

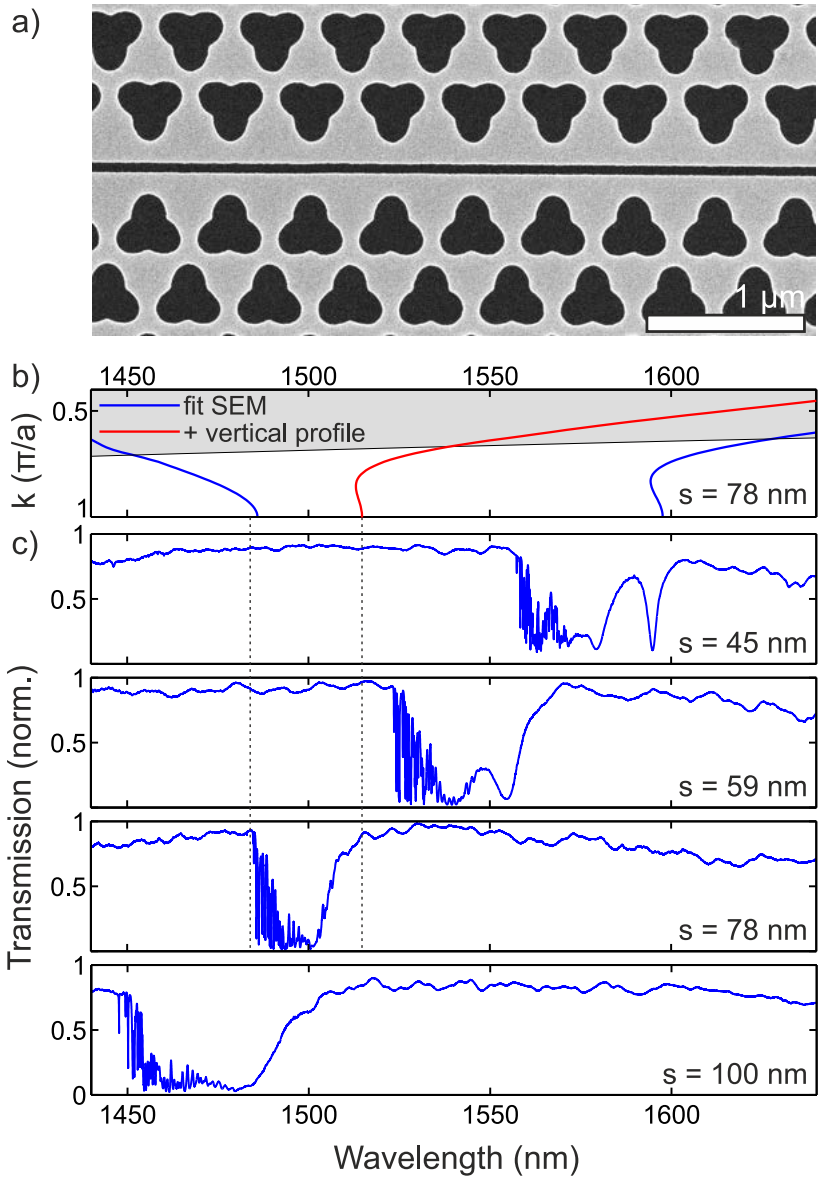

Figure 5.34: Fiber-taper optical characterization of slotted shamrock photonic crystal waveguides (sPhCWs). (a) Normal-incidence SEM micrograph of a $s = 78$ nm shamrock sPhCW, with its band diagram given in (b). The bands using the in-plane geometry obtained from the mean value of a set of fitted shamrocks are given with (red) and without (blue) the vertical profiile shown in Fig. 5.23. (c) Fiber-taper transmission spectra of waveguides with different slot widths s, clearly evidencing the deterministic tuning of the overall band region.

micrograph of a waveguide with $s = 59$ nm is shown. Compared to the shamrocks shown in Fig. 5.14 (fabricated at ICN2), the shamrocks here are less rounded despite sharing the same nominal parameters. This makes the fit using a perfect shamrock more suited for this situation. We extract the mean parameters of the shamrock holes by using normal-incidence SEM micrographs which results in the band structure shown in blue in Fig. 5.34(b). We observe again a shift $\Delta\lambda$ of of over 100 nm between the simulated and measured cutoff clearly indicating that we

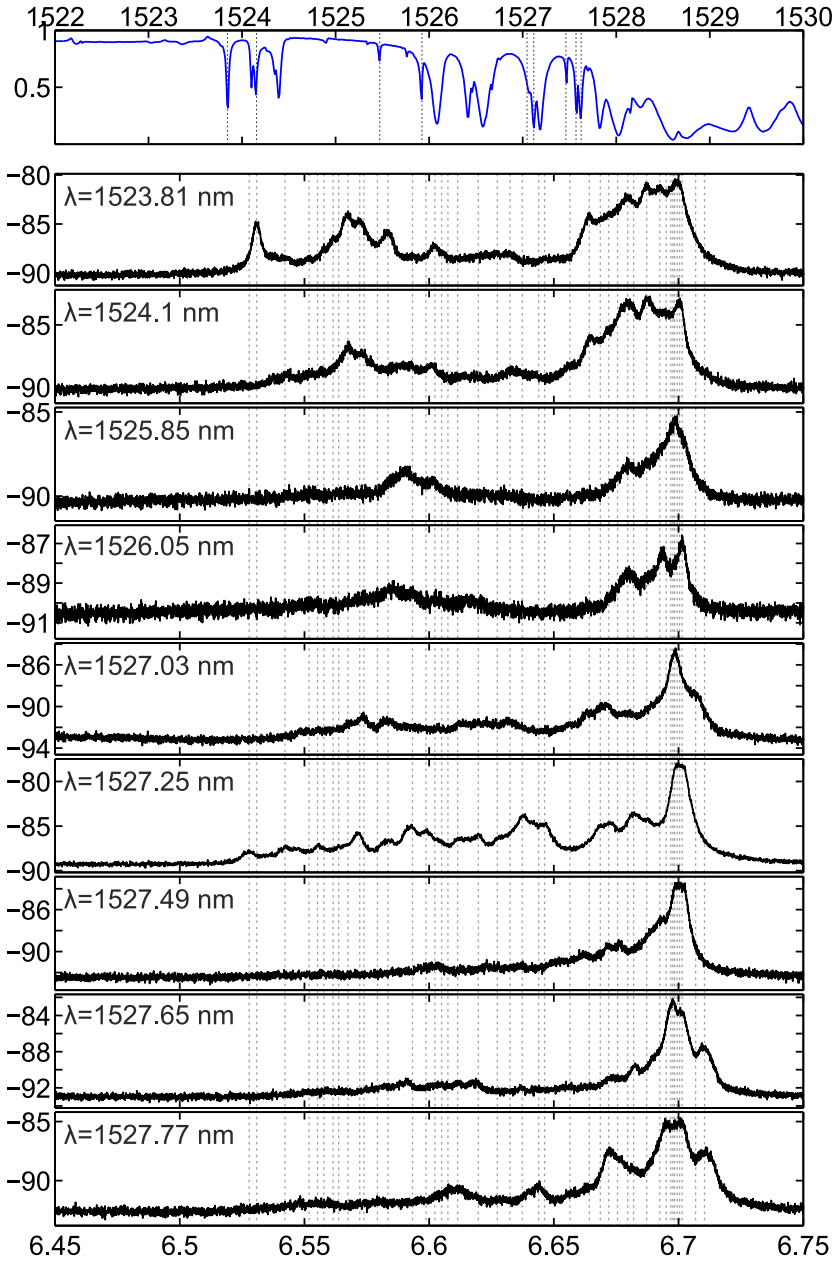

Figure 5.35: Optomechanical (OM) transduction of GHz-motion with Anderson-localized optical modes in a slotted shamrock photonic crystal waveguide (sPhCW). The driving of an Anderson-localized mode at moderate laser power leads to the OM transduction of the thermally active motion of multiple GHz mechanical modes. (Top) Optical spectrum of a shamrock sPhCW with $s = 59$ nm around the band edge of the slot-guided mode. The vertical dashed lines mark the optical resonances for which the RF spectra are shown (bottom). Multiple mechanical resonances are evidenced, with the dashed grey lines marking the central frequency of all of the transduced modes in a larger set of RF spectra.

need to account for the vertical profile. Using the same profile shown in Fig. 5.23 results instead in the band structure shown in red. With this vertical profile, bands originating from TM-like modes (not shown for clarity) are responsible for features like the broad dip in the $s = 45$ nm transmission spectrum. Again, the vertical profile does not suffice to account for the disagreement and an additional shift of $\delta\lambda \sim 30$ nm would be necessary.

We observe two different families of mechanical modes when the Anderson-localized mode is driven and the outcoupled laser light is detected with the fast photoreceiver and analyzed with the ESA. The first, spanning 0 to 1 GHz (maximum), corresponds to the in-plane differential modes already described for the sPhCWs with circular holes, which are not discussed any further in this section. In addition, a second group of closely packed resonances is observed in the frequency range spanning 6.5 to 6.75 GHz. This is shown in Fig. 5.35 for the shamrock sPhCW with $s = 59$ nm. The optical spectrum of the measured waveguide is given on top, with the vertical dashed lines marking the optical modes probed to obtain the transduced spectra shown below. As done for the low-frequency mechanical spectra of Fig. 5.27, the peaks in at least one of the spectra are marked with vertical dashed lines across all panels in order to obtain a good approximation of the local density of mechanical states. Comparison of the observed mechanical spectrum to the simulated guided mechanical bands did not provide a clear picture of what region of the guided bands shown in Fig. 5.2(b) we were observing, neither of the nature/origin of the obseverd mechanical modes, although the observation of common mechanical modes probing localized optical resonances at different points in the waveguide suggest that these extend over the full system. To observe FP mechanical resonances that enable us to reconstruct the mechanical band structure, another chip with waveguides based on the same unit cell design but with considerably shorter lengths was fabricated at DTU Fotonik.

Fabry-Perot acoustic resonances

To achieve a better level of mechanical confinement as well as improved optical quality factors Q in moderate-length waveguides, air trenches are introduced at each termination. An example of a shamrock sPhCW of length $L = 40a$ and slot width $s = 48$ nm is shown in the SEM micrograph of Fig. 5.36(a). The waveguides are characterized by using the fiber taper evanescent coupling technique, with the fiber placed right at the center of the waveguide. The optical spectrum of the structure shown is depicted in Fig. 5.36(b), along with the band dispersion, which already takes into account the, once again, irregular etch profile. The presence of a higher Q-factor optical mode in between lower Q resonances underlines the non-monotone nature of the band. The highest Q is typically found for the mode closer to the band edge due to either the higher effective index impedance mismatch or to its localized nature if $\xi < L$. The focus is set here in understanding the underlying mechanical guided modes

Driving that optical resonance at a power of $P_{in} = 7$ mW results in the transduction of a set of well-defined Lorentzian mechanical resonances as shown in Fig. 5.36(d) in a frequency range close to that shown previously in Fig. 5.35,

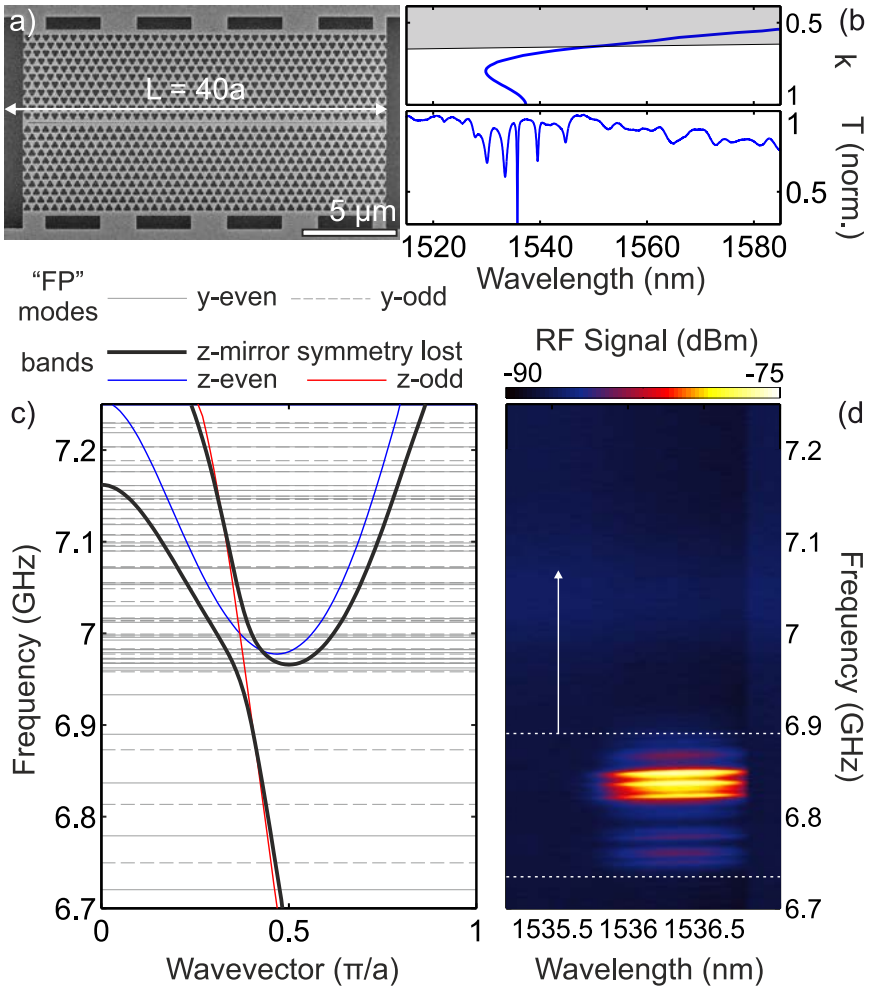

Figure 5.36: Fabry-Pérot (FP) like mechanical modes in a short shamrock slotted photonic crystal waveguide (sPhCW). (a) A shamrock sPhCW with slot width $s = 48$ nm and length $L = 40$a. Etched trenches are introduced in the terminations to achieve better optical and mechanical confinement. (b) Band dispersion and transmission optical spectrum of the structure shown in (a). (c) Band structure of the guided mechanical bands with the as-fabricated vertical profile (black) and with vertical sidewalls (blue for z-even and red for z-odd). The horizontal solid and dashed grey lines provide the calculated eigenfrequencies in a simulated device of length $L = 40a$. (b) RF spectral map of the high-Q optical mode highlighted in (b) when driven at $P_{in} = 7mW$. The white arrow highlights the spectral mismatch between the calculated bands and the measured mechanical modes.

the minor difference coming from the overall scaling Γ of the structure measured here. We observe the same shift when a long open waveguide is measured on the new chip, which rules out that the difference originates from a finite size effect. The waveguided mechanical modes of an $L = 40a$ structure can be simulated with the available computational resources even when the irregular etch profile is considered. The simulated structure has no in-plane disorder and modes are therefore split into y-even and y-odd modes with respect to the mirror plane defined by the waveguide axis and the thickness. The eigenfrequencies of the supported modes

are shown with solid and dashed grey lines in Fig. 5.36(c). The same panel shows the mechanical band structure for the same frequency region (thick black lines). The loss of the vertical symmetry hybridizes the z-even (blue) and z-odd (red) bands, as evidenced by the anticrossing. This also mixes the OM darkness or brightness of the modes. A rather constant free spectral range is observed within the region spanning 6.7 to 6.98 GHz, where the guided mechanical band has fairly constant slope. However, the eigenspectrum is more intricate in the region above 6.98 GHz, where the waveguide simultaneously supports three guided modes. An additional complication is introduced by the free surfaces at the etched terminations, which also support guided modes that can couple to those of the waveguide under study. In addition, the splitting of modes into y-even and y-odd modes is probably lost in the measured spectrum due to the presence of the fiber taper in contact. In summary, the observed mechanical resonances in (d) have a considerably smaller FSR than that shown in (c) for the same frequency region. In addition, they lie at frequencies where the guided mode is mainly odd with respect to the mid plane, i.e. any FP-like mechanical mode from that band is expected to be weakly coupled to the light field. Last, the OM coupling in an extended structure is expected for modes originating close to the Γ point, where neighboring unit cells add-up constructively in the integral defining g_o (Subsection 3.5.2 of Chapter 3). For these facts, the calculated bands are shifted with respect to the real underlying bands. We attribute the observed modes to FP-like modes from the originally z-even band. The shift is schematically represented on Fig. 5.36(c) with a white arrow, although what really shifts is the underlying band structure.

5.4.2 Dynamical back-action amplification

The backaction of the Anderson-localized cavity light field on the high-frequency mechanics is observed on some of the longer shamrock sPhCWs. This is shown in Fig. 5.37 for a waveguide of length $L = 400a$ and slot width $s = 48$ nm belonging to the varying-length series of the device shown in Fig. 5.36. Fig. 5.37(a) shows the low and high ($P_{in} = 2$ mW) power optical transmission spectra of the probed optical mode, which possesses both surprisingly low Q-factor and high TO effect. The RF spectral map as a function of laser wavelength is given below and evidences the presence of two different type of mechanical modes: the low-frequency in-plane modes and a single high-frequency GHz mode with frequency $f_m = 6.842$ GHz. The spectrum at the wavelength marked with the white dashed line is shown in Fig. 5.37(b). The high-amplitude peak at f_m corresponds to the mechanical mode undergoing OM self-sustained oscillations. We were not able to obtain the temporal trace due to the limited bandwith of our oscilloscope, but the coherence of the high amplitude signal induces the sidebands appearing around the carrier peak, which are replicas of the low-frequency MHz modes. This is also evidenced by the zoomed-in RF spectral map shown in Fig. 5.37(c) and the different spectra of Fig. 5.37(d), where a progressive linewidth narrowing and stiffening is observed before reaching the self-sustained oscillations. Again, as in Fig. 5.30, the oscillation frequency f_{OMO} then decreases when the detuning is further reduced. Note that with the measured $Q \approx 9500$ and mechanical frequency, the

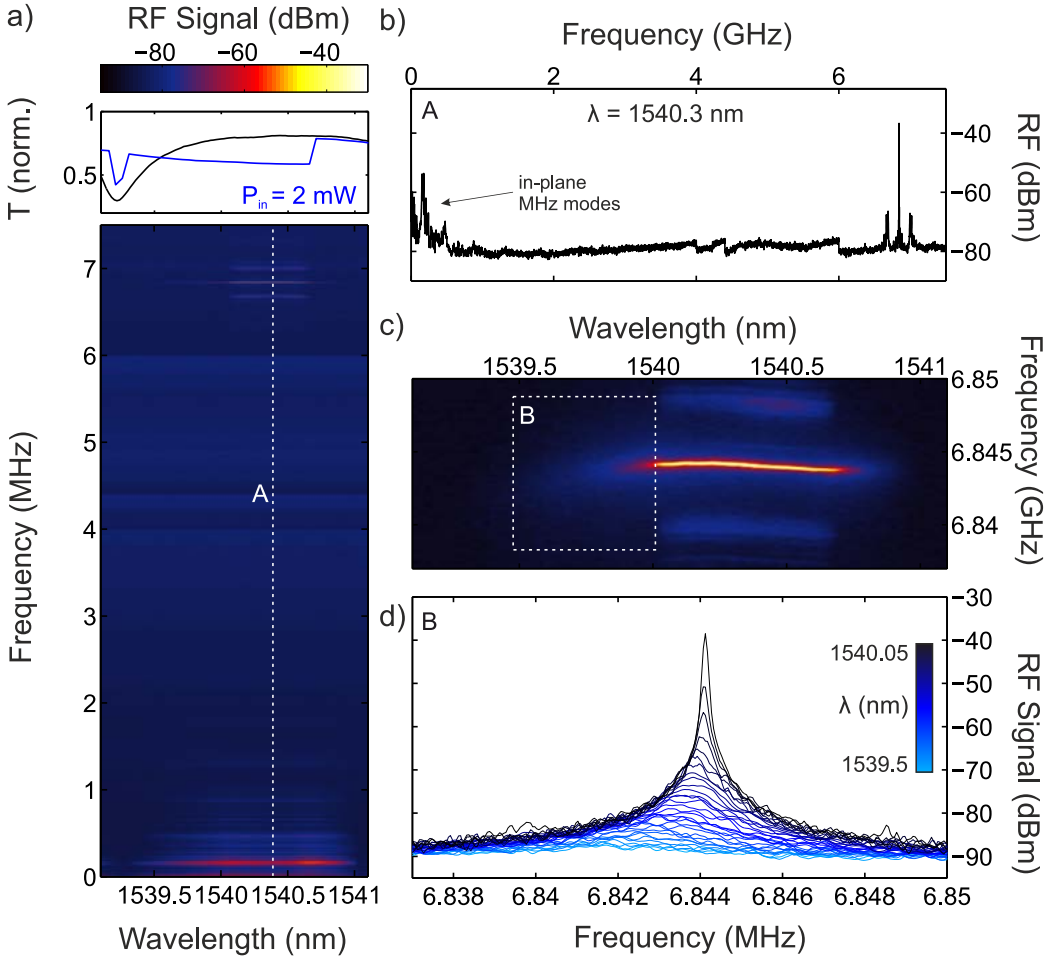

Figure 5.37: Dynamical backaction amplification and optomechanical (OM) oscillation with an Anderson-localized optical mode and a GHz mechanical mode (a) Optical transmission spectrum and radiofrequency (RF) spectral map of an Anderson-localized mode driven at $P_{in} = 2$ mW, where both transduction of low-frequency in-plane mechanical motion and of a high-frequency mode at $f_m = 6.842$ GHz are evidenced. The RF spectrum at position A -marked with a white dashed line- is given in (b). (c) Detailed RF spectral map around f_m, with the region leading to self-oscillation marked with a white dashed box. Representative spectra in that region are shown separately in (d), evidencing both stiffening and amplification of the motional state as the characteristic dynamical-backaction path towards self-oscillation.

system is still largely sideband unresolved since $\frac{\kappa}{\Omega_m} \sim 3$, but the highest Q-factor modes measured on the same waveguides are such that $\kappa \approx \Omega_m$, which suggests that the sideband resolved regime with Anderson-localized optical modes is at experimental reach.

The transduced mechanical spectra in long open waveguides (Fig. 5.35) might originate from FP-like mechanical resonances or from localized mechanical modes. The spectral information gathered does not allow a clear identification of their spatial features. However, the observed dynamical backaction amplification in this system, where a single mechanical mode is visible and an

Anderson-localized optical mode is employed, are hints for its localized nature. For a localized optical mode with a small mode volume V_o, we expect a rather low OM coupling if $V_m \gg V_o$, with V_m the mechanical mode volume, since most of the mechanical mode volume does not participate in the coupling. Both the measured $g_o \approx 2\pi \cdot$ 62 kHz with a frequency-modulation technique (Subsection 5.3.2) and the observed rich dynamics point towards a localized interaction. In addition, the frequency of the mechanical mode probed here matches well the position of the highest frequency modes observed in Fig. 5.36(d), which would correspond to the mechanical band edge if the suggested shift in Fig. 5.36(c,d) is real. Nevertheless, more experimetal data are needed to unambiguosly determine the nature of the modes.

Chapter 6

Conclusions and perspectives

We summarise the main results of this thesis and discuss their relevance. We also suggest possible extensions to this work that could further facilitate the observation of Anderson-localized mechanical excitations in the GHz range enabled by optomechanics. Pursuing this fundamental objective and the concepts used to address it has also led to another major scientific question with important technological implications, namely, how can we instead attempt to prevent the subtle but dramatic effects that disorder has on photon-phonon transport and use their cumulative interaction over increasing lengths? During the last months of the research reported here, we studied how the field of topological bosonics could offer an answer to this question. We briefly present the results obtained since these constitute an example of how the knowledge acquired can be applied to fast-growing fields like topological photonics or acoustics. The chapter has two blocks: how can optomechanics be used to understand phonon transport in the presence of disorder, and, how can we minimize its effects to guarantee lossless transport.

6.1 How to harness disorder?

In this thesis, we have used both simulations and experiment to design and demonstrate various optomechanical systems where the localization of photons via disorder can be used as a local probe for mechanical spectroscopy, with a special emphasis on how to observe mechanical Anderson localization at high frequencies. Studies on the Anderson localization of elastic waves above the MHz range are scarce compared to the broad variety of systems/frequencies explored in the case of electromagnetic waves. This is probably due to the current limited range of generation and detection methods as compared to photons. While the latter are easily generated, injected into the device under test and detected even far away from it, the former require much more elaborate experimental schemes. Generating GHz-phonons and injecting them into the region of interest (a disordered structure in this case) requires either dedicated material platforms exhibiting piezoelectricity and the required patterning of resonant nanostructures including interdigitated transducers (IDTs), or high-power pulsed lasers in coherent phonon pump-probe spectroscopy, as discussed in Chapter 4. The detection is then typically achieved

using optical techniques, e.g. reflectometry, interferometry or vibrometry. In the case of mechanical vibrations in a disordered nanostructure, the expected localized nature of the supported excitations make this task even more complex. Ideally, one would like to measure the spatio-spectral properties of the thermally-activated mechanical motion with an in-situ transducer. In this thesis, we have identified the critical parameters to achieve such a goal by using simultaneously confined photons and phonons in disordered optomechanical structures.

The spatial co-localization of photons and phonons is the first condition to enable their interaction in nanostructured media. In conventional optomechanical schemes this is granted by design, but nothing ensures it is in the Anderson-localization regime due to the random and independent nature of the two interference processes. We have presented (part of Chapter 4) a numerical analysis of simultaneous Anderson localization of the two wave fields in a particular set of random superlattices, a 1D photonic/phononic crystal, with emphasis on their spatial overlap and their acousto-optic interaction. Our calculations provide quantitative evidence of the role played by spatial co-localization of mechanical and optical excitations in GaAs/AlAs superlattices in which the likelyhood of spatial overlap is greatly enhanced as a consequence of a material property that ensures *perfect* co-localization between certain photon-phonon pairs. The coupling of the cavity light field to the mechanical motion in GaAs/AlAs DBR-based cavity structures appears to be a natural and appropriate choice to observe Anderson localization of phonons at frequencies $\sim$ 20 GHz and even to explore Anderson localization of coupled excitations [25]. While we have focused in the numerical simulation of such structures, the growth of disordered GaAs/AlAs DBRs using molecular beam epitaxy (MBE) would in principle allow for a verification of the numerical findings. GaAs/AlAs nanophononic structures are regularly grown with a wedge along a particular direction [232,252,432,433] to allow frequency-detuning of the drive laser with respect to, e.g., a nanophotonic cavity mode. In principle, one could grow a wafer with continously increasing level of disorder along the radial direction by randomly choosing the wedge direction and sample rotation between layers also randomly. Moreover, due to the optomechanical nature of standard coherent phonon generation/detection experiments in GaAs/AlAs mutilayers, the conditions for read-out are well understood in terms of the optomechanical coupling g_o. The integration of quantum emitters [434] during MBE growth could enable cavity quantum-electrodynamics experiments in the Anderson-localization regime coupled to the motion of high frequency nano-mechanical oscillators, as well as to explore the role of phonon-mediated dephasing in random lasers [402]. Finally, the discussed structures can be scaled down to study Anderson localization of sub-THz vibrations with extended light modes or etched into micropillars to study 3D-confined coupled excitations [282].

We have then transitioned to 3D dielectric nanostructures in the form of photonic crystal waveguides (PhCWs) in a planar silicon slab. Substantial spectral evidence of Anderson localization of light with quality factors up to $Q \sim 10^5$ has been gathered via optical spectroscopy using a fiber taper evanescent-coupling technique in both standard and slotted PhCWs (sPhCWs). The inclusion of the subwavelength air-slot has allowed the observation of the thermal motion

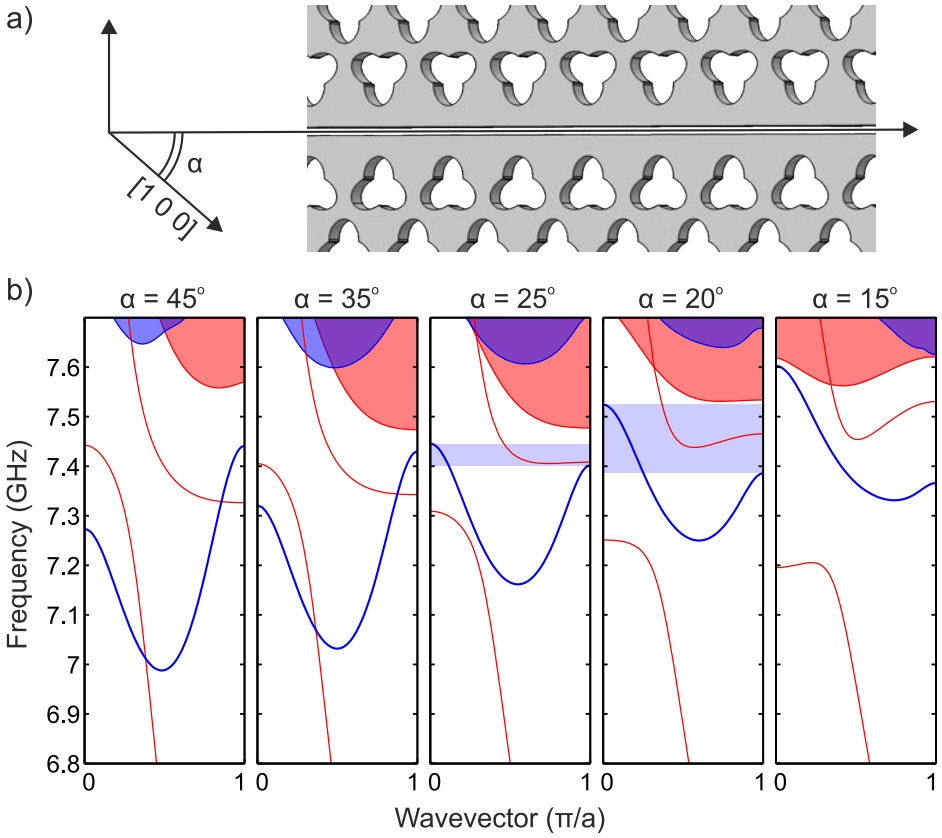

Figure 6.1: Single-mode mechanical guided resonance. The mechanical band structure can be tuned by changing the relative orientation of the waveguide axis with respect to the crystalline axis. (a) Schematic of the mechanical waveguide explored and its orientation at an angle α with respect to the [1 0 0] silicon axis. The case experimentally shown corresponds to $\alpha = 45°$, i.e. the waveguide along the [1 1 0] direction. (b) Phononic band diagram as a function of the angle α. The shaded regions in panels $\alpha = 25°$ and 20° mark the regions where the z-symmetric band (blue) is single mode close to the Γ point.

associated to MHz in-plane differential modes and GHz guided modes of long (L up to 200 μm) suspended structures. Optomechanical coupling to Anderson optical modes with rates g_o as high as $2\pi\cdot$ 300 kHz has been measured for slots of width $s = 40$ nm. The achieved g_o and the high optical Q of the localized optical modes lead to amplification of the motional amplitude of particular mechanical modes at moderate (sub-mW for MHz modes to several mW for GHz modes) drive powers. Self-sustained oscillations using dynamical backaction with the driven Anderson-localized cavity field are reported at both frequency ends. While the extended in-plane modes are immune to fabrication disorder, the high-frequency modes are expected to be. The inference of the spatial extension of the observed GHz mechanical modes via their spectral properties remains nonetheless elusive due to the complicated dispersion of the optomechanically bright band and its coupling to isofrequency bands due to the deviation from vertical side-wall during dry-etching. However, the proposed design can be minimally altered to produce a band structure that could elucidate this question. While the optical properties are, in principle, not affected by rotating the waveguide axis with respect to the

silicon crystalline axis, the mechanical properties are. The mechanical bands of a shamrock sPhCW evolve continuously with the angle α between the axis and the [100] direction (Fig. 6.1). The experimentally probed waveguides, corresponding to $\alpha = 45°$ or a [110]-oriented axis, have no z-symmetric single-mode bandwith around the Γ point, but this is achieved for a specific range of angles around 20-25°. With such design, the fluctuations of the group velocity as extracted from Fabry-Pérot mechanical resonances would be an invaluable fingerprint of Anderson-localization as is the case for the optical modes. While the regime of disorder-induced localization is considerably exploited in PhCWs, with evidence of strong-coupling cavity quantum electrodynamics [366] and low-threshold random lasing [402] in GaAs, little work exists on phononic crystal waveguides [435,436] operating at GHz frequencies and on the effect of fabrication disorder on the propagation of slow sound. The work presented here constitutes an important step towards achievieng such regime.

These results and the simple design improvement make shamrock sPhCWs an excellent platform for two-dimensional optomechanical experiments in the Anderson-localization regime, and not just limited to it. Although most milestone experiments in the field of cavity optomechanics use one-dimensional nanobeam optomechanical crystal (OMC) cavities, often surrounded by two-dimensional phononic shields, the initial efforts on two-dimensional OMC cavities [63,167,411] are recently regaining momentum. The higher dimensionality of the platform enables efficient thermalization as compared to nanobeam OMCs which have limited thermal conductance [169], thus cirumventing a main roadblock for the quantum manipulation of such devices at millikelvin temperatures. Engineered OMC cavities in dual photonic and phononic band gap structures relying on a simple geometry, e.g. the shamrock, promise to be an important building block for quantum information processing and quantum sensing with optomechanical degrees of freedom. The inclusion of the air slot in the shamrock waveguides could also allow a strong ultracold atom-photon-phonon (tripartite) interaction [437], enabling optomechanics at the quantum level.

6.2 How to fight disorder?

The role of both intentional and unintentional disorder in periodic-on-average optical and acoustic nanostructures hosting propagating modes depends on a myriad of aspects such as the dimensionality of the structure, the periodic pattern, the type and level of disorder, the field profile of the supported modes, etc. Ultimately, the effect of all of these parameters on the transport properties of low-dimensional nanostructures is quantified via the localization length ξ. As extensively discussed in this thesis, ξ is a key figure of merit in determining the characteristic length-scale of Anderson-localized modes. This has led us to consider OMC waveguides, where the optical localization length has been shown to be of only several unit cells, as the most adequate platform to study phonon localization enabled by optomechanics. However, the opposite objective, minimizing the effect of disorder by maximizing ξ is equally relevant as a means to quantify the robustness of nanoscale transport. We have shown how ξ generally depends on the operating

frequency and related the dependence to the dispersive density of states of the unperturbed system. In the case of light, the group index n_g, the slowdown factor of the group velocity of the propagating mode with respect to the speed of light in vacuum, and ξ are intimately linked via the density of optical states (DOS), i.e. a larger n_g leads to a smaller ξ. A general conclusion that we extract from the work carried out in this thesis is that these two figures of merit, ξ and n_g, have to be taken into account when quantifying the robustness of (slow-light) transport against fabrication imperfection. Therefore, these figures of merit are critical to claim on the improved performance of a waveguide design over another, a key issue for technological applications requiring slow light.

In the last years, topology, the mathematical branch of conserved properties under continuous deformations, has emerged as a new fundamental degree of freedom to predict and control the propagation of light [438] or sound [439]. In this thesis, we have numerically and experimentally demonstrated a high frequency (200 GHz) acoustic interface state between two concatenated superlattices and discussed its emergence in terms of the differing topological phases of the bulk superlattices. The bridge between the topological invariants, the Zak phases, and the resulting interface state is provided by the reflection phases in a spacerless Fabry-Pérot cavity and linked to the symmetry properties of the band edge modes. The use of coherent phonon spectroscopy with selection rules sensitive to these particular symmetries has allowed the clear assignment of the experimentally observed acoustic mode to a topological interface state. The reasoning used to proof the existence of the interface state constitutes a form of the bulk-edge correspondence [440], the fundamental principle called to justify the emergence of the edge states in topological photonics and/or acoustics. Inspired by the dissipationless transport of interfacial electrons in topological insulators, this suggests the possibility of back-scatter immune propagation of photons with the potential of achieving slow light that is insensitive to disorder, or, in other words, to prevent Anderson localization. However, several implementations of photonic topological edge states have been proposed and the level of protection may vary considerably. The most robust implementations use time-reversal symmetry broken edge states [441], for which the time-reversed state at -**k** does not exist, preventing direct elastic backscattering of the propagating mode. However, it requires strong magnetic effects which at visible and near-infrared wavelengths are very weak and challenging to implement [146]. In time-invariant topological insulators based on the quantum-spin Hall effect [442] and the valley-Hall effect [443], topology emanates from the breaking of particular spatial symmetries. In such implementations, the counterpropagating state at -**k** is granted by reciprocity, but carries the opposite value of a binary degree of freedom, i.e., a pseudo-spin [442]. In this case, the key open question we tackle here is whether backscattering is reduced for such implementation. Does the existing structural disorder preserve the pseudo-spin value, or not? Recent ground breaking experiments have reported robustness to structural back-reflection when precisely-shaped local defects were introduced in different topological waveguides [444–449]. However, this claimed robustness still needs to be systematically quantified against fabrication imperfection, the real limitation in slow-light transport. It is also crucial to compare these values to

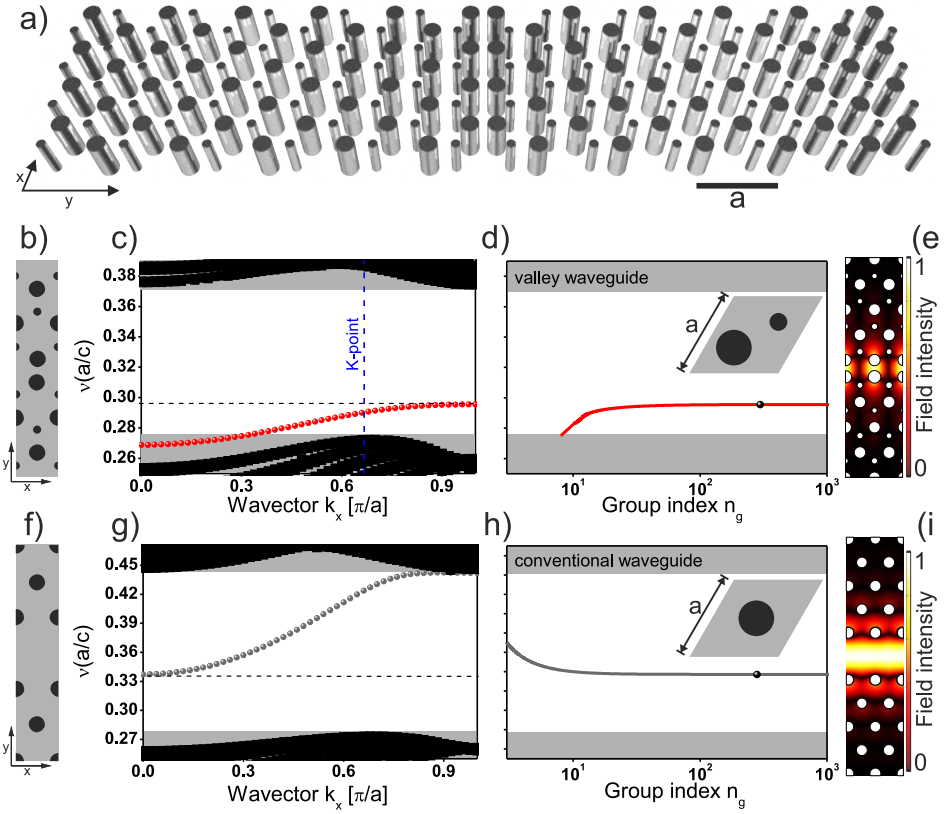

Figure 6.2: Slow light in a valley-Hall topological waveguide. (a) llustration of a valley-Hall topological waveguide formed at the interface of two valley crystals with different topological invariants as proposed in Ref. [443]. (b) Distribution of the dielectric function in the structure: black corresponds to silicon and gray to air. Each valley crystal is formed as a triangular periodic lattice with a unit cell composed by two pillars with different diameters to break the spatial inversion symmetry. (c) Dispersion relation, $\nu = \nu(k)$, and (d) calculated group index of the interface topological edge state. The projection of the K point in the waveguide unit cell is marked with a vertical dashed line. The unit cell of each crystal is detailed in the inset. For reference, we design a conventional photonic waveguide obtained by leaving a row of pillars from a triangular lattice (f) with a dispertion relation and a group index plotted in (g) and (h), respectively. The black point in the group index curves denotes the frequency at which each waveguide has a group index of $n_g \approx 300$. The electromagnetic field intensities calculated at these frequencies and for perfect (non-disordered) waveguides are plotted in (e) and (i).

existing conventional designs to determine if this approach is valid or not. Despite the substantial work on ξ in conventional waveguides we have referred to along this thesis, this parameter has only been explored recently in topological waveguides [450] although ignoring the precise value of n_g. Besides this, only intrinsic out-of plane losses of topological guided modes in non-disordered photonic crystal slabs have been analyzed [451].

We compare a standard W1 waveguide in a two-dimensional photonic crystal made of silicon pillars in air with a Valley-Hall (VH) waveguide created at the

interface between two VH photonic crystals [452] using the same materials. The latter is made by interfacing the photonic crystal shown in the inset to Fig. 6.2(d) with its mirrored version across the plane defined by the horizontal lattice vector. The two-dimensional layout of the two waveguides is plotted in Figs. 6.2(b) and (f). Both waveguides support a guided mode along the interface, as shown in Figs. 6.2(c,d,g,h). While the former originates from a standard line defect, the latter can be understood in terms of the topological properties of the bounding crystals. When the two silicon pillars in the unit cell are equal, i.e. $d_1 = d_2$, the system preserves the C_{6v} symmetry of the lattice and supports a symmetry-protected gapless band structure between the first and second lowest energy bands for TM light. When spatial inversion symmetry is broken, a bandgap between these two bands opens at the K point in the Brillouin Zone and the band structure acquires a local non-trivial topology [447]. Due to the bulk-edge correspondance, interfacing two topology unequal crystals, as is the case with a crystal and its mirrored version, leads to an interface edge state [440]. The group index of the topological and the conventional edge modes respectively diverge at the X and Γ points, evidencing how both support extreme slow-light (Figs. 6.2(d) and (h)). The ideal spatial field-intensity distributions in both waveguides, i.e., in absence of any perturbation, and at frequencies corresponding to $n_g = 300$ in both cases are plotted in Figs. 6.2(e) and (i) for reference, evidencing a similar level of light confinement.

We randomize the full phase by introducing positional disorder in the pillars, thus mimicking the effect of imperfection in real systems. The backscattering mean free path ξ of the waveguides is then numerically obtained as done in Chapter 5. For disorder levels of $\sigma = 0.001a$ (Fig. 6.3(a)) the topological waveguide (solid-red circles) is more robust than the conventional slow-light waveguides (open-black circles). Does this difference stem from topological protection? We know now that small geometrical perturbations in the pillars of the waveguides result in small energy shifts $\pm\triangle\nu$ of the dispersion relation of a guided mode [266], shifting the guided-mode cutoff frequency ν. These frequency fluctuations result in a collection of barriers at random positions along the waveguide, responsible for breaking down ballistic propagation. To quantify how large are these barriers at a fixed σ we calculate ν of the guided mode by solving the bands for a disordered supercell of length $N_x = 11a$. Fig. 6.3(b) and (c) plot the distributions of these deviations, $\Delta\nu$, for 10^4 different configurations normalized by the unperturbed cut-off ν_0. This figure shows unambiguously that for the same amount of positional disorder the impact, in terms of the standard deviation of the distribution σ_ν, is stronger for the topological edge state than for the conventional guided mode. We evaluate the linear dependence of σ_ν on positional disorder strength for a wide range of values in both waveguides, where the proportionality constant ϕ quantifies the effective impact of disorder. As plotted in Fig. 6.3(d), the topological waveguide suffers a larger effective impact of disorder than the conventional one. This underlines even more the potential of the topological protection observed here at very large values of n_g and for a considerable slow-light operational bandwith. Even if the dependence of ξ on σ is markedly different on both waveguides and topological protection is lost above a critical disorder strength σ_c [453], these results constitute a first evidence of the role of topology in state-of-the-art

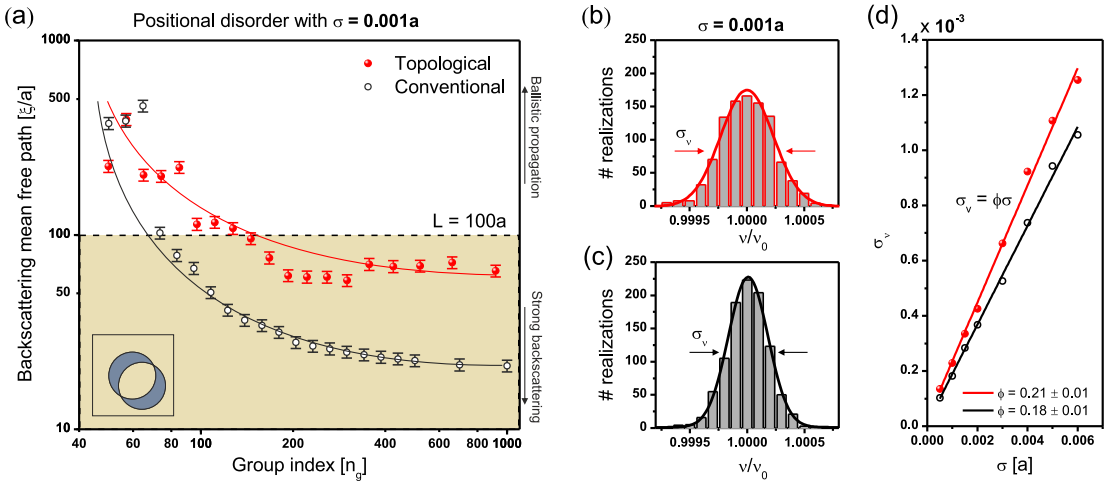

Figure 6.3: Backscattering length versus group index in topological waveguides. (a) Backscattering length calculated for different frequencies corresponding to different values of the group index in a valley (solid-red circles) and a conventional photonic crystal waveguide (open-black circles). The positions of the pillars have been randomized around their ideal values with a standard deviation of $\sigma = 0.001a$. The shaded area indicates the crossover between ballistic transport and strong backscattering for a waveguide of length $L = 100a$. The error bars are a conservative estimate of the fitting error to the exponential decay used to extract ξ. The red and black lines are guides to the eye. (b,c) Distributions of the cutoff frequency calculated in a topological and a conventional waveguide of 11 cells in the x-direction for 10^4 different configurations of positional disorder with $\sigma = 0.001a$. The calculated frequency is normalized to the frequency of the unperturbed structures ν_0. (d) Standard deviation of the distribution of the frequency shifts $\pm\triangle\nu$ as calculated in (b) and (c) vs. the strength of the perturbation. From the relation $\sigma_v = \phi\sigma$, we quantify the effective impact of disorder in the waveguides with the parameter ϕ.

extreme slow-light.

In conclusion, we show how to quantify the robustness of a topological edge states against white noise depending on its structural parameters. Calculating the backscattering length linked to the group index enables us to do that. We conclude that current proposals of topological photonic phases relying on the breaking of different parity symmetries may quantitatively be more robust than standard conventional waveguides with small disorder levels. Although this analysis is carried out on a particular design and for a particular system of silicon pillars surrounded by air, the approach is completely generic and can be implemented for any other single-mode waveguide with arbitrary design. Future work to evaluate topological invariants [454] of different topological implementations will provide additional insight on the relationship between the backscattering length evolution with disorder level and the topological invariants of perturbed phases. The large values of the group index calculated here, $n_g \simeq 1000$, affected by a relatively weak backscattering, show the potential of topological edge states for highly efficient strong light-matter interaction [455] where photon transmission over hundreds of

microns is relatively backscattering-free. These propagating edge states promise to extend the effective length of optomechanical circuits and boost the Brillouin gain, opening the door to a range of applications in silicon photonic circuits.

Appendix A

Guided-Mode-Expansion

Photonic crystal slabs are slabs with an embedded periodicity in the in-plane directions. In the same way as we use plane waves in Plane Wave Expansion (PWE) as a reasonable basis to develop the solution to Maxwell's equations in systems exhibiting periodicity in some direction(s) of space and translational invariance in the rest, it appears as natural to use homogeneous dielectric slab waveguide modes of an effective slab as a basis in which to project Maxwell's equations in photonic crystal slabs (PCSs). Since the index profile in the z direction in such structures has the shape of a square function, the use of PWE as a numerical tool to obtain dispersion diagrams becomes numerically inefficient since large number of wave-vectors in reciprocal space are required to reproduce the desired profile. The Guided Mode Expansion (GME) has the advantage of requiring very few effective dielectric slab modes since those reproduce well the field-structure of the real solution. The basis of guided modes of an effective homogeneous dielectric slab is not a complete basis and GME is therefore an approximate method by definition. Nevertheless, this method has proven computationally reliable and efficient [159], specially to compute the dispersion diagram of the lower energy bands and the intrinsic losses of quasi-guided modes [159,339,456,457]. The aim of this Appendix is to describe the formalism to calculate band diagrams for such structures and a way to estimate the optical losses due to coupling with radiative modes by using a first order perturbation theory approach, equivalent to a Fermi Golden's rule in quantum mechanics. The formalism is based on [159,458].

A.0.1 Photonic dispersion band diagram

All macroscopic electromagnetism phenomena are governed by the four Maxwell's equations in matter, and propagation in complex structures is not an exception. Under often verified assumptions such as linear dependence of the material's polarization and homogeneous constant magnetic permeability $\mu = 1$, the second-order equation for the magnetic field $\mathbf{H}$ with harmonic time dependence writes

$$\nabla \times [\frac{1}{\varepsilon(\mathbf{r})} \nabla \times \mathbf{H}] = \frac{\omega^2}{c} \mathbf{H} \tag{A.1}$$

with the additional condition that the magnetic field needs to be divergence-free; i.e. $\nabla \cdot \mathbf{H} = 0$. In order to solve this equation, we can expand the magnetic field in an orthonormal set of basis states

$$\sum_{\mu} c_\mu \mathbf{H}_\mu((r)) \quad \text{with orthogonality condition} \tag{A.2a}$$

$$\int \mathbf{H}^*_\mu((r)) \cdot \mathbf{H}_\nu((r)) d\mathbf{r} = \delta_{\mu\nu} \tag{A.2b}$$

Inserting A.2a into A.1 and using condition A.2b bears

$$\sum_{nu} H_{\mu\nu} c_\nu = \frac{\omega^2}{c} c_\nu \tag{A.3}$$

with matrix element

$$H_{\mu\nu} = \int \frac{1}{\varepsilon(\mathbf{r})} (\nabla \times \mathbf{H}^*_\mu(\mathbf{r})) \cdot (\nabla \times \mathbf{H}_\nu(\mathbf{r})) d\mathbf{r} \tag{A.4}$$

Obtaining the electric field is direct once the magnetic field is known, by applying

$$\mathbf{E}(\mathbf{r}) = \frac{ic}{\omega \varepsilon(\mathbf{r})} \nabla \times \mathbf{H}(\mathbf{r}) \tag{A.5}$$

To solve this problem numerically requires the choice of a given basis and a way to make this linear eigenvalue problem of finite-dimension. For the type of geometries we are concerned with, the chosen basis for this method are the guided modes of an effective homogeneous slab surrounded by two semi-infinite effective layers. We define the effective dielectric constants $\overline{\varepsilon}_1, \overline{\varepsilon}_2, \overline{\varepsilon}_3$ of the three layers as their average dielectric constant over their respective 2D-unit cells (u.c.),

$$\overline{\varepsilon}_i = \frac{1}{A_{u.c.}} \int_{u.c.} \varepsilon_i(\mathbf{x}) d\mathbf{x} \tag{A.6}$$

with $\mathbf{x} \equiv (x, y)$ the coordinate in the x,y-plane. The choice is not unique and by no means globally optimal, but it turns out to be computationally convenient for most of the cases this work was concerned with. In any case, we must have $\overline{\varepsilon}_2, \overline{\varepsilon}_1, \overline{\varepsilon}_3$ to define guided modes in this dielectric structure. Here, we restrict our basis to actual guided modes of the effective slab because the relevant photonic modes of the structures lie below the light cone do not couple to the radiative field. The formalism has been extended to include the leaky modes of the dielectrib slab [459].

Let us now properly define the basis of guided modes of the effective slab. The spatial profile of the magnetic field $\mathbf{H}$ of such modes writes

$$\mathbf{H}_\mathbf{g}(\mathbf{x}, z) = \frac{e^{i\mathbf{g}\cdot\mathbf{x}}}{\sqrt{A}} B_1(-q_1 \hat{\mathbf{g}} + i|\mathbf{g}|\hat{\mathbf{z}}) e^{q_1(z+\frac{d}{2})}, \qquad z \leq -\frac{d}{2} \tag{A.7a}$$

$$i\frac{e^{i\mathbf{g}\cdot\mathbf{x}}}{\sqrt{A}} (A_2(-q_2 \hat{\mathbf{g}} + |\mathbf{g}|\hat{\mathbf{z}}) e^{iq_2 z} + B_2(q_2 \hat{\mathbf{g}} + |\mathbf{g}|\hat{\mathbf{z}}) e^{-iq_2 z}), \quad |z| \leq \frac{d}{2} \tag{A.7b}$$

$$\frac{e^{i\mathbf{g}\cdot\mathbf{x}}}{\sqrt{A}} A_3(q_3 \hat{\mathbf{g}} + i|\mathbf{g}|\hat{\mathbf{z}}) e^{-q_3(z-\frac{d}{2})}, \qquad z \geq -\frac{d}{2} \tag{A.7c}$$

for transverse electric (TE) polarization and

$$\mathbf{H}_{\mathbf{g}}(\mathbf{x},z) = \frac{e^{i\mathbf{g}\cdot\mathbf{x}}}{\sqrt{A}}\hat{\boldsymbol{\epsilon}}_{\boldsymbol{g}} D_1 e^{q_1(z+\frac{d}{2})}, \qquad z \leq -\frac{d}{2} \tag{A.8a}$$

$$\frac{e^{i\mathbf{g}\cdot\mathbf{x}}}{\sqrt{A}}\hat{\boldsymbol{\epsilon}}_{\boldsymbol{g}} (C_2 e^{iq_2 z} + D_2 e^{-iq_2 z}), \qquad |z| \leq \frac{d}{2} \tag{A.8b}$$

$$\frac{e^{i\mathbf{g}\cdot\mathbf{x}}}{\sqrt{A}}\hat{\boldsymbol{\epsilon}}_{\boldsymbol{g}} C_3 e^{-q_3(z-\frac{d}{2})}, \qquad z \geq -\frac{d}{2} \tag{A.8c}$$

for transverse magnetic (TM) polarization. Here $\mathbf{g}$ denotes the in-plane wave-vector, $\hat{\mathbf{g}}$ the unit vector in the same direction and $\hat{\boldsymbol{\epsilon}}_{\boldsymbol{g}} \equiv \hat{\mathbf{z}} \times \hat{\mathbf{g}}$ perpendicular to both $\hat{\mathbf{z}}$ and $\hat{\mathbf{g}}$, while

$$q_1 = \sqrt{|\mathbf{g}|^2 - \overline{\varepsilon}_1 \frac{\omega^2}{c^2}} \tag{A.9a}$$

$$q_2 = \sqrt{\overline{\varepsilon}_1 \frac{\omega^2}{c^2} - |\mathbf{g}|^2} \tag{A.9b}$$

$$q_3 = \sqrt{|\mathbf{g}|^2 - \overline{\varepsilon}_3 \frac{\omega^2}{c^2}} \tag{A.9c}$$

are the out-of-plane component of the wave-vectors in the corresponding layers where the fact that $c|\mathbf{g}|/n_2 \leq \omega \leq c|\mathbf{g}|/max(n_1, n_3)$ for core-guided modes has been taken into account. The normalization parameter A is not relevant here. Applying Maxwell's boundary conditions on the two interfaces and the normalization condition determines all the coefficients and imposes the following implicit dispersion relation on the allowed modes

$$q_2(q_1+q_3)\cos(q_2 d) + (q_1 q_3 - q_2^2)\sin(q_2 d) = 0, \qquad \text{for TE modes} \tag{A.10a}$$

$$\frac{q_2}{\overline{\varepsilon}_2}\left(\frac{q_1}{\overline{\varepsilon}_1} + \frac{q_3}{\overline{\varepsilon}_3}\right)\cos(q_2 d) + \left(\frac{q_1 q_3}{\overline{\varepsilon}_3 \varepsilon_3} - \left(\frac{q_2}{\overline{\varepsilon}_2}\right)^2\right)\sin(q_2 d) = 0, \qquad \text{for TM modes} \tag{A.10b}$$

The solutions to A.10 are organized in bands, such that for a fixed value of $\mathbf{g}$ we have a discrete set of solutions with ω real. Here, we label the guided-modes with a single parameter μ, where this one has the information on the wave-vector $\mathbf{g}$ and the band-index α such that $\mu \equiv (\mathbf{g}, \alpha)$.

The solutions to A.1 in a photonic crystal slab obey Bloch's theorem and it is easy to then verify that the wave-vectors $\mathbf{g}$ of interest for the basis described above can be redefined as $\mathbf{g} = \mathbf{k_{Bloch}} + \mathbf{G}$ where $\mathbf{k_{Bloch}}$ is the Bloch wavevector of the solution in the first Brillouin zone and $\mathbf{G}$ is a reciprocal lattice vector. For simplicity we will note now $\mathbf{k_{Bloch}} \equiv \mathbf{k}$. Thus, the solution we seek can be written as:

$$\mathbf{H}_{\mathbf{k}} = \sum_{\mathbf{G},\alpha} c_{\mathbf{k}+\mathbf{G},\alpha} \mathbf{H}_{\mathbf{k}+\mathbf{G},\alpha}(\mathbf{r}) \tag{A.11}$$

where $\mathbf{H}_{\mathbf{k}+\mathbf{G},\alpha}$ will include both TE and TM modes.

The basis being defined, we can now compute the matrix elements of Equation A.4 where we set $\mu = (\mathbf{k}+\mathbf{G}, \alpha)$ and $\nu = (\mathbf{k}+\mathbf{G}', \alpha')$. Four different types

of combinations (TE-TE,TE-TM,TM-TE,TM-TM) yield the following different matrix elements

$$\begin{aligned} H_{\nu\mu}^{TE-TE} =&(\frac{\omega_\mu}{c})^2(\frac{\omega_\nu}{c})^2(\hat{\boldsymbol{\epsilon}}_{\boldsymbol{k+G}}\cdot\hat{\boldsymbol{\epsilon}}_{\boldsymbol{k+G'}})\{(\overline{\varepsilon}_1)^2\eta_1(\mathbf{G},\mathbf{G}')B_{1,\mu}^*B_{1,\nu}I_1 \\ &+(\overline{\varepsilon}_3)^2\eta_3(\mathbf{G},\mathbf{G}')A_{3,\mu}*A_{3,\nu}I_3+(\overline{\varepsilon}_2)^2\eta_2(\mathbf{G},\mathbf{G}')[(A_{2,\mu}^*A_{2,\nu} \\ &+B_{2,\mu}^*B_{2,\nu})I_{2,-}+(A_{2,\mu}^*B_{2,\nu}+B_{2,\mu}^*A_{2,\nu})I_{2,+}]\} \end{aligned} \tag{A.12a}$$

$$\begin{aligned} H_{\nu\mu}^{TE-TM} =&(\frac{\omega_\mu}{c})^2(\hat{\boldsymbol{\epsilon}}_{\boldsymbol{k+G}}\cdot\widehat{(\mathbf{k}+\mathbf{G}')})\{-\overline{\varepsilon}_1\eta_1(\mathbf{G},\mathbf{G}')B_{1,\mu}^*D_{1,\nu}q_{1,\nu}I_1 \\ &+\overline{\varepsilon}_3\eta_3(\mathbf{G},\mathbf{G}')A_{3,\mu}^*C_{3,\nu}q_{3,\nu}I_3+i\overline{\varepsilon}_2\eta_2(\mathbf{G},\mathbf{G}')q_{2,\nu}[(-A_{2,\mu}^*C_{2,\nu} \\ &+B_{2,\mu}^*D_{2,\nu})I_{2,-}+(A_{2,\mu}^*D_{2,\nu}-B_{2,\mu}^*C_{2,\nu})I_{2,+}]\} \end{aligned} \tag{A.12b}$$

$$\begin{aligned} H_{\nu\mu}^{TM-TE} =&(\frac{\omega_\nu}{c})^2((\widehat{\mathbf{k}+\mathbf{G}})\cdot\boldsymbol{\epsilon}_{\boldsymbol{k+G'}})\{-\overline{\varepsilon}_1\eta_1(\mathbf{G},\mathbf{G}')D_{1,\mu}^*B_{1,\nu}q_{1,\mu}I_1 \\ &+\overline{\varepsilon}_3\eta_3(\mathbf{G},\mathbf{G}')C_{3,\mu}^*A_{3,\nu}q_{3,\mu}I_3-i\overline{\varepsilon}_2\eta_2(\mathbf{G},\mathbf{G}')q_{2,\mu}[(-C_{2,\mu}*A_{2,\nu} \\ &+D_{2,\mu}^*B_{2,\nu})I_{2,-}+(D_{2,\mu}^*A_{2,\nu}-C_{2,\mu}^*B_{2,\nu})I_{2,+}]\} \end{aligned} \tag{A.12c}$$

$$\begin{aligned} H_{\nu\mu}^{TM-TM} =&\eta_1(\mathbf{G},\mathbf{G}')D_{1,\mu}*D_{1,\mu}(q_{1,\mu}q_{1,\nu}\widehat{\mathbf{k}+\mathbf{G}}\cdot\widehat{\mathbf{k}+\mathbf{G}'}+|\mathbf{k}+\mathbf{G}||\mathbf{k}+\mathbf{G}'|)I_1 \\ &+\eta_3(\mathbf{G},\mathbf{G}')C_{3,\mu}*C_{3,\mu}(q_{3,\mu}q_{3,\nu}\widehat{\mathbf{k}+\mathbf{G}}\cdot\widehat{\mathbf{k}+\mathbf{G}'}+|\mathbf{k}+\mathbf{G}||\mathbf{k}+\mathbf{G}'|)I_3 \\ &+\eta_2(\mathbf{G},\mathbf{G}')[(C_{2,\mu}*C_{2,\nu}+D_{2,\mu}*D_{2,\nu})(q_{2,\mu}q_{2,\nu}\widehat{\mathbf{k}+\mathbf{G}}\cdot\widehat{\mathbf{k}+\mathbf{G}'} \\ &+|\mathbf{k}+\mathbf{G}||\mathbf{k}+\mathbf{G}'|)I_{2,-}+(C_{2,\mu}*D_{2,\nu}+D_{2,\mu}*C_{2,\nu})(-q_{2,\mu}q_{2,\nu} \\ &\widehat{\mathbf{k}+\mathbf{G}}\cdot\widehat{\mathbf{k}+\mathbf{G}'}+|\mathbf{k}+\mathbf{G}||\mathbf{k}+\mathbf{G}'|)I_{2,+}] \end{aligned} \tag{A.12d}$$

where I_j correspond to the following definite integrals

$$I_1=\int_{-\infty}^{-\frac{d}{2}}e^{(q_{1,\mu}+q_{1,\nu})(z+\frac{d}{2})}dz=\frac{1}{q_{1,\mu}+q_{1,\nu}} \tag{A.13a}$$

$$I_{2,+/-}=\int_{-\frac{d}{2}}^{\frac{d}{2}}e^{i(q_{2,\mu}+q_{2,\nu})z}dz=2\frac{\sin((q_{2,\mu}\pm q_{2,\nu})\frac{d}{2})}{(q_{2,\mu}\pm q_{2,\nu})} \tag{A.13b}$$

$$I_3=\int_{\frac{d}{2}}^{\infty}e^{-(q_{3,\mu}+q_{3,\nu})(z-\frac{d}{2})}dz=\frac{1}{q_{3,\mu}+q_{3,\nu}} \tag{A.13c}$$

and $\eta_j(\mathbf{G},\mathbf{G}')$ is the inverse dielectric matrix element

$$\eta_j(\mathbf{G},\mathbf{G}')=\frac{1}{A_{u.c}}\int_{u.c.}\varepsilon(\mathbf{x})^{-1}e^{i(\mathbf{G}'-\mathbf{G})\cdot\mathbf{x}}\mathbf{dx} \tag{A.14}$$

where here $\varepsilon(\mathbf{x})$ are the real index x,y-profiles in the photonic crystal of each one of the three layers. First, one computes the $\varepsilon_j(\mathbf{G},\mathbf{G}')$ matrix and then inverts it numerically. This operation is more adapted to truncation rules for Fourier series in the presence of discontinuous functions [460]. Note that the Fourier transform of any arbitrary closed polygon has an analytic Fourier transform [461], which allows fast computation of $\varepsilon_j(\mathbf{G},\mathbf{G}')$.

Finally, we need to render the problem finite-dimensional. This is achieved by defining a α_{max} and a G_{max}, the former being the maximum number of TE and

TM bands considered and the latter a bound for the norm of the reciprocal space wavevectors used. Doing so, the expansion A.11 becomes finite and the linear eigenvalue problem A.3 numerically solvable. Additional physical constraints in the problem can be used to find suitable numerical schemes for the eigenvalue algorithms. An example is the fact that for PhC slabs that are invariant under reflection through the mirror plane bisecting the slab, the problem can be decoupled in finding so-called *quasi-TE* and *quasi-TM* modes, which are even and odd modes with respect to that symmetry plane. The standard structures used in this work based on patterned free-standing silicon based on under-etched silicon-on-insulator (SOI) samples are well represented by this situation and the decoupling can be used.

A.0.2 Intrinsic diffraction losses

Photonic modes in the PhC slab that lie above the cladding light line(s) are coupled to the radiative field due to diffraction induced by the in-plane dielectric modulation, and become quasi-guided. As a consequence, eigenmodes and eigenvalues obtained in Subsection A.0.1 and lying above such lines require some additional calculation in order to assess their level of coupling to leaky modes.

Such out-of-plane intrinsic losses can be captured with an imaginary part of the eigenfrequency $\mathrm{Im}(\omega)$. In the GME's framework, this imaginary part is computed using time-dependent perturbation theory, and given by

$$\mathrm{Im}((\frac{\omega_k}{c})^2) = \pi \sum_{\mathbf{G}'} \sum_{t=TE,TM} \sum_{j=1,3} |W_{\mathbf{k},rad}|^2 \rho_j(\mathbf{k}+\mathbf{G}', (\frac{\omega_k}{c})^2) \tag{A.15}$$

with coupling matrix element

$$W_{\mathbf{k},rad} = \int \frac{1}{\varepsilon(\mathbf{r})} (\nabla \times \mathbf{H}^*_{\mathbf{k}}(\mathbf{r})) \cdot (\nabla \times \mathbf{H}^{\mathrm{rad}}_{\mathbf{k}+\mathbf{G}',t,j}(\mathbf{r})) d\mathbf{r} \tag{A.16}$$

and $\rho_j(\mathbf{k}+\mathbf{G}', (\frac{\omega_k}{c})^2)$ the 1D density of optical states (DOS) at a given in-plane wavevector of the effective slab and outgoing in the medium corresponding to j. These can be written as

$$\rho_j(\mathbf{g}, (\frac{\omega}{c})^2) = \int_0^\infty \delta((\frac{\omega_k}{c})^2 - \frac{|\mathbf{g}|^2 + k_z^2}{\overline{\varepsilon}_j}) \frac{dk_z}{2\pi} \tag{A.17}$$

To compute A.15, the field profile of the radiation modes of the effective dielectric slab are required. These can be written as

$$\mathbf{H_g}^{rad}(\mathbf{x},z) = \frac{e^{i\mathbf{g}\cdot\mathbf{x}}}{\sqrt{A}} i\frac{c}{\omega}[W_1(-q_1\hat{\mathbf{g}}+|\mathbf{g}|\hat{\mathbf{z}})e^{iq_1(z+\frac{d}{2})} + X_1(q_1\hat{\mathbf{g}}+|\mathbf{g}|\hat{\mathbf{z}})e^{-iq_1(z+\frac{d}{2})}], \quad z \leq -\frac{d}{2} \tag{A.18a}$$

$$\frac{e^{i\mathbf{g}\cdot\mathbf{x}}}{\sqrt{A}} i\frac{c}{\omega}[W_2(-q_2\hat{\mathbf{g}}+|\mathbf{g}|\hat{\mathbf{z}})e^{iq_2z} + X_2(q_2\hat{\mathbf{g}}+|\mathbf{g}|\hat{\mathbf{z}})e^{-iq_2z}], \quad |z| \leq \frac{d}{2} \tag{A.18b}$$

$$\frac{e^{i\mathbf{g}\cdot\mathbf{x}}}{\sqrt{A}} i\frac{c}{\omega}[W_3(-q_3\hat{\mathbf{g}}+|\mathbf{g}|\hat{\mathbf{z}})e^{iq_3(z-\frac{d}{2})} + X_3(q_3\hat{\mathbf{g}}+|\mathbf{g}|\hat{\mathbf{z}})e^{-iq_3(z-\frac{d}{2})}], \quad z \leq -\frac{d}{2} \tag{A.18c}$$

for TE polarization and

$$\mathbf{H_g}^{rad}(\mathbf{x},z) = \frac{e^{i\mathbf{g}\cdot\mathbf{x}}}{\sqrt{A}} \hat{\boldsymbol{\epsilon}}_{\boldsymbol{g}}[Y_1 e^{iq_1(z+\frac{d}{2})} + X_1 e^{-iq_1(z+\frac{d}{2})}], \quad z \leq -\frac{d}{2} \tag{A.19a}$$

$$\frac{e^{i\mathbf{g}\cdot\mathbf{x}}}{\sqrt{A}} \hat{\boldsymbol{\epsilon}}_{\boldsymbol{g}}[Y_2 e^{iq_2z} + X_2 e^{-iq_2z}], \quad |z| \leq \frac{d}{2} \tag{A.19b}$$

$$\frac{e^{i\mathbf{g}\cdot\mathbf{x}}}{\sqrt{A}} \hat{\boldsymbol{\epsilon}}_{\boldsymbol{g}}[Y_3 e^{iq_3(z-\frac{d}{2})} + Z_3 e^{-iq_3(z-\frac{d}{2})}], \quad z \leq -\frac{d}{2} \tag{A.19c}$$

for TM polarization. Here all q_j's are defined as $q_j = \sqrt{\bar{\varepsilon}_j \frac{\omega^2}{c^2} - |\mathbf{g}|^2}$, where now q_1, q_3 can take up real or imaginary values depending on what region of the radiation space (defined by $\omega \geq c|\mathbf{g}|/\max(n_1, n_3)$ we are in. For most of the cases we dealt with, $\bar{\varepsilon}_1 = \bar{\varepsilon}_3$ and therefore all radiation modes exhibit real q_1 and q_3.

With such radiation fields and after using the expansion in A.11, the matrix element A.16 between a guided mode of the PhC slab and a radiation mode becomes

$$W_{\mathbf{k},\text{rad}} = \sum_{\mathbf{G},\alpha} c^*_{\mathbf{k}+\mathbf{G},\alpha} W_{\text{guided,rad}} \tag{A.20}$$

with

$$W_{\text{guided,rad}} = \int \frac{1}{\varepsilon(\mathbf{r})} (\nabla \times \mathbf{H}^*_{\mathbf{k}+\mathbf{G},\alpha}(\mathbf{r})) \cdot (\nabla \times \mathbf{H}^{\text{rad}}_{\mathbf{k}+\mathbf{G}',t,j}) d\mathbf{r} \tag{A.21}$$

For these matrix elements A.21 we set guided $= \mu = (\mathbf{k}+\mathbf{G}, \alpha)$ and rad $= r = (\mathbf{k}+\mathbf{G}', \omega, j)$. Four different types of combinations (TE-TE,TE-TM,TM-TE,TM-TM) yield the following different matrix elements

$$W^{TE-TE}_{\text{guided,rad}} =(\frac{\omega_\mu}{c})^2\frac{\omega_r}{c}(\hat{\boldsymbol{\epsilon}}_{\boldsymbol{k+G}}\cdot\hat{\boldsymbol{\epsilon}}_{\boldsymbol{k+G'}})\{(\overline{\varepsilon}_1)^2\eta_1(\mathbf{G},\mathbf{G}')B^*_{1,\mu}(W_{1,r}I_{1,+}+X1,rI1,-) + (\overline{\varepsilon}_3)^2\eta_3(\mathbf{G},\mathbf{G}')A^*_{3,\mu}(W_{3,r}I_{3,-}+X_{3,r}I_{3,+})+(\overline{\varepsilon}_2)^2\eta_2(\mathbf{G},\mathbf{G}')[(A^*_{2,\mu}W_{2,r} + B^*_{2,\mu}X_{2,r})I_{2,-}+(A^*_{2,\mu}X_{2,r}+B^*_{2,\mu}W_{2,r})I_{2,+}]\} \tag{A.22a}$$

$$W^{TE-TM}_{\text{guided,rad}} =i(\frac{\omega_\mu}{c})^2(\hat{\boldsymbol{\epsilon}}_{\boldsymbol{k+G}}\cdot\widehat{(\mathbf{k}+\mathbf{G}')})\{\overline{\varepsilon}_1\eta_1(\mathbf{G},\mathbf{G}')B^*_{1,\mu}q_{1,r}(Z_{1,r}I_{1,-}-Y_{1,r}I_{1,+}) + \overline{\varepsilon}_3\eta_3(\mathbf{G},\mathbf{G}')A^*_{3,\mu}q_{3,\nu}(Z_{3,r}I_{3,+}-Y_{3,r}I_{3,-})+\overline{\varepsilon}_2\eta_2(\mathbf{G},\mathbf{G}')q_{2,r}[(-A^*_{2,\mu}Y_{2,r} + B^*_{2,\mu}Z_{2,r})I_{2,-}+(A^*_{2,\mu}Z_{2,r}-B^*_{2,\mu}Y_{2,R})I_{2,+}]\} \tag{A.22b}$$

$$W^{TM-TE}_{\text{guided,rad}} =\frac{\omega_r}{c}(\widehat{(\mathbf{k}+\mathbf{G})}\cdot\boldsymbol{\epsilon}_{\boldsymbol{k+G'}})\{-\overline{\varepsilon}_1\eta_1(\mathbf{G},\mathbf{G}')D^*_{1,\mu}q_{1,\mu}(W_{1,r}I_{1,+}-X_{1,r}I_{1,-}) + \overline{\varepsilon}_3\eta_3(\mathbf{G},\mathbf{G}')C^*_{3,\mu}q_{3,\mu}(W_{3,r}I_{3,-}-X_{3,r}I_{3,+})-i\overline{\varepsilon}_2\eta_2(\mathbf{G},\mathbf{G}')q_{2,\mu}[(-C_{2,\mu}*W_{2,r} + D^*_{2,\mu}X_{2,r})I_{2,-}+(D^*_{2,\mu}W_{2,r}-C^*_{2,\mu}X_{2,r})I_{2,+}]\} \tag{A.22c}$$

$$\begin{aligned}W^{TM-TM}_{\text{guided,rad}} =&\eta_1(\mathbf{G},\mathbf{G}')D^*_{1,\mu}[(iq_{1,\mu}q_{1,r}\widehat{\mathbf{k}+\mathbf{G}}\cdot\widehat{\mathbf{k}+\mathbf{G}'}+|\mathbf{k}+\mathbf{G}||\mathbf{k}+\mathbf{G}'|)Y_{1,r}I_{1,+}\\ &+(-iq_{1,\mu}q_{1,r}\widehat{\mathbf{k}+\mathbf{G}}\cdot\widehat{\mathbf{k}+\mathbf{G}'}+|\mathbf{k}+\mathbf{G}||\mathbf{k}+\mathbf{G}'|)Z_{1,r}I_{1,-}]\\ &+\eta_3(\mathbf{G},\mathbf{G}')C^*_{3,\mu}[(-iq_{3,\mu}q_{3,r}\widehat{\mathbf{k}+\mathbf{G}}\cdot\widehat{\mathbf{k}+\mathbf{G}'}+|\mathbf{k}+\mathbf{G}||\mathbf{k}+\mathbf{G}'|)Y_{3,r}I_{3,-}\\ &+(iq_{3,\mu}q_{3,r}\widehat{\mathbf{k}+\mathbf{G}}\cdot\widehat{\mathbf{k}+\mathbf{G}'}+|\mathbf{k}+\mathbf{G}||\mathbf{k}+\mathbf{G}'|)Z_{3,r}I_{3,+}]\\ &+\eta_2(\mathbf{G},\mathbf{G}')[(C^*_{2,\mu}Y_{2,r}+D^*_{2,\mu}Z_{2,r})(q_{2,\mu}q_{2,r}\widehat{\mathbf{k}+\mathbf{G}}\cdot\widehat{\mathbf{k}+\mathbf{G}'}\\ &+|\mathbf{k}+\mathbf{G}||\mathbf{k}+\mathbf{G}'|)I_{2,-}+(C^*_{2,\mu}Z_{2,r}+D^*_{2,\mu}Y_{2,r})(-q_{2,\mu}q_{2,r}\widehat{\mathbf{k}+\mathbf{G}}\cdot\widehat{\mathbf{k}+\mathbf{G}'}\\ &+|\mathbf{k}+\mathbf{G}||\mathbf{k}+\mathbf{G}'|)I_{2,+}]\end{aligned} \tag{A.22d}$$

The expression of this coefficients given, the formulation to obtain dispersion relations and diffraction losses of quasi-guided modes is easily implemented in any programming language using the truncation already explained in the end of Subsection A.0.1 and an additional bound to $|\mathbf{G}'|$ in A.15.

Appendix B

Sample fabrication

This Appendix describes the different steps of the nanofabrication process employed for samples fabricated at ICN2 and at DTU Fotonik.

B.1 Fabrication at ICN2-CNM

Although most of the reported measurements in this thesis were carried out in samples fabricated elsewhere, an important part of this PhD has been devoted to acquiring skills and hands-on practice in nanofabrication. Samples fabricated during the thesis will hopefully produce publishable results soon. This section gives the basic fabrication flow followed using equipment at both ICN2 and CNM.

SOI stack and sample preparation

The structures are fabricated using a silicon-on-insulator (SOI) SOITEC wafer. The top silicon layer has a thickness of 250 nm (resistivity $\rho \sim 1 - 10\Omega \cdot cm$, p-doping of $\sim 10^{15} cm^{-3}$), the buried oxide layer a thickness of 3 μm and the silicon substrate a thickness of 675 μm. The usually 15x15 mm chips are cleaned via a 5 min O_2-plasma exposure (PVA Tepla). The power is set to 400 W and the chamber pressure is kept at $\sim$ 200 mTorr using an oxygen flow of 50 sccm. With the chip directly placed under the vacuum chuck of the spinner, the chemically semi-amplified positive resist AR-P 6200.09 (CSAR-62) is spin-coated on the sample using a first step at 500 rpm for 5 secs and a second step at 4000 rpm during 60 sec. The acceleration in between steps is set to 8000 rpm/s. The chip is finally soft baked on a hot plate at 145°C for 1 min, which typically results in a 200 nm thick film of CSAR as measured with a profilometer.

Electron beam lithography and development

Electron-beam lithography is either done at ICN2 using an EBL-converted SEM (Inspect F50) from Raith or on a dedicated electron-beam lithography system (Raith150-TWO) at CNM. The masks to expose are generated as GDS-files by using the Java-scripted NIST Nanolithography Toolbox [462] or directly on text .ASC files using the language supported by the Raith Elphy Quantum Software

suite generated via Matlab scripts. For the standard optomechanical structures with pitches $\sim$ 500 nm, the acceleration voltage is set to 30 kV in both systems, while the currents are set around 160 pA (CNM) and 20 pA (ICN2). The large difference in current stems from the lower speed electronics of the beam blanker used by the ICN2 equipment. The chosen writefields are respectively calibrated and aligned using a chessboard reference sample (ICN2) or a reference mark (CNM). The exposure base-dose is set to 70 μC/cm^2 and various exposures using dose-factors between 0.9 and 1.1 are typically done.

After e-beam exposure, the development of the CSAR resist is done by a 1 min inmersion and rinsing in AR-600-546, the dedicated developer by AllResist for CSAR-62. This is followed by inmersion and rinsing in isopropanol (IPA) to stop the developing process and clean the residues. Finally, the chip is gently dried with a N_2 gun and baked at 135°C in a hot plate to enhance the plasma etching resistance.

Reactive ion etching and resist strip

The pattern is transferred to silicon using a Bosch process in an ICP-DRIE (Alcatel AMS-110DE) system. The source power is set to 500 W and the pulsed flows of SF_6 and C_4F_8 gases set to 150 sccm for 1.5 secs and 100 sccm for 2 secs, respectively. The cycle repeats up to a total process time which depends on the size of the feature to transfer but is typically around 1 min 15 sec for a membrane thickness of 250 nm. The etch rates are respectively $\sim$200 nm/min for silicon and 45 nm/min for the CSAR resist. After pattern transfer, the remaining resist is ashed by using the same O_2 plasma step used for the chip surface cleaning. On the last samples fabricated, the plasma ashing was replaced by inmersion in remover AR-600-71, the dedicated remover by AllResist for CSAR-62. This last step improves the matching of the fabricated and nominal parameters since it avoids increased oxidation of the hole sidewalls during the plasma and subsequent etching during the release.

Membrane release

The top silicon layer is realeased by isotropic wet-etching of the buried oxide using a hydrofluoric acid (50%). The etch rate is $\sim$ 20 nm/s and the chip is inmersed in the solution for 2 min and 30 sec, leading to full etching of the oxide in the vertical direction and to 3 μm underetched regions around the exposed patterns. The chip is then sequentially transferred (always under inmersion) to water and IPA and then undergoes a critical point drying process (Tousimis Automegasamdri-915B Series C) for 1 hour to avoid stiction and/or collapse of the structures during the drying process.

B.2 Fabrication at DTU Fotonik

A considerable part of the samples shown in Chapter 5 of this thesis were fabricated at DTU Fotonik by PhD student Marcus Albrechtsen. This section gives

credit to his work.

SOI stack and sample preparation

The structures are fabricated using a silicon-on-insulator (SOI) SOITEC wafer. The top silicon layer has a thickness of 240 nm (resistivity $\rho \sim$ 13.5-22.5 Ω·cm, p-doping of $\sim 10^{15} cm^{-3}$), the buried oxide layer a thickness of 3 μm and the silicon substrate a thickness of 675 μm. The 25x25 mm chips are cleaned sequentially in acetone (1 min), IPA, deionized water (1 min), IPA, and blow-dried with an N_2 gun. The chip is then placed for 10 min on a hotplate at 200°C for dehydration. The sample is then attached to the center of a 4" Si-carrier wafer with a carrier-bonding substante. The 4" carrier with the sample is spin-coated in a fully-automatic robot. Exactly 6 mL of CSAR-62 are deposited on the sample surface and then followed by a first acceleraction step of 10000 rpm/s and then kept at 6000 rpm during 1 min. The sample is then soft baked on a hot plate at 200∘C for 185 sec, which typically results in a 180 nm thick film of CSAR. Prior to e-beam exposure, a 20 nm Al layer is thermally-evaporated on top of the resist. This is done at a rate of 1 $\mathring{A}$/s, with the sample upside down in a chamber pumped down to a pressure $p < 1.3 \cdot 10^{-}5$ mbar.

Electron beam lithography and development

The superior quality of the e-beam lithtography step at DTU is both due to the electron beam itself and to the pre-processing of the exposed pattern. The GDS-file is first loaded into the pre-processor GenISys BEAMER v5.3.6 [463], which removes polygon overlaps and merges adjacent polygons. The mask is therefore flattened. The resulting geometry is then proximity effect corrected (PEC) [464] for long-range effects using a Gaussian approximation with $\beta = 30$ μm and $\eta = 0.5$, which equalizes the real dose received by the different features of the mask, e.g. it boosts the dose in the corners. The GDS file is then converted into the v30 format supported by the used electron beam equipment (JEOL JBX-9500FSZ) using conventional fracturing and an exposure grid of 1 nm. The file is then loaded into the e-beam software and exposed with an acceleration voltage of 100 keV and a current of 0.2 nA. The exposure base-dose is set at 235 μ C/cm^2, but the structure is PEC-corrected and therefore every polygon recieves a slightly different dose.

The development step is comprised of two steps. First, the 20 nm aluminum layer is removed by inmersion in 2.38% TMAH for 60 secs and then cleaned with DIW for 60 sec and spun-dried. The etch rate of the 2.8% TMAH is 0.5 nm/s for the aluminium layer and 0.05 nm/s for the CSAR layer; thus all aluminium is gone after 40-50 secs and the first nm of CSAR is etched away to ensure no Al remains. Then the CSAR is developed in AR-600-546 for 60 sec and cleaned in IPA for 20 sec. Finally, it is spun-dried under N_2 flow.

Reactive ion etching and resist strip

ICP reactive ion-etching of the silicon thin layer is done on a SPTS Pegasus ICP reactor using a cryogenic continuous process. Two gases, C_4F_8 at 75 sccm and SF_6 at 38 sccm are used. The chamber pressure is kept at 4 mTorr, with a 3 secs initial strike at 15 mTorr to ensure instantaneous ignition of the plasma. The ICP coil power is set at 800 W, while the chuck power is fixed at 40 W. The chiller temperature is set at -19∘C. These set of parameters lead to a silicon etch rate of approximately 190 nm/min with a total process time of 80 secs. The etch rate for CSAR is approximately 80 nm/min, leaving approximately a 75 nm thick layer left. Once the RIE completed, the remaining resist is removed by inmersion in AR-600-71. Last, the sample is then sequentially cleaned in acetone (1 min), IPA, DIW (1 min), IPA, and blow-dried with an N_2 gun.

Membrane release

The top silicon layer is realeased by a slow isotropic wet-etching of the buried oxide using an SiO-etch, which is a buffered HF solution in water. The etch rate is $\sim$ 100 nm/min and the chip is inmersed in the solution for 35 min, leading to 3.5 μm underetched regions around the exposed patterns. The sample is then sequentially transferred to water twice and left to dry for 15 min inside a metallic chamber filled with ethanol vapor.

Bibliography

[1] G. Feher and E. A. Gere, *Electron Spin Resonance Experiments on Donors in Silicon. II. Electron Spin Relaxation Effects*, Physical Review **114**, 1245–1256 (1959).

[2] P. W. Anderson, *Absence of Diffusion in Certain Random Lattices*, Physical Review **109**, 1492–1505 (1958).

[3] H. Kunz and B. Souillard, *Sur le spectre des opérateurs aux différences finies aléatoires*, Communications in Mathematical Physics **78**, 201–246 (1980).

[4] R. Carmona and J. Lacroix, *Spectral Theory of Random Schrödinger Operators*, Birkhäuser, Basel (1990).

[5] P. W. Anderson, *Local Moments and Localized States*, Science **201**, 307–316 (1978).

[6] A. P. Vinogradov and A. M. Merzlikin, *Band theory of light localization in one-dimensional disordered systems*, Physical Review E **70**, 026610 (2004).

[7] G. I. Menon and P. Ray, *The physics of disordered systems*, Hindustan Book Agency, New Delhi (2012).

[8] P. W. Anderson, *The question of classical localization A theory of white paint?*, Philosophical Magazine B **52**, 505–509 (1985).

[9] E. Guazzelli, E. Guyon, and B. Souillard, *On the localization of shallow water waves by a random bottom*, Journal de Physique Lettres **44**, 837–841 (1983).

[10] M. Segev, Y. Silberberg, and D. N. Christodoulides, *Anderson localization of light*, Nature Photonics **7**, 197–204 (2013).

[11] H. Hu, A. Strybulevych, J. H. Page, S. E. Skipetrov, and B. A. van Tiggelen, *Localization of ultrasound in a three-dimensional elastic network*, Nature Physics **4**, 945–948 (2008).

[12] N. Garcia and A. Z. Genack, *Anomalous photon diffusion at the threshold of the Anderson localization transition*, Physical Review Letters **66**, 1850–1853 (1991).

[13] D. S. Wiersma, P. Bartolini, A. Lagendijk, and R. Righini, *Localization of light in a disordered medium*, Nature **390**, 671–673 (1997).

[14] F. Scheffold, R. Lenke, R. Tweer, and G. Maret, *Localization or classical diffusion of light?*, Nature **398**, 206–207 (1999).

[15] S. E. Skipetrov and J. H. Page, *Red light for Anderson localization*, New Journal of Physics **18**, 021001 (2016).

[16] A. A. Chabanov, M. Stoytchev, and A. Z. Genack, *Statistical signatures of photon localization*, Nature **404**, 850–853 (2000).

[17] P. D. García and P. Lodahl, *Physics of Quantum Light Emitters in Disordered Photonic Nanostructures*, Annalen der Physik **529**, 1600351 (2017).

[18] R. L. Weaver, *Anderson localization of ultrasound*, Wave Motion **12**, 129–142 (1990).

[19] L. Brillouin, *Diffusion de la lumière et des rayons X par un corps transparent homogène - Influence de l'agitation thermique*, Annales de Physique **9**, 88–122 (1922).

[20] M. Aspelmeyer, T. J. Kippenberg, and F. Marquardt, *Cavity optomechanics*, Reviews of Modern Physics **86**, 1391–1452 (2014).

[21] M. Eichenfield, J. Chan, R. M. Camacho, K. J. Vahala, and O. Painter, *Optomechanical crystals*, Nature **462**, 78–82 (2009).

[22] G. S. MacCabe, H. Ren, J. Luo, J. D. Cohen, H. Zhou, A. Sipahigil, M. Mirhosseini, and O. Painter, *Nano-acoustic resonator with ultralong phonon lifetime*, Science **370**, 840–843 (2020).

[23] S. John, *Strong localization of photons in certain disordered dielectric superlattices*, Physical Review Letters **58**, 2486–2489 (1987).

[24] A. H. Safavi-Naeini and O. Painter, "Optomechanical Crystal Devices", *Cavity Optomechanics: Nano- and Micromechanical Resonators Interacting with Light*, ed. by M. Aspelmeyer, T. J. Kippenberg, and F. Marquardt(2014), pp. 195–231.

[25] T. F. Roque, V. Peano, O. M. Yevtushenko, and F. Marquardt, *Anderson localization of composite excitations in disordered optomechanical arrays*, New Journal of Physics **19**, 013006 (2017).

[26] J. Kepler, *De cometis libelli tres ...* Typis Andreæ Apergeri, sumptibus Sebastiani Mylii bibliopolæ Augustani (1619).

[27] J. C. Maxwell, *A Treatise on Electricity and Magnetism*, Clarendon Press, Oxford (1873).

[28] D. de Mairan, *Traité Physique Et Historique De L'aurore Boréale*, Wentworth Press (2019).

[29] A. Bennet and R. Kaye, *A new suspension of the magnetic needle, intended for the discovery of minute quantities of magnetic attraction: also an air vane of great sensibility; with new experiments on the magnetism of iron filings and brass*, Philosophical Transactions of the Royal Society of London **82**, 81–98 (1792).

[30] A. Fresnel, *Note sur la répulsion récrproque que des corps échauffés exercent les uns sur les autres à des distances sensibles*, Annales Chimie et Physique **3**, 107 (1825).

[31] L. d. Broglie, *XXXV. A tentative theory of light quanta*, The London, Edinburgh, and Dublin Philosophical Magazine and Journal of Science **47**, 446–458 (1924).

[32] W. Crookes, *XV. On attraction and repulsion resulting from radiation*, Philosophical Transactions of the Royal Society of London **164**, 501–527 (1874).

[33] P. Lebedew, *Untersuchungen über die Druckkräfte des Lichtes*, Annalen der Physik **311**, 433–458 (1901).

[34] E. F. Nichols and G. F. Hull, *The Pressure due to Radiation*, The Astrophysical Journal **17**, 315 (1903).

[35] T. W. Hänsch and A. L. Schawlow, *Cooling of gases by laser radiation*, Optics Communications **13**, 68–69 (1975).

[36] D. J. Wineland and W. M. Itano, *Laser cooling of atoms*, Physical Review A **20**, 1521–1540 (1979).

[37] A. Ashkin, *Trapping of Atoms by Resonance Radiation Pressure*, Physical Review Letters **40**, 729–732 (1978).

[38] S. Chu, L. Hollberg, J. E. Bjorkholm, A. Cable, and A. Ashkin, *Three-dimensional viscous confinement and cooling of atoms by resonance radiation pressure*, Physical Review Letters **55**, 48–51 (1985).

[39] M. H. Anderson, J. R. Ensher, M. R. Matthews, C. E. Wieman, and E. A. Cornell, *Observation of Bose-Einstein Condensation in a Dilute Atomic Vapor*, Science **269**, 198–201 (1995).

[40] G. I. Harris, D. L. McAuslan, E. Sheridan, Y. Sachkou, C. Baker, and W. P. Bowen, *Laser cooling and control of excitations in superfluid helium*, Nature Physics **12**, 788–793 (2016).

[41] P. S. Jessen and I. H. Deutsch, *Optical Lattices*, Advances in Atomic, Molecular and Optical Physics **37**, 95–138 (C 1996).

[42] V. S. Letokhov, V. G. Minogin, and B. D. Pavlik, *Cooling and capture of atoms and molecules by a resonant light field*, Soviet Physics JETP Letters **45**, 698 (1977).

[43] F. Diedrich, J. C. Bergquist, W. M. Itano, and D. J. Wineland, *Laser Cooling to the Zero-Point Energy of Motion*, Physical Review Letters **62**, 403–406 (1989).

[44] D. Leibfried, R. Blatt, C. Monroe, and D. Wineland, *Quantum dynamics of single trapped ions*, Reviews of Modern Physics **75**, 281–324 (2003).

[45] O. Mandel, M. Greiner, A. Widera, T. Rom, T. W. Hänsch, and I. Bloch, *Controlled collisions for multi-particle entanglement of optically trapped atoms*, Nature **425**, 937–940 (2003).

[46] M. Anderlini, P. J. Lee, B. L. Brown, J. Sebby-Strabley, W. D. Phillips, and J. V. Porto, *Controlled exchange interaction between pairs of neutral atoms in an optical lattice*, Nature **448**, 452–456 (2007).

[47] R. Penrose, *On Gravity's role in Quantum State Reduction*, General Relativity and Gravitation **28**, 581–600 (1996).

[48] J. Aasi et al., *Advanced LIGO*, Classical and Quantum Gravity **32**, 074001 (2015).

[49] V. B. Braginsky and A. B. Manukin, *Ponderomotive effects of electromagnetic radiation*, Soviet Physics JETP Letters **25**, 653–655 (1967).

[50] M. Dykman, *Heating and cooling of local and quasilocal vibrations by a nonresonance field*, Sov. Phys. Solid State **8**, 1306–1311 (1978).

[51] V. B. Braginsky, F. Y. Khalili, and K. S. Thorne, *Quantum Measurement*, Cambridge University Press, Cambridge (1992).

[52] LIGO Scientific Collaboration and Virgo Collaboration et al., *Observation of Gravitational Waves from a Binary Black Hole Merger*, Physical Review Letters **116**, 061102 (2016).

[53] V. B. Braginsky, Y. I. Vorontsov, and K. S. Thorne, *Quantum Nondemolition Measurements*, Science **209**, 547–557 (1980).

[54] C. Fabre, M. Pinard, S. Bourzeix, A. Heidmann, E. Giacobino, and S. Reynaud, *Quantum-noise reduction using a cavity with a movable mirror*, Physical Review A **49**, 1337–1343 (1994).

[55] W. Marshall, C. Simon, R. Penrose, and D. Bouwmeester, *Towards Quantum Superpositions of a Mirror*, Physical Review Letters **91**, 130401 (2003).

[56] S. Mancini, V. Giovannetti, D. Vitali, and P. Tombesi, *Entangling Macroscopic Oscillators Exploiting Radiation Pressure*, Physical Review Letters **88**, 120401 (2002).

[57] J. D. Cohen, S. M. Meenehan, G. S. MacCabe, S. Gröblacher, A. H. Safavi-Naeini, F. Marsili, M. D. Shaw, and O. Painter, *Phonon counting and intensity interferometry of a nanomechanical resonator*, Nature **520**, 522–525 (2015).

[58] S. M. Meenehan, J. D. Cohen, G. S. MacCabe, F. Marsili, M. D. Shaw, and O. Painter, *Pulsed Excitation Dynamics of an Optomechanical Crystal Resonator near Its Quantum Ground State of Motion*, Physical Review X **5**, 041002 (2015).

[59] S. Hong, R. Riedinger, I. Marinković, A. Wallucks, S. G. Hofer, R. A. Norte, M. Aspelmeyer, and S. Gröblacher, *Hanbury Brown and Twiss interferometry of single phonons from an optomechanical resonator*, Science **358**, 203–206 (2017).

[60] S. Gröblacher, J. B. Hertzberg, M. R. Vanner, G. D. Cole, S. Gigan, K. C. Schwab, and M. Aspelmeyer, *Demonstration of an ultracold micro-optomechanical oscillator in a cryogenic cavity*, Nature Physics **5**, 485–488 (2009).

[61] E. Verhagen, S. Deléglise, S. Weis, A. Schliesser, and T. J. Kippenberg, *Quantum-coherent coupling of a mechanical oscillator to an optical cavity mode*, Nature **482**, 63–67 (2012).

[62] J. Chan, T. P. M. Alegre, A. H. Safavi-Naeini, J. T. Hill, A. Krause, S. Gröblacher, M. Aspelmeyer, and O. Painter, *Laser cooling of a nanomechanical oscillator into its quantum ground state*, Nature **478**, 89–92 (2011).

[63] E. Gavartin, R. Braive, I. Sagnes, O. Arcizet, A. Beveratos, T. J. Kippenberg, and I. Robert-Philip, *Optomechanical Coupling in a Two-Dimensional Photonic Crystal Defect Cavity*, Physical Review Letters **106**, 203902 (2011).

[64] R. Thijssen, T. J. Kippenberg, A. Polman, and E. Verhagen, *Plasmomechanical Resonators Based on Dimer Nanoantennas*, Nano Letters **15**, 3971–3976 (2015).

[65] G. P. Srivastava, *The Physics of Phonons*, CRC Press (1990).

[66] G. Mie, *Beiträge zur Optik trüber Medien, speziell kolloidaler Metallösungen*, Annalen der Physik **330**, 377–445 (1908).

[67] C. Baker, W. Hease, D.-T. Nguyen, A. Andronico, S. Ducci, G. Leo, and I. Favero, *Photoelastic coupling in gallium arsenide optomechanical disk resonators*, Optics Express **22**, 14072–14086 (2014).

[68] T. J. Kippenberg, H. Rokhsari, T. Carmon, A. Scherer, and K. J. Vahala, *Analysis of Radiation-Pressure Induced Mechanical Oscillation of an Optical Microcavity*, Physical Review Letters **95**, 033901 (2005).

[69] A. Schliesser, P. Del'Haye, N. Nooshi, K. J. Vahala, and T. J. Kippenberg, *Radiation Pressure Cooling of a Micromechanical Oscillator Using Dynamical Backaction*, Physical Review Letters **97**, 243905 (2006).

[70] E. Yablonovitch, *Inhibited Spontaneous Emission in Solid-State Physics and Electronics*, Physical Review Letters **58**, 2059–2062 (1987).

[71] S. G. Johnson, S. Fan, P. R. Villeneuve, J. D. Joannopoulos, and L. A. Kolodziejski, *Guided modes in photonic crystal slabs*, Physical Review B **60**, 5751–5758 (1999).

[72] J. D. Joannopoulos, S. G. Johnson, J. N. Winn, and R. D. Meade, *Photonic Crystals: Molding the Flow of Light*, 2nd ed., Princeton University Press (2011).

[73] J. Chan, A. H. Safavi-Naeini, J. T. Hill, S. Meenehan, and O. Painter, *Optimized optomechanical crystal cavity with acoustic radiation shield*, Applied Physics Letters **101**, 081115 (2012).

[74] K. Karrai, I. Favero, and C. Metzger, *Doppler Optomechanics of a Photonic Crystal*, Physical Review Letters **100**, 240801 (2008).

[75] T. K. Paraïso, M. Kalaee, L. Zang, H. Pfeifer, F. Marquardt, and O. Painter, *Position-Squared Coupling in a Tunable Photonic Crystal Optomechanical Cavity*, Physical Review X **5**, 041024 (2015).

[76] M. Pinard, Y. Hadjar, and A. Heidmann, *Effective mass in quantum effects of radiation pressure*, The European Physical Journal D - Atomic, Molecular, Optical and Plasma Physics **7**, 107–116 (1999).

[77] W. P. Bowen and G. J. Milburn, *Quantum Optomechanics*, CRC Press (2015).

[78] A. O. Caldeira and A. J. Leggett, *Influence of Dissipation on Quantum Tunneling in Macroscopic Systems*, Physical Review Letters **46**, 211–214 (1981).

[79] A. A. Clerk, M. H. Devoret, S. M. Girvin, F. Marquardt, and R. J. Schoelkopf, *Introduction to quantum noise, measurement, and amplification*, Reviews of Modern Physics **82**, 1155–1208 (2010).

[80] C. Gardiner and P. Zoller, *Quantum Noise: A Handbook of Markovian and Non-Markovian Quantum Stochastic Methods with Applications to Quantum Optics*, 3rd ed., Springer-Verlag, Berlin Heidelberg (2004).

[81] G. W. Ford, J. T. Lewis, and R. F. O'Connell, *Quantum Langevin equation*, Physical Review A **37**, 4419–4428 (1988).

[82] V. Giovannetti and D. Vitali, *Phase-noise measurement in a cavity with a movable mirror undergoing quantum Brownian motion*, Physical Review A **63**, 023812 (2001).

[83] H. A. Haus, *Waves and Fields in Optoelectronics*, Prentice Hall, Englewood Cliffs, NJ (1983).

[84] M. Cai, O. Painter, and K. J. Vahala, *Observation of Critical Coupling in a Fiber Taper to a Silica-Microsphere Whispering-Gallery Mode System*, Physical Review Letters **85**, 74–77 (2000).

[85] J. Bochmann, A. Vainsencher, D. D. Awschalom, and A. N. Cleland, *Nanomechanical coupling between microwave and optical photons*, Nature Physics **9**, 712–716 (2013).

[86] M. Davanço, S. Ates, Y. Liu, and K. Srinivasan, *Si3N4 optomechanical crystals in the resolved-sideband regime*, Applied Physics Letters **104**, 041101 (2014).

[87] M. J. Burek, J. D. Cohen, S. M. Meenehan, N. El-Sawah, C. Chia, T. Ruelle, S. Meesala, J. Rochman, H. A. Atikian, M. Markham, D. J. Twitchen, M. D. Lukin, O. Painter, and M. Lončar, *Diamond optomechanical crystals*, Optica **3**, 1404–1411 (2016).

[88] K. Schneider, Y. Baumgartner, S. Hönl, P. Welter, H. Hahn, D. J. Wilson, L. Czornomaz, and P. Seidler, *Optomechanics with one-dimensional gallium phosphide photonic crystal cavities*, Optica **6**, 577–584 (2019).

[89] R. Stockill, M. Forsch, G. Beaudoin, K. Pantzas, I. Sagnes, R. Braive, and S. Gröblacher, *Gallium Phosphide as a Piezoelectric Platform for Quantum Optomechanics*, Physical Review Letters **123**, 163602 (2019).

[90] M. Forsch, R. Stockill, A. Wallucks, I. Marinković, C. Gärtner, R. A. Norte, F. van Otten, A. Fiore, K. Srinivasan, and S. Gröblacher, *Microwave-to-optics conversion using a mechanical oscillator in its quantum ground state*, Nature Physics **16**, 69–74 (2020).

[91] J. Leuthold, C. Koos, and W. Freude, *Nonlinear silicon photonics*, Nature Photonics **4**, 535–544 (2010).

[92] Q. Lin, O. J. Painter, and G. P. Agrawal, *Nonlinear optical phenomena in silicon waveguides: Modeling and applications*, Optics Express **15**, 16604–16644 (2007).

[93] P. E. Barclay, K. Srinivasan, and O. Painter, *Nonlinear response of silicon photonic crystal microresonators excited via an integrated waveguide and fiber taper*, Optics Express **13**, 801–820 (2005).

[94] T. J. Johnson, M. Borselli, and O. Painter, *Self-induced optical modulation of the transmission through a high-Q silicon microdisk resonator*, Optics Express **14**, 817–831 (2006).

[95] N. Cazier, X. Checoury, L.-D. Haret, and P. Boucaud, *High-frequency self-induced oscillations in a silicon nanocavity*, Optics Express **21**, 13626–13638 (2013).

[96] D. Navarro-Urrios, N. E. Capuj, J. Gomis-Bresco, F. Alzina, A. Pitanti, A. Griol, A. Martínez, and C. M. Sotomayor Torres, *A self-stabilized coherent phonon source driven by optical forces*, Scientific Reports **5**, 15733 (2015).

[97] D. Navarro-Urrios, J. Gomis-Bresco, N. E. Capuj, F. Alzina, A. Griol, D. Puerto, A. Martínez, and C. M. Sotomayor-Torres, *Optical and mechanical mode tuning in an optomechanical crystal with light-induced thermal effects*, Journal of Applied Physics **116**, 093506 (2014).

[98] L. Zhang, Y. Fei, T. Cao, Y. Cao, Q. Xu, and S. Chen, *Multibistability and self-pulsation in nonlinear high-Q silicon microring resonators considering thermo-optical effect*, Physical Review A **87**, 053805 (2013).

[99] M. Brunstein, A. M. Yacomotti, I. Sagnes, F. Raineri, L. Bigot, and A. Levenson, *Excitability and self-pulsing in a photonic crystal nanocavity*, Physical Review A **85**, 031803 (2012).

[100] D. Navarro-Urrios, N. E. Capuj, M. F. Colombano, P. D. García, M. Sledzinska, F. Alzina, A. Griol, A. Martínez, and C. M. Sotomayor-Torres,

Nonlinear dynamics and chaos in an optomechanical beam, Nature Communications **8**, 14965 (2017).

[101] E. E. Coddington and N. Levinson, *Theory of Ordinary Differential Equations*, McGraw-Hill, New York (1955).

[102] T. Van Vaerenbergh, M. Fiers, J. Dambre, and P. Bienstman, *Simplified description of self-pulsation and excitability by thermal and free-carrier effects in semiconductor microcavities*, Physical Review A **86**, 063808 (2012).

[103] J. Yang, T. Gu, J. Zheng, M. Yu, G.-Q. Lo, D.-L. Kwong, and C. Wei Wong, *Radio frequency regenerative oscillations in monolithic high-Q/V heterostructured photonic crystal cavities*, Applied Physics Letters **104**, 061104 (2014).

[104] Y. Hadjar, P. F. Cohadon, C. G. Aminoff, M. Pinard, and A. Heidmann, *High-sensitivity optical measurement of mechanical Brownian motion*, EPL (Europhysics Letters) **47**, 545 (1999).

[105] P. Stoica and R. L. Moses, *Spectral Analysis of Signals*, Pearson Prentice Hall, Upper Saddle River, N.J (2005).

[106] D. T. Gillespie, *The mathematics of Brownian motion and Johnson noise*, American Journal of Physics **64**, 225–240 (1996).

[107] A. Khintchine, *Korrelationstheorie der stationären stochastischen Prozesse*, Mathematische Annalen **109**, 604–615 (1934).

[108] P. Hänggi and G.-L. Ingold, *Fundamental aspects of quantum Brownian motion*, Chaos: An Interdisciplinary Journal of Nonlinear Science **15**, 026105 (2005).

[109] A. H. Safavi-Naeini, J. Chan, J. T. Hill, T. P. M. Alegre, A. Krause, and O. Painter, *Observation of Quantum Motion of a Nanomechanical Resonator*, Physical Review Letters **108**, 033602 (2012).

[110] A. Dorsel, J. D. McCullen, P. Meystre, E. Vignes, and H. Walther, *Optical Bistability and Mirror Confinement Induced by Radiation Pressure*, Physical Review Letters **51**, 1550–1553 (1983).

[111] F. Marquardt, J. G. E. Harris, and S. M. Girvin, *Dynamical Multistability Induced by Radiation Pressure in High-Finesse Micromechanical Optical Cavities*, Physical Review Letters **96**, 103901 (2006).

[112] A. G. Krause, J. T. Hill, M. Ludwig, A. H. Safavi-Naeini, J. Chan, F. Marquardt, and O. Painter, *Nonlinear Radiation Pressure Dynamics in an Optomechanical Crystal*, Physical Review Letters **115**, 233601 (2015).

[113] G. Arregui, M. F. Colombano, J. Maire, A. Pitanti, N. E. Capuj, A. Griol, A. Martínez, C. M. S. Torres, and D. N. Urrios, *Injection locking in an optomechanical coherent phonon source*, arXiv:2009.09012 [cond-mat, physics:nlin, physics:physics] (2020), arXiv: 2009.09012.

[114] D. Mason, J. Chen, M. Rossi, Y. Tsaturyan, and A. Schliesser, *Continuous force and displacement measurement below the standard quantum limit*, Nature Physics **15**, 745–749 (2019).

[115] J. D. Jackson, *Classical Electrodynamics*, 3rd ed., Wiley, New York (1998).

[116] R. W. Boyd and D. Prato, *Nonlinear Optics*, 3rd ed., Academic Press, Amsterdam (2008).

[117] C. M. Soukoulis, *Photonic Band Gap Materials*, Springer Netherlands (1996).

[118] K. Sakoda, *Optical Properties of Photonic Crystals*, 2nd ed., Springer-Verlag, Berlin Heidelberg (2005).

[119] R. Shankar, *Principles of Quantum Mechanics*, 2nd ed., Plenum Press (2011).

[120] D. Christodoulides and J. Yang, *Parity-time Symmetry and Its Applications*, Springer, New York (2018).

[121] C. E. Rüter, K. G. Makris, R. El-Ganainy, D. N. Christodoulides, M. Segev, and D. Kip, *Observation of parity–time symmetry in optics*, Nature Physics **6**, 192–195 (2010).

[122] A. Regensburger, C. Bersch, M.-A. Miri, G. Onishchukov, D. N. Christodoulides, and U. Peschel, *Parity–time synthetic photonic lattices*, Nature **488**, 167–171 (2012).

[123] P. Lalanne, W. Yan, K. Vynck, C. Sauvan, and J.-P. Hugonin, *Light Interaction with Photonic and Plasmonic Resonances*, Laser & Photonics Reviews **12**, 1700113 (2018).

[124] N. Moiseyev, *Non-Hermitian Quantum Mechanics*, Cambridge University Press, Cambridge (2011).

[125] U. Fano, *Effects of Configuration Interaction on Intensities and Phase Shifts*, Physical Review **124**, 1866–1878 (1961).

[126] J. R. d. Lasson, P. T. Kristensen, J. Mørk, and N. Gregersen, *Semianalytical quasi-normal mode theory for the local density of states in coupled photonic crystal cavity-waveguide structures*, Optics Letters **40**, 5790–5793 (2015).

[127] A. Settimi, S. Severini, and B. J. Hoenders, *Quasi-normal-modes description of transmission properties for photonic bandgap structures*, JOSA B **26**, 876–891 (2009).

[128] P. Fauché, S. G. Kosionis, and P. Lalanne, *Collective scattering in hybrid nanostructures with many atomic oscillators coupled to an electromagnetic resonance*, Physical Review B **95**, 195418 (2017).

[129] M. K. Dezfouli, C. Tserkezis, N. A. Mortensen, and S. Hughes, *Nonlocal quasinormal modes for arbitrarily shaped three-dimensional plasmonic resonators*, Optica **4**, 1503–1509 (2017).

[130] C. Sauvan, J. P. Hugonin, I. S. Maksymov, and P. Lalanne, *Theory of the Spontaneous Optical Emission of Nanosize Photonic and Plasmon Resonators*, Physical Review Letters **110**, 237401 (2013).

[131] B. Vial, F. Zolla, A. Nicolet, and M. Commandré, *Quasimodal expansion of electromagnetic fields in open two-dimensional structures*, Physical Review A **89**, 023829 (2014).

[132] E. A. Muljarov and W. Langbein, *Resonant-state expansion of dispersive open optical systems: Creating gold from sand*, Physical Review B **93**, 075417 (2016).

[133] C. Kittel, *Introduction to Solid State Physics*, 8th ed., Wiley, New York (2004).

[134] J. W. Rudnicki, *Fundamentals of Continuum Mechanics*, Wiley (2014).

[135] P. Helnwein, *Some remarks on the compressed matrix representation of symmetric second-order and fourth-order tensors*, Computer Methods in Applied Mechanics and Engineering **190**, 2753–2770 (2001).

[136] M. A. Hopcroft, W. D. Nix, and T. W. Kenny, *What is the Young's Modulus of Silicon?*, Journal of Microelectromechanical Systems **19**, 229–238 (2010).

[137] A.-W. El-Sayed and S. Hughes, *Quasinormal mode theory of elastic Purcell factors and Fano resonances of optomechanical beams*, arXiv:2006.14809 [cond-mat, physics:physics] (2020), arXiv: 2006.14809.

[138] A. N. Bolgar, D. D. Kirichenko, R. S. Shaikhaidarov, S. V. Sanduleanu, A. V. Semenov, A. Y. Dmitriev, and O. V. Astafiev, *A phononic crystal coupled to a transmission line via an artificial atom*, Communications Physics **3**, 1–6 (2020).

[139] M. Skorobogatiy and J. Yang, *Fundamentals of Photonic Crystal Guiding*, Cambridge University Press (2009).

[140] M. Oudich and M. Badreddine Assouar, *Complex band structures and evanescent Bloch waves in two-dimensional finite phononic plate*, Journal of Applied Physics **112**, 104509 (2012).

[141] H. Watanabe and L. Lu, *Space Group Theory of Photonic Bands*, Physical Review Letters **121**, 263903 (2018).

[142] F. Maurin, C. Claeys, E. Deckers, and W. Desmet, *Probability that a band-gap extremum is located on the irreducible Brillouin-zone contour for the 17 different plane crystallographic lattices*, International Journal of Solids and Structures **135**, 26–36 (2018).

[143] R. G. G. Sachs, *The Physics of Time Reversal*, University of Chicago Press (1987).

[144] V. Allori, *Quantum mechanics, time and ontology*, Studies in History and Philosophy of Science Part B: Studies in History and Philosophy of Modern Physics **66**, 145–154 (2019).

[145] M. G. Silveirinha, *Time-reversal Symmetry in Antenna Theory*, Symmetry **11**, 486 (2019).

[146] Z. Wang, Y. Chong, J. D. Joannopoulos, and M. Soljačić, *Observation of unidirectional backscattering-immune topological electromagnetic states*, Nature **461**, 772–775 (2009).

[147] T. Terzibaschian and B. Enderlein, *The irreducible representations of the two-dimensional space groups of crystal surfaces. Theory and applications*, physica status solidi (b) **133**, 443–461 (1986).

[148] E. Yablonovitch, T. J. Gmitter, and K. M. Leung, *Photonic band structure: The face-centered-cubic case employing nonspherical atoms*, Physical Review Letters **67**, 2295–2298 (1991).

[149] J. E. G. J. Wijnhoven and W. L. Vos, *Preparation of Photonic Crystals Made of Air Spheres in Titania*, Science **281**, 802–804 (1998).

[150] Y. A. Vlasov and S. J. McNab, *Coupling into the slow light mode in slab-type photonic crystal waveguides*, Optics Letters **31**, 50–52 (2006).

[151] S. Y. Lin, J. G. Fleming, D. L. Hetherington, B. K. Smith, R. Biswas, K. M. Ho, M. M. Sigalas, W. Zubrzycki, S. R. Kurtz, and J. Bur, *A three-dimensional photonic crystal operating at infrared wavelengths*, Nature **394**, 251–253 (1998).

[152] J. G. Fleming, S. Y. Lin, I. El-Kady, R. Biswas, and K. M. Ho, *All-metallic three-dimensional photonic crystals with a large infrared bandgap*, Nature **417**, 52–55 (2002).

[153] S. Noda, K. Tomoda, N. Yamamoto, and A. Chutinan, *Full Three-Dimensional Photonic Bandgap Crystals at Near-Infrared Wavelengths*, Science **289**, 604–606 (2000).

[154] M. Qi, E. Lidorikis, P. T. Rakich, S. G. Johnson, J. D. Joannopoulos, E. P. Ippen, and H. I. Smith, *A three-dimensional optical photonic crystal with designed point defects*, Nature **429**, 538–542 (2004).

[155] T. Tajiri, S. Takahashi, Y. Ota, K. Watanabe, S. Iwamoto, and Y. Arakawa, *Three-dimensional photonic crystal simultaneously integrating a nanocavity laser and waveguides*, Optica **6**, 296–299 (2019).

[156] J. Millen, T. S. Monteiro, R. Pettit, and A. N. Vamivakas, *Optomechanics with levitated particles*, Reports on Progress in Physics **83**, 026401 (2020).

[157] O. Romero-Isart, A. C. Pflanzer, F. Blaser, R. Kaltenbaek, N. Kiesel, M. Aspelmeyer, and J. I. Cirac, *Large Quantum Superpositions and Interference of Massive Nanometer-Sized Objects*, Physical Review Letters **107**, 020405 (2011).

[158] F. L. Pedrotti, *Introduction to Optics*, 3rd ed., Cambridge University Press (2017).

[159] L. C. Andreani and D. Gerace, *Photonic-crystal slabs with a triangular lattice of triangular holes investigated using a guided-mode expansion method*, Physical Review B **73**, 235114 (2006).

[160] J. Hu and C. R. Menyuk, *Understanding leaky modes: slab waveguide revisited*, Advances in Optics and Photonics **1**, 58–106 (2009).

[161] L. J. Armitage, M. Doost, W. Langbein, and E. Muljarov, *Resonant-state expansion applied to planar waveguides*, Physical Review A **89**, 053832 (2014).

[162] T. Ochiai and K. Sakoda, *Nearly free-photon approximation for two-dimensional photonic crystal slabs*, Physical Review B **64**, 045108 (2001).

[163] P. Lodahl, S. Mahmoodian, and S. Stobbe, *Interfacing single photons and single quantum dots with photonic nanostructures*, Reviews of Modern Physics **87**, 347–400 (2015).

[164] S. Mohammadi, A. A. Eftekhar, A. Khelif, and A. Adibi, *Simultaneous two-dimensional phononic and photonic band gaps in opto-mechanical crystal slabs*, Optics Express **18**, 9164–9172 (2010).

[165] M. Borselli, T. J. Johnson, C. P. Michael, M. D. Henry, and O. Painter, *Surface encapsulation for low-loss silicon photonics*, Applied Physics Letters **91**, 131117 (2007).

[166] A. H. Safavi-Naeini and O. Painter, *Design of optomechanical cavities and waveguides on a simultaneous bandgap phononic-photonic crystal slab*, Optics Express **18**, 14926–14943 (2010).

[167] A. H. Safavi-Naeini, J. T. Hill, S. Meenehan, J. Chan, S. Gröblacher, and O. Painter, *Two-Dimensional Phononic-Photonic Band Gap Optomechanical Crystal Cavity*, Physical Review Letters **112**, 153603 (2014).

[168] C. Brendel, V. Peano, O. Painter, and F. Marquardt, *Snowflake phononic topological insulator at the nanoscale*, Physical Review B **97**, 020102 (2018).

[169] H. Ren, M. H. Matheny, G. S. MacCabe, J. Luo, H. Pfeifer, M. Mirhosseini, and O. Painter, *Two-dimensional optomechanical crystal cavity with high quantum cooperativity*, Nature Communications **11**, 3373 (2020).

[170] H. Ren, T. Shah, H. Pfeifer, C. Brendel, V. Peano, F. Marquardt, and O. Painter, *Topological phonon transport in an optomechanical system*, arXiv:2009.06174 [cond-mat, physics:physics] (2020), arXiv: 2009.06174.

[171] F. Wen, S. David, X. Checoury, M. E. Kurdi, and P. Boucaud, *Two-dimensional photonic crystals with large complete photonic band gaps in both TE and TM polarizations*, Optics Express **16**, 12278–12289 (2008).

[172] I. Söllner, L. Midolo, and P. Lodahl, *Deterministic Single-Phonon Source Triggered by a Single Photon*, Physical Review Letters **116**, 234301 (2016).

[173] S. Benchabane, A. Khelif, A. Choujaa, B. Djafari-Rouhani, and V. Laude, *Interaction of waveguide and localized modes in a phononic crystal*, EPL (Europhysics Letters) **71**, 570 (2005).

[174] F.-C. Hsu, C.-I. Lee, J.-C. Hsu, T.-C. Huang, C.-H. Wang, and P. Chang, *Acoustic band gaps in phononic crystal strip waveguides*, Applied Physics Letters **96**, 051902 (2010).

[175] Y. Pennec, B. D. Rouhani, C. Li, J. M. Escalante, A. Martinez, S. Benchabane, V. Laude, and N. Papanikolaou, *Band gaps and cavity modes in dual phononic and photonic strip waveguides*, AIP Advances **1**, 041901 (2011).

[176] J. Gomis-Bresco, D. Navarro-Urrios, M. Oudich, S. El-Jallal, A. Griol, D. Puerto, E. Chavez, Y. Pennec, B. Djafari-Rouhani, F. Alzina, A. Martínez, and C. M. S. Torres, *A one-dimensional optomechanical crystal with a complete phononic band gap*, Nature Communications **5**, 4452 (2014).

[177] M. Oudich, S. El-Jallal, Y. Pennec, B. Djafari-Rouhani, J. Gomis-Bresco, D. Navarro-Urrios, C. M. Sotomayor Torres, A. Martínez, and A. Makhoute, *Optomechanic interaction in a corrugated phoxonic nanobeam cavity*, Physical Review B **89**, 245122 (2014).

[178] L. Mercadé, L. L. Martín, A. Griol, D. Navarro-Urrios, and A. Martínez, *Microwave oscillator and frequency comb in a silicon optomechanical cavity with a full phononic bandgap*, Nanophotonics **9**, 3535–3544 (2020).

[179] N. W. Ashcroft and N. D. Mermin, *Solid State Physics*, Saunders College, Philadelphia (1976).

[180] P. D. García, R. Bericat-Vadell, G. Arregui, D. Navarro-Urrios, M. Colombano, F. Alzina, and C. M. Sotomayor-Torres, *Optomechanical coupling in the Anderson-localization regime*, Physical Review B **95**, 115129 (2017).

[181] J.-P. Berenger, *A perfectly matched layer for the absorption of electromagnetic waves*, Journal of Computational Physics **114**, 185–200 (1994).

[182] A. W. Snyder and J. Love, *Optical Waveguide Theory*, Springer (1983).

[183] K. Srinivasan and O. Painter, *Momentum space design of high-Q photonic crystal optical cavities*, Optics Express **10**, 670–684 (2002).

[184] J. M. Geremia, J. Williams, and H. Mabuchi, *Inverse-problem approach to designing photonic crystals for cavity QED experiments*, Physical Review E **66**, 066606 (2002).

[185] Y. Akahane, T. Asano, B.-S. Song, and S. Noda, *High- Q photonic nanocavity in a two-dimensional photonic crystal*, Nature **425**, 944–947 (2003).

[186] B.-S. Song, S. Noda, T. Asano, and Y. Akahane, *Ultra-high- Q photonic double-heterostructure nanocavity*, Nature Materials **4**, 207–210 (2005).

[187] J. Chan, M. Eichenfield, R. Camacho, and O. Painter, *Optical and mechanical design of a "zipper" photonic crystal optomechanical cavity*, Optics Express **17**, 3802–3817 (2009).

[188] M. H. Matheny, *Enhanced photon-phonon coupling via dimerization in one-dimensional optomechanical crystals*, Applied Physics Letters **112**, 253104 (2018).

[189] R. Leijssen, G. R. La Gala, L. Freisem, J. T. Muhonen, and E. Verhagen, *Nonlinear cavity optomechanics with nanomechanical thermal fluctuations*, Nature Communications **8**, ncomms16024 (2017).

[190] I. Ghorbel, F. Swiadek, R. Zhu, D. Dolfi, G. Lehoucq, A. Martin, G. Moille, L. Morvan, R. Braive, S. Combrié, and A. De Rossi, *Optomechanical gigahertz oscillator made of a two photon absorption free piezoelectric III/V semiconductor*, APL Photonics **4**, 116103 (2019).

[191] F. G. S. Santos, Y. A. V. Espinel, G. O. Luiz, R. S. Benevides, G. S. Wiederhecker, and T. P. M. Alegre, *Hybrid confinement of optical and mechanical modes in a bullseye optomechanical resonator*, Optics Express **25**, 508–529 (2017).

[192] I. Favero and K. Karrai, *Optomechanics of deformable optical cavities*, Nature Photonics **3**, 201–205 (2009).

[193] M. Stoehr, G. Gerlach, T. Härtling, and S. Schoenfelder, *Analysis of photoelastic properties of monocrystalline silicon*, Journal of Sensors and Sensor Systems **9**, 209–217 (2020).

[194] Y. Pennec, V. Laude, N. Papanikolaou, B. Djafari-Rouhani, M. Oudich, S. E. Jallal, J. C. Beugnot, J. M. Escalante, and A. Martínez, *Modeling light-sound interaction in nanoscale cavities and waveguides*, Nanophotonics **3**, 413–440 (2014).

[195] M. Stocchi, D. Mencarelli, Y. Pennec, B. Djafari-Rouhani, and L. Pierantoni, *Rigorous simulation of nonlinear optomechanical coupling in micro- and nano-structured resonant cavities*, International Journal of Optomechatronics **12**, 11–19 (2018).

[196] H. A. Bethe and J. Schwinger, *Perturbation Theory for Cavities*, Massachusetts Institute of Technology, Radiation Laboratory, Cambridge (1943).

[197] J. Yang, H. Giessen, and P. Lalanne, *Simple Analytical Expression for the Peak-Frequency Shifts of Plasmonic Resonances for Sensing*, Nano Letters **15**, 3439–3444 (2015).

[198] T. Weiss, M. Mesch, M. Schäferling, H. Giessen, W. Langbein, and E. Muljarov, *From Dark to Bright: First-Order Perturbation Theory with Analytical Mode Normalization for Plasmonic Nanoantenna Arrays Applied to Refractive Index Sensing*, Physical Review Letters **116**, 237401 (2016).

[199] A. G. Primo, N. C. Carvalho, C. M. Kersul, N. C. Frateschi, G. S. Wiederhecker, and T. P. Alegre, *Quasinormal-Mode Perturbation Theory for Dissipative and Dispersive Optomechanics*, Physical Review Letters **125**, 233601 (2020).

[200] A. N. Cleland, *Foundations of Nanomechanics: From Solid-State Theory to Device Applications*, Springer-Verlag, Berlin Heidelberg (2003).

[201] A. Gillespie and F. Raab, *Thermally excited vibrations of the mirrors of laser interferometer gravitational-wave detectors*, Physical Review D **52**, 577–585 (1995).

[202] S. G. Johnson, M. Ibanescu, M. A. Skorobogatiy, O. Weisberg, J. D. Joannopoulos, and Y. Fink, *Perturbation theory for Maxwell's equations with shifting material boundaries*, Physical Review E **65**, 066611 (2002).

[203] P. T. Kristensen, K. Herrmann, F. Intravaia, K. Busch, and K. Busch, *Modeling electromagnetic resonators using quasinormal modes*, Advances in Optics and Photonics **12**, 612–708 (2020).

[204] W. Yan, R. Faggiani, and P. Lalanne, *Rigorous modal analysis of plasmonic nanoresonators*, Physical Review B **97**, 205422 (2018).

[205] J. Chan, "Laser Cooling of an Optomechanical Crystal Resonator to Its Quantum Ground State of Motion", PhD thesis, California Institute of Technology, 2012.

[206] K. Koshelev, G. Favraud, A. Bogdanov, Y. Kivshar, and A. Fratalocchi, *Nonradiating photonics with resonant dielectric nanostructures*, Nanophotonics **8**, 725–745 (2019).

[207] M. Minkov, U. P. Dharanipathy, R. Houdré, and V. Savona, *Statistics of the disorder-induced losses of high-Q photonic crystal cavities*, Optics Express **21**, 28233–28245 (2013).

[208] S. H. Mousavi, A. B. Khanikaev, and Z. Wang, *Topologically protected elastic waves in phononic metamaterials*, Nature Communications **6**, 8682 (2015).

[209] P. Sheng, *Introduction to Wave Scattering, Localization and Mesoscopic Phenomena*, 2nd ed., Springer-Verlag, Berlin Heidelberg (2006).

[210] I. M. Lifshitz, *The energy spectrum of disordered systems*, Advances in Physics **13**, 483–536 (1964).

[211] S. R. Huisman, G. Ctistis, S. Stobbe, A. P. Mosk, J. L. Herek, A. Lagendijk, P. Lodahl, W. L. Vos, and P. W. H. Pinkse, *Measurement of a band-edge tail in the density of states of a photonic-crystal waveguide*, Physical Review B **86**, 155154 (2012).

[212] H. Thyrrestrup, S. Smolka, L. Sapienza, and P. Lodahl, *Statistical Theory of a Quantum Emitter Strongly Coupled to Anderson-Localized Modes*, Physical Review Letters **108**, 113901 (2012).

[213] J. P. Vasco and S. Hughes, *Statistics of Anderson-localized modes in disordered photonic crystal slab waveguides*, Physical Review B **95**, 224202 (2017).

[214] M. C. W. van Rossum and T. M. Nieuwenhuizen, *Multiple scattering of classical waves: microscopy, mesoscopy, and diffusion*, Reviews of Modern Physics **71**, 313–371 (1999).

[215] C. W. J. Beenakker, *Random-matrix theory of quantum transport*, Reviews of Modern Physics **69**, 731–808 (1997).

[216] M. Charbonneau-Lefort, E. Istrate, M. Allard, J. Poon, and E. H. Sargent, *Photonic crystal heterostructures: Waveguiding phenomena and methods of solution in an envelope function picture*, Physical Review B **65**, 125318 (2002).

[217] P. D. García, A. Javadi, H. Thyrrestrup, and P. Lodahl, *Quantifying the intrinsic amount of fabrication disorder in photonic-crystal waveguides from optical far-field intensity measurements*, Applied Physics Letters **102**, 031101 (2013).

[218] J. Orton and T. Foxon, *Molecular Beam Epitaxy: A Short History*, Illustrated edition, Oxford University Press, Oxford (2015).

[219] M. Born and E. Wolf, *Principles of Optics: Electromagnetic Theory of Propagation, Interference and Diffraction of Light*, 7th ed., Cambridge University Press, Cambridge (1999).

[220] C. Colvard, T. A. Gant, M. V. Klein, R. Merlin, R. Fischer, H. Morkoc, and A. C. Gossard, *Folded acoustic and quantized optic phonons in (GaAl)As superlattices*, Physical Review B **31**, 2080–2091 (1985).

[221] M. Cardona and G. Güntherodt, *Light Scattering in Solids V: Superlattices and Other Microstructures*, Springer-Verlag, Berlin Heidelberg (1989).

[222] B. Jusserand, D. Paquet, F. Mollot, F. Alexandre, and G. Le Roux, *Influence of the supercell structure on the folded acoustical Raman line intensities in superlattices*, Physical Review B **35**, 2808–2817 (1987).

[223] V. Laude, Y. Achaoui, S. Benchabane, and A. Khelif, *Evanescent Bloch waves and the complex band structure of phononic crystals*, Physical Review B **80**, 092301 (2009).

[224] D. W. L. Sprung, H. Wu, and J. Martorell, *Scattering by a finite periodic potential*, American Journal of Physics **61**, 1118–1124 (1993).

[225] P. A. Kalozoumis, G. Theocharis, V. Achilleos, S. Félix, O. Richoux, and V. Pagneux, *Finite-size effects on topological interface states in one-dimensional scattering systems*, Physical Review A **98**, 023838 (2018).

[226] A. Settimi, S. Severini, N. Mattiucci, C. Sibilia, M. Centini, G. D'Aguanno, M. Bertolotti, M. Scalora, M. Bloemer, and C. M. Bowden, *Quasinormal-mode description of waves in one-dimensional photonic crystals*, Physical Review E **68**, 026614 (2003).

[227] F. Alpeggiani, N. Parappurath, E. Verhagen, and L. Kuipers, *Quasinormal-Mode Expansion of the Scattering Matrix*, Physical Review X **7**, 021035 (2017).

[228] D. E. Muller, *A Method for Solving Algebraic Equations Using an Automatic Computer*, Mathematical Tables and Other Aids to Computation **10**, 208–215 (1956).

[229] E. Anemogiannis and E. N. Glytsis, *Multilayer waveguides: efficient numerical analysis of general structures*, Journal of Lightwave Technology **10**, 1344–1351 (1992).

[230] M. Trigo, A. Bruchhausen, A. Fainstein, B. Jusserand, and V. Thierry-Mieg, *Confinement of Acoustical Vibrations in a Semiconductor Planar Phonon Cavity*, Physical Review Letters **89**, 227402 (2002).

[231] N. D. Lanzillotti-Kimura, A. Fainstein, A. Lemaitre, B. Jusserand, and B. Perrin, *Coherent control of sub-terahertz confined acoustic nanowaves: Theory and experiments*, Physical Review B **84**, 115453 (2011).

[232] F. R. Lamberti, M. Esmann, A. Lemaître, C. Gomez Carbonell, O. Krebs, I. Favero, B. Jusserand, P. Senellart, L. Lanco, and N. D. Lanzillotti-Kimura,

Nanomechanical resonators based on adiabatic periodicity-breaking in a superlattice, Applied Physics Letters **111**, 173107 (2017).

[233] G. Arregui, N. Lanzillotti-Kimura, C. Sotomayor-Torres, and P. García, *Anderson Photon-Phonon Colocalization in Certain Random Superlattices*, Physical Review Letters **122**, 043903 (2019).

[234] J. Zak, *Berry's phase for energy bands in solids*, Physical Review Letters **62**, 2747–2750 (1989).

[235] N. D. Lanzillotti-Kimura, A. Fainstein, C. A. Balseiro, and B. Jusserand, *Phonon engineering with acoustic nanocavities: Theoretical considerations on phonon molecules, band structures, and acoustic Bloch oscillations*, Physical Review B **75**, 024301 (2007).

[236] G. Panzarini, L. C. Andreani, A. Armitage, D. Baxter, M. S. Skolnick, V. N. Astratov, J. S. Roberts, A. V. Kavokin, M. R. Vladimirova, and M. A. Kaliteevski, *Exciton-light coupling in single and coupled semiconductor microcavities: Polariton dispersion and polarization splitting*, Physical Review B **59**, 5082–5089 (1999).

[237] S. A. Maier, *Plasmonics: Fundamentals and Applications*, Springer US (2007).

[238] A. V. Kavokin, I. A. Shelykh, and G. Malpuech, *Lossless interface modes at the boundary between two periodic dielectric structures*, Physical Review B **72**, 233102 (2005).

[239] Y. Tsurimaki, J. K. Tong, V. N. Boriskin, A. Semenov, M. I. Ayzatsky, Y. P. Machekhin, G. Chen, and S. V. Boriskina, *Topological Engineering of Interfacial Optical Tamm States for Highly Sensitive Near-Singular-Phase Optical Detection*, ACS Photonics **5**, 929–938 (2018).

[240] G. Bastard, *Wave Mechanics Applied to Semiconductor Heterostructures*, Wiley-Interscience (1991).

[241] W. Chen, Y. Lu, H. J. Maris, and G. Xiao, *Picosecond ultrasonic study of localized phonon surface modes in Al/Ag superlattices*, Physical Review B **50**, 14506–14515 (1994).

[242] S. Willard, *General Topology*, Illustrated edition, Dover Publications, Mineola, N.Y (2004).

[243] Y.-D. Wu, *Topological properties in one-dimensional periodic systems*, arXiv:1706.02370 [cond-mat] (2019), arXiv: 1706.02370.

[244] J. K. Asbóth, L. Oroszlány, and A. Pályi, *A Short Course on Topological Insulators: Band Structure and Edge States in One and Two Dimensions*, Springer International Publishing (2016).

[245] M. V. Berry, *Quantal phase factors accompanying adiabatic changes*, Proceedings of the Royal Society of London. A. Mathematical and Physical Sciences **392**, 45–57 (1984).

[246] M. Xiao, G. Ma, Z. Yang, P. Sheng, Z. Q. Zhang, and C. T. Chan, *Geometric phase and band inversion in periodic acoustic systems*, Nature Physics **11**, 240–244 (2015).

[247] M. Atala, M. Aidelsburger, J. T. Barreiro, D. Abanin, T. Kitagawa, E. Demler, and I. Bloch, *Direct measurement of the Zak phase in topological Bloch bands*, Nature Physics **9**, 795–800 (2013).

[248] X. Z. Zhang and Z. Song, *Partial topological Zak phase and dynamical confinement in a non-Hermitian bipartite system*, Physical Review A **99**, 012113 (2019).

[249] M. Xiao, Z. Zhang, and C. Chan, *Surface Impedance and Bulk Band Geometric Phases in One-Dimensional Systems*, Physical Review X **4**, 021017 (2014).

[250] P. St-Jean, V. Goblot, E. Galopin, A. Lemaître, T. Ozawa, L. Le Gratiet, I. Sagnes, J. Bloch, and A. Amo, *Lasing in topological edge states of a one-dimensional lattice*, Nature Photonics **11**, 651–656 (2017).

[251] Z. Yang, F. Gao, and B. Zhang, *Topological water wave states in a one-dimensional structure*, Scientific Reports **6**, 29202 (2016).

[252] M. Esmann, F. R. Lamberti, P. Senellart, I. Favero, O. Krebs, L. Lanco, C. Gomez Carbonell, A. Lemaître, and N. D. Lanzillotti-Kimura, *Topological nanophononic states by band inversion*, Physical Review B **97**, 155422 (2018).

[253] W. Kohn, *Analytic Properties of Bloch Waves and Wannier Functions*, Physical Review **115**, 809–821 (1959).

[254] W. P. Su, J. R. Schrieffer, and A. J. Heeger, *Solitons in Polyacetylene*, Physical Review Letters **42**, 1698–1701 (1979).

[255] J. Shapiro, *The bulk-edge correspondence in three simple cases*, Reviews in Mathematical Physics **32**, 2030003 (2019).

[256] A. R. McGurn, K. T. Christensen, F. M. Mueller, and A. A. Maradudin, *Anderson localization in one-dimensional randomly disordered optical systems that are periodic on average*, Physical Review B **47**, 13120–13125 (1993).

[257] S. A. Bulgakov and M. Nieto-Vesperinas, *Competition of different scattering mechanisms in a one-dimensional random photonic lattice*, JOSA A **13**, 500–508 (1996).

[258] L. I. Deych, D. Zaslavsky, and A. A. Lisyansky, *Statistics of the Lyapunov Exponent in 1D Random Periodic-on-Average Systems*, Physical Review Letters **81**, 5390–5393 (1998).

[259] S.-i. Tamura and F. Nori, *Acoustic interference in random superlattices*, Physical Review B **41**, 7941–7944 (1990).

[260] N. Nishiguchi, S.-i. Tamura, and F. Nori, *Phonon-transmission rate, fluctuations, and localization in random semiconductor superlattices: Green's-function approach*, Physical Review B **48**, 2515–2528 (1993).

[261] R. Venkatasubramanian, *Lattice thermal conductivity reduction and phonon localizationlike behavior in superlattice structures*, Physical Review B **61**, 3091–3097 (2000).

[262] P. Han and C. Zheng, *Effects of structural periodicity on localization length in one-dimensional periodic-on-average disordered systems*, Physical Review E **77**, 041111 (2008).

[263] L. Miglio, *Introduction to the theory of disordered systems*, Il Nuovo Cimento D **11**, 1375–1376 (1989).

[264] C. A. Müller and D. Delande, *Disorder and interference: localization phenomena*, Oxford University Press ().

[265] S. John and R. Rangarajan, *Optimal structures for classical wave localization: an alternative to the ioffe-regel criterion*, Physical Review B **38**, 10101–10104 (1988).

[266] R. Faggiani, A. Baron, X. Zang, L. Lalouat, S. A. Schulz, B. O'Regan, K. Vynck, B. Cluzel, F. de Fornel, T. F. Krauss, and P. Lalanne, *Lower bound for the spatial extent of localized modes in photonic-crystal waveguides with small random imperfections*, Scientific Reports **6**, 27037 (2016).

[267] P. D. García, G. Kiršanskė, A. Javadi, S. Stobbe, and P. Lodahl, *Two mechanisms of disorder-induced localization in photonic-crystal waveguides*, Physical Review B **96**, 144201 (2017).

[268] S. Hughes, L. Ramunno, J. F. Young, and J. E. Sipe, *Extrinsic Optical Scattering Loss in Photonic Crystal Waveguides: Role of Fabrication Disorder and Photon Group Velocity*, Physical Review Letters **94**, 033903 (2005).

[269] L. S. Froufe-Pérez, M. Yépez, P. A. Mello, and J. J. Sáenz, *Statistical scattering of waves in disordered waveguides: From microscopic potentials to limiting macroscopic statistics*, Physical Review E **75**, 031113 (2007).

[270] P. D. García, S. Smolka, S. Stobbe, and P. Lodahl, *Density of states controls Anderson localization in disordered photonic crystal waveguides*, Physical Review B **82**, 165103 (2010).

[271] P. D. García, R. Sapienza, L. S. Froufe-Pérez, and C. López, *Strong dispersive effects in the light-scattering mean free path in photonic gaps*, Physical Review B **79**, 241109 (2009).

[272] R. C. McPhedran, L. C. Botten, J. McOrist, A. A. Asatryan, C. M. de Sterke, and N. A. Nicorovici, *Density of states functions for photonic crystals*, Physical Review E **69**, 016609 (2004).

[273] V. S. C. Manga Rao and S. Hughes, *Single quantum-dot Purcell factor and beta factor in a photonic crystal waveguide*, Physical Review B **75**, 205437 (2007).

[274] R. Carmona, *Exponential localization in one dimensional disordered systems*, Duke Mathematical Journal **49**, 191–213 (1982).

[275] Y. A. Godin, S. Molchanov, and B. Vainberg, *The effect of disorder on the wave propagation in one-dimensional periodic optical systems*, Waves in Random and Complex Media **21**, 135–150 (2011).

[276] H.-J. Sommers, Y. V. Fyodorov, and M. Titov, *S-matrix poles for chaotic quantum systems as eigenvalues of complex symmetric random matrices: from isolated to overlapping resonances*, Journal of Physics A: Mathematical and General **32**, L77–L85 (1999).

[277] M. Weiss, J. A. Méndez-Bermúdez, and T. Kottos, *Resonance width distribution for high-dimensional random media*, Physical Review B **73**, 045103 (2006).

[278] P. W. Anderson, D. J. Thouless, E. Abrahams, and D. S. Fisher, *New method for a scaling theory of localization*, Physical Review B **22**, 3519–3526 (1980).

[279] A. Fainstein, N. D. Lanzillotti-Kimura, B. Jusserand, and B. Perrin, *Strong Optical-Mechanical Coupling in a Vertical GaAs/AlAs Microcavity for Subterahertz Phonons and Near-Infrared Light*, Physical Review Letters **110**, 037403 (2013).

[280] S. Adachi, *GaAs and Related Materials: Bulk Semiconducting and Superlattice Properties*, World Scientific (1994).

[281] P. Sesin, P. Soubelet, V. Villafañe, A. E. Bruchhausen, B. Jusserand, A. Lemaître, N. D. Lanzillotti-Kimura, and A. Fainstein, *Dynamical optical tuning of the coherent phonon detection sensitivity in DBR-based GaAs optomechanical resonators*, Physical Review B **92**, 075307 (2015).

[282] S. Anguiano, A. Bruchhausen, B. Jusserand, I. Favero, F. Lamberti, L. Lanco, I. Sagnes, A. Lemaître, N. Lanzillotti-Kimura, P. Senellart, and A. Fainstein, *Micropillar Resonators for Optomechanics in the Extremely High 19–95-GHz Frequency Range*, Physical Review Letters **118**, 263901 (2017).

[283] O. Ortiz, P. Priya, A. Rodriguez, A. Lemaitre, M. Esmann, and N. D. Lanzillotti-Kimura, *Topological optical and phononic interface mode by simultaneous band inversion*, arXiv:2007.14753 [cond-mat, physics:physics] (2020), arXiv: 2007.14753.

[284] Y. Léger, *Double Magic Coincidence in an Optomechanical Laser Cavity*, Physics **6** (2013).

[285] Y. Ezzahri, S. Grauby, J. M. Rampnoux, H. Michel, G. Pernot, W. Claeys, S. Dilhaire, C. Rossignol, G. Zeng, and A. Shakouri, *Coherent phonons in Si/SiGe superlattices*, Physical Review B **75**, 195309 (2007).

[286] A. I. Sharkov, T. I. Galkina, and A. Y. Klokov, *Probing of the multilayer Si/SiGe structure with a flux of nonequilibrium acoustic phonons*, Physics of the Solid State **51**, 2040 (2009).

[287] M. Hijazi and M. Kazan, *Phonon heat transport in superlattices: Case of Si/SiGe and SiGe/SiGe superlattices*, AIP Advances **6**, 065024 (2016).

[288] S. Gehrsitz, F. K. Reinhart, C. Gourgon, N. Herres, A. Vonlanthen, and H. Sigg, *The refractive index of AlxGa1-xAs below the band gap: Accurate determination and empirical modeling*, Journal of Applied Physics **87**, 7825–7837 (2000).

[289] O. Matsuda and O. B. Wright, *Laser picosecond acoustics in multilayer structures*, Ultrasonics **40**, 753–756 (2002).

[290] P. Ruello and V. E. Gusev, *Physical mechanisms of coherent acoustic phonons generation by ultrafast laser action*, Ultrasonics **56**, 21–35 (2015).

[291] O. Matsuda and O. B. Wright, *Reflection and transmission of light in multilayers perturbed by picosecond strain pulse propagation*, JOSA B **19**, 3028–3041 (2002).

[292] K. Mizoguchi, M. Hase, S. Nakashima, and M. Nakayama, "Study of coherent folded acoustic phonons in GaAs/AlAs superlattices by two-color pump-probe technique", *Ultrafast Phenomena XI*, ed. by T. Elsaesser, J. G. Fujimoto, D. A. Wiersma, and W. Zinth(1998), pp. 269–271.

[293] C. Thomsen, J. Strait, Z. Vardeny, H. J. Maris, J. Tauc, and J. J. Hauser, *Coherent Phonon Generation and Detection by Picosecond Light Pulses*, Physical Review Letters **53**, 989–992 (1984).

[294] C. Thomsen, H. T. Grahn, H. J. Maris, and J. Tauc, *Surface generation and detection of phonons by picosecond light pulses*, Physical Review B **34**, 4129–4138 (1986).

[295] C. A. Paddock and G. L. Eesley, *Transient thermoreflectance from thin metal films*, Journal of Applied Physics **60**, 285–290 (1986).

[296] N.-W. Pu, *Ultrafast excitation and detection of acoustic phonon modes in superlattices*, Physical Review B **72**, 115428 (2005).

[297] T. H. K. Barron, *Anharmonicity, Thermal Expansion and Thermal Resistance in a Dielectric Solid*, Nature **178**, 871–871 (1956).

[298] O. B. Wright, *Ultrafast nonequilibrium stress generation in gold and silver*, Physical Review B **49**, 9985–9988 (1994).

[299] B. G. M. Tavares, M. A. Tito, and Y. A. Pusep, *Influence of energy structure on recombination lifetime in GaAs/AlGaAs multilayers*, Journal of Applied Physics **119**, 234305 (2016).

[300] M. V. Fischetti and J. M. Higman, "Theory and Calculation of the Deformation Potential Electron-Phonon Scattering Rates in Semiconductors", *Monte Carlo Device Simulation: Full Band and Beyond*, ed. by K. Hess(1991), pp. 123–160.

[301] S. A. Akhmanov and V. E. Gusev, *Laser excitation of ultrashort acoustic pulses: New possibilities in solid-state spectroscopy, diagnostics of fast processes, and nonlinear acoustics*, Physics-Uspekhi **35**, 153–191 (1992).

[302] P. Babilotte, O. Diallo, L.-P. T. H. Hue, M. Kosec, D. Kuscer, and G. Feuillard, *Electrical excitation and optical detection of ultrasounds in PZT based piezoelectric transducers*, Journal of Physics: Conference Series **278**, 012027 (2011).

[303] T. E. Stevens, J. Kuhl, and R. Merlin, *Coherent phonon generation and the two stimulated Raman tensors*, Physical Review B **65**, 144304 (2002).

[304] V. Gusev, *Generation of inhomogeneous bulk plane acoustic modes by laser-induced thermoelastic grating near mechanically free surface*, Journal of Applied Physics **107**, 114906 (2010).

[305] M. F. Pascual-Winter, A. Fainstein, B. Jusserand, B. Perrin, and A. Lemaître, *Spectral responses of phonon optical generation and detection in superlattices*, Physical Review B **85**, 235443 (2012).

[306] Y. C. Shen, T. Lo, P. F. Taday, B. E. Cole, W. R. Tribe, and M. C. Kemp, *Detection and identification of explosives using terahertz pulsed spectroscopic imaging*, Applied Physics Letters **86**, 241116 (2005).

[307] M. Kuriakose, N. Chigarev, S. Raetz, A. Bulou, V. Tournat, A. Zerr, and V. E. Gusev, *In situimaging of the dynamics of photo-induced structural phase transition at high pressures by picosecond acoustic interferometry*, New Journal of Physics **19**, 053026 (2017).

[308] B. F. Spencer, W. F. Smith, M. T. Hibberd, P. Dawson, M. Beck, A. Bartels, I. Guiney, C. J. Humphreys, and D. M. Graham, *Terahertz cyclotron resonance spectroscopy of an AlGaN/GaN heterostructure using a high-field pulsed magnet and an asynchronous optical sampling technique*, Applied Physics Letters **108**, 212101 (2016).

[309] A. Abbas, Y. Guillet, J.-M. Rampnoux, P. Rigail, E. Mottay, B. Audoin, and S. Dilhaire, *Picosecond time resolved opto-acoustic imaging with 48 MHz frequency resolution*, Optics Express **22**, 7831–7843 (2014).

[310] F. Pérez-Cota, R. J. Smith, E. Moradi, L. Marques, K. F. Webb, and M. Clark, *High resolution 3D imaging of living cells with sub-optical wavelength phonons*, Scientific Reports **6**, 39326 (2016).

[311] A. Bartels, R. Cerna, C. Kistner, A. Thoma, F. Hudert, C. Janke, and T. Dekorsy, *Ultrafast time-domain spectroscopy based on high-speed asynchronous optical sampling*, Review of Scientific Instruments **78**, 035107 (2007).

[312] A. Bruchhausen, R. Gebs, F. Hudert, D. Issenmann, G. Klatt, A. Bartels, O. Schecker, R. Waitz, A. Erbe, E. Scheer, J.-R. Huntzinger, A. Mlayah, and T. Dekorsy, *Subharmonic Resonant Optical Excitation of Confined Acoustic Modes in a Free-Standing Semiconductor Membrane at GHz Frequencies with a High-Repetition-Rate Femtosecond Laser*, Physical Review Letters **106**, 077401 (2011).

[313] *Laser Manufacturer and Supplier | Laser Sources.*

[314] R. Merlin, *Generating coherent THz phonons with light pulses*, Solid State Communications **102**, 207–220 (1997).

[315] G. F. Simmons, *Differential Equations with Applications and Historical Notes*, 3rd ed., Chapman and Hall/CRC (2016).

[316] D. G. Duffy, *Green's Functions with Applications*, 2nd ed., Chapman and Hall/CRC (2018).

[317] R. Legrand, A. Huynh, B. Jusserand, B. Perrin, and A. Lemaître, *Direct measurement of coherent subterahertz acoustic phonons mean free path in GaAs*, Physical Review B **93**, 184304 (2016).

[318] M. Nakayama, K. Kubota, H. Kato, and N. Sano, *Finite-size effects on Raman scattering from GaAs-AlAs superlattices*, Journal of Applied Physics **60**, 3289–3292 (1986).

[319] P. Etchegoin, J. Kircher, M. Cardona, C. Grein, and E. Bustarret, *Piezo-optics of GaAs*, Physical Review B **46**, 15139–15149 (1992).

[320] B. Jusserand, A. Poddubny, A. Poshakinskiy, A. Fainstein, and A. Lemaitre, *Polariton Resonances for Ultrastrong Coupling Cavity Optomechanics in GaAs/AlAs Multiple Quantum Wells*, Physical Review Letters **115**, 267402 (2015).

[321] N. D. Lanzillotti-Kimura, A. Fainstein, A. Huynh, B. Perrin, B. Jusserand, A. Miard, and A. Lemaître, *Coherent Generation of Acoustic Phonons in an Optical Microcavity*, Physical Review Letters **99**, 217405 (2007).

[322] A. Savitzky and M. J. E. Golay, *Smoothing and Differentiation of Data by Simplified Least Squares Procedures.* Analytical Chemistry **36**, 1627–1639 (1964).

[323] C. Thomsen, H. T. Grahn, H. J. Maris, and J. Tauc, *Picosecond interferometric technique for study of phonons in the brillouin frequency range*, Optics Communications **60**, 55–58 (1986).

[324] A. Huynh, N. D. Lanzillotti-Kimura, B. Jusserand, B. Perrin, A. Fainstein, M. F. Pascual-Winter, E. Peronne, and A. Lemaître, *Subterahertz Phonon Dynamics in Acoustic Nanocavities*, Physical Review Letters **97**, 115502 (2006).

[325] M. Notomi, K. Yamada, A. Shinya, J. Takahashi, C. Takahashi, and I. Yokohama, *Extremely Large Group-Velocity Dispersion of Line-Defect Waveguides in Photonic Crystal Slabs*, Physical Review Letters **87**, 253902 (2001).

[326] S. G. Johnson, P. R. Villeneuve, S. Fan, and J. D. Joannopoulos, *Linear waveguides in photonic-crystal slabs*, Physical Review B **62**, 8212–8222 (2000).

[327] C. Jamois, R. B. Wehrspohn, L. C. Andreani, C. Hermann, O. Hess, and U. Gösele, *Silicon-based two-dimensional photonic crystal waveguides*, Photonics and Nanostructures - Fundamentals and Applications **1**, 1–13 (2003).

[328] S. Mazoyer, J. P. Hugonin, and P. Lalanne, *Disorder-Induced Multiple Scattering in Photonic-Crystal Waveguides*, Physical Review Letters **103**, 063903 (2009).

[329] T. F. Krauss, *Why do we need slow light?*, Nature Photonics **2**, 448–450 (2008).

[330] B. Corcoran, C. Monat, C. Grillet, D. J. Moss, B. J. Eggleton, T. P. White, L. O'Faolain, and T. F. Krauss, *Green light emission in silicon through slow-light enhanced third-harmonic generation in photonic-crystal waveguides*, Nature Photonics **3**, 206–210 (2009).

[331] H. Takesue, N. Matsuda, E. Kuramochi, and M. Notomi, *Entangled photons from on-chip slow light*, Scientific Reports **4**, 3913 (2014).

[332] T. F. Krauss, *Slow light in photonic crystal waveguides*, Journal of Physics D: Applied Physics **40**, 2666–2670 (2007).

[333] L. V. Hau, S. E. Harris, Z. Dutton, and C. H. Behroozi, *Light speed reduction to 17 metres per second in an ultracold atomic gas*, Nature **397**, 594–598 (1999).

[334] Z. Shi, R. W. Boyd, R. M. Camacho, P. K. Vudyasetu, and J. C. Howell, *Slow-Light Fourier Transform Interferometer*, Physical Review Letters **99**, 240801 (2007).

[335] J. Topolancik, B. Ilic, and F. Vollmer, *Experimental Observation of Strong Photon Localization in Disordered Photonic Crystal Waveguides*, Physical Review Letters **99**, 253901 (2007).

[336] Zhang Daozhong, Hu Wei, Zhang Youlong, Li Zhaolin, Cheng Bingying, and Yang Guozhen, *Experimental verification of light localization for disordered multilayers in the visible-infrared spectrum*, Physical Review B **50**, 9810–9814 (1994).

[337] J. Bertolotti, S. Gottardo, D. S. Wiersma, M. Ghulinyan, and L. Pavesi, *Optical Necklace States in Anderson Localized 1D Systems*, Physical Review Letters **94**, 113903 (2005).

[338] H. H. Sheinfux, Y. Lumer, G. Ankonina, A. Z. Genack, G. Bartal, and M. Segev, *Observation of Anderson localization in disordered nanophotonic structures*, Science **356**, 953–956 (2017).

[339] V. Savona, *Electromagnetic modes of a disordered photonic crystal*, Physical Review B **83**, 085301 (2011).

[340] M. Qiu, *Effective index method for heterostructure-slab-waveguide-based two-dimensional photonic crystals*, Applied Physics Letters **81**, 1163–1165 (2002).

[341] A. García-Martín and J. J. Sáenz, *Universal Conductance Distributions in the Crossover between Diffusive and Localization Regimes*, Physical Review Letters **87**, 116603 (2001).

[342] A. Baron, S. Mazoyer, W. Smigaj, and P. Lalanne, *Attenuation Coefficient of Single-Mode Periodic Waveguides*, Physical Review Letters **107**, 153901 (2011).

[343] N. Le Thomas, H. Zhang, J. Jágerská, V. Zabelin, R. Houdré, I. Sagnes, and A. Talneau, *Light transport regimes in slow light photonic crystal waveguides*, Physical Review B **80**, 125332 (2009).

[344] M. Patterson, S. Hughes, S. Combrié, N.-V.-Q. Tran, A. De Rossi, R. Gabet, and Y. Jaouën, *Disorder-Induced Coherent Scattering in Slow-Light Photonic Crystal Waveguides*, Physical Review Letters **102**, 253903 (2009).

[345] W. Song, R. A. Integlia, and W. Jiang, *Slow light loss due to roughness in photonic crystal waveguides: An analytic approach*, Physical Review B **82**, 235306 (2010).

[346] R. J. P. Engelen, D. Mori, T. Baba, and L. Kuipers, *Two Regimes of Slow-Light Losses Revealed by Adiabatic Reduction of Group Velocity*, Physical Review Letters **101**, 103901 (2008).

[347] S. Mondal, R. Kumar, M. Kamp, and S. Mujumdar, *Optical Thouless conductance and level-spacing statistics in two-dimensional Anderson localizing systems*, Physical Review B **100**, 060201 (2019).

[348] M. Okano, T. Yamada, J. Sugisaka, N. Yamamoto, M. Itoh, T. Sugaya, K. Komori, and M. Mori, *Analysis of two-dimensional photonic crystal L-type cavities with low-refractive-index material cladding*, Journal of Optics **12**, 075101 (2010).

[349] J. P. Vasco and S. Hughes, *Anderson Localization in Disordered LN Photonic Crystal Slab Cavities*, ACS Photonics **5**, 1262–1272 (2018).

[350] W. Bogaerts, D. Taillaert, B. Luyssaert, P. Dumon, J. V. Campenhout, P. Bienstman, D. V. Thourhout, R. Baets, V. Wiaux, and S. Beckx, *Basic structures for photonic integrated circuits in Silicon-on-insulator*, Optics Express **12**, 1583–1591 (2004).

[351] S. Gröblacher, J. T. Hill, A. H. Safavi-Naeini, J. Chan, and O. Painter, *Highly efficient coupling from an optical fiber to a nanoscale silicon optomechanical cavity*, Applied Physics Letters **103**, 181104 (2013).

[352] D. Taillaert, W. Bogaerts, P. Bienstman, T. F. Krauss, P. V. Daele, I. Moerman, S. Verstuyft, K. D. Mesel, and R. Baets, *An out-of-plane grating coupler for efficient butt-coupling between compact planar waveguides and single-mode fibers*, IEEE Journal of Quantum Electronics **38**, 949–955 (2002).

[353] X. Zhou, I. Kulkova, T. Lund-Hansen, S. L. Hansen, P. Lodahl, and L. Midolo, *High-efficiency shallow-etched grating on GaAs membranes for quantum photonic applications*, Applied Physics Letters **113**, 251103 (2018).

[354] G. Z. Masanovic, V. M. N. Passaro, and G. T. Reed, *Dual grating-assisted directional coupling between fibers and thin semiconductor waveguides*, IEEE Photonics Technology Letters **15**, 1395–1397 (2003).

[355] X. Chen, C. Li, and H. K. Tsang, *Fabrication-Tolerant Waveguide Chirped Grating Coupler for Coupling to a Perfectly Vertical Optical Fiber*, IEEE Photonics Technology Letters **20**, 1914–1916 (2008).

[356] J. D. Cohen, S. M. Meenehan, and O. Painter, *Optical coupling to nanoscale optomechanical cavities for near quantum-limited motion transduction*, Optics Express **21**, 11227–11236 (2013).

[357] T. G. Tiecke, K. P. Nayak, J. D. Thompson, T. Peyronel, N. P. d. Leon, V. Vuletić, and M. D. Lukin, *Efficient fiber-optical interface for nanophotonic devices*, Optica **2**, 70–75 (2015).

[358] H. S. Dutta, A. K. Goyal, V. Srivastava, and S. Pal, *Coupling light in photonic crystal waveguides: A review*, Photonics and Nanostructures - Fundamentals and Applications **20**, 41–58 (2016).

[359] P. Pottier, M. Gnan, and R. M. D. L. Rue, *Efficient coupling into slow-light photonic crystal channel guides using photonic crystal tapers*, Optics Express **15**, 6569–6575 (2007).

[360] C.-Y. Lin, X. Wang, S. Chakravarty, B. S. Lee, W.-C. Lai, and R. T. Chen, *Wideband group velocity independent coupling into slow light silicon photonic crystal waveguide*, Applied Physics Letters **97**, 183302 (2010).

[361] J. P. Hugonin, P. Lalanne, T. P. White, and T. F. Krauss, *Coupling into slow-mode photonic crystal waveguides*, Optics Letters **32**, 2638–2640 (2007).

[362] X. Chen, W. Jiang, J. Chen, L. Gu, and R. T. Chen, *20dB-enhanced coupling to slot photonic crystal waveguide using multimode interference coupler*, Applied Physics Letters **91**, 091111 (2007).

[363] C. P. Reardon, I. H. Rey, K. Welna, L. O'Faolain, and T. F. Krauss, *Fabrication and characterization of photonic crystal slow light waveguides and cavities*, Journal of Visualized Experiments: JoVE, e50216 (2012).

[364] M. Spasenović, D. M. Beggs, P. Lalanne, T. F. Krauss, and L. Kuipers, *Measuring the spatial extent of individual localized photonic states*, Physical Review B **86**, 155153 (2012).

[365] S. Smolka, H. Thyrrestrup, L. Sapienza, T. B. Lehmann, K. R. Rix, L. S. Froufe-Pérez, P. D. García, and P. Lodahl, *Probing the statistical properties of Anderson localization with quantum emitters*, New Journal of Physics **13**, 063044 (2011).

[366] L. Sapienza, H. Thyrrestrup, S. Stobbe, P. D. Garcia, S. Smolka, and P. Lodahl, *Cavity Quantum Electrodynamics with Anderson-Localized Modes*, Science **327**, 1352–1355 (2010).

[367] F. Riboli, P. Barthelemy, S. Vignolini, F. Intonti, A. D. Rossi, S. Combrie, and D. S. Wiersma, *Anderson localization of near-visible light in two dimensions*, Optics Letters **36**, 127–129 (2011).

[368] M. Lee, J. Lee, S. Kim, S. Callard, C. Seassal, and H. Jeon, *Anderson localizations and photonic band-tail states observed in compositionally disordered platform*, Science Advances **4**, e1602796 (2018).

[369] C. P. Michael, M. Borselli, T. J. Johnson, C. Chrystal, and O. Painter, *An optical fiber-taper probe for wafer-scale microphotonic device characterization*, Optics Express **15**, 4745–4752 (2007).

[370] K. Srinivasan, P. E. Barclay, M. Borselli, and O. Painter, *Optical-fiber-based measurement of an ultrasmall volume high-Q photonic crystal microcavity*, Physical Review B **70**, 081306 (2004).

[371] C. Grillet, C. Smith, D. Freeman, S. Madden, B. Luther-Davies, E. C. Magi, D. J. Moss, and B. J. Eggleton, *Efficient coupling to chalcogenide glass photonic crystal waveguides via silica optical fiber nanowires*, Optics Express **14**, 1070–1078 (2006).

[372] P. E. Barclay, K. Srinivasan, M. Borselli, and O. Painter, *Probing the dispersive and spatial properties of photonic crystal waveguides via highly efficient coupling from fiber tapers*, Applied Physics Letters **85**, 4–6 (2004).

[373] M. W. Lee, C. Grillet, C. G. Poulton, C. Monat, C. L. C. Smith, E. Mägi, D. Freeman, S. Madden, B. Luther-Davies, and B. J. Eggleton, *Characterizing photonic crystal waveguides with an expanded k-space evanescent coupling technique*, Optics Express **16**, 13800–13808 (2008).

[374] L. Ding, C. Belacel, S. Ducci, G. Leo, and I. Favero, *Ultralow loss single-mode silica tapers manufactured by a microheater*, Applied Optics **49**, 2441–2445 (2010).

[375] J. D. Love, W. M. Henry, W. J. Stewart, R. J. Black, S. Lacroix, and F. Gonthier, *Tapered single-mode fibres and devices. I. Adiabaticity criteria*, IEE Proceedings J - Optoelectronics **138**, 343–354 (1991).

[376] R. Garcia-Fernandez, W. Alt, F. Bruse, C. Dan, K. Karapetyan, O. Rehband, A. Stiebeiner, U. Wiedemann, D. Meschede, and A. Rauschenbeutel, *Optical nanofibers and spectroscopy*, Applied Physics B **105**, 3 (2011).

[377] J. E. Hoffman, S. Ravets, J. A. Grover, P. Solano, P. R. Kordell, J. D. Wong-Campos, L. A. Orozco, and S. L. Rolston, *Ultrahigh transmission optical nanofibers*, AIP Advances **4**, 067124 (2014).

[378] H. L. Sørensen, "A Waveguide Platform for Collective Light-Atom Interaction", PhD thesis, phd: The Niels Bohr Institute, Faculty of Science, University of Copenhagen, 2015.

[379] J.-B. Béguin, J. Müller, J. Appel, and E. Polzik, *Observation of Quantum Spin Noise in a 1D Light-Atoms Quantum Interface*, Physical Review X **8**, 031010 (2018).

[380] E. Kuramochi, M. Notomi, S. Hughes, A. Shinya, T. Watanabe, and L. Ramunno, *Disorder-induced scattering loss of line-defect waveguides in photonic crystal slabs*, Physical Review B **72**, 161318 (2005).

[381] L. O'Faolain, T. P. White, D. O'Brien, X. Yuan, M. D. Settle, and T. F. Krauss, *Dependence of extrinsic loss on group velocity in photonic crystal waveguides*, Optics Express **15**, 13129–13138 (2007).

[382] J. Topolancik, F. Vollmer, R. Ilic, and M. Crescimanno, *Out-of-plane scattering from vertically asymmetric photonic crystal slab waveguides with in-plane disorder*, Optics Express **17**, 12470–12480 (2009).

[383] C. M. Patil, "Experiments on Glide-Symmetric Photonic-Crystal Waveguides", PhD thesis, Niels Bohr Institute, Faculty of Science, University of Copenhagen, 2020.

[384] D. J. Thouless, *Maximum Metallic Resistance in Thin Wires*, Physical Review Letters **39**, 1167–1169 (1977).

[385] M.-K. Kim, J.-Y. Kim, J.-H. Kang, B.-H. Ahn, and Y.-H. Lee, *On-demand photonic crystal resonators*, Laser & Photonics Reviews **5**, 479–495 (2011).

[386] M. Eichenfield, R. Camacho, J. Chan, K. J. Vahala, and O. Painter, *A picogram- and nanometre-scale photonic-crystal optomechanical cavity*, Nature **459**, 550–555 (2009).

[387] T. Kottos and T. Kottos, "Statistics of Resonances and Delay Times in High Dimensional Random Media", *Frontiers in Optics (2006), paper FWY1*, Frontiers in Optics(2006), FWY1.

[388] F. A. Pinheiro, *Statistics of quality factors in three-dimensional disordered magneto-optical systems and its applications to random lasers*, Physical Review A **78**, 023812 (2008).

[389] H. T. Nielsen, *Quantum Electrodynamics in Photonic Crystal Waveguides*, Technical University of Denmark (2011).

[390] P. Gregory, *Bayesian Logical Data Analysis for the Physical Sciences: A Comparative Approach with Mathematica Support*, Cambridge University Press, Cambridge (2005).

[391] E. Abrahams, P. W. Anderson, D. C. Licciardello, and T. V. Ramakrishnan, *Scaling Theory of Localization: Absence of Quantum Diffusion in Two Dimensions*, Physical Review Letters **42**, 673–676 (1979).

[392] P. D. García, S. Stobbe, I. Söllner, and P. Lodahl, *Nonuniversal Intensity Correlations in a Two-Dimensional Anderson-Localizing Random Medium*, Physical Review Letters **109**, 253902 (2012).

[393] G. Arregui, D. Navarro-Urrios, N. Kehagias, C. M. S. Torres, and P. D. García, *All-optical radio-frequency modulation of Anderson-localized modes*, Physical Review B **98**, 180202 (2018).

[394] S. M. Sze and K. K. Ng, *Physics of Semiconductor Devices*, 3rd edition, Wiley-Interscience, Hoboken, N.J (2006).

[395] M. Dinu, F. Quochi, and H. Garcia, *Third-order nonlinearities in silicon at telecom wavelengths*, Applied Physics Letters **82**, 2954–2956 (2003).

[396] R. A. Soref and B. R. Bennett, *Electrooptical effects in silicon*, IEEE Journal of Quantum Electronics **23**, 123–129 (1987).

[397] T. Tanabe, H. Sumikura, H. Taniyama, A. Shinya, and M. Notomi, *All-silicon sub-Gb/s telecom detector with low dark current and high quantum efficiency on chip*, Applied Physics Letters **96**, 101103 (2010).

[398] G. Cocorullo and I. Rendina, *Thermo-optical modulation at 1.5 mu m in silicon etalon*, Electronics Letters **28**, 83–85 (1992).

[399] I. V. Shadrivov, K. Y. Bliokh, Y. P. Bliokh, V. Freilikher, and Y. S. Kivshar, *Bistability of Anderson Localized States in Nonlinear Random Media*, Physical Review Letters **104**, 123902 (2010).

[400] N. Cherroret, *A self-consistent theory of localization in nonlinear random media*, Journal of Physics: Condensed Matter **29**, 024002 (2016).

[401] P. Stano and P. Jacquod, *Suppression of interactions in multimode random lasers in the Anderson localized regime*, Nature Photonics **7**, 66–71 (2013).

[402] J. Liu, P. D. Garcia, S. Ek, N. Gregersen, T. Suhr, M. Schubert, J. Mørk, S. Stobbe, and P. Lodahl, *Random nanolasing in the Anderson localized regime*, Nature Nanotechnology **9**, 285–289 (2014).

[403] D. S. Wiersma, *Disordered photonics*, Nature Photonics **7**, 188–196 (2013).

[404] V. R. Almeida, Q. Xu, C. A. Barrios, and M. Lipson, *Guiding and confining light in void nanostructure*, Optics Letters **29**, 1209–1211 (2004).

[405] J. D. Hood, A. Goban, A. Asenjo-Garcia, M. Lu, S.-P. Yu, D. E. Chang, and H. J. Kimble, *Atom–atom interactions around the band edge of a photonic crystal waveguide*, Proceedings of the National Academy of Sciences **113**, 10507–10512 (2016).

[406] M. P. Hiscocks, C.-H. Su, B. C. Gibson, A. D. Greentree, L. C. L. Hollenberg, and F. Ladouceur, *Slot-waveguide cavities for optical quantum information applications*, Optics Express **17**, 7295–7303 (2009).

[407] M. G. Scullion, T. F. Krauss, and A. Di Falco, *Slotted Photonic Crystal Sensors*, Sensors (Basel, Switzerland) **13**, 3675–3710 (2013).

[408] J. Gao, J. F. McMillan, M.-C. Wu, J. Zheng, S. Assefa, and C. W. Wong, *Demonstration of an air-slot mode-gap confined photonic crystal slab nanocavity with ultrasmall mode volumes*, Applied Physics Letters **96**, 051123 (2010).

[409] A. Di Falco, L. O'Faolain, and T. F. Krauss, *Chemical sensing in slotted photonic crystal heterostructure cavities*, Applied Physics Letters **94**, 063503 (2009).

[410] J. Jágerská, H. Zhang, Z. Diao, N. L. Thomas, and R. Houdré, *Refractive index sensing with an air-slot photonic crystal nanocavity*, Optics Letters **35**, 2523–2525 (2010).

[411] A. H. Safavi-Naeini, T. P. M. Alegre, M. Winger, and O. Painter, *Optomechanics in an ultrahigh-Q two-dimensional photonic crystal cavity*, Applied Physics Letters **97**, 181106 (2010).

[412] P. Seidler, K. Lister, U. Drechsler, J. Hofrichter, and T. Stöferle, *Slotted photonic crystal nanobeam cavity with an ultrahigh quality factor-to-mode volume ratio*, Optics Express **21**, 32468–32483 (2013).

[413] X. Sun, J. Zheng, M. Poot, C. W. Wong, and H. X. Tang, *Femtogram Doubly Clamped Nanomechanical Resonators Embedded in a High-Q Two-Dimensional Photonic Crystal Nanocavity*, Nano Letters **12**, 2299–2305 (2012).

[414] R. Leijssen and E. Verhagen, *Strong optomechanical interactions in a sliced photonic crystal nanobeam*, Scientific Reports **5**, 15974 (2015).

[415] K. E. Grutter, M. I. Davanço, and K. Srinivasan, *Slot-mode optomechanical crystals: a versatile platform for multimode optomechanics*, Optica **2**, 994–1001 (2015).

[416] W. Shimizu, N. Nagai, K. Kohno, K. Hirakawa, and M. Nomura, *Waveguide coupled air-slot photonic crystal nanocavity for optomechanics*, Optics Express **21**, 21961–21969 (2013).

[417] J. Zheng, Y. Li, M. Sirin Aras, A. Stein, K. L. Shepard, and C. Wei Wong, *Parametric optomechanical oscillations in two-dimensional slot-type high-Q photonic crystal cavities*, Applied Physics Letters **100**, 211908 (2012).

[418] L. D'Alessandro, B. Bahr, L. Daniel, D. Weinstein, and R. Ardito, *Shape optimization of solid–air porous phononic crystal slabs with widest full 3D bandgap for in-plane acoustic waves*, Journal of Computational Physics **344**, 465–484 (2017).

[419] M. Winger, T. D. Blasius, T. P. M. Alegre, A. H. Safavi-Naeini, S. Meenehan, J. Cohen, S. Stobbe, and O. Painter, *A chip-scale integrated cavity-electro-optomechanics platform*, Optics Express **19**, 24905–24921 (2011).

[420] A. D. Falco, M. Massari, M. G. Scullion, S. A. Schulz, F. Romanato, and T. F. Krauss, *Propagation Losses of Slotted Photonic Crystal Waveguides*, IEEE Photonics Journal **4**, 1536–1541 (2012).

[421] J. Li, Q. X. Zhang, A. Q. Liu, W. L. Goh, and J. Ahn, *Technique for preventing stiction and notching effect on silicon-on-insulator microstructure*, Journal of Vacuum Science & Technology B: Microelectronics and Nanometer Structures Processing, Measurement, and Phenomena **21**, 2530–2539 (2003).

[422] Y. Fu, N. Bryan, O. Shing, and N. Hung, *Influence of the Redeposition effect for Focused Ion Beam 3D Micromachining in Silicon*, The International Journal of Advanced Manufacturing Technology **16**, 877–880 (2000).

[423] M. L. Gorodetksy, A. Schliesser, G. Anetsberger, S. Deleglise, and T. J. Kippenberg, *Determination of the vacuum optomechanical coupling rate using frequency noise calibration*, Optics Express **18**, 23236–23246 (2010).

[424] T. Kodama, J. Hofs, S. Jin, and T. Tanabe, "High-Resolution Spectrometer with Random Photonic Crystals", *2020 Conference on Lasers and Electro-Optics (CLEO)*, 2020 Conference on Lasers and Electro-Optics (CLEO)(2020), pp. 1–2.

[425] S. Forstner, E. Sheridan, J. Knittel, C. L. Humphreys, G. A. Brawley, H. Rubinsztein-Dunlop, and W. P. Bowen, *Ultrasensitive Optomechanical Magnetometry*, Advanced Materials **26**, 6348–6353 (2014).

[426] M. Colombano, G. Arregui, F. Bonell, N. Capuj, E. Chavez-Angel, A. Pitanti, S. Valenzuela, C. Sotomayor-Torres, D. Navarro-Urrios, and M. Costache, *Ferromagnetic Resonance Assisted Optomechanical Magnetometer*, Physical Review Letters **125**, 147201 (2020).

[427] X. Zhang, T. Lin, F. Tian, H. Du, Y. Zou, F. S. Chau, and G. Zhou, *Mode competition and hopping in optomechanical nano-oscillators*, Applied Physics Letters **112**, 153502 (2018).

[428] L. Fan, K. Y. Fong, M. Poot, and H. X. Tang, *Cascaded optical transparency in multimode-cavity optomechanical systems*, Nature Communications **6**, 5850 (2015).

[429] P. Piergentili, W. Li, R. Natali, N. Malossi, D. Vitali, and G. Di Giuseppe, *Two-membrane cavity optomechanics: non-linear dynamics*, arXiv:2009.04694 [nlin, physics:physics, physics:quant-ph] (2020), arXiv: 2009.04694.

[430] U. Kemiktarak, M. Durand, M. Metcalfe, and J. Lawall, *Mode Competition and Anomalous Cooling in a Multimode Phonon Laser*, Physical Review Letters **113**, 030802 (2014).

[431] L. Bakemeier, A. Alvermann, and H. Fehske, *Route to Chaos in Optomechanics*, Physical Review Letters **114**, 013601 (2015).

[432] G. Rozas, M. F. P. Winter, B. Jusserand, A. Fainstein, B. Perrin, E. Semenova, and A. Lemaître, *Lifetime of THz Acoustic Nanocavity Modes*, Physical Review Letters **102**, 015502 (2009).

[433] M. F. Pascual Winter, A. Fainstein, B. Jusserand, B. Perrin, and A. Lemaître, *Optimized optical generation and detection of superlattice acoustic phonons*, Applied Physics Letters **94**, 103103 (2009).

[434] T. Czerniuk, C. Brüggemann, J. Tepper, S. Brodbeck, C. Schneider, M. Kamp, S. Höfling, B. A. Glavin, D. R. Yakovlev, A. V. Akimov, and M. Bayer, *Lasing from active optomechanical resonators*, Nature Communications **5**, 4038 (2014).

[435] K. Fang, M. H. Matheny, X. Luan, and O. Painter, *Optical transduction and routing of microwave phonons in cavity-optomechanical circuits*, Nature Photonics **10**, 489–496 (2016).

[436] R. N. Patel, Z. Wang, W. Jiang, C. J. Sarabalis, J. T. Hill, and A. H. Safavi-Naeini, *Single-Mode Phononic Wire*, Physical Review Letters **121**, 040501 (2018).

[437] J.-B. Béguin, Z. Qin, X. Luan, and H. J. Kimble, *Coupling of light and mechanics in a photonic crystal waveguide*, Proceedings of the National Academy of Sciences **117**, 29422–29430 (2020).

[438] L. Lu, J. D. Joannopoulos, and M. Soljačić, *Topological photonics*, Nature Photonics **8**, 821–829 (2014).

[439] G. Ma, M. Xiao, and C. T. Chan, *Topological phases in acoustic and mechanical systems*, Nature Reviews Physics **1**, 281–294 (2019).

[440] M. G. Silveirinha, *Bulk-edge correspondence for topological photonic continua*, Physical Review B **94**, 205105 (2016).

[441] S. Raghu and F. D. M. Haldane, *Analogs of quantum-Hall-effect edge states in photonic crystals*, Physical Review A **78**, 033834 (2008).

[442] L.-H. Wu and X. Hu, *Scheme for Achieving a Topological Photonic Crystal by Using Dielectric Material*, Physical Review Letters **114**, 223901 (2015).

[443] T. Ma and G. Shvets, *All-Si valley-Hall photonic topological insulator*, New Journal of Physics **18**, 025012 (2016).

[444] X.-T. He, E.-T. Liang, J.-J. Yuan, H.-Y. Qiu, X.-D. Chen, F.-L. Zhao, and J.-W. Dong, *A silicon-on-insulator slab for topological valley transport*, Nature Communications **10**, 872 (2019).

[445] S. Barik, A. Karasahin, C. Flower, T. Cai, H. Miyake, W. DeGottardi, M. Hafezi, and E. Waks, *A topological quantum optics interface*, Science **359**, 666–668 (2018).

[446] Z. Wang, Y. D. Chong, J. D. Joannopoulos, and M. Soljačić, *Reflection-Free One-Way Edge Modes in a Gyromagnetic Photonic Crystal*, Physical Review Letters **100**, 013905 (2008).

[447] M. I. Shalaev, W. Walasik, A. Tsukernik, Y. Xu, and N. M. Litchinitser, *Robust topologically protected transport in photonic crystals at telecommunication wavelengths*, Nature Nanotechnology **14**, 31–34 (2019).

[448] N. Parappurath, F. Alpeggiani, L. Kuipers, and E. Verhagen, *Direct observation of topological edge states in silicon photonic crystals: Spin, dispersion, and chiral routing*, Science Advances **6**, eaaw4137 (2020).

[449] S. Arora, T. Bauer, R. Barczyk, E. Verhagen, and L. Kuipers, *Direct quantification of topological protection in symmetry-protected photonic edge states at telecom wavelengths*, Light: Science & Applications **10**, 9 (2021).

[450] B. Orazbayev and R. Fleury, *Quantitative robustness analysis of topological edge modes in C6 and valley-Hall metamaterial waveguides*, Nanophotonics **8**, 1433–1441 (2019).

[451] E. Sauer, J. P. Vasco, and S. Hughes, *Theory of intrinsic propagation losses in topological edge states of planar photonic crystals*, Physical Review Research **2**, 043109 (2020).

[452] J.-W. Dong, X.-D. Chen, H. Zhu, Y. Wang, and X. Zhang, *Valley photonic crystals for control of spin and topology*, Nature Materials **16**, 298–302 (2017).

[453] G. Arregui, J. Gomis-Bresco, C. M. Sotomayor-Torres, and P. D. Garcia, *Quantifying the Robustness of Topological Slow Light*, Physical Review Letters **126**, 027403 (2021).

[454] M. B. d. Paz, C. Devescovi, G. Giedke, J. J. Saenz, M. G. Vergniory, B. Bradlyn, D. Bercioux, and A. García-Etxarri, *Tutorial: Computing Topological Invariants in 2D Photonic Crystals*, Advanced Quantum Technologies **3**, 1900117 (2020).

[455] A. Goban, C.-L. Hung, S.-P. Yu, J. D. Hood, J. A. Muniz, J. H. Lee, M. J. Martin, A. C. McClung, K. S. Choi, D. E. Chang, O. Painter, and H. J. Kimble, *Atom–light interactions in photonic crystals*, Nature Communications **5**, 3808 (2014).

[456] M. Minkov and V. Savona, *Automated optimization of photonic crystal slab cavities*, Scientific Reports **4**, 5124 (2014).

[457] M. Minkov, I. A. D. Williamson, L. C. Andreani, D. Gerace, B. Lou, A. Y. Song, T. W. Hughes, and S. Fan, *Inverse Design of Photonic Crystals through Automatic Differentiation*, ACS Photonics **7**, 1729–1741 (2020).

[458] M. Minkov, *Numerical study and optimization of photonic crystals*, Infoscience, 2016.

[459] S. Neale and E. A. Muljarov, *Resonant-state expansion for planar photonic crystal structures*, Physical Review B **101**, 155128 (2020).

[460] L. Li, *Use of Fourier series in the analysis of discontinuous periodic structures*, JOSA A **13**, 1870–1876 (1996).

[461] Shung-Wu Lee and R. Mittra, *Fourier transform of a polygonal shape function and its application in electromagnetics*, IEEE Transactions on Antennas and Propagation **31**, 99–103 (1983).

[462] K. Coimbatore Balram, D. Westly, M. Davanco, K. Grutter, Q. Li, T. Michels, C. Ray, R. Kasica, C. Wallin, I. Gilbert, B. Bryce, G. Simelgor, J. Topolancik, N. Lobontiu, Y. Liu, P. Neuzil, V. Svatos, K. Dill, N. Bertrand, and R. Ilic, *The Nanolithography Toolbox*, Journal of Research of the National Institute of Standards and Technology **121**, 464 (2016).

[463] J. R. Bickford, G. Lopez, N. Belic, and U. Hofmann, *Hydrogen silsesquioxane on SOI proximity and microloading effects correction from a single 1D characterization sample*, Journal of Vacuum Science & Technology B **32**, 06F511 (2014).

[464] G. Owen and P. Rissman, *Proximity effect correction for electron beam lithography by equalization of background dose*, Journal of Applied Physics **54**, 3573–3581 (1983).